SAPIENZA
UNIVERSITÀ DI ROMA

From hydrophilic to hydrophobic metal nanoparticles: the role of surface functionality on chemical properties

Faculty of Mathematics, Physics and Natural Sciences

Department of Chemistry Ph.D. in Chemical Sciences – XXXVIII Cycle

Beatrice Pennacchi

ID number 1795097

Supervisor

Prof. Ilaria Fratoddi

PhD Coordinator

Prof. Paola D'Angelo

A.Y. 2024/2025

A thesis submitted in partial fulfilment of the requirements for the degree of Doctor of Philosophy in Chemical Sciences

From hydrophilic to hydrophobic metal nanoparticles: the role of surface functionality on chemical properties

Ph.D. thesis – Sapienza University of Rome

beatrice.pennacchi@uniroma1.it

This page is intentionally left blank

Abstract

This PhD thesis provides a comprehensive investigation into the synthesis, characterization, and application of metal nanoparticles (MNPs), with particular emphasis on gold nanoparticles (AuNPs) and the role of the thiol ligands on the gold surface and how they influence the application potential of nanoparticles.

The nanoparticles were synthesised via chemical reduction methods, yielding spherical nanoparticles with controlled diameters predominantly below 10 nm. The research is structured into two main parts.

The first focused on hydrophilic AuNPs for biomedical applications, in this respect, a highly stable and reproducible system was developed using a mixed thiols ligand layer (sodium 3-mercapto-1-propanesulfonate, 3MPS, and 2-(diethylamino)ethanethiol hydrochloride, DEA). These nanoparticles were thoroughly characterized, including with the innovative μ-liquid jet XPS technique at the SOLEIL Synchrotron, which can investigate the structural and chemical properties of free thiols in solution and thiol-capped on gold surface in the native colloidal state of AuNPs. Thanks to the small size (*ca.* 10 nm) and high stability, this AuNPs system has been successfully used as versatile drug delivery platform of an anticancer drug (Methotrexate) and a therapeutic antibody (Trastuzumab); in both cases, the AuNPs platform significantly enhanced the therapeutic effect compared to the free drug, proving its potential in nanomedicine.

The second part of the thesis explored hydrophobic nanoparticles for materials science and sensing applications. Here, the precise control over surface chemistry enabled the creation of "smart" systems, responsive to external stimuli. By functionalizing AuNPs with dodecanethiol (DDT) and 4-aminothiophenol (Ani) in mixture, three distinct self-assemblies were achieved: supramolecular, covalent, and transient covalent self-assembly. Furthermore, the use of rigid, bifunctional π-conjugated ligands allowed for the construction of covalent networks of AuNPs, AgNPs, and PdNPs with tunable interparticle distances, opening perspectives for optoelectronics. Fine-tuning the 2D/3D arrangement of AuNPs networks is possible using a monofunctional ligand in mixture with the bifunctional ligands yielding promising preliminary results as chemiresistive sensors for volatile organic compounds like benzene and toluene. Finally, hydrophobic and interconnected AuNPs were incorporated into different polymer matrices (poly(phenylacetylene), PPA; poly(3-hexylthiophene-2,5-diyl), P3HT; polylactic acid, PLA) to create hybrid organic-inorganic nanocomposites. These blends consistently demonstrated significant enhancements in electrical conductivity,

showing a synergistic effect between the nanoparticles and the polymers. The thesis concludes with a preliminary study into chirality, functionalizing AuNPs with enantiopure [2.2]paracyclophane synthetic derivatives, laying the foundations for future studies on chiral plasmonics.

Contents

List of abbreviations

3MPS	sodium 3-mercapto-1-propanesulfonate
2AET	2-(anthracen-9-ylmethyl)thio)ethane-1-thiol
4BBT	4-bromobenzene thiol
ACAs	Activated Carboxylic Acids
AFM	Atomic Force Microscopy
AgNPs	Silver Nanoparticles
Ani	4-Aminothiophenol
Ani2	4-Aminophenyl disulfide
AniFITC	1-(3',6'-dihydroxy-3-oxo-3H-spiro[isobenzofuran-1,9'-xanthen]-5-yl)-3-(4-(methylthio)phenyl)thiourea
ATR	Attenuated Total Reflectance
AuNPs	Gold Nanoparticles
AuNPs_1	AuNPs-3MPS-CysFITC
AuNPs_2	AuNPs-3MPS-AniFITC
BE	Binding Energy
BTX	benzene, toluene, xylene
CD	Circular Dichroism
CSA	Covalent Self-Assembly
cTSA	covalent Transient Self-Assembly
CuNPs	Copper Nanoparticles
Cys	Cysteamine hydrocloride
Cys2	Cystamine dihydrochloride
CysFITC	1-(3',6'-dihydroxy-3-oxo-3H-spiro[isobenzofuran-1,9'-xanthen]-5-yl)-3-(2-(methylthio)ethyl)thiourea
D	diameter
DBBA	4,4'-(dodecane-1,12-diylbis(oxy)) dibenzylidene-butylamine
DDT	Dodecanethiol
DEA	2-(diethylamino)ethanethiol hydrochloride
DEBP	4,4’-diethynylbiphenyl
DF	Dark Field
DLS	Dynamic Light Scattering
DMEM-F12	Dulbecco’s modified Eagle medium/Ham’s F-12 50/50 Mix
DOTA	1,4,7,10-Tetraazacyclododecane-1,4,7,10-tetraacetic acid
EDS	energy dispersive X-ray spectroscopy
EPR	enhanced permeability and retention
FE-SEM	Field Emission Scanning Electron Microscopy
FITC	Fluorescein isothiocyanate isomer I
FL	9,9-didodecyl-2,7-bis(acetylthio)fluorene
FT-IR	Fourier Transform Infrared Spectroscopy
FWHM	Full Width at Half-Maximum
GISAXS	Grazing-incidence small-angle X-ray scattering

GIWAXS	Grazing Incident Wide Angle X-Ray Scattering
H_2O_{up}	Ultra-Pure water
HEPES	4-(2-hydroxyethyl)-1-piperazineethanesulfonic acid
HR-TEM	high-resolution Transmission Electron Microscopy
LSPR	Localised Surface Plasmon Resonance
MNPs	Metal Nanoparticles
MO_xNPs	Metal Oxide Nanoparticles
MTX	Methotrexate
MUL	Multilayers
NHCs	N-Heterocyclic Carbenes
NMR	nuclear magnetic resonance
NPs	Nanoparticles
P3HT	poly(3-hexylthiophene-2,5-diyl)
PCP	[2.2] Paracyclophane
PCP_1	[2.2]Paracyclophan-4-thiol
PCP_2 (PCP)	[2.2]Paracyclophan-4-yl)methanethiol
PDI	Polydispersity Index
PdNPs	Palladium Nanoparticles
PLA	polylactic acid
PPA	poly(phenylacetylene)
PtDEBP	*trans,trans*-[dithioacetyldibis(tributylphosphine)diplatinum(II)-4,4'-diethynylbiphenyl]
PtFL	2,7-Bis[2-(trans-acetylthio-bis-(tributylphosphine)platinumII)ethynyl]-9,9-didodecyl-9H-fluorene
QDs	Quantum Dots
QSE	Quantum Size Effect
SAM	Self-Assembled Monolayers
SAXS	Small angle X-ray scattering
SEM	Scanning Electron Microscopy
SPR	Surface Plasmon Resonance
SR-XPS	high-resolution synchrotron radiation induced X-ray photoelectron spectroscopy
SSA	Supramolecular Self-Assembly
TBA	tribromo acetic acid
TEM	Transmission Electron Microscopy
TFA	trifluoroacetic acid
TOAB	Tetraoctylammonium Bromide
TZ	Trastuzumab
UV-Vis	UV-visible spectroscopy
VOCs	Volatile Organic Compounds
XPS	X-ray Photoelectron Spectroscopy
XPS m-LJ	X-ray Photoelectron Spectroscopy micro-Liquid-Jet

Chapter 1. Introduction

1.1. Overview of Nanomaterials

Nanomaterials are a class of materials that exhibit exceptional properties due to their dimensions at the nanoscale, typically with at least one dimension between 1 and 100 nm.[1] At this scale, the materials show unique physico-chemical behaviours that are different from their bulk counterparts.[2] For example, if the bulk gold appears yellow, at the nanoscale the gold exhibits a purple or red colour due to size-dependent optical properties.[3] The nanomaterials are characterized by a high surface-to-volume ratio (often 35–45% times higher as compared to large particle[4]) which results in an high percentage of atoms or molecules on the surface[5]. This very large surface area and high particle number per mass unit, the increased fraction of atoms at the surface in nanomaterials and the fewer direct neighbours for the atoms on the surface lead the unique surface-dependent properties of nanomaterials.[6] The remarkable features can drastically alter the physical, chemical, biological, and mechanical characteristics of the materials[7]. Nanomaterials demonstrate unique optical, thermal, electrical, magnetic, and catalytic functionalities that are not observed in the bulk counterparts.[8,9] Tuning the material size is possible tailor their size-dependent properties.[10,11] The combination of unique physico-chemical properties and the possibility to fine-tune them sparked the interest in studying nanomaterials and in their application in different fields. Nowadays, nanoparticles and nanostructured materials in general are synthesized in a large scale and play a crucial role in different fields such as medicine, electronics, energy, environmental remediation, agriculture, and food processing.[12] Nanomaterials differ in dimensions, shapes, sizes, compositions, porosity, phases, and uniformity. The widespread use and study of nanostructured materials resulted in a clear definition and classification. In summary, nanomaterials are materials that have one or more external dimensions, or an internal structure, at the nanoscale.

Several classifications have been used to categorize them and from a structural point of view, based on the dimensions of nanoscale (<100 nm) they are classified [13,14], as reported in **Figure 1**:

Zero-dimensional nanomaterials (0D): All dimensions are in the nanoscale *e.g.* Quantum dots (QDs), Metal nanoparticles (MNPs), clusters. These materials often show size-dependent optical and electronic properties.

One-dimensional nanomaterials (1D): Two dimensions are in the nanoscale, with the third being significantly larger. Nanorods, nanowires and nanofiber are in this class. These are usually used in nanoelectronics and photonics.

Two-dimensional nanomaterials (2D): Thickness is at the nanoscale, while length and width are much larger (e.g., thin films, plates, graphene sheets). These materials exhibit outstanding mechanical, thermal, and electronic properties.

Three-dimensional nanomaterials (3D): Composed of many nanoscale units interconnected in all three dimensions (e.g., polycrystal, liposomes), or porous nanostructures.

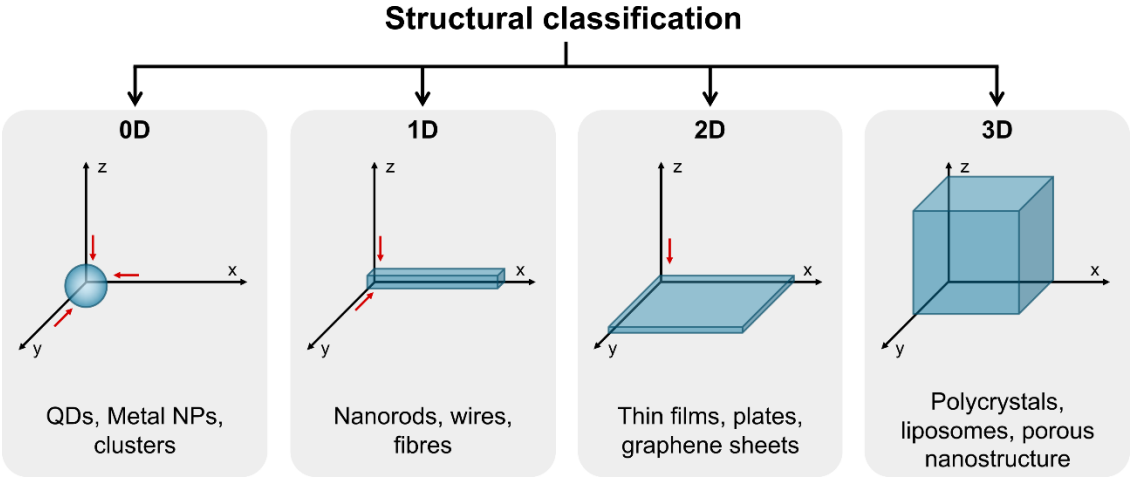

Figure 1. *Classification of nanomaterials size dimensions*

Nanomaterials can be classified based on the composition into four main categories: carbon-based, inorganic-based, organic-based, and composite-based nanomaterials (schematized in **Figure 2**). [2,15]

Inorganic-based nanomaterials are non-carbon-based nanomaterial and can be summarize into metals nanoparticles (MNPs), metal oxides nanoparticles (MO_xNPs) or other inorganic compounds such as semiconductor quantum dots (e.g. cadmium selenide, CdSe).

MNPs are characterized by high surface-to-volume ratio, particular optical properties, reactivity and sensitivity. Common examples of MNPs are gold (AuNPs), silver (AgNPs) palladium (PdNPs), and copper (CuNPs) nanoparticles. MNPs are widely used in different fields *i.e.*, nanomedicine (drug delivery, therapy, diagnostic procedures)[16,17], sensing[18], biosensing[19], catalysis[20], electronics and optoelectronics.

This thesis will specifically focus on metal nanoparticles based on noble metals, such as gold, silver, and palladium, owing to their unique optical properties (surface plasmon

resonance *vd.* 1.2), high chemical stability, and superior performance in catalytic, biomedical, and sensing applications.

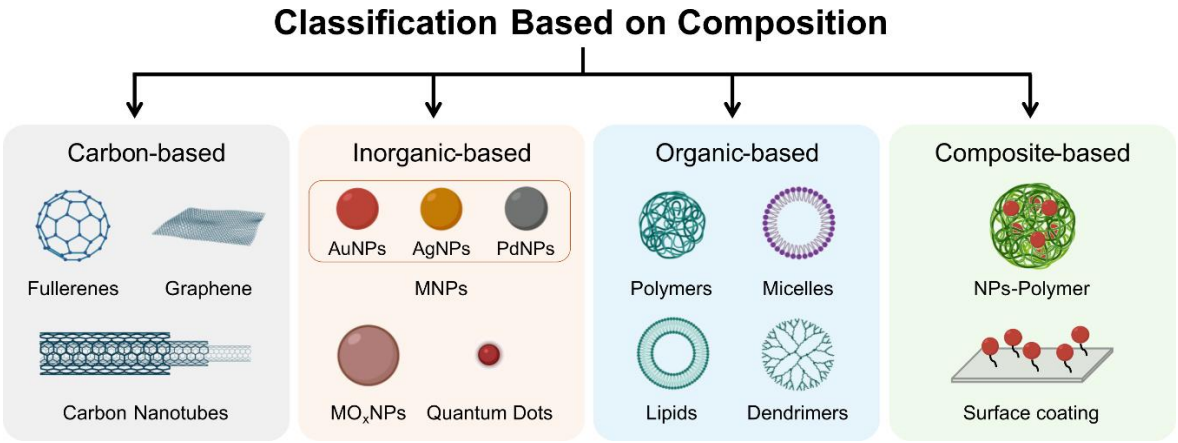

Figure 2. *Nanomaterials classification based on composition.*

1.2. Metal Nanoparticles: Chemical and Physical Properties

As previously described, metal nanoparticles (MNPs) are inorganic-based nanomaterials, among them, noble metal nanoparticles, particularly gold (AuNPs), silver (AgNPs), and palladium (PdNPs), have attracted considerable attention due to their unique physicochemical and optical properties. Noble metal nanoparticles are particularly renowned for their intense and tuneable colours, a property exploited historically, even if unknowingly. In fact, humans have employed MNPs since as early as the 3rd millennium BC when natural asbestos nanofibers were used to reinforce ceramic materials.[21] A notable example of use of nanoparticles in human history is the Lycurgus Cup (4th century AD), which shows a complex colour and scattering effects of the glass depending on the incident light, a phenomenon now understood to result from the presence of AuNPs and AgNPs in it.[22] The scientific understanding of this coloration began with Faraday's studies on noble MNPs and then it was theoretically explained by Gustav Mie, who derived solutions to Maxwell's equations for spherical NPs.[23]

These optical phenomena are primarily governed by Surface Plasmon Resonance (SPR) which is an important optical phenomenon of plasmonic MNPs. To understand these optical phenomena and how to control and tune physical and chemical properties of a nanoparticles it is useful analyse the differences between nanoscale materials and their bulk counterparts. According to band theory, in metallic solids the valence band and the conduction band are continuous or overlap. In contrast, in semiconductors, the valence band and the conduction

band are separated by a well-defined energy gap. The overlap of the valence band and the conduction band allows electrons to move freely throughout the material, encountering no significant energy barriers. From this perspective, a material is classified as a metal only if its valence electrons can move freely. This distinction becomes particularly important at the nanoscale. For instance, MNPs composed of only a few atoms of metals (diameter, D: 5 nm; N_{Au} ~ 4000)[24] can exhibit electronic structures with a valence band and conduction band well separated that means the energy gaps is more significant than the thermal energy. The discreteness of the energy levels leads to opening a HOMO–LUMO gap, leading to molecular-like optical and electronic properties rather than bulk metallic behaviour.[25] This phenomenon is the Quantum Size Effect (QSE) and, as shown in **Figure 3a**, the energy bandgap increases as the sample size decreases, *i.e.*, from the bulk metal materials where valence band overlaps the conduction band, to a small nanoparticle, and finally the molecules with discrete energy levels. This effect is also known as the "quantum confinement" effect, which affects optical, conduction, and magnetic properties.

Upon irradiation, due to QSE, the free electrons of MNPs respond to an electromagnetic wave and oscillate with an appropriate wavelength. In response to incident electromagnetic radiation, the quantization of the collective oscillations of the free electrons is described as plasmons, *i.e.*, one type of quasiparticle. When light has a frequency below the plasma frequency, it is reflected by the material, in contrast, light with a frequency above the plasma frequency is transmitted. Surface plasmons are oscillations confined to the surfaces of conducting materials and interact strongly with light. Irradiating MNPs with light at their plasmon frequency generates intense electric fields at the surface of the nanoparticles due to interaction between light and surface electrons (as illustrate in **Figure 3b**). The specific frequency at which the amplitude of these oscillations reaches its maximum is known as the SPR frequency. In the SPR phenomenon, the collective oscillation of electrons has two modes: surface plasmon–polarization (SPP) and localized surface plasmon resonance (LSPR). Propagation of SPP takes place along the interface between metal and dielectric, while LSPR surrounds the isolated MNPs by covering the small volume.[26]

The intensity and position of the LSPR band are highly sensitive and depend on various parameters, notably the type of metal, because the plasmonic response is strongly influenced by the dielectric function of the material.[27,28]

MNPs that exhibit strong LSPR absorption bands in the visible region include AuNPs, AgNPs and CuNPs. The bands are typically between 500-600 nm for AuNPs, 400-500 nm for AgNPs and 550-650 nm for CuNPs, as show in **Figure 3c**. In contrast, other metals show

broader and weaker plasmonic bands, often located in the ultraviolet region. However, the stability of the plasmonic response also varies with the metal: silver nanostructures are prone to oxidation over time, which significantly degrades their plasmonic performance. Copper oxidizes even more rapidly than silver, further limiting its plasmonic stability. [29],[30]

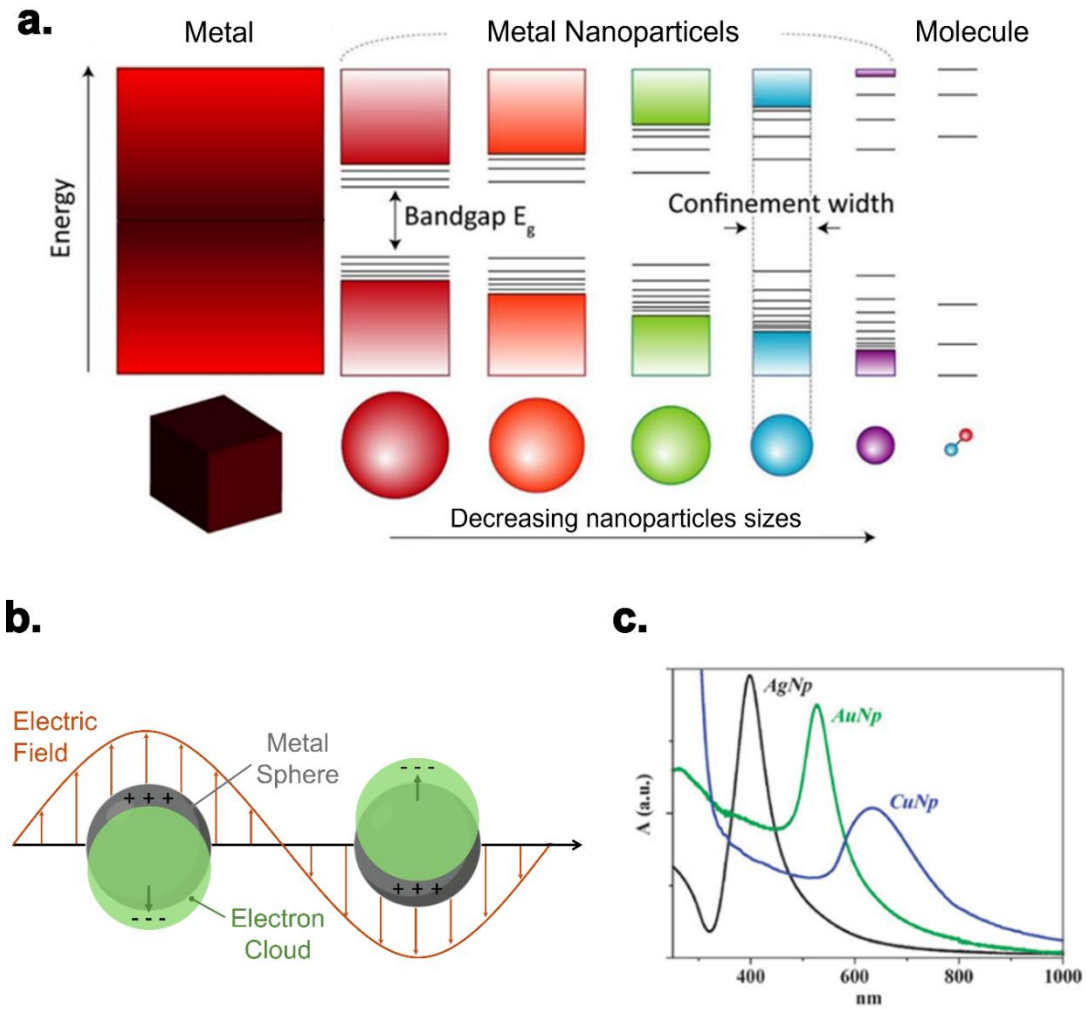

Figure 3. *a) Quantum size effect comparing bulk, NPs and molecules, b) Surface Plasmon Resonance in metal nanoparticles, c) Typical UV-Vis LSPR band of Ag, Au and Cu nanoparticles* [30].

1.2.1. Physical properties of AuNPs

Plasmonic AuNPs represent a major area of research among metal-based nanomaterials due to their chemical stability against oxidation and colloidal aggregation, tunable reactivity. Moreover, advances in nanochemistry have made possible a precise control the size and shape of AuNPs, allowing the synthesis of both isotropic and anisotropic morphologies, as well as highly monodisperse size distributions. The unique optical properties, combined with

exceptional chemical stability and size-dependent electrochemical behaviour, have established AuNPs as a model system for investigating a wide range of physical, chemical, and biological phenomena. Their plasmonic nature makes them especially suitable for optical applications, including imaging, sensing and biosensing and therapeutic targeting.[26,31,32] This level of synthetic precision allows for accurate modulation of the optical properties, which are highly size and shape dependent. Isotropic (spherical) AuNPs, for instance, exhibit a strong and single LSPR absorption band typically in the range of 500–600 nm[29], while more anisotropic structures possess multiple plasmon bands. Several examples of anisotropic gold nanoparticles are reported in the literature, including nanobipyramids[33] (**Figure 4a**), nanorods[34] (**Figure 4b, 4c**), nanostars[35].

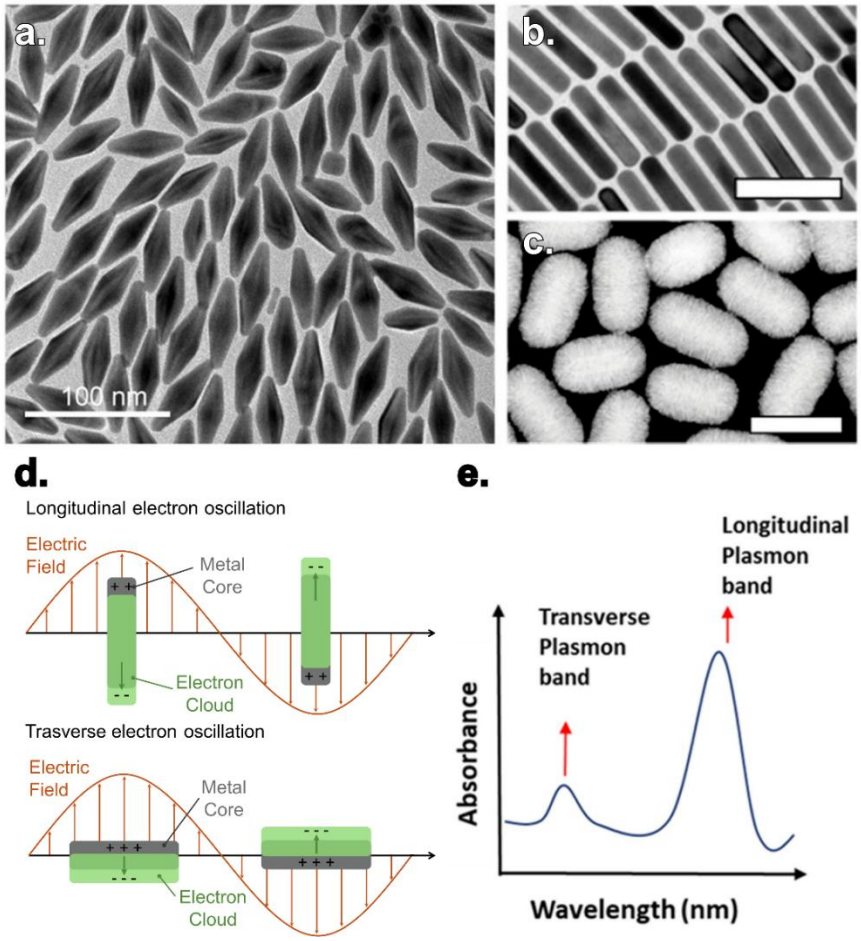

Figure 4. *a) TEM image of gold nanobipyramids[33] b) TEM image of gold nanorods (scale bars: 100 nm)[34], c) STEM image of chiral gold nanorods (scale bar: 200 nm)[34], d) Surface Plasmon Resonance of rod shape nanoparticles, e) Typical UV-Vis spectrum of rod shaped plasmonic gold nanoparticles[36].*

In terms of optical properties, anisotropic structures, such as nanorods and nanobipyramids, exhibit a transverse plasmon band (λ_{max} ~ 520 nm), associated with electron oscillations along the short axis, and a longitudinal plasmon band (λ_{max} ranging from ~ 600 to 800 nm), as schematically reported in **Figure 4d, 4e**. The relative intensity of the bands is tunable based on the aspect ratio of AuNPs.

The optical response of AuNPs is not only influenced by particle shape but is also significantly modulated by factors such as particle size, interparticle spacing and the surrounding chemical environment (e.g., solvent dielectric constant).

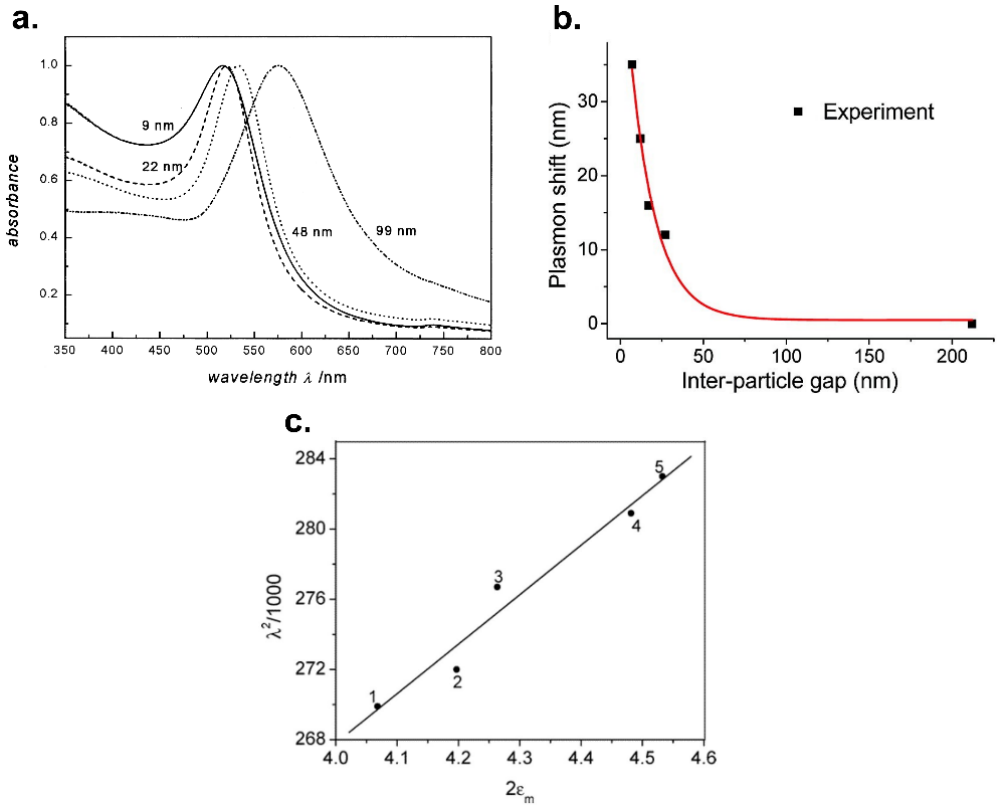

Figure 5. *a) UV−vis absorption spectra of 9, 22, 48, and 99 nm gold nanoparticles in water,[38] b) Shift in the plasmon wavelength maximum of a pair of Au nanodiscs as a function of the interparticle edge-to-edge separation gap,[37] c) Plot of the square of the absorption maxima vs. square of solvent refractive index. 1, 2, 3, 4, 5 on the curve represent cyclohexane, chloroform, carbon tetrachloride, toluene, and o-xylene.[41]*

In the specific case of isotropic AuNPs, numerous studies have been conducted to investigate the correlation between the LSPR peak position and particle diameter. While Mie theory originally predicted that the plasmon resonance peak position for spherical particles would

be independent of size, experimental observations have shown a clear size-dependent redshift in the LSPR wavelength as particle diameter increases, as report in **Figure 5a**.

This discrepancy arises because, at the nanoscale, the dielectric function of gold becomes size dependent as the particle diameter approaches or falls below the free path of conduction electrons. As a result, a redshift in the LSPR peak is commonly observed with increasing AuNPs size. Furthermore, the broadening of the plasmon band in larger particles (> 100 nm) is often attributed to retardation effects. Additionally, the increase in linewidth can be qualitatively explained by the coupling between higher-order electron oscillations, which progressively disrupt the collective plasmon oscillation.[38]

The LSPR of AuNPs is highly sensitive to interparticle distance. When the AuNPs are in very close proximity, strong plasmon coupling occurs and causes both red-shifting and a large broadening of the plasmonic band of colloidal AuNPs. This is due to the coupling of the plasmon modes and the generation of a broad range of complex plasmon modes absorbing at different wavelengths.[39] As shown in **Figure 5b**, the closer the particles are to each other, the more pronounced the shift in the LSPR band becomes. Conversely, when the particles are sufficiently spaced (typically few nm[40]), plasmonic coupling is absent and the LSPR band remains essentially unshifted.

Moreover, the surrounding environment plays a critical role. In non-polar solvents (e.g., cyclohexane, chloroform, carbon tetrachloride, toluene, and *o*-xylene), the λ_{max} of the LSPR of AuNPs gradually red-shifts with the increase in solvent refractive index (**Figure 5c**). This behaviour is due to the plasmon resonance condition that depends on the dielectric contrast between the metal and its environment. In polar solvents such as acetonitrile, tetrahydrofuran, dimethylformamide, and dimethyl sulfoxide often induce nonlinear shifts in the LSPR position. This deviation arises from electronic interactions between the solvent molecules and surface gold atoms, which are coordinatively unsaturated and possess available orbitals capable of accepting electron density.

Through donor-acceptor interactions, these solvents can donor electrons to the AuNPs, altering its free electron density and, consequently, its dielectric function. The modulation of the conduction electron density leads to a shift of λ_{max} of the LSPR band.[41] **Table 1** summarizes the variation of the LSPR λ_{max} (nm) for AuNPs in both polar and non-polar solvents, as a function of the solvent refractive index.

	Solvent	Reflective index (n)	λ_{max} (nm)
Non-polar solvents	cyclohexane	1.4262	519.5
	chloroform	1.4486	521.5
	carbon tetrachloride	1.4600	526
	toluene	1.4969	530
	o-xylene	1.5054	532
Polar solvents	acetonitrile	1.3441	545.5
	tetrahydrofuran	1.4072	526
	dimethylformamide	1.4282	549
	dimethyl sulfoxide	1.4790	542

Table 1. *λ_{max} (nm) of LSPR for AuNPs stabilized with cetylpyridinium chloride in different solvent and solvent refractive index.* [41]

Due to QSE, AuNPs exhibit distinctive thermal and electrical properties that differ significantly from their bulk counterparts. For example, AuNPs show an excellent photothermal conversion efficiency, making them highly efficient in absorbing light and converting it into heat, a property widely exploited in photothermal therapy. Their small size enhances surface scattering of phonons, altering their thermal conductivity compared to bulk gold.[42] Moreover, the conductivity of gold is sensitive to particle size, shape, surface chemistry, and interparticle distance at the nanoscale. These size-dependent electrical behaviours make AuNPs promising candidates for applications in nanoelectronics, sensors.[43] The conductivity can be improved with the functionalization of the nanoparticles creating, for example, a molecular network in a matrix. In the formed network, the nanoparticles act as electronic contacts between the molecules and exhibit photoconductive properties.[44] AuNPs could also improve the mechanical properties of bulk materials when are in a composite-based nanomaterials due to higher particle surface binding without loss of composite ductility when used in similar volume fractions compared to micro sized fillers.

1.3. Synthesis Method

Nanoparticles can be synthesized through two main strategies: top-down and bottom-up approaches.[1,45,46] Top-down is a destructive method, bulk materials are broken down into nanoscale structures through destructive processes such as, ball milling[47], thermal decomposition[48], laser ablation, and physical vapor deposition.

In contrast, bottom-up techniques follow the opposite path: they start from atoms, ions or small molecules, through the nucleation of clusters and growth of particles, then to colloidal nanoparticles. Common bottom-up techniques include chemical reduction, sol-gel synthesis[49], microemulsion, co-precipitation[50]. The idea of top-down and bottom-up strategies is illustrated in **Figure 6**.

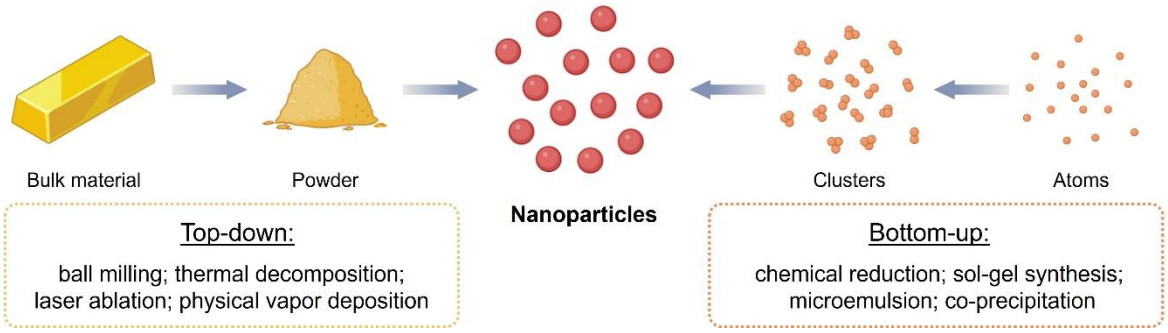

Figure 6. *The synthesis of nanomaterials via top-down and bottom-up approaches.*

This thesis will focus on noble metal nanoparticles (AuNPs, AgNPs and PdNPs) obtained *via* a bottom-up method: chemical reduction.

1.3.1. Chemical Reduction

The chemical reduction method involves the reduction of the metal precursor (M^{n+}) to its metallic state (M^0). For AuNPs, the most commonly used metal precursor is tetrachloroauric acid $HAuCl_4$, whereas for AgNPs, silver nitrate ($AgNO_3$) is typically employed, and for PdNPs, potassium tetrachloropalladate (K_2PdCl_4). A wide range of reducing agents, such as sodium citrate[51], sodium borohydride, ascorbic acid[52], and amines[53], are employed to achieve this reduction. At the same time, small organic molecules (like thiols) or polymers should be added to the system to prevent the aggregation of the formed nanoparticles.[54] Historically, Faraday was the first to synthesize AuNPs, using white phosphorus in diethyl ether as a reducing agent, yielding nanoparticles with an average diameter of 5 nm. Later, in 1951, Turkevich introduced a widely adopted method (**Figure 7a**) based on trisodium citrate as both a reducing and capping agent. Variations of this method focus on adjusting the citrate-to-gold ratio, pH, and reaction temperature to control particle size and stability.

The sodium borohydride method (**Figure 7b**) involves employing $NaBH_4$ as the reducing agent and replacing citrate with stabilizing agents such as thiols. A key advantage of this approach lies in the ability to covalently stabilize gold nanoparticles using a wide variety of molecules (the role of stabilizing agents will be discussed in detail in *paragraph 1.4*). This

method is commonly used to obtain hydrophilic nanoparticles, as only water-soluble capping agents can be used. Moreover, the use of $NaBH_4$ simplifies the synthesis by eliminating the need for a heating step (in Turkevich method the reducing agent operates at 100 °C).

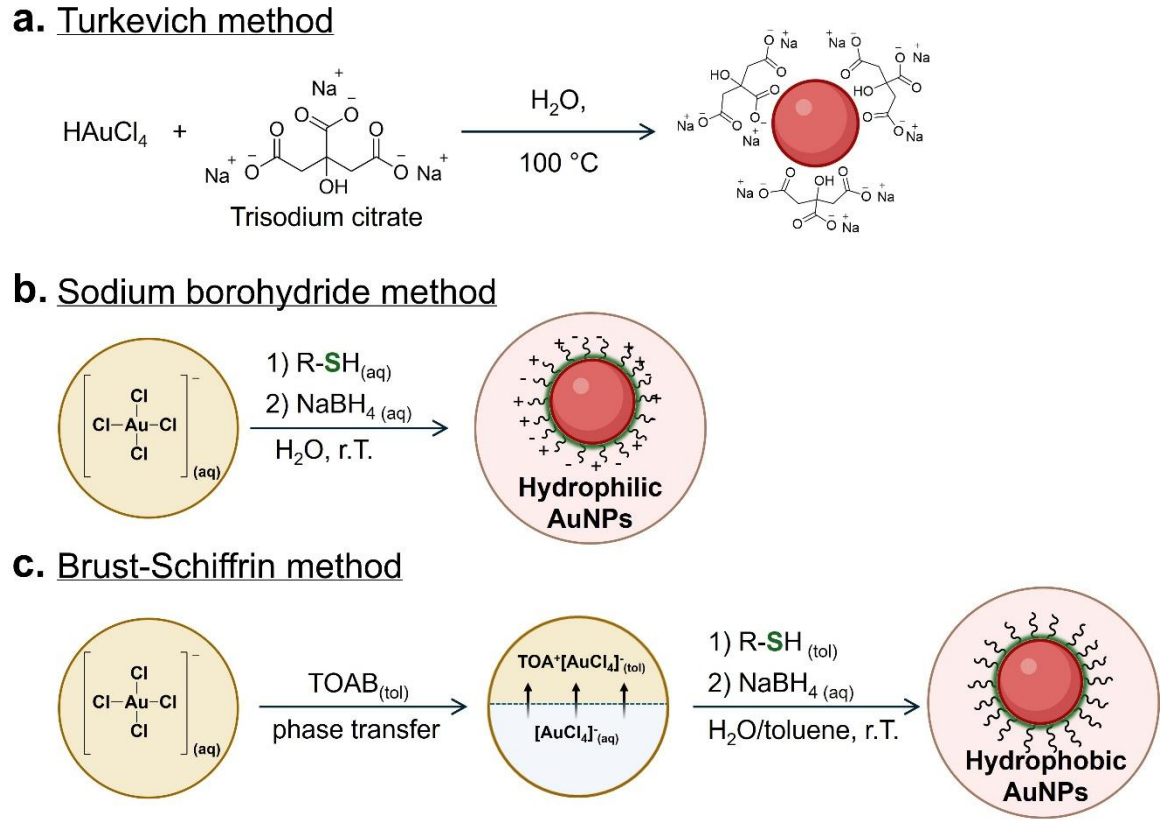

Figure 7. *Synthesis scheme for AuNPs with a) Turkevich, b) sodium borohydride, and c) Brust-Schiffrin methods.*

$NaBH_4$ is usually employed as a reducing agent in the synthesis of MNPs due to its exceptionally high reducing power. Its redox potential is - 1.24 V vs. SHE at pH 14, decreasing to - 0.48 V at pH 0.[55] In aqueous solution, $NaBH_4$ dissociates into sodium cations and borohydride anions (BH_4^-). At pH < 9.24, the dominant boron species is boric acid (H_3BO_3), its redox reaction and potential are described by the following equations:

$$BH_4^- + 3H_2O \rightarrow H_3BO_3 + 7H^+ + 8e^- \quad E^0 = -0.481\ V \quad (1)$$

At pH > 9.24, the dominant species is tetrahydroxyborate ($B(OH)_4^-$), produced via

$$BH_4^- + 8OH^- \rightarrow B(OH)_4^- + 4H_2O + 8e^- \quad E^0 = -0.413\ V \quad (2)$$

In the case of gold nanoparticles, the stepwise reduction of the gold precursor $[AuCl_4]^-$ to metallic gold (Au^0) involves two electrochemical processes[56]:

$$[AuCl_4]^- + 2e^- \rightarrow AuCl_2^- + 2Cl^- \quad E^0 = 0.926\ V \quad (3)$$

$$AuCl_2^- + e^- \rightarrow Au^0 + 2Cl^- \quad E^0 = 1.154\ V \quad (4)$$

These reactions take place in parallel with the intrinsic reducing activity of surface ligands, particularly thiols, which are known to actively participate in reducing processes of the metal precursor.

The strongly negative redox potentials of both reactions ensure that $NaBH_4$ is thermodynamically capable of reducing Au^{3+} species rapidly and efficiently under a wide range of conditions, enabling fast nucleation and the formation of small, monodisperse nanoparticles without the need for heating. Furthermore, its ability to operate in mild conditions makes it compatible with various stabilizing ligands, facilitating control over particle size and surface chemistry. Due to its strong reducing power, sodium borohydride can also be employed for the synthesis of other MNPs, such as CuNPs, AgNPs, and PdNPs. **Table 2** reports the standard reduction potentials of the $Mn^{+}/M^{0}_{(aq)}$ redox couples for these metals.

Metal	Redox Couple	E^0 (M^{n+}/M^0_{aq}) V vs SHE [57]
Copper	$Cu^{+}_{(aq)}/Cu^0$	2.57
Silver	$Ag^{+}_{(aq)}/Ag^0$	1.74
Palladium	$Pd^{2+}_{(aq)}/Pd^0$	0.81

Table 2. *Standard reduction potentials M^{n+}/M^0_{aq} versus SHE.*

One of the most well-known ways to synthesize hydrophobic AuNPs is the two-phase Brust-Schiffrin method (**Figure 7c**). This method was originally proposed for the synthesis of highly stable gold nanoparticles and, thanks to its remarkable versatility, is now used to produce nanoparticles of various noble metals, including silver[58], copper[59], and palladium[60]. The method involves transferring of metal precursor ($[AuCl_4]^-$ for AuNPs) into an organic phase (toluene) using a phase transfer (tetraoctylammonium bromide, TOAB), followed by the addition of the caping agent (thiols, more specifically dodecanethiol), which strongly binds to the gold surface and limits nanoparticle growth. $NaBH_4$ is then added as a reducing agent under vigorous stirring. After several purification steps involving ethanol precipitation by centrifuge and washing, nanoparticles with an average diameter of ~2.5 nm are obtained.[61] It was widely held, that TOAB transfers $[AuCl_4]^-$ into toluene by forming a complex with it through the following reaction[62]:

$$H^+ [AuCl_4]^-_{(aq)} + (R_8)_4N^+Br^-_{(org)} \rightarrow (R_8)_4N^+[AuCl_4]^-_{(org)} + HCl_{(aq)} \qquad (5)$$

Before the reduction step with $NaBH_4$, the thiols reduce some of the Au^{3+} into Au^{1+}. However, with the typical thiol:Au ratios being less than 3:1 in the conventional methods, only a small fraction of the Au^{3+} is reduced to Au^{1+} through the following reaction[63]:

$$(R_8)_4N^+[AuCl_4]^- + 3RSH \rightarrow -(AuSR)_n + RSSR + (R_8)_4N^+ + 4Cl^- + 3H^+ \quad (6)$$

At this point of the process, the organic phase comprised TOAB, dialkyldisulfide (RSSR), Au^{1+} in the form of a –(AuSR)– polymer, and either $AuCl_4^-$ complexed with TOA^+ ions and an excess of RSH. The final reduction of Au^{3+} and Au^{1+} into Au^0 by $NaBH_4$ occurs at the organic-aqueous interface.

The size of nanoparticles is influenced by several factors, including temperature[64], reaction time[65], ligand concentration[66], the balance between the capping rate and the particle growth rate. A faster capping rate generally results in smaller particles. For S/Au ratios below 1:4, the available thiol is insufficient to fully cap the particles, and the particle size is mainly determined by the reduction kinetics of the metal precursor. Conversely, when the S/Au ratio exceeds 1:4, a "capping-based control" mechanism dominates.[67]

The final shape achieved with all three methods described in this paragraph is generally spherical.

1.4. The Role of Ligands in the Surface Stabilization and Functionalization

Ligands of NPs play a dual role; they stabilize the nanoparticles against the aggregation and functionalize the surface with specific functionalities for different applications.

Due to Van der Waals attraction between particles and the constant Brownian motion, without any capping agents (**Figure 8a**), nanoparticles tend to the aggregated state. Uncapped nanoparticles are in a non-favoured energetic state compared to bulk materials under standard temperature and pressure. To contrast the persistent Van der Waals attraction, the nanoparticles require the introduction of effective repulsion mechanism. Stability can be achieved through three main mechanisms: electrostatic, steric, and electrosteric stabilization.[68] In electrostatic stabilization (**Figure 8b**), Coulombic repulsion between particles with the same surface charge prevents close contact. This is typically achieved by using capping agents with charged moieties, such as citrate, which produces AuNPs capped with a negative charge. In steric stabilization (**Figure 8c**) a physical barrier, often provided by polymers, is adsorbed or bounded on AuNPs surface. The attractive van der Waals forces become stronger with decreasing particle-particle distance, these chains prevent particles

from being too closely, acting as physical spacers. Finally, electrosteric stabilization (**Figure 8d**) combines both effects, it provides simultaneous electrostatic and steric protection against aggregation.[69,70]

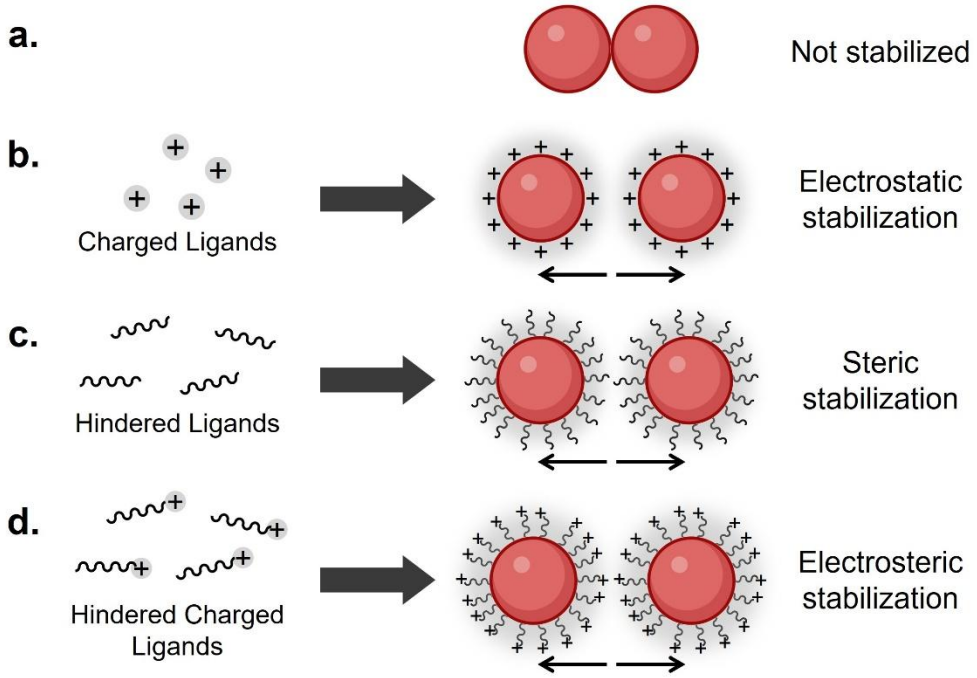

Figure 8. *Schematic illustration a) not stabilized, b) electrostatic, c) steric, and d) electrosteric stabilization of NPs achieved with b) charged, c) hindered, and d) charged hindered ligands.*

After establishing the role of capping agents in colloidal stabilization of nanoparticles, attention is now directed to the chemical interactions established between ligands and the nanoparticle surface. One of the earliest stabilizing agents employed was citric acid, introduced by Turkevich in 1951 (*vd.* 1.3.1). The interaction between carboxylate groups and the gold surface is relatively weak (6.7 kJ/ mol)[71] when compared to a covalent Au–O bond.[72] On the other hand, the weak binding affinity of citrate can be advantageous when a post-synthetic ligand exchange is desired. In fact, citrate-protected AuNPs readily undergo ligand exchange due to the loose attachment of citrate to the nanoparticle surface.[73] Numerous exchanges with ligands bearing various anchoring groups, such as thiolates and amines, have been reported, often improving both the colloidal stability and the biocompatibility of the nanoparticles. Other notable examples of ligands containing carboxylate groups include tannic acid and sodium acrylate[74]. These compounds follow mechanisms of nanoparticle

formation similar to the case of citrate, acting both as reducing agents and stabilizing the MNPs through carboxylate groups.

Another category of stabilizing molecules is represented by surfactants, characterized by an ammonium ion as a polar head group that interacts with the metal surface and long aliphatic chain(s) for the steric stabilization of NPs. Among them, cetyltrimethylammonium bromide (CTAB) is one of the most widely used surfactants reported in the literature for the synthesis of nanostructures. Other examples include cetyltrimethylammonium chloride (CTAC), decyltrimethylammonium bromide (DTAB), and tetraoctylammonium bromide (TOAB).[75]

In addition to being used as a phase-transfer agent in the two-phase Brust–Schiffrin method, TOAB can be used as a stabilizer for nanoparticles dispersible in organic media. The advantages of using surfactants over other capping agents are their capacity to form micelles and other aggregates. The formation of nanoparticles is highly sensitive to process parameters such as temperature, stirring rate, surfactant concentration, and the reduction potential of the chosen reducing agent. Surfactants are extensively employed in the synthesis of both spherical and, most notably, anisotropic nanoparticles. In the case of anisotropic nanostructures, they are often used in seed-mediated growth approaches to produce shapes such as nanorods and nanobipyramids.[76]

The most widely used molecules for both the synthesis and stabilization of noble MNPs are the thiols. Their popularity stems from their strong affinity for metal surfaces, (in case of AuNPs, Au-S bond strength of 40 kcal mol^{-1}[77]), which ensures robust protection against aggregation. Thiolate ligands typically yield nanoparticles with excellent colloidal stability and enables precise control over nanoparticle properties. The most widely accepted model for the Au–thiol interaction involves the binding of a deprotonated sulfhydryl group (forming a thiyl radical) to the gold surface. In its protonated form, the –SH group can only bind through the lone pair electrons on the sulphur atom, forming coordination-type bonds.[73] AuNPs stabilized by thiolate ligands possess remarkable stability in solution due to the robustness of the sulphur–gold bonds and the aurophilic interactions between Au(I) atoms. This unique sulphur–Au(I) chemistry has also enabled the synthesis of atomically precise gold nanoclusters with well-defined sizes and structures, paving the way for a broad range of emerging applications.[78]

Unlike thiols, phosphines bind to Au via the phosphorus' lone electron pair. This type of bond is stronger than the electrostatic interactions between citrate and Au, but still not as strong as the sulphur−Au bond, thus allowing for facile ligand exchange. The mechanism by which NPs are stabilized by phosphines is believed to arise from both charge and steric

interactions owing to the bulky aromatic rings on phosphines derivatives. However, applications of phosphine-capped AuNPs have mainly focused on asymmetric catalysis or the creation of precursors for the synthesis of AuNPs capped with other ligands. The limited use of phosphines as capping agents for AuNPs is due to their susceptibility to oxidation and the fact that they promote the formation of ultrasmall particles during synthesis.[79]

Over the last decade, N-heterocyclic carbenes (NHCs) have emerged as a promising family of surface ligands for gold nanoparticles.[80] Possessing a formally divalent carbon atom, NHCs form strong covalent bonds with surface metal atoms, with Au–NHC bonds estimated to be ~90 kJ mol^{-1} stronger than the corresponding Au–phosphine bonds and roughly twice as strong as metal–sulphide bonds in molecular complexes.[81] DFT calculations reported by Crudden et al. for the NHC–Au system predict the C–Au bond energy to be 150 ± 10 kJ mol^{-1}.[82]

Polymers and biomolecules can also serve as effective stabilizing agents for metal nanoparticles, providing steric and/or electrostatic protection through physisorption or chemisorption onto the particle surface. Although less frequently employed than other ligands, biomolecules such as glutathione, containing functional groups like thiols, amines, phosphines, or carboxylates, have been successfully used to stabilize AuNPs.[73]

All these ligands are schematically reported in **Figure 9**.

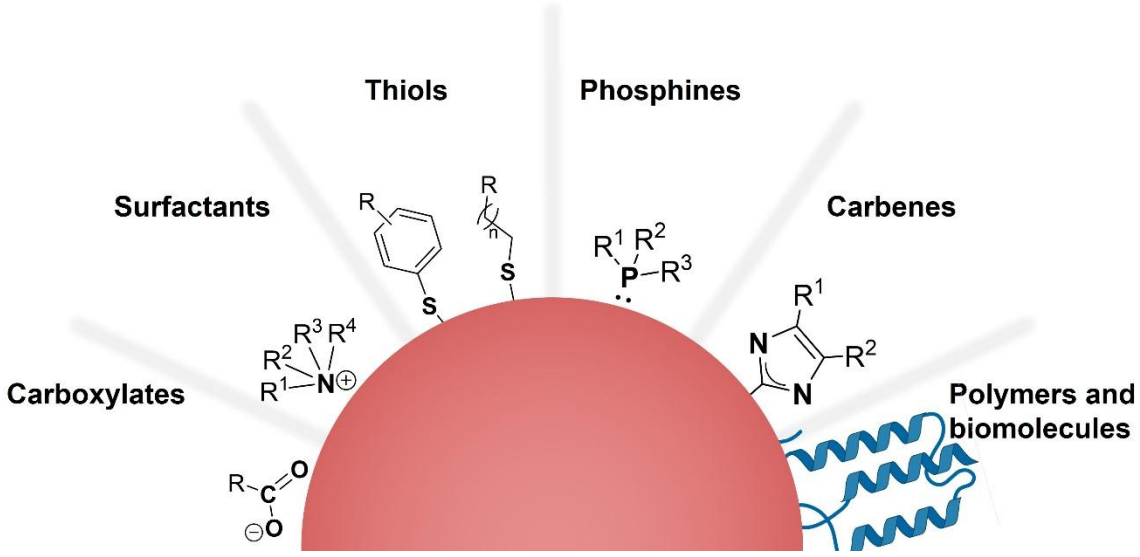

Figure 9. *Surface functionalization of AuNPs.*

In the case of covalent stabilization of noble MNPs, thiols prove to be the best candidates due to their high affinity with the surface metal. The organic ligands on the surface of metal nanoparticles (MNPs) can generally be divided into three main components. The first is the

anchoring group, which directly interacts with the surface metal atoms. In the case of thiols, this anchoring point is the sulphur atom, forming strong covalent bonds with the metal surface, as discussed previously. The nature of the anchoring group not only affects the stability of the ligand–nanoparticle interaction but also plays a decisive role in determining the overall structure and physicochemical properties of the nanoparticles.

The second component is the ligand backbone, which may consist of alkyl chains of varying lengths, aromatic rings, or other structural units. This segment influences the interligand interactions through forces such as hydrophobic effects and van der Waals interactions, thereby affecting steric hindrance, electron transfer, and nanoparticle stability and morphology. The third component is the terminal functional group, often present in hydrophilic ligands, such as hydroxyl (–OH), carboxyl (–COOH), amine (– NH_2), nitro (– NO_2), sulfonate ($-SO_3^-$) groups.[83] These functional groups influence suspensibility, surface charge, and interfacial properties, playing a key role in how the nanoparticles interact with their surrounding environment, including solvents, biomolecules, analytes. Taken together, these three components act synergistically to define the physical, chemical, and functional characteristics of ligands.[78]

By carefully choice of the ligand backbone and terminal functional group, it is possible to obtain nanoparticles that are dispersible either in aqueous or in organic media, each with tailored properties according to the final application of the nanomaterial. Ligands used for this purpose include charged, dye, hydrophobic, chiral, dithiol-functionalized, and organometallic ligands. All of these categories of ligand, used individually or in combination, have been employed in the synthesis of metal nanoparticles, particularly gold nanoparticles, described in this thesis, (schematized in **Figure 10**)

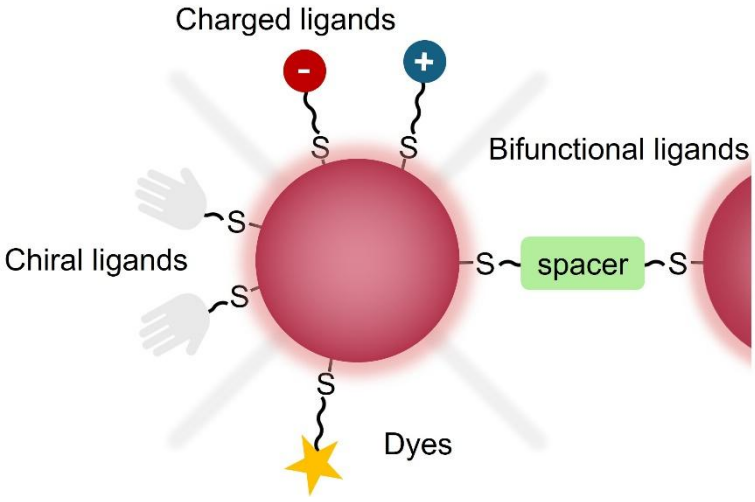

Figure 10. *AuNPs functionalised with charged, chiral, bifunctional thiols and dyes.*

Charged ligands are commonly employed in the synthesis of hydrophilic nanoparticles, which are typically applied in nanomedicine, drug delivery, and biosensing. Among these, sulfonate[84], carboxylate[85], and amine moieties are particularly utilized. For instance, Ngernpimai et al.[85] reported the use of carboxylate-terminated ligands to stabilize AuNPs, which were used to load a monoclonal antibodies for the detection of Listeria monocytogenes, demonstrating their strong potential in biosensing applications.

Regarding dyes, the covalent bond between a chromophore and the surface of plasmonic nanoparticles, such as AuNPs and AgNPs, creates a synergic effect between the optical properties of the fluorophore and the intrinsic optical properties of the nanoparticle. The interaction fluorophores-plasmonic nanoparticles is complex, in fact both fluorescence enhancement and quenching are reported. This apparent contradiction arises from multiple factors, including nanoparticle size and shape, the fluorophore-surface distance, the orientation of the fluorophore dipole moment, and the spectral overlap between the fluorophore emission and the nanoparticle plasmon resonance.[86] Common commercial dyes such as fluorescein isothiocyanate isomer I (FITC) and rhodamine B isothiocyanate (RBITC) have been successfully employed to functionalize AuNPs and AgNPs for applications in biosensing and imaging.[87]

Bifunctional thiols, aromatic and organometallic, can lead the organization of nanoparticles into 2D/3D networks with controlled size and spacing, allowing precise tuning of their electronic and optoelectronic properties. In particular, rigid π-conjugated spacers, such as fluorene derivatives or platinum-containing fluorenes, are highly attractive they have a very rigid π-conjugated structure that favour the charge delocalization. Such ordered nanoparticle arrays are promising for advanced applications in nanodevices, light-emitting systems, solar cells, and electronic switches.[88] In addition, nanoparticles stabilized with bifunctional thiols can be mixed with other functional materials to enhance optoelectronic performance. For instance, when combined with semiconducting polymers (such as poly(3-hexylthiophene-2,5-diyl), P3HT), they can improve conductivity, giving rise to composite-based nanomaterials. As a result, they display not only improved mechanical, thermal behaviour but also unique multifunctional properties tailored for specific technological applications.[12]

Chiral ligands, on the other hand, represent an emerging frontier in nanoparticle research. They can be used to synthesize nanoparticles with intrinsic chiral morphologies[89] or isotropic particles functionalized with enantiopure ligands. The latter are particularly attractive for use as enantioselective probes, enabling the discrimination of molecular enantiomers in sensing applications[90].

Although, in the last decades, the terminal functional group of ligands have been exploited to manipulate and control the colloidal state of MNPs through external stimuli like light, magnetic/electric fields, pH, temperature.[91,92] Particularly for the achievement of dynamic aggregates, sensitive to external physical or chemical stimuli.[93] Responsive nanoparticles can be at the basis of smart materials developed for different purposes (sensors,[94] catalysis for nanoconfinement,[95] nanocarrying of biomolecules[96]). In general, formation of nanoparticle aggregates could be driven by supramolecular[97] or covalent interactions.[98] In the first case, the dynamic assembly/disassembly of NPs is easily achieved through intermolecular non-covalent interactions that can be broken via external stimuli such as temperature[99] or pH[100]. Whereas covalent interaction involves the formation and breaking of covalent bonds obtaining a covalent self-assembly[101]. An example of a gold nanoparticle system in which the terminal groups of the ligands were exploited to achieve both reversible and irreversible covalent aggregation, using external stimuli, will be discussed in detail in the following sections (*vd.* 3.1.1.). Examples have been reported by Klajn (light stimulus) and Boekhoven (chemical stimulus) and others.[102,103,104,105]

1.5. Applications of Metal Nanoparticles

The use of metal nanoparticles has rapidly expanded across diverse fields, including molecular biology, physics, organic and inorganic chemistry, medicine, and materials science, sensing and optoelectronic marking the advent of the nanotechnology era.[106]

1.5.1. Nanoparticles in Nanomedicine and Drug Delivery

In particular, their integration into medical and healthcare treatments has led to a true revolution, opening new possibilities for diagnostics and therapies. AuNPs stand out in the biomedical field, where they find wide applications in diagnostics, therapy, and theragnostic. They have also emerged as excellent candidates for the targeted delivery of a broad range of payloads, from small drug molecules to larger biomolecules such as DNA, RNA, antibodies and proteins. In some cases, drug molecules can be directly conjugated to AuNPs through non-covalent interaction or via ionic and covalent interactions. To further improve their performance as drug carriers, the presence of specific functional groups on the metal surface is necessary to enhance their affinity toward biological molecules and increasing their specificity. Current approaches to AuNPs functionalization typically exploit one or a

combination of different functional groups, tailoring the nanoparticles for their intended biomedical applications.[107,108]

Nanocarriers focus on the appropriate release speed and enhancement of delivery capability with the aim to increase the amount of drug at the target site reducing the side effects. For example, the aim is to deliver anticancer drugs to a specific site and avoid damage to surrounding healthy tissues.[109,110] Many studies have demonstrated the synergistic effect between nanocarrier and drug, showing that the therapeutic effect is significantly enhanced when the drug is delivered through nanoparticles.

1.5.2. Nanoparticles in Sensing

Another important field of application of nanomaterials is sensing. Thanks to their conductive and optical properties, nanomaterials can act as probes to enhance sensor performance by improving sensitivity, selectivity, and response time.[111] Their outstanding physicochemical features, such as small size, high surface-to-volume ratio, tunable composition (e.g., metals), diverse size and shape, and unique target-binding characteristics, allow a markedly improved response to analytes. Nanomaterials have been employed in both biosensors and chemical sensors. In the latter case, they are often applied for the detection of small molecules, including volatile organic compounds (VOCs). Several chemical classes of VOCs can be found in the atmosphere, such as pyrazines, benzenoids, terpenes, organic acids, ketones, alcohols, and alkenes.[112] Among aromatic hydrocarbons, benzene, toluene, and the three xylene isomers (*m*-xylene, *o*-xylene, and *p*-xylene) are categorized as BTX.[113] VOCs show a substantial impact on human health and their vapours can cause various health diseases such as nausea and pain in body organs; moreover, some VOCs are carcinogenic and teratogenic.[114,115] Over the years, three main sensing technologies have been investigated: electrochemical, optical/colorimetric, and chemiresistive sensors.[116] Among these, chemiresistive gas sensors are reported in literature as a good choice for BTX gas detection due to high sensitivity, simple fabrication, compactness, low operating temperature, and reduced power consumption.[117,118,119] These gas sensors are resistive-based and detect the gas by converting the analyte concentration into an electrical signal, measuring the resistance charge of sensor.[120] Typically, the sensing material is deposited on electrodes (line electrode, parallel electrodes, and interdigitated electrodes) printed/stamped on a substrate (paper, plastic or silica substrate).[121] Chemiresistive sensors that operate at room temperature are suitable to reduce energy consumption and cost, increasing security

and stability of sensors. To obtain room temperature operative sensors, surface functionalized MNPs can be used and deposited on interdigitated electrodes producing stable films and superstructure formation. To date, there is no extensive literature on functionalized MNPs-based sensors.[122,123]

1.5.3. Nanoparticles in Optoelectronics

Recent advances in nanomaterials science have expanded the role of metal nanoparticles, driving innovation in fields such as electronics, optoelectronics, photonics, and bioelectronics. These research areas span from information technology and solar energy to high-density data storage, life sciences, and security. Among the most promising systems, hybrid nanomaterials have attracted considerable attention, particularly for their potential in optoelectronic applications. The nanocomposites of polymeric semiconductors and gold nanoparticles, for example, exploit the surface plasmon resonance of gold nanoparticles to induce unique photophysical phenomena such as hot-electron injection and plasmon-induced resonance energy transfer, making them highly relevant for photovoltaic devices.[124] The development of next generation flexible functional materials has further stimulated interest in inorganic/organic hybrid blends. In this context, metal nanoparticle–polymer hybrid nanostructures showed promising applications as passive or active layers in optoelectronic devices.[125] Among different nanomaterials type, AuNPs were intensively studied for these purposes, due to their great stability under standard conditions (compared with the reactivity shown by other MNPs)[126] and their size-dependent optical properties (like LSPR).[127] Due to these characteristics, incorporating AuNPs into polymer matrices not only enhances the intrinsic properties of the host material but can also give rise to novel multifunctional features through a synergistic interplay between the two components. Notably, polymer nanocomposites with nanoscale fillers exhibit significant improvements in performance at much lower loadings compared to conventional polymer composites.[128]

1.6. Aim of the Work

The aim of this work can be divided into two:

1. Hydrophilic Gold Nanoparticles: synthesis, characterization, and applications in nanomedicine.
2. Hydrophobic Metal (mostly Au) Nanoparticles: synthesis, characterization, and applications in optoelectronics.

The synthesis of hydrophilic AuNPs was carried out through a single-phase aqueous reduction of a gold precursor, and two different systems were optimized (**Figure 11**):

a. AuNPs stabilized with a mixture of two thiols, *i.e.*, sodium 3-mercaptopropanesulfonate (3MPS) and 2-(diethylamino)ethanethiol hydrochloride (DEA). The careful choice of these ligands enhances the hydrophilicity and overall bioactivity of drug-loaded AuNPs. A thorough characterization, using the innovative μ-liquid jet XPS technique, allowed to study the nanoparticles in their native colloidal state. After the synthesis and characterization, the employment of AuNPs in drug delivery was tested: the loading of synthetic DOTA derivatives was studied, then we moved on to loading the drug MTX, and finally, increasing the degree of complexity, proceeded with the loading of the antibody TZ. The objective was to study the interaction between the drug and the thiols capped on the gold surface, but also to verify an enhancement of the therapeutic effect thanks to the loading on AuNPs.

b. AuNPs stabilized with a dye and 3MPS. The dyes used were two synthetic derivatives of fluorescein isothiocyanate (CysFITC and AniFITC), modified to introduce a thiol moiety to the fluorophore molecule. The role of 3MPS was to stabilize the synthesized colloid due to the low solubility of CysFITC and AniFITC. The objective was to obtain a synergistic combination of the intrinsic optical properties of the nanoparticles and the fluorescent characteristics of the dyes.

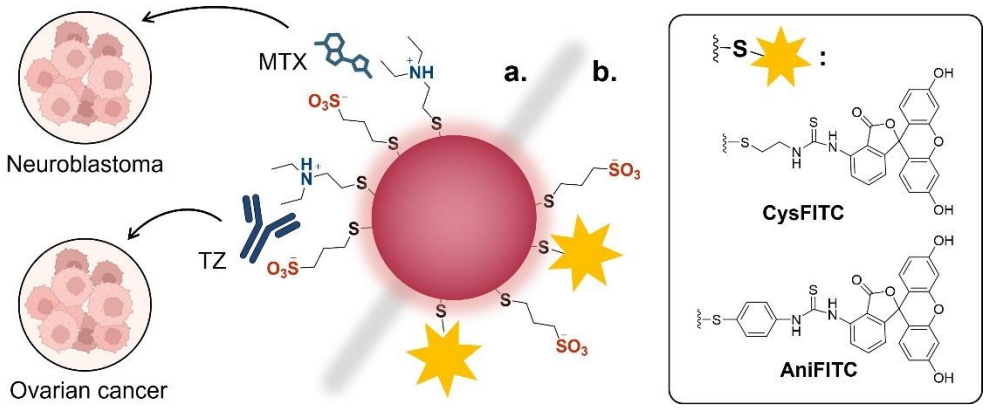

Figure 11. *a) AuNPs functionalized by different hydrophilic ligands, i.e. sodium 3-mercapto-1-propanesulfonate (3MPS) and 2-(diethylamino)ethanethiol hydrochloride (DEA). Methotrexate (MTX) and trastuzumab (TZ) loaded on AuNPs for nanomedicine: treatment of neuroblastoma cells for AuNPs-MTX bioconjugate and treatment of ovarian cancer cells for AuNPs-TZ bioconjugate. b) AuNPs functionalized by 3MPS and FITC synthetic derivatives (CysFITC or AniFITC).*

The synthesis of hydrophobic AuNPs was carried out through a modified two-phase Brust-Schiffrin method and the types of systems studied can be divided into three groups, as highlighted in **Figure 12**:

a. AuNPs stabilized with a mixture of two thiols, *i.e.*, dodecanethiol (DDT) and 4-aminothiophenol (Ani). The aim was to manipulate and control the colloidal state of the AuNPs using external stimuli, starting from an initial state of isolated nanoparticles. The different colloidal states achieved were: Supramolecular Self-Assembly (SSA), which is a non-covalent self-assembly between the AuNPs; Covalent Self-Assembly (CSA), which is an irreversible self-assembly formed by new covalent bonds; and Covalent Transient Self-Assembly (cTSA), where the covalent self-assembly is transient over time, when the external stimulus ends, the covalent bonds break, restoring the system of isolated nanoparticles.

b. Networks of Metal Nanoparticles: to obtain them, it is necessary to employ bifunctional ligands (molecules having two thiol moieties). These ligands are synthetic derivates and are characterized by a rigid structure and an extended π-conjugation. These characteristics are necessary to obtain MNPs for chemiresistive sensors or for optoelectronic applications. Bifunctional ligands were used in a mixture with monofunctional thiols to tune the 2D/3D arrangement of the network. That was required

to obtain chemiresistive sensors for benzene and toluene. To enhance the optoelectronic properties, organic-inorganic blends using AuNPs and polymers were studied.

c. Gold Nanoparticles functionalized with chiral ligands. The objective was to obtain nanoparticles where the chirality of the thiol is maintained in the nanostructure. To achieve this, a thiolbenzyl derivative of PCP was synthesized and used to stabilize the nanoparticles.

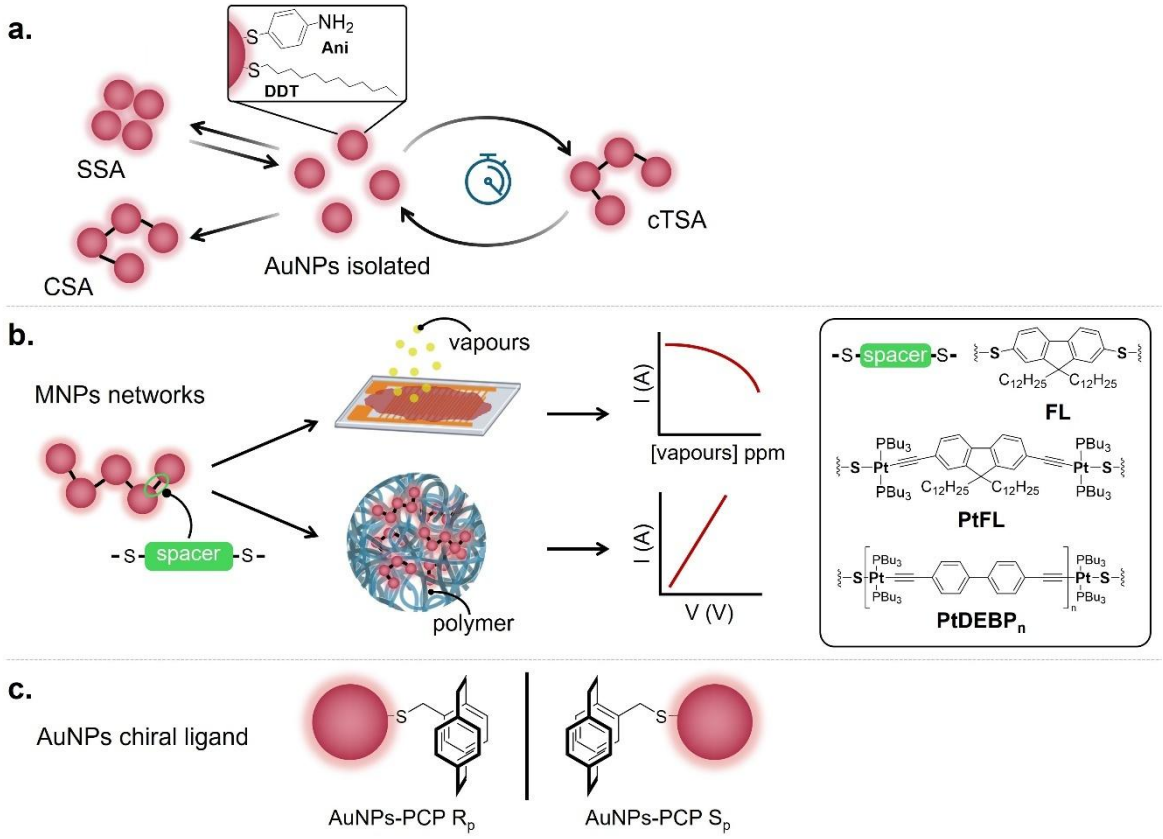

Figure 12. *a) AuNPs functionalized by dodecanethiol (DDT) and 4-aminothiophenol (Ani), and schematic depiction of Supramolecular Self-Assembly (SSA), Covalent Self-Assembly (CSA), and Covalent Transient Self-Assembly (cTSA) of AuNPs; b) Network of MNPs functionalized by bifunctional ligands (FL, PtFL and PtDEBPn) for vapours sensors and in polymeric blends for optoelectronics; c) AuNPs functionalized by chiral ligands.*

Chapter 2. Hydrophilic Gold Nanoparticles

In this chapter synthesis, characterization and application of hydrophilic gold nanoparticles are explored, with a special focus on the field of drug delivery and nanomedicine.

The nanoparticles discuss in this chapter were synthesized using the sodium bromide method, described in detail in *Section 1.3.1*, and stabilized with a mixture of thiols. The choice of employing mixed thiols was made to introduce multiple functional groups and to anchor different molecules (for example dyes) onto the nanoparticle surface. This strategy enables the preparation of multifunctional AuNPs while providing greater control over colloidal size and stability, ultimately allowing the development of diverse approaches in nanomedicine.

The first part of the chapter describes AuNPs functionalized with two thiols in mixture, *i.e.*, sodium 3-mercaptopropanesulfonate (3MPS) and 2-(diethylamino) ethanethiol hydrochloride (DEA). The AuNPs synthesized were small sized, very stable, even under harsh conditions such as elevated temperature and prolonged time, while also displaying excellent monodispersity. After a thorough characterization, the nanoparticle system was investigated at the Soleil Synchrotron (Proposal No. 20221610 'Hydration chemistry of functionalized gold nanoparticles suited for drug delivery'), using the innovative μ-liquid jet XPS technique. Unlike conventional solid-state XPS, this approach enables experiments to be carried out directly in the colloidal state, which represents the natural environment of the nanomaterial during its practical applications.

Thanks to their high colloidal stability, the nanoparticles were further tested upon interaction with molecules, two synthetic derivatives of DOTA (1,4,7,10-Tetraazacyclododecane-1,4,7,10-tetraacetic acid).

Encouraged by these results, the system was then successfully employed as a versatile platform for the delivery of an anticancer drug (methotrexate, MTX) and, subsequently, of an antibody (trastuzumab, TZ), highlighting its strong potential in the field of nanomedicine.

Finally, the last section of the chapter presents a preliminary study on nanoparticles functionalized with 3MPS and a synthetic derivative of the commercial dye FITC. The aim was to obtain nanoparticles with unique optical characteristics, arising from the synergistic combination of the intrinsic optical properties of the nanoparticles and the fluorescent characteristics of the dyes.

2.1. AuNPs functionalised by mixed thiols: 3MPs and DEA

Synthesis of gold nanoparticles functionalised with 3MPS and DEA mixed thiols was carried out following a wet reduction procedure in water[61] and schematically shown in **Figure 13a** and reported in detail in *Appendix C1.1*.

Gold nanoparticles (AuNPs) were synthesized using $[AuCl_4]^-$ as the metal precursor, while 3MPS and DEA were employed in mixture as capping and functionalizing agents. Sodium borohydride was added as the reducing agent. The synthesis was carried out under mild conditions (room temperature and atmospheric pressure) for 2 hours, using ultrapure water as solvent. Different molar ratios between the Au precursor and the two thiols were explored; in this study, we focused on the Au/3MPS/DEA = 1/4/10 molar ratio. The resulting nanoparticles AuNPs were purified and extensively characterized.

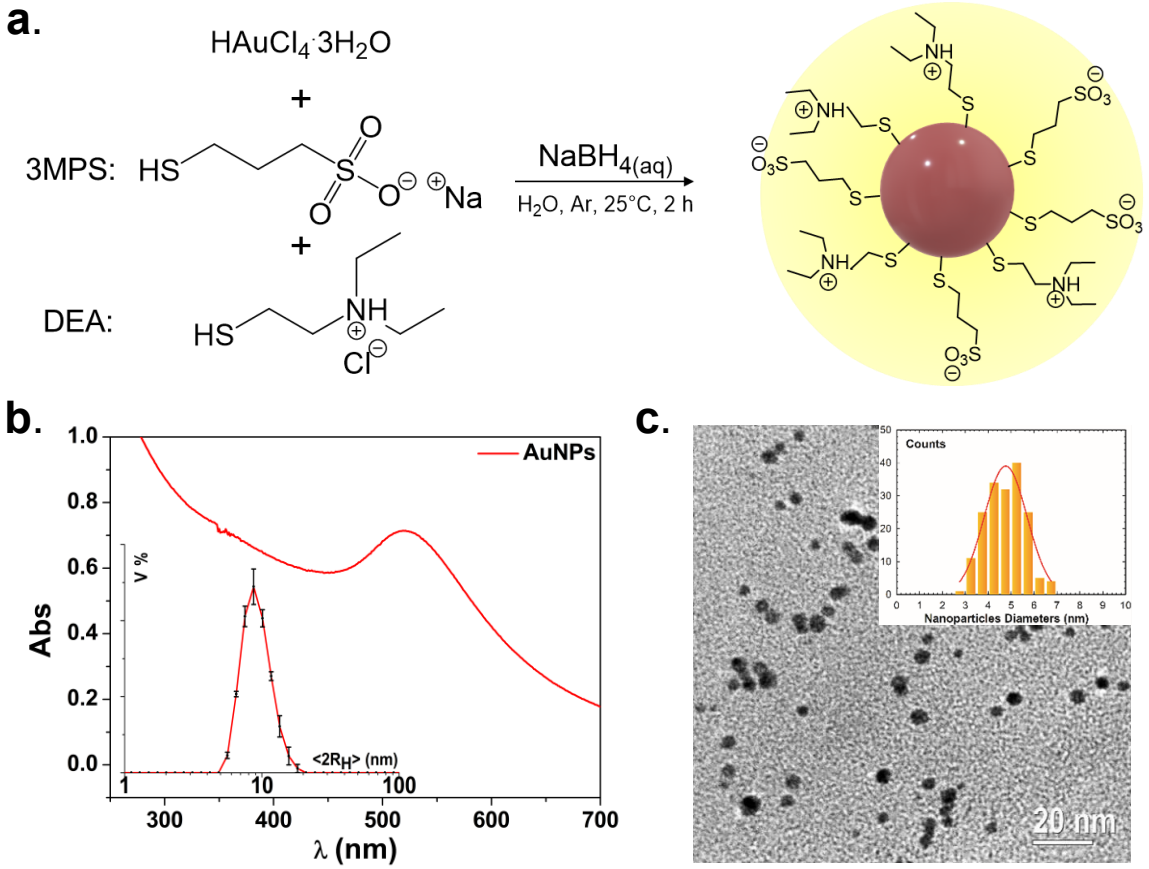

Figure 13. *a) Scheme of synthetic process of the AuNPs, b) UV-Vis spectrum of AuNPs in H_2O_{up} at concentration 50 µg/mL (λ_{max} = 516 nm), inset: hydrodynamic size distribution of AuNPs at concentration 50 µg/mL ($<2R_H>$ = (9 ± 2) nm), c) High resolution TEM image of AuNPs, inset: frequency distribution of the nanoparticles size and data fitted by Gaussian function (red line).*

The obtained AuNPs were small in size and highly stable, as confirmed by UV-Vis spectroscopy and DLS measurements (**Figure 13b**). The LSPR band, centred at *ca.* 520 nm, is consistent for particles with diameter of approximately 10 nm[41], in agreement with the hydrodynamic diameter measured by DLS ($<2R_H> = 9 \pm 2$ nm). The narrow LSPR band also indicates a good monodispersity of the sample.

To have a better understanding of the size and shape of the nanoparticles, high resolution TEM image (**Figure 13c**) shows nanoparticles with a diameter of (4.76 ± 0.09) nm in average. The size difference (*ca.* 5 nm) between a solvent mediated measurement such as DLS and a solid-state technique such as HR-TEM is because DLS considers the presence of the thiols surrounding the metal core, as well as the solvation shell, whereas with electron microscopy studies, only the metal core can be measured.

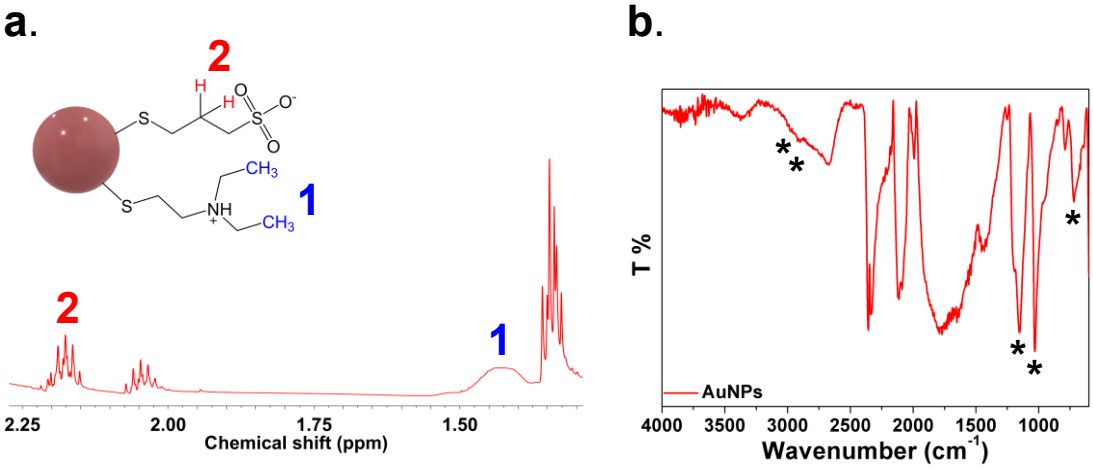

Figure 14. *a) ^{1}H NMR spectra of AuNPs in D_2O, inset: AuNPs and surface thiol structure; b) FTIR spectrum of AuNPs. Relevant bands are marked with and asterisk (ν = 2978, 2920, 1150, 1027, 718 cm^{-1}).*

NMR and FTIR were carried out to investigate the surface chemistry of AuNPs and the stoichiometric ratio between the two thiol ligands. **Figure 14a** shows a detail of the ^{1}H spectrum of AuNPs (for full spectra *Figure C1*), where the presence of both thiols on the surface of the nanoparticles can be confirmed, as the signals of the central methylene of the aliphatic chain of 3MPS and the signal of the terminal methyl groups of DEA thiol can be distinguished (δ=2.18 ppm and δ=1.43 ppm, respectively). The signals at higher fields that are visible on the spectrum pertain to the free thiol in solution, unbound on the nanoparticle surface.[129] This observation is in agreement with literature reports, where physically sorbed thiols are often found even after purification.[130] By comparing the integrals of these two signals, the molar ratio between the two thiols on the surface of the nanoparticles can be

calculated; it was found to be *ca.* 1/2 in favour of 3MPS. **Figure 14b** shows the FTIR spectrum of AuNPs. The spectrum, as well as the spectra of the two thiols alone (*cfr. Figure A1*), was collected in the attenuated total reflectance mode (ATR) on the dry samples. The FTIR spectrum exhibits the typical asymmetric stretching (ν_{as}) of $-SO_3^-$ at 1027 cm^{-1} and symmetric stretching (ν_s) of $-SO_3^-$ at 1150 cm^{-1} related to the presence of 3MPS on AuNPs surface. Being a tertiary amide the are no absorption associated with $-N(CH_3)_2$ of DEA, whereas C–N stretching vibration is partially overlapped with $\nu_{as}(-SO_3^-)$ at 1027 cm^{-1}. Asymmetric stretching of $-CH_2$ and $-CH_3$ can be found at 2920 and 2978 cm^{-1}, respectively. Thiol related carbon sulphur single bond stretching resonates at 718 cm^{-1}.

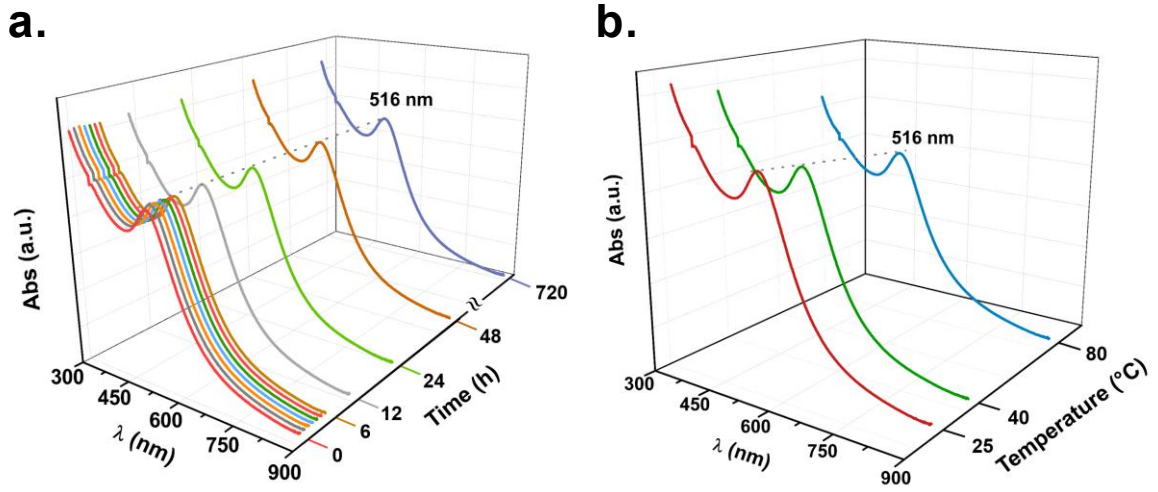

Figure 15. *Stability studies: values of the maxima of the plasmon band (λ_{LSPR}) for the UV-Vis studies on the stability of the AuNPs in a) time and b) temperature. All spectra recorded in water. AuNPs concentration 0.1 g/L in H_2O_{up}.*

To assess the colloidal stability of AuNPs, different studies were carried out. **Figure 15** shows a summary of such studies; the gold nanoparticles were firstly tested for their stability in time (**Figure 15a**) with UV-visible measurements, measuring the same suspension from freshly prepared nanoparticles up to 1 month (720 hours). The results show no aggregation or precipitation in the colloidal suspension, as the maximum of the plasmon band remains centred at 516-517 nm (instrument error ± 1 nm), and no enlargement of the band can be seen, with the maximum indicating small sized nanoparticles and the FWHM giving an indication on the polydispersion of the sample. **Figure 15b**, on the other hand, represent the stability of the AuNPs system when measured at different temperature, three points were investigated: first, room temperature (25°C), then a spectrum of the same suspension was recorded after overnight thermal treatment at 40°C, and lastly, the AuNPs were treated

overnight at 80°C. As it can be seen, the results are the same as the experiments in time, both the thermal treatment have no effect on size and polydispersity of the sample.

2.1.1. µ-liquid jet XPS technique

The XPS technique usually requires AuNPs in the form of solid samples (*e.g.*, a drop cast of the AuNPs dispersion on a surface) preventing to characterize the functionalizing agents in more *operando* conditions, *i.e.*, aqueous solvent. Hence, we decided to explore the use of X-ray photoemission µ-liquid jet (XPS µ-LJ) to investigate the structural and chemical properties of thiols and thiol-capped gold nanoparticles in water (**Figure 16**).

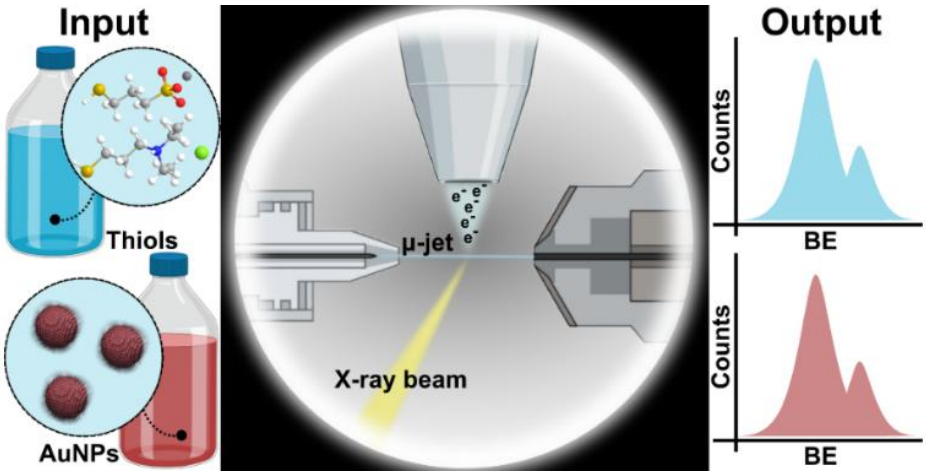

Figure 16. *Schematic representation of free thiols' (3MPS and DEA) and AuNPs' µLJ-XPS measurement.*

Then, we faced the challenge of characterizing gold nanoparticles functionalized with 3MPS and DEA, which provide AuNPs with well-studied applications in drug delivery.[131] The functionalization with two thiols (3MPS and DEA) in the appropriate molar ratio allowed to obtain exceptionally stable AuNPs, even at high concentrations (2.8 g/L), that could resist to the necessary temperature and pressure conditions of the experiment, allowing at the same time for their recycling without any sample waste.

While XPS is an established tool to analyse NPs deposits on solid surfaces[131], its implementation for the characterization of colloidal NPs dispersions counts on a few case studies,[132,133,134,135] due to the challenges posed by NPs aggregation phenomena that may occur during the measurements. Moreover, the cited literature reports few examples about the characterization of commercial nanoparticles. In this regard, our study represents one of

the rare examples of AuNPs used in a XPS μ-LJ experiment. The presented results showed how the XPS μ-LJ appears as a versatile and efficient tool to unravel the electronic structure of functionalized gold nanoparticles and molecules in their native – aqueous – environment. The XPS μ-LJ measurements were performed at the French synchrotron radiation facility SOLEIL (Paris, France) at the PLÉIADES beamline which is dedicated to spectroscopic studies of dilute systems (atoms, molecules, ions, clusters). For this experiment a system with two recycling bottles was implemented behind the catcher. One bottle was used only for alignment of the liquid jet compared to the synchrotron and for optimization of the electron signal. When the optimal conditions were found, the sample was directed towards the second clean recycling bottle, for its collection. At the end of the available sample, a new switch to the first recycling bottle is made, to be able to retrieve and run tests or purification on the recycled sample. For the sample preparation, 3MPS thiol solutions (0.5-1.0 L) were prepared in H_2O_{up} at 200 mM concentration at the native pH (2.90) and adjusted to obtain solutions at pH 5 and 10. DEA solutions were prepared (0.5-1.0 L) H_2O_{up} at a 200 mM concentration at the native pH (3.50) and adjusted with NaOH to obtain solutions at pH = 5 and pH = 9. The 3MPS/DEA mix solution (MIX) was prepared by mixing 500 mL of 3MPS 200 mM, with 500 mL of DEA 500 mM, obtaining a molar ratio of 1:2.5 (that corresponds to the stoichiometric molar ratio between the two thiols during the AuNPs synthesis, *vd. Appendix C.1.1.*) in H_2O_{up} and measured at native pH = 4.25. AuNPs were suspended in water at a 2.8 g/L concentration at native pH (5.0). All the samples were filtered on a bottle-top vacuum filter system equipped with cellulose acetate membrane, pore size 0.22 μm. (solutions were analysed by UV-vis spectra to assess the quality of the colloidal suspensions). For all experimental details *vd. D1.1.*)

M-liquid jet XPS allowed to investigate the hydration chemistry and the structure of the AuNPs and surface thiols in the colloidal state, obtaining information complementary to the ones provided by "conventional" UHV-XPS techniques, which are used to probe solid state samples.

Focusing on the stabilizing ligands, 3MPS and DEA, we studied the impact of different aqueous pH conditions in solution on their structures before investigating the stability and hydration chemistry of the gold nanoparticles system. **Figure 17** highlights the XPS spectra in solution of the two thiols, recorded at the S 2p (**Figure 17a**) and N 1s (**Figure 17b**) core levels.

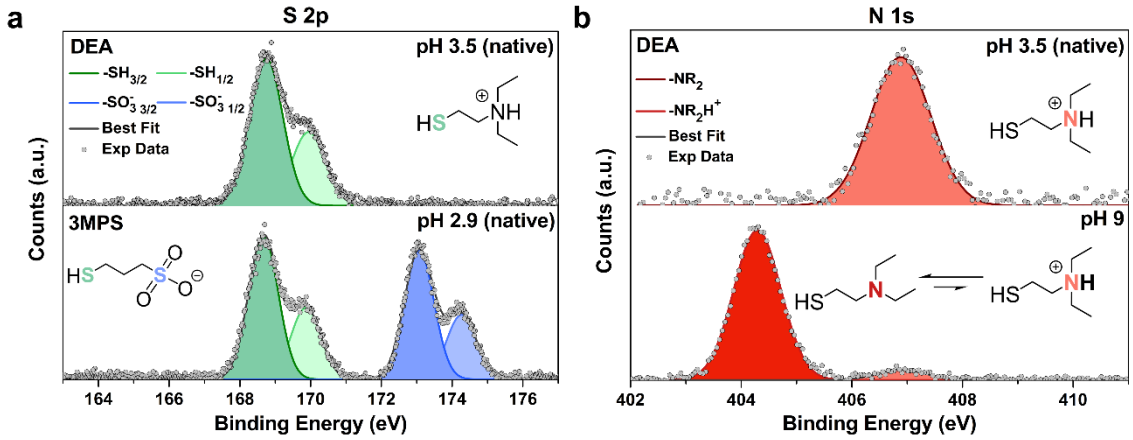

Figure 17. *a) XPS μ-liquid jet spectra of DEA at its native pH (top) and 3MPS at its native pH (bottom), recorded at S 2p core level;b) XPS μ-liquid jet spectra of DEA at its native pH (top) and at pH = 9 (bottom), recorded at N 1s core level. The insets in the figures show the molecular structures of the analysed thiols.*

Figure 17a in the panel shows the S 2p core level XPS spectra of the two thiols at their native pHs (3.5 – DEA, 2.9 – 3MPS); the measured S 2p core level in DEA (**Figure 17a** top) consists in a single pair of spin-orbit components relative to -SH group. As for the 3MPS (**Figure 17a** bottom), the S 2p signal appears composite, and it is possible to identify two spin-orbit components, the one at lower BE (3/2 spin-orbit component, green) pertains to the thiol group, as in DEA; at higher BE, the sulfonate moiety can be found. The observed core-level shift (ΔBE) between the two S2p signals is of about 4.2 eV, as expected for these two types of sulphur groups[136]. In **Figure 17b**, the spectra taken at N 1s core level are reported: the graph on the top of the image pertains to DEA in solution at pH 3.5 (native), only one component can be seen, pertaining to the protonated nitrogen in the amine (as expected for a tertiary amine at this pH); the lower spectrum, taken at pH 9, highlights the presence of an equilibrium between the protonated and deprotonated amine, with the deprotonated molecule being strongly prevalent at this pH; the BE splitting for the deprotonated (dark red) - protonated (salmon) N1s signals is of about 1.5 eV, as expected by the literature[137]

In the *Appendix D1.1.* the spectra of C 1s, S 2p, N1s core levels of the two thiols at different pHs are reported (*Figure D1-2.*), alongside all Binding Energy (BE) values, FWHM and atomic ratios (*Table D2.*).

After characterizing the free 3MPS and DEA ligands solutions, we proceeded with the study of the AuNPs dispersion. The nanostructured system used in this work (AuNPs functionalised with 3MPS and DEA), as already mentioned (*cfr.* 2.1.). For XPS liquid μ-LJ

measurements, a 400 mL water suspension of gold nanoparticles (2.8 g/L) at their native pH (5) was prepared. The choice of this concentration was determined by the amount of nanoparticles needed to obtain an acceptable signal during the experiment and is also driven by the upper limit of concentration after which the colloidal suspension would not be stable anymore and the nanoparticles would aggregate.

Determining the molar mass of nanoparticles is challenging, due to the necessity of a monodisperse population to accurately calculate it. However, as this system has shown high monodispersity, and assuming a diameter of the metal core of 5 nm (from TEM images 4.76 ± 0.09, *vd.* 2.1.), the molecular weight of a nanoparticle was calculated to be 757940 g/mol, thus yielding a concentration of the solution equal to $3.7 \cdot 10^{-3}$ mM (*cfr.* Eq. 7)[24]. This calculation is done with the approximation of not considering the molecular weight of the surface thiols, as their contribution is much lower than the Au atoms.

$$\text{molar concentration}_{\text{AuNPs}} = \frac{\text{weight concentration}_{\text{AuNPs}}\ [\text{g}\cdot\text{L}^{-1}]}{\text{molecular weight}_{\text{AuNPs}}\ [\text{g}\cdot\text{mol}^{-1}]} = \frac{\text{weight concentration}_{\text{AuNPs}}\ [\text{g}\cdot\text{L}^{-1}]}{N_{Au}\cdot m_{Au}\ [\text{g}\cdot\text{mol}^{-1}]} = \frac{2.8\ \text{g}\cdot\text{L}^{-1}}{3848\cdot 196.97\ \text{g}\cdot\text{mol}^{-1}} \qquad (7)$$

AuNPs concentration was much higher if compared with the amount needed for more conventional structural characterizations (*i.e.*, solid state XPS, NMR, FTIR, for which normally the concentration is in the 0.1-1 mg/mL range). In a report on similar gold nanoparticles, coated only with 3-mercaptopropionic acid[138], on the surface of the nanoparticles, an average ligand density of 7.8 molecules·nm^{-2} of chemisorbed thiol was calculated. Assuming the same ligand density for a two-thiol system such as the one used in this work, and the experimental molar ratio between 3MPS and DEA calculated with ^{1}H NMR (2:1) (*vd.* 2.1.), we estimate 1.51 mM of chemisorbed 3MPS and 0.755 mM of DEA, which amounts to be much less than the amount used for the characterization of the free thiols (200 mM for 3MPS, 100 mM for DEA; in the mix solution: 200 mM 3MPS, 500 mM DEA, according to the synthetic molar ratio).

For the characterization of the free ligands, we prepared 1 L solutions in the 100-500 mM range (*vd. supra*) with a flow during the experiments of 2.7 mL/min; To obtain an acceptable signal-to-noise ratio with the AuNPs suspension, however, its recovery and repeating the measurements was necessary. Measuring only 400 mL of a 100 times less concentrated suspension once would not have yielded a readable signal.

This was possible only thanks to the exceptional stability of this nanostructured system, which could be recycled without it losing its physico-chemical properties. To confirm this

stability, UV-Vis spectroscopy and DLS measurements were performed (**Figure 18**). The results are fully consistent with those obtained for the AuNPs before the μ-LJ XPS experiments: the LSPR peak remains centred at 520 nm, and the DLS profile shows a single population with an average size of (8 ± 2) nm.

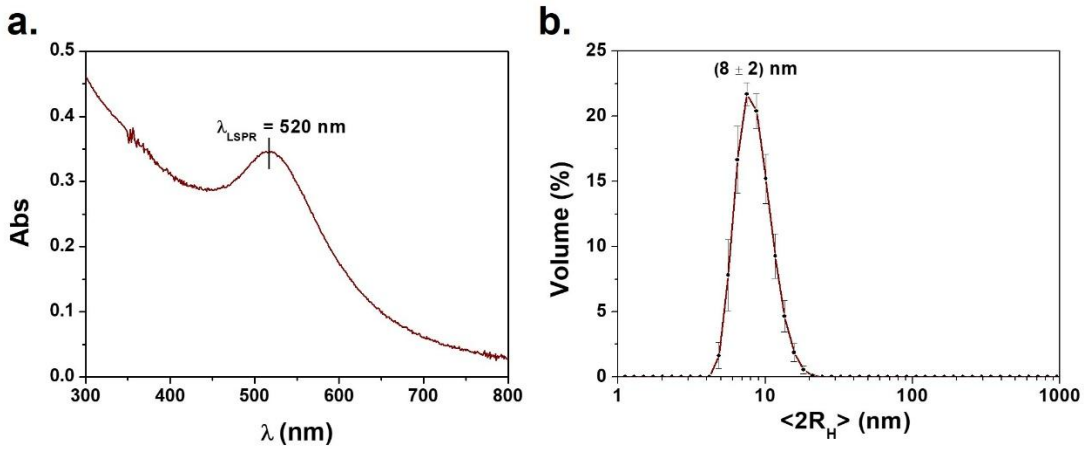

Figure 18. *a) UV-Vis spectrum and b) DLS graph of the AuNPs after the measurement; both measurements were recorded in water.*

After the characterization of the free ligands' solutions, and before measuring the gold nanoparticles suspension, a solution comprising of both thiols in solution ("mix") was prepared. In this solution, the molar ratio between the two thiols was kept the same as in the synthesis process (3MPS:DEA 1:2.5). **Figure 19** shows a comparison of liquid jet XPS spectra of the mix solution and the AuNPs dispersion.

In **Figure 19a**, the top spectrum relates to the 3MPS-DEA mix solution, collected at S 2p core level; two doublets can be distinguished in both spectra, the one at lower BE values pertains to the sulphur in the –SH group, in the "mix" (green), whereas at higher BE values the signal of the sulphur in the $–SO_3^-$ group can be found (blue); the observed ΔBE = 4.2 eV is in excellent agreement with the same measurement carried out on pure 3MPS ligand solution reported in **Figure 17**.

The S2p core-level spectrum of AuNPs reported at the bottom of **Figure 19a** is much broader than the mixed ligands one due to the lower S/N ratio; this is probably related to the low nanoparticles' concentration needed to prevent aggregation, as well as the presence of the colloidal suspension that causes inhomogeneities in the sample. As in the spectrum above, it is possible to individuate two sulphur signals with a binding energy splitting of about 4.2 eV respectively assigned to -SH (green) and $–SO_3^-$ (blue) groups. Due to the very large FWHM

it is possible that other spectral components also contribute to the detected signals. Indeed, by comparison with solid state measurements, a low-intensity contribution arising by sulphur atoms covalently bonded to gold atoms at the NP surface (Au-S-R) is expected at lower BE than -SH (expected ΔBE = 1.5 – 2.0 eV). However, the signal/to/noise ratio is not high enough to be able to finely distinguish the different components. The noticeable amount of -SH groups is not surprising since, even after thorough purification, physically adsorbed thiols cannot be fully removed[130]. Interestingly, the relative intensity of the two -SH and -SO_3^- doublets changes in the AuNPs S 2p spectrum, with the –SO_3^- component becoming more prevalent when compared with the –SH. The latter is in both thiols, while the former is present only in 3MPS, and such a noticeable shift in the relative intensity agrees closely with the previous studies which predicted an experimental molar ratio of 2:1 in favour of 3MPS (*vd. supra*).

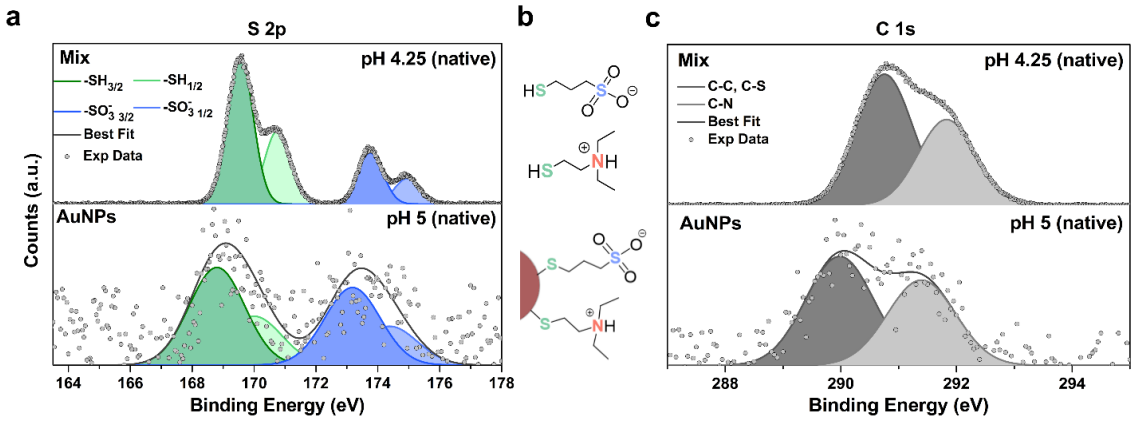

Figure 19. *a) XPS spectra collected at S 2p core level of a solution of the mix of the two thiols (top), and the colloidal suspension of AuNPs (bottom); b) structure of the thiols (top) and of the AuNPs-3MPS-DEA (bottom); c) XPS spectra collected at C 1s core level of a solution of the mix of the two thiols (top), and the colloidal suspension of AuNPs-3MPS-DEA (bottom).*

Figure 19c relates to the C 1s spectra of the "mix" (top) and of AuNPs; as expected, both spectra show two components: one related to C-C and C-S groups at lower BE values (dark grey), and another one at higher BE values which pertains to C-N (light grey, ΔBE =1.0-1.5, as expected[139]). Notably, the synthesis and purification process do not affect the molecular stability of the system, as C 1s spectrum does not change significantly between the "mix" and the AuNPs; as for the S2p core-level spectrum, measurements carried out on

nanoparticles suspension have a lower S/N ratio and the core-level signals appear much broader than those detected for the single and mixed thiols in aqueous solution.

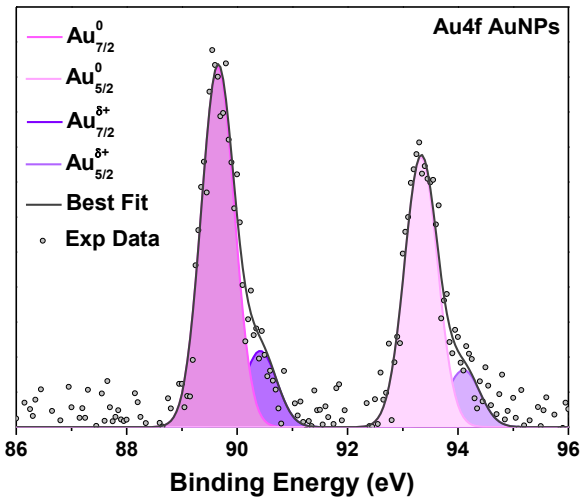

Figure 20. *XPS μ-liquid jet spectrum of gold nanoparticles taken at Au4f core level.*

Figure 20 shows the spectrum of the AuNPs dispersion taken at the Au4f core level; in this case, as it can be seen from the spectrum, two doublets pertaining to two components are distinguishable. The most intense component at low BE values is associated to the $Au^0_{7/2}$ (dark pink), pertaining to Au atoms in the core of the nanoparticles, the corresponding 5/2 component can be found at higher BE with the expected spin-orbit splitting Δs-o = 3.6 eV (light pink)[140]. Quite interestingly, by applying a peak-fitting procedure it is possible to distinguish a second doublet (light purple) of small intensity at higher BE (ΔBE = 0.6 eV). This signal confirms the presence of positively charged gold atoms at the nanoparticles surface, compatible with the spectral component usually observed in solid-state measurements and assigned to Au(δ+) atoms covalently linked to thiols end-groups (Au-S-R).

2.1.2. Conjugate AuNPs-DOTA derivate

Further evidence of the stability of this nanoparticle system was obtained by studying the interaction of 3MPS/DEA-functionalized AuNPs with two synthetic derivatives of DOTA. DOTA is among the most potent chelators for theragnostic applications, owing to the high thermodynamic stability and kinetic inertness of its complexes with radiometals such as yttrium.[141] Two DOTA derivates (DOTA_1 and DOTA_2) were synthesized by Professor

Dante Rotili and group (at the Department of Pharmaceutical chemistry and technology, Sapienza University of Rome) and both derivates featuring a 1,2-dithiolane group bounded to the chelating core through linkers of different lengths.

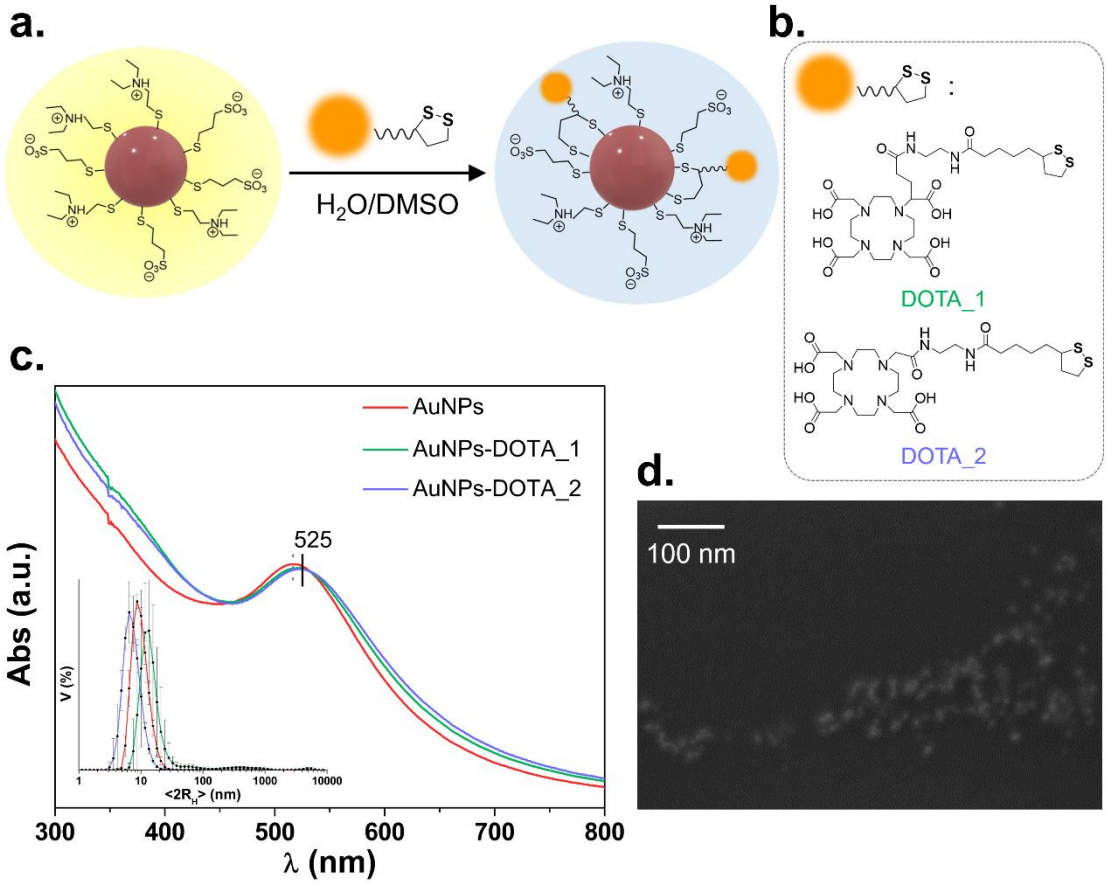

Figure 21. *a) schematic representation of interaction between AuNPs and synthetic derivates of DOTA; b) chemical structures of DOTA_1 and DOTA_2; c) UV-Vis spectra and DLS graphs of AuNPs and AuNPs conjugate with DOTA_1 and DOTA_2; d) FESEM image of AuNPs conjugate with DOTA_1.*

The dithiolane moiety is able to interact with the AuNP surface breaking the disulfide bond of 1,2-dithiolane group, leading to the formation of a covalent Au–S bond.[142] The process that results in the AuNPs-DOTA conjugates and the chemical structures of the two DOTA derivatives, are illustrated in **Figure 21a,b**. Due to the limited solubility of the DOTA derivatives in water, the conjugation reactions were carried out in a H_2O/DMSO mixture, described in detail in the *appendixD1.2.* After the interaction and subsequent purification to remove the unreacted DOTA and residual DMSO, the system was thoroughly characterized. UV-Vis spectra (**Figure 21c**) confirmed the preservation of colloidal stability after conjugation: well-defined plasmonic bands were observed even in the presence of the

chelators (green and blue lines). The interaction induced a slight red shift of the plasmon maximum to 525 nm. DLS data (**Figure 21c**, inset) further supported these findings: prior to interaction, the AuNPs exhibited a hydrodynamic diameter of 9 ± 3 nm, which remained essentially unchanged upon binding within experimental error with the size distribution of DOTA_1 centred at (13 ± 4 nm) and of DOTA_2 at (7 ± 2) nm, again indicating preserved stability. These results are corroborated by FESEM imaging (**Figure 21d**), which confirms the maintenance of particle morphology and dispersion after conjugation.

This conclusion demonstrates the stability of AuNPs system and that the 3MPS and DEA ligands remained bound to the gold surface after the interaction with DOTA derivatives. As a result, the final AuNPs-DOTA conjugates retained excellent colloidal stability in aqueous suspension.

2.2. Bioconjugates based on AuNPs: a new platform for drug delivery

Gold nanoparticles hold great promise in nanomedicine[143], owing to their low toxicity, high versatility, and straightforward synthesis. [144,145] Interest in the biomedical applications is growing exponentially, especially in cancer therapy, where AuNPs can simultaneously serve as diagnostic and for therapeutic tools.[146,147,148] In tumour treatment, thanks to their small size, AuNPs can accumulate in neoplastic tissues through the enhanced permeability and retention (EPR) effect.[149] In drug delivery, the loading hydrophobic or poorly soluble drugs on AuNPs surface provides an effective strategy to enhance their bioavailability.[150] Moreover, AuNPs can accommodate a wide range of molecules, from small drugs to larger biomolecules such as antibodies, which can be used for targeted delivery or therapeutic purposes.

In this context, AuNPs functionalized with the two different thiols 3MPS (with a negative charge, sulfonate moiety), DEA (with a positive charge, amine moiety) were employed. The careful choice of these ligands enhances the hydrophilicity and overall bioactivity of drug-loaded AuNPs. The first bioconjugate developed and studied in this PhD thesis is between these AuNPs and methotrexate (MTX), an inhibitor of dihydrofolate reductase (DHFR). Both AuNPs-MTX nanoconjugate and pristine AuNPs, were used to assess the cytotoxic activity for *in vitro* studies and administered to two different neuroblastoma cell lines: SJNKP and IMR5 with overexpressed n-Myc. These studies were conducted in collaboration

with prof. E. Agostinelli, at the Department of Molecular Medicine, Sapienza University of Rome.

Furthermore, in a complementary strategy, these AuNPs were conjugated with trastuzumab (AuNPs–TZ), an antibody that targets and blocks the HER2 protein on cancer cells. This bioconjugate was then employed in combination with extracellular targeting and with the intracellular tumour-suppressive activity of miR-200c, which was overexpressed in SKOV3 ovarian cancer cells. These studies were conducted in collaboration with Prof P. Trivedi, Prof. E. Anastasiadou and Dr. T.A. Salamonente

2.2.1. Bioconjugate AuNPs-MTX

Gold nanoparticles have already been explored as platforms for MTX delivery, as well as biopolymer-based colloids. [131, 151] However, they have never been investigated in the context of a mixed-thiol system, where the surface charge plays a crucial role in governing the electrostatic interactions between the nanoparticle surface and the drug.[152] Employing a nanocarrier for MTX delivery can help mitigate the adverse effects associated with the drug, which becomes highly toxic at elevated doses. By carefully selecting the two ligands, it is possible to enhance both the hydrophilicity and the overall bioactivity of MTX-loaded AuNPs.[153]

In this work, we developed a nanoconjugate between methotrexate (MTX), a dihydrofolate reductase (DHFR) inhibitor, and small hydrophilic gold nanoparticles (AuNPs, <10 nm) functionalized with two thiols (3MPS and DEA, *cfr* 2.1.). The cytotoxic activity of both the AuNPs-MTX conjugate and pristine AuNPs was evaluated *in vitro* on two neuroblastoma cell lines, SJNKP and IMR5, which overexpress n-Myc. Given their small size, these AuNPs have the potential to cross the blood–brain barrier (BBB), making them suitable candidates for testing in neuroblastoma models. A schematic representation in **Figure 22**.

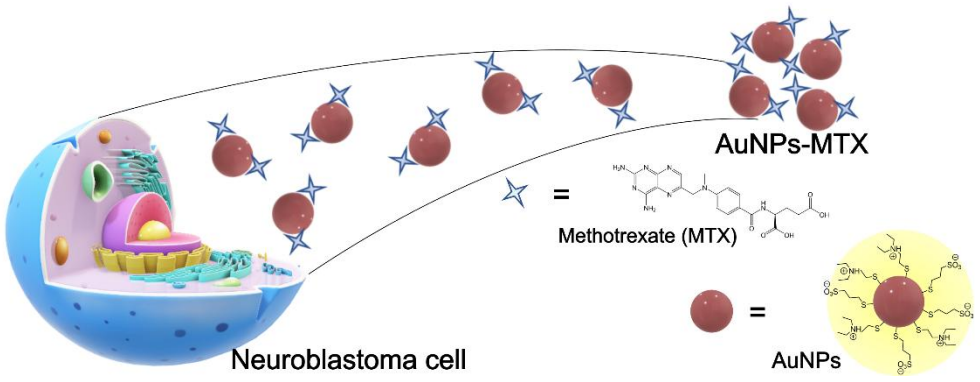

Figure 22. *Scheme of AuNPs-MTX on neuroblastoma cell lines.*

2.2.1.a. Study of chemical interaction between MTX and AuNPs surface

MTX was subsequently loaded onto the AuNPs according to the procedure reported in *Appendix D1.3.* and schematically reported in **Figure 23a**, yielding the AuNPs–MTX nanoconjugate. Concerning the UV-Vis spectrum (**Figure 23b**), it indicates no significant aggregation due to the presence of MTX, as the λ_{LSPR} is centred at around 520 nm, the same values as before the interaction with the drug (*cfr.* **Figure 13b**). The three MTX bands appear at lower wavelength values (260, 303, and 370 nm), and the one at λ_{max} of 303 nm was used as a marker, (UV-Vis spectrum of free MTX in *Figure D3a*). The DLS graph of the bioconjugate is reported in the inset of **Figure 23b**, and, similarly to the UV-visible measurements, it indicates that no relevant aggregation occurred after the MTX loading. The mean hydrodynamic diameter of AuNPs-MTX is $<2R_H> = (9 \pm 3)$ nm, whereas the DLS of pristine AuNPs showed a hydrodynamic diameter equal to $<2R_H> = (9 \pm 2)$ nm (*cfr.* Inset of **Figure 13b**).

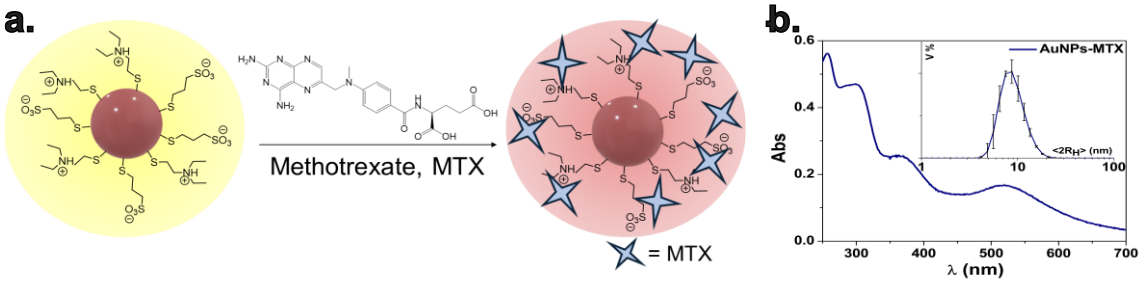

Figure 23. *a) Schematic representation of MTX loading on AuNPs to obtain AuNPs-MTX; b) Spectroscopic characterisation of AuNPs-MTX nanoconjugate in H_2O_{up} at concentration AuNPs 10 µg/mL loaded with 17 µM of MTX (λ_{max} = 520 nm). The band associated with MTX has a maximum at 303 nm, in accordance with literature reports[154], inset: Hydrodynamic size distribution of loaded AuNPs-MTX nanoconjugate (AuNPs 10 µg/mL and MTX 17 µM in H_2O_{up}), ($<2R_H> = (9 \pm 3)$ nm).*

XPS measurements were carried out to have structural information. The C1s, N1s, O1s, S2p and Au4f core levels on pristine AuNPs, free MTX, AuNPs-MTX, spectra were carried out depositing following a drop-casting procedure onto proper substrates. C1s, O1s, N1s, Au4f and S2p spectra were analysed following a peak-fitting procedure, allowing to individuate the components arising by chemical elements with different atomic environment (*i.e.*, in different functional groups); all peak positions BE (Binding Energies), Full-Width at Half

Maximum (FWHM) values, atomic ratios (relative intensities) and assignments are reported in *Appendix D142., Table D4-D6* and *Figure D4-D6*.

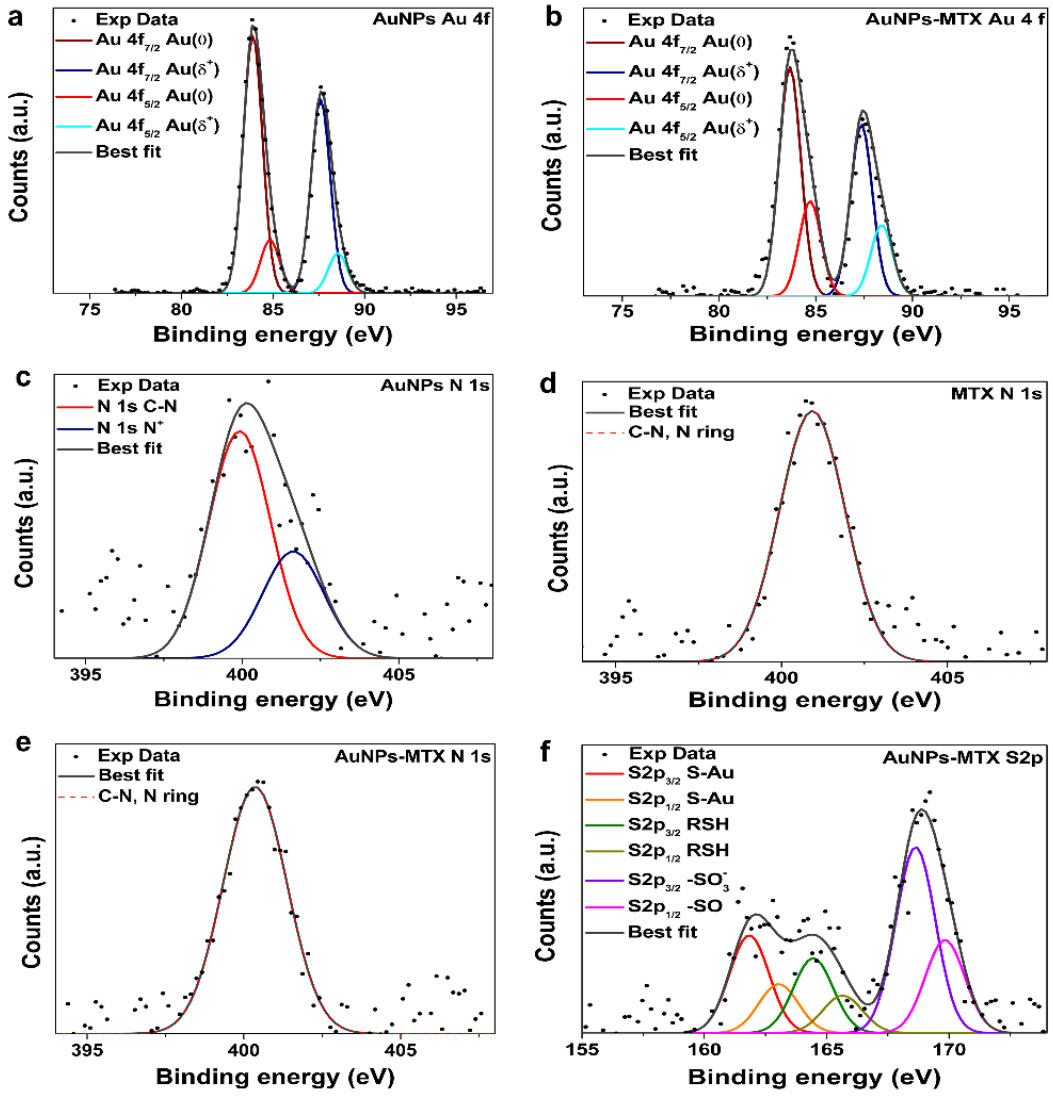

Figure 24. *XPS spectra of a) AuNPs at Au4f core level; b) AuNPs-MTX at Au4f core level; c) AuNPs at N1s core level; d) MTX at N1s core level; e) AuNPs-MTX at N1s core level; f) AuNPs-MTX at S2p core level.*

The most interesting signals to evaluate the AuNPs stability and interaction with MTX are Au4f, S2p and N1s core levels, and they will be here discussed in detail. Au4f core level spectrum of AuNPs (**Figure 24a**) is composed of two spin–orbit doublets ($Au4f_{7/2}$, $Au4f_{5/2}$); the more intense $Au4f_{7/2}$ component, due to metallic Au (0) atoms, is usually taken as reference (BE = 83.9 eV). As expected for small nanoparticles, the high surface to volume ratio allows us to observe also the Au4f signal related to substrate-thiol interface atoms: the spin–orbit pairs at higher BE values ($Au4f_{7/2}$ = 84.9 eV) appear as a pronounced shoulder on

all the Au4f measured spectra.[155] N1s spectrum of pristine AuNPs (**Figure 24c**) has two components both indicative of DEA presence and stability: a main signal at 399.9 eV due to amine terminal groups of DEA thiol, and a small peak at 401.6 eV usually attributed to charged amine groups.[156]

N1s spectrum of MTX (**Figure 24d**) shows a single peak related to aliphatic and aromatic amine groups, centred at 400.9 eV. Au4f core level spectrum of AuNPs-MTX (**Figure 24b**), in analogy with the pristine sample shows the two spin-orbit doublets ($Au4f_{7/2}$, $Au4f_{5/2}$) with the $Au4f_{7/2}$ component centred at 83.7 eV for Au(0) and 84.7 eV attributed to Au(δ+) atoms on the surface covalently linked to sulphur atoms.

Looking at S2p spectra of AuNPs-MTX reported in **Figure 24f**, the B.E. value of $S2p_{3/2}$ signal, taken as a reference for the $S2p_{3/2\text{-}1/2}$ spin–orbit pair, proves whether the sulphur atom is linked to the metal surface with a covalent bond or not. For thiols covalently anchored on metals, as well as on metal nanoparticles surface, an $S2p_{3/2}$ BE value of *circa* 161.5 eV is expected; $S2p_{3/2}$ signals around 163 eV are usually assigned to non-covalently bonded thiols or thiolates.[156] Both components are observed for conjugated nanoparticles sample, suggesting that the thiol interaction with gold atoms at NPs surface is stable and not affected by the AuNPs functionalization with MTX. The S2p signal component at high BE ($S2p_{3/2}$ BE around 168 eV) arises from the sulphonate end-group of 3MPS.

AuNPs-MTX N1s spectrum (**Figure 24e**) only has one component at 400.3 eV associated to C-N and N-ring nitrogen, as does the MTX N1s spectrum (**Figure 24d**), centred at 400.9 eV. The absence of the signal pertaining to the charged amine of DEA, and the presence of only the MTX-related signal can be interpreted as further evidence of an electrostatic interaction between MTX and the charged group functionalities of AuNPs, specifically the charged terminal amine of DEA. Furthermore, the slight shift in BE (0.6 eV) shown in the N1s spectrum related to the MTX before and after the interaction with the gold nanoparticles could support the hypothesis of a cation-π interaction between the charged moiety of DEA and the aromatic rings of MTX. The permanence of all MTX-related signals in AuNPs-MTX systems indicates that MTX molecules interact with AuNPs with weak chemical forces, then the molecular structure and functional groups of MTX are fully conserved in the adduct formation. The presence of weak interactions between the drug and the thiols on the AuNPs surface suggests that methotrexate could maintain its biological activity.

To study the nature of the interaction and its influence on the structure of the nanomaterial, a detail characterization of the nanoconjugate AuNPs-MTX have been conducted. **Figure 25a** shows the FTIR spectra of drug loaded AuNPs (in blue line) and free MTX (dark red

line). A shift in characteristic MTX bands before and after the interaction with the surface thiols on the AuNPs is observed. The shifts can help to interpret the nature of the chemical interaction between MTX and thiols functional groups. The infrared spectrum of pristine MTX (dark red) highlights the presence of the typical C=O stretching band of the carboxylic acid at 1643 cm^{-1}, at 1596 cm^{-1}, the aromatic skeletal stretching vibrations give rise to a strong band, whereas the aromatic out of plane bending band is centred at 830 cm^{-1}.[157]

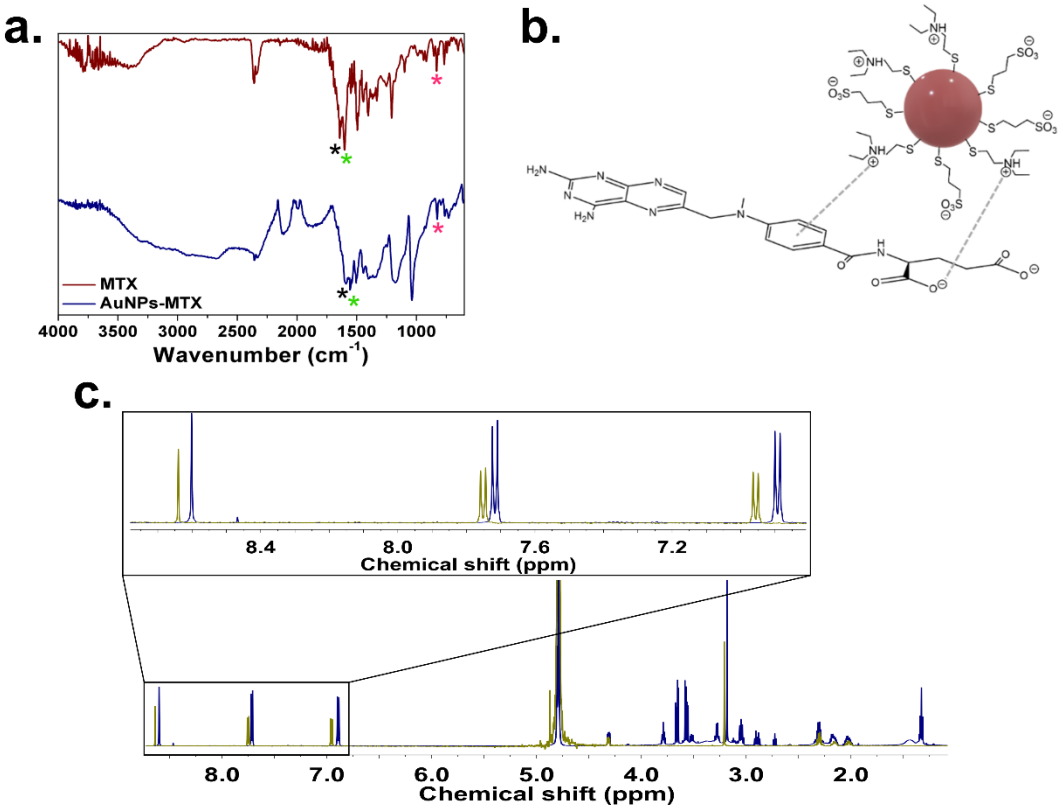

Figure 25. *a) FTIR superimposed spectra of AuNPs-MTX nanoconjugate (blue) and MTX (dark red). C=O stretching band (MTX 1643 cm^{-1}, AuNPS-MTX 1589 cm^{-1}) is marked with a black asterisk, the green asterisk represents the skeletal aromatic stretching band (MTX 1596 cm^{-1}, AuNPS-MTX 1557 cm^{-1}), and the magenta asterisk is used for the out of plane aromatic bending (MTX 830 cm^{-1}, AuNPS-MTX 830 cm^{-1}). Spectra were recorded in ATR mode on solid samples. b) chemical structure illustrating the AuNPs-MTX interaction, c) ^{1}H NMR superimposed spectra of AuNPs-MTX (blue) and MTX (dark yellow) alone; inset: aromatic portion of the spectra. The solvent of all spectra is D_2O (4.76 ppm, broad).*

In the AuNPs-MTX spectrum (blue line), the corresponding bands are shifted towards lower wavenumber values, the carboxylic acid band shifts to 1589 cm^{-1}, whereas the aromatic stretching band shifts to 1557 cm^{-1}; the out of plane bending band does not shift notably.

The vibration bands pertaining to the C=O stretching and to the aromatic stretching are shifted considerably, for the C=O band, $\Delta\nu$ = -54 cm^{-1}, for the aromatic band, $\Delta\nu$ = -39 cm^{-1}. An interaction between carboxyl group and aromatic group pertaining to MTX and the end group functionalities of the thiol ligands can be envisaged.

More in depth, NMR studies were carried out to understand the interaction. ^{1}H-NMR spectrum of AuNPs-MTX (blue) was compared with spectrum of free methotrexate (dark yellow) in **Figure 25c**; the inset is a detail of the aromatic portion of the spectrum, where only signals pertaining to the drug are present. In the rest of the spectrum, no visible difference in the chemical shift of the MTX related signals can be seen, whereas, in the 6.90-8.70 region a clear shift in the two doublets and one singlet aromatic signals of MTX is evident. The chemical shift values before and after are: δ=8.64, 7.76, 6.94ppm, before the interaction and δ=8.60, 7.72, 6.90 ppm after the interaction. All the MTX aromatic proton signals are more shielded after the interaction with the surface of the nanoparticle; as this is the only significant shift in the ^{1}H NMR spectra, it can be inferred that the aromatic portion of methotrexate is directly involved in the interaction with the thiols on the surface of the nanoparticles, presumably with the positively charged portion of DEA.[158]

These analyses support the hypothesis that the interaction between the drug and the AuNPs is of twofold nature: electrostatic, through the interaction of the carboxylate groups of MTX and the ammonium of DEA, and also a cation-π interaction between the ammonium and the aromatic moiety of MTX[159], as schematised in **Figure 25b**.

The formation of small sized and stable colloidal suspensions also upon MTX interaction makes the AuNPs stabilised with DEA and 3MPS in mixture particularly suitable for nanomedicine.

Small angle X-ray scattering (SAXS) measurements allowed to characterise the size and shape in solution of the as-synthesised nanoparticles and of the AuNPs-MTX nanoconjugate. **Figure 26** shows the scattering profiles of AuNPs and of AuNPs-MTX and the best fits according to a homogeneous sphere model with a lognormal distribution of the radius (in the lower inset), in accordance with the expected spherical shape of the AuNPs. The obtained values of the average radius and distribution width were (2.53 ± 0.23) nm for AuNPs sample and (2.49 ± 0.21) nm for the AuNPs-MTX, indicating that most of the nanoparticles have a diameter of 5 nm in both cases. A positive deviation of the experimental SAXS profiles from the model intensity for $q < 0.3$ nm^{-1} was observed. The inspection of the Guinier plot (shown for the pristine AuNPs in the upper inset of **Figure 26a**) and of the pair distance distribution functions obtained by indirect Fourier transform (**Figure 26b**) also suggests that the samples

contain a non-negligible fraction of particles with overall size larger than 5 nm. Allowing for a certain fraction of the spherical NPs to be structured within larger clusters, helped to fit the SAXS data at $q < 0.3$ nm^{-1} as well. The clusters were described by considering that a fraction of the spheres with 5 nm diameter is correlated by a fractal structure factor (fitting parameters reported in *Tables D7-D8*). The fractal dimension, the maximum distance for the correlations and the number density of spheres involved were best fitted to reproduce the SAXS data. The best-fit fractal dimension was 1.3 in both cases, the maximum correlation size was 107 nm for pristine AuNPs and 65 nm for AuNPs-MTX, whereas the fraction of particles involved in clusters increased from 28% to 45% with addition of MTX, due to a decrease of the number of particles in the non-clustered population, as inferred form the distributions shown in the lower inset of **Figure 26a**.

Hence the size of the gold nanoparticles does not relevantly change upon interaction with methotrexate, nor the presence of the drug triggers significant aggregation in the system.

In order to deeply understand the interaction with MTX, AuNPs before and after drug loading were studied by GISAXS and GIWAXS experiments at the P03 beamline (MINAXS), PETRA III in Hamburg (all details *vd*. *Appendix D1.5.*). The influence of MTX on *inter*- and *intra*- particles degree of order was studied and in **Figure 26c** the GISAXS and in **Figure 26d** the GIWAXS scattering profiles of AuNPs and AuNPs-MTX are compared. In the GISAXS profile of AuNPs (**Figure 26c**) a peak centred at 1.134 nm^{-1} for pristine gold nanoparticles is found; this peak is shifted to lower q values (0.64 nm^{-1}) after the interaction with MTX. This could confirm the non-covalent interaction between the thiols and the drug, as the interparticle distance increases when MTX is added (5.54 nm for pristine AuNPs, 9.82 nm for AuNPs-MTX), suggesting the presence of the drug on the surface of the AuNPs, which would increase the size of the shell surrounding the metal core (see inset of **Figure 26c**).

GIWAXS scattering profiles, shown in Figure 6d, show a Bragg peak centred at 26.8 nm^{-1} for pristine (111) AuNPs which substantially decreased and was slightly shifted to smaller *q*-values after drug interaction. A similar behaviour was found for the less prominent (200) peak at higher q values. Moreover, the lower intensity of the peak at about 22.5 nm^{-1} in **Figure 26d** associated with interaction between the thiols is completely gone after MTX addition. This confirms a strong influence on interparticle arrangement and a certain loss in the internal order of the AuNPs after being exposed to the drug. 2D GISAXS and GIWAXS data are collected in *Figure D7*.

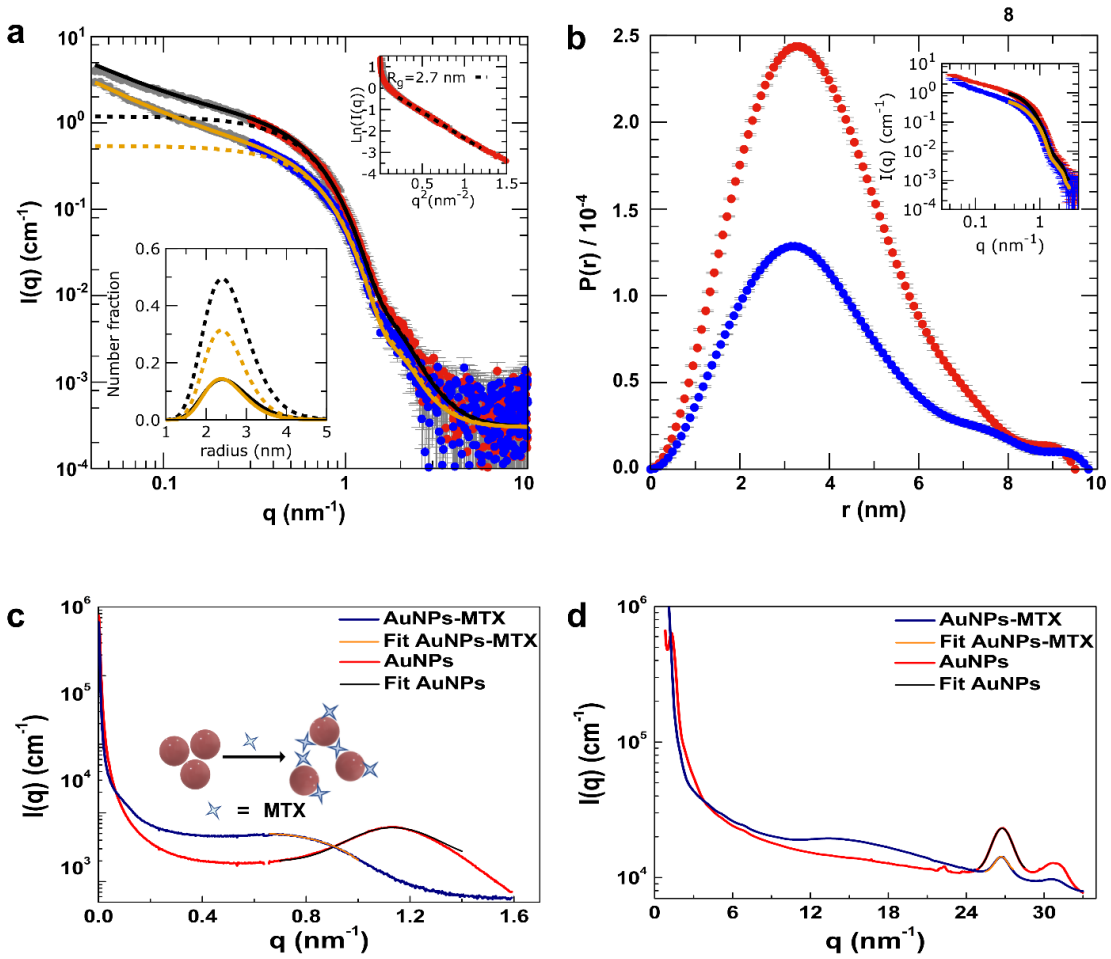

Figure 26. *a) SAXS profiles of AuNPs (red dots) and AuNPs-MTX (blue dots) with the relative best fit curves for a distribution of spheres (black and orange dotted curve, respectively). The fits considering a fraction of the spheres to be structured within < 100 nm clusters are reported as solid lines. The corresponding distributions for the sphere radius are shown in the lower inset. In the upper inset, the Guinier plot for AuNPs is shown together with the linear fit* $ln(I)=ln(I_0)-(R_g/3)q^2$*, according to a radius of gyration* $R_g=2.7$*. b) Pair distance distribution functions obtained by indirect Fourier transform from the AuNPs (red dots) and AuNPs-MTX (blue dots) SAXS data. The corresponding fits are shown in the inset. GISAXS superimposed profiles of AuNPs and AuNPs-MTX (c), GIWAXS superimposed profiles of pristine and drug loaded AuNPs (d). Best fits are superimposed on the curves. Inset of c) schematic depiction of AuNPs and AuNPs-MTX after the interaction. Peaks centres, GISAXS: pristine AuNPs, 1.13* nm^{-1}*; AuNPs-MTX, 0.64* nm^{-1}*; GIWAXS: pristine AuNPs, 26.8* nm^{-1}*; AuNPs-MTX, 26.7* nm^{-1}*.*

2.2.1.b. Study of load and release of MTX, cell viability and the uptake of AuNPs

To evaluate the possibility of the use of the system as a drug nanocarrier, the *Molar Drug Encapsulation Efficiency (η%)* and *Drug Loading (L%)* were studied, evaluating the quantity of loaded MTX via UV-Vis with the calibration curve of MTX (R^2=0.9994; ε_0 = (20,540 ± 2630) M^{-1} cm^{-1}) (*Figure D3b*)[160]. The obtained *η%* was optimized to be 70% by using the AuNPs/MTX 5:1 weight ratio, testing the loading in different AuNPs/MTX weight ratios as reported in *Table D3*. The samples used for the cell studies were the 1/20, 1/1 and 5/1 wt/wt ratios, with respective final concentrations of nanoparticles of 0.5 µg/mL, 10 µg/mL, and 50 µg/mL.

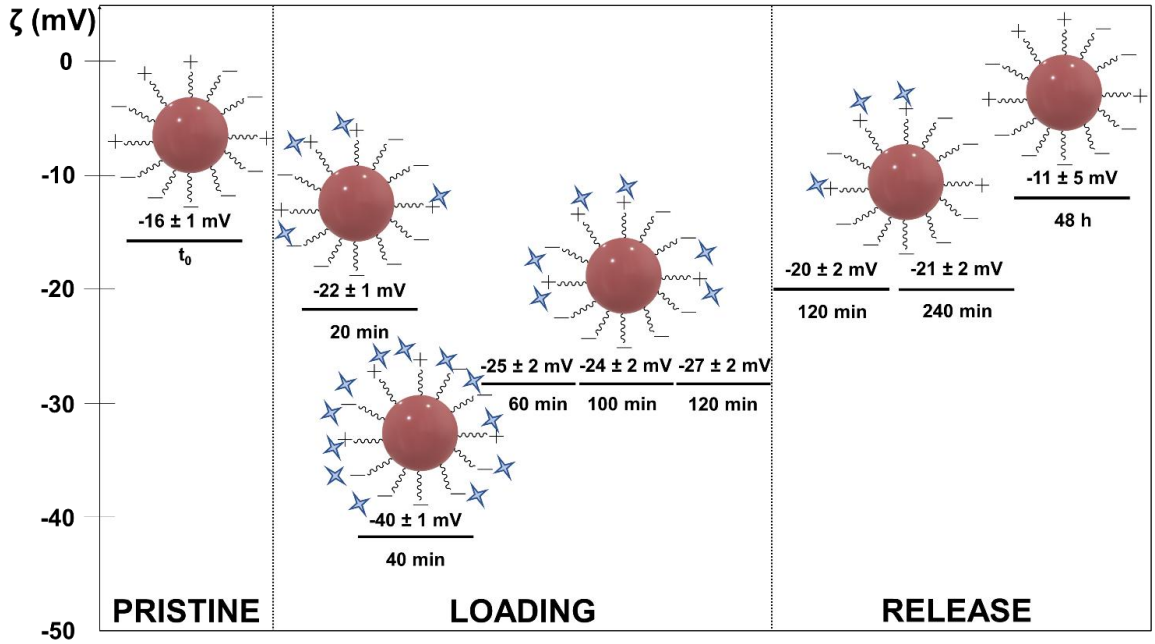

Figure 27. *Study of the surface ζ-potential in H_2O_{up} of pristine, loaded and released AuNPs (AuNPs/MTX 5/1 wt/wt), at different time points during the loading (every 20 minutes up to 2 hours) and release (after 2, 4 and 48 hours) process. The blue star represents MTX.*

The ζ-potential provides information on the surface charge of the nanoparticles and on the loading and release of the drug from the surface of the nanoparticles. In **Figure 27**, a study over time of the ζ-potential of AuNPs is reported. The gold nanoparticles used in this study are functionalised with the two thiols, which at pH = 7 exhibit two charges, a negative (3MPS) and a positive (DEA) one.[161,162] As a consequence of the two charges on the AuNPs, the surface charge is a result of the net sum of the two. The value of the ζ-potential was found equal to (-16 ± 1) mV, in accordance with the presence of the different charges, and

with the molar ratio between the two thiols calculated from the NMR (it was found to be *ca.* 1/2 in favour of 3MPS, *cfr*. **Figure 14a**). As shown in **Figure 27**, after 40 minutes, the value reaches a minimum of ζ-potential = (-40 ± 1) mV, and subsequently, after 60 minutes and for the remaining hour of the reaction sets to a value of around -30 mV, with a final value at 2 hours of ζ-potential = (-27 ± 2) mV. After the loading, the release of the drug from the AuNPs was evaluated, with the value of the ζ-potential increasing to (-21 ± 2) mV after 4 hours and reaching the value (-11 ± 5) mV after 48 h, which could be ascribed to a complete release of MTX loaded on AuNPs. The ζ-potential trend during the loading and release processes indicates that the positive charge on the surface of the AuNPs is partially shielded by the presence of MTX. This suggests that the interaction between the nanostructure and the drug is mainly driven by DEA-methotrexate interaction.

To assess the long-term stability of AuNPs at 37°C in DMEM-F12 culture medium, UV-Vis studies in time were carried out. The aggregation dynamics can be studied by following the shift of the λ_{LSPR} over time; it was found that the aggregation over 14 days was noticeable in the first two days, with a wavelength value of 520 nm for the pristine AuNPs, which increased to only 528 nm after 2 days in DMEM-F12 at 37°C and stayed stable at that value up to 14 days (*Figure D8*).

Pristine and MTX loaded AuNPs were used to assess the cell viability on neuroblastoma SJNKP and IMR5 cell lines, by MTT assays. The treatment was performed with a range of concentration of MTX on AuNPs, (0.015-0.124 μM) as shown in **Figure 28** and resume in **Table 3**. SJNKP and IMR5 cells were treated for 48 h and cell viability was evaluated by MTT. The number of seeded cells was $5x10^3$ cells/well. All three concentrations of AuNPs loaded with the respective MTX concentrations show a significant effect, compared to both SJNKP and IMR5 control cells. The values ***p = 0.0005 and ***p = 0.0006 are obtained for 0.015 μM MTX on AuNPs 0.5 μg/mL, for SJNKP and IMR5, respectively, with cell viability (43.40 ± 2.8) % for SJNKP (number of cells 17360 ± 3140) and (52.03 ± 4.24) % for IMR5 (number of cells 20810 ± 5000); ***p=0.0004 and ***p=0.0003 are related to 0.031 μM on AuNPs 10 μg/mL for SJNKP and IMR5, respectively, with cell viability (42.38 ± 1.98) % for SJNKP (number of cells 16950 ± 2050) and (48.92 ± 2.13) % for IMR5 (number of cells 19570 ± 3730); ***p=0.0007 and ***p=0.0008 refer to 0.124 μM on AuNPs 50 μg/mL for SJNKP and IMR5, respectively, with cell viability (45.75 ± 5.59) % for SJNKP (number of cells 18300 ± 4130) and (52.90 ± 8.14) % for IMR5 (number of cells 21160 ± 5300). 0.015 μM free MTX didn't show any significant effect, compared to control cells, while 0.124 μM free MTX shows a significant effect compared to SJNKP and IMR5

control cells; ***p=0.0005; ***p=0.0009, respectively, with cell viability (44.11 ± 5.29) % for SJNKP (number of cells 17650 ± 3050) and (53.69 ± 3.04) % for IMR5 (number of cells 21480 ± 6870). The lowest concentration of AuNPs, loaded with 0.015 µM of MTX, show a significant effect compared to the free drug in both cell lines: ***p=0.0004; **p=0.002, respectively. 0.031 µM of MTX bound to 10 µg/mL of AuNPs shown a significant effect in reducing cell viability of SJNKP and IMR5 cells, compared to the free drug (0.031 µM) with *p=0.02 and *p=0.04, respectively. Free nanoparticles did not show any cytotoxic effect on SJNKP cell line, while a mild cytotoxic effect for the highest concentration (50 µg/mL) was observed on IMR5 cells, with *p=0.03. This cytotoxicity occurred in small cases of experiments, which can be considered negligible for further studies.

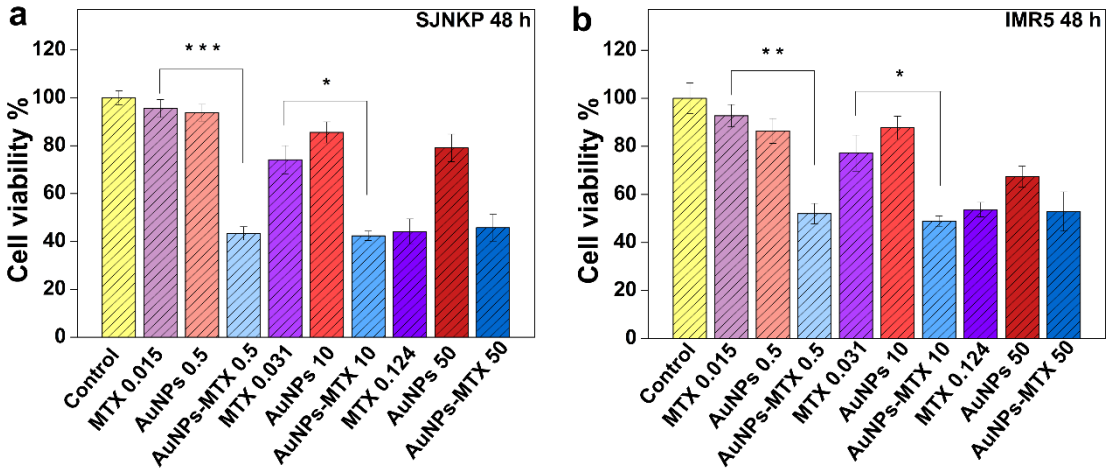

Figure 28. *a, b) MTT assays at 48 hours for low MTX concentrations. The nanoconjugate is compared with pristine AuNPs and drug at three different AuNPs concentrations (0.5 µg/mL, 10 µg/mL, 50 µg/mL). MTX concentrations on AuNPs-MTX and free MTX are 0.015 µM, 0.031 µM, 0.124 µM; loaded on AuNPs 0.5 µg/mL, 10 µg/mL, 50 µg/mL, respectively; ***p = 0.0009 and **p = 0.004 are obtained for 0.015 µM MTX on AuNPs 0.5 µg/mL, for SJNKP and IMR5, respectively; *p=0.03 and *p=0.04 are related to 0.031 µM on AuNPs 10 µg/mL for SJNKP and IMR5, respectively.*

A dose–response study of MTX using an MTT assay showed that MTX exerted significant cytotoxic effects on SJNKP cells starting from 0.05 µM, with IC50 values of 0.0793 µM at 24 h and 0.0220 µM at 48 h. In IMR5 cells, MTX reduced cell viability from 0.2 µM at 24 h (IC50 = 0.1080 µM) and from 0.05 µM at 48 h (IC50 = 0.0318 µM). Based on these results,

three MTX concentrations were selected for binding to AuNPs: 0.015 μM (AuNPs 0.5 μg/mL), 0.031 μM (AuNPs 10 μg/mL), and 0.124 μM (AuNPs 50 μg/mL).

Treatment Condition	Cell Line	Cell Viability (%)	Cell Number (mean ± SD)
0.015 μM MTX on AuNP 0.5 μg/mL	SJNKP IMR5	43.40 ± 2.8 52.03 ± 4.24	17360 ± 3140 20810 ± 5000
0.031 μM MTX on AuNP 10 μg/mL	SJNKP IMR5	42.38 ± 1.98 48.92 ± 2.13	16950 ± 2050 19570 ± 3730
0.124 μM MTX on AuNP 50 μg/mL	SJNKP IMR5	45.75 ± 5.59 52.90 ± 8.14	18300 ± 4130 21160 ± 5300
0.015 μM Free MTX	SJNKP IMR5	(No significant effect vs control)	
0.124 μM Free MTX	SJNKP IMR5	44.11 ± 5.29 53.69 ± 3.04	17650 ± 3050 21480 ± 6870
Pristine AuNP 50 μg/mL	SJNKP IMR5	(No cytotoxic effect) (Mild cytotoxic effect)	

Table 3. *Cytotoxicity of MTX-loaded AuNPs on neuroblastoma cells. SJNKP and IMR5 cell viability (%) and cell counts after 48 h treatment with the indicated concentrations of free MTX, pristine AuNPs, or MTX-conjugated AuNPs. Data are presented as mean ± SD.*

Concentrations of MTX loaded onto AuNPs in the range 0.015 – 0.031 μM induce a marked cytotoxic effect compared to the free MTX. Pristine AuNPs demonstrated to be prevalently not cytotoxic towards NB cell lines. Considering the high toxicity of MTX alone, this strategy allows to deliver a lower amount of the drug, following a synergic and potentiated effect upon loading. These results suggest a new and promising therapeutic approach in clinical applications for the for the treatment of neuroblastoma tumours. Further studies will be performed to investigate the localisation of this nanosystem in neuroblastoma tumour mass and the biochemical and molecular mechanism of cytotoxicity.

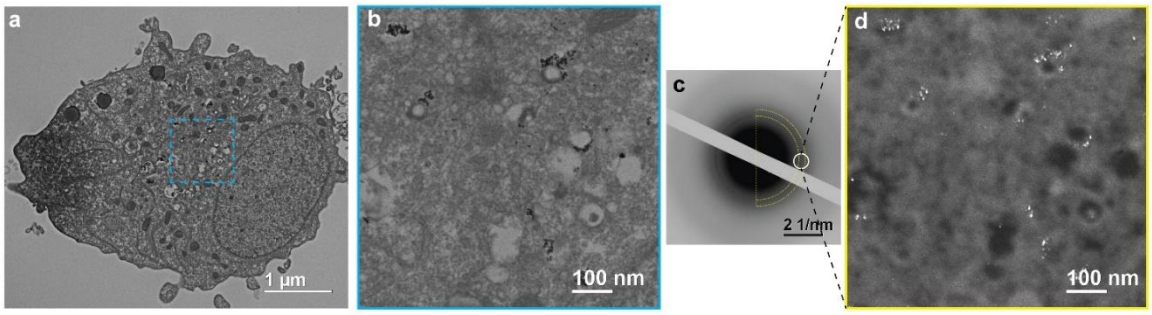

Figure 29. *Morphostructural observations of AuNPs uptake by neuroblastoma cells. a) Cross-section of IMR5 cell with smallest AuNPs nanoaggregates internalised near perinuclear region (blue dot line square) and b) the corresponding magnified area. c) EDP taken from Figure 29b) shows diffraction rings belonging to the face-centred-cubic Au phase (yellow dot line arcs). d) DF TEM image of Figure 29a) obtained by selecting both reflections of (111) and (200) of the AuNPs, labelled by a white circle in Figure 29c). Intense white spots belong to smallest Au nanoparticles.*

Direct imaging evidence of AuNPs uptaken by cells, TEM images confirm the potential ability of the AuNPs to be well sequestered by IMR5 cells (**Figure 29**). Smallest aggregates of dark nanoparticles distributed around the perinuclear region are displayed in the magnified image of bright-field TEM image (**Figure 29b**). To identify experimentally the internalised nanoparticles, selected area electron diffraction experiments were carried out. This allowed to characterise the atomic and structural compositions of the nanoconjugates. The electron diffraction pattern (EDP) shows two weak diffraction rings produced by the polycrystalline material in a random orientation (**Figure 29c**). The weak diffraction signal is due to the high diffusion beam of the resin, embedding the cell. By measuring the d-spacing of the diffraction rings, we were able to identify the face-centred-cubic (fcc) Au with a space group *Fm*3*m* of the (111) and (200) Au reflections (yellow dot line arcs). To visualize the crystalline feature of the AuNPs, dark-field (DF) imaging was applied. DF images have been obtained by placing the objective aperture around both diffracted beams of the Debye rings (white circle of **Figure 29c**). Therefore, the DF image well shows bright dots in **Figure 29d**, having same position in **Figure 29b** (dark dots) and confirming experimentally the golden nature of the nanoparticles. The smallest nanoparticles, efficiently uptake by cell, are observed either isolated or nanoaggregate states probably dependent from the internalization mechanisms of the engaged biological processes.

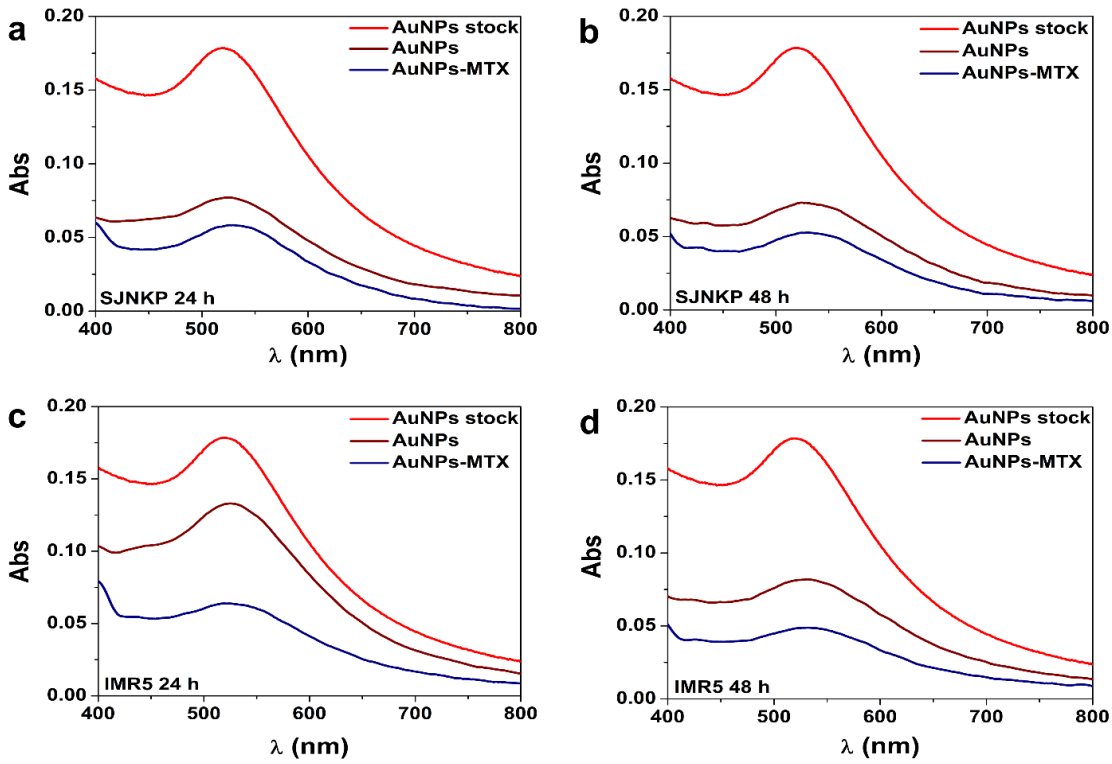

Figure 30. *UV-visible spectra of AuNPs (dark red) and AuNPs-MTX (blue) compared to AuNPs stock solution (red) permeation tests, at different time points (24 and 48 h) on SJNKP a), b) and IMR5 c), d) cell lines.*

The permeation of AuNPs inside the cell membrane was evaluated *via* UV-vis; absorbance intensity of AuNPs and AuNPs-MTX supernatant solution after 24 and 48 h of MTT assay were compared to the intensity of the stock AuNPs solution (**Figure 30**). By doing so, it was possible to infer by difference the relative quantity of AuNPs that permeated inside the cells at 24 and 48 h. As seen in **Figure 30a,b**, IMR5 cells showed a higher permeation of AuNPs-MTX compared to pristine AuNPs (24 h: 25% AuNPs, 63% AuNPs-MTX; 48 h: 54% AuNPs, 73% AuNPs-MTX), at both time points. The same behaviour can be observed for SJNKP cells, see **Figure 30c,d** (24 h: 57% AuNPs, 67% AuNPs-MTX; 48 h: 58% AuNPs, 70% AuNPs-MTX). This experiment suggests that the synergistic effect of the small size of the hydrophilic nanoparticles, together with the presence of an antifolate drug, increases the absorption of the probe by the cells.

This work reports on highly hydrophilic, small, stable, and non-cytotoxic gold nanoparticles (AuNPs) as drug carriers for cancer therapy. Methotrexate (MTX), a lipophilic anti-folate drug, was successfully loaded onto thiol-functionalized AuNPs, improving its bioavailability while preserving colloidal stability and reducing cytotoxicity. Advanced characterizations

(ζ-potential, NMR, XPS, FTIR, GIWAXS/GISAXS, SAXS) revealed that MTX interacts with surface thiols through both electrostatic and cation–π interactions. In vitro tests on two neuroblastoma cell lines (SJNKP and IMR5, n-Myc overexpressed) showed that pristine AuNPs were non-cytotoxic, whereas AuNPs-MTX exhibited significantly higher cytotoxicity compared to free MTX, likely due to improved cellular penetration. These conclusions highlight the potential of hydrophilic AuNPs as effective drug delivery systems, warranting further in vivo studies.

2.2.2. Bioconjugate AuNPs-TZ

MicroRNAs (miRNAs) are fragments of RNA and they play a role in controlling how genes are expressed. They can act in two opposite ways: as tumour suppressors or as oncogenic drivers, supporting tumour growth. This duality makes them both fascinating and challenging study and exploit their potential is the new tools in cancer therapy.[163,164,165].

Among the MiRNAs, miR-200c has attracted attention. In earlier studies, overexpressing miR-200c in ovarian cancer cells reduced their growth.

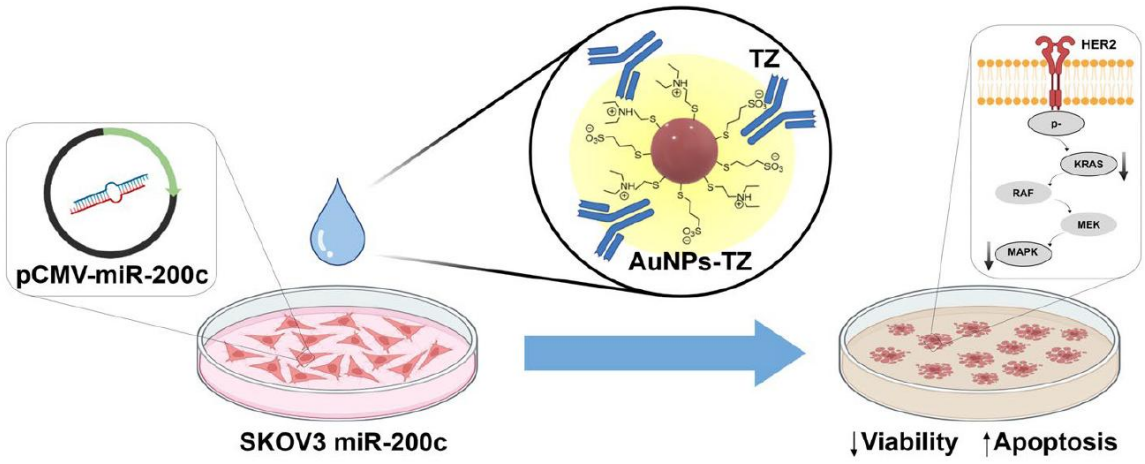

Figure 31. *Overexpression of miR-200c in SKOV3 cells and subsequent treatment with AuNPs-TZ reduces cell viability and induces apoptosis in SKOV3 cells via the HER2/MAPK pathway.*

Another important player in ovarian cancer is HER2, a receptor encoded by the erbB2 gene. When overproduced, as it is in about 10–30% of ovarian cancers, HER2 activates growth-promoting pathways, driving uncontrolled cell division and metastasis. A well-known drug, Trastuzumab (Herceptin®), was developed to block HER2 activity and has shown great success in breast cancer. Unfortunately, its effect in HER2-positive ovarian cancer is far less impressive, partly because of resistance mechanisms[166].

Gold nanoparticles (AuNPs), when carefully functionalized with thiol groups, offer a promising solution. Their ability to remain stable in biological environments, accumulate selectively in tumour tissue, and serve as carriers for therapeutic molecules makes them ideal candidates for drug delivery. With this in mind, our approach was to design a smart nanocarrier system that combines the tumour-suppressing activity of miR-200c with the targeted anti-HER2 action of Trastuzumab (TZ). This dual strategy could not only enhance treatment efficacy but also help to overcome resistance in HER2-positive ovarian cancer.

In this respect, recent studies have proven that antibodies can be delivered on the surface of gold nanoparticles, serving as targeting or therapeutic agents.[167],[168] While antibody-loaded AuNPs have shown great promise in targeted therapy by enhancing drug delivery and tumour targeting, combining this approach with miRNA-based therapies might offer a novel synergistic strategy to tackle complex diseases like cancer (scheme in **Figure 31**).

TZ was loaded on the AuNPs, through a mild procedure exploiting non-covalent interactions occurring between the surface thiols and the antibody (described in detail in *Appendix D1.7.*). The extensive characterization of the pristine AuNPs has already been reported by us previously (*vd.* 2.1.).

As shown in the UV-Vis spectra in **Figure 32a**, the plasmon band of AuNPs (red), initially centred at 516 nm, shifts to 525 nm after TZ loading (cyan), as highlighted in the zoomed-in section. This red shift suggests that the nanoparticles move closer to each other due to the presence of TZ, while still maintaining excellent colloidal stability. Only in the AuNPs-TZ spectrum a peak at *ca.* 280 nm can be seen, ascribed to the antibody's presence. **Figure 32b** shows the ζ-potential of the nanoparticles before and after the loading process (red bar and cyan bar, respectively). After the loading, the ζ-potential switches from a negative value, (-16 ± 1) mV, to a positive one, (19± 1) mV. This can be an indication of the negatively charged 3MPS thiol interacting with the antibody, thus leaving a positive charge on the surface of the nanoparticles. The DLS graph, shown in **Figure 32c**, highlights an increase in the hydrodynamic diameter from (9 ± 2) nm to (825 ± 300) nm, with a smaller population centred at *ca.* 150 nm. However, such a dramatic change in the diameter shown by the DLS graph is likely influenced by the increased complexity when a macromolecule such as TZ is inserted into the system. A decrease in the interparticle distance (as shown by the UV-visible spectrum) is to be expected with the presence of an antibody on the surface of the gold nanoparticles. As it can be observed by the FESEM image in **Figure 32d** small, isolated nanoparticles are present, together with larger aggregates probably arising from the film

deposition and drying procedure. It can be observed that AuNPs are quite uniformly dispersed in the antibody medium, without AuNPs coalescence.

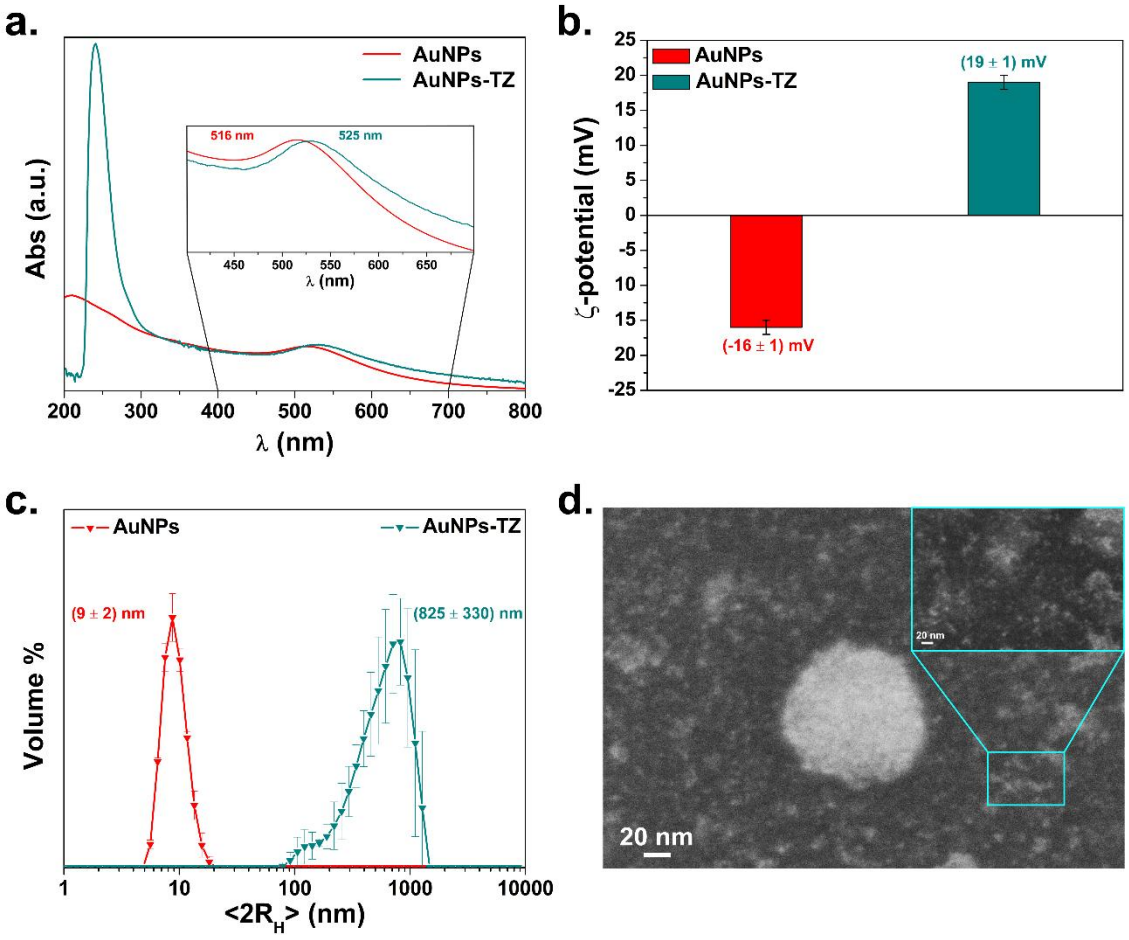

Figure 32. *a) superimposed UV-vis spectra of AuNPs (red) and loaded AuNPs-TZ (cyan); b) ζ-potential values of AuNPs (red) and AuNPs-TZ (cyan); c) DLS graph of AuNPs (red) and AuNPs-TZ (cyan); All spectra are recorded in H_2O_{up}. d) FESEM image of drop-cast AuNPs-TZ.*

Two different weight ratios were tested to optimize the loading: a 1:2 and 1:1 ratio between the antibody and gold nanoparticles. As shown in **Figure 33a**, it was found that the 1:1 ratio resulted in a (41 ± 4) % loading percentage, and thus, this optimized weight ratio was chosen for the cell studies. The TZ concentration in AuNPs-TZ nanoconjugate was calculated from the Bradford assay, equal to 0.041 µg/ml for a 0.1 µg/ml nanoparticles concentration. **Figure 33b** shows the release of the antibody from the AuNPs. The results show a non-relevant difference in the release percentage after one hour at 37°C and 48 hours, with a release (in

detail in *Appendix D1.7.*) percentage between 60% and 40%, thus supporting the labile, non-covalent interaction.

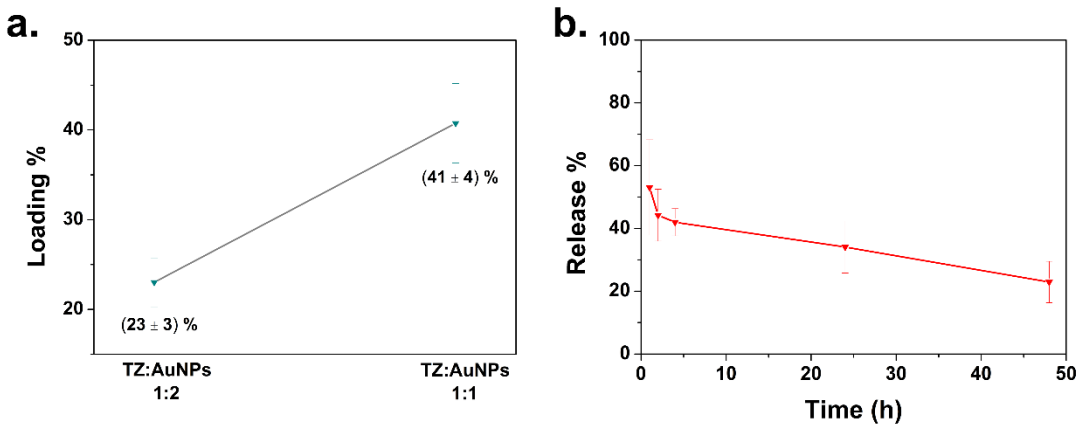

Figure 33. *Loading a) and release b) curves for AuNPs-TZ.*

To assess the cytotoxicity of AuNPs and the AuNPs-TZ nanoconjugates, SKOV3 Vector and SKOV3 miR-200c were treated at three different concentrations: 0.1, 0.5, and 1 µg/ml and at three time points 24, 48, and 72 h. AuNPs alone did not affect the viability of the parental (dark grey-colored bars) and miR-200c transfected cells (light grey-colored bars) at all three concentrations and time points (**Figure 34a,b,c**). On the contrary, at 48 h, AuNPs-TZ treatment significantly decreased SKOV3 miR-200c viability (**Figure 34b**, pink-colored bars). Significant differences in cell viability emerged at 48 hours (**Figure 34b**), with SKOV3 miR-200c cells showing a stronger response to AuNPs-TZ treatment than vector controls, especially at the lowest concentration (0.1 µg/ml). At 72 hours, the effect on the viability of AuNPs-TZ (**Figure 34c**) treatment decreased in miR-200c transfected cells at 0.1 and 0.5 µg/ml. This suggests a time-dependent and miR-200c-specific sensitization to AuNPs-TZ. We also compared the effect of miR-200c and vector control in untreated or TZ-treated conditions (0.041 µg/ml, which corresponds to the concentration of TZ on the surface of the AuNPs at 0.1 µg/ml nanoparticles concentration) over 24, 48, and 72 hours (**Figure 34c**). The results showed that TZ treatment slightly decreased cell viability in the parental and the miR-200c transfected cell line (**Figure 34d**).

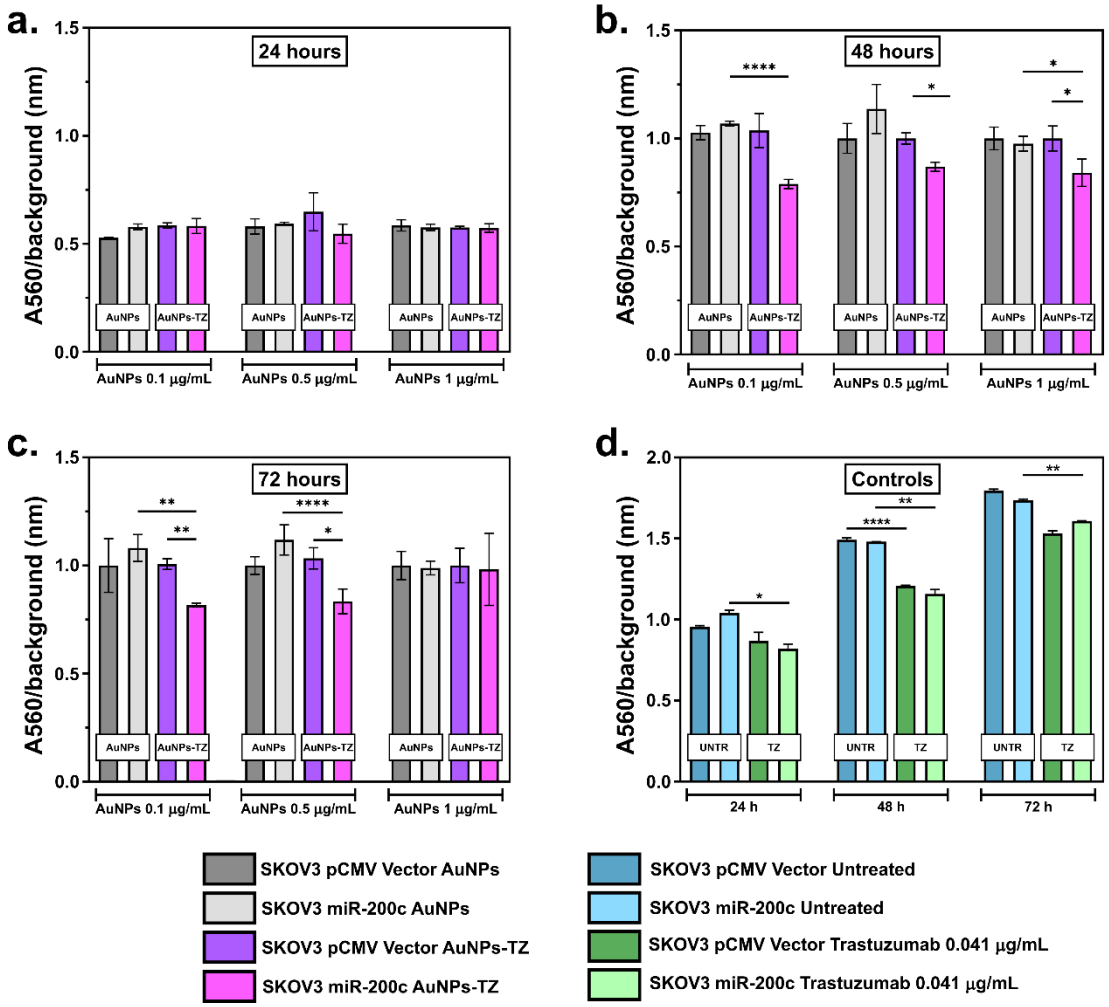

Figure 34. *a),b) and c) depict the absorbance measurements (A560/background in nm) of SKOV3 cells treated with various concentrations of gold nanoparticles (AuNPs), and AuNPs conjugated with trastuzumab (AuNPs-TZ) over different time points (24, 48, and 72 hours). d) compares the effects of miR-200c and vector control under untreated or TZ-treated conditions (0.041 µg/ml) over 24, 48, and 72 hours. Dark gray bars represent the SKOV3 pCMV Vector (V) cell line, while light gray bars indicate SKOV3 miR-200c-transfected cells treated with pristine AuNPs. Purple bars depict SKOV3 V. cells, and pink bars represent SKOV3 miR-200c cells treated with AuNPs-TZ. Blue bars represent the untreated SKOV3 Vector cells, while light blue is the miR-200c transfected ones; dark green and light green bars depict TZ treated vector and miR-200c transfected cells, respectively. The results are presented as mean ± SD of three replicates measured at A560nm, obtained from three experiments. (*p<0.05, **p<0.01, ***p<0.001, ****p<0.0001). Experimental details Appendix D1.8.*

However, TZ treatment did not impact overall cell viability, as the parental and miR-200c cells remained viable at 72 hours (**Figure 34d**). These results indicate that: a) AuNPs alone do not have any cytotoxic effect at all three concentrations (0.1, 0.5, and 1 μg/ml) over time (up to 72 h) (**Figure 34a,b,c**); b) the presence of miR-200c sensitized SKOV3 cells to TZ treatment and c) 0.1 μg/ml AuNPs-TZ concentration at 48 h had the most significant and synergic effect on SKOV3 miR-200c viability over time. Thus, the 0.1 μg/ml concentration of AuNPs-TZ and the time point of 48 h were chosen for further studies.

To further confirm the cytotoxic effect of AuNPs-TZ and miR-200c on SKOV3 cells, we evaluated whether the observed decrease in cell viability was due to apoptosis. While untreated or AuNP-treated cells remained largely viable, TZ treatment induced a modest increase in late apoptosis, particularly in miR-200c-transfected cells. The strongest effect was observed with the combined AuNPs-TZ and miR-200c treatment, which reduced cell viability to ~64% and significantly increased late apoptotic and necrotic populations. These results indicate a synergistic effect, where miR-200c enhances the apoptotic response of SKOV3 cells to AuNPs-TZ beyond what is achieved with each treatment alone.

For a precise localization of the AuNPs loaded with TZ in treated cells, TEM images were analysed to find any morphological differences between the untreated and treated SKOV3 and SKOV3 miR-200c cells. *Figure D9* and **Figure 35** show TEM micrographs of untreated vector and miR-200c transfected cells and AuNPs-TZ treated miR-200c transfected cells, respectively. SKOV3 cells, which are a model of ovarian cancer, typically show features associated with aggressive tumours. They have a very large nucleus compared to the cytoplasm, indicating high proliferation, and their cytoplasm is poorly differentiated, meaning the cells are not specialized or well-structured. The connections between neighbouring cells are weak and underdeveloped, and their surface is covered with irregular and disorganized microvilli (*Figure D9A-C*). When miR-200c is introduced, however, these cells begin to change their appearance and behaviour. They start to look more like healthy epithelial cells: their cell–cell junctions become stronger and more developed, and the microvilli on their surface appear more numerous and well-organized, especially along the borders of the structures they form together. In other words, miR-200c seems to push SKOV3 cells away from a highly malignant state and toward a more differentiated and orderly epithelial-like phenotype (*Figure D9D-F*).

48 hours after treatment with the AuNPs-TZ nanoconjugates, the SKOV3-miR-200c cells show clear signs that the nanoparticles are actively interacting with their internal structures. Under the microscope (**Figure 35**), the AuNPs can be seen gathering close to the cell

membrane, likely because some are still being taken up, or because they remain attached to the surface. Many nanoparticles are also found inside the cell, particularly in acidic compartments and multivesicular bodies, which suggests they mainly enter through endocytosis, a natural uptake process, and that part of them are directed towards degradation.

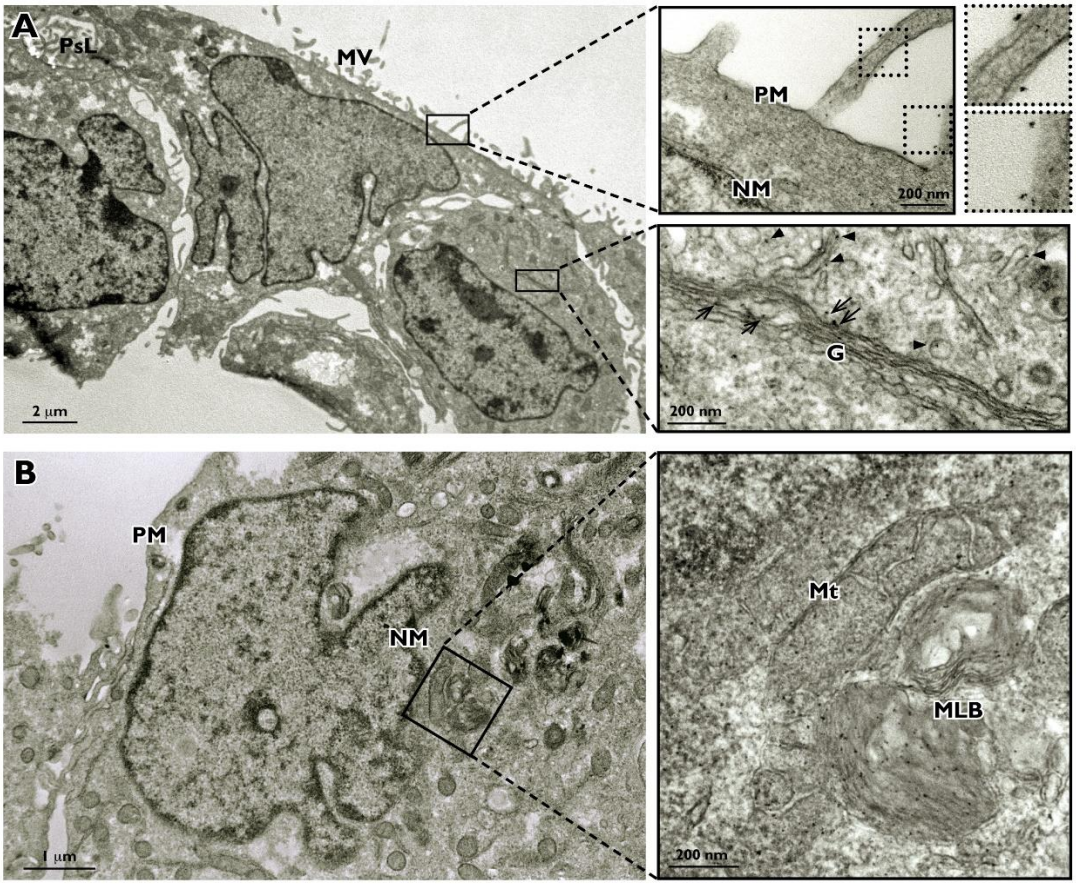

Figure 35. *Intracellular distribution of AuNPs-TZ in miR-200c-transfected SKOV3 cells. A-B: at 48 hours post-treatment, AuNPs-TZ are still observable near the plasma membrane (inset in A). They also appear concentrated in multilamellar structures associated with multivesicular bodies, associated with Golgi membranes (black arrows in the inset in A), and within several intracellular vesicles (black arrowheads in the inset in B). Sparse AuNPs are also observed within the mitochondria (see inset in B), near the nuclear membrane, and free in the cytoplasm. [Legend: MV: microvilli; PM: plasma membrane; NM: nuclear membrane; PsL: pseudolumen; Mt: mitochondrion; G: Golgi apparatus. TEM micrographs; staining: uranyl acetate/lead citrate].*

This study explored the use of small, hydrophilic thiol-functionalized gold nanoparticles (<10 nm) to deliver trastuzumab into HER2-positive ovarian cancer cells (SKOV3). These

cells are normally resistant to TZ and lack miR-200c. The AuNPs provided high stability, biocompatibility, and an efficient non-covalent TZ loading, (41 ± 4) %. When combined with miR-200c overexpression, AuNPs-TZ treatment led to a marked reduction in cell viability, increased apoptosis. TEM analysis revealed that AuNPs-TZ were internalized via endocytic pathways, localized in endosomes and multivesicular bodies, and sometimes free in the cytoplasm, suggesting receptor-mediated uptake.

Compared to free TZ or miR-200c alone, the combination therapy was significantly more effective, indicating a synergistic mechanism: AuNPs improve TZ delivery and stability, while miR-200c downregulates KRAS, a key player in the HER2/MAPK pathway.

Morphological changes in SKOV3-miR-200c cells (greater epithelial differentiation and junction formation) further supported improved nanoparticle uptake.

2.3. Dye-stabilized Gold Nanoparticles

Among fluorescent probes, fluorescein is one of the most widely used. The chemical structure is reported in **Figure 36a**[169] Fluorescein rapidly became one of the most ubiquitous tools in biological research for its intense fluorescence, pH sensitivity (**Figure 36c**), chemical stability, and low cytotoxicity. Today, fluorescein is a reference standard in biomedicine, particularly for its strong fluorescence and sensitivity at pH around neutrality. Since most biological systems operate under physiological conditions (pH ~7.3), fluorescein has become a benchmark probe for monitoring pH variations in living cells.

Fluorescein isothiocyanate (FITC), a functional derivative of fluorescein (**Figure 36b**), maintains these properties and offers additional versatility. Through its isothiocyanate group, FITC can easily conjugate with molecules containing amine groups, including fluorophores, targeting agents, proteins, polymers, or small molecules. The resulting thiourea linkage is stabilized by hydrogen bonding.[170]

To combine the plasmonic properties of gold nanoparticles with fluorescence-based tracking, we functionalized AuNPs with synthetic derivatives of FITC. This strategy allowed us to create a hybrid nanomaterial in which the optical features of FITC complement the stability and biocompatibility of AuNPs, enabling both functional delivery and imaging capabilities.

To obtain gold nanoparticles with FITC covalently bound to their surface, we first derivatized FITC using cystamine (Cys2) (see synthetic protocol, *Appendix B1.1.1.*) and 4-Aminophenyl disulfide (Ani2). Both molecules were selected because contain an amine group and a thiol group. The amine group was exploited to react with the isothiocyanate

moiety of FITC[171] to obtain the thiourea derivative, while the thiol group (temporarily protected as a disulfide to prevent unwanted nucleophilic attack on FITC) served as the anchoring functionality for covalent attachment of the resulting fluorophore to the gold nanoparticle surface.

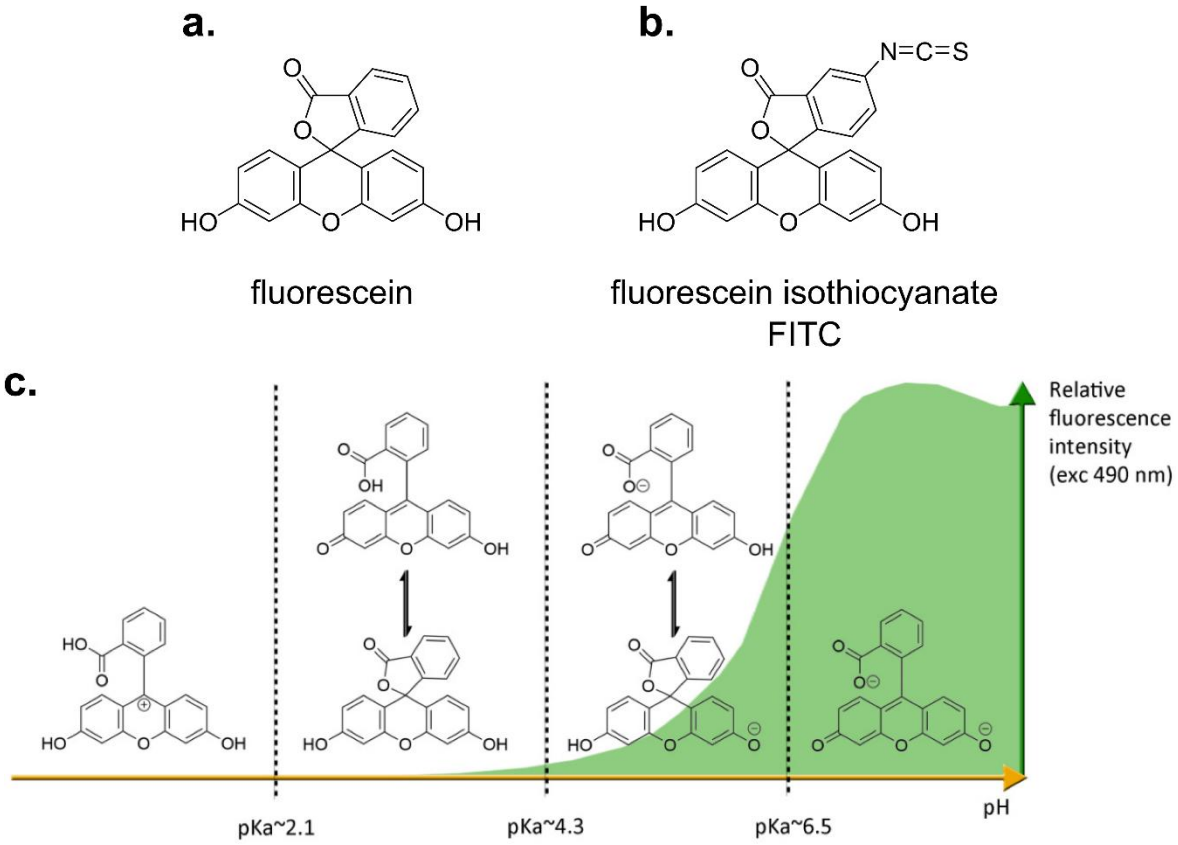

Figure 36. *Chemical structure of a) fluorescein and b) fluorescein isothiocyanate (FITC); c) Ionic forms of fluorescein according to the pH domains and their relative fluorescence intensities*[170].

The amine group was exploited to react with the isothiocyanate moiety of FITC[172] to obtain the thiourea derivative, while the thiol group (temporarily protected as a disulfide to prevent unwanted nucleophilic attack on FITC) served as the anchoring functionality for covalent attachment of the resulting fluorophore to the gold nanoparticle surface. To explore whether the chemical environment of the linker could influence the optical of the dye, we chose two different molecules to derivatize the FITC: one with a short aliphatic chain (two carbon atoms, Cys2) and one with an aromatic ring (Ani2). The synthetic schemes are described in detail in *Appendices C1.1 and C1.2*. The chemical structures of the two FITC derivatives obtained, CysFITC and AniFITC, are shown in **Figure 37a, b**. The ^{1}H, ^{13}C-NMR spectra of

the synthesized products were challenging to interpret because the chromophore exists in multiple tautomeric forms depending on pH (see **Figure 36c**), but it was possible the products identification. The spectra were acquired in D_2O under basic conditions in the presence of K_2CO_3, in order to favour the predominance of the tautomeric form shown on the right in **Figure 36c**. The ^{1}H-NMR spectra of CysFITC and AniFITC showed notable differences in the aromatic region when compared to commercial FITC (*Figure B3a*). The aromatic signals of CysFITC and AniFITC shift to higher fields, and this observation supports the substitution of the electron-withdrawing isothiocyanate group with a thiourea derivative.

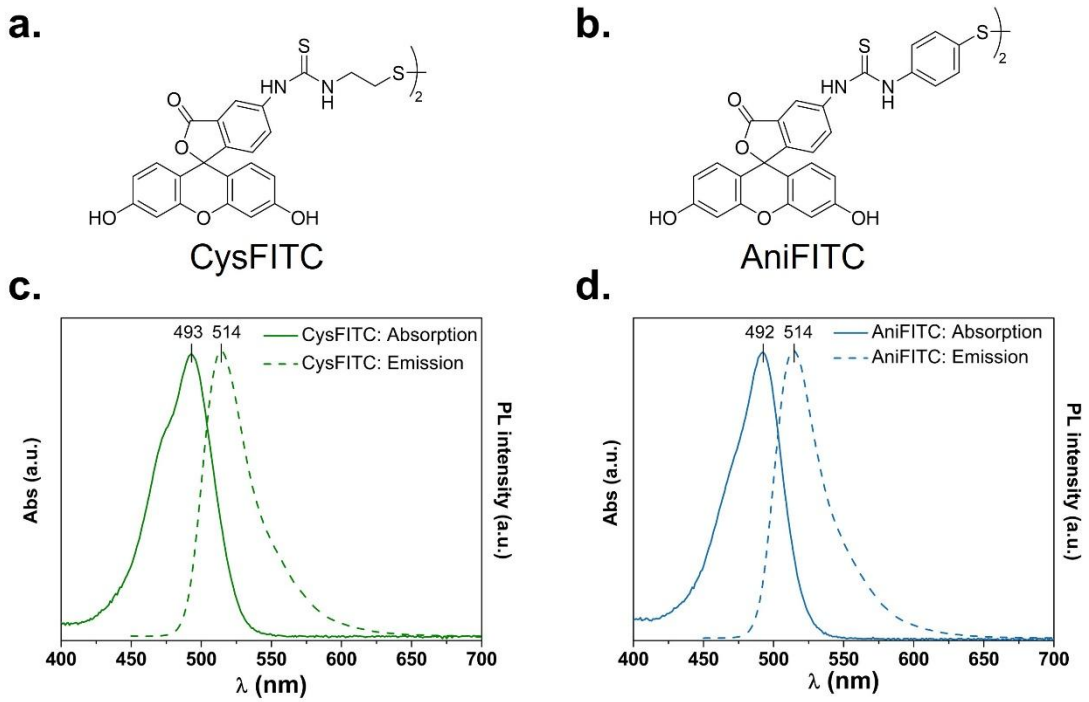

Figure 37. *Chemical structures of a) CysFITC and b) AniFITC; normalized adsorption and emission (excitation at λ = 440 nm) spectra of c) CysFITC and d) AniFITC. All the spectra were collected in H_2O pH 8 with phosphate buffer.*

The full ^{1}H-NMR spectrum of FITC is reported in *Figure A2*. Additional evidence for the successful synthesis of CysFITC was obtained from its ^{1}H-NMR spectrum (*Figure B1*). A peak at 3.92 ppm and a triplet at 3.01 ppm can be attributed to the aliphatic protons of Cys2 conjugated to FITC, comparing the integrals of these two signals with the aromatic signals are compatible. Similarly, in the ^{1}H-NMR spectrum of AniFITC (*Figure B2*), the signals of the aromatic ring of Ani2 were observed at 7.63 ppm and 7.07 ppm. The latter overlaps with the aromatic proton signals of the FITC fluorophore. The ^{13}C-NMR spectra of both CysFITC

and AniFITC (*Figure B3b*) displayed a distinct resonance at 182.7 ppm, consistent with the carbon signal of the thiourea moiety[173], further confirming the success of the derivatization. The emission properties of CysFITC and AniFITC were evaluated before their conjugation with AuNPs to determine if structural variations in the spacer (Cys or Ani) could influence the optical behaviour of the conjugated dye. Absorption and emission spectra are reported in **Figure 37c,d** and were recorded at pH 8 in phosphate buffer, ensuring maximum fluorescence intensity. The absorption spectra show a maximum centred at 493 nm for CysFITC and at 492 for AniFITC. The emission spectra were acquired upon excitation at 440 nm, and both fluorophores displayed an emission band with a maximum at 514 nm.

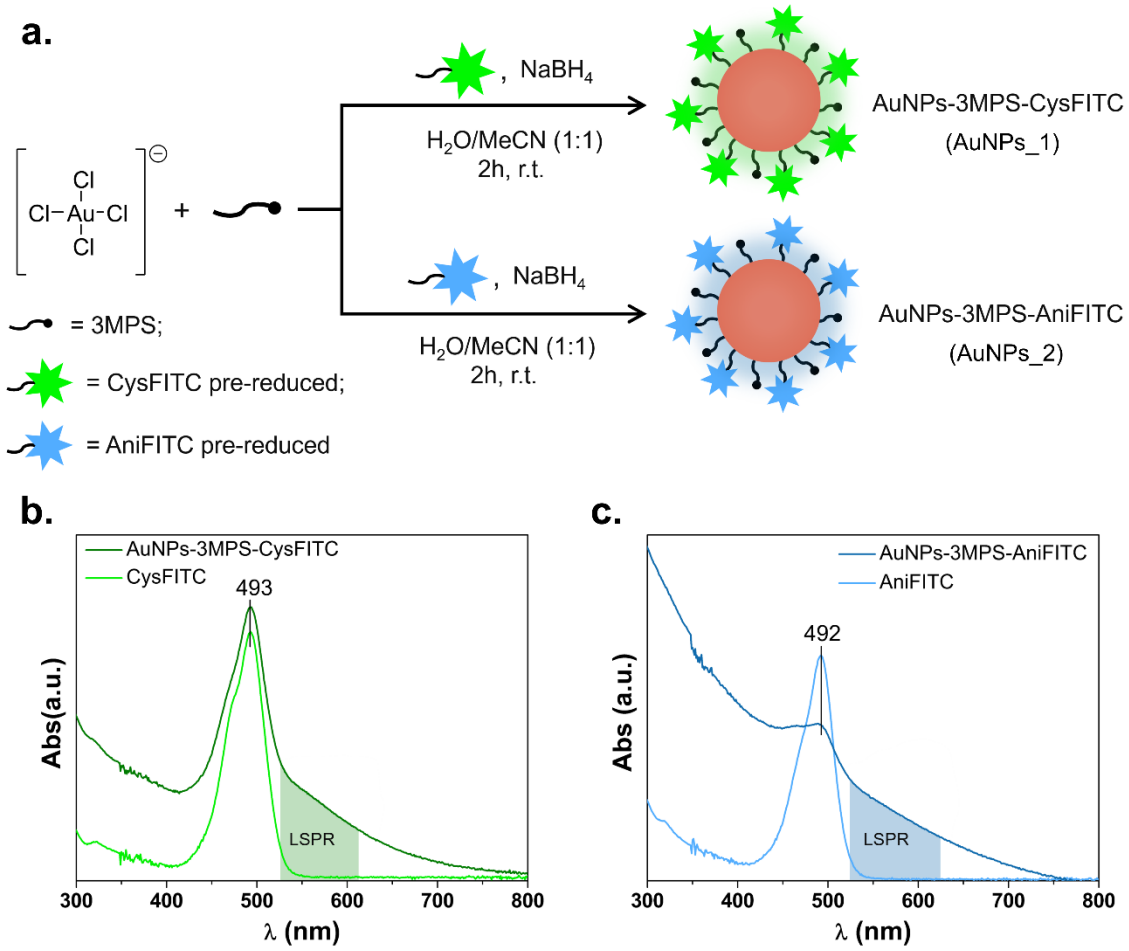

Figure 38. *a) schematic depiction of the AuNPs synthesis process; b) UV-Vis spectra of CysFITC (light green) and AuNPs-3MPS-CysFITC (dark green); c) UV-Vis spectra of AniFITC (light blue) and AuNPs-3MPS-AniFITC (dark blue). All UV-Vis spectra are collected in H_2O pH 8 (phosphate buffer).*

Compared to the commercial FITC spectrum recorded under the same conditions (*Figure A3,* λ_{max} = 516 nm), there is a slight blue-shift of approximately 2 nm. Although modest, this

spectral shift indicates that the substitution of the isothiocyanate group with a thiourea linkage, mediated by either Cys2 or Ani2, perturbs the electronic environment of the fluorescein chromophore, thereby influencing its photophysical behaviour.

As previously described in *Section 2.1.*, the synthesis of gold nanoparticles was carried out using a one-pot wet chemical reduction method using $[AuCl_4]^-$ complex as metal precursor, $NaBH_4$ as reducing agent and two thiols in mixture, for these synthesises: 3MPS and CysFITC or AniFITC, as capping agents. The synthesis method was adapted to account for the presence of FITC derivatives, as described in detail in *Appendix C1.2*. Since CysFITC and AniFITC exist in their disulfide forms, they were pre-reduced with $NaBH_4$ prior to use. Furthermore, to overcome their poor solubility in water, the synthesis of AuNPs was conducted in a H_2O/MeCN (1/1, v/v) solution. Different molar ratio between the precursor were tested ($Au/S_{3MPS}/S_{Dye}$: 1/4/4, 1/4/2, 1/4/1, 1/1/0.5) and stable AuNPs were produced with a molar ratio of $Au/S_{3MPS}/S_{Dye}$ = 1/4/0.5 generating AuNPs-3MPS-CysFITC (or AuNPs_1) and the AuNPs-3MPS-AniFITC (or AuNPs_2), as schematized in **Figure 38a**. The role of 3MPS is fundamental, as its sulfonate groups contribute to electrostatic stabilization of the synthesized nanoparticles and significantly enhance their aqueous dispersibility.

After careful purification to remove the unreacted thiols, AuNPs were successfully obtained, as evidenced by the UV-visible spectra reported in **Figure 38b,c**.

In both cases, the absorption band of the FITC derivatives is clearly visible (λ_{max}: 493 nm for AuNPs_1, **Figure 38b** dark green; λ_{max}: 492 nm for AuNPs_2, **Figure 38c** dark blue) and appears to largely overlap with the LSPR of the nanoparticles ($\lambda_{LSPR} \approx 545$ nm for AuNPs_1; $\lambda_{LSPR} \approx 550$ nm for AuNPs_2,). The absorption band of AniFITC in AuNPs_2 appears less intense compared to that of CysFITC in AuNPs_1. This difference is likely due to the lower solubility of AniFITC under synthesis conditions, which may reduce its effective interaction with the gold surface. In addition, although not sharply defined, the plasmonic band of AuNPs_2 appears to be slightly red shifted compared to that of AuNPs_1. This observation may suggest that AuNPs_1 are smaller in size than the nanoparticles functionalized with AniFITC. This view is further supported by both DLS measurements and FESEM images, as reported in **Figure 39**. Comparing the DLS graphs of AuNPs-3MPS-CysFITC (AuNPs_1) and AuNPs-3MPS-AniFITC (AuNPs_2), **Figures 39a,b**, it is possible observe that AuNPs_1 have a smaller size in fact it presents a single population with a hydrodynamic diameter centred at (28 ± 14) nm instead AuNPs_2 present two populations with $<2R_H>$ = (68 ± 20) and (295 ± 19) nm. The polydispersity index (PDI) confirms that AuNPs_1 is more

monodisperse than AuNPs_2 (PDI_{AuNPs_1} = 0.238 ± 0.012; PDI_{AuNPs_2} = 0.394 ± 0.070). To have a better understanding of the size and shape of the nanoparticles, electron microscopy images are reported in **Figure 39c,d**. AuNPs_1 and AuNPs_2 were observed by FESEM, and the images confirm the spherical shapes of both systems.

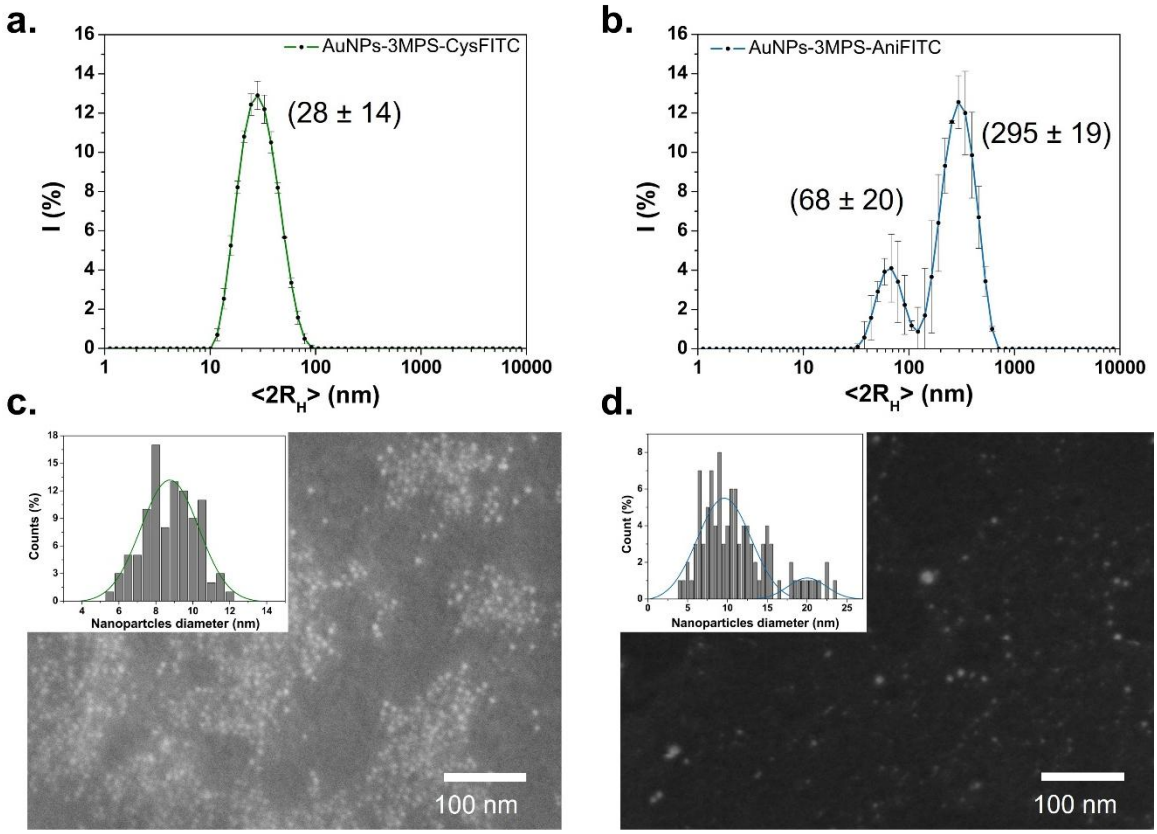

Figure 39. *Hydrodynamic size distribution of a) AuNPs-3MPS-CysFITC (AuNPs_1), $<2R_H>$ = (28 ± 14) nm, PDI = (0.238 ± 0.012), b) AuNPs-3MPS-AniFITC (AuNPs_2), $<2R_H>$ = (68 ± 20), (295 ± 19) nm, PDI = (0.394 ± 0.070), measurements carried out in H_2O; morphological observation: FESEM images of c) AuNPs_1 inset: distribution of the nanoparticles diameter and data fitted by Gaussian function (8.7 ± 1.5) nm (green line), d) AuNPs_2 inset: distribution of the nanoparticles diameter and data fitted by Gaussian function (9.6 ± 3.4) nm (20.0 ± 2.4) nm (blue line).*

For AuNPs_ 1, the image shows nanoparticles with a diameter of (8.7 ± 1.5) nm in average (**Figure 39c** and inset), instead for AuNPs_ 2 the distribution of particles diameters is a little bit different. It is possible observe two main populations, the biggest one centred at (9.6 ± 3.4) nm and the latter at (20.0 ± 2.4) nm (**Figure 39d** and inset). The size differences between a solvent mediated measurement such as DLS and a solid-state technique such as FESEM is due to the solvation shell, which is taken into account by DLS, whereas solid state studies

such as FESEM can only investigate the metal core. Furthermore, DLS measurements have high experimental errors (relative error up to 50%), and the measurements are strongly influenced by the presence of dynamic aggregates of AuNPs formed in suspension. It is also important to note that the intensity of the curves in DLS is not directly proportional to the concentration of aggregates of a given size, since larger populations carry greater weight in the correlation function of dynamic light scattering. These factors had a significant impact on the DLS analysis which indicated a population centred at (295 ± 19) nm that is not observed in FESEM images. Nevertheless, DLS and FESEM data are consistent regarding the polydispersity of the samples: FESEM images confirm that AuNPs_1 are more monodisperse, displaying a single population, while AuNPs_2 are more polydisperse and feature two distinct populations.

Focusing again on the colloidal state, both nanoparticle systems exhibit good colloidal stability, as demonstrated by their ζ-potentials: (–49 ± 9) mV for AuNPs_1 and (–30 ± 9) mV for AuNPs_2. The negative surface charge is consistent with the presence of sulfonate groups from 3MPS as well as negatively charged tautomers of the FITC derivatives. ζ-potentials measurements were carried out in H_2O pH native of AuNPs.

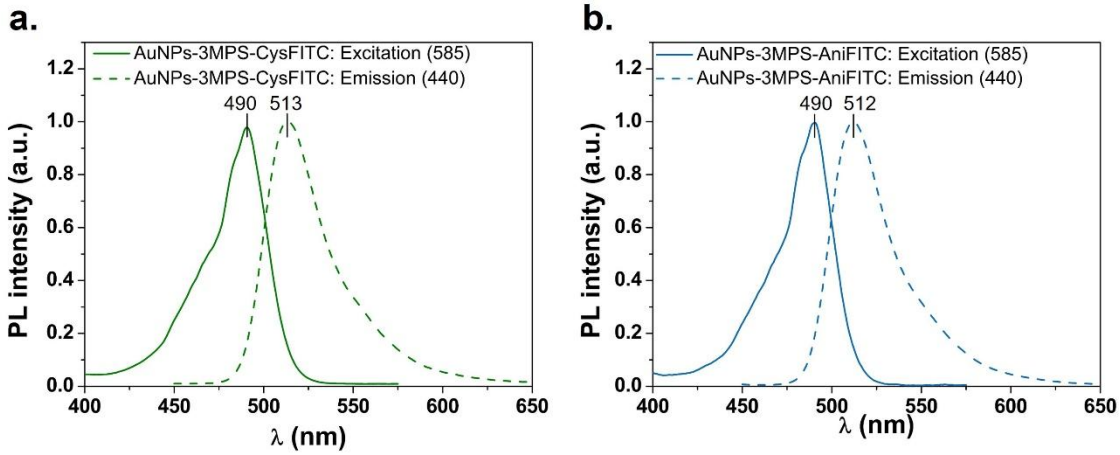

Figure 40. *Normalized excitation (emission at λ = 585 nm) and emission (excitation at λ = 440 nm) spectra of a) AuNPs-3MPS-CysFITC and b) AuNPs-3MPS-AniFITC. All the spectra were collected in H_2O pH 8 with phosphate buffer.*

The emission properties of AuNPs were evaluated to give a better understanding of the impact of the synthesis protocol on the nanoparticle applications. To exploit potential applications of AuNPs_1 and AuNPs_2, the emission properties were evaluated (**Figure 40**). **Figure 40a** shows the excitation and emission spectra of AuNPs_1 and **Figure 40b** the excitation and emission spectra of AuNPs_2. Excitation spectra were acquired by monitoring

the emission at λ = 585 nm, whereas emission spectra were recorded upon excitation at λ = 440 nm. In both systems, the excitation profiles revealed no evidence of fluorescence enhancement, consistent with the absence of plasmon-mediated effects, and displayed a maximum at 490 nm. Interestingly, the emission spectra exhibited a slight blue shift when compared to the spectra of the free FITC derivatives: AuNPs_1 showed a 1 nm shift (λ_{em} = 513 nm, resolution 0.5 nm), while AuNPs_2 displayed a 2 nm shift (λ_{em} = 512 nm, resolution 0.5 nm). These subtle spectral shifts are likely associated with modifications of the electronic states of the dye molecules upon interaction with the nanoparticle surface.

The covalent conjugation of fluorophores molecules on the surface of AuNPs open perspectives in the field of nanomedicine. Indeed, fluorescent NPs hold several advantages over free fluorescent dyes for clinical application, such as biocompatibility and photostability and greater retention time within the body than small molecules, allowing for improved imaging over a longer period. Non-specific binding by biomolecules present in biological medium can deactivate the fluorescence of small fluorescent probes, ultimately leading to its removal through the hepatobiliary or renal system. Covalent bound of dyes on NPs surface prevent quenching of dye molecules, as demonstrated by fluorescence spectroscopy for both studied systems *i.e.* AuNPs-3MPS-CysFITC (AuNPs_1) and AuNPs-3MPS-AniFITC (AuNPs_2). The high surface-to-volume ratio and synthetic versatility of AuNPs allows to conjugate both dye molecules and therapeutic moieties with application as theranostic platform. Moreover, the intensity of the fluorescent emission can be tuned according to the size of NPs.

2.4. Final Remarks

Using a wet-reduction synthesis starting from the metal precursor $AuCl_4^-$, hydrophilic Gold Nanoparticles functionalized thiols in a mixture were successfully synthesized. This study on hydrophilic AuNPs demonstrates the versatility of chosen synthesis method, as it yielded small, monodisperse, and stable nanoparticles synthetized. The synthesized nanoparticles (AuNPs-3MPS-DEA, AuNPs-3MPS-CysFITC, and AuNPs-3MPS-AniFITC) were thoroughly characterized to study not only their morphology but also their surface chemistry and optical properties. Among them, the AuNPs-3MPS-DEA nanoparticles proved to be a versatile platform, successfully employed for the delivery of an anticancer drug (methotrexate, MTX) and subsequently of an antibody (trastuzumab, TZ). These results highlight their strong potential of hydrophilic AuNPs in nanomedicine.

Chapter 3. Hydrophobic Gold Nanoparticles

The synthetic versatility of noble metal nanoparticles (AuNPs, AgNPs, PdNPs) allows the preparation of stable NPs in organic solvents. In this chapter, we focus on hydrophobic nanoparticles synthesized through the two-phase Brust–Schiffrin method, described in detail in *Section 1.3.1*. The MNPs surface can be functionalized with a wide range of molecules, from simple monofunctional thiols to more complex bifunctional ligands, enabling the formation of interconnected nanoparticle networks.

In the first part of the chapter, AuNPs functionalized with a mixture of dodecanethiol (DDT) and 4-aminothiophenol (Ani) are discussed. The aim was to manipulate and control the colloidal state of the AuNPs, starting from isolated AuNPs and generating nanoparticle networks through external stimuli, by exploiting the aromatic amine group of Ani anchored on the nanoparticle surface. In this work, the colloidal and isolated state of AuNPs was manipulated with external stimuli to obtain either irreversible or reversible nanoparticle networks. That was achieved taking advantage of transimination chemistry. The studies were conducted in collaboration with Prof. S. Di Stefano and PhD student Dr. G. Melchiorre of Department of Chemistry of Sapienza University of Rome.

Subsequently, metallic nanoparticles (AuNPs, AgNPs, and PdNPs) functionalized with bifunctional ligands are presented. These ligands include both synthetic organic bifunctional molecules and organometallic bifunctional ligands based on platinum complexes. In this context, the use of bifunctional ligands is particularly advantageous for the formation of 2D and 3D nanoparticle networks, where the optoelectronic properties of individual nanoparticles can be extended to the whole system, leading to enhanced overall performance. Such nanostructures have found applications in sensing and optoelectronics.

Finally, the chapter deals gold nanoparticles functionalized with chiral thiol derivatives of [2.2]paracyclophane (PCP). The synthesis of PCP-thiol derivatives was carried out during a three-month research period at the École Nationale Supérieure d'Ingénieurs de Caen (ENSICaen), France, in CARMeN group under the supervision of Prof. C. Lemouchi and Prof. S. Perrio.

3.1. Self-Assembly of AuNPs: irreversible and transient covalent networks

The colloidal state of AuNPs can be manipulated and controlled through external stimuli influencing the self-assembly of nanoparticles.[91] The self-assembly of nanoparticles in the last decades gained a lot of interest, is driven by supramolecular[97] or covalent interactions.[101] In supramolecular interaction the dynamic assembly/disassembly of AuNPs is governed by intermolecular non-covalent interactions; while in covalent interaction the formation and breaking of covalent bonds are required for the dynamic self-assembly.

Among different strategies, activated carboxylic acids (ACAs)[174,175] represent structurally simple stimuli capable of driving reversible covalent self-assembly of systems containing at least one basic moiety.

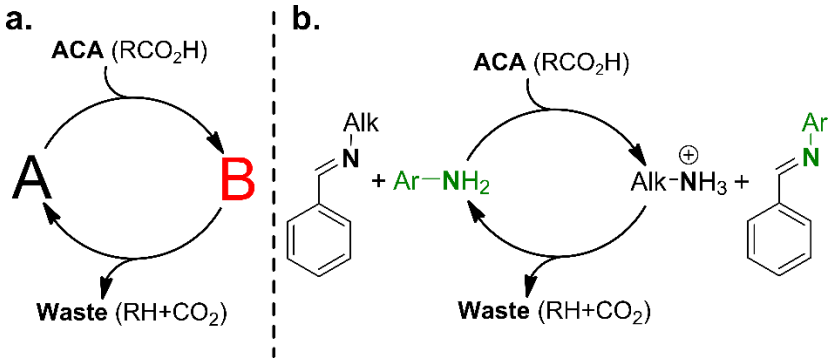

Figure 41. *a) General scheme of an equilibrium state A converted into an activated one B through ACA addition. ACA exhaustion reverts the starting state A with the parallel formation of waste products. b) Transient variation of imines dynamic library composition obtained through ACA addition.*

As shown in **Figure 41a**, the system can be protonated by ACA and shift from a neutral state (A) to a protonated state (B). The conjugate base of ACA then spontaneously decarboxylates, generating a very strong base that deprotonates the system (B), thereby restoring the neutral state (A).[176] The greater the amount of ACA introduced, the longer its dissipation time, and consequently, the longer the system remains in the protonated state (B). This principle has been successfully applied to control the composition of a dynamic library of imines, as studied by Di Stefano *et al*. and illustrated in **Figure 41b**.[177,178,179]

The equilibrium of this library is normally shifted to the left, favouring the *N*-alkylimine over the *N*-arylimine. Upon addition of stoichiometric or excess amounts of ACA, the alkylamine, the strongest base in solution, is quantitatively protonated to alkylammonium.

As a result, alkylamine is withdrawn from the equilibrium, which shifts toward the right side. This new composition persists as long as ACA remains present. Once decarboxylation and back-proton transfer occur, the original equilibrium is restored.

The precise choice of thiol capping agents with a specific terminal group influences the behaviour of the colloid.[107]

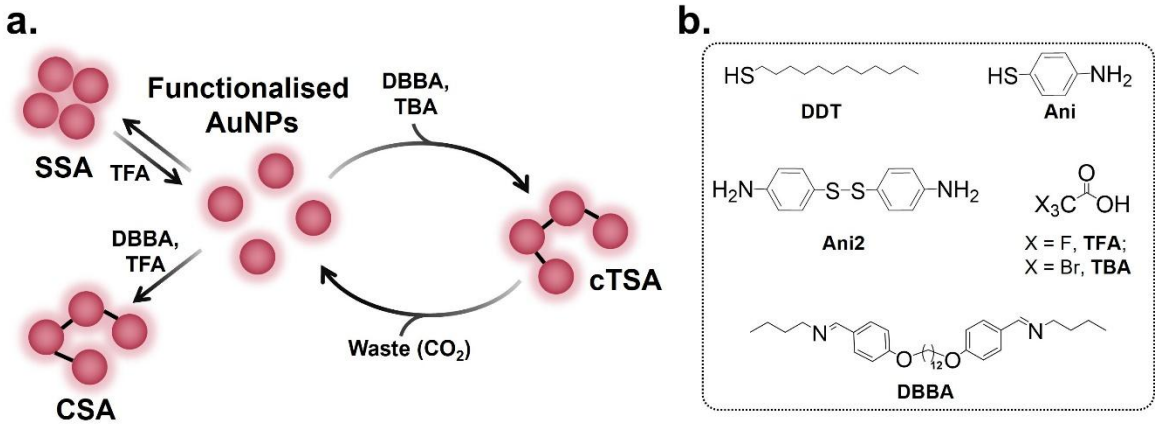

Figure 42. *a) schematic representation of Supramolecular Self-Assembly (SSA), Covalent Self-Assembly (CSA), and covalent Transient Self-Assembly (cTSA) of AuNPs; b) chemical structures of DDT, Ani, Ani2, TFA, TBA, DBBA.*

In this work, three different types of assemblies of AuNPs were achieved through precise surface functionalization: Supramolecular Self-Assembly (SSA), Covalent Self-Assembly (CSA), and covalent Transient Self-Assembly (cTSA), summarized in **Figure 42a**.

Gold nanoparticles were functionalized with two ligands: 1-dodecanethiol (DDT) and 4-aminobenzenethiol (Ani), the latter generated *in situ* from 4-aminophenyl disulfide (Ani2). Both ligands play a key role in the different self-assembly processes.

In the SSA system, the aliphatic chains of DDT covalently bound to the AuNPs surface were crucial in driving spontaneous aggregation. The co-presence of Ani enabled the use of trifluoroacetic acid (TFA) allow the system to switch between aggregated and isolated AuNPs.

In the CSA system, covalent networks were obtained by introducing an external linker, an *N*-aliphatic di-imine (4,4'-(dodecane-1,12-diylbis(oxy)) dibenzylidene-butylamine, DBBA), under TFA stimulation. In this case, the aromatic amine groups of Ani on the AuNPs surface reacted with DBBA through a transimination process, forming covalent bonds between nanoparticles.

In the cTSA system, the same covalent linkage was made transient by replacing TFA with an ACA. After protonating the system, ACA spontaneously decarboxylates, restoring the initial state. In this work, tribromoacetic acid (TBA) was selected as the ACA to drive the transient assembly. In **Figure 42b** all the molecules are reported.

3.1.1. Design of functionalized AuNPs

To obtain hydrophobic AuNPs, the two-phase Brust–Schiffrin method[180] was adapted to the selected substrates, following the procedure schematized in **Figure 43a**.

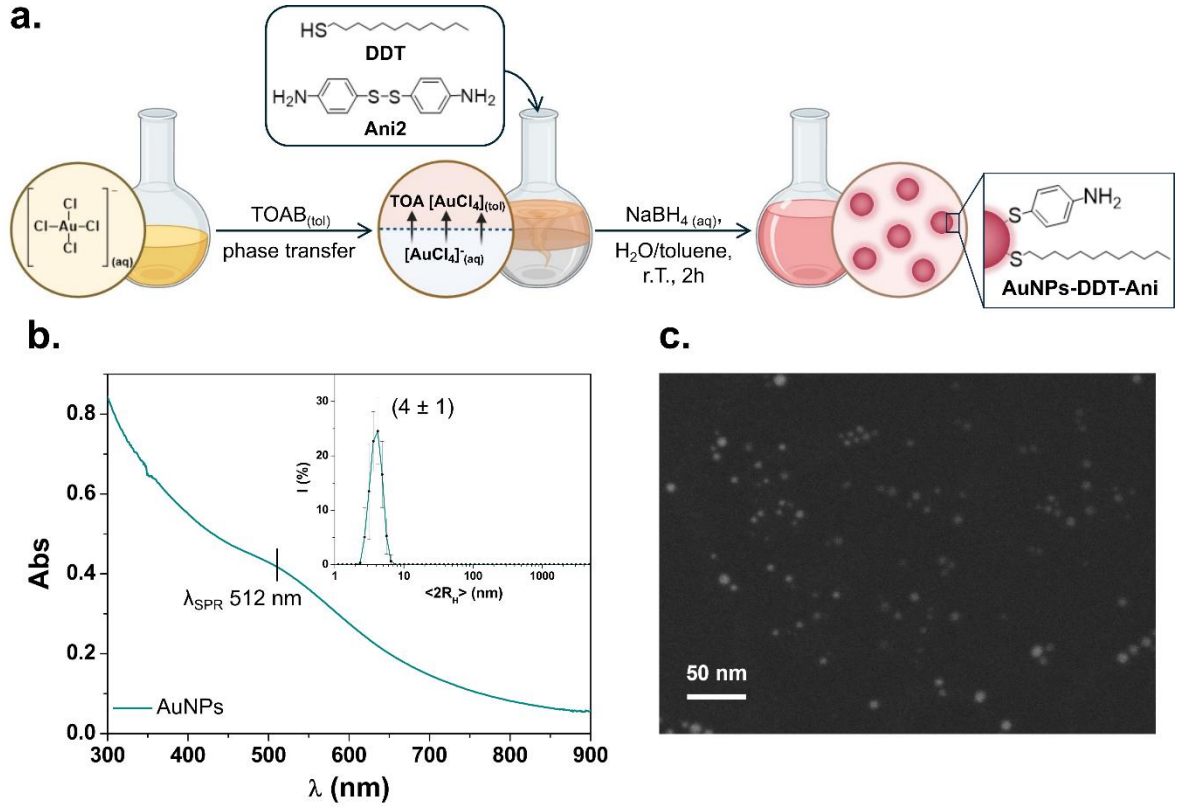

Figure 43. *a) schematic representation of synthesis of AuNPs; b) UV-Vis spectrum of AuNPs, λ_{LSPR} = 512 nm, inset: DLS graph of AuNPs $<2R_H>$ = (4 ± 1) nm, all the measurements were conducted in DCM; c) FESEM image of AuNPs.*

The phase transfer of the square-planar complex ion $[AuCl_4]^-$ was assisted by TOAB, after thiols were added in different molar ratios. The subsequent addition of $NaBH_4$ reduced the gold and, at the same time, the disulfide bonds of the commercial precursor (Ani2), yielding the corresponding thiol (Ani). The complete synthesis procedure is reported in *Appendix C2.1*. Different molar ratios between the gold precursor $HAuCl_4 \cdot 3H_2O$, the sulphur atoms from DDT (S_{DDT}), and those from Ani (S_{Ani}) were investigated. The Au/S_{DDT}/S_{Ani} molar ratios studied were 1/4/0.5, 1/4/1, 1/4/2, and 1/4/4. The colloidal properties of the resulting

nanoparticles were analysed by UV-Vis spectroscopy and DLS measurements. The UV-Vis spectra and DLS graphs are shown in *Figures C2 and C3*, respectively, and the results are summarized in *Table C1*.

The optimal colloidal stability and degree of functionalization were achieved for the sample synthesized with an $Au/S_{DDT}/S_{Ani}$ molar ratio of 1/4/2 (hereafter referred to as AuNPs), obtained with a yield of (34 ± 5) %. The UV-Vis spectrum and DLS graph of as prepared nanoparticles are reported in **Figure 43b**. The UV-Vis spectrum displays the characteristic plasmonic band centred at 512 nm, DLS analysis revealed a monodisperse population with a small hydrodynamic diameter of (4 ± 1) nm (inset in **Figure 43b**). The formation of spherical AuNPs was further confirmed by electron microscopy. As reported in **Figure 43c**, the FESEM image highlights the homogeneous distribution of nanoparticles, showing morphology and dimensions consistent with the size estimated from DLS analysis. The as prepared AuNPs mainly form small aggregates composed of a few nanoparticles, while some isolated particles are also visible with an average size of (4.7 ± 1.3) nm, in agreement with the DLS results.

To confirm the successful surface functionalization with both thiols, ^{1}H-NMR and FTIR-ATR spectra were recorded.

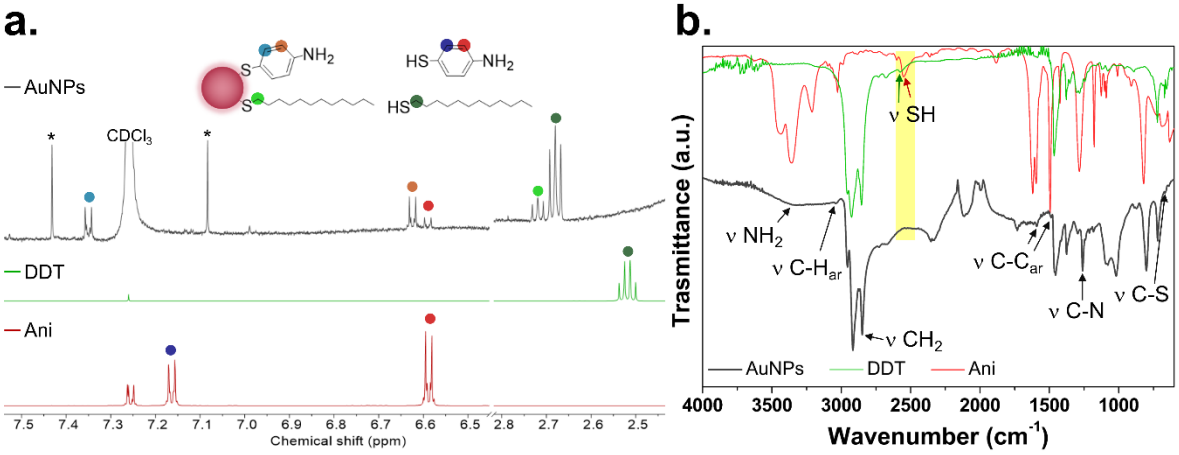

Figure 44. *a) ^{1}H-NMR spectra of AuNPs (top, grey), DDT (middle, green) and Ani (bottom, red). All spectra were collected in $CDCl_3$ (7.26 ppm); b) FTIR-ATR spectra of AuNPs (grey), DDT (green) and Ani (red).*

In the ^{1}H-NMR spectrum of AuNPs (**Figure 44a**, grey line), the most relevant peaks can be attributed to: the methylenic protons α to the sulfhydryl group of DDT (t, 2.72 ppm); the aromatic protons ortho to the amine group of Ani (d, 6.62 ppm); the aromatic protons ortho to the thiol group of Ani (d, 7.35 ppm). By comparing the corresponding integral values, it

was possible to calculate the molar ratio of the two thiols bound to the gold surface. The ratio between DDT and Ani ligands was found to be approximately 2:1, in favour of DDT, consistent with the stoichiometric ratio ($Au/S_{DDT}/S_{Ani}$ = 1/4/2) employed during synthesis.
Further confirmation of the interaction between the thiols and the AuNP surface is provided by the downfield shifts observed when comparing the capped thiols with the free ligands in solution (DDT = green line, Ani = red line). Specifically, a shift of 0.2 ppm was observed for the CH_2 protons adjacent to the SH group in DDT and for the aromatic protons ortho to the thiol group in Ani. A smaller shift of 0.03 ppm was recorded for the aromatic protons ortho to the amine function of Ani, as these protons are more distant from the gold surface.
Signals corresponding to physisorbed thiols are also visible in the AuNPs spectrum at higher fields (t, 2.68 for DDT; d, 6.59 for Ani)[181]. The presence of physically adsorbed thiols is quite common: they contribute to the stabilization of the nanoparticles, often remain detectable even after purification, and do not negatively affect the colloidal stability.[130]
The FTIR-ATR spectrum of the stabilized AuNPs (**Figure 44b**, grey line) clearly shows the characteristic bands of the DDT ligand: the sharp band at 2954 cm^{-1}, the intense bands at 2916 cm^{-1} and 2848 cm^{-1}, corresponding to the symmetric and antisymmetric stretching of aliphatic chains [$\nu_s(CH_3)$, $\nu_s(CH_2)$, $\nu_{as}(CH_2)$], the ν(C–S) vibration at 667 cm^{-1}.[182]
Concerning the Ani ligand, the spectrum displays: the aromatic ring vibrations $\nu(C–H_{Ar})$ at 3042 cm^{-1}, $\nu(C–C_{Ar})$ at 1591 cm^{-1}, and $\gamma(C–H_{Ar})$ at 800 cm^{-1}, the band at 3350–3170 cm^{-1} (ν(N–H)) and the band at 1296 cm^{-1} (ν(C–N)), confirming the presence of the amine group on AuNPs. The possible presence of other N-based functionalities was also investigated. Importantly, the spectrum shows the absence of signals due to undesired azo by-products (expected at 1457 cm^{-1} and 1513 cm^{-1})[183,184]. Moreover, the absence of ν(S–H) signals in AuNPs spectrum, centred at 2575 cm^{-1} for DDT and 2550 cm^{-1} typical of Ani, confirms the functionalization of both ligands on the AuNP surface. The complete FT-IR band assignments for Ani, DDT, and AuNPs are reported in *Table C2*.
Overall, the obtained AuNPs show good colloidal stability and a well-defined degree of functionalization with both thiols (DDT and Ani), making them a suitable nanomaterial for the subsequent studies.

3.1.2. Supramolecular Self-Assembly (SSA) of AuNPs

AuNPs, when left in dichloromethane (DCM) suspension for 24 h, tend to spontaneously organize into a dynamic aggregation state, referred to as Supramolecular Self-Assembly

(SSA). Interestingly, when the SSA of AuNPs is treated with an acid, specifically trifluoroacetic acid (TFA), the system reverts to a state of well-isolated nanoparticles in suspension. TFA was chosen due to its strong acidity and solubility in organic solvents such as DCM. These equilibria are schematized in **Figure 45a** (with the legend reported **in Figure 45b**). The SSA process and the subsequent recovery of isolated nanoparticles upon TFA addition were investigated by UV–Vis spectroscopy, DLS measurements, and FESEM imaging. The UV–Vis spectra (*Figure D10*) did not reveal significant variations: the plasmonic band remained centred at 512 nm without appreciable shifts.

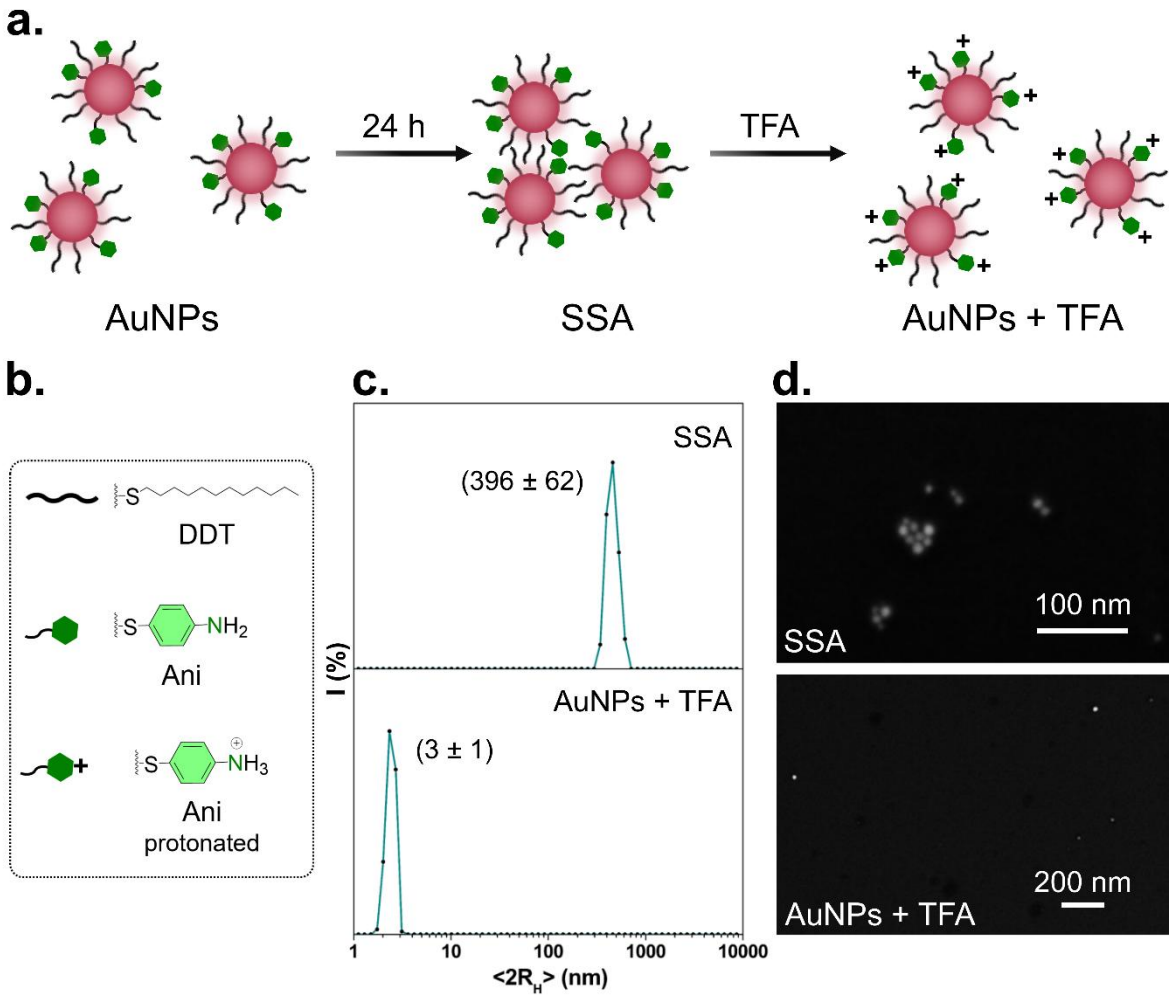

Figure 45. *a) schematic representation of formation of SSA and* the return to a state of isolated AuNPs*; b) legend; c) DLS graphs of SSA of AuNPs and after TFA treatment, SSA: <2R_H> = (396 ± 62) nm; AuNPs + TFA: <2R_H> = (3 ± 1) nm. All the measurements were conducted in DCM; d) FESEM images of SSA and AuNPs + TFA.*

Conversely, DLS measurements (**Figure 45c**) highlighted substantial differences. After 24 h in DCM suspension, a single population with a hydrodynamic diameter centred at (396 ±

62) nm was observed, indicating the formation of a dynamic aggregate due to SSA of AuNPs. Upon treatment with TFA, the DLS results showed a new population centred at (3 ± 1) nm, consistent with the dimensions of as prepared nanoparticles (**Figure 43b**, inset) indicating that the addition of TFA restored the system to its initial state, a single population with a hydrodynamic diameter centred at ~ 4 nm.

FESEM images corroborated these results, showing that AuNPs, in DCM suspension after 24 h, display a strong tendency to aggregate, confirming the SSA state. After TFA treatment, the images clearly reveal well-isolated nanoparticles with an average size of (5.2 ± 1.0) nm, in agreement with the DLS data.

A possible explanation for the SSA behaviour of AuNPs lies in the interaction between the aliphatic chains of dodecanethiol. Upon addition of TFA to the colloidal suspension, the system returns to a state of isolated nanoparticles, as the aromatic amine group of Ani is protonated to form $-NH_3^+$. The presence of positively charged *N*-aromatic amines on the AuNPs surface induces electrostatic repulsion, which counteracts the supramolecular aggregation.

3.1.3. Covalent Self-Assembly (CSA) of AuNPs

A covalent self-assembly of AuNPs based on a transimination reaction was achieved using 4,4'-(dodecane-1,12-diylbis(oxy))dibenzyliden-butylamine (DBBA), a linker precursor containing two *N*-aliphatic imine groups. Under acidic conditions induced by TFA, the amino groups of the Ani moieties on the AuNPs surface undergo transimination with DBBA, leading to the formation of stable covalent bonds between the nanoparticles. The reaction proceeds with the release of butylammonium ions, which shifts the equilibrium toward the formation of aromatic imines and drives the assembly of a covalently interconnected nanoparticle network. It is noteworthy that, during the equilibration period of three days required for the AuNPs–DBBA system, the nanoparticles tend to undergo SSA, driven by non-covalent interactions (*vide supra,* par. 3.1.2). Upon addition of TFA, this supramolecular equilibrium is disrupted and the SSA is broken down. At the same time, the acidic environment promotes the transimination reaction[185] between the amino groups of Ani and the DBBA linker, leading to the formation of aromatic imines on the AuNPs surface. As a result, a covalent and permanent self-assembly (CSA) of AuNPs is established as shown in **Figure 46a** (legend in **Figure 46b**).

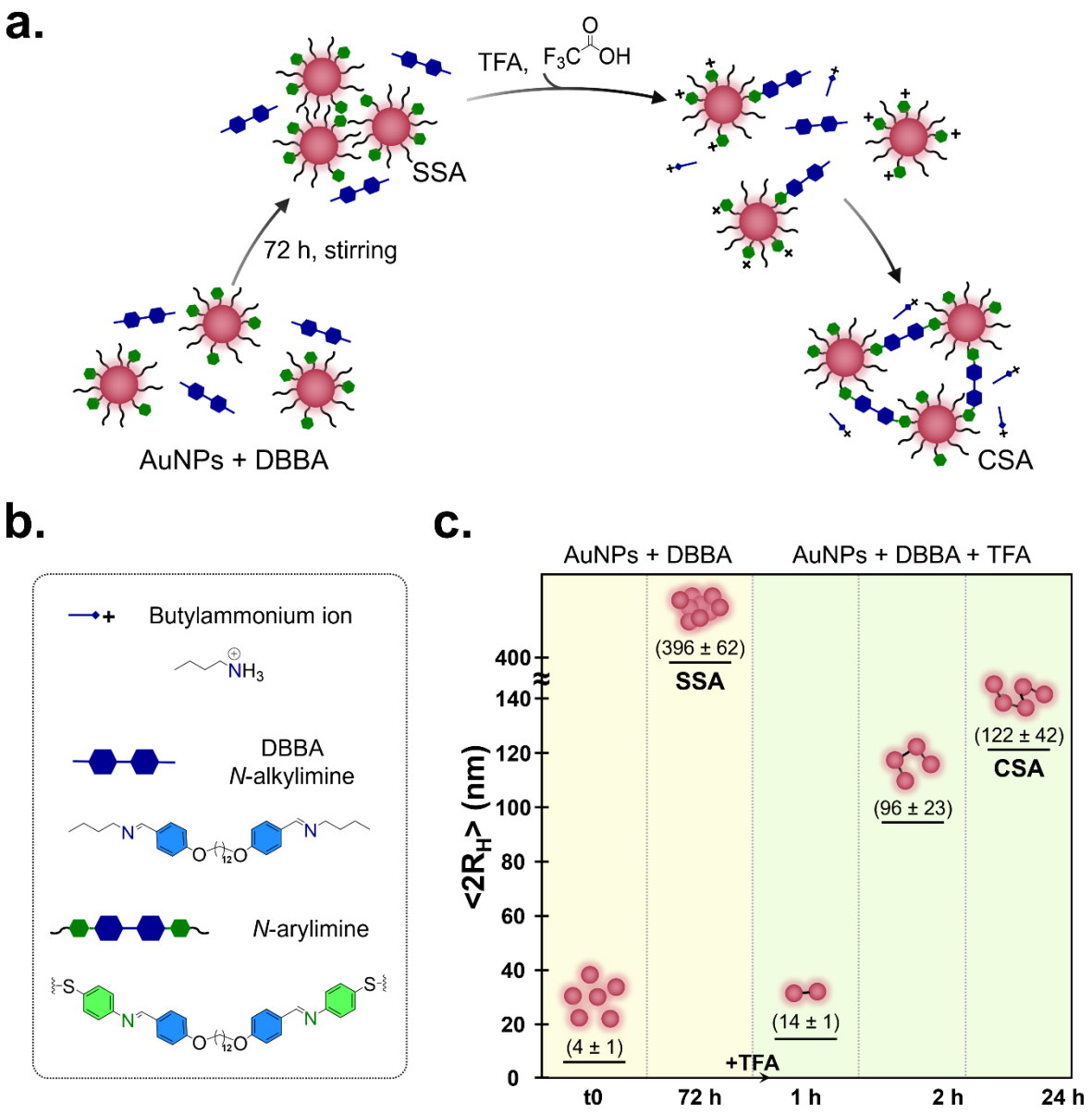

Figure 46. *a) schematic representation of CSA of AuNPs: AuNPs + DBBA were stirred for 72 hours and SSA occurred, the adding of TFA disrupted the SSA and generated CSA; b) legend; c) relevant results of DLS measurements of AuNPs + DBBA mixture in DCM at t0 and 72 h, AuNPs + DBBA + TFA at 1h, 2h, 24h.*

The system was first investigated by DLS in DCM suspension. All DLS graphs are reported in *Figure D11*, while **Figure 46c** highlights the most relevant results. At t0, the AuNPs in the presence of the DBBA showed a population centred at (4 ± 1) nm, indicating that the linker precursor does not affect the initial colloidal stability of the nanoparticles. After 72 hours of equilibration, in agreement with the observations described in paragraph 3.1.2, the AuNPs underwent SSA, giving rise to a population centred at (396 ± 62) nm, driven by interactions among the aliphatic chains of DDT on the gold surface. Once the equilibrium

between AuNPs and DBBA was reached, the addition of TFA disrupted the SSA and generated covalent self-assembly (CSA). One hour after TFA addition, DLS revealed a population centred at (14 ± 1) nm, while after 2 hours a new population at (96 ± 23) nm appeared, suggesting the progressive formation of a nanoparticle network. After 24 hours, the system reached a plateau, showing a single population centred at (122 ± 42) nm. These results confirm the establishment of a covalent nanoparticle network, while maintaining colloidal stability in DCM suspension.

Further studies were carried out to verify the effective interaction between AuNPs and DBBA. To this aim, FTIR and UV-Vis spectroscopies were employed. Spectra were collected for the free DBBA, for the AuNPs + DBBA mixture (before CSA), and for the CSA of AuNPs. The spectra of the AuNPs + DBBA mixture were used to check if, in the absence of TFA (necessary to generate CSA), the linker precursor interacts covalently with AuNPs.

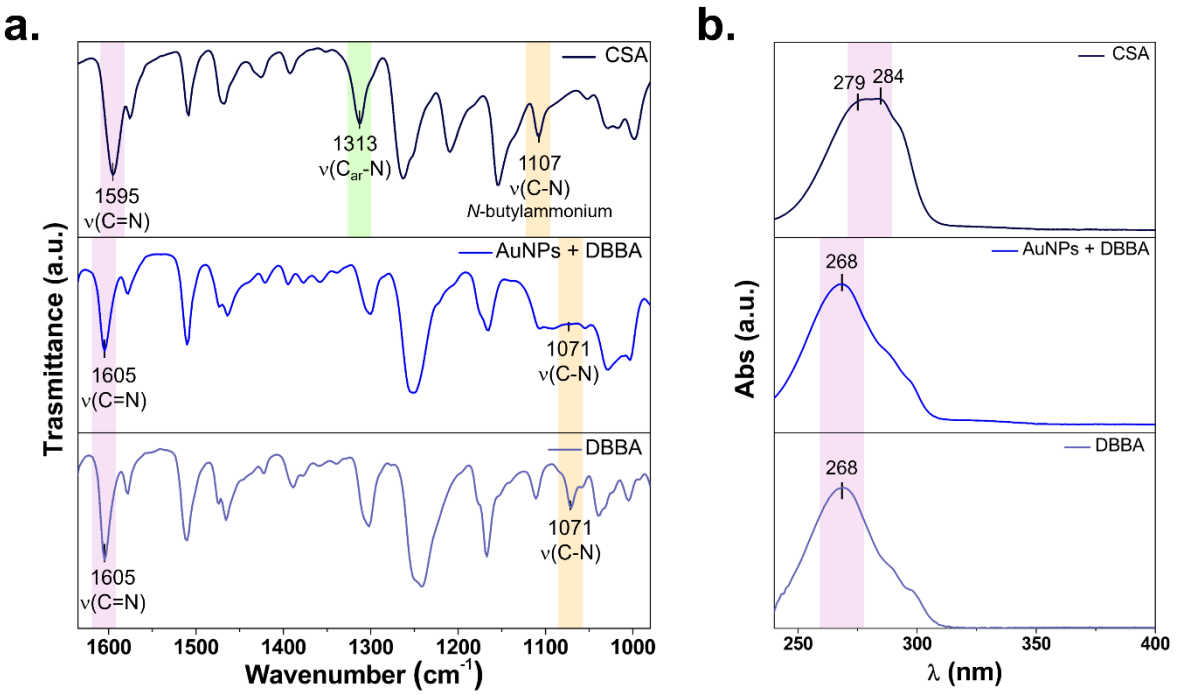

Figure 47. *a)FTIR spectra of DBBA (bottom), mixture of AuNPs + DBBA (middle) and CSA of AuNPs (top), highlighted: in purple the stretching band of C=N of aliphatic imine (in DBBA and AuNPs + DBBA miture) and of aromatic imine; in green the stretching band of Car-N of aromatic imine; in orange the stretching band of C-N in aliphatic imine (DBBA and AuNPs + DBBA) and C-N of N-butylammonium; b)UV-Vis spectra of DBBA (bottom), mixture of AuNPs + DBBA (middle) and CSA of AuNPs (top) .*

As reported in **Figure 47a** (complete FTIR spectra in *Figure D12*, with band assignments in *Table D10*), no changes in the wavenumber of DBBA peaks are observed when mixed with AuNPs, confirming the absence of covalent interactions prior to TFA addition. In contrast, the FTIR spectrum of CSA of AuNPs shows the appearance of a new band at 1313 cm^{-1}, assigned to the stretching of the newly formed aromatic imine bond (νC_{Ar}-N). In addition, the band at 1605 cm^{-1} in free DBBA shifts to 1595 cm^{-1} in CSA of AuNPs, further supporting *N*-aromatic imine formation. The presence of the coproduct *N*-butylamine is also indicated by new peaks at 3360 cm^{-1} (νNH_2) and 1107 cm^{-1} (νC–N). Small shifts are also visible in the ether region, from 1242 to 1251 cm^{-1} (ν_{as}C–O–C) and from 1040 to 1030 cm^{-1} (ν_sC–O–C). UV-Vis analysis (**Figure 47b**) confirms these. The spectrum of AuNPs + DBBA, prior to TFA addition, overlaps with that of free DBBA (both with a maximum at 268 nm), indicating that the linker precursor remains stable. After TFA addition, however, the spectrum undergoes a significant change: two new peaks appear at 279 and 284 nm, consistent with increased conjugation associated with the formation of aromatic imine bonds. Monitoring the surface plasmon resonance band, even after CSA formation the plasmon band remains centred at ~512 nm and no substantial modification, indicating that nanoparticle morphology is preserved. The complete spectra are reported in *Figure D13*.

3.1.4. Covalent Transient Self-Assembly (cTSA) of AuNPs

A covalent Transient Self-Assembly (cTSA) of AuNPs can be obtained by exploiting the same transimination reaction described for CSA but using tribromoacetic acid (TBA) as a transient chemical stimulus (**Figure 48a**). Initially, AuNPs and DBBA are left to equilibrate for 72 h, during which SSA occurs, as previously discussed. When TBA is added, two processes occur simultaneously: the SSA breaks down into isolated AuNPs, as the protonation of the aromatic amines produces $-NH_3^+$ groups that generate Coulombic repulsion, and the acidic environment promotes transimination between DBBA and the surface amines, leading to the formation of a covalent network of AuNPs. However, TBA is not stable once deprotonated: it undergoes decarboxylation, generating a strong carbanion base. This base regenerates *N*-butylamine, which progressively back-reacts via transimination, cleaving the covalent linkers. As a result, the covalent assembly exists only transiently. Once TBA has fully decarboxylated, the system returns to isolated AuNPs, with bromoform ($CHBr_3$) as the by-product.

DLS measurements proved to be a valuable tool to monitor the formation of cTSA of AuNPs. All DLS graphs is reported in *Figure D14*, while only the most significant populations are shown in **Figure 48b**.

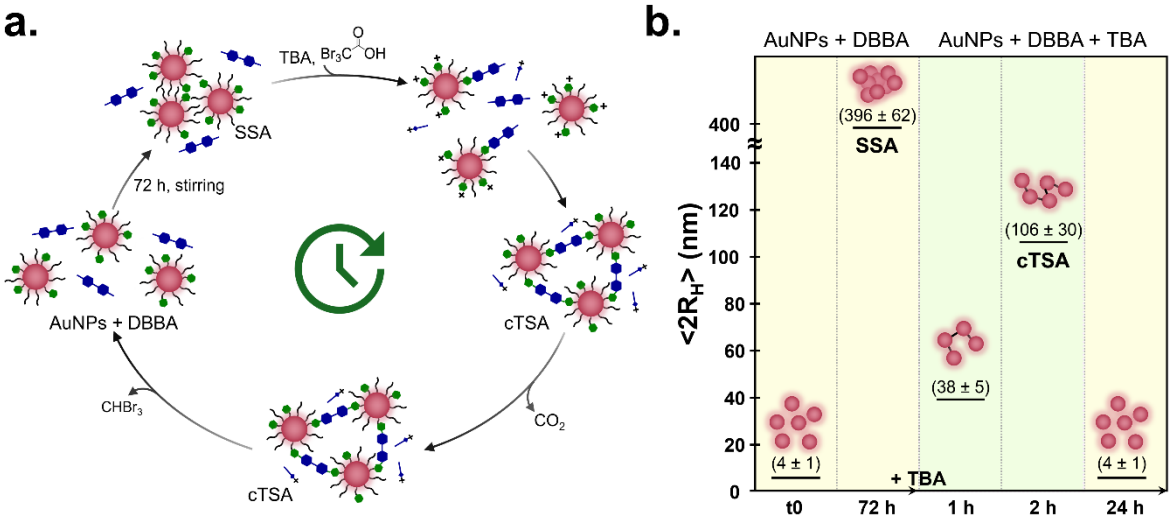

Figure 48. *a) schematic representation of cTSA of AuNPs: the isolated AuNPs and DBBA were stirred for 72 hours and SSA occurred, the adding of TBA disrupted the SSA and generated cTSA, the decarboxylation of TBA induced the restore of the system obtaining the isolated AuNPs and $CHBr_3$ as waste ; b) relevant results of DLS measurements of AuNPs + DBBA mixture in DCM at t0 and 72 h, AuNPs + DBBA + TBA at 1h, 2h, 24h.*

At the initial time (t0), the hydrodynamic diameter of AuNPs in the presence of DBBA was centred at (4 ± 1) nm, confirming that the precursor linker does not affect the colloidal stability. After 72 hours, a single population centred at (396 ± 62) nm was detected, as a consequence of SSA formation. Upon addition of TBA, a dynamic evolution of the system was observed. After 1 hour, three populations appeared: a one centred at (38 ± 5) nm, attributed to the formation of the covalent network, and two populations at (6 ± 1) nm and (468 ± 59) nm, imputable to isolated AuNPs and residual SSA aggregates, respectively. These latter two were not included in **Figure 48b** since they are not essential for illustrating the dynamic cycle of the cTSA. After 2 hours, the system reorganized into a single population centred at (106 ± 30) nm, pointing to the progressive stabilization of the covalent network. Finally, after 24 hours, the DLS results revealed a single population centred at (4 ± 1) nm, indicating the recovery of isolated AuNPs. This behaviour can be explained by the deprotonation and subsequent decarboxylation of TBA, which regenerates the DBBA linker and restores the initial state of the system.

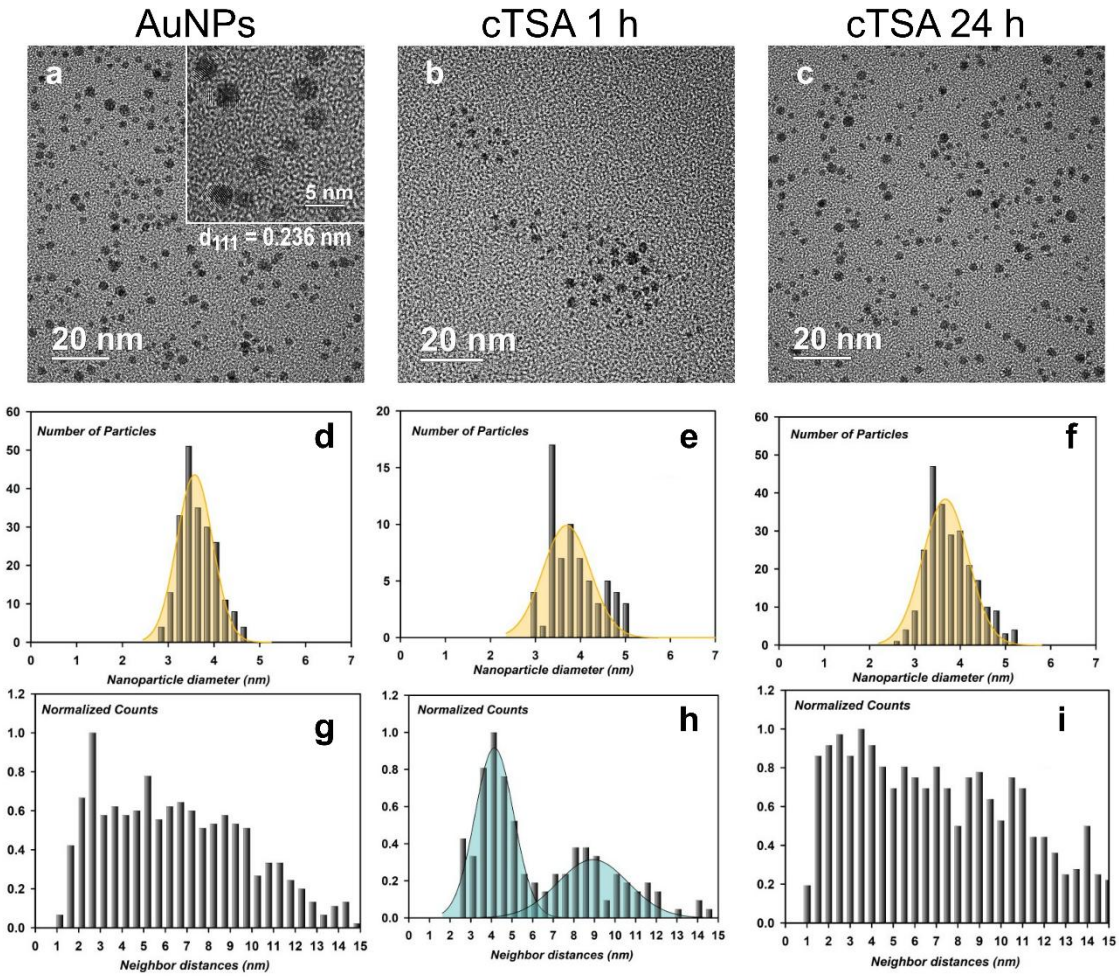

Figure 49. *HR-TEM images of a) AuNPs, inset: micrograph with crystalline lattices spacing d(111) =0.236 nm; b) cTSA after 1 hour of reaction and c) cTSA after 24 hours of reaction. Distribution graphs of nanoparticles diameter of d) AuNPs; e) cTSA after 1 hour of reaction and f) cTSA after 24 hours of reaction cTSA. Distribution graphs of inter-nanoparticles distance of g) AuNPs; f) cTSA after 1 hour of reaction and i) cTSA after 24 hours of reaction cTSA. Support grid: carbon amorphous film grid. Distribution of the nanoparticles diameter and distances fitted by Gaussian function.*

More detailed morpho-structural insights into the cTSA process were obtained through HR-TEM analyses. Images were collected for the pristine AuNPs, as well as for the cTSA system after 1 hour and 24 hours of reaction (**Figure 49a-c**). In all cases, the nanoparticle diameter remained constant at ~4 nm (AuNPs: 3.7 ± 0.8 nm; cTSA 1 h: 3.7 ± 1.1 nm; cTSA 24 h: 3.6 ± 0.9 nm), indicating that the covalent transient assembly process does not affect the individual particle size. Instead, significant differences were observed in the interparticle organization. In the initial state (**Figure 49a**), the nanoparticles appear randomly distributed,

as confirmed by the broad interparticle distance distribution reported in **Figure 49g**. After 1 h from the addition of TBA (**Figure 49b**), the nanoparticles arrange into aggregates, with a non-random distribution of interparticle distances. Indeed, the histogram in **Figure 49h** reveals two preferential distances, at 4.2 ± 1.9 nm and 8.8 ± 3.4 nm. This bimodal distribution can be attributed to the flexibility of the linker: its long aliphatic chain (12 carbon atoms) can adopt two predominant conformations, leading to distinct spacing regimes. However, this ordered state is only transient. After 24 h (**Figure 49c**), the nanoparticles are once again dispersed in a random fashion, as demonstrated by the interparticle distance distribution shown in **Figure 49i**, consistent with the reversibility of the cTSA process.

The inset of **Figure 49a** further highlights the nanocrystalline character of the AuNPs. Lattice fringe measurements confirmed the typical face-centred cubic gold structure (space group $Fm\bar{3}m$), with an interplanar spacing of d(111) = 0.236 nm, in agreement with literature values[186,187].

The reaction between AuNPs and DBBA in the presence of TBA was investigated by UV-Vis spectroscopy and ^{1}H-NMR (**Figure 50**).

UV-Vis spectrum of the mixture was studied and in **Figure 50a**. After 72 h and before addition of TBA, the AuNPs and linker do not covalent interact each other (λ_{max} = 268 nm). After 1 h of TBA interaction, a red shift was observed in the spectrum, indicating that the linker has been reacting with the *N*-aromatic amine of the gold surface obtaining *N*-aromatic imines. The red shift is still present after 2 h, and the maximum is still centred at 273 nm.

After 24 hours, however, the maximum shifted back to 268 nm, consistent with the restoration of *N*-aliphatic imines as a consequence of the dynamic transimination process. Monitoring of the surface plasmon resonance band confirmed that, also during cTSA, the plasmonic absorption remained centred at ~512 nm, with no substantial spectral changes observed.

The reaction was also investigated by ^{1}H-NMR. The signals of covalently bound ligands on the gold surface are weak, due to both restricted mobility at the nanoparticle interface and strong metal–ligand interactions[188]. For this reason, the ^{1}H-NMR analysis reported in **Figure 50b** mainly focuses on the processes occurring in solution, while **Figure 50c** provides a view of the 6.55–6.80 ppm region to monitor the aromatic proton of the Ani moiety directly bound to the AuNPs. In **Figure 50b** the ^{1}H-NMR spectra of the AuNPs + DBBA mixture were collected at equilibrium and at different times after the addition of TBA (40 min, 2 h, and 5 days). The equilibrium spectrum (**Figure 50b**, bottom) shows the characteristic signals of DBBA: doublets at 7.64 and 6.90 ppm (purple and green) from the aromatic moieties, and a

triplet at 3.57 ppm (red) assigned to the α-CH_2 of the imine. After 40 minutes from TBA addition, the triplet at 3.57 ppm disappears, while a new singlet at ~3.0 ppm (orange), attributed to the CH_2 of the *N*-butylammonium ion, appears and persists up to 2 h. At the same time, the aromatic doublets at 7.64 and 6.90 ppm are no longer detected, confirming that the DBBA moieties are involved in the transimination reaction.

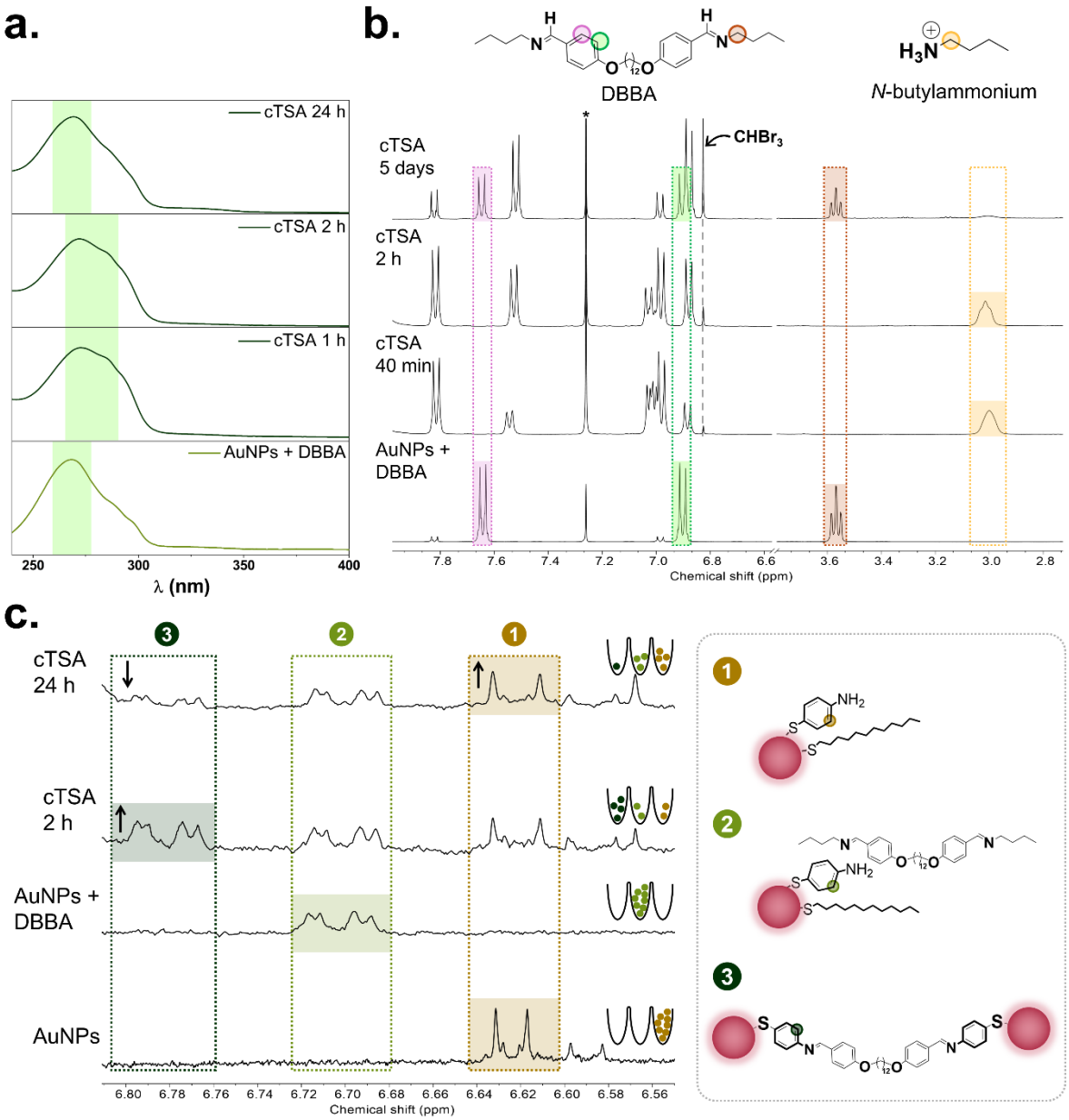

Figure 50. *a) UV-Vis spectra in DCM of AuNPs + DBBA mixture and after the addition of TBA (1 h, 2 h, and 24 h); 1H-NMR spectra in CDCl3 of b) AuNPs + DBBA mixture and after the addition of TBA (40 min, 2 h, and 5 days) and c) AuNPs, AuNPs + DBBA mixture and after the addition of TBA (2 h, and 24 h).*

The spectrum recorded 5 days after TBA addition (**Figure 50b**, top) shows the reappearance of the DBBA diagnostic peaks: the aromatic doublets (7.64 and 6.90 ppm) and the α-CH_2 imine triplet at 3.57 ppm (red), while the *N*-butylammonium signal at 3.0 ppm (orange) is no longer present. During the experiment, however, a significant hydrolysis of the imine was observed, leading to the formation of the corresponding benzaldehyde units (doublets at 7.82 and 6.98 ppm). In parallel, a singlet at 6.83 ppm, assigned to bromoform, is detected, confirming the occurrence of TBA decarboxylation and the transimination cycle. Additional peaks, a singlet at 4.31 ppm and a triplet at 2.57 ppm not shown in the figure (*vd. Figure D15*), were tentatively assigned to the formation of an adduct between bromoformate and the aliphatic amine moieties[189].

Quantitative analysis indicates that, after 5 days, bromoform accounts for about 47% of the initially expected amount, while benzaldehyde represents ~15%. Overall, the final spectrum suggests that the DBBA is progressively restored, consistent with the transient nature of the covalent assembly.

Monitoring the aromatic protons of the Ani moiety directly bound to the AuNPs, a clear shift of the ortho-proton signal of the amine group is observed (**Figure 50c**). In the spectrum of AuNPs alone (bottom), the doublet is centred at 6.62 ppm. In the equilibrium spectrum of the AuNPs + DBBA mixture, the signal shifts to 6.70 ppm, suggesting a non-covalent interaction between the precursor linker and the Ani moiety. After 2 h from the addition of TBA, three distinct signals are visible: one at 6.62 ppm, attributable to a small fraction of non-interacting Ani; a second at 6.70 ppm, corresponding to Ani occupied in non-covalent interactions with DBBA; and a third new doublet at 6.78 ppm, assigned to the formation of *N*-aromatic imines within the covalent network of AuNPs. The spectrum recorded after 24 h still shows the three signals, but their relative intensities change: the covalent signal at 6.78 ppm decreases drastically, while the contribution of non-interacting Ani increases. This evolution provides further evidence of the transient nature of the nanoparticle covalent network.

In conclusion, the SSA, CSA, and cTSA approaches enabled the development of stimuli-responsive nanoparticles capable of generating distinct self-assembly pathways, thereby highlighting their potential as versatile building blocks for dynamic and tunable nanostructures.

3.2. Network of AuNPs stabilized by bifunctional ligands

Network based on MNPs (schematic representation in **Figure 51**) have attracted a lot of interest due to their electronic and optoelectronic properties. By varying parameters such as size or interparticle distance, the electronic behaviour of the MNPs arrays can be substantially tuned and controlled. In general, when MNPs are in close proximity each other, the interparticle coupling effect becomes very important and the properties of regularly packed aggregates show tuneable optical properties and enhancement of photocurrents[190]. Rigid organic and organometallic bifunctional molecules, having two thiols moieties as anchoring groups, with an extended π-conjugated electronic system were used as bridges for the synthesis of covalently linked MNPs with tunable interparticle distances.

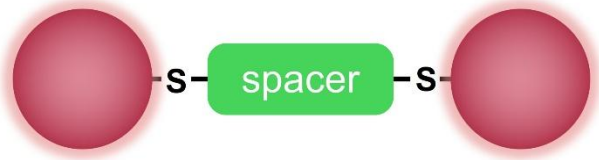

Figure 51. *Schematic representation of MNP covalent network.*

It this thesis, to modulate the interparticle distances in MNPs covalent networks, organic and organometallic ligands with different spacer were synthetised to functionalise MNPs. The ligands used are reported in **Figure 52**.

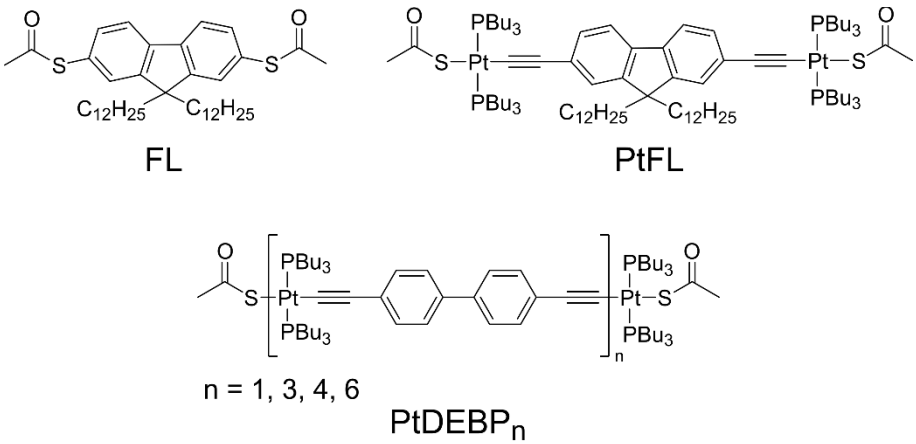

Figure 52. *Chemical structure of bifunctional ligand: 9,9-didodecyl-2,7-bis(acetylthio)fluorene (FL); bis[2-(trans-acetylthio-bis-(tributylphosphine) platinum(II))ethynyl]-9,9-didodecyl-9H-fluorene (PtFL); trans,trans-[dithioacetyldibis (tributylphosphine)diplatinum(II)-4,4'-diethynylbiphenyl] (PtDEBP).*

Ligands based on platinum complex can be used as bifunctional ligands, it is known that Pt(II) centres in MNPs can induce a synergistic effect at the electronic level, and a modulation of the physicochemical properties of MNPs with promising applications in organic electronic devices, sensing, and biocatalysis.

The synthetic pathways of the ligands in **Figure 52** are reported in *appendix B*, the thiols moieties are protected with acyl ending groups, the deprotection takes place *in-situ* during the nanoparticle synthesis with the acidic conditions. In this section different system of interconnected MNPs will be analysed. The first part focuses on a comparison between AuNPs, AgNPs and PdNPs functionalized with a single bifunctional organometallic ligand *i.e.* $PtDEBP_n$ with n = 1 (PtDEBP). Then we move to comparison between AuNPs functionalised with bifunctional ligands (FL or PtFL) with AuNPs functionalised with monofunctional and bifunctional ligands in mixture (DDT, see paragraph 3.1.1, and FL or PtFL). The aim was fine-tune the 2D/3D arrangement of the networks. Subsequently, preliminary studies on the use of these systems as chemoresistive sensors for Volatile Organic Compounds (VOCs) vapours is presented, with a short introduction about the importance of VOCs detection.

Finally, three different systems of AuNPs functionalized with monofunctional and bifunctional ligands in mixture is analysed in semiconductive polymeric blends for optoelectronic applications.

3.2.1. AuNPs, AgNPs and PdNPs counterparts-based Networks

The first system of interconnected nanoparticles was obtained using PtDEBP ($PtDEBP_n$ with n = 1). The investigated nanoparticles included gold, silver, and palladium (AuNPs, AgNPs, and PdNPs). The aim was to assess the formation of a trinuclear covalent M–S–Pt bond between the bifunctional organometallic thiolate complex and MNPs (AuNPs, AgNPs and PdNPs) surface. The size, shape and crystalline structure of these thiol functionalized metal nanoparticles were determined by transmission electron microscopy (TEM), energy dispersive X-ray spectroscopy (EDS), ^{1}H and ^{31}P nuclear magnetic resonance (NMR), and high-resolution synchrotron radiation induced X-ray photoelectron spectroscopy (SR-XPS).

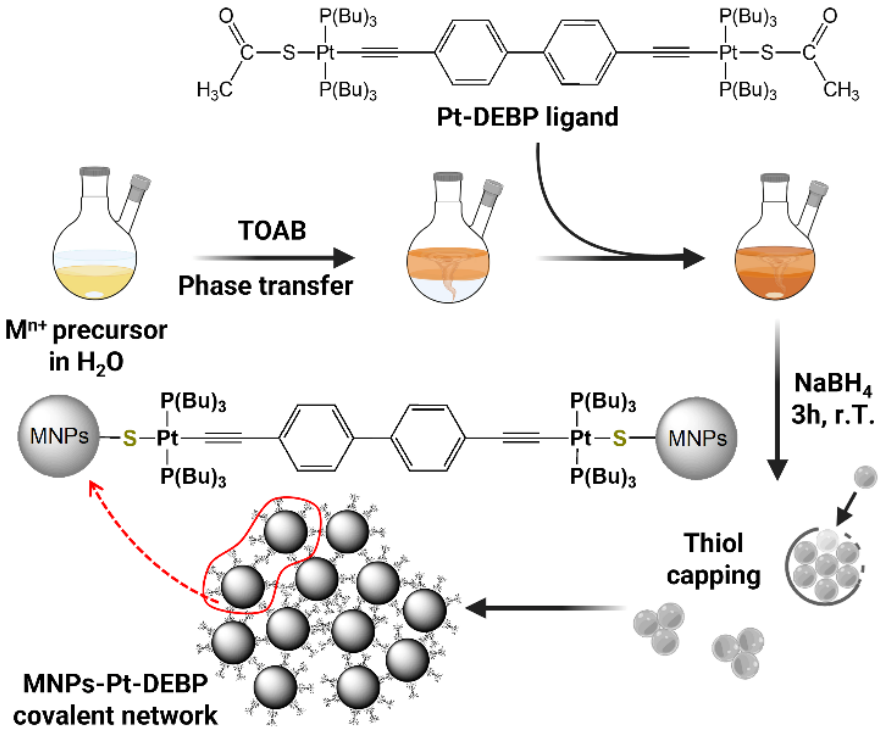

Figure 53. *Schematic synthesis procedure for MNPs-PtDEBP (M=Au, Ag, Pd).*

The latter allowed to probe the intermolecular interaction occurring between adjacent rod-like dithiols, involving Pt(II) centers and biphenyl rings considerably stabilizing the organic moieties arrangement. In order to provide useful models to understand the complex data achieved on the as-synthesized MNPs, self-assembled monolayers (SAM) and multilayers (MUL) of PtDEBP on gold surfaces were also prepared and investigated. Platinum(II) ethynylated complexes are excellent candidates for optoelectronics and sensing applications due to their well-assessed electronic properties that arise from inter- and intrachain charge transport mechanisms.

MNPs stabilized by the organometallic bifunctional thiol (PtDEBP) (metal precursor/sulphur 2:1 molar ratio) were prepared by a modified two-phase wet chemical reduction method, as already reported in **paragraph 3.1.1** and in detail described in *appendix C.2.2*. During the synthesis, the organometallic thioester is subjected to an *in-situ* deacetylation due to the presence of acidic conditions, this reaction promotes the formation of the S-metal bond. The final MNPs-PtDEBP were obtained following the one-pot procedure depicted in **Figure 53**. Spectroscopic characterization of pristine PtDEBP ligand and Au-, Ag-, and PdNPs-PtDEBP and are reported in **Figure 54**. However, for nanometre-sized PdNPs, the absorption profile does not feature a well-defined absorption such as surface plasmon resonance (SPR) band of AuNPs-PtDEBP (λ_{SPR} (AuNPs) = 525 nm) and AgNPs-PtDEBP (λ_{SPR} (AgNPs) =420 nm);

whereas, for PdNPs within 1-10 nm size range, only the Mie scattering spectra can be observed, thus confirming the nanoparticles formation.

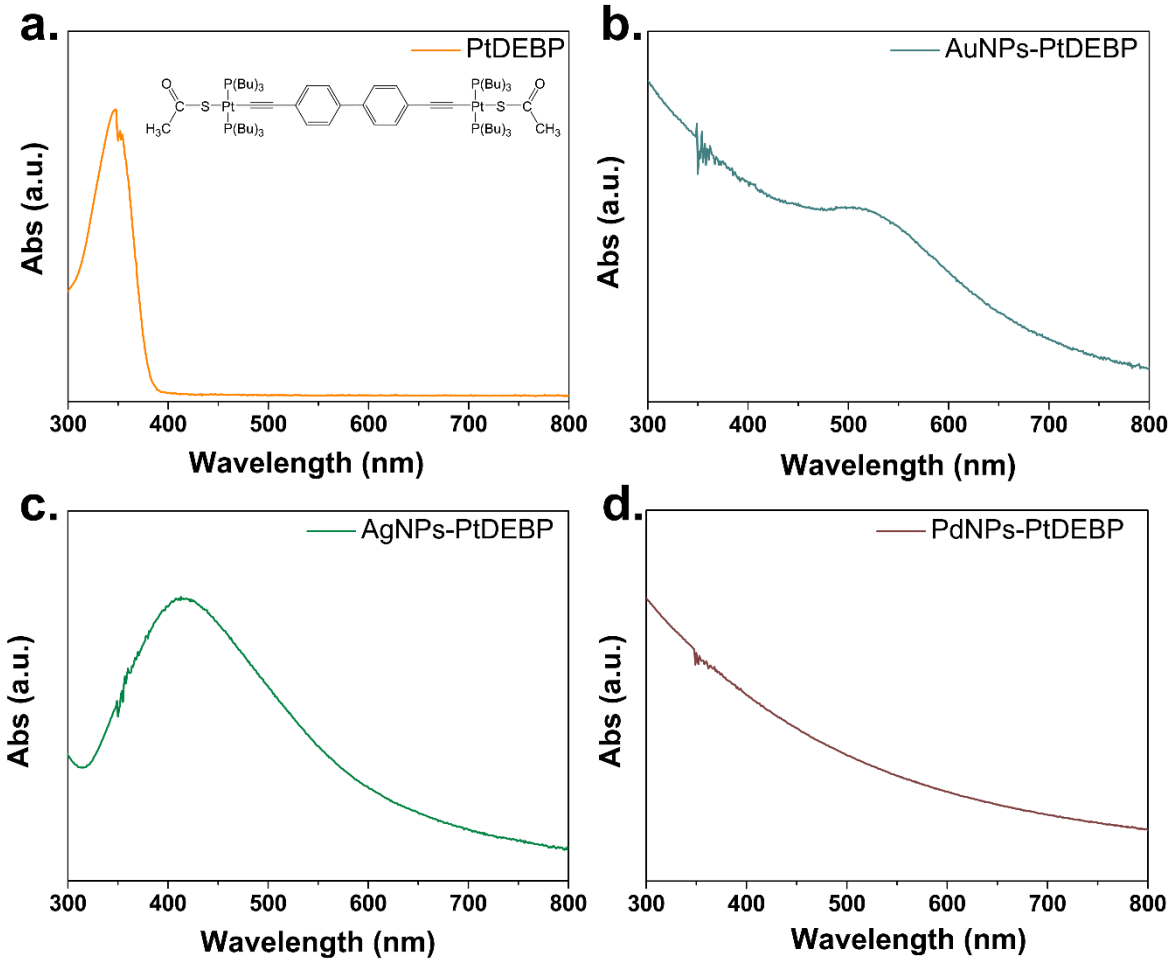

Figure 54. *UV-Vis absorption spectra of a)PtDEBP; b) AuNPs-PtDEBP; c) AgNPs-PtDEBP and d) PdNPs-PtDEBP. Solvent: dichloromethane.*

Powerful complementary information about the chemical composition at the surface of NPs were from energy dispersive X-ray spectroscopy (EDS), ^{1}H and ^{31}P nuclear magnetic resonance (NMR). NMR spectra of AuNPs-Pt-DEBP dispersed in $CDCl_3$ are reported as representative sample in *Figure C4*. In the ^{1}H-NMR spectrum, the four resonances in the alkyl-proton region (0.90−2 ppm) can be assigned to $-CH_2$ and $-CH_3$ protons of tributylphosphine linked to Pt(II) centers, whereas resonances associated to aromatic DEBP moiety in the ligand structure can be seen in the 7.00−7.60 ppm region. Additionally, corresponding resonance due to internal phosphines on Pt(II) was observed in the ^{31}P-NMR spectrum at 3.09 ppm, in agreement with a square planar Pt(II) center in *trans* configuration.

The morphology and surface modification of Au-, Ag-, and PdNPs-PtDEBP was investigated by TEM. The morphology and morphometric characterization of well-separated nanoparticles forming an extensive network are reported in **Figure 55** (PdNPs-PtDEBP) and **Figure 56** (Au- and AgNPs-PtDEBP). Bright-field (BF) transmission electron microscopy shows a monolayer of separated dark NPs deposited by drop casting from their colloidal suspensions on a carbon amorphous film.

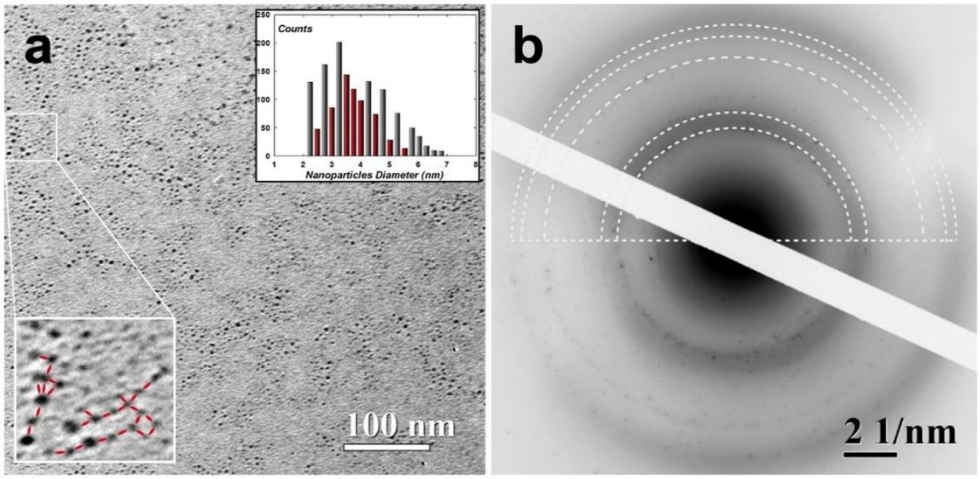

Figure 55. *Morphological study of PdNPs self-assembled in a monolayer network by PtDEBP bifunctional organometallic thiols. a) BF-TEM image of the inorganic–organic 2D-network of PdNPs-PtDEBP, inset: magnified region (white square) showing similar distances among nanoparticles evidenced by red rods (bottom-left) and histogram plot shows the frequency distribution of the nanoparticle dimension (top-right); b) EDP taken from Figure 55a showing distinct diffraction rings corresponding to the crystalline phases of Pd nanocrystal (grey dot line arcs).*

Appropriate imaging analyses have been exploited to perform accurate quantitative measurements of the size and spatial distribution of individual nanoparticles, paying attention to the statistical analysis. Since all the nanoparticles systems seem assembled into a bi-dimensional monolayer network with regular spatial distributions, quantitative morphometric measurements and a possible topological relationship among the NPs have been investigated. The case of PdNPs-PtDEBP is reported as representative sample. By measuring the diameter of 1555 selected palladium nanoparticles in enlarged statistical imaging analyses revealed an overlapping of a bimodal size distributions. The higher-counts distribution is centered at (3.35 ± 0.48) nm with a polydispersity of about 15%, while the second bin distribution of low-counts value is centred at (3.52 ± 0.36) nm with a

polydispersity of about 10%. It should be noticed that the bimodal size distribution exhibits the smallest difference, and the applied synthesis was able to limit the growth of the nanoparticles. In fact, the histogram of the nanoparticle diameter clearly exhibits a linear increase of the dimension from about 2 nm to 3.5 nm and later a rapid decrease in counts can be observed, locking the growth mechanisms. A magnified region of the white line square evidences well separated PdNPs in which red rods of same length have been drawn among neighbour dark nanoparticles only to show that the unnatural rods could be associated to the organometallic spacer (PtDEBP, Inset of **Figure 55a**). To explore how the organometallic bridge may have involved the organization of the palladium interparticle distance into a 2D self-assembled network, an image analysis technique has been involved to quantify the distribution among surface-to-surface nearest neighbor distances of about 2.1 nm. In order to obtain more experimental information on the 2D-network, selected area electron diffraction (SAED) measurements were performed for identifying the atomic and structural compositions of the observed hybrid aggregate. The corresponding electron diffraction pattern (EDP) exhibits diffraction rings produced by a random orientation of the polycrystalline material (**Figure 55b**). By measuring the d-spacing of the diffraction rings, we were able to identify the typical Pd crystallites with a face centred-cubic (fcc) structure of a space group Fm3m (American Mineralogist Crystal Structure Database, amcsd 0014952), confirmed also by the intensive ring of d_{111} = 0.224 nm (grey dot arcs). Similar TEM morphology and morphometric characterization have been performed for gold and silver nanoparticles samples showing a well-organized 2D-network.[191,192]

Therefore, BF-TEM and SAED observations have been reported **Figure 56**. Herein, imaging analysis estimated AuNPs and AgNPs diameter of (3.95 ± 0.56) nm and of (3.54 ± 0.62) nm closer to previous investigations and the estimated interparticle distances remain similar to the length of the organometallic spacer PtDEBP of about 2.1 nm (theoretical S-to-S distance for PtDEBP ligand 2.034 nm[193]). To identify the atomic and structural compositions of the samples, SAED investigations have been probed. The corresponding EDPs of the AuNPs and AgNPs display several diffraction rings with different planes assigned to the typical Au and Ag crystallites both with a face centred-cubic (fcc) structure of a space group Fm3m, confirmed also by the intensive ring of d_{111} = 0.236 nm. These morphometric investigations of the noble metal NPs regarding the dimensions and their similar interparticle distances let us see the strong influence of the organometallic spacer that links covalently the surface of the NPs forming a self-assembled monolayer independently from the noble metal species used through the wet-chemistry approach.

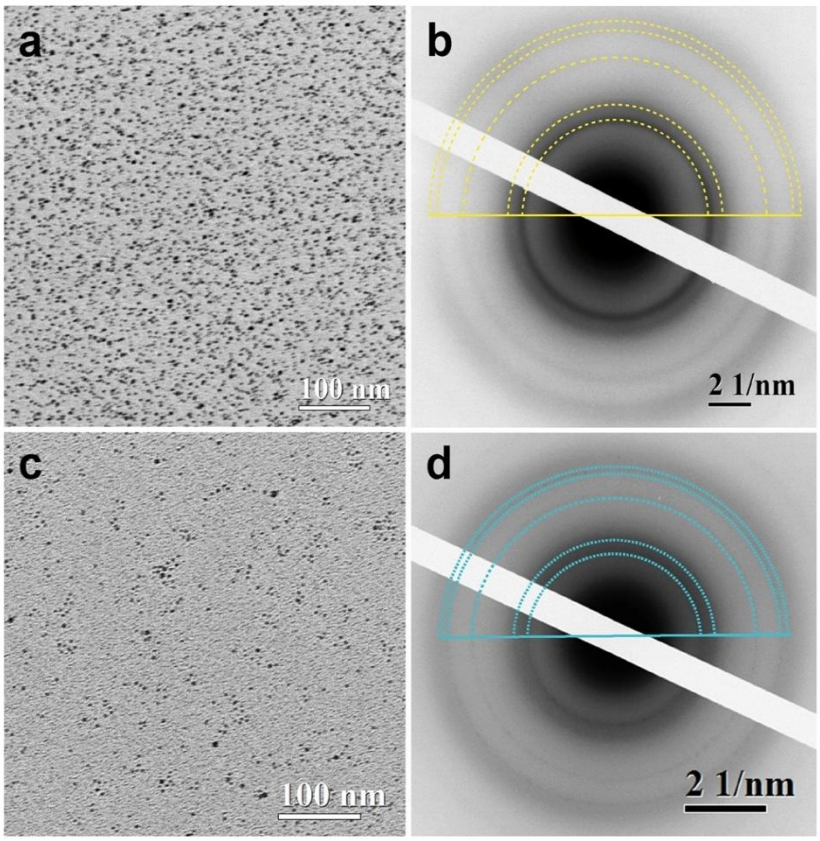

Figure 56. *Morphological study of gold and silver nanoparticles self-assembled in a monolayer network by PtDEBP bifunctional organometallic thiols. a) BF-TEM image of the inorganic–organic 2D-network of AuNPs-PtDEBP; b) EDP taken from Figure 54a showing distinct diffraction rings corresponding to the crystalline phases of Au (yellow line arcs); c) BF-TEM image of the inorganic–organic 2D-network of AgNPs-PtDEBP; d) 2D contour map of the 2D-network distribution. d) EDP taken from Figure 54c showing distinct diffraction rings corresponding to the crystalline phases of Ag (blue dot line arcs).*

3.2.1.a. SR-Induced X-Ray Photoelectron Spectroscopy Investigation.

With the aim to probe the chemical and electronic interaction at the interface between noble metal NPs and rod-like PtDEBP ligand, high resolution SR-XPS experiments were performed. Measurements were carried out at P2p, S2p, Pt4f, and Au4f or Pd3d or Ag3d core levels for all the considered samples (for complete BE, FWHM, atomic ratio values and assignments, see *Table C3*). Data collected on SAM and multilayer of the same molecules anchored on polycrystalline gold substrates (Au/Si(111) wafers) were also analysed for comparison; in particular, the S2p signal analysis performed for SAM and multilayer samples was used as reference for the interpretation of the sulphur spectra collected on the stabilized NPs. For all the NPs samples, $P2p_{3/2}$ BE values were found at about 130 eV

(*Figure C5*), whereas for and Pt4f$_{7/2}$ at ca. 72.6 eV (*Figure C6*), as expected for binuclear compounds of PtDEBP-like Pt(II) dimers, evidencing that the organometallic molecules are all surface associated and that Pt−S bond cleavage and/or phosphines oxidation and degradation is not occurring, thus allowing to assess the ligands molecular structure stability after the synthesis procedure. Furthermore, SR-XPS measurements allowed to assess the anchoring of the organometallic thiols onto gold substrates as well as to gold, silver, and palladium nanoparticles surfaces. To characterize the chemical structure of the ligands on monolayers and multilayers, the metal and sulphur core level spectra were collected. For SAM, a single pair of spin-orbit components is detected in the Au4f signal with the main Au4f$_{7/2}$ component at 83.89 eV BE related to metallic gold atoms, as expected for a polycrystalline gold substrate covered by a very thin molecular substrate (monolayer). In the multilayer sample**,** Au4f signal intensity is very low, due to the attenuation of the thick overlayer. Concerning the stabilized NPs, metal core-level signals (*i.e.*, Pd3d, Au4f and Ag3d) were collected and analysed (**Figure 57**).

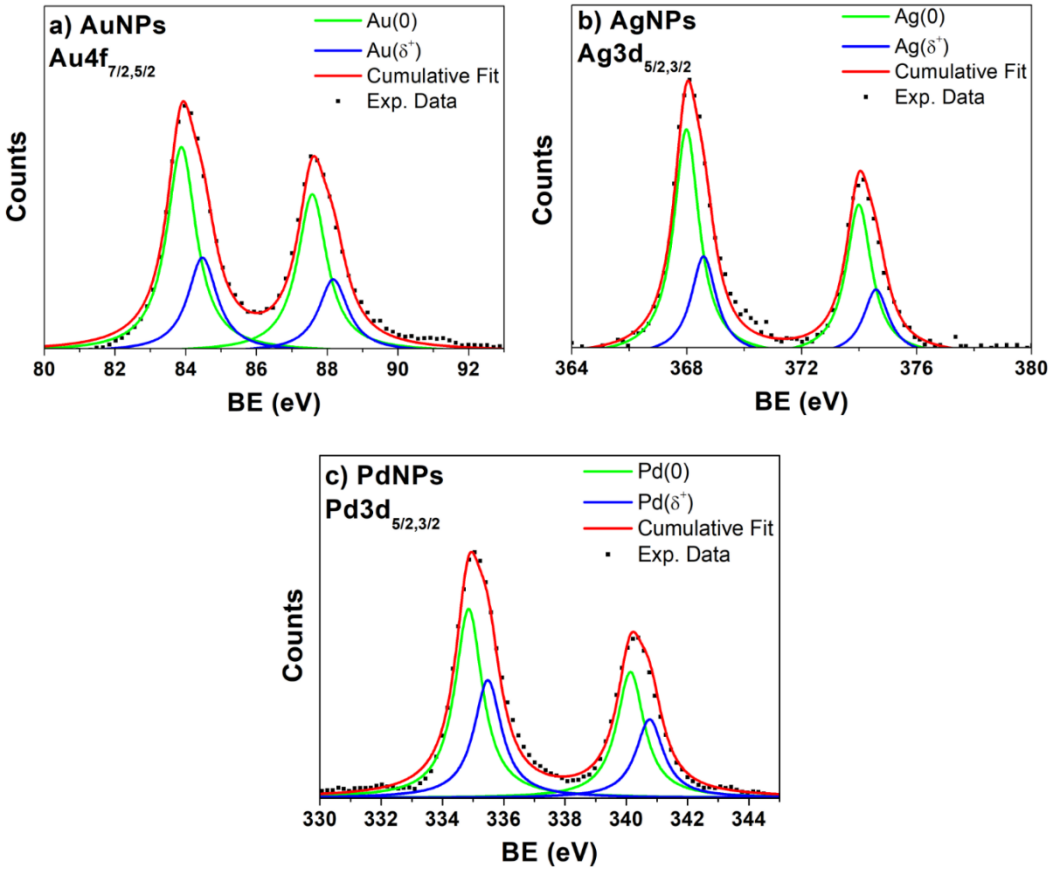

Figure 57*. SR-XPS at a) Au4f$_{7/2,5/2}$ core level for AuNPs-PtDEBP, b) Ag3d$_{5/2,3/2}$ for AgNPs-PtDEBP and c) Pd3d$_{5/2,3/2}$ of PdNPs-PtDEBP.*

By a curve-fitting analysis, two spin-orbit pairs can be observed (in all cases) and associated to metal atoms involved in different chemical environments. Characteristically, the signal at lower BE values is attributed to metallic atoms in NPs bulk; on the other hand, the spectral component that occurs at a higher BE value is associated with metal sites coordinating the electron acceptor thiol ligands. More in detail, in Au4f spectrum of AuNPs (**Figure 57a**) a main spin-orbit pair is found at BE values expected for the metallic gold signal ($Au4f_{7/2}$ BE = 83.87 eV), and a less intense couple of components at higher BE ($Au4f_{7/2}$ BE = 84.47 eV) coherently with positively charged Au atoms belonging to the NP surface and chemically interacting with sulphur (about 46% in the gold atomic percent); for the Ag3d SR-XPS spectrum of AgNPs (**Figure 57b**) two doublets can be observed: a main spin-orbit pair at 367.99 eV, as expected for metallic silver, related to the core NPs atoms and a second component at about 368.59 eV, associated to the surface metallic atoms involved in Ag−S−R bridges and corresponding to a 44% in the atomic percent. Likewise, to probe the electronic interaction at PdNP/thiol interface, the Pd3d core level was measured (**Figure 57c**).

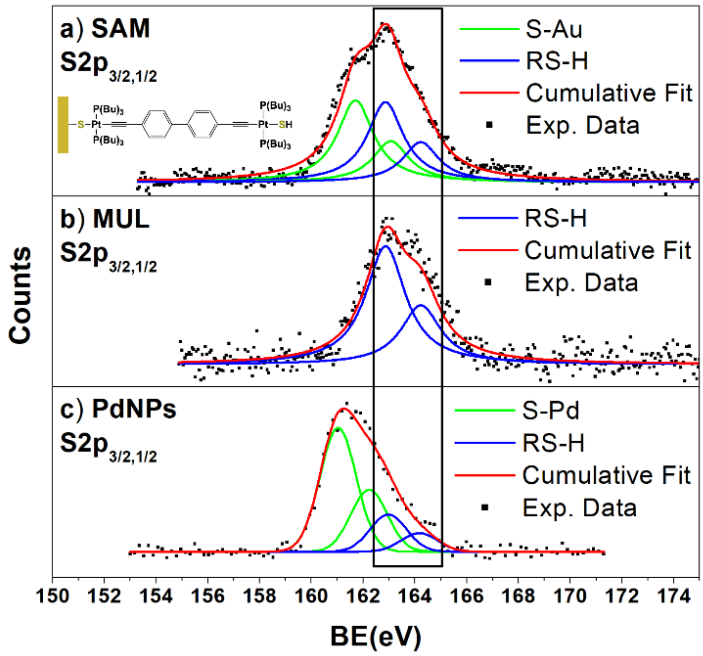

***Figure 58**. SR-XPS at $S2p_{3/2,1/2}$ core level of a) self-assembled monolayer (SAM), b) self-assembled multilayer (MUL) and c) PdNPs-PtDEBP. The component associated to the free thiol terminal group is evidenced.*

The peak fitting procedure allows to identify two pairs of spin-orbit doublets: the spin-orbit pair at lower BEs, $Pd3d_{5/2}$ BE = 334.85 eV, is due to the metallic palladium signal. The signal

at higher BE (335.48 eV) is associated with palladium atoms that are partially positively charged because of the chemical bond with the thiol. The surface palladium atoms involved in the Pd−S bond correspond to a 62% in the atomic percent.

S2p spectra collected on SAM and multilayer provided useful references for the interpretation of NPs data, as reported in the following. As shown in **Figure 58a**, the sulphur signal collected on SAM shows two doublets ($S2p_{3/2}$ BE = 162.3 eV and $S2p_{3/2}$ BE = 163.3 eV), whereas for the multilayer sample (**Figure 58b**) only a single spin-orbit pair is detected, with the 3/2 component at about 163.3 eV in BE. According to the literature, the spin-orbit doublet at lower binding energy is due to organometallic thiols chemically linked to metals through a covalent S–metal bond, while the signal at higher BE values is associated with sulphur atoms of free thiol terminal groups. It is noteworthy that the atomic ratio between the two components is 1:1 for SAM, suggesting the formation of a monolayer in which each molecule is anchored on the gold surface while preserving a free terminal group (inset in **Figure 58a**). Conversely, S2p spectra of AuNPs, AgNPs and PdNPs showed a single signal at low BE values, similarly to the low BE signal observed in SAM (*i.e.*, around 160–162 eV in BE) and attributed to organometallic thiols chemically bonded to metals through a S−metal bond, suggesting that all thiol groups of MNPs are involved in sulphur-metal chemical bonds (S2p spectrum collected on PdNPs is reported as an example in **Figure 58c**, all the S2p spectra are reported in *Figure C7*). This finding supports the hypothesis of the formation of a NPs network organized in a "thiol bridges" configuration, coherently with TEM images. According to SAM and MUL spectra interpretation, in the PdNPs S2p spectrum (**Figure 58c**) two spin-orbit pairs can be found: at lower BEs the spin-orbit component is due to organometallic thiol chemically interacting with NPs surface through Pd-S covalent bond (77%), whereas signals at higher BE (162.97 eV) can associated with sulphur atoms of free thiol end-groups (ca. 23%). The latter are due to a fraction of terminal sulphide groups not interacting with the NPs surface or physisorbed thiols.[194]

Pt4f SR-XPS spectra gave interesting information about the interaction between adjacent ligand molecules. Molecular self-assembling is commonly observed in films of polymeric conjugated systems containing transition metal centres σ- or π-bonded to organic main chain. For the here discussed samples, except for the SAM, all Pt4f spectra showed a second component, at higher BE values (ca. 73-74 eV) respect to the previously discussed signal related to square-planar Pt(II). This secondary feature observed in Pt4f spectra can be attributed to the Pt atoms electronically interacting with the ethynyl-biphenyl groups of adjacent molecules, as expected for rod-like polyynes, giving rise to intra and inter-

molecular charge transfer between metal and ligand. BE, FWHM, atomic ratio values and assignments of Pt4f collected on all the presented samples here are reported in the following **Table 4**.

Sample	BE	FWHM	I ratio[a]	Assignment
SAM	72.83	1.45	1	PtDEBP-like
MUL	72.59	1.74	85.05%	PtDEBP-like
	73.44	1.74	14.95%	Pt(δ^+)
AuNPs	72.61	1.68	84.60%	PtDEBP-like
	73.59	1.68	15.40%	Pt(δ^+)
AgNPs	72.63	1.64	82.13%	PtDEBP-like
	73.34	1.64	17.87%	Pt(δ^+)
PdNPs	72.80	1.82	77.69%	PtDEBP-like
	74.04	1.82	22.31%	Pt(δ^+)

Table 4. *SR-XPS $Pt4f_{7/2}$ collected on SAM and MUL of Pt polyynes Pt-DEBP and on NPs stabilized by Pt-DEBP (BE, FWHM, atomic ratios and assignments). [a] I ratio = I_{peak}/I_{tot} signal for the selected element.*

As a matter of fact, a variety of d-transition metal complexes involving metal ions like Ru(II), Re(I), Pt(II) and Ir(III) show interesting optical properties related to inter- and intra-molecular charge transfer (CT). Among these metal complexes, square-planar Pt(II) complexes are quite interesting, since they show metal-to-ligand CT (MLCT), ligand-centred (LC), and/or metal-metal-to-ligand CT (MMLCT) optical emission, depending on ligand structure, temperature, medium and concentration.[195,196] It can be noticed a switching between metal-to-ligand charge transfer, intra-ligand charge transfer (ILCT), ligand-to-ligand charge transfer (LLCT), or intra-ligand (IL) transitions in platinum(II) complexes. These excited states might be interchanged by a change of solvent or pH, or by the introduction of metal ions, thereby yielding a variety of interesting photophysical properties.[197]

Therefore the presence of a second doublet in the Pt4f of multilayer and NPs samples (**Figure 59**) seems to be due to inter-chain interactions arising between metal centres and adjacent acetylene moieties and aromatic rings. This behaviour in the self-assembling organization of dinuclear Pt(II)-based complexes and organometallic polyynes was already observed and reported in previous works.[198] Conversely, the Pt4f signal of SAM shows a single spin-orbit pair, confirming the formation of a monolayer without inter-chain interactions[199], probably due to the larger interchain distances and/or to a different molecular packing that does not allow Pt–phenyl ring communication. Generally speaking, Pt4f and

S2p spectra collected on SAM suggest the presence of a molecular orientation, as already observed in thin films of Pt-DEBP and Pd-DEBP deposited onto Au/Si(111) substrates and investigated by angular dependent NEXAFS spectroscopy[200]; this aspect will be subject to a future investigation.

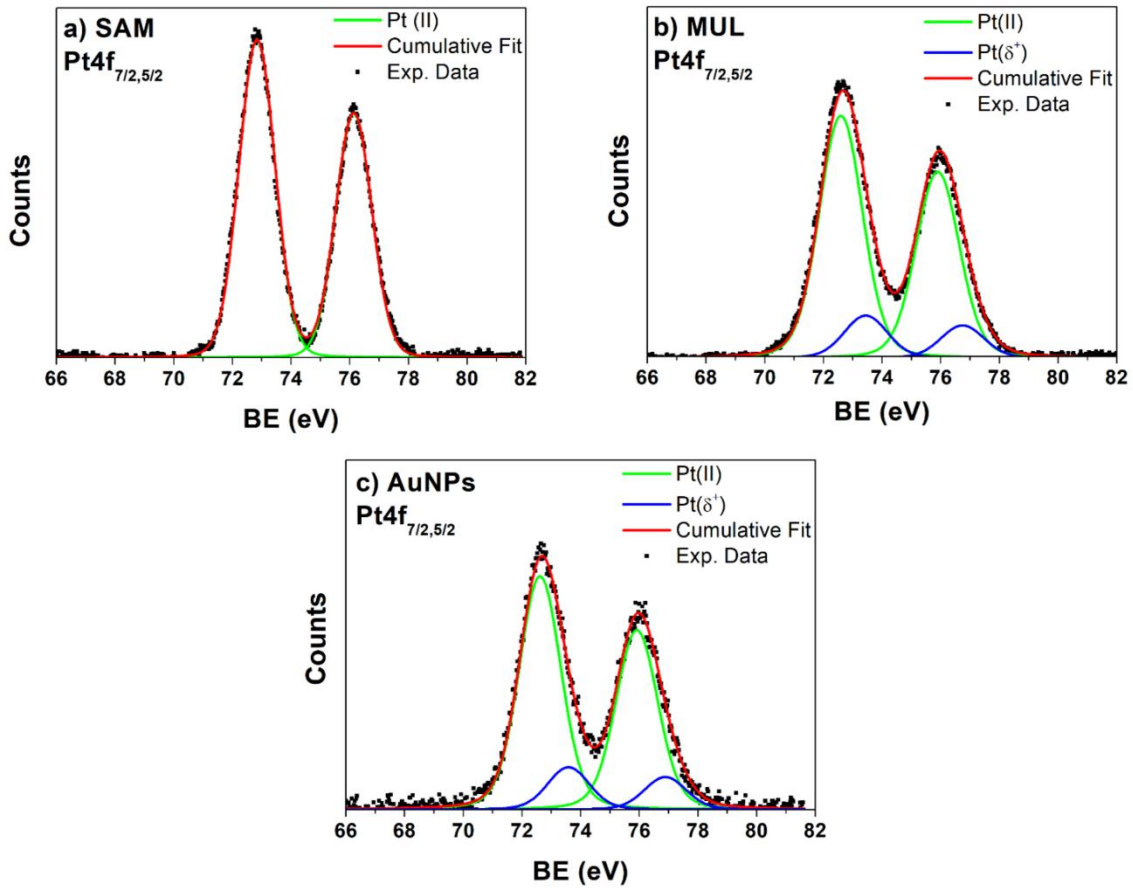

***Figure 59**. SR-XPS at $Pt4f_{7/2,5/2}$ core level of a) self-assembled monolayer (SAM), b) self-assembled multilayer (MUL) and c) AuNPs-Pt-DEBP.*

The synthesis and characterization of gold nanoparticles (AuNPs) stabilized by a novel bifunctional thiolate organometallic complex containing Pt(II) centres (AuNPs-PtDEBP) is reported and compared with Ag- and PdNPs-PtDEBP. A self-assembled monolayer (SAM) and a multilayer (MUL) of the organometallic complex deposited onto a "flat" gold surface were prepared and investigated as a reference. UV-Visible spectroscopy allowed to confirm the nanoparticles formation, whereas EDS and ^{1}H,^{31}P-NMR were used to assess the chemical composition and the presence of PtDEBP ligand on the surface of NPs, respectively. The morphology of the nanoparticles was characterized by TEM analyses highlighting NPs with

an average diameter of (3.95 ± 0.56) nm, AuNPs; (3.54 ± 0.62) nm, AgNPs; (3.35 ± 0.48) nm, PdNPs). The linkage between the MNPs has an estimated interparticle distance of about 2.1 nm, in agreement with PtDEBP length. SR-XPS measurements allowed to assess the covalent attachment of the sulphur atoms as thiolates to the surface of metals. S2p spectra of PdNPs showed a single signal, suggesting that the organometallic dithiol can graft vicinal nanoparticles with both terminal groups in dyads, supporting TEM observations. The new hybrids show a direct link between Pt(II) and Au nanoparticles through a single S bridge, confirming the hypothesized achievement of 2D or 3D networks. Furthermore, the comparison between SR-XPS data collected on MNPs, SAM and MUL of the pristine rod-like dithiols deposited onto a polycrystalline gold surfaces lead to ascertain that an electronic interaction occurs between the Pt(II) centres and the biphenyl moieties of adjacent ligands, stabilizing the organic part of the network. This behaviour was observed for all noble-metal NPs, *i.e.*, AuNPs, AgNPs and PdNPs. In conclusion, the here demonstrated ability to obtain networks of regularly spaced noble metal nanoparticles (successfully tested on three different noble metals) opens outstanding perspectives in the field of optoelectronics.

3.2.2. AuNPs networks fictionalised by mixed thiols for chemiresistive sensors

The increasing presence of pollutants in the atmosphere is a steadily increasing problem; and among them volatile organic compounds (VOCs)[201,202]are considered the most critical indoor contaminants by the World Health Organization (WHO). [203] VOCs are low-molecular weight compounds and exhibit high vapour pressure, low boiling point, and are easily volatile under atmosphere conditions.[204] VOCs show a substantial impact on human health and their vapours can cause various health diseases such as nausea and pain in body organs; moreover, some VOCs are carcinogenic and teratogenic.[114,115] In the atmosphere, VOCs include several chemical classes such as pyrazines, benzenoids, terpenes, organic acids, ketones, alcohols, and alkenes.[112] Among aromatic hydrocarbons, benzene, toluene, and the three xylene isomers (*m*-xylene, *o*-xylene, and *p*-xylene) are categorized as BTX.[113] Simultaneous detection of BTXs is challenging, various techniques are currently employed for this scope, although with some limitations. The most common techniques include gas chromatography – mass spectrometry (GC-MS), Raman spectroscopy, attenuated total reflection mid-infrared spectroscopy; all these methods are limited by low-cost effectiveness and necessity of specialised technicians.[205,206,207] . Hence, the development of highly

selective, sensitive, and real-time sensors is essential. Up to now, among various platforms, chemiresistive gas sensors are reported in literature as a good choice for BTX gas detection due to high sensitivity, ease of fabrication, compactness, lower operating temperature, and low power consumption[117] In such devices, the sensing material is deposited on electrodes (e.g. line electrode, parallel electrodes, and interdigitated electrodes) that are printed/stamped on a substrate like paper, plastic or silica substrate.[121] Gas adsorption is detected as a resistance change, which is directly correlated to the analyte concentration. Metal oxide semiconductors have shown great potential in sensing applications[208,209] but they usually operate at high temperature (between 100 °C to 500 °C)[210,211,212] that can cause degradation of sensing performance changing the microstructure of the materials. To obtain room temperature operative sensors, surface functionalized MNPs can be used and deposited on interdigitated electrodes producing stable films and superstructure formation. To date, there is no extensive literature on functionalized MNPs-based sensors.[122] MNPs provide a high surface-to-volume ratio, offering numerous active sites for gas adsorption and thereby enhancing sensitivity, selectivity, and response time.[213] Among them, AuNPs are particularly promising candidates, as their surface electronic properties can be finely tuned by an appropriate choice of ligands.[111] Rigid bifunctional ligands enable the formation of interconnected and conjugated AuNP films, while aromatic ligands can exploit π–π interactions with BTX molecules, opening the way to highly efficient chemiresistive sensors for these hazardous pollutants.[214]

In this contest, interconnected AuNPs functionalised with FL or PtFL were synthesized and compared with systems functionalized with two ligands in mixture (DDT/FL and DDT/PtFL). After a precise characterization, they were used as VOCs chemiresistive sensors.

3.2.2.a. Comparison between single-ligand and mixed-ligand systems

AuNPs were synthesized according to a modified Brust-Schiffrin method. Four systems of AuNPs were synthesised and characterized. The systems of AuNPs stabilized with single bifunctional ligand (FL or PtFL) were obtained in accordance with previous works of the group [215,216]. To fine-tune the 2D/3D arrangement of the networks, modulate the quantity of optically active ligand (FL or PtFL) and increase the stability and suspensibility in organic solvents of AuNPs, the ligand dodecanethiol (DDT) was added into the reaction mixture and AuNPs functionalized with 2 thiols in mixture were obtained *i.e.* AuNPs-DDT-FL and AuNPs-DDT-PtFL (as schematized in **Figure 60**).

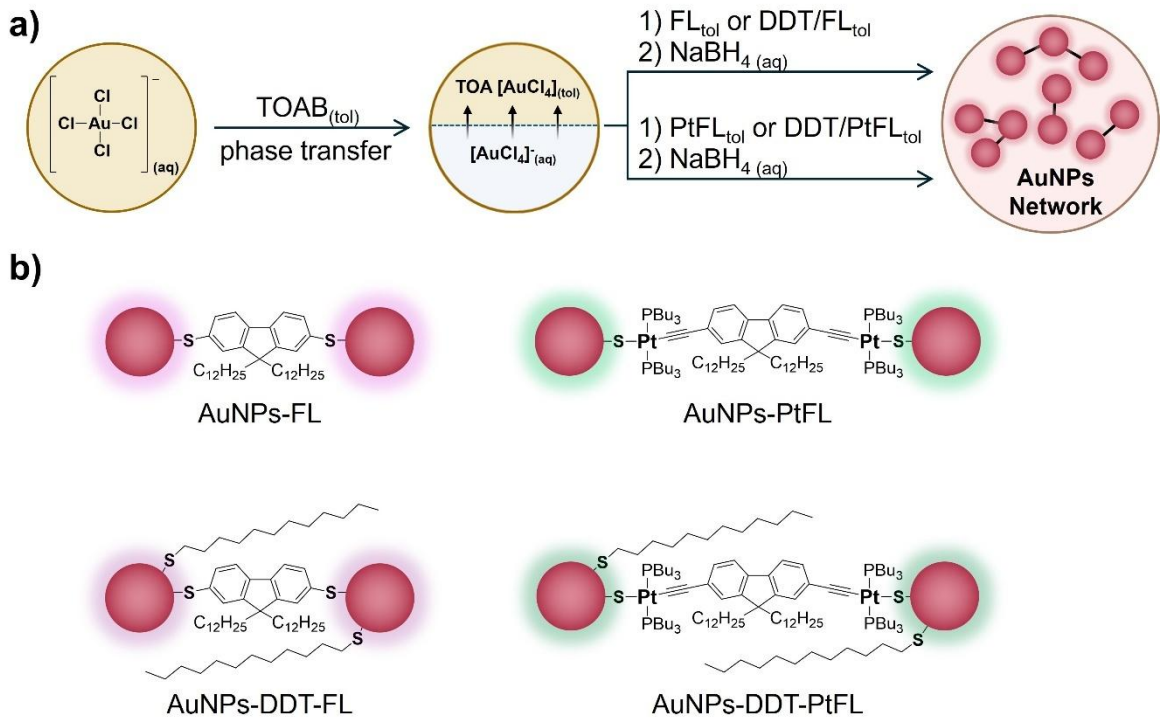

Figure 60. *a) schematic representation of synthesis of AuNPs; b) representation of the four systems of AuNPs synthesised and characterized in this section.*

The synthesis protocol for mixed-thiol nanoparticles was optimized, yielding stable AuNPs with the following molar ratios between the precursors: $Au/S_{FL}/S_{DDT}$ = 1/2/1 for AuNPs-DDT-FL and $Au/S_{PtFL}/S_{DDT}$ = 1/1/1 for AuNPs-DDT-PtFL. The detailed synthetic procedure is reported in *Appendix C2.3*.

After purification, the formation of colloidal thiol-functionalized AuNPs was confirmed by the presence of the characteristic surface plasmon resonance (SPR) absorption band in all systems, centred between 515 and 550 nm. **Figure 61a** shows the UV–Vis spectra of the ligand FL, AuNPs-FL, and AuNPs-DDT-FL. In both nanoparticles, a peak at 336 nm corresponding to the optically active ligand FL is clearly visible. Focusing on the plasmonic bands, AuNPs functionalized with FL exhibit an SPR band centred at 520 nm, whereas AuNPs prepared with the two thiols in mixture show a blue-shifted of plasmonic band centred at 515 nm. This effect may indicate: the nanoparticles formed with mixed ligands have a smaller metallic core, or the covalent assembly mediated by the bifunctional FL is less extensive when DDT is present on the surface, that means a successful fine-tuning of the 2D/3D arrangement was achieved.

A similar trend is observed in **Figure 61b**, which reports the UV–Vis spectra of PtFL, AuNPs-PtFL, and AuNPs-DDT-PtFL. Again, the characteristic absorption of the optically

active ligand is observed at 385 nm for both nanoparticles. However, the SPR bands show a clear shift: AuNPs-PtFL exhibit an LSPR centred at 550 nm, while in the mixed-ligand system (AuNPs-DDT-PtFL) the band is blue-shifted to 530 nm. As before, this behaviour can be attributed either to a reduced particle size or, more plausibly, to the formation of a less extended covalent network.

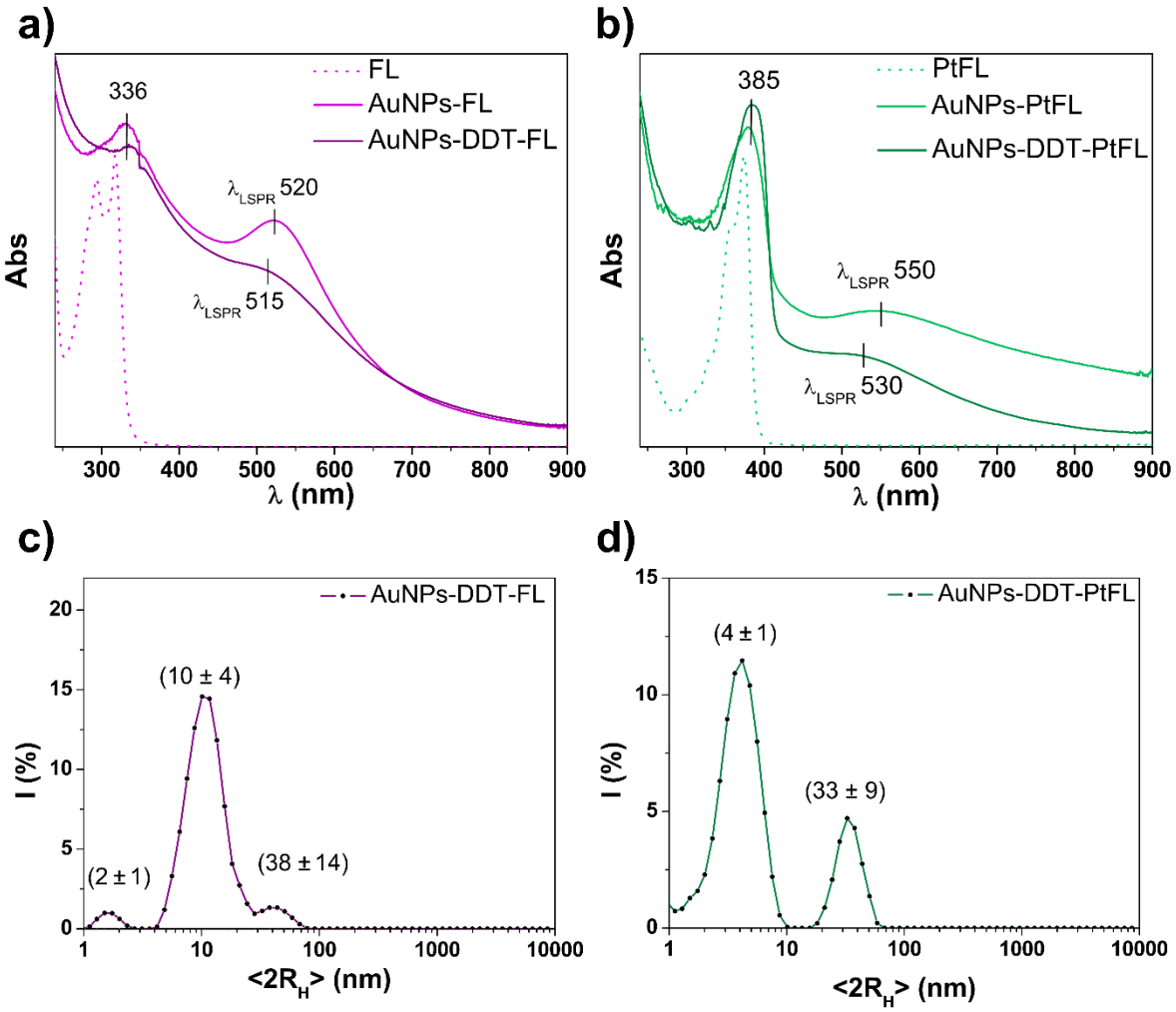

Figure 61. *UV-Vis spectra of a) FL, AuNPs-FL, AuNPs-DDT-FL and of b) PtFL, AuNPs-PtFL, AuNPs-DDT-PtFL. DLS graph of c) AuNPs-DDT-FL and d) AuNPs-DDT-PtFL. All the measurements were collected in* CH_2Cl_2.

The DLS measurements support the hypothesis that the addition of DDT to the nanoparticle surface modulates the networking. As shown in the graphs reported in *Appendix C* (*Figure C8, C9*), AuNPs functionalized with FL display two size populations, with hydrodynamic diameters centred at (16 ± 8) nm and (113 ± 29) nm, while the system functionalized with

PtFL exhibits a single broader population centred at (69 ± 35) nm. These suggest an extended networking in both systems.

In **Figure 61c**, the DLS profile of the AuNPs-DDT-FL system is reported, showing three distinct populations centred at (2 ± 1) nm, (10 ± 4) nm, and (38 ± 14) nm. These results suggest that the suspension contains both isolated nanoparticles ((2 ± 1) nm) as well as networks of different extents: ((10 ± 4) nm and (38 ± 14) nm). A similar behaviour is observed for the AuNPs-DDT-PtFL system as shown in the DLS graph in **Figure 61d**, both isolated nanoparticles ((4 ± 1) nm) and nanoparticle networks ((33 ± 9) nm) are present.

Overall, the networks formed in mixed-ligand systems are less extended compared to those observed in the corresponding single-ligand systems, improving the suspendability of the colloidal systems.

To confirm the presence of thiols on the gold surface, FT-IR spectroscopy was performed. **Figure 62a** reports the spectra of AuNPs functionalized with FL (light purple) and with a mixture of DDT and FL (dark purple). The complete band assignments are provided in *Appendix C2.3*; here, the most significant features are discussed. In both systems, characteristic signals of the symmetric and asymmetric stretching vibrations of aliphatic -CH_2 groups are observed: for AuNPs-FL, $\nu_{as}(\text{-}CH_2)$ = 2922 cm^{-1} and $\nu_{s}(\text{-}CH_2)$ = 2851 cm^{-1}, while for AuNPs-DDT-FL the corresponding bands appear at 2924 cm^{-1} and 2853 cm^{-1}. These confirm the presence of aliphatic chains from FL and, in the mixed system, from both FL and DDT. Another diagnostic feature is the weak band assigned to the aromatic $\nu(C\text{-}C)_{Ar}$ stretching of the FL phenyl rings, detected at 1597 cm^{-1} for AuNPs-FL and slightly shifted to 1595 cm^{-1} for AuNPs-DDT-FL. Such small shifts can be considered not significant. Finally, the stretching vibrations of the C-S bonds provide further evidence of surface binding: for AuNPs-FL, a $\nu(C_{Ar}\text{-}S)$ band is observed at 615 cm^{-1}, whereas in AuNPs-DDT-FL two distinct signals appear, at 658 cm^{-1} ($\nu(C_{aliph}\text{-}S)$) and 626 cm^{-1} ($\nu(C_{Ar}\text{-}S)$), confirming the simultaneous presence of aromatic and aliphatic thiols on the gold surface.

Figure 62b shows the spectra of AuNPs functionalized with PtFL and with DDT and PtFL in mixture. The complete band assignments are reported in *Appendix C2.3*. The -CH_2 stretching bands are clearly visible: for AuNPs-PtFL, $\nu_{as}(\text{-}CH_2)$ = 2926 cm^{-1} and $\nu_{s}(\text{-}CH_2)$ = 2855 cm^{-1}; for AuNPs-DDT-PtFL, $\nu_{as}(\text{-}CH_2)$ = 2924 cm^{-1} and $\nu_{s}(\text{-}CH_2)$ = 2853 cm^{-1}. A distinctive feature of both systems is the signal at 2098 cm^{-1}, attributed to the C≡C stretching of the platinum complex. The weak band assigned to aromatic $\nu(C\text{–}C)_{Ar}$ stretching appears at 1603 cm^{-1} for both AuNPs-PtFL and AuNPs-DDT-PtFL. The presence of DDT on AuNPs-DDT-PtFL is further supported by a weak signal at 664 cm^{-1}, assigned to $\nu(C_{aliph}\text{–}S)$.

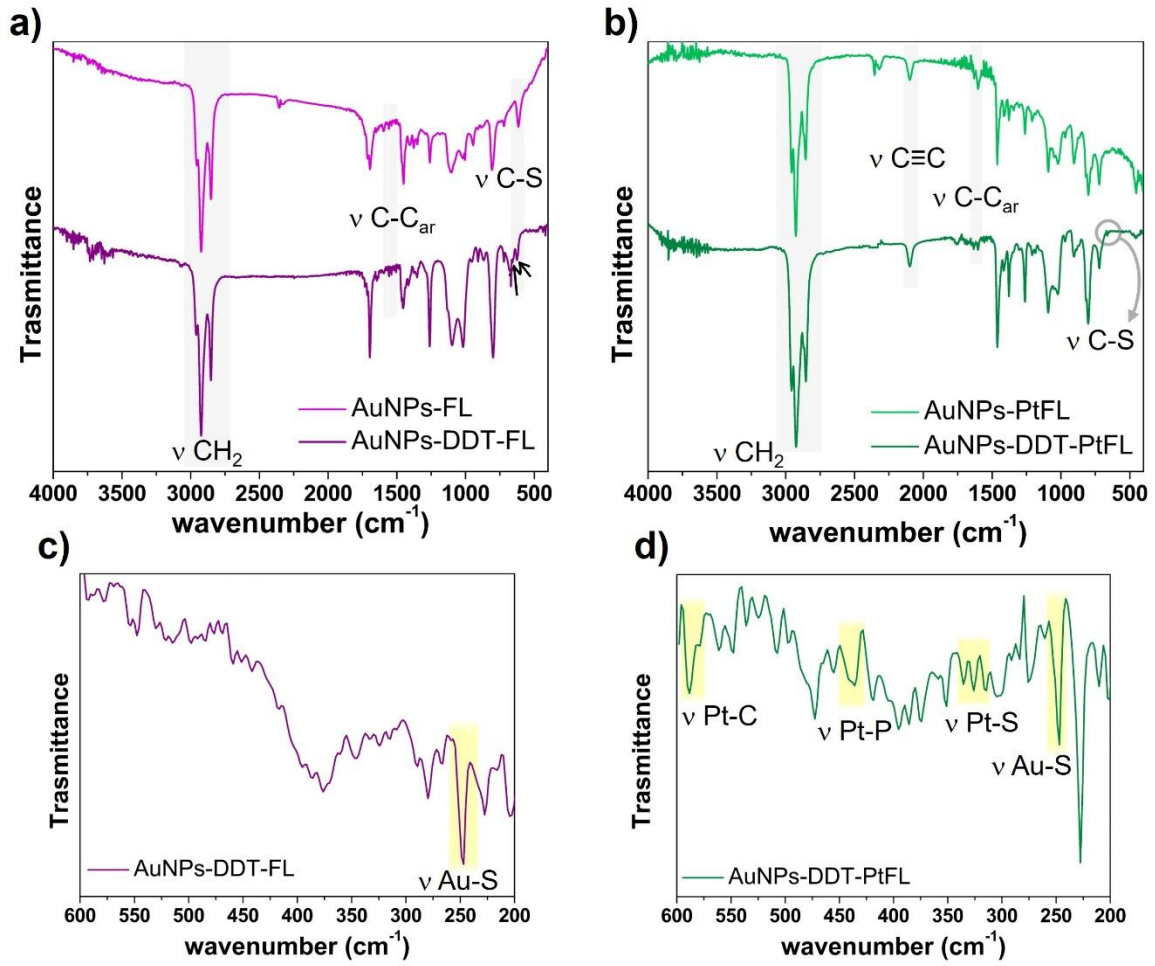

Figure 62. *FT-IR spectra of a) AuNPs-FL and AuNPs-DDT-FL, b) AuNPs-PtFL and AuNPs-DDT-PtFL. Samples were deposited as a thin film from CH_2Cl_2 on a KRS-5 plate. FarIR spectra of c) AuNPs-DDT-FL and d) AuNPs-DDT-PtFL. Samples were deposited as a thin film from iPr-OH on a PE plate and air dried.*

Additional confirmation of thiol binding on the surface of the mixed-ligand AuNPs is provided by the FAR-IR spectra shown in **Figure 62c, d**. In **Figure 62c**, the Au-S stretching band at 247 cm^{-1} is clearly detectable, confirming the covalent bond of thiols to the nanoparticle surface. In **Figure 62d**, the Au-S signal at 247 cm^{-1} is also observed, together with the characteristic bands of the platinum complex: ν(Pt-C) = 588 cm^{-1}, ν(Pt-P) = 436 cm^{-1}, and ν(Pt-S) = 326 cm^{-1}.[216]

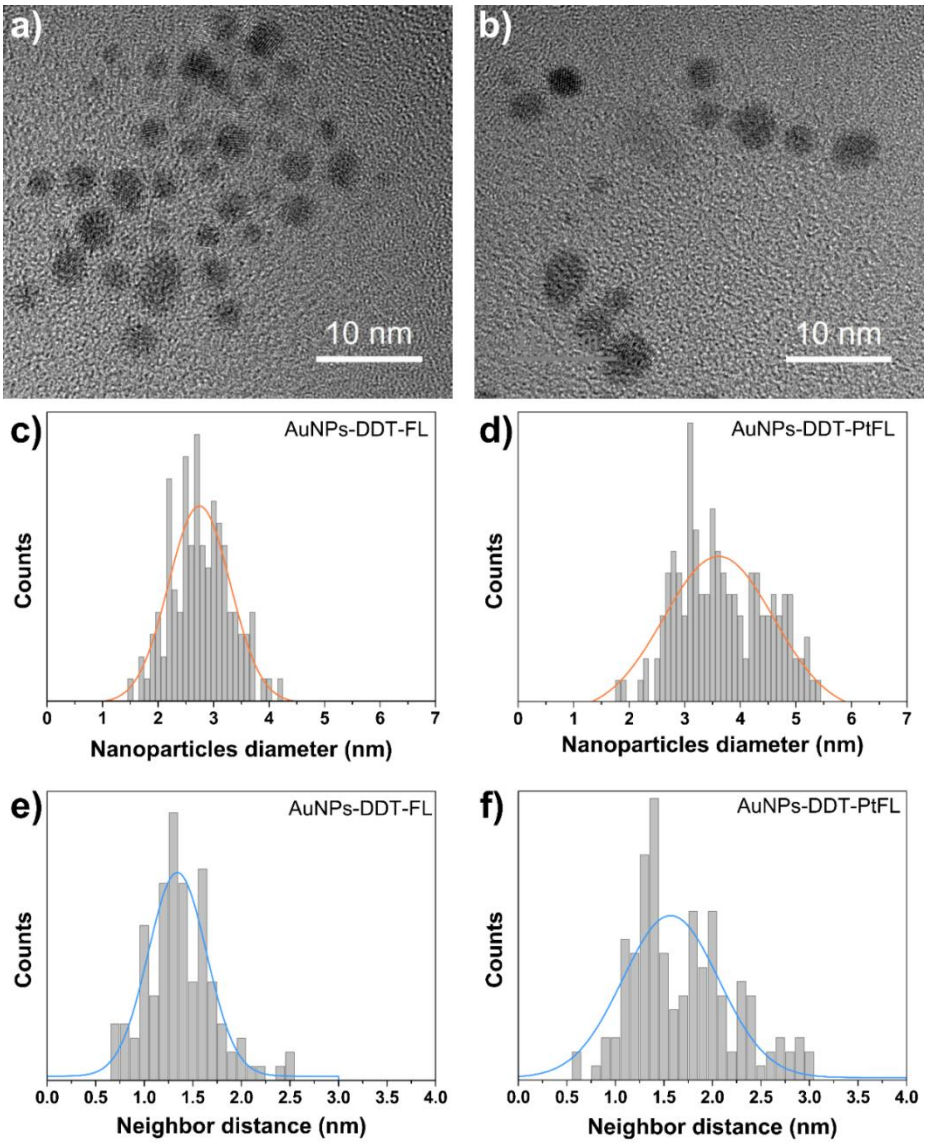

Figure 63. *TEM images of AuNPs functionalised with a) DDT and FL, b) DDT and PtFL. Distribution of nanoparticles diameter and data fitted by Gaussian function of c) AuNPs-DDT-FL (2.7 ± 0.6) nm and d) AuNPs-DDT-PtFL (3.6 ± 1.0) nm. Distribution of neighbour distance of NPs: e) for AuNPs-DDT-FL (1.3 ± 0.3) nm and f) AuNPs-DDT-PtFL (1.6 ± 0.5) nm. Data fitted by Gaussian function.*

After confirming the presence of thiols on the nanoparticle surface, the morphological features were investigated by TEM. This analysis allowed us to visualize the shape and measure the size of the nanoparticles obtained with mixed thiols, as well as their interparticle distance. Representative TEM images of AuNPs-DDT-FL and AuNPs-DDT-PtFL are shown in **Figure 63a,b**, respectively. The images confirm the spherical shape of the nanoparticles. The corresponding size distributions, fitted with Gaussian functions (**Figure 63c,d**), indicate an average diameter of (2.7 ± 0.6) nm for AuNPs-DDT-FL and (3.6 ± 1.0) nm for AuNPs-

DDT-PtFL, in good agreement with the DLS results (**Figures 63c,d**). The size were consistent with those obtained for AuNPs-FL and AuNPs-PtFL.[215,216] The interparticle distances were evaluated, and their distributions, plotted and fitted in **Figure 63e,f**, show non-random organization. The mean interparticle distance was found to be (1.3 ± 0.3) nm for AuNPs-DDT-FL and (1.6 ± 0.5) nm for AuNPs-DDT-PtFL, values consistent with the expected lengths of the two spacers (FL, PtFL)[186].

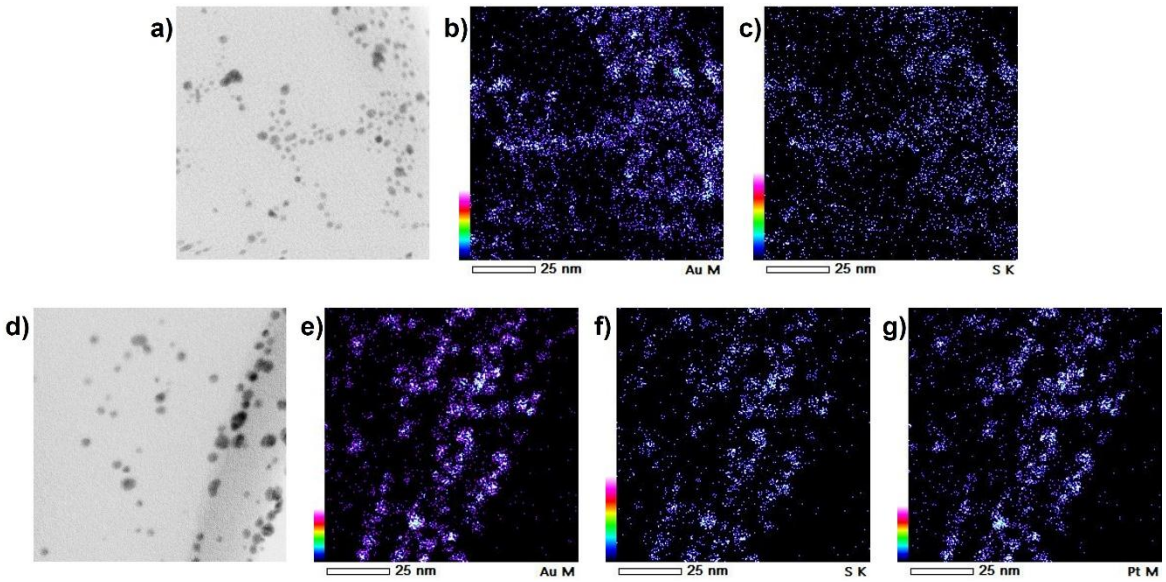

Figure 64. *Mapping of a) AuNPs-DDT-FL: b) Au and c) S. Mapping of d) AuNPs-DDT-PtFL: e) Au f) S and g) Pt.*

Mapping images (**Figure 64**) confirm that the darkest features observed in both systems (**Figure 64a,d**) correspond to AuNPs, as shown by the gold signals (**Figure 64b,e**). The sulphur signals (**Figure 64c,f**) overlap with the gold distribution, further confirming the surface functionalization of the AuNPs. In addition, the platinum signal detected in **Figure 64g** provides clear evidence of the presence of PtFL on the nanoparticle surface.

3.2.2.b. AuNPs networks as chemiresistive sensors

A preliminary evaluation of the sensing properties at room temperature (20 °C) of hydrophobic AuNPs networks towards organic vapours (VOCs), *i.e.* benzene and toluene, was conducted. The assessment was performed by depositing a thin film of AuNPs onto the surface of interdigitated electrodes[123], using a measurement chamber provided with a flux system of the selected vapours.

The output characteristics (current versus voltage curves) recorded at room temperature and controlled humidity are presented in **Figure 65a**. AuNPs functionalized with a mixture of thiols exhibited a linear ohmic response (adhering to Ohm's law) across both positive and negative bias voltages (from −1 to +1 V), that suggests the formation of an ohmic contact between the gold electrodes and the AuNPs. Different slope was observed, yielding resistances of R = (6.3 ± 0.1) GΩ and R = (0.606 ± 0.003) GΩ for AuNPs-DDT-FL and AuNPs-DDT-PtFL, respectively.

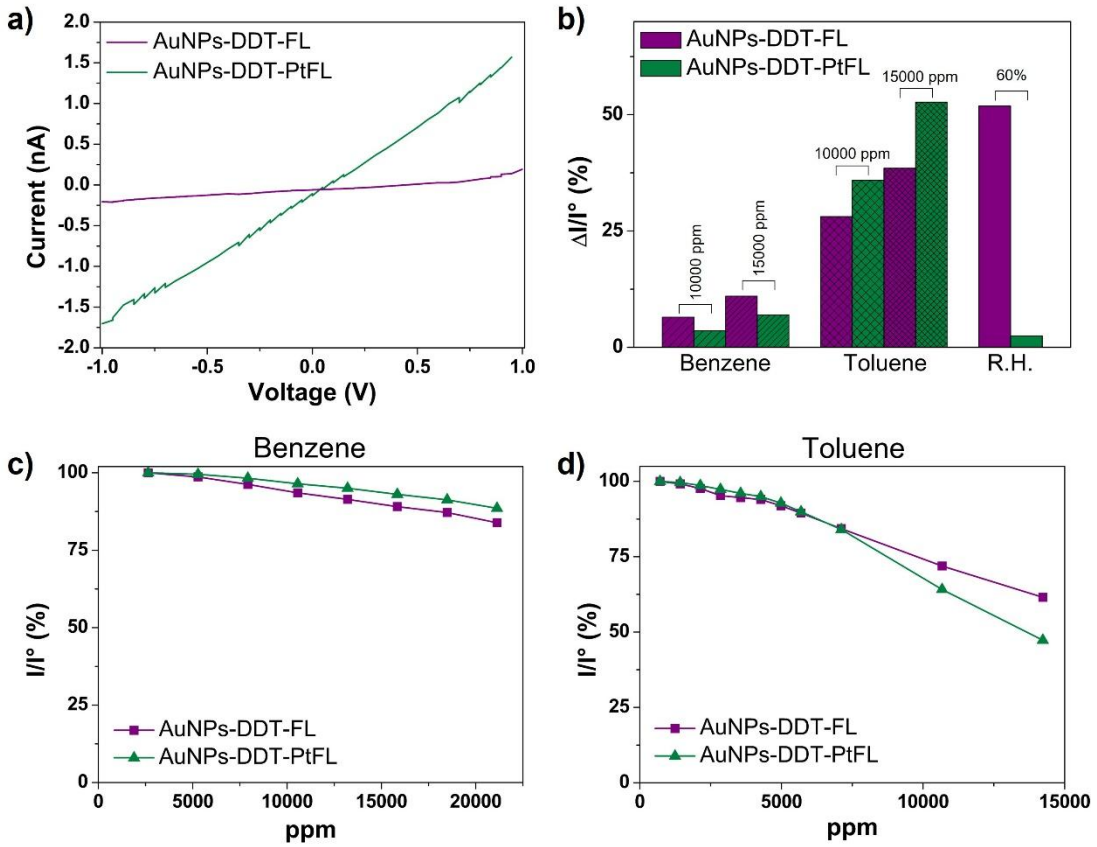

Figure 65. *a) I/V curves of AuNPs-DDT-FL (purple) and AuNPs-DDT-PtFL (green); b) responses against benzene, toluene, R.H. of AuNPs-DDT-FL (purple) and AuNPs-DDT-PtFL (green); c) response versus benzene concentration plot of AuNPs-DDT-FL (purple) and AuNPs-DDT-PtFL (green); d) response versus toluene concentration plot of AuNPs-DDT-FL (purple) and AuNPs-DDT-PtFL (green).*

In contrast, AuNPs functionalized with the bifunctional thiols (AuNPs-FL and AuNPs-PtFL) displayed an atypical behaviour. The system functionalized with the organometallic ligand (AuNPs-PtFL) exhibited conductivity that was anomalously high compared to the mixed-thiol systems and literature results[123]. This could be influenced by the low stability of the

nanoparticles, leading to aggregation and collapse of the colloidal network following deposition onto the interdigitated electrode. Conversely, the system functionalized with FL showed very low conductivity compared to the mixed-thiol particles. This can be explained by its inferior colloidal stability in suspension, preventing the formation of a uniform nanoparticle film upon deposition. The I/V curves for these two systems are reported in *Figure D16* and *Figure D17*. Based on these electrical behaviours, the sensing properties were evaluated exclusively for the mixed-thiol nanoparticles.

The selectivity of AuNPs-DDT-FL and AuNPs-DDT-PtFL was investigated by exposing the samples to different organic vapours (toluene and benzene) and to relative humidity at room temperature (the experimental setup is described in *Appendix D2.3.)*.

Figure 65b shows the results of the selectivity tests. The response to VOCs vapours was studied in the concentration ranges of 0-10,000 ppm and 0-15,000 ppm for benzene and toluene, considering the potential interference of relative humidity (0–60%).

Regarding benzene, **Figure 65b** indicates that both systems are slightly sensitive to its presence, with the system functionalized with the organic ligand (AuNPs-DDT-FL) showing higher sensitivity. An opposite trend is observed for toluene interaction; the AuNPs-DDT-PtFL system is significantly more sensitive than AuNPs-DDT-FL. Furthermore, the AuNPs-DDT-PtFL system is insensitive to humidity (60% R.H.), unlike the AuNPs-DDT-FL system, whose electrical resistance is influenced by moisture. These preliminary studies indicate that AuNPs-DDT-PtFL possesses an ability to discriminate toluene gas.

The variation in resistance upon exposure to different concentrations of benzene and toluene was measured to demonstrate the potential utility of these AuNPs for vapour sensing as chemiresistive layers. Normalized data are reported in **Figure 65c** for the ranges of 0–20,000 ppm for benzene and in **Figure 65d** for the ranges of 0–15,000 ppm for toluene, illustrating the differing sensitivities of the two nanomaterials towards these gases. AuNPs-DDT-FL shows a higher sensitivity to benzene up to 5,000 ppm. Regarding toluene, both systems showed almost the same sensitivity up to 7,000 ppm, beyond which AuNPs-DDT-PtFL becomes substantially more sensitive to the vapour.

In conclusion, four distinct systems of interconnected nanoparticles were synthesised and characterized. Two were functionalized with bifunctional ligands (FL and PtFL), in accordance with previous works [215,216], while the other two systems were obtained by functionalizing the particle surface with two thiols in mixture (FL or PtFL together with DDT). The role of DDT was to fine-tune the extent of the nanoparticle networks and, importantly, to enhance colloidal stability. These mixed-thiol systems have also proven

promising as chemiresistive sensors for VOCs compounds in these preliminary results. The development of sensors capable of detecting VOCs at room temperature remains a challenge, and these materials represent a step towards addressing it.

3.2.3 AuNPs networks in polymeric blends for optoelectronics

The inception of next generation flexible functional materials has energized the area of inorganic/organic hybrid blends. In this context, metal nanoparticle–polymer hybrid nanostructures showed promising applications as passive or active layers in optoelectronic devices.[124,125] Among different nanomaterials type, AuNPs are particularly attractive due to their great stability under standard conditions and their size-dependent optical properties (LSPR). The LSPR of AuNPs is highly sensitive to the chemical surrounding, causing variation in optical response of a single particle compared with bulk material,[217] and it is easily tunable according to the surface functionalization, which play a crucial role in achieving suitable properties for optoelectronics applications.[218,219] The incorporation of AuNPs into different polymer matrices leads to inorganic/organic hybrid blends that allow to combine the intrinsic properties of both counterparts, often enhancing existing features. Indeed, polymer nanocomposite blends with nano-scale fillers show significant property creation at much lower loadings compared to undoped polymer composites.[128] For example, concerning electrical properties of semiconducting polymers (*e.g.*, intrinsic carrier mobility), the intrinsic charge carrier mobility is strongly dependent on the planarity of the conjugated backbone and intermolecular stacking. However, in many cases the charge carrier mobilities is insufficient and need to be further improved to optimize device performances. It has been shown that the electronic properties of conjugated polymers could be enhanced by tailoring the stacking and ordering in the form of thin film. [220]

Among semiconducting polymers, poly(3-hexylthiophene-2,5-diyl) (P3HT) stands out as one of the most studied p-type materials for organic thin-film transistors (OTFTs)[221] and organic solar cells.[222] The charge carrier mobility of P3HT strongly depends on its crystallinity and structural order which in turn is heavily influenced by (i) the regioregularity of P3HT chains, and (ii) the interchain interactions between crystalline and amorphous regions of the polymer (especially near the film-substrate interface), and is determinant to obtain good electrical performances with reasonable light absorption.[223] Indeed, pristine P3HT possess high HOMO energy level (estimated to be in the range of 5.1–5.2 eV)[224] and wide energy band gap (2.1 eV)[225] which limits the absorption of red and infrared

wavelengths (the most intense parts of solar radiations).[226] The light absorption of P3HT is also impeded by its low charge carrier mobility (generally less than 10^{-4}-10^{-1} cm^2/Vs)[227] that restrict the thickness of the organic active layer to < 100 nm.[226] Another drawback which limits P3HT technological applications is due to polymer photodegradation by the simultaneous action of incident light, oxygen, and humidity.[228] Thus, the dispersion of functionalized AuNPs into P3HT matrix to enhance polymer charge transport properties and device performances is a topic of great interest to the scientific community for the development of functional hybrid materials.[229]

The conducting behaviour of P3HT in films is strongly influenced by its morphology, where the inter-chain electron transport can be enhanced if the polymer is confined in nanostructured domains.[230] Nanodomains morphology can be obtained *via* electrodeposition or use of a templating agent.[231],[232] Another technique that can be used to obtain nano-domains of P3HT is through phase separation of polymer blends. P3HT blended with a polymer that has different solubility parameters, leads to films with phase separation and segregation in nanostructured domains.[233,234] In thin films obtained *via* spin-coating, dip-coating or drop-casting[235,236], the morphology of the polymers in the film is influenced by mechanisms of phase separation[237,238], with the films behaving differently than the bulk due to substrate/film and film/air interfaces.[239] In such techniques, the resulting blend is in a thermodynamically metastable state, due to the quick evaporation of the solvent.[240] P3HT blends obtained with spin coating have been studied in the literature. P3HT blended with poly(methyl methacrylate) (PMMA) resulted in a stratified layer morphology due to the surface energy difference of the polymers, with P3HT at the air interface.[241]

Based on these considerations, three different inorganic/organic blend based on AuNPs are investigated in this section. The first is blend with poly(phenylacetylene) (PPA), as a preliminary model to study the interaction of functionalized interconnected AuNPs with a simple polymer matrix. Then a blend with P3HT is analysed, the aim is study how the length of the spacer between the AuNPs can influence the charge transport and optoelectronic response through synergistic effects between the semiconducting polymer and AuNPs. Finally, a ternary bled is studied, a blend of polylactic acid (PLA), P3HT and AuNPs. The presence of PLA allows the formation of heterojunctions and opens perspectives for multifunctional nanocomposites.

This progressive approach enables the systematic evaluation of how AuNPs affect the morphology, charge transport, and optoelectronic performance of polymer matrices, from simple to more complex systems, and highlights their potential for the development of next-

generation functional hybrid materials. In **Figure 66** the chemical structures of the polymers are reported.

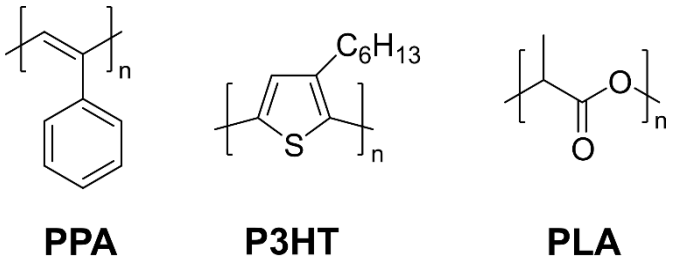

Figure 66. *Chemical structure of poly(phenylacetylene) (PPA), poly(3-hexylthiophene-2,5-diyl) (P3HT), polylactic acid (PLA)*

3.2.3.a. AuNPs functionalised by 2AET and FL in PPA blends

In this work (scheme in **Figure 67**) we synthesized organic suspensible AuNPs functionalized with two different organic, π-conjugated synthetic thiols, *i.e.*, 9,9-didodecyl-2,7-bis(acetylthio)fluorene (FL) and 2-(anthracen-9-ylmethyl)thio)ethane-1-thiol (2AET), both bearing an activable thiolate group (−SH or $-SCOCH_3$), which can be exploited for covalent binding with the gold surface. Attention has been given to optimizing synthesis conditions for mixed functionalized gold nanoparticles, namely AuNPs-2AET-FL_1 (molar ratio 2AET:FL 1:1), AuNPs-2AET-FL_2 (molar ratio 2AET:FL 1:2), and AuNPs-2AET-FL_4 (molar ratio 2AET:FL 1:4). The fluorene derivative was chosen due to its fluorescence in the 300-400 nm range with negligible quenching effect after AuNPs conjugation and its proven conductivity enhancement when used in polymer blends.[242] Fluorescent 2AET was synthesized by Dr. Damiano Cirri of Department of Chemistry and Industrial Chemistry, University of Pisa. 2EAT with its anthracene moiety has been designed to exploit an electron-rich structure with absorption/emission not overlapping with the typical SPR band of AuNPs, thus showing optically active behaviour in the near-UV region. With potential applications in optoelectronics, AuNPs-2AET-FL_2 has been used as inorganic fillers in a semiconducting poly(phenylacetylene) (PPA) matrix at different weight ratios (from 10/90 to 90/10 AuNPs/PPA %wt.) to obtain hybrid organic/inorganic nanocomposites *via* simple blending approach at room temperature. Compared with pristine AuNPs, nanocomposite arrangement is more prone to applications in miniaturized, flexible devices.[226] PPA has been chosen as a π-conjugated model polymer in the nanocomposite architecture due to its dynamic helical structure, opening the possibility for preparing materials with combined fluorescent-electrical and potential dynamic chiral plasmon response.[243] To obtain insight

into the structural and optical behaviour of these colloidal nanoparticles and nanocomposites, a combination of characterization techniques has been exploited. UV-Vis and photoluminescence (PL) assessed their optical properties. Infrared spectroscopy (FTIR, Far-IR) and synchrotron radiation-induced X-ray photoelectron spectroscopy (SR-XPS) were employed for extensive structural characterization, whereas, at solid-state, morpho-structural analyses have been carried out using atomic force microscopy (AFM), and high-resolution transmission electron microscopy (HR-TEM). In organic solvent suspension, the hydrodynamic diameter value ($<2R_H>$) has been estimated by dynamic light scattering (DLS). The electrical response of both pristine gold nanoparticles and nanocomposites was evaluated *via* electrical (I/V) measurements in the form of spin-coated thin films onto interdigitated ITO electrodes.

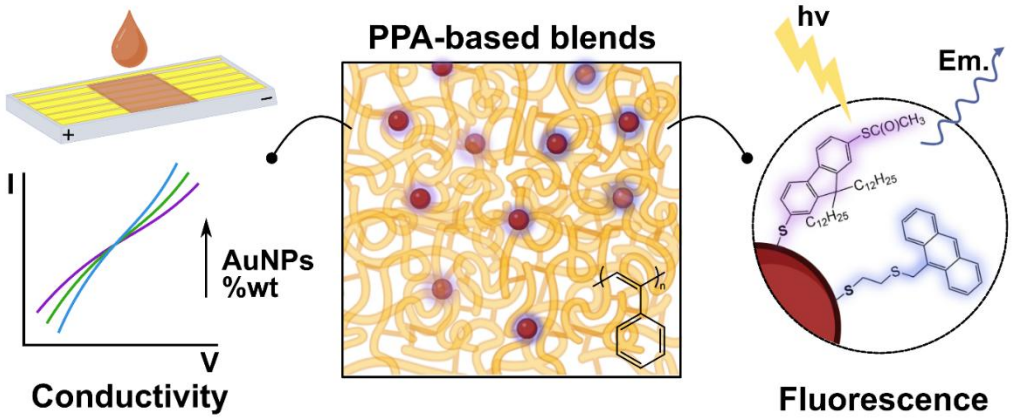

Figure 67. *Scheme of AuNPs-FL-2AET in PPA-based blend for optoelectronic applications.*

AuNPs were synthesized under optimized conditions according to a modified Brust-Schiffrin method. It is noteworthy that the FL ligand bears two thiol-ending groups, and it is a suitable linker for the formation of interconnected nanoparticles, leading to super-aggregates. The synthesis procedure is schematized in **Figure 68a**. After the purification steps, the formation of colloidal thiol-functionalized AuNPs-2AET-FL was confirmed by the appearance of the characteristic SPR absorption band centred at 533 nm (**Figure 68b**). The shape of the SPR band reflects the morphology of nanoparticles and the presence of a single absorption maximum suggested the formation of spherical nanoparticles.[244] Importantly, a further absorption band in the 300–400 nm range was detected, associated with the presence of 2AET dye on AuNPs surface, partially overlapping with that of FL ligand at 318 nm. An estimation of the relative quantity of the thiol ligands on each colloidal freshly prepared AuNPs can be extrapolated from the UV-Vis considering the following ratio (Q, equation 8):

$$Q = \frac{Abs_{peak}}{Abs_{372\ nm}} \quad (8)$$

where Abs_{peak} is the wavelength at the maximum absorption of FL (λ_{max}=318) or at the λ_{SPR}=533 nm, respectively. The ratio considers the normalization to maximum absorption of 2AET dye (λ_{max}=372 nm), since its quantity is fixed in the synthesis protocol. For AuNPs-2AET-FL_1 calculated Q between 2AET/FL gave a 1:1.02 absorbance ratio with a AuNPs/thiols 0.54:1, for AuNPs-2AET-FL_2, 2AET/FL Q value was 1:0.98 and AuNPs/thiols 0.54:1, whereas for AuNPs-2AET-FL_4 Q between 2AET/FL was 1:1.03 and AuNPs/thiols 0.46:1. These results evidenced that, for the molar ratios herein explored, a 1:1 ratio between ligands is maintained through samples, although in the case of AuNPs-2AET-FL_4 a low AuNPs yield was obtained. In all cases, AuNPs showed a single, broad plasmon band, with a calculated full-width-at-half-maximum (FWHM) value of (205 ± 1) nm. The FWHM value (or SPR peak width) is known to depend on the size distribution of colloidal nanoparticles but also on the coupling effect between gold cores in the case of close or interconnected AuNPs.[245,246]

A more accurate evaluation of the super-aggregates size in colloidal suspension was obtained from dynamic light scattering (DLS) analysis. Intensity-weighted hydrodynamic diameter distributions of AuNPs are reported in **Figure 68c**. For AuNPs-2AET-FL_1 (**Figure 68c**, dark cyan trace), there was a small population centred at (12 ± 2) nm and the most intense population was found at (60 ± 25) nm, overlapping with that at (185 ± 65) nm. For AuNPs-2AET-FL_2 **Figure 68c**, red trace) two less intense populations were found at (30 ± 5) nm and at (68 ± 15) nm, whereas the most intense was centred at (260 ± 70) nm. In the AuNPs-2AET-FL_4 sample, a curve at (205 ± 30) nm appeared in the size distribution profile along with single populations at (37 ± 5) nm, and at (3 ± 1) nm (**Figure 68c**, magenta trace). The use of a higher amount of FL ligand determines an increase in the polydispersity of the sample was found (for example comparing AuNPs-2AET-FL_1 with AuNPs-2AET-FL_4). It is worth mentioning that the FL ligand is used as bifunctional thioacetate derivative in the synthesis procedure, thus potentially leading to the formation of interconnected nanoparticles super-aggregates[247], contributing to the biggest population in the DLS profile, broadness of the SPR band and increased polydispersity.

Interestingly, after one year aging in CH_2Cl_2 suspension at room temperature and in a dark environment, UV-Vis analysis showed that the suspension of AuNPs-2AET-FL_2 (**Figure 68d**) maintained its colloidal stability towards aggregation with a red-shift in the SPR band

at 545 nm and a smaller FWHM value (66 nm) with respect to the freshly prepared sample in **Figure 68b**.

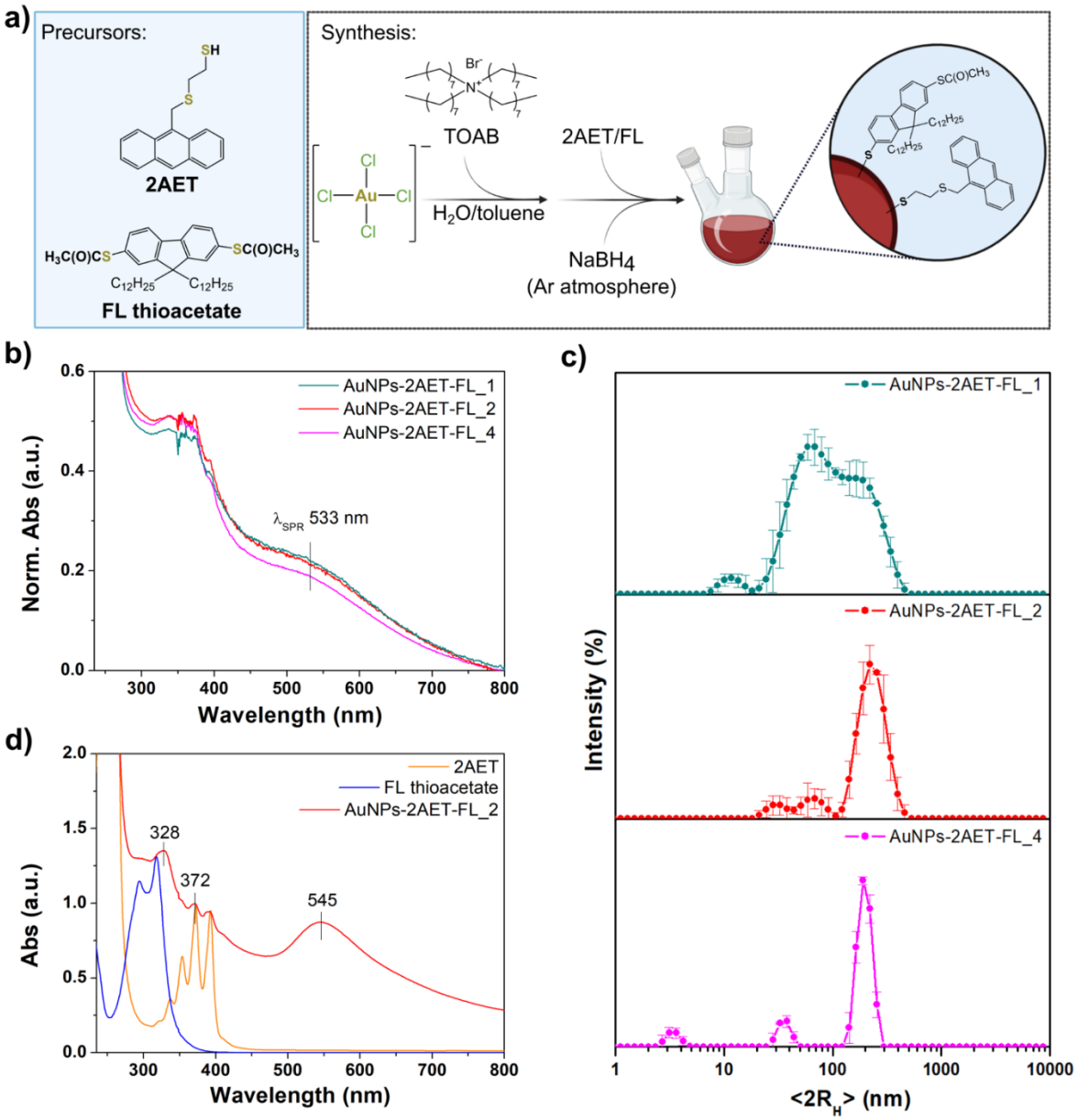

Figure 68. *Preparation and preliminary characterizations of AuNPs. a) Two-phase water/toluene synthesis scheme of AuNPs-2AET-FL adopted in this work. b) UV-Vis extinction spectra of freshly prepared colloidal AuNPs suspensions recorded in CH_2Cl_2. c) DLS particle size distribution in CH_2Cl_2 for freshly prepared AuNPs-2AET-FL_1 (dark cyan trace), AuNPs-2AET-FL_2 (red trace), AuNPs-2AET-FL_4 (magenta trace). d) UV-Vis extinction spectra of aged (1 year) AuNPs-2AET-FL_2 (red line), free 2AET (orange line) and FL thioacetate (blue line) ligands.*

Absorption belonging to FL at 328 nm and 2AET at 372 nm also emerged from the UV-Vis profile. Conversely, AuNPs-2AET-FL_1 and AuNPs-2AET-FL_4 underwent irreversible aggregation, as demonstrated by the broadening of the SPR band in the aged samples (*Figure C8*). The reported behaviour can be ascribed to the partial time-induced release of the physisorbed thiol shell around gold core, which contributes to colloidal gold nanoparticles stabilization. According to the reported spectroscopic data, the profile, FWHM, and position of the plasmon band in three spectra (especially in the spectral region of 500–600 nm), freshly prepared AuNPs were similar in terms of shape (spherical NPs), composition (*Q* ratio between counterparts), and size distribution. This experimental procedure evidenced the ultimately reproducible synthesis protocol among molar ratio variations between reagents. However, long-term aging evidenced a different colloidal stability between samples, with the AuNPs-2AET-FL_2 showing the highest stability. This sample was selected for the preparation of the blends (see following paragraphs).

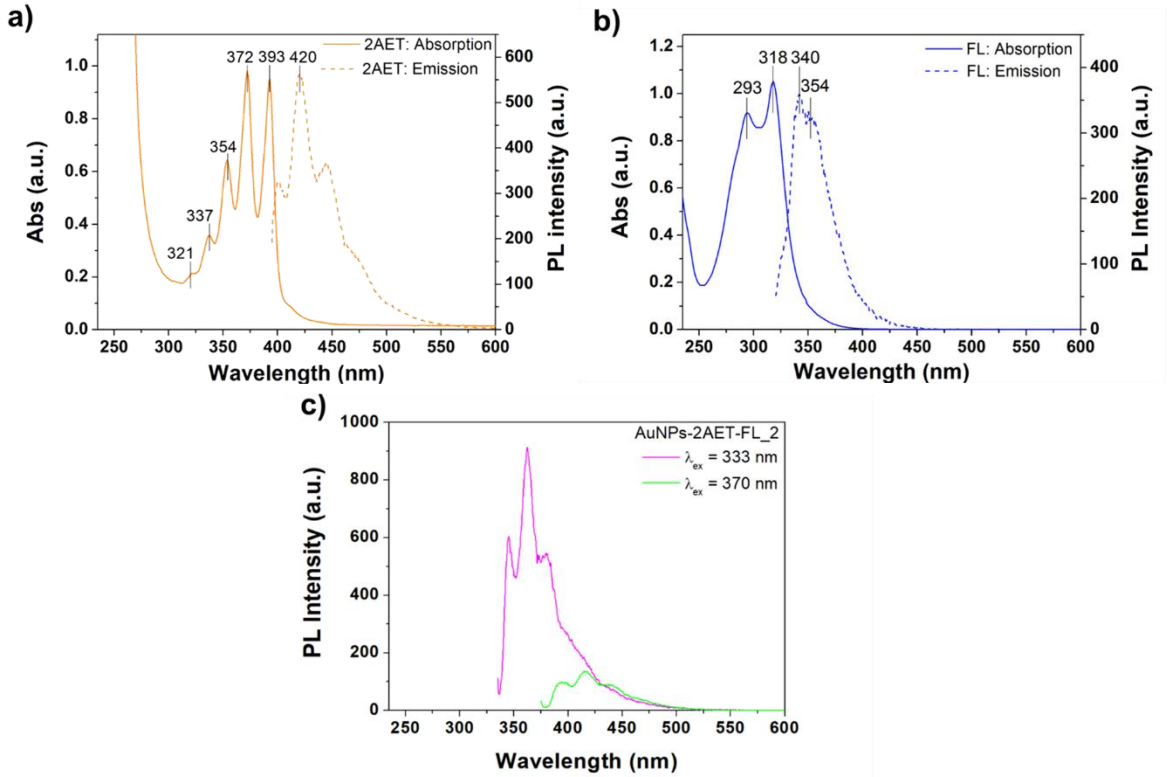

Figure 69. *Spectroscopic characterizations (UV-Vis, PL) of free 2AET and FL thiols and AuNPs-2AET-FL_2. a) Absorption (continuous line) and emission (dotted line) of 2AET dye in CH_2Cl_2 (λ_{ex}=375 nm). b) Absorption (continuous line) and emission (dotted line) of FL thioacetate ligand in CH_2Cl_2 (λ_{ex}=285 nm). c) Emission spectra of AuNPs recorded at two different excitation wavelengths: 333 nm (magenta line) and 370 nm (green line).*

The emission properties of 2AET/FL-functionalized AuNPs were evaluated to give a better understanding of the impact of the synthesis protocol on the nanoparticle applications. The emission spectra of pristine 2AET dye and FL thioacetate were recorded using information-rich photoluminescence excitation-emission matrices (EEMs). In the case of 2AET in a dichloromethane solution, excitation was in the λ_{ex} = 335-395 nm wavelength range, with λ_{ex} = 375 nm being the wavelength of the maximum emission intensity for free dye (*Figure C9a*). The fluorophore showed an emission band with a maximum at 420 nm (**Figure 69a**). On the other hand, EEM obtained for FL evidenced that excitation at 285 nm gave rise to the most intense emission spectrum (*Figure C9b*), with maximum corresponding emissions at 340 and 354 nm (**Figure 69b**).

The measured emission spectra from aged functionalized AuNPs-2AET-FL_2 are reported in **Figure 69c**, whereas spectra of AuNPs-2AET-FL_1 and AuNPs-2AET-FL_4 are reported in *Figure C10*. For the excitation, two different wavelengths were explored: λ_{ex} = 333 nm (magenta line in **Figure 69c**) and λ_{ex} = 370 nm (green line in **Figure 69c**), the former capable of exciting the emission of both molecular components based on previous UV-Visible studies on aged samples. Excitation at 333 nm allowed to induce emission from both 2AET and FL, which overlapped in this spectral region with a significant contribution of the latter. Indeed, AuNPs-2AET-FL_2 sample excited at λ_{ex} = 333 nm showed an intense emission with λ_{em} = 362 nm, due to the presence of FL and 2AET ligands directly bonded to the gold surface, similar to that of AuNPs-2AET-FL_4 (*Figure C10*). Compared with spectral features of 2AET and FL, a change in the spectral shape of functionalized AuNPs emission occurred, which goes beyond the trivial overlap of free ligands spectra. This result can be ascribed to the possible formation of Au–S bond, as reported for similar noble metal-interacted dyes.[248] In the case of AuNPs-2AET-FL_1 (*Figure C10*), excitation at 333 nm did not produce considerable emission (same spectral shape around 360 nm, with much weaker intensity), which is in agreement with the lowest 2AET/FL (1:1) molar ratio. Selective emission from 2AET was evidenced at λ_{ex} = 370 nm, in which AuNPs-2AET-FL_2 showed a less intense emission with a maximum at λ_{em} = 416 nm, slightly blue-shifted compared with free 2AET dye. Results showed that modulation it is possible to tune gold colloids emission properties, taking advantage of the presence of mixed 2AET and FL on AuNPs according to different excitation wavelengths. In all cases, excitation in the proximity of surface plasmon resonance did not result in emission from gold cores or gold to thiols charge transfer phenomena (*Figure C10*), confirming that spherical AuNPs with a diameter >10 nm do not show intrinsic fluorescence.

Surface characterization of aged AuNPs was carried out by FTIR in the mid (4000–400 cm^{-1}) and far-infrared (600–200 cm^{-1}) regions. Spectra of AuNPs-2AET-FL_2 are reported in **Figure 70a, b**, whereas AuNPs-2AET-FL_1 and AuNPs-2AET-FL_4 spectra are reported in *Figure C11*.

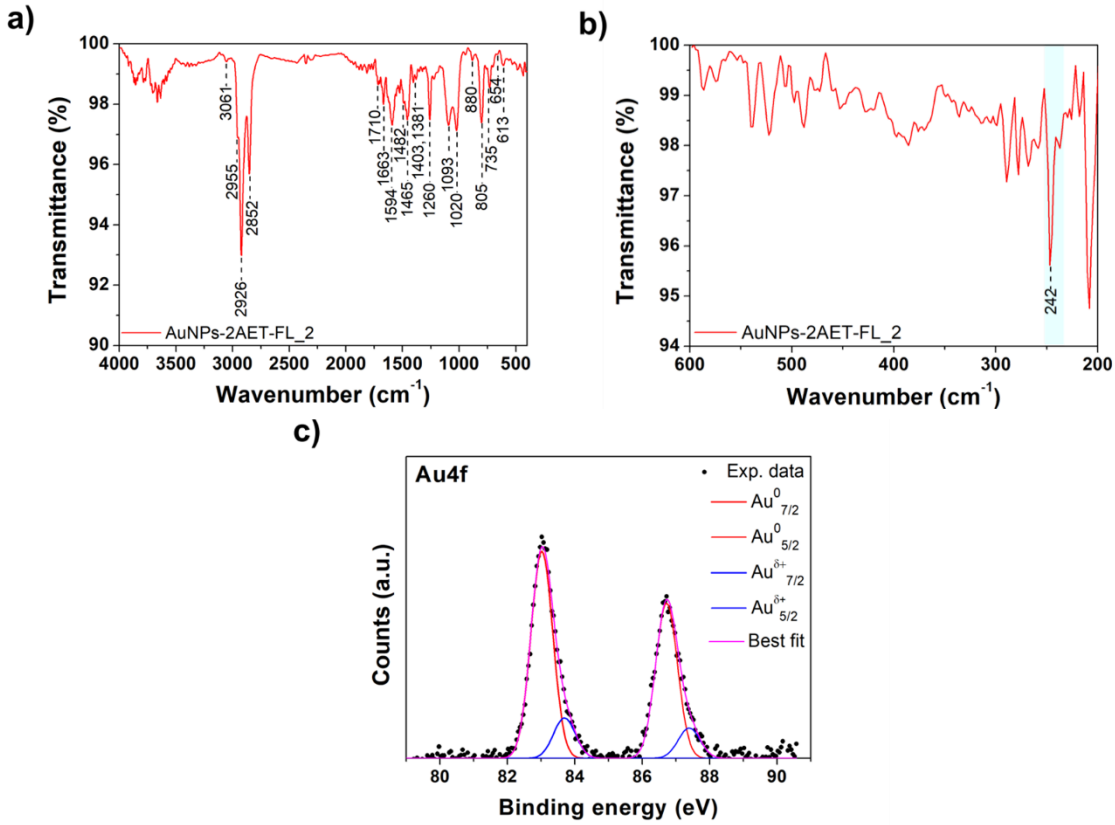

Figure 70. *Structural characterizations of AuNPs-2AET-FL_2. a) FT-IR in the 4000–400 cm^{-1} wavenumber range. b) Far-IR spectrum in the 600–200 cm^{-1} wavenumber range, Au–S stretching vibration at ca. 242 cm^{-1} is evidenced. c) Au4f core level spectrum. All analyses were conducted on dried solid thin film.*

The FTIR spectrum of AuNPs-2AET-FL_2 (**Figure 70a**) showed typical vibrations of aromatic portions of ligands: stretching (ν) of (=C–H) at 3061 cm^{-1} together with their *in-plane* bending δ(=C–H) at 1093, 1020 cm^{-1} and *out-of-plane* bending δ(=C–H) at 735 cm^{-1}, and those of ν(C–C) of the rings at 1663, 1594, 1482 cm^{-1}. Typical (C–C) deformations modes appeared at 880, 805 cm^{-1}. Aliphatic side chains of 2AET and FL gave rise to ν_{as}(–CH_3) at 2955 cm^{-1} (due to terminal carbons in –$C_{12}H_{25}$ chains of FL), whereas asymmetric ν_{as}(–CH_2) and symmetric ν_s(–CH_2) were found at 2926 and 2852 cm^{-1}, respectively. Less intense peaks ascribable to δ(–CH_3) at 1403 cm^{-1}, scissoring δ_s(–CH_2) at 1465 cm^{-1} and γ(–CH_2) at 1381 cm^{-1} were also found in the fingerprint region. Carbon-sulfur vibrations with

different intensities at 654 and 613 cm^{-1} originate from aliphatic ν(C–S) of 2AET and aromatic ν(=C–S–C(O)CH_3) of FL, respectively. The weak signal at 1710 cm^{-1} was ascribed to ν(C=O), highlighting the presence of a small portion of unreacted thioacetate ending groups of FL. Notably, no signals corresponding to free ν(S–H) from 2AET ligand were found in the 2550–2600 cm^{-1} spectral region.

To better evidence the successful functionalization, Far-IR spectra were recorded for AuNPs samples (**Figure 70b** and *Figure C11*). The region between 590–325 cm^{-1} was dominated by *in-plane* and *out-of-plane* ring deformation modes (523, 477, 326 cm^{-1}), whereas at ca. 300 cm^{-1} the band corresponding to –S–C–C deformation of 2AET aliphatic chain was found. Vibrations < 300 cm^{-1} were mainly due to ρ(–CH_2), although in this region, the most important signal was detected at 242 cm^{-1}, attributed to the (Au–S) stretching vibration in AuNPs samples. This latter is normally found in the 280–170 cm^{-1} range, exhibiting two or three peaks depending on the sulphur binding modes.

SR-induced XPS measurements were carried out at the C1s, S2p and Au4f core levels. Full XPS data (BE, FWHM, atomic ratios) are reported in *Table C4*. C1s spectrum (*Figure C12*) is made of three components. The first, fixed at 284.7 eV, is assigned to aromatic and C-S carbons; the second and the third at 286.8 and 288.9 eV to C-O and COOH carbons of contamination, respectively. S2p spectrum (*Figure C12*) is made of five couples of spin-orbit doublets ($S2p_{3/2}$, $S2p_{1/2}$) of which the $S2p_{3/2}$ signal is taken as reference. $S2p_{3/2}$ signal at 161.4 eV is relative to thiols covalently bonded to gold nanoparticle surface. S2p3/2 signal at 163.0 eV is usually assigned to physisorbed thiols or disulfides. The last components at higher BE are due to oxidized sulphur atoms.[249]

Au4f spectrum (**Figure 70c**) shows two couples of spin-orbit ($Au4f_{7/2}$, $Au4f_{5/2}$) doublets, of which we consider as reference the $Au4f_{7/2}$ component. The $Au4f_{7/2}$ signal at 83.0 eV is due to metallic bulk Au(0) atoms of NPs, while those around 83.7 eV to surface Au atoms of nanoparticle involved in the covalent bond with sulphur atoms of functionalizing thiol ligands.

Morphological characterization of AuNPs was carried out by tapping mode AFM onto spin-coated samples from dichloromethane suspension. The corresponding AFM topography images of AuNPs-2AET-FL_2 dried on a glass substrate are shown in **Figure 71a, b**. As it can be seen, the observed nanostructures showed slightly elongated morphology with a maximum height in the 3–7 nm range, interconnected by an extended amorphous layer underneath. More detailed morpho-structural imaging analyses have been provided using HR-TEM imaging. The HR-TEM images exhibit small nanoparticles with a darker contrast,

chemically identified using EDX (**Figure 71c** and *Figure C13*). The EDX spectrum evidences the high purity of the aggregates, showing intense peaks belonging to Au species (Ni peaks are from the support grid). The small sulphur peak can be ascribed to the S atoms belonging to the thiol ligands. The morphometric imaging analysis of **Figure 71c** identified quasi-spherical shape AuNPs, with a measured mean diameter of (4.1 ± 0.7) nm, having a polydispersity of about 17%. It is noteworthy that the surface-to-surface distance of the nearest-neighbor nanoparticles has been estimated at about 1.30 nm, in agreement with to the organic FL bridge length. This result supports the formation of interconnected AuNPs networks.

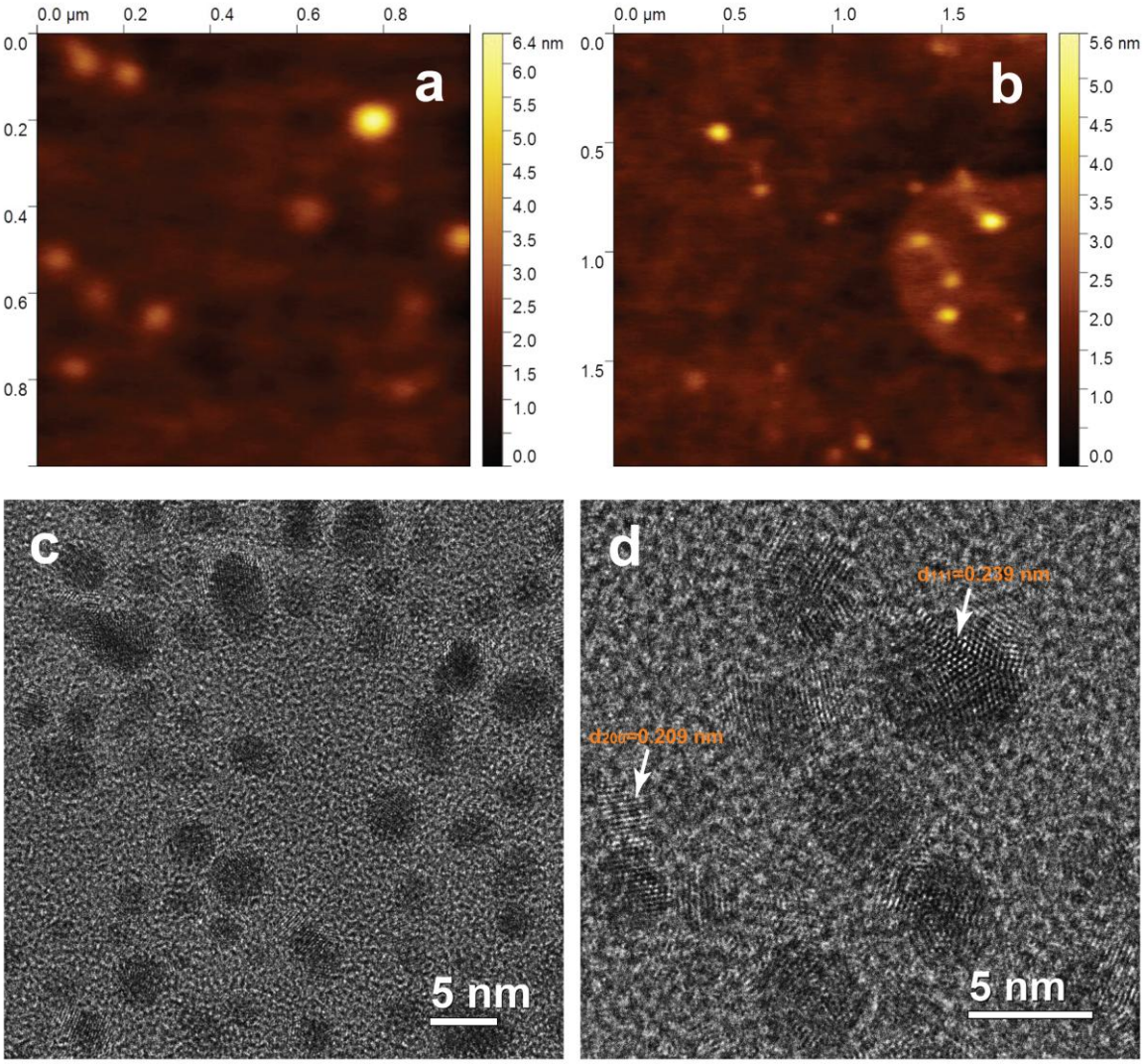

Figure 71. *Morpho-structural observations on AuNPs-2AET-FL_2. a-b) AFM measurements at different magnifications on AuNPs spin-coated onto Si/SiO_2 substrate from CH_2Cl_2 suspension and air dried. c) TEM image of crystalline AuNPs at medium magnification onto carbon amorphous film grid. d) HR-TEM micrograph of AuNPs with crystalline lattices spacing $d_{(200)}$=0.206 nm and $d_{(111)}$=0.239 nm.*

High-resolution image (**Figure 71d**) evidences the nanocrystal character of the typical AuNPs.[186] By measuring the crystalline lattices, the typical gold nanostructure of space group $Fm\bar{3}m$ with spacing $d_{(200)}=0.206\ nm$ and $d_{(111)}=0.239\ nm$ has been identified.

Poly(phenylacetylene) (PPA) was used as a π-conjugated model polymer to obtain nanocomposite hybrid blends with AuNPs. Nanocomposite samples consisting of PPA and AuNPs-2AET-FL_2 were obtained at ambient temperature by mixing precalculated weight ratios of both PPA and AuNPs dopant in $CHCl_3$ according to **Table 5** (experimental details are reported in paragraph *D2.4.*).

Sample	AuNPs-2AET-FL_2 (%wt.)	PPA (%wt.)
B10	10	90
B30	30	70
B50	50	50
B70	70	30
B90	90	10

Table 5. *Conditions used for the nanocomposites sample preparation.*

Characteristic UV-Vis extinction spectra of nanocomposites, pristine fresh AuNPs and pure PPA are reported in **Figure 72a**. Pure PPA showed a predominant *cis*-transoid conformation with intense absorptions centred at 250 nm due to the π–π* transitions of the phenyl groups and broad, less intense shoulder bands at 330 nm and 394 nm due to the π-π* transition of conjugated main chain between HOMO and LUMO along their axis direction.[250,251] Nanocomposite samples can be distinguished by the appearance of the typical SPR band of AuNPs at 533 nm, which becomes more evident in the B90 sample (**Figure 72b**), whereas for B10 and B30 the absorption is still clearly dominated by the polymer. The SPR band of AuNPs did not show reasonable changes compared to pristine AuNPs, both in terms of position and width, thus demonstrating that blending with PPA did not induce nanoparticle aggregation. The stability towards aggregation can be ascribed to a chemical matching between surface functionalizing agents on NPs surface bearing aryl moieties and the phenyl rings of the polymer matrix.[252] All spectra were characterized by the main absorption edge at ca. 250 nm mainly consistent with the presence of PPA and a red shift up to 260 nm by increasing the AuNPs amount (sample B90). Moreover, in B70 and B90, this band appears to be distorted. Notably, a change also occurs in the absorptions in the 300-450 nm wavelength range (those associated with π-π* transitions of the polymer chain double

bonds). In this region, B10 and B30 profiles linearly follow that of the polymer, whereas changes in the absorption intensities were found for B50, B70, B90 samples. The reported shifts and distortions in the UV-vis bands could be ascribed to (i) a change in the crystalline phase in the nanocomposites and thus, in the optical energy gap (E_g)[253], and (ii) the formation of interfacial non-covalent π–π stacking between PPA chains and aromatic thiols on AuNPs, as previously reported in AuNPs/P3HT polymer blends, highlighting the complexity of AuNPs/polymer interactions. In particular, the hypsochromic shift and intensity decrease in the visible band of PPA (300-500 nm) is the result of a decrease in the main-chain conjugation.[254,255]

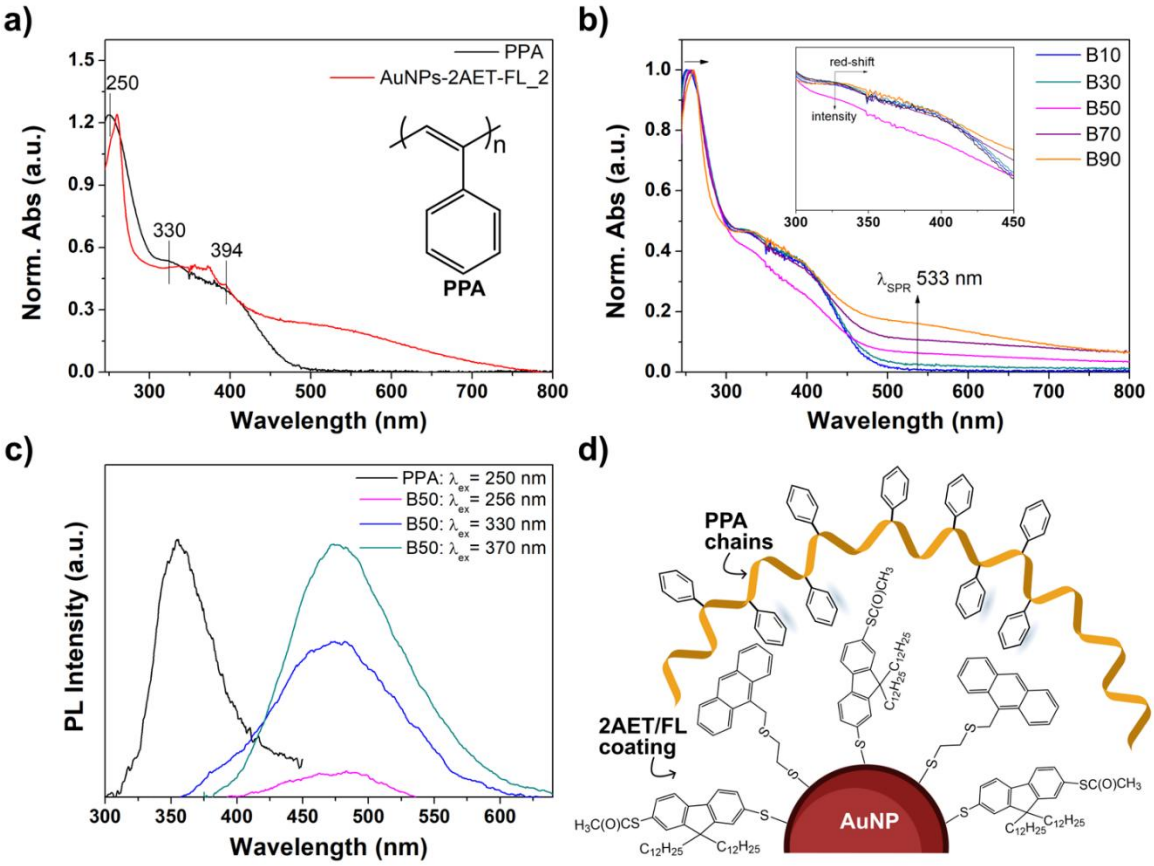

Figure 72 *Spectroscopic characterizations (UV-Vis, PL) of pure PPA and related AuNPs blends. a) UV-visible extinction spectra of pure PPA ($CHCl_3$) and pristine AuNPs-2AET-FL_2 (CH_2Cl_2). Inset: chemical structure of PPA. b) UV-visible spectra of AuNPs-2AET-FL_2/PPA nanocomposite blends containing different amounts of AuNPs. c) Emission spectra in CH_2Cl_2 of PPA (black line) and B50 at different excitation wavelengths. For labels refer to Table 1. d) Possible interaction mechanism occurring between AuNPs-2AET-FL_2 and PPA in the nanocomposites.*

The shortening of the extent delocalization of π-electrons can be ascribed to charge-transfer phenomena across the metal/organic interfaces probably interacting through weak π–π stacking which proved to facilitate the electron transfer process.[256,257]
schematized in **Figure 72d**.

Selected photoluminescence spectra of pure PPA and B50 nanocomposites are given in **Figure 72c**. Pristine polymer showed an emission maximum at 356 nm at λ_{ex} = 250 nm, whereas at λ_{ex} = 330 nm and λ_{ex} = 394 nm PPA resulted in a less intense emission at 384 and 471 nm, respectively (*Figure D18*). In the AuNPs/PPA B50 blend, excitation at 256 nm gave only a small contribution (*Figure D18*), arising from the polymeric counterpart. Conversely, λ_{ex} = 330 nm resulted in an emission spectrum with a maximum at 475 nm and a shoulder band at 390 nm (whose profile linearly follows that at λ_{ex} = 325 nm, see *Figure D18*). The shoulder band in the nanocomposite originates from PPA and disappeared for λ_{ex} = 330 nm with an increase in the emission intensity at 475 nm. The latter can be ascribed to the 2AET dye functionalizing AuNPs, with a red shift of 56 nm compared with the emission of pristine functionalized AuNPs. The redshift can be due to the formation of exciplex (hole-transporting molecules which provide electrons and electron-transporting materials able to accept electrons) in the blended system originating from interchain interactions. [258,259] In this specific case, this behaviour is reflected in the suppression of radiative decay in favour of charge transfer phenomena likely due to polymer addition. The possible interaction is

The morphology of PPA and nanocomposite blends spin-coated as thin films on a solid substrate was investigated by AFM. Nanometric imaging of PPA in the absence of AuNPs at two different magnifications is shown in **Figure 73a**. Neat polymer showed an irregular flat morphology (with cavities induced by solvent evaporation), forming a layer of (4 ± 1) nm average thickness, partially wrapped at the edge of the cavities. AFM topography of NPs/PPA blend image is displayed in **Figure 73b**. Qualitatively, at the AuNPs concentrations herein used, the general structure of PPA was not altered by the addition of NPs, the thickness of the blend being almost unaltered and estimated to be (4.6 ± 0.8) nm (*Figure D19*). However, in this case, several nanostructures were found entrapped inside the polymer matrix since the alone NPs of 4.1 nm were estimated by HR-TEM. The images clearly show the presence of round-shaped protrusions uniformly distributed within the polymer, which cause a remarkable variation in the maximum sample dimension in z direction.

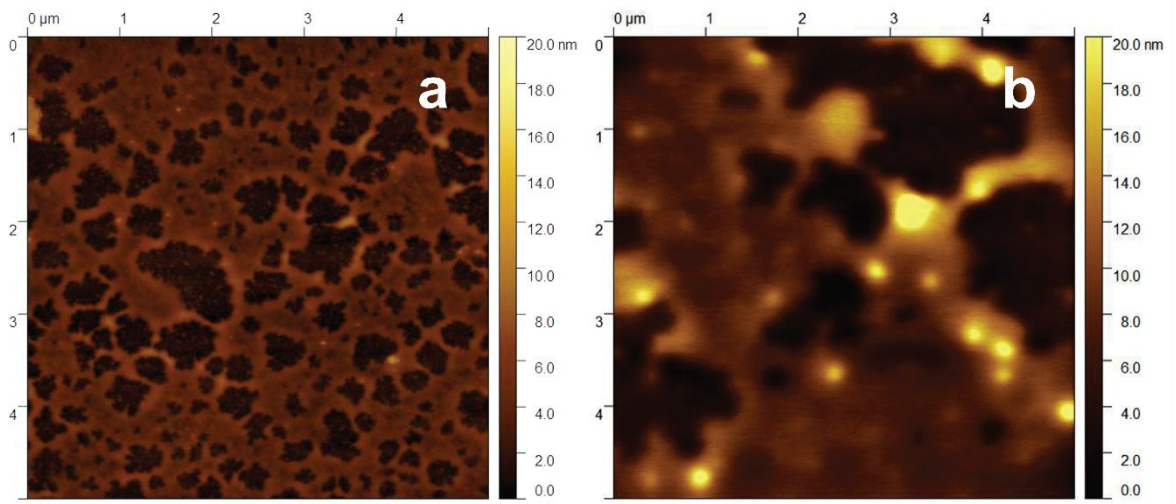

Figure 73. *AFM topography images of a) pure PPA and b) AuNPs-2AET-FL_2/PPA 50:50 %wt. nanocomposite blend. Samples were spin-coated onto Si/SiO₂ substrate from their organic suspensions and air dried.*

Band gap energy (E_g) of pristine functionalized AuNPs, PPA and related blends was estimated using the Tauc plot method, further developed by Davis and Mott from UV-Vis extinction spectra.[260] First, the energy-dependent absorption coefficient α was calculated by the Lambert–Beer's modulus following equation (9):

$$\alpha(\nu) = 2.303 \cdot \left(\frac{A}{d}\right) \qquad (9)$$

where α is estimated by absorbance (A) and thickness of the optical path length (d, in cm). The absorption coefficient α dependent on the incident photon energy can be expressed by the typical equation (10):

$$(\alpha h\nu) = \beta\left(h\nu - E_g\right)^{\gamma} \text{ for } h\nu > E_g \qquad (10)$$

where β is the absorption constant (associated with the separation of electrical conductivity and energy level), h is the Planck's constant (J·s), ν is the photon's frequency (s^{-1}), and the γ exponent factor is related to the nature of possible electronic transition: γ = 2 (indirect transition) allowed and γ = 1/2 (direct transition), respectively.[261]

Spectra obtained by plotting $(\alpha h\nu)^2$ and $(\alpha h\nu)^{1/2}$ as a function of energy (hν) are reported in *Figure D20*, and results summarized in **Table 6**. Herein, only the optical transition band gaps (involved in the excitation of electrons from the valance band to conduction band using photons of selected frequency) will be considered. It is worth noting that the optical band gap herein considered is important for applications such as solar cells, whereas the electronic band gap (removal or injection of electrons from the semiconductor valence band), usually

higher than the optical band gap, should be considered for devices such as light emitting diodes and laser diodes. However, for amorphous materials it is hard to estimate whether the band is direct or indirect.[262]

Sample	**Optical Band gap (eV) ± 0.05 eV**	
	Direct	Indirect
AuNPs-2AET-FL_2	4.13	4.50
PPA	2.47	2.75
B10	2.44	2.73
B30	2.41	2.72
B50	2.35	2.76
B70	2.34	2.69
B90	2.15	2.68

Table 6. *Direct and indirect optical band gap values obtained for AuNPs-2AET-FL_2, pure PPA, and AuNPs/PPA nanocomposite blends.*

Gold nanoparticles showed optical E_g values of about 4.0 eV, consistent with an insulating behaviour (>4 eV), whereas a lower E_g of ca. 2 eV value was found for typical semiconductor PPA.[263,264] For AuNPs/PPA nanocomposites, gold nanoparticles incorporation causes a variation in the E_g values. Optical band gap values decrease from 2.47 to 2.15 eV for direct transitions, whereas they decrease from 2.75 to 2.68 eV for indirect transitions (with respect to pure PPA) with increasing the concentration of gold nanoparticles (**Table 6**). Thus, the band gap value can be tuned according to AuNPs filling, achieving a reduction (13% for direct transitions, 3% for indirect transitions) when compared to the values for AuNPs functionalized with 1-dodecanthiol in P3HT:PCBM film[265], and similar values to those of oleylamine-functionalized Au- and AgNPs/P3HT:PCBM blends,[266] and AuNP-doped P3HT[267]. These results can be clarified in terms of (1) increase in the disorder caused by the polymer structural alteration, *e.g.*, deformities caused by localized states within the energy bandgap after AuNPs addition, and (2) creation of charge transfer complexes between functionalized gold nanoparticles and PPA structures.[268]

Electrical conductivity at room temperature (σ) for AuNPs-2AET-FL_2, PPA, and nanocomposites was calculated using equation (11) and equation (12)[269]:

$$\sigma = \frac{G \cdot L}{t \cdot W} \tag{11}$$

$$Norm.relative\ conductivity\ (\%) = \frac{(\sigma - \sigma_{AuNPs})}{\sigma_{AuNPs}} \cdot 100 \qquad (12)$$

where G is the conductance (1/R in 1/Ω = S) derived from the slope of I/V measurements, t is the thickness of each film (in m) measured by AFM of (4.6 ± 0.8) nm, L is the length between electrodes (in m) and W is the electrode length (in m) both depending on electrode design. In this case, electrical conductivity was in the range of $(9.3 \pm 0.9)\cdot 10^{-8}$ S m^{-1} (pure PPA) to $(23 \pm 2)\cdot 10^{-8}$ S m^{-1} in polymer blends (*Table D11*). Herein, a similar film thickness was assumed for all formulations, since it is mainly governed by spin coating conditions (rotational speed, suspension concentration, rate of solvent evaporation).[270] Normalized relative conductivity percentages reported in **Figure 74** clearly showed a conductivity increase as the AuNPs content increased.

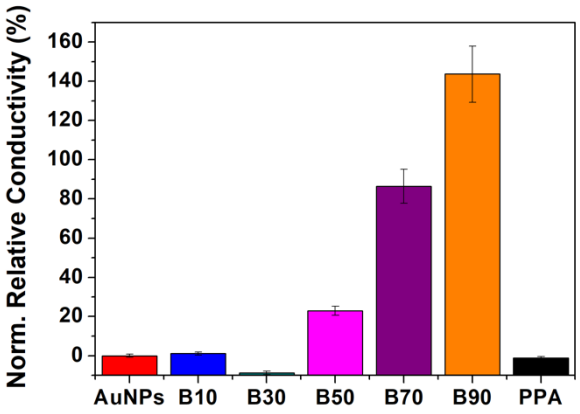

Figure 74. *Relative electrical conductivity (%) calculated for pristine AuNPs-2AET-FL_2, pure PPA and related nanocomposite blends. All values are normalized according to AuNPs electrical conductivity (σ).*

In particular, B50, B70, B90 significantly deviate with respect to other samples with (23 ± 2) %, (86 ± 9) %, and (144 ± 14) % conductivity gain to that of pristine functionalized AuNPs (considered as 100%), respectively. In particular, a significant enhancement in the conductivity was found with respect to pure PPA, which acts as a doping material for AuNPs in B70 and B90 nanocomposites. It is worth mentioning that processing methods, secondary doping and post-treatments have been verified to affect electrical conductivity values[271] and they are strongly dependent on the molecular arrangement of the polymer chains in the film (*e.g.*, edge-on, face-on configurations) that leads to different interface resistances.[272] Concerning practical applications, relative current ($\Delta I/I_0$ %)[273] was plotted for different samples at 5 V and 10 V (*Figure D21*). For both, a similar trend was found with a 60%

current improvement after 90% wt. of AuNPs addition. As reported for similar AuNPs/polymer nanocomposites, the enhancement of the electrical properties after blending procedure may be attributed to an increase in the amorphous phase of the polymeric matrix (due to the inclusion of AuNPs), which lowers the energy barrier and permits ion transport.[274]
In conclusion, a typical two-phase wet chemical reduction method produced gold nanoparticles functionalized with two different thiols: a bifunctional synthetic FL and a synthetic organic fluorescent dye 2AET to obtain AuNPs-2AET-FL colloids. Different molar ratios among precursors were explored, finding that freshly prepared samples were quite similar, showing an SPR band at 533 nm, as evidenced by UV-Vis measurements. At higher FL content during synthesis, smaller gold nanoparticles were obtained (with hydrodynamic diameter $<2R_H>$ of about 3 nm), together with an increase in the polydispersity of the sample. After one year of aging, the AuNPs-2AET-FL_2 (2AET/FL 1:2 molar ratio) remained stable in its dichloromethane suspension, with a sharp surface plasmon band at 545 nm and typical absorptions arising from surface functionalizing thiols. Solid-state morphological analysis (TEM, AFM) conducted on the latter evidenced AuNPs of quasi-spherical shape with a measured diameter of (4.1 ± 0.7) nm on average, with a polydispersity of about 17%. Surface characterization (FTIR, Far-IR, SR-XPS) confirmed the occurred functionalization. Photoluminescence measurements evidenced that it is possible to modulate the AuNPs emission: excitation at 333 nm induced emission from both 2AET and FL, whereas 2AET selective emission was found with λ_{ex} = 370 nm, whereas no fluorescence arose from the gold core (λ_{ex} = 533 and 545 nm). New nanocomposites were synthesized using a simple blending approach based on a poly(phenylacetylene) (PPA) matrix doped with the produced AuNPs. Blends varying AuNPs-2AET-FL/poly(phenylacetylene) (PPA) composition were obtained: 10/90, 30/70, 50/50, 70/30, 90/10%. After blending, a blue-shift in the UV-Vis spectra (300-500 nm spectral region) of the B50 and B90 samples was ascribed to a reduction of the extent of delocalization of π-electrons and the appearance of charge-transfer phenomena across the metal/organic interfaces, possibly interacting through π–π stacking. Charge-transfer reduced the radiative decay of the PPA matrix in emission spectra, with a consequent red shift in the emission maxima of functionalizing agents on AuNPs compared with pristine nanoparticles. Electrical characterization revealed a reduction in the band gap up to 2.15 eV for direct transitions and up to 2.68 eV for indirect transitions after addition of 90 %wt of AuNPs in the PPA matrix. Nanocomposites deposited as thin films (thickness of 4.6 ± 0.8 nm) showed a progressive increase in the electrical conductivity with respect to pristine, functionalized AuNPs reaching 144% gain in the case of B90 with respect to

pristine, functionalized AuNPs. In particular, an increase of about 2.5 times the relative conductivity value of pure PPA was obtained at 90% AuNPs loading.

3.2.3.b. AuNPs functionalised by PtDEBP$_n$ in P3HT blends

This work is a detailed study on synthesis and characterization of gold nanoparticles stabilized with the synthetic rigid rod-like organometallic Pt-based *i.e.* PtDEBP$_n$ ligands having different chain length (*n*) and their related hybrid composite blends with regioregular P3HT polymer. Organometallic oligomers involving three (*n*=3, PtDEBP$_3$) to six (*n*=6, PtDEBP$_6$) repeating units were employed as capping agents during nanoparticles synthesis. The chain-length dependence of the optical, morphological, and structural properties of the AuNPs-PtDEBP$_n$ (n=1–6) were investigated in solution and on thin dry films. Then, AuNPs-PtDEBP$_n$ were incorporated into P3HT matrix through a simple blending approach at room temperature, and different weight ratios (%wt/wt) between AuNPs/P3HT were studied (from 10/90 to 90/10). The organization and dispersion of AuNPs-PtDEBP$_n$ within P3HT-based spin coated thin films were studied *via* scanning electron microscopy. Complementary techniques, namely spectroscopic UV-Visible, Fourier-Transform Infrared (FT-IR), Dynamic Light Scattering (DLS), ^{1}H- and ^{31}P-NMR, and Atomic Force Microscopy (AFM) techniques were used for a comprehensive characterization of gold colloids and AuNPs-PtDEBP$_n$/P3HT nanocomposites. The influence of different chain lengths on the electric conductivity of nanocomposite blends was also examined.

Rod-like organometallic platinum(II) oligomers were synthesized starting from commercially available K_2PtCl_4, tri-*n*-butylphosphine, and synthetic 4,4'-diethynylbiphenyl (H-C≡C-C_6H_4-C_6H_4-C≡C-H, DEBP) as precursors following the procedure in *Appendix B1.3*.**Errore. Il segnalibro non è definito.** The increase in the chain length of oligomers determined a r ed shift of the extinction maxima following the trend **L6** (364 nm) > **L4** (362 nm) > **L3** (352 nm) (**Figure 75a**). These UV–Vis absorption bands (in CH_2Cl_2) are due to π–π* transitions of the alkynyl ligands. the red shifted can be assigned to the intraligand (IL) transition of DEBP ligands and to the Pt → C≡CR metal-to-ligand charge transfer (MLCT) transition from a filled metal d orbital to vacant π* DEBP orbitals, thus being best described as a mixture of $\pi\rightarrow\pi^*$(C≡CR) IL/d_π(Pt(II))$\rightarrow\pi^*$(C≡CR) MLCT.[275,276] Structural assessment was carried out *via* FT-IR spectroscopy in the mid- and far-infrared regions. A comparison between FT-IR spectrum of halogenated Pt-DEBP$_6$ oligomer and its thioacetate derivative is shown in **Figure 75b**. In both compounds, the presence of aromatic DEBP moiety gave rise to the aromatic =C–H stretching (ν) vibration at 3027 cm^{-1}, ν(C=C) at 1602 cm^{-1}, and the

out-of-plane bending (δ) vibration of aromatic ring at 826 cm^{-1}. Triple C≡C stretching was observed at 2102 cm^{-1}.[277] Tri-*n*-butylphosphine aliphatic chains on Pt atoms showed typical asymmetric (as) and symmetric (s) stretching: $\nu_{as}(-CH_3)$=2958 cm^{-1} partially overlapped with $\nu_{as}(-CH_2)$=2931 cm^{-1}, and the corresponding $\nu_s(-CH_3)$=2873 cm^{-1}. Aliphatic $-CH_2/-CH_3$ also shown the δ_{as} band at 1462 cm^{-1} of medium intensity. The two bands of relatively low intensity at 1094 cm^{-1} and 1045 cm^{-1} were assigned to typical *in-plane* CH deformation (βCH) vibration of aromatic rings. Noticeable differences among the Pt-$DEBP_6$–Cl and Pt-$DEBP_6$–$SCOCH_3$ trace was from the strong signal at 1730 cm^{-1} due to terminal C=O functional groups and C–S stretching vibration which appears as a weak band centred at 636 cm^{-1} with splitting due to vibration coupling.[278]

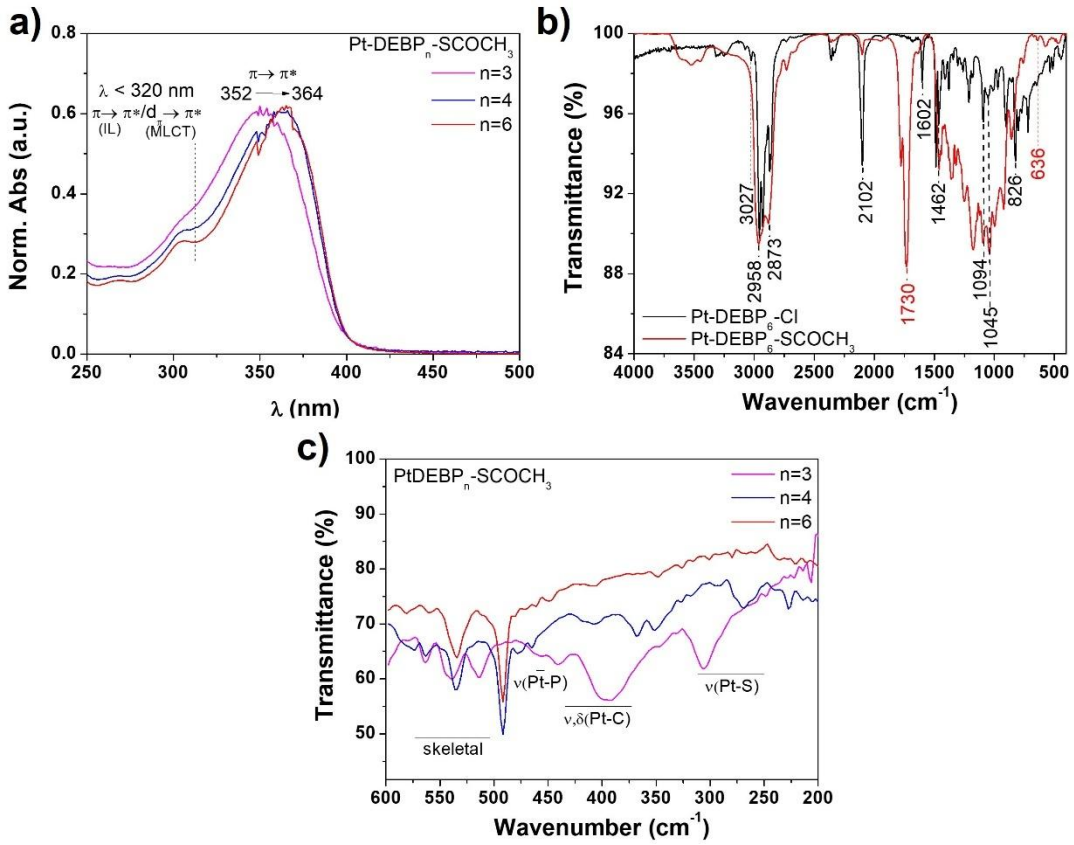

Figure 75. *a) UV-Vis spectra of oligomers recorded in CH_2Cl_2. b) FTIR spectra comparison of Pt-$DEBP_n$-Cl (black line) and Pt-$DEBP_n$-$SCOCH_3$. (red line). Samples were deposited as a thin film from CH_2Cl_2 on a KRS-5 plate. c) Superimposed Far-IR spectra of Pt-$DEBP_n$-Cl (black line) and Pt-$DEBP_n$-$SCOCH_3$ (red line). Samples were deposited as a thin film from iPr-OH on a PE plate and air dried.*

Vibrations involving the Pt-DEBP$_n$–SCOCH$_3$ were investigated by Far-IR in the 600-200 cm^{-1} wavenumber range. As can be seen from **Figure 75c**, the three higher-frequency bands were assigned to skeletal vibrations at ca. 580 cm^{-1} (very weak, in-plane and out-of-plane aromatic ring deformations, two bands), 560 cm^{-1} and 535 cm^{-1} due to and combination of ν(Pt–C) and C_nH_{2n+1} and C–C–C alkyl chain deformation modes, consistent with literature values for bis-phosphine Pt(II) alkynyl complexes.[279] The vibrations at ca. 490 cm^{-1}, and 410 cm^{-1} were further assigned to ν(Pt–C) of the bridging alkynyl ligands (Pt–C≡C).[280] The bands of medium intensity centred at 450 cm^{-1} were due to ν(Pt–P), whereas the signals at 390 cm^{-1} can be assigned to the δ(C–C–P).[281]

Metal-sulphur stretching frequencies ν(M–S), lie in the range 298-205 cm^{-1} for the transition-metal complexes[282], allowing to assign the band at about 300 cm^{-1} to the ν(Pt–S) which is shifted to lower frequency with respect to simple thiolate complexes owing to the strong *trans* influence of the alkynyl ligand. The same band was absent in the Pt-DEBP$_n$–Cl spectrum. Conversely, in the halogenated oligomer, a band was present at 305 cm^{-1}, typically assigned to terminal ν_s(Pt–Cl) in *trans* configuration (see *Figure B4*).[283]

AuNPs functionalized with the bifunctional *trans*,*trans*-[CH$_3$CO–S–(Pt(PBu$_3$)$_2$–(C≡C–C$_6$H$_4$–C$_6$H$_4$–C≡C–))$_n$Pt(PBu$_3$)$_2$–S–COCH$_3$] (AuNPs–PtDEBP$_n$, n=3,4,6) (**Figure 76**) were obtained through reduction of Au^{3+} precursor in a two-phase Brust-Schiffrin procedure (in details in *Appendix C2.5*. As previously explained, the acidic conditions of HAuCl$_4$ aqueous solution (pH < 2 at a concentration of 25 mM) allowed a *in-situ* deprotection of the thiol groups of Pt–DEBP$_n$–SCOCH$_3$ oligomers, which rapidly react with the gold precursor to form AuNPs-PtDEBP$_n$ colloids after addition of NaBH$_4$ reductant.

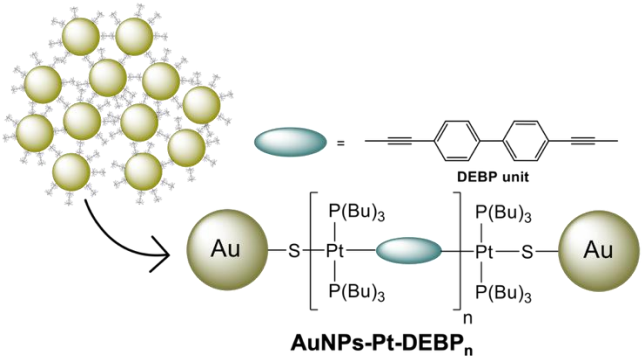

Figure 76. *Schematic representation of AuNPs functionalised by PtDEBP$_n$ (n = 3, 4, 6).*

The UV-Vis spectra of the as-obtained AuNPs stabilized by the organometallic ligands with different chain lengths (n = 3, 4, 6) are shown in **Figure 77a**. All the spectra clearly showed a single SPR band in the 525–530 nm region, typical of spherical AuNPs with a diameter

<10 nm[284], and the absorption of $PtDEBP_n$ oligomers functionalizing the AuNPs surface at $\lambda < 400$ nm.

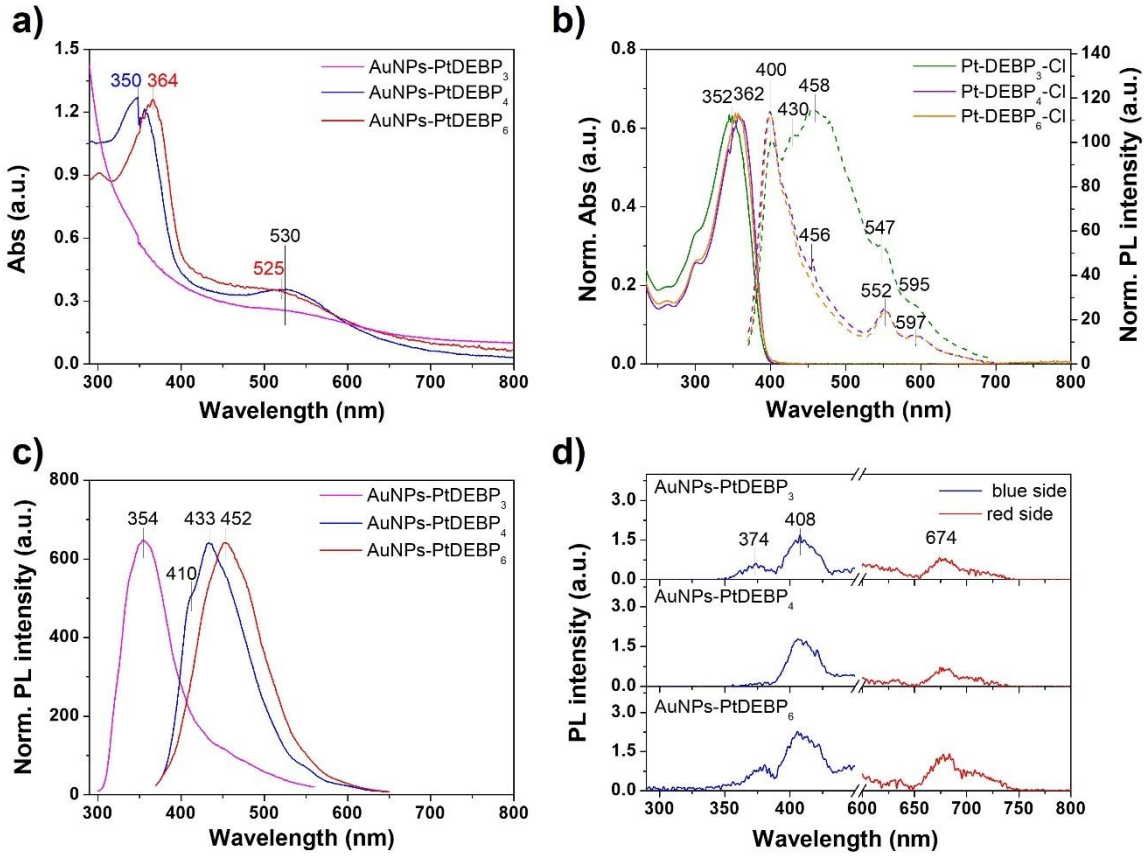

Figure 77. *a) UV-Vis spectra of AuNPs-PtDEBP$_3$ (pink line) AuNPs-PtDEBP$_4$ (blue line) AuNPs-PtDEBP$_6$ (red line); b) absorption and emission spectra of Pt-DEBPn-Cl (n = 3, 4, 6); emission spectra of AuNPs-PtDEBPn (n = 3, 4, 6) with c) λ_{ex} at 290 nm for AuNPs–PtDEBP$_3$ and at 350 nm for AuNPs–PtDEBP$_4$ and AuNPs–PtDEBP$_6$ d) λ_{ex} at 530 nm.*

Compared with pristine oligomers, the absorption related to Pt-based ligand remains mostly unaffected in the case of AuNPs–$PtDEBP_6$ (centered at ca. 364 nm in both cases), whereas a consistent blue shift occurred in the case of AuNPs–$PtDEBP_3$, from 352 nm of pristine ligand to <300 nm on AuNPs, and AuNPs–$PtDEBP_4$ (from 362 nm to 350 nm on AuNPs). Upon covalent binding of Pt(II) oligomers to the surface of AuNPs involving the sulphur donor atoms, an interfacial orbital mixing can occur causing changes in the HOMO-LUMO transition energy, thus determining a length-dependent blue shift in the oligomer absorption. These results illustrated that the ligand electronic properties represent a significant (and potentially predictable) degree of tunability for the functionalized AuNPs electronic structure, though a precise accounting of the origin of this effect is currently outstanding[285]

Notably, AuNPs capped with six-residues oligomer (AuNPs-PtDEBP$_6$, red line in **Figure 77a**) showed a 5 nm blue-shift in the LSPR maximum value (λ_{SPR} = 525 nm) compared with AuNPs-PtDEBP$_3$ and AuNPs-PtDEBP$_4$ (λ_{SPR} = 530 nm). The reported effect could be ascribed to the interparticle coupling effect occurring interacting AuNPs. Indeed, the extinction spectra of nanoparticles is very sensitive to the separation distance between AuNPs and is strongly influenced by the interparticle coupling of nearby particles; a blue-shift in the LSPR band typically occurs with increasing nanoparticle spacing.[286] In this case, the PtDEBP oligomers behave as a bifunctional functionalizing agent (having the availability of two sulphur ending groups) and considering a theoretical length for a single PtDEBP unit of 2.034 nm (experimental 2.1 nm[287]), the calculated S-to-S distance of PtDEBP$_3$ was 5.1692 nm, whereas for PtDEBP$_6$ was 9.872 nm, allowing a qualitative assessment of the formation of an interconnected AuNPs network with different NP-NP distance. The three samples showed different full width at half-maximum (FWHM) value of SPR band, with AuNPs-PtDEBP$_4$ having the smaller FWHM compared with AuNPs-PtDEBP$_3$ and AuNPs-PtDEBP$_6$. Normally, the different bandwidth accounts for different polydispersity of the samples, the narrower the FWHM the lower the polydispersity.[288] However, the extinction spectra of very close AuNPs also comprise interband absorptions of AuNPs and coupled LSPR band (*via* near-field interaction, resulting in coupled plasmon modes) of interacting AuNPs which contribute to LSPR band broadening.[289] Thus, based on the UV–Vis results, it is possible to hypothesize the formation of Pt–DEBP$_n$-capped AuNPs arranged into 3D-network of super-aggregates of different sizes[290], also assuming the formation of isolated nanoparticles to some extent. The luminescence spectra for the chlorinated platinum complexes, n=3,4,6, were recorded in CH_2Cl_2 at room temperature (**Figure 77b**). The excitation wavelengths (λ_{exc}) were chosen as they correspond to the absorption UV-Vis maxima of the complexes reported herein (see **Figure 77b**), being λ_{exc} = 353 nm for Pt–DEBP$_3$–Cl, λ_{exc} = 360 nm for Pt–DEBP$_4$–Cl and Pt–DEBP$_6$–Cl. All the samples exhibited a significant PL emission. For n = 4,6 the emission spectra overlap, with a negligible difference in the λ_{em} maxim. The luminescence properties of longer organometallic complexes are predominantly DEBP-centred transitions ($\pi \rightarrow \pi^*$)[291], and green/yellow photoluminescent characteristics (λ_{em}=552–597 nm) which can be ascribed metal-to-ligand charge transfer (MLCT) transitions and ligand-to-ligand charge transfer (LLCT).[292] Interestingly, the profile of Pt–DEBP$_3$–Cl strongly differed from other complexes under study, showing a broader and red-shifted emissions in the 400–500 nm. Once covalently linked on the AuNPs, the PL properties were studied (**Figure 77c**). AuNPs–PtDEBP$_4$ and AuNPs–PtDEBP$_6$ were studied at the optimal

excitation (350 nm), the emission spectra are centred at 434 and 452 nm, respectively. Notably, for AuNPs–PtDEBP$_3$, the optimal excitation was found at 290 nm, with a broad emission band centred at 354 nm. This evidence further corroborates the presence of functionalizing Pt(II) interacting with the AuNPs surface. PL recorded on the AuNPs LSPR band provides insight into multiple emissive pathways (**Figure 77d**). Excitation at 530 nm, close to the LSPR of AuNPs, yielded unexpected high-energy bands at about 374, 408, and 675 nm, with no significant spectral shifts among all the samples. In this case, the emission reasonably comes from the Pt(II) complexes functionalizing the surface, since only small sized clusters (< 2nm) are known to exhibit intrinsic luminescence.[293] The long-wavelength emission found in functionalized AuNPs was rather close to that of the free Pt–DEBP$_n$–Cl (λ_{em} at about 547, 595 nm), thus it can be attributed to PtDEBP$_n$ MLCT transitions, slightly modified by the covalent interaction with AuNPs. In particular, the higher rigidity of the system provided by the formation of covalent AuNPs network suppress non-radiative deactivation pathways, intermolecular quenching, and probably hydrogen-bonding/π-stacking interactions, featuring the red-shifted emission band at ca. 670 nm.[294]

In order to confirm previous assumptions about different sample polydispersity, hydrodynamic diameter (<2R$_H$>, nm) evaluation was carried out by DLS analysis (**Figure 78**).

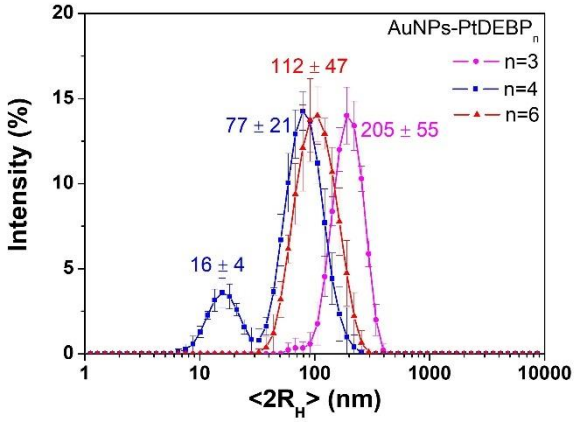

Figure 78. *DLS graphs of AuNPs-PtDEBP$_n$ with n = 3, 4, 6. Graphs collected in CH_2Cl_2.*

For AuNPs-PtDEBP$_3$, the first population, not very intense, was found at (72 ± 11) nm, with the biggest at (205 ± 55) nm (PDI = 0.32 ± 0.05) indicating the coexistence of AuNPs network of different sizes; for AuNPs-PtDEBP$_4$ the first population was centred at (16 ± 11) nm and the second one at (77 ± 21) nm (PDI = 0.4 ± 0.2), which agreed with the presence of smaller, isolated AuNPs, at least in a higher percentage than in the previous sample, as also

demonstrated by the different PDI values. Conversely, the AuNPs-PtDEBP$_6$ showed a single distribution at (112 ± 47) nm (PDI = 0.29 ± 0.04) consistent with more uniform AuNPs networks.

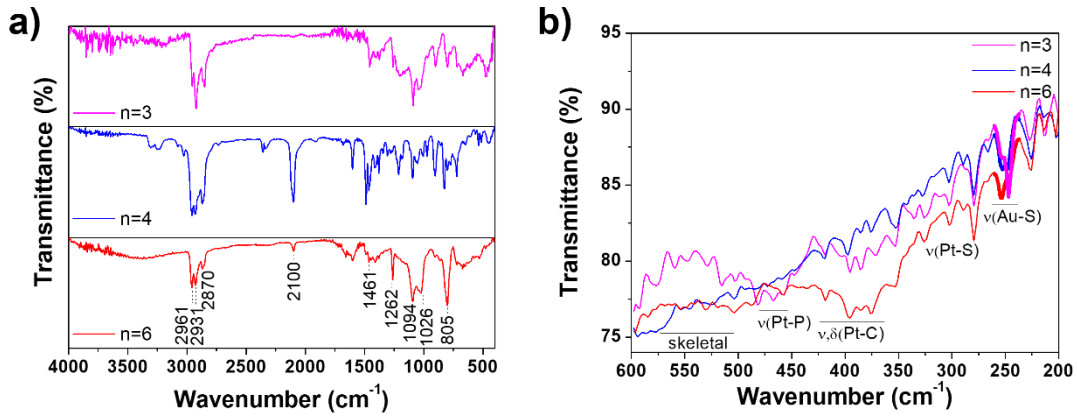

Figure 79. *a) FTIR spectrum of AuNPs–PtDEBP$_n$ recorded in transmittance mode (4000-400 cm^{-1}) deposited on KRS-5 cells. b) Far-IR spectrum (600-250 cm^{-1}) of AuNPs-Pt-DEBP$_n$ deposited on PE cells.*

Occurred surface functionalization was assessed by FTIR spectroscopy. Infrared spectra of AuNPs-PtDEBP$_n$ are reported in **Figure 79a**. As first evidence, the spectrum recorded on AuNPs did not show the 1730 cm^{-1} stretching band of >C=O functional groups, due to the occurred deacetylation reaction of terminals –SCOCH$_3$ in acidic conditions, followed by the formation of metal–sulphur bond. According to ligand structure, signals assigned to ν_{as}(–CH$_3$)=2962 cm^{-1}, ν_{as}(–CH$_2$)=2931 cm^{-1} and ν_s(–CH$_3$)=2869 cm^{-1} of aliphatic tri-*n*-butylphosphine chains on platinum atoms were found, together with scissoring vibration of –CH$_2$ overlapped with that of asymmetric deformation mode of –CH$_3$ groups at 1461 cm^{-1} and ν(C–C) at 1262 cm^{-1}. Intrachain DEBP moiety unambiguously gave rise to a ν(C≡C) band at 2100 cm^{-1} typical of disubstituted acetylenes. Aromatic rings showed signals at 1094 and 1026 which represent the *in-plane* CH deformation vibration of 1,4 disubstituted ring, as also reported for pristine chloride and thioacetate oligomers. The strong C–H *out-of-plane* deformation vibration of disubstituted aromatic ring was found at 805 cm^{-1}. Signals at 3300 cm^{-1} and 1620 cm^{-1} were due to absorbed water and assigned to ν(–OH) and δ(–OH), respectively.

In the far-infrared spectra of the AuNPs (**Figure 79b**) several vibrations were consistently observed. Bands in the 580–530 cm^{-1} and 490–380 cm^{-1} region are assigned to skeletal and Pt–C stretching and bending vibrations arising from both the tributylphosphine ligands and the DEBP moiety, in line with reported ranges for pristine complexes. Most notably, all three

samples displayed a strong absorption centred at ~250 cm^{-1}, characteristic of the ν(Au–S) vibration. As expected, this band occurs at substantially lower frequency than the corresponding ν(Pt–S) in Pt(II) complexes (typically 298–205 cm^{-1}). The presence of these well-defined ν(Au–S) absorptions across all samples provides evidence for the covalent anchoring of the oligomer to the AuNPs surface through thiolate bonds, while the higher-frequency bands confirm the retention of alkynyl and phosphine coordination motifs in the nanostructure.

After an accurate characterization of the system, the studies of AuNPs/P3HT blend were carried out. The AuNPs–$PtDEBP_n$/P3HT polymer blends were synthesized varying the AuNPs weight percent (%wt) between 10 to 90, respect to the polymer. Nanocomposites were obtained by blending the AuNPs and regioregular P3HT suspensions in $CHCl_3$ under air atmosphere and room temperature (for experimental details refers to *Appendix D2.4.*). The presence of gold colloids inside the P3HT was investigated in suspension *via* DLS. As can be seen from **Figure 80a**, the presence of larger aggregates of $<2R_H>$ = 140–230 nm range prevailed over a small population centred at about 20 nm. The presence of a bimodal population was detected after polymeric blending (pristine AuNPs–$PtDEBP_4$ showed populations at (16 ± 4) nm and (77 ± 21) nm), although a slight increase in the most intense size distribution was found in all cases, as the presence of P3HT matrix further contribute with a solvated corona due to interactions with the –$PtDEBP_4$ on the AuNPs surface to some extent. A detailed morphological analysis was carried out on pristine P3HT and AuNPs–$PtDEBP_4$/P3HT 50/50 (as a representative sample) using tapping mode AFM. Pristine regioregular P3HT (*Figure D22*) showed a porous morphology with porous depth that ranged between 45 and 100 nm. In the nanocomposite, considering the interconnected nature of AuNPs–$PtDEBP_4$, the bright aggregates in **Figure 80** were due to the presence of AuNPs networks uniformly distributed within the polymer matrix with no apparent clustering of NPs at the P3HT/air interface (3D profiles can be found in *Figure D22*). These observations were consistent with a good miscibility between the AuNPs functionalized with rigid π-conjugated organometallic polymer and the P3HT chains. Indeed, the interactions between the AuNPs surface ligand and mixed polymer chains largely determine the thermodynamics/miscibility and hence the morphology of films.[295]

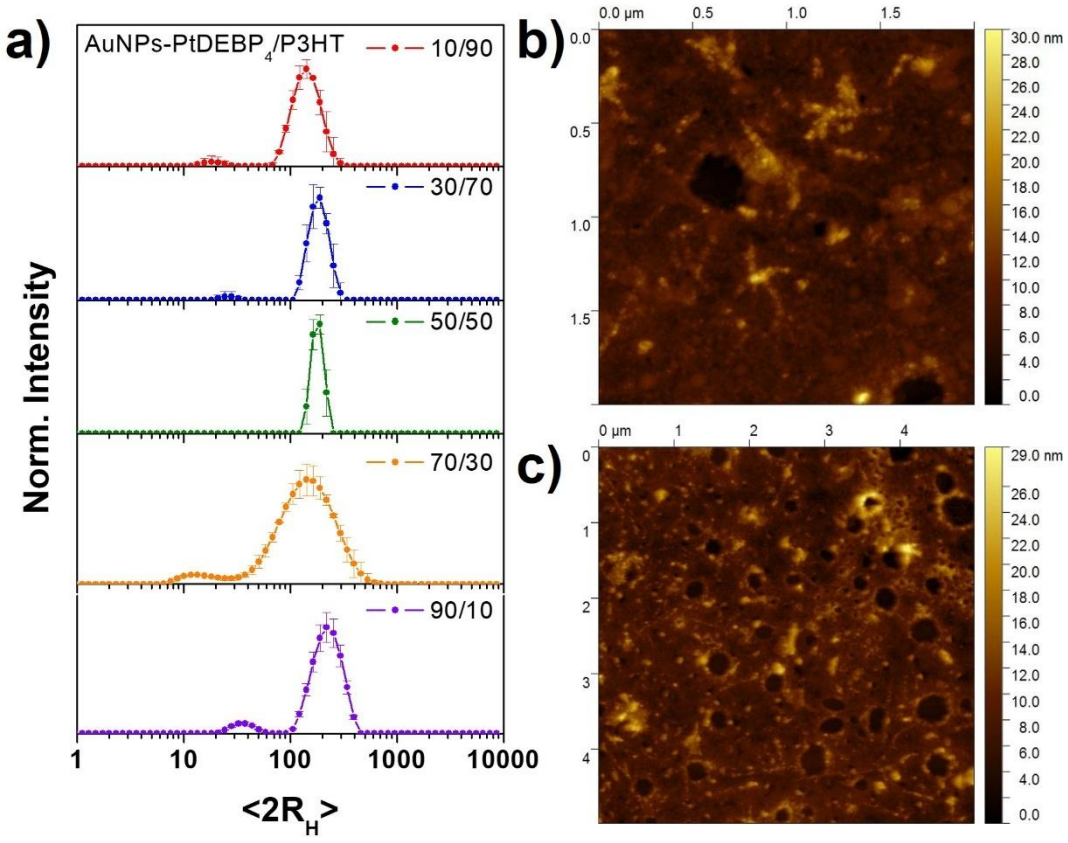

Figure 80. *a) Normalized DLS intensity weighted size distributions of AuNPs–PtDEBP$_4$/P3HT blends: % wt 10/90 (<2R$_H$> = 19 ± 4 nm and 140 ± 34 nm), 30/70 (<2R$_H$> = 26 ± 4 nm and 196 ± 41 nm), 50/50 (<2R$_H$> = 176 ± 22 nm), 70/30 (<2R$_H$> = 14 ± 5 nm and 170 ± 105 nm), 90/10 (<2R$_H$> = 36 ± 8 nm and 229 ± 66 nm) recorded in CHCl$_3$. b,c) AFM profiles of AuNPs–PtDEBP$_4$/P3HT 50/50 blend spin coated onto Si/SiO$_2$ substrate from their CHCl$_3$ suspension and air dried.*

A direct comparison of the electrical behaviour was done based on the current-voltage response in the interval of -10 V to +10 V (**Figure 81a,b,c**). Blends were spin coated onto interdigitated electrodes resulting in a mean film thickness of 3 ± 1 nm (evaluated by AFM). The P3HT electrical measurements are reported in *Figure D22*, for comparison. Although the absolute current densities varied among the three samples, all exhibited a fully linear I/V dependence, indicative of ohmic transport. These trends can be explained based on (1) the absence of a contact energy barrier between the AuNPs and the P3HT matrix, *i.e.*, a good Ohmic contact, owing to the favourable alignment between HOMO level of P3HT (in the range 5.1–5.2 eV) and the work function of gold in the range (5.0–5.1 eV), and (2) a high concentration of free charges at the thermal equilibrium.[296] The AuNPs–PtDEBP$_4$/P3HT

blends showed the highest variation among the different formulations (**Figure 81b**), probably owing to a more efficient dispersion and distribution within the P3HT matrix which reduced the resistance and boosted the current response to different bias. A comparison of the electrical properties of blends at specific DC (Direct Current) voltage levels used in electronic devices and systems, *i.e.*, 5 V and 10 V, is presented in **Figure 81d**. The AuNPs/P3HT samples showed the same electrical trend for both applied voltages and, in all cases, the AuNPs/P3HT 10/90 composition represented the optimized weight ratio. The best results were obtained for the AuNPs–PtDEBP$_4$/P3HT 10/90, with an increase in the current intensity of more than 30 times the pristine P3HT.

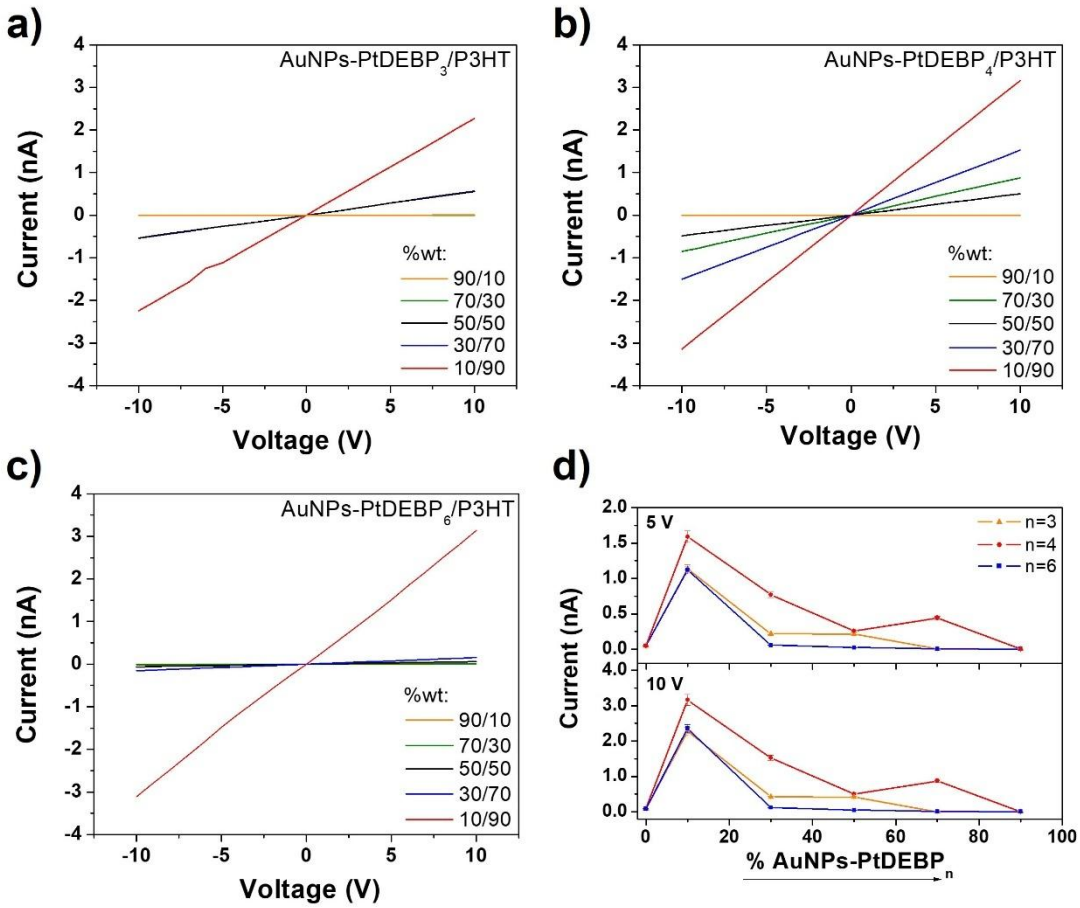

Figure 81. *Electrical measurements performed on AuNPs/P3HT blends deposited by spin-coating onto interdigitated electrodes. a) AuNPs–PtDEBP$_3$/P3HT. Data of 70/30, 50/50, and 30/70 are overlapped. b) AuNPs–PtDEBP$_4$/P3HT. c) AuNPs–PtDEBP$_6$/P3HT. d) Comparison of the electrical response at 5 V and 10 V. 0% means P3HT only.*

In conclusion, colloidal, hydrophobic gold nanoparticles (AuNPs) were synthesized in the presence of platinum-containing polyynes with different chain length and incorporated into

poly(3-hexylthiophene-2,5-diyl) (P3HT) matrix for potential optoelectronics and storage devices uses. Blending AuNPs–$PtDEBP_n$ with regioregular P3HT produced nanocomposites with a mean thickness of 3 ± 1 nm and uniform distribution of AuNPs within the polymer matrix, as evidenced by DLS and AFM, indicating a good miscibility between counterparts. At room temperature, electrical I vs V measurements (± 10 V range) were carried out on AuNPs/P3HT hybrid blends with different composition (10/90 to 90/10 %wt) and spin-coated onto an interdigitated ITO substrate, being the AuNPs/P3HT 10/90 %wt the best composition with an improvement of the electrical conducibility with respect to pristine homo-polymer of about 30 times.

3.2.3.c. AuNPs functionalised by 4BBT and FL in P3HT/PLA blends

In this work, we sought to fabricate thin films of P3HT and the insulating polymer PLA, exploiting the phase separation phenomena occurring when blending these two polymers and spin-coating them on silicon wafers or interdigitated electrodes. By varying the molecular weight of PLA and different parameters such as the weight concentration of the blend in the solution and the weight ratio of the polymers, we intended to obtain different morphologies where P3HT was confined in nanodomains, or was able to a form continuous phases, in order to see how the confinement influenced molecular orientation and electrical conductivity of the polymer. Moreover, it was possible to selectively remove PLA with acetic acid.

Together with the P3HT/PLA system, in the blend, we included a network of hydrophobic AuNPs networks, functionalised with two sulphur-based ligands: 4-bromobenzene thiol (4BBT), an aromatic thiol and 9,9-didodecyl-2,7-bis(acetylthio)fluorene (FL), a bifunctional ligand[293]. The inclusion of functionalised gold nanoparticles aimed to improve the transport properties of P3HT segregated in nanodomains.

The functionalised AuNPs networks were firstly characterized morphostructurally, *i.e.* with UV-visible spectroscopy, FT-IR spectroscopy, HR-Transmission Electron Microscopy (HR-TEM). The obtained hybrid systems, where we used two different PLA molecular weights and different concentrations of the polymers and the AuNPs to influence the morphology of the spin-coated film, were then characterized using UV-visible spectroscopy, Atomic Force Microscopy (AFM), to understand their morphology. Lastly, the influence of the morphology on the transport behaviour was investigated through the comparison of absorption spectra with electrical measurements.

AuNPs were prepared following a typical two-phase synthesis in water and toluene (*vd. Appendix C2.8.*). The obtained nanoparticles were stabilised against aggregation thanks to the presence of two thiol linkers in mixture. The presence of two aromatic thiols improves both the dispersibility and the colloidal stability, the long aliphatic chains in FL interact with the solvents giving the system good dispersibility in organic solvents such as chloroform and dichloromethane. Moreover, the bifunctional FL induced the formation of direct interconnection between AuNPs. 4BBT, at the same time, being a smaller, aromatic, and monofunctional ligand, links to the surface of the single gold nanoparticles, contrasting the rigidity of the system if only FL was used, thus giving it further colloidal stability.

Figure 82 shows the reaction scheme of the interconnected AuNPs network, together with their UV-vis and DLS characterizations. The plasmon band is centred at 520 nm, in accordance with the presence of gold nanoparticles (**Figure 82b**, UV-vis). In **Figure 82c**, the DLS highlights the presence of a population of nanoparticles with a hydrodynamic diameter of (44 ± 24) nm, with a shoulder centred at around 10 nm in hydrodynamic diameter, as expected with such systems.

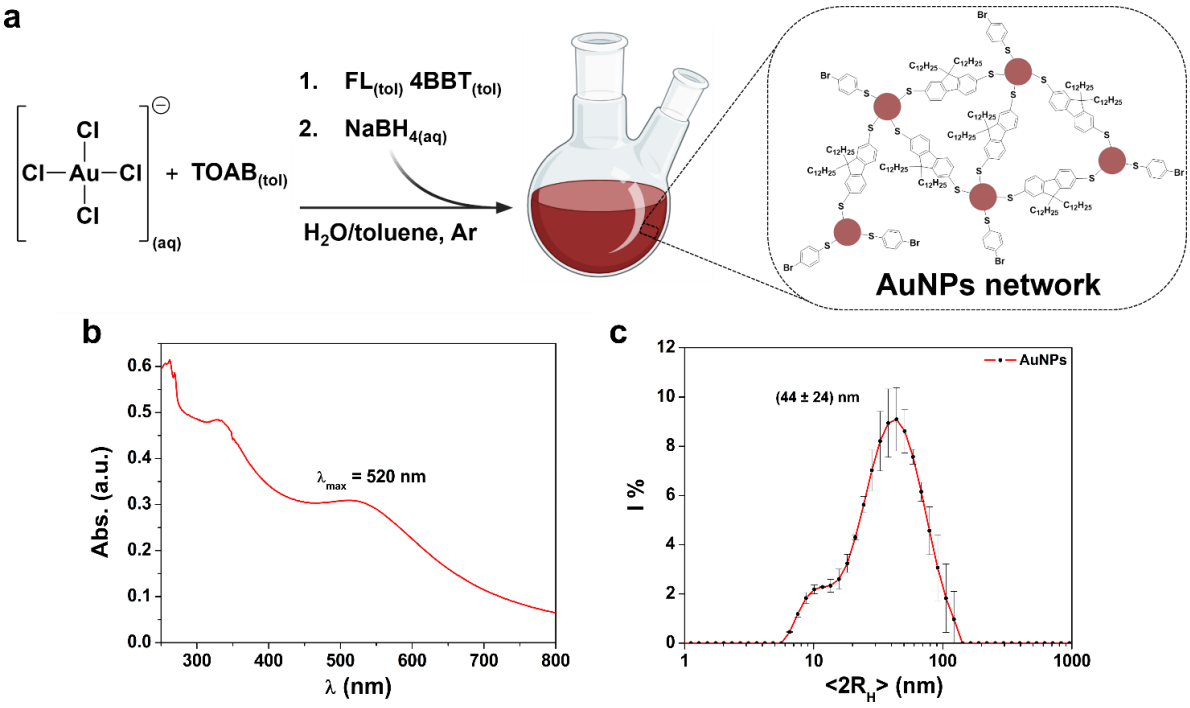

Figure 82. *a) reaction scheme; b) UV-vis spectrum of AuNPs; c) DLS graph of AuNPs. UV-vis and DLS were recorded in dichloromethane.*

FT-IR was performed to structurally analyse the system, *i.e.*, to confirm the presence of both thiols on the surface of the nanoparticles. In the AuNPs FT-IR spectrum, shown in *Figure C14a*, signals of both FL and 4BBT can be seen: the peak in the 2800-3000 cm^{-1} range pertains to sp^3 C-H stretching, which can be ascribed to the two aliphatic chains (12 C atoms) of FL. On the other hand, at 480 cm^{-1}, the C-Br stretching peak, relative to 4BBT, is distinguishable, confirming the presence of both thiols. Quite relevantly, in the spectra of the pristine thiols (*Figure C14b,c*), the peak relative to S-H stretching at 2565 cm^{-1} (4BBT, *Figure C14c*), and, for FL, the peak at 1710 cm^{-1} of the C=O stretching in the thioacetate group can be seen. These two signals, as expected, are not present in the functionalised AuNPs IR spectrum, as the sulphur links to the gold surface and thiol and thioacetate groups are not present anymore, giving further confirmation of the chemical functionalisation.

The morphology and structure of the functionalised AuNPs networks were investigated using a combination of electron microscopy (HR-TEM, FFT, IFFT and EDX) and image processing techniques (**Figure 83**). The morpho-structural investigation confirmed a nanoparticle arrangement into a monodimensional network (**Figure 83a**)[290]. The corresponding high resolution IFFT evidenced crystalline lattice fringes with preferential orientations of spacing $d_{111} = 0.237$ nm of the gold phase. The morphometric analysis identified AuNPs of quasi-spherical shape with evident rough surfaces, arranged in a network. The measured diameter provided an average value of (3.69 ± 0.93) nm having a polydispersity of about 25% (**Figure 83a**). To increase the electron scattering signal at high resolution, a different nanometric region with overlapping layers is shown in **Figure 83b**. The inset shows a crystalline lattice with a spacing of 0.251 nm, oriented along the (200) crystallographic plane, belonging to the crystalline phase of gold sulphide (Au_2S)[297]. The presence of the expected chemical species was confirmed by EDX spectroscopy probed on **Figure 83b** (Au, S, Br, **Figure 83b**-EDX). The fast Fourier transform of **Figure 83b** exhibits a nanodiffraction rings produced by a random orientation of the polycrystalline material (**Figure 83b**-FFT). By measuring the d-spacing of the diffraction rings, we were able to identify a superimposition of two different diffraction patterns. The signal of the diffraction rings indicated by yellow dot-arcs belongs to the typical Au crystallites with a face-centered-cubic (fcc) structure of a space group $Fm\bar{3}m$, confirmed also by the ring of $d_{111} = 0.237$ nm. The overlapped nanodiffraction pattern showed the presence of gold sulphide (Au_2S) phase of a cubic space group Pn3m (orange arcs). This confirmed the measured interplanar spacing of the crystalline lattice of the nanoparticle reported in the inset of **Figure 83b**.

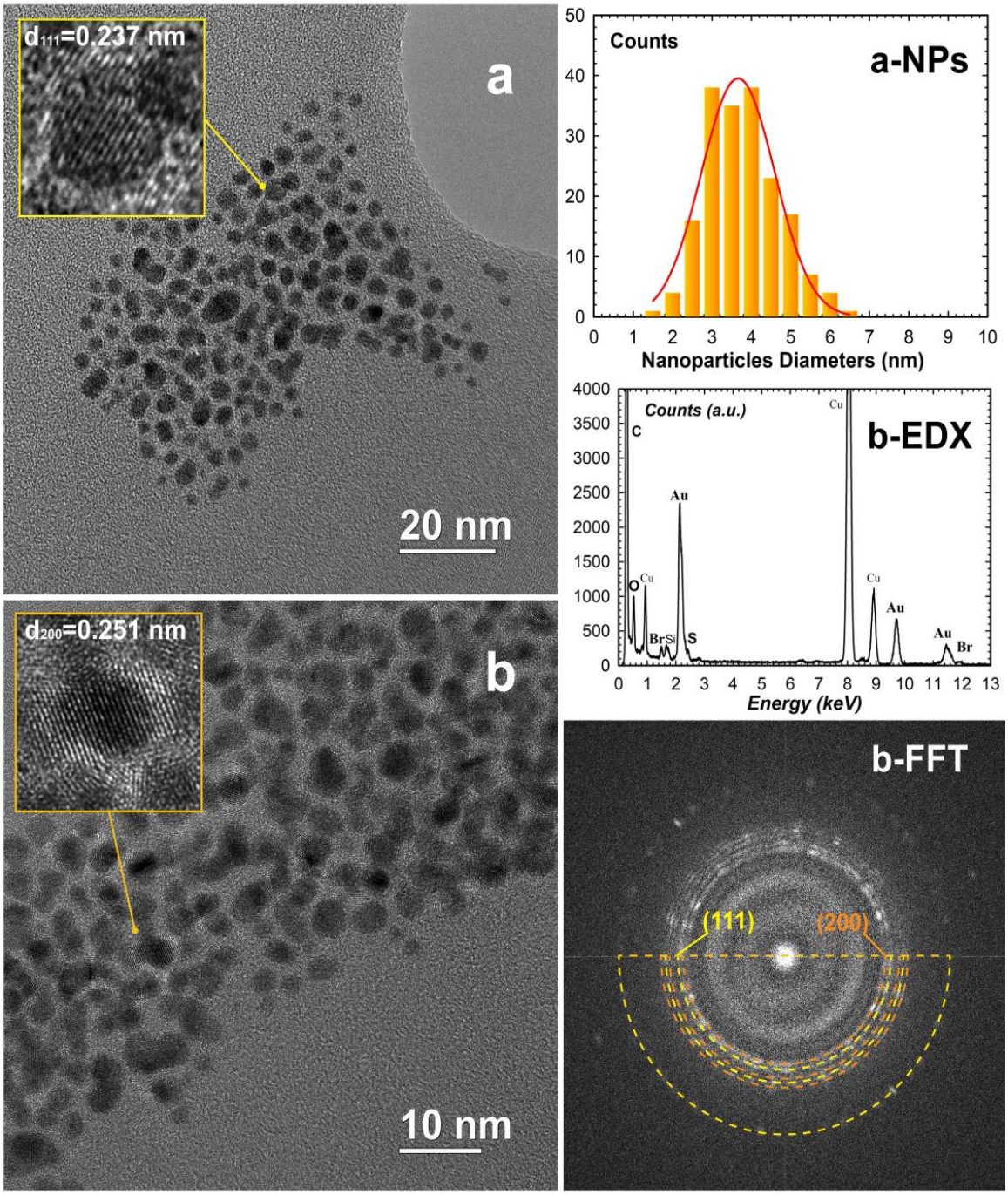

Figure 83. *Morpho-structural studies of AuNPs. a) BF-HRTEM image of AuNPs layer. Inset: high-resolution IFFT image illustrating crystalline lattice of a single gold nanoparticle, and plot showing the frequency distribution of the nanoparticle size histogram of a; b) BF-HRTEM image of AuNPs overlapping layers; inset: high-resolution IFFT image illustrating crystalline lattice of single gold sulphide nanoparticle; b-EDX: EDX spectral image of b; b-FFT: FFT image illustrating showing distinct diffraction rings corresponding to the crystalline phases of Au_2S (orange line arcs) and of Au (yellow line arcs).*

Firstly, binary blends (only P3HT and PLA) were studied in order to optimise the morphology control and be able to obtain thin films with different nanophases. A homogeneous solution of the blend was obtained using a common solvent for the polymers, with chloroform being chosen. These two polymers have quite different chemical structures and are immiscible. When a blend of these two polymers is spin-coated from $CHCl_3$, the evaporation of the solvent, together with the different chemical nature of the polymers, give rise to two phases and the morphology of the film can be tuned by varying parameters such as weight ratio, molecular weight, and concentration[298].

Morphological characterisations on the blends were carried out by means of Atomic Force Microscopy (AFM), in tapping mode. Weight ratio and molecular weight, together with the different chemistry of the two polymers, play a key role in the phase separation process, and thus in the morphology of the blended thin film. These parameters were tweaked in order to obtain different morphologies and thickness of the films, which could be controlled by changing the concentration of the dispersion pre-spinning.[299]

After the binary blends fabrication, hybrid blends – P3HT/PLA/AuNPs were studied. Adding AuNPs in the blends, which accumulated in the P3HT phase due to chemical affinity, caused some morphology changes with respect to binary blends. The shift in morphology, obtaining a continuous P3HT phase with AuNPs dispersed inside, allowed for a better transport behaviour and optical response for the hybrid blends.

Binary blends of poly(lactic acid) and poly(3-hexylthiophene-2,5-diyl) were spin coated from chloroform, obtaining different morphologies due to phase separation phenomena. In collaboration with Christophe Sinturel from Université d'Orléans, France, weight ratios and molecular weight for the polymer blend dispersions were tested, with the aim of obtaining co-continuous phases. Firstly, a PLA with a M_n of 85-95 kDa (PLA_1) was employed, and with the 50-50 weight ratio (P3HT-PLA_1 50-50, BB_1 50) a continuous phase of isolated domains distributed in a continuous layer of lower elevation was obtained and studied *via* AFM. As shown in *Figure D22*, the molecular weight of PLA was varied, using a polymer with a lower M_n – 15-25 kDa – PLA_2. The lowering the molecular weight of one or both polymers in a binary blend increases their miscibility, thus allowing a morphology close to co-continuous phases, or at least with one continuous phase (see **Figure 84**)[300, 301]

Figure 84 shows AFM images of P3HT-PLA binary blends at different weight ratios and varying parameters. **Figure 84a** depicts a 70-30% wt:wt P3HT-PLA blend (BB_2 70), **Figure 84b**, a 90-10% wt:wt P3HT-PLA blend (BB_2 10). **Figure 84c** and d show an example of P3HT confined in almost continuous nano-domains (size across approximately 200-500 nm),

which was obtained with a 50-50% wt:wt P3HT-PLA blend (BB_2 50). **Figure 84d** is the blend BB_2 50 after AcOH treatment to remove PLA.

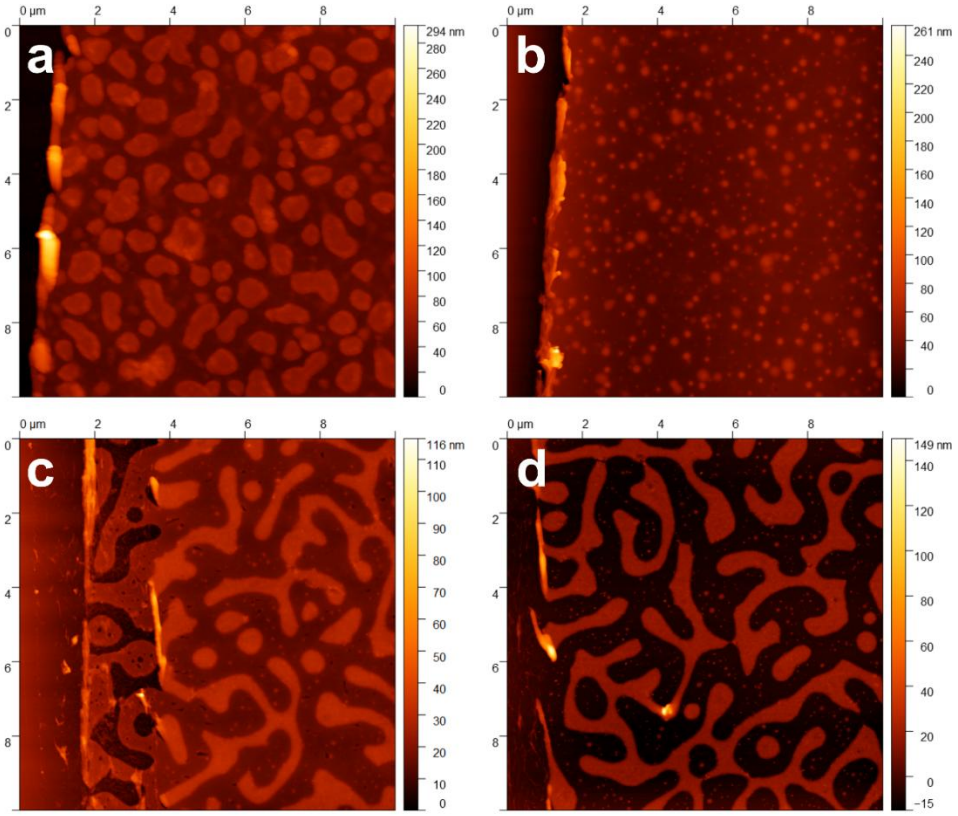

Figure 84. *AFM images of thin films taken in tapping mode, a) P3HT-PLA_2 40-60; b) P3HT-PLA_2 10-90; c) P3HT-PLA2 50-50; d) P3HT-PLA2 50-50 after AcOH treatment. All samples spin coated from $CHCl_3$.*

Moreover, the films shown in **Figure 84c-d** were spin-coated from a 5 mg/mL solution, resulting in a thickness of approximately 30 nm.

P3HT confined in domains in the nanoscale is desirable to obtain confinement of the semiconducting polymer, to modulate the orientation of P3HT and the morphology of the nanophase, thus its conductivity. Moreover, the fabrication of a fully continuous phase of nanometric size serves the purpose of maximising the interface area while maintaining interconnectivity of the conducting phase.

After obtaining different morphologies, optimising the control of the confinement effect of P3HT varying different parameters only with P3HT and PLA, AuNPs were included inside the blends, at varying concentrations and in different morphologies. The different weight

concentrations used were: 10%, 25%, 33%, 50%, with respect to the total blend concentration.

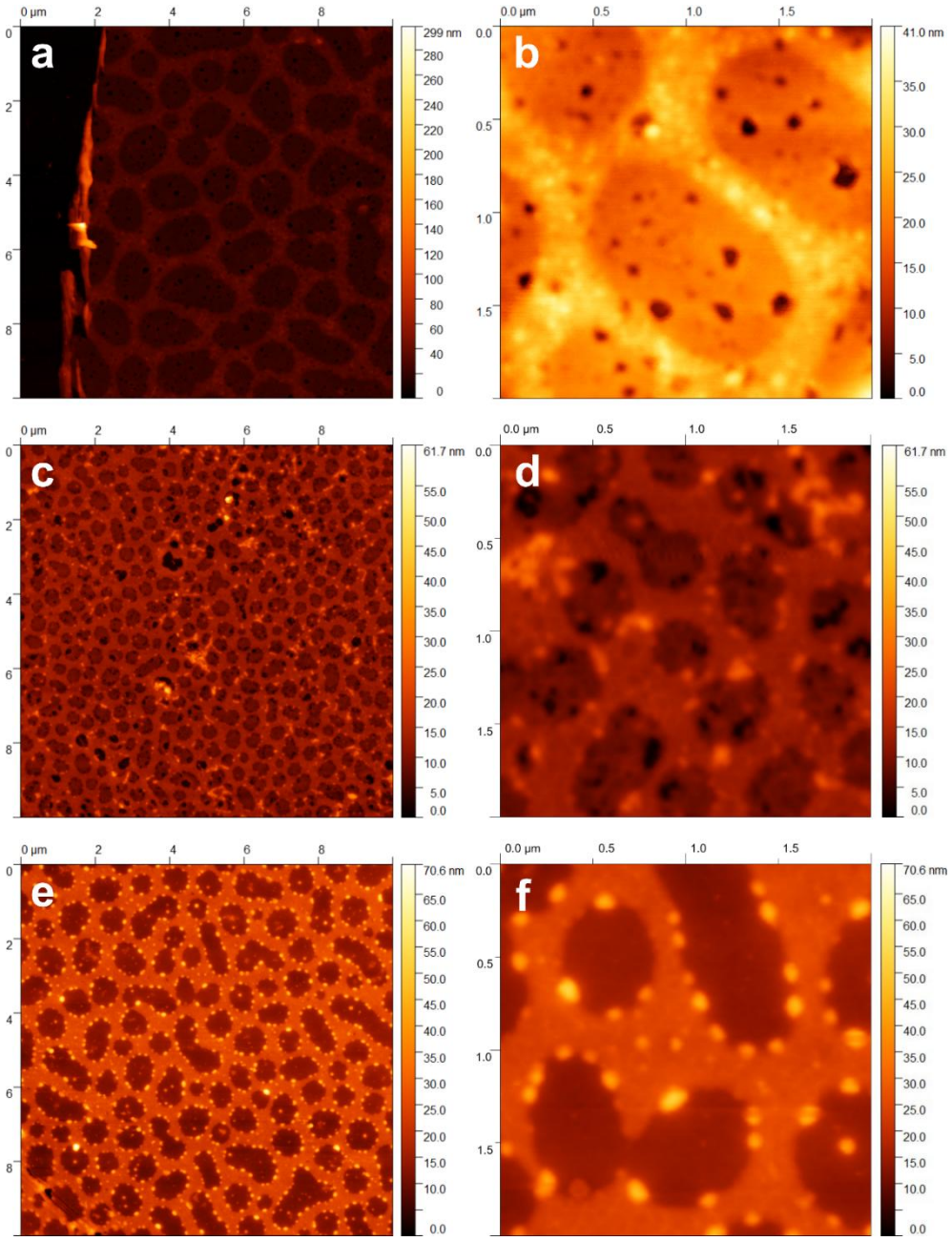

Figure 85. *Polymers-AuNPs thin films, a) HB 10, 10x10 µm^2; b) HB 10, 2x2 µm^2; c) HB 25, 10x10 µm^2; d) HB 25, 2x2 µm^2; e) HB 33, 10x10 µm^2; f) HB 33, 2x2 µm^2.*

AuNPs were included in thin films with different morphologies, by keeping the relative ratio between the polymers the same as the one without the nanoparticles in the blend (BB_2 50). As expected, the AuNPs accumulated inside and/or at the interface with P3HT phase due to its chemical affinity with the thiol ligands. **Figure 85** shows AFM images of three different

thin films of P3HT-PLA-AuNPs. In **Figure 85a** a 45-45-10 blend is presented, HB 10, with **Figure 85b** showing a magnification highlighting the presence of AuNPs in the P3HT phase. When adding more AuNPs in the blends, 25% (HB 25) and 33% (HB 33), **Figure 85c,d**, **Figure 85e,f**, respectively, while keeping the relative ratio of the polymers the same (37.5-37.5-25 and 33.3-33.3-33.3, respectively), the continuous morphology of P3HT is retained as well, however, it can be seen that the AuNPs accumulate at the interface of the two phases, rather than being well dispersed in the P3HT phase, probably due to their higher concentration. Arguably, in terms of morphology, the addition of AuNPs could influence the phase behaviour of the P3HT/PLA blend, from both energetic and rheological perspectives, triggering an interconnected domain in the PLA matrix. Moreover, AuNPs are fully dispersed in the semiconducting polymer phase, paving the way for the possibility of the improvement of the transport behaviour of P3HT.

Figure 86 shows the optical characterization of the different blends (all UV-vis spectra were recorded in chloroform), both binary and hybrid with different weight percentages of AuNPs, compared with pristine P3HT. The absorption spectrum of pure P3HT (orange curve, **Figure 86a**) shows the typical features of the polymer, *i.e.* a more intense transition with a maximum at 447 nm and a less intense peak at 610 nm with a shoulder at *ca.* 570 nm. The 447 nm peak is related to the coiled conformation of the polymer, while the two peaks at higher wavelength pertain to the inter-chain π-π* transitions, which are an indication of the presence of crystalline aggregates[302]. The spectra are normalized on the maximum at 447 nm.

In semiconducting polymers such as P3HT, alongside the amorphous coiled conformation of the chains, the presence of crystalline regions improves the charge transport and thus the electrical conductivity of the polymer[303,304].

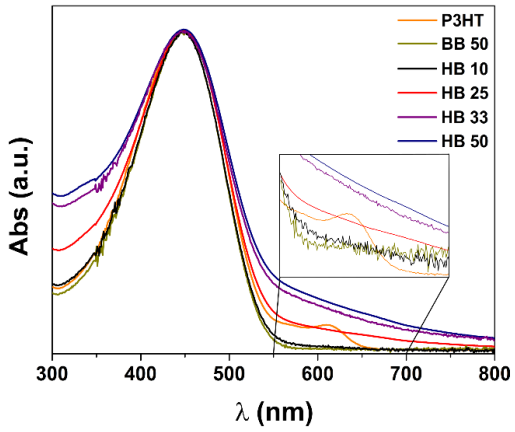

Figure 86. *UV-visible spectra of pristine P3HT and blends, all collected in $CHCl_3$.*

In **Figure 86a**, blending P3HT with PLA and with AuNPs has a strong influence on the optical behaviour of P3HT; the binary blend between the two P3HT and PLA polymers shows a complete quenching of the peak at 610 nm (dark yellow curve), thus indicating that the presence of the other polymer disturbs the crystalline order of P3HT. Conversely, as AuNPs are inserted in the blend, an absorption is gradually restored at that wavelength, indicating an interaction between gold nanoparticles networks and P3HT chains which influences the morphology, and, crucially, the interchain π-π interactions of the polymer.

To evaluate possible uses of the hybrids for optoelectronics, the electrical behaviour of the thin films was studied. The thin films were deposited *via* spin coating on interdigitated indium tin oxide (ITO) electrodes and their conductivity was studied with a switchboard. The applied voltages were from -1 V to 1 V with 0.05 V steps.

Figure 87 shows the current improvement while compared with BB_2 50, expressed in percentage, measured at 1 V at 20 °C for increasing quantity of AuNPs in the blends and only AuNPs (100%). All measurements were conducted in a dry N_2 atmosphere.

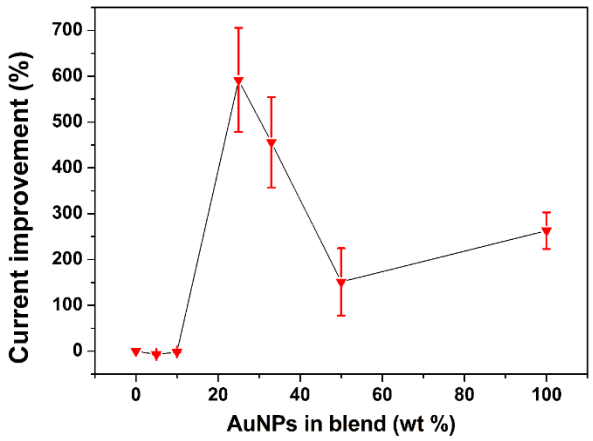

Figure 87. *Current improvement at 1 V for the different blends and AuNPs alone.*

Quite interestingly, 25% of AuNPs in weight increase the conductivity of the blend of *ca.* 600% compared to the blend without gold nanoparticles (BB_2 50), whereas an increased percentage of AuNPs does not improve the conductivity of the blend or it does so less efficiently, probably due to the well dispersion of the nanoparticles inside the blend and appropriate concentration, which avoided their aggregation (which is visible in the blends with a higher percentage of AuNPs) and improved the charge transport properties of P3HT. As discussed in previous sections, morphological evaluations through AFM did indeed show that the blend with 25 % AuNPs showed well dispersed nanoparticles networks in the interconnected and nano-confined P3HT phase, at the same time, optical characterisation

with UV-vis of the blends showed that adding AuNPs in the blend in the dispersed state, the π-π interactions are favoured by the presence of gold nanoparticles, giving the possibility of increase transport properties when adding AuNPs in the blends.

3.3. AuNPs stabilized with chiral ligands

In this section AuNPs functionalised with chiral ligand will be explored. The chiral ligands synthesis was carried out at the École Nationale Supérieure d'Ingénieurs de Caen (ENSICaen), France, in CARMeN group under the supervision of Prof. Cyprien Lemouchi and Prof. Stéphane Perrio.

The chiral ligand used are thiol derivatives of the [2.2]paracyclophane ([2.2]PCP).

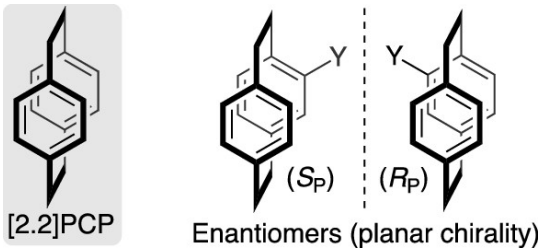

Figure 88. *[2.2]PCP chemical structure and planar chiral monosubstituted derivatives.*[305]

[2.2]PCP is the smallest stable co-facially stacked pro-chiral 3D strained scaffold where two benzene rings are rigidly held in a face-to-face orientation by two short ethylene bridges -$[CH_2]_2$- in their *para*-positions. [2.2]PCP belongs to the D_{2h} point group, which is broken by the first substituent, resulting in planar chiral enantiomers (**Figure 88**). The stereochemical notations R_p-, and S_p- define the planar chirality of the PCP enantiomers. PCP-derived being one of the most prominent examples of planar chiral ligands employed in diverse synthetic transformations shows that planar chirality is a viable alternative to the most conventional central/point chirality and offers new opportunities for the development of efficient ligand/catalyst systems.[306]

During my research period in Caen, two [2.2]PCP derivates were studied. In one derivate (PCP_1)[307,308], a sulphur atom is positioned directly on the aromatic ring, while in the other (PCP_2), the sulphur is located at the benzylic position (**Figure 89a**). For both molecules, the racemic as well as the two enantiopure forms (R_p and S_p) were isolated, the synthetic procedure for PCP_2 is reported in *Appendix B1.4*. Thiol derivatives of [2.2]PCP were synthesized with the aim of producing spherical AuNPs functionalized with a chiral ligand and AuNPs with chiral shape transferred by the enantiopure forms. The synthesis of hydrophobic AuNPs exhibiting a chiral shape presents a significant challenge, and the

corresponding protocol is currently undergoing optimization. The synthesis of AuNPs was carried out at Sapienza University, to obtain the spherical AuNPs functionalised with chiral ligand, a modified Brust-Schiffrin method was used (schematized in **Figure 89b** and described in detail in *Appendix C2.7.*).

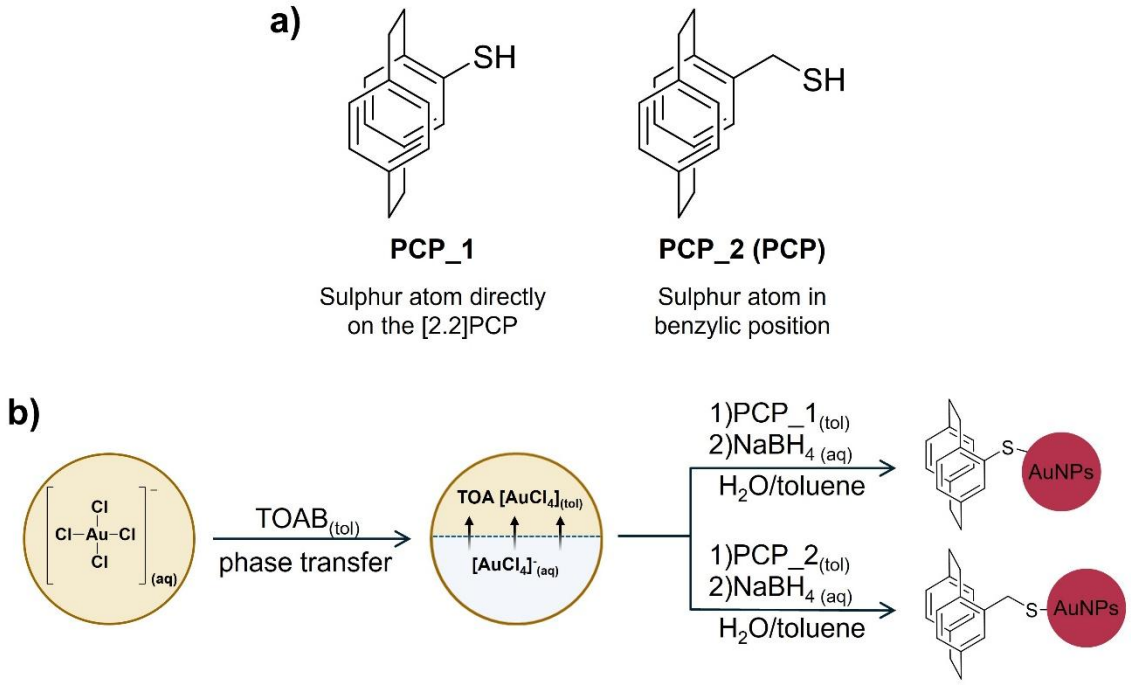

Figure 89. *a) chemical structure of thiol derivate PCP: [2.2]Paracyclophan-4-thiol (PCP_1) with the sulphur atom directly on the aromatic ring; [2.2]Paracyclophan-4-yl)methanethiol (PCP_2 or PCP) with the sulphur atom in benzylic position. b) schematic description of the synthesis of AuNPs functionalized with PCP_1 and PCP_2.*

It was observed that the nanoparticles functionalized with PCP_1 were less stable and were obtained in lower yield compared to those obtained with PCP_2. The poor stability of the AuNPs-PCP_1 may be attributed to the significant steric hindrance of the two aromatic rings, which are not sufficiently distanced from the thiol moiety.

Only the results obtained with nanoparticles functionalized by PCP_2 will be reported hereafter; from this point forward, PCP_2 will be named as PCP. AuNPs functionalized with the racemic PCP form, as well as with the enantiopure forms (PCP S_p and PCP R_p), were synthesized and purified. These nanoparticles were thoroughly characterized. The first evidence of nanoparticle formation was provided by UV-Vis spectroscopy (**Figure 90a**). Indeed, the characteristic plasmonic band can be observed for all three nanoparticles: the racemic and the two enantiopure forms. The plasmon band is centred at 515 nm, indicating that the particles are small in size.

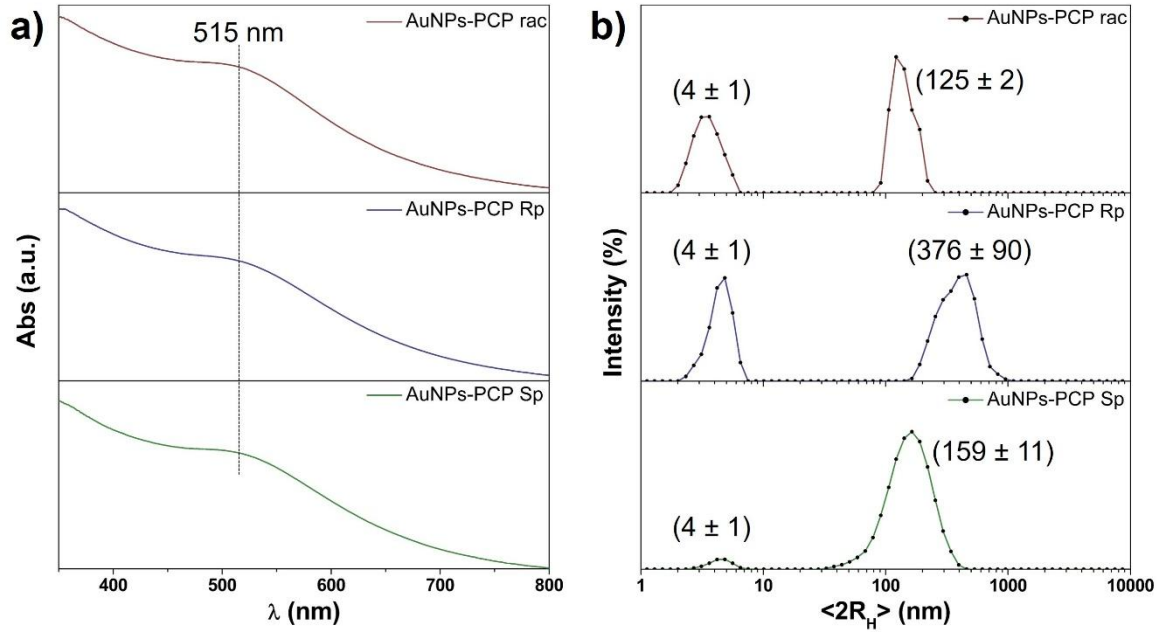

Figure 90. *a) UV-Vis spectra of AuNPs-PCP rac (top), AuNPs-PCP Rp (middle), AuNPs-PCP Sp (bottom); b) DLS graphs of AuNPs-PCP rac (top), AuNPs-PCP Rp (middle), AuNPs-PCP Sp (bottom). All the measurements were conducted in CH_2Cl_2.*

The DLS graphs (**Figure 90b**) reveal that all three nanoparticles contain a population of nanoparticles with a hydrodynamic diameter centred at (4 ± 1) nm, as well as a population in the range of a few hundred nanometres, *i.e.*, AuNPs-PCP rac = (125 ± 2) nm, AuNPs-PCP Rp = (376 ± 90) nm, AuNPs-PCP Sp = (159 ± 11) nm. These larger populations can be attributed to the presence of dynamic nanoparticle aggregates in dichloromethane.

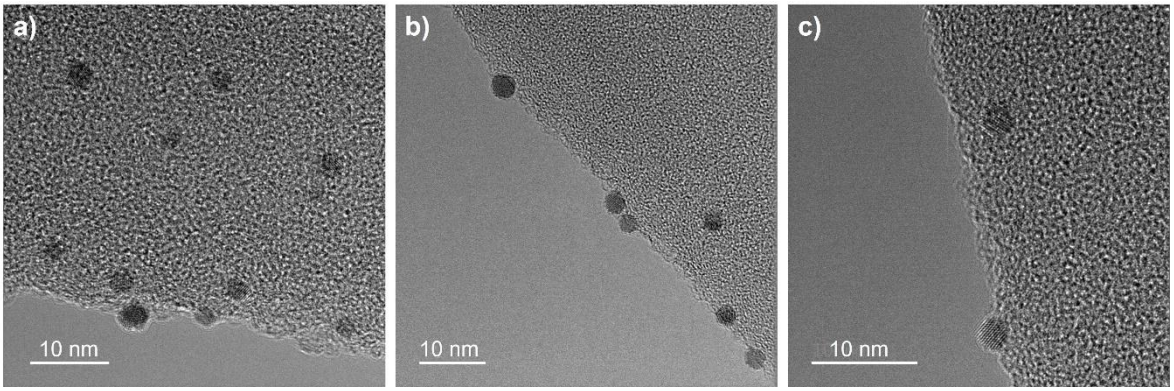

Figure 91. *TEM images of a) AuNPs-PCP rac; b) AuNPs-PCP R_p; c) AuNPs-PCP S_p.*

TEM images of the AuNPs-PCP rac, AuNPs-PCP S_p, and AuNPs-PCP R_p are reported in **Figure 91** and provided direct confirmation of the spherical shape of AuNPs and that the size distribution is under 10 nm. A statistical size analysis on 50 nanoparticles for each sample revealed the following core diameters: AuNPs functionalized with the racemic PCP ligand measured (3.09 ± 0.51) nm, AuNPs with the R_p enantiomer (3.09 ± 0.54) nm, and those with the S_p enantiomer (2.85 ± 0.45) nm. This analysis not only confirms the nanoscale dimensions but also highlights a notably uniform dispersity in all samples.

The presence of PCP on the nanoparticle surface was verified by FT-IR spectroscopy in ATR mode, with the samples deposited on a glass slide from a CH_2Cl_2 suspension (**Figure 92**). The spectra of the three nanoparticles are nearly superimposable, differing primarily in peak intensities, which is likely a consequence of the concentration of the deposited sample.

In all spectra, the characteristic peaks of the PCP ligand are easily identifiable. The signals at approximately 2960 cm^{-1} and 2920 cm^{-1} (specifically 2963 and 2922 for AuNPs-PCP rac, 2954 and 2920 for AuNPs-PCP R_p, and 2964 and 2922 for AuNPs-PCP S_p) are attributable to the -CH_2- bridging groups between the aromatic rings and linked to the sulphur. Peaks attributed to the aromatic rings are also clearly visible. The most intense of these is at 795 cm^{-1}, attributable to the δ(CC)Ar deformation modes, and the signal at 630 cm^{-1} is attributable to the C-S stretching vibration of the ligand. Furthermore, the S-H stretching band at 2565 cm^{-1} is absent in all three spectra, indicating that the ligand has interacted with the metal surface of the nanoparticle.

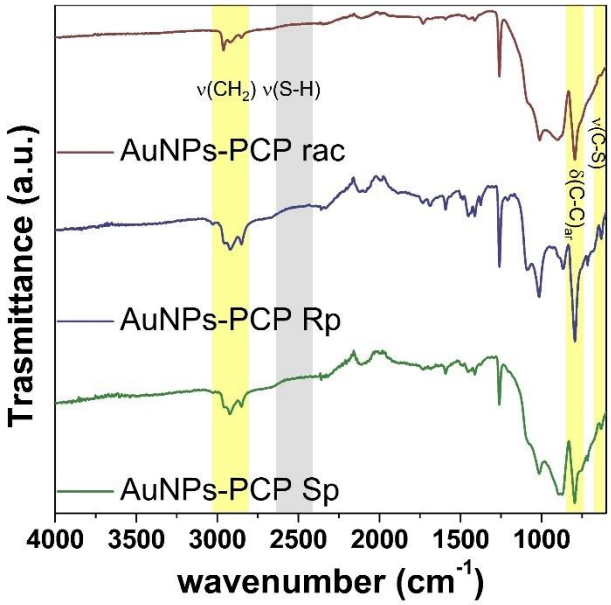

Figure 92. *FT-IR ATR spectra of AuNPs-PCP rac (red), AuNPs-PCP Rp (blue) and AuNPs-PCP Sp (green).*

The PCP ligands exhibit a strong Circular Dichroism (CD) response, showing essentially mirror-image CD spectra in the region of 250 to 350 nm (**Figure 93a**). Specifically, the PCP S_p and PCP R_p enantiomers display distinct dichroic signals, with the former being positively polarized and the latter negatively polarized. As expected, the racemate shows no CD response, confirming it is a racemic mixture of the two enantiomers.

To analyse the possible influence of the chiral thiol on the nanoparticle surfaces, circular dichroism analyses were also conducted on the particles functionalized with PCP rac, PCP S_p, and PCP R_p (**Figure 93b**). The g-factors were calculated, as defined in *Appendix A2*. The spectra for the enantiopure functionalized nanoparticles showed essential mirror images in the 250–350 nm region, where chiroptical signals are expected to arise from the intrinsic chirality of the ligand. It must be noted that no apparent CD signal was detected in the localized surface plasmon resonance (LSPR) wavelength range of 500-600 nm. Regarding the signal of the AuNPs-PCP rac, the absence of peaks indicates that the two enantiomers interact identically with the gold surface.

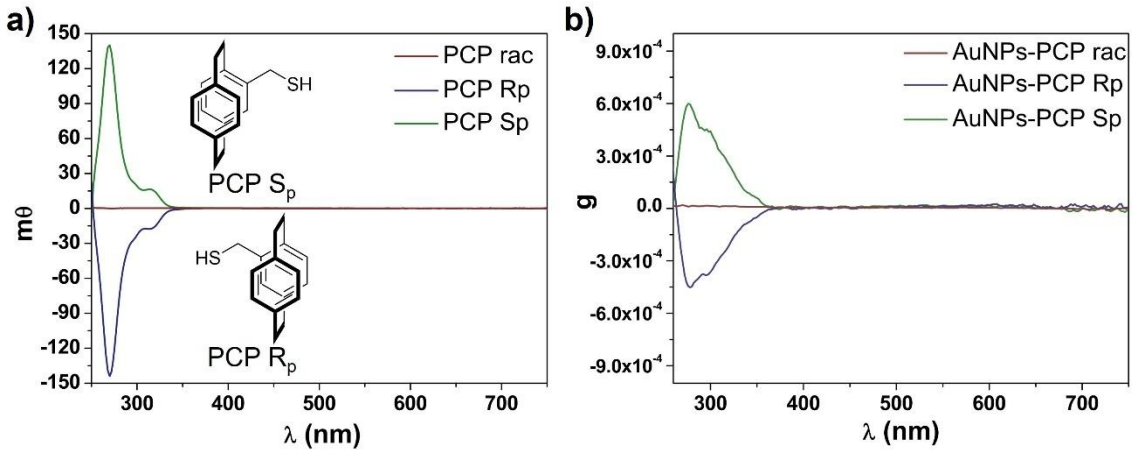

Figure 93. *Circular Dichroism spectra of a) ligands: PCP rac (in red), PCP R_p (in blue) and PCP S_p (in green); and b) AuNPs stabilized with PCP rac (in red), PCP R_p (in blue) and PCP S_p (in green).*

In conclusion, spherical hydrophobic gold nanoparticles functionalized with a ligand exhibiting planar chirality were successfully synthesized. The resulting nanoparticles are stable in organic solvents, monodisperse, and the intrinsic chirality of the ligand is preserved upon binding to the gold surface. Future studies are aimed at achieving nanoparticles where the chirality of the ligand is transmitted to the particle's morphology and, consequently, to its plasmonic properties. To achieve this goal, a seed-mediated growth approach for AuNPs

is currently being investigated. This involves new synthetic methodologies using gold nanoseeds stabilized by surfactants such as cetyltrimethylammonium bromide (CTAB). This represents a highly interesting and promising field of research, and investigations are currently ongoing through the collaboration with the University of Caen.

3.4. Final Remarks

This chapter demonstrates the versatility of hydrophobic Metal Nanoparticles.

The modified two-phase Brust-Schiffrin method proved to be highly effective for all the thiols used (monofunctional with reactive groups, bifunctional, and chiral) and for all the metals employed (Au, Ag, Pd). This chapter established that the self-assembled state of the nanoparticles can be controlled through external stimuli, leading to Supramolecular Self-Assembly, Covalent Self-Assembly, and Covalent Transient Self-Assembly.

Furthermore, nanoparticle networks can be created by using ligands with two thiol moieties. This approach allows for tuning not only the interparticle distance but also the 2D/3D arrangement of the network, a crucial factor for optoelectronic applications.

Nanoparticles functionalized with chiral ligands were successfully synthesized. Achieving chirality transfer to the particle plasmon remains a challenge; this aspect is currently being optimized through the collaboration with the University of Caen.

Chapter 4. Conclusions

This PhD Thesis has been dedicated to the synthesis and characterization of MNPs (AuNPs, AgNPs and PdNPs), with particular emphasis on the role of the thiol ligand on the surface of gold nanoparticles and how they influence the application potential of AuNPs. Thanks to the peculiar characteristics of nanomaterials *i.e.* optical and electronic properties and surface chemistry; the obtained materials were tested for applications in various fields, like drug delivery, sensing experiments were carried out, and the potential use of metal nanoparticles in optoelectronics was explored. Chemical reduction is the wet method adopted for the synthesis of nanoparticles yielding spherical shape with controlled diameters predominantly below 10 nm.

The first part of this research focused on the synthesis and characterization of hydrophilic nanoparticles, with a particular attention on their potential in drug delivery.

A highly stable and reproducible system based on gold nanoparticles functionalized with two thiols ligand in mixture (*i.e.* 3MPS and DEA) was developed. This optimized synthesis produced small, monodisperse AuNPs ($<2R_H> = 9 \pm 2$ nm) exhibiting exceptional colloidal stability, even under demanding conditions such as elevated temperatures (up to 80 °C) and over extended periods (up to one month, years at the solid state).

After a thorough characterization, the AuNPs were investigated at the Soleil Synchrotron (Proposal No. 20221610 ‘Hydration chemistry of functionalized gold nanoparticles suited for drug delivery’), using the innovative μ-liquid jet XPS technique. Unlike conventional solid-state XPS, this very innovative approach enables experiments directly in the colloidal state. It was possible to investigate the structural properties of the thiols alone, together with the functionalised AuNPs, by carrying out μ-liquid jet XPS experiments at the C1s, N1s, S2p, and Au4f core levels.

Thanks to their high colloidal stability, these AuNPs were further tested upon interaction with molecules, synthetic derivatives of DOTA yielded a very promising preliminary studies demonstrating a controlled interaction with the AuNPs surface.

Encouraged by these results, the system was successfully employed as a versatile platform for the delivery of an anticancer drug (methotrexate, MTX) and, subsequently, of an antibody (trastuzumab, TZ), highlighting its strong potential in the field of nanomedicine. The bioconjugate AuNPs-MTX was extensively studied and the interaction between the positively charged ammonium group of DEA and the negatively charged carboxylate moieties of MTX, together with the aromatic rings of MTX was investigated. Furthermore,

in vitro tests against two neuroblastoma cell lines (SJNKP and IMR5) confirmed the advantage of loading MTX on AuNPs rather than employing it alone, as a greater cytotoxic effect could be seen. Lastly, the permeation of the AuNPs inside the cells was studied, both qualitatively and quantitatively. Subsequently, the bioconjugate AuNPs-TZ was then employed in combination with extracellular targeting and with the intracellular tumour-suppressive activity of miR-200c, which was overexpressed in SKOV3 ovarian cancer cells. In this therapeutic approach *in vitro*, the role of the nanoparticle platform again proved to be decisive in enhancing the therapeutic effect of TZ.

Finally, the last section of the chapter on hydrophilic nanoparticles is about nanoparticles functionalized with 3MPS and synthetic derivatives of the commercial dye FITC. Two distinct FITC derivatives (*i.e.* CysFITC and AniFITC) were successfully synthesized by exploiting the reaction between the primary amines of cysteamine (Cys) and thioaniline (Ani) with the isothiocyanate group of FITC. Subsequently, nanoparticles were synthetized using 3MPS in combination with either CysFITC or AniFITC. Comprehensive characterization revealed that the AuNPs-3MPS-CysFITC system was monodisperse with a diameter of (8.7 ± 1.5) nm. The AuNPs-3MPS-AniFITC system, however, exhibited a bimodal size distribution with populations of (9.6 ± 3.4) nm and (20.0 ± 2.4) nm. Crucially, the optical properties of the fluorescent ligand were effectively transferred to the nanostructured system, confirming the synergistic combination of the intrinsic optical properties of the nanoparticles and the fluorescent characteristics of the dyes.

The second part of this research focused on hydrophobic nanoparticles. The first system synthesized and characterized consisted in gold nanoparticles (AuNPs) functionalized with a mixture of DDT and Ani. These nanoparticles exhibited a hydrodynamic diameter of (4 ± 1) nm. The aim was to manipulate and control the colloidal state of the AuNPs using external stimuli. Through precise surface functionalization, three distinct types of AuNP assemblies were achieved: Supramolecular Self-Assembly (SSA), Covalent Self-Assembly (CSA), and Covalent Transient Self-Assembly (cTSA). Both ligands used to functionalize the gold surface played a key role in these different self-assembly processes. In the SSA, the aliphatic chain of DDT on AuNPs surface was crucial in driving spontaneous aggregation. The co-presence of Ani allowed the system to switch from supramolecular self-assembly to isolated AuNPs using TFA that protonates the amine group of Ani inducing electrostatic repulsion between nanoparticles. In the CSA, covalent networks were obtained by using a linker, DBBA, under acid stimulation (with TFA). In this case, the aromatic amine groups of Ani

on the AuNPs surface reacted with DBBA through a transimination process, forming irreversible covalent bonds between nanoparticles, as highlighted by techniques such as DLS. In the cTSA, the same covalent linkage was made transient by replacing TFA with an Activated Carboxylic Acid (ACA). After protonating the system, the ACA spontaneously decarboxylates, restoring the initial state. TBA was selected as the ACA to drive this transient assembly. Evidence for the formation of a transient network was obtained from several characterization techniques, the most evident is DLS. It can be observed that the system starts from a state of isolated particles with hydrodynamic diameter of (4 ± 1) nm. After the nanoparticles interact with DBBA and TBA, a transient network forms, leading to self-assembly with hydrodynamic sizes of (106 ± 30) nm. After 24 hours of interaction, the particles return to their isolated state, and DLS shows a single population of nanoparticles with a hydrodynamic diameter of (4 ± 1) nm.

The discussion then moves to covalent networks based on MNPs (AuNPs, AgNPs, and PdNPs). Rigid organic and organometallic bifunctional molecules, featuring two thiol moieties as anchoring groups and an extended π-conjugated electronic system, were used as bridges for the synthesis of covalent network of MNPs with tunable interparticle distances. Several organic and organometallic derivatives were successfully synthesized, *i.e.*, synthetic derivatives of fluorene (FL and PtFL) and metal-polyyne derivatives of DEBP ($PtDEBP_n$, with n = 1, 3, 4, 6).

A comparison was made between AuNPs, AgNPs, and PdNPs functionalized with a single bifunctional organometallic ligand, $PtDEBP_n$ with n = 1 (PtDEBP). All three nanoparticle systems were successfully synthesized, resulting in stable materials. The morphology of the nanoparticles was characterized, and TEM analyses highlight NPs with an average diameter of (3.95 ± 0.56) nm (AuNPs), (3.35 ± 0.48) nm (PdNPs), and (3.54 ± 0.62) nm (AgNPs). SR-XPS measurements allowed for the assessment of the covalent attachment of the sulphur atoms as thiolates in all of three different metal surfaces. We demonstrated that the ability to obtain networks of regularly spaced noble metal nanoparticles, successfully tested on three different noble metals, opens outstanding perspectives in the field of optoelectronics.

Subsequently, the work moved to a comparison between AuNPs functionalized solely with a bifunctional ligand (FL or PtFL) and AuNPs functionalized with a mixture of monofunctional and bifunctional ligands (DDT with FL or PtFL). The aim was to fine-tune the 2D/3D arrangement of the networks. The addition of DDT to the nanoparticle surface successfully allowed for the tuning of the AuNPs network arrangement. Furthermore, the presence of the additional monofunctional ligand increased the colloidal stability of the two

systems. Preliminary studies on the use of these systems as chemoresistive sensors for toluene and benzene were then conducted. Both nanoparticle systems functionalized with DDT and a bifunctional ligand (*i.e.*, AuNPs-DDT-FL and AuNPs-DDT-PtFL) proved to be sensitive to the two analytes in question. In detail, AuNPs-DDT-FL was more sensitive to benzene than its organometallic counterpart, while AuNPs-DDT-PtFL was more sensitive to toluene than its organic counterpart. These preliminary results are very promising for the application of hydrophobic AuNPs networks as chemiresistive sensors for BTX.

AuNPs functionalized with bifunctional molecules were incorporated into different polymer matrices leads to inorganic/organic hybrid blends that combine the intrinsic properties of both counterparts, often resulting in enhanced features. Three different inorganic/organic blends based on AuNPs were investigated in this section. The first was a blend with PPA, serving as a preliminary model to study the interaction of functionalized, interconnected AuNPs with a simple polymer matrix. Subsequently, a blend with P3HT was analysed, with the aim of studying how the spacer length between AuNPs can influence charge transport and optoelectronic response through synergistic effects between the semiconducting polymer and the nanoparticles. Finally, a ternary blend of PLA, P3HT, and AuNPs was studied. The presence of PLA allows for the formation of heterojunctions, opening perspectives for developing multifunctional nanocomposites.

For the PPA blend, AuNPs were functionalized with two different organic, π-conjugated synthetic thiols, *i.e.*, FL and 2AET. The nanoparticle synthesis was optimized, and the particles obtained from the Au:2AET:FL 1:1:2 molar ratio were the most stable. After thorough characterization using UV-Vis, PL, FTIR, Far-IR, and SR-XPS spectroscopies, an extensive morpho-structural characterization in the solid-state was carried out using AFM and HR-TEM. This analysis evidenced quasi-spherical AuNPs with an average diameter of (4.1 ± 0.7) nm, a polydispersity of about 17%, and the hydrodynamic diameter in organic solvent suspension was estimated by DLS. The electrical response of both the pristine gold nanoparticles and the nanocomposites was evaluated via I/V measurements on spin-coated thin films deposited onto interdigitated ITO electrodes. Blends with varying AuNPs-2AET-FL/PPA compositions were obtained: 10/90, 30/70, 50/50, 70/30, and 90/10%. The nanocomposites, deposited as thin films (thickness of 4.6 ± 0.8 nm), showed a progressive increase in electrical conductivity increasing the AuNPs amount compared to the pristine reaching a 144% gain in the case of the blend with 90% of AuNPs.

Moving to the second blend studied, colloidal, hydrophobic AuNPs were synthesized in the presence of platinum-containing polyynes with different chain lengths ($PtDEBP_n$, n = 3, 4,

6) and incorporated into a P3HT matrix. Blending AuNPs-PtDEBP$_n$ with regioregular P3HT produced nanocomposites with a mean thickness of 3 ± 1 nm and a uniform distribution of AuNPs within the polymer matrix, as evidenced by DLS and AFM, indicating good miscibility between the components. At room temperature, I/V measurements (± 10 V range) were carried out on AuNPs/P3HT hybrid blends with different compositions (from 10/90 to 90/10 %wt) spin-coated onto an interdigitated ITO substrate. The AuNPs/P3HT 10/90 %wt composition was found to be the best, showing an improvement in electrical conductivity of about 30 times compared to the pristine homopolymer.

The final blend utilized nanoparticles functionalized with a mixture of two thiols: the bifunctional FL and the monofunctional aromatic 4BBT. Spherical nanoparticles with a diameter of (3.69 ± 0.93) nm and a polydispersity of about 25% were obtained, as determined by TEM microscopy. Prior to the fabrication of the ternary AuNPs/P3HT/PLA blend, the binary blend of the two polymers (P3HT and PLA) was studied to optimize morphology control and obtain thin films with distinct nanophases. Following this, the P3HT/PLA/AuNPs hybrid blends were investigated using different weight concentrations of AuNPs: 10%, 25%, 33%, and 50%. To evaluate potential uses in optoelectronics, the electrical behaviour of the thin films was studied. The films were deposited via spin coating on interdigitated ITO electrodes, and their conductivity was measured with an applied voltage sweep from -1 V to +1 V. A loading of 25% AuNPs by weight increased the conductivity of the blend by approximately 600% compared to the blend without gold nanoparticles.

The final section of this thesis concerns hydrophobic nanoparticles functionalized with chiral ligands. The thiol ligands (PCP) are synthetic derivatives of [2.2]PCP, and the racemic mixture and the enantiopure forms were isolated. The nanoparticles were functionalized with the racemic mixture and two enantiopure ligands (R_p and S_p). The resulting nanoparticles are spherical with a diameter of *ca.* 3 nm for all three systems, are stable in organic solvents, and monodisperse. The intrinsic chirality of the ligand is preserved upon binding to the gold surface. Future studies are aimed at achieving nanoparticles where the chirality of the ligand is transmitted to the particle's morphology and, consequently, to its plasmonic properties.

Acknowledgements

Some of the characterisations and applicative studies were done in collaboration with people outside my research group:

- Cell studies on neuroblastoma cell lines with the bioconjugate AuNPs-MTX were possible thanks to Prof. E. Agostinelli, of Sapienza University of Rome;
- Cell studies on SKOV3 cells with the bioconjugate AuNPs-TZ were conducted by Prof. P. Trivedi Prof. E. Anastasiadou and Dr. T.A. Salamone, of Sapienza University of Rome;
- Morphological studies, TEM and FESEM, were possible thanks to Dr. R. Matassa, of University of Camerino;
- AFM measurements were conducted by Dr. F. A. Scaramuzzo, of Sapienza University of Rome and by Prof. C. Sinturel, of ICMN institute at the CNRS, Orléans;
- FESEM measurements were conducted by Dr. F. Mura of Sapienza Nanotechnology and Nanoscience Laboratory (SNN-Lab CNIS);
- XPS and SR-XPS measurements were possible thanks to Prof. C. Battocchio, of University of Roma Tre;
- μ-liquid jet SR-XPS experiments were possible thanks to Prof. C. Battocchio, University of Roma Tre, Dr. V. Lanzilotto, University of Trieste, Dr. C. Nicholas, of SOLEIL synchrotron;
- Sensing measurements were carried out by Dr. A. Bearzotti, of CNR, Institute of Atmospheric Pollution Research;
- GIWAXS and GISAXS studies were possible thanks to Prof. S. Grigorian, of the University of Siegen;
- SAXS experiments were conducted by Dr. A. Del Giudice, of Sapienza University of Rome;
- NMR experiments were possible thanks to Prof. F. Sciubba, of Sapienza University of Rome;
- Circular Dichroism experiments were possible thanks to Prof. C. Fasolato, of Sapienza University of Rome;
- Fluorescence experiments were possible thanks to Prof. C. Fasolato and Prof. M. Giustini of Sapienza University of Rome;

Plots, schemes, and figures were drawn with BioRender, ChemDraw Professional, OriginLab.

This work was partially supported by Sapienza grant “Avvio alla Ricerca 2024” AR12419078A01A21.

I am profoundly grateful to Prof. Stefano Di Stefano and Dr. Gabriele Melchiorre, without whom I would not have had the opportunity to be introduced to the study of kinetics applied to nanoparticle self-assembly.

I wish to thank Prof. Cyprien Lemouchi, Prof. Stéphane Perrio and Dr. Arthur Le-Coz for hosting me at the École Nationale Supérieure d’Ingénieurs de Caen (ENSICaen) for three months. My sincere thanks for the stimulating scientific exchange. I am very pleased with this collaboration and look forward to its future development.

I sincerely acknowledge my colleagues Sara Cerra, Tommaso A. Salamone, Martina Mercurio, Carla Sappino, Federico Milanese and all other members of the laboratory for their useful discussions and the mutual support.

I would like to express my sincere gratitude to my supervisor, Professor Ilaria Fratoddi, for her insightful guidance, for providing many opportunities that have contributed significantly to my development, both professionally and personally. A sincere thank you.
谢谢!

Appendix A

A1. Materials and chemicals

Tetrachloroauric(III) acid trihydrate ($HAuCl_4$, 99.0%, M.W. 393.83 g mol^{-1}), potassium tetrachloroplatinate(II) (K_2PtCl_4 99.99%, M.W. 415.09 g mol^{-1}), silver nitrate ($AgNO_3$, ≥ 99.0%, 169.87 g mol^{-1}), potassium tetrachloropalladate (K_2PdCl_4, 326.42 g mol^{-1}), tetraoctylammonium bromide (TOAB, $(CH_3(CH_2)_7)_4N^+Br^-$, 98%, M.W. 546.79 g mol^{-1}), sodium 3-mercapto-1-propanesulfonate (3MPS, $HS(CH_2)_3SO_3Na$, 90%, M.W. 178.21 g mol^{-1}), 2-(diethylamino)ethanethiol hydrochloride (DEA, $(C_2H_5)_2NCH_2CH_2SH{\cdot}HCl$, 95%, M.W. 169.72 g mol^{-1}), 4-bromobenzenethiol (4BBT, BrC_6H_4SH, M.W. 189.07 g mol^{-1}), 1-Dodecanethiol (DDT, $CH_3(CH_2)_{11}SH$, ≥ 98%, M.W. 202.40 g mol^{-1}), 4-Aminophenyl disulfide (Ani2, $(H_2NC_6H_4S\text{-})_2$, 98%, M.W. 248.37 g mol^{-1}), cysteamine hydrochloride (Cys, $HSCH_2CH_2NH_2{\cdot}HCl$, 98%, M.W. 113.61 g mol^{-1}), sodium borohydride ($NaBH_4$, ≥98.0%, M.W. 37.83 g mol^{-1}), 9,9-didodecyl-2,7-dibromofluorene (FL-Br, $C_{37}H_{56}Br_2$, 97.0%, M.W. 660.65 g mol^{-1}), sodium methanethiolate (CH_3SNa, ≥90.0%, M.W. 70.09 g mol^{-1}), dimethylformamide (C_3H_7NO, DMF, anhydrous, M.W. 73.10 g mol^{-1}), 1,3-dimethyl-2-imidazolidinone (DMI, $C_5H_{10}N_2O$, ≥99.5%, M.W. 114.15 g mol^{-1}),
acetyl chloride (CH_3COCl, ≥99.0%, M.W. 78.50 g mol^{-1}), tri-*n*-butylphosphine ($C_{12}H_{27}P$, 99%, M.W. 202.32 g mol^{-1}), potassium thioacetate (CH_3COSK 98.0%, M.W. 114.21 g mol^{-1}), 4,4'-diethynylbiphenyl (H-C≡C-C_6H_4-C_6H_4-C≡C-H, DEBP) was prepared as previously reported.[309] 1,12-dibromododecane ($Br(CH_2)_{12}Br$, 98%, M.W. 328.13 g mol^{-1}), 4-hydroxy-benzaldehyde ($C_7H_6O_2$, 98%, M.W. 122.12 g mol^{-1}), fluorescein isothiocyanate isomer I (FITC, $C_{21}H_{11}NO_5S$, ≥98%, M.W. 389.38 g mol^{-1}), titanium chloride ($TiCl_4$, M.W. 189.68 g mol^{-1}), dichloromethyl methyl ether ($C_2H_4Cl_2O$, M.W. 114.95 g·mol^{-1}), [2.2]Paracyclophane (PCP, $C_{16}H_{16}$, M.W. 208.30 g mol^{-1}), boron trifluoride diethyl etherate (BF_3OEt_2, $BF_3{\cdot}O(C_2H_5)_2$, M.W. 141.93 g mol^{-1}), triethylsilane (Et_3SiH, M.W. 116.28 g mol^{-1}), potassium tert-butoxide solution 1.0 M in THF (tBuOK 1M in THF, M.W. 112.21 g mol^{-1}), methyl 3-mercaptopropionate ($HSCH_2CH_2COOCH_3$, M.W. 120.17 g mol^{-1}), acetic acid (CH_3COOH, AcOH), acetone (CH_3COCH_3, ≥99.5%), acetonitrile (MeCN, C_2H_3N), chloroform ($CHCl_3$, ≥99.5%), chloroform-d ($CDCl_3$), deuterium oxide (D_2O), deuterated toluene ($C_6D_5CD_3$, 99.6%), dichloromethane (DCM, CH_2Cl_2, ≥99.9%), diethyl ether (Et_2O, $C_2H_{10}O$, 99%), diethylamine ($(CH_3CH_2)_2NH$), dimethyl sulfoxide (DMSO, $(CH_3)_2SO$), ethanol (EtOH 96%, CH_3CH_2OH), ethanol (EtOH, CH_3CH_2OH), ethyl acetate ($CH_3COOC_2H_5$, ≥99.7%), isopropyl alcohol (*i*-PrOH, $(CH_3)_2CHOH$, ≥99.8%), *n*-butylamine

($CH_3(CH_2)_3NH_2$, 99.5%), *n*-hexane (C_6H_{14}, ≥98%), *n*-pentane (C_5H_{12}, 99%,), petroleum ether (40-60 °C, ≥ 90%), tetrahydrofuran (THF, C_4H_8O), toluene ($C_6H_5CH_3$, ≥99.5%), methotrexate hydrate (MTX, $C_{20}H_{22}N_8O_5 \cdot xH_2O$, 4-Amino-10-methyl folic acid hydrate, ≥98%, M.W. 454.44 g mol^{-1} anhydrous basis), 3-(4,5-dimethylthiazol-2-yl)-2,5-diphenyltetrazolium bromide dye (MTT), 4-(2-hydroxyethyl)-1-piperazineethanesulfonic acid 0.1 M (HEPES, $C_8H_{18}N_2O_4S$), ethylenediaminetetraacetic acid tetrasodium salt (EDTA, $C_{10}H_{16}N_2O_8$), phosphate buffered saline (PBS), potassium carbonate (K_2CO_3, 99%, M.W. 138.21 g mol^{-1}), sodium sulphate anhydrous (Na_2SO_4, M.W. 142.04 g mol^{-1}), magnesium sulfate anhydrous ($MgSO_4$, M.W. 120.366 g mol^{-1}), trifluoroacetic acid (TFA, CF_3COOH, M.W. 114.02 g mol^{-1}), tribromoacetic acid (TBA, CBr_3COOH, 99%, M.W. 296.74 g mol^{-1}), hydrochloric acid (HCl, ≥37%), nitric acid (HNO_3, ≥65%), sodium hydroxide (NaOH, ≥98%) were used as received from Merck and used without purification.

Previously synthetized stereoregular *cis*-transoid poly(phenylacetylene) (PPA) was used.[225]

Polylactic acid ($(C_3H_4O_2)_n$, PLA_2, M_n: 15-25 kDa; PLA_1, M_n: 85-95 kDa) was purchased from PolySciTech. Poly(3-hexylthiophene-2,5-diyl) (P3HT, M.W. 60,000 g mol^{-1}, PDI 2.1 and the regioregularity higher than 96.8%) was purchased by Rieke RMI-00IEE.

Solvents used for kinetics were treated with molecular sieves 4Å for one night.

Cellulose acetate dialysis tubing with molecular weight cut-offs (MWCO) = 12,000 Da (Merck) were used upon pre-conditioning with distilled water for 12 h.

All cell cultures, flasks, dishes, RPMI-1640 medium and Dulbecco's modified Eagle medium/Ham's F-12 50/50 Mix (DMEM-F12) containing fetal bovine serum (FBS) at 10% (v/v), L-glutamine, 1% Penicillin (100 IU/mL), Streptomycin (100 µg/mL), without phenol red, were purchased from Corning.

Ultrapure water (H_2O_{up}, 18.3 MΩ·cm) produced with a Zeneer Power I Scholar-UV water purification system (Fulltech Instruments, Rome, Italy) was used in all aqueous solutions.

A high-speed micro-centrifuge (Scilogex, Rocky Hill, Connecticut, USA) was used for purification of the colloidal suspensions.

Thin-layer chromatography (TLC) separation was performed on silica gel (TLC-PET foils) with fluorescent indicator 254 nm (Merck, Milan, Italy).

For thin film deposition an Electron mec PRS 5V Spinner (Electron mec, Milan, Italy) was used (speed 600 rpm, 1 min).

Bolt™ 4-12%, Bis-Tris Plus WedgeWell™ Gel: ThermoFisher Scientific; BD Pharmingen™ PE Annexin V Apoptosis Detection Kit I: BD Biosciences; Trastuzumab 21 mg/mL: San Camillo Hospital, Rome, Italy, 0,041 µg/ml - 0,22 µg/ml; HER2: HER2

antisera, 1:5000; Human anti- Phospho-HER2/ErbB2 (Tyr1221/Tyr1222) Rabbit monoclonal antibody, 6B12: Cell signaling Technology, 1:1000; Human anti-K-Ras Rabbit monoclonal antibody, E2M9G: Cell signaling Technology, 1:1000; Human anti-p44/42 MAPK (Erk1/2) Mouse monoclonal antibody, L34F12: Cell signaling Technology, 1:1000; Human anti-Phospho-p44/42 MAPK (Erk1/2) (Thr202/Tyr204) Rabbit monoclonal antibody, D13.14.4E: Cell signaling Technology, 1:2000; Human anti-β-actin Mouse monoclonal, C4: Santa Cruz, 1:5000; Goat-anti-rabbit IgG Antibody, HRP conjugate: Advasta, 1:10000; Goat anti-Mouse IgG Antibody, HRP conjugate: Merck, 1:5000.

A1.1 Chemicals reference

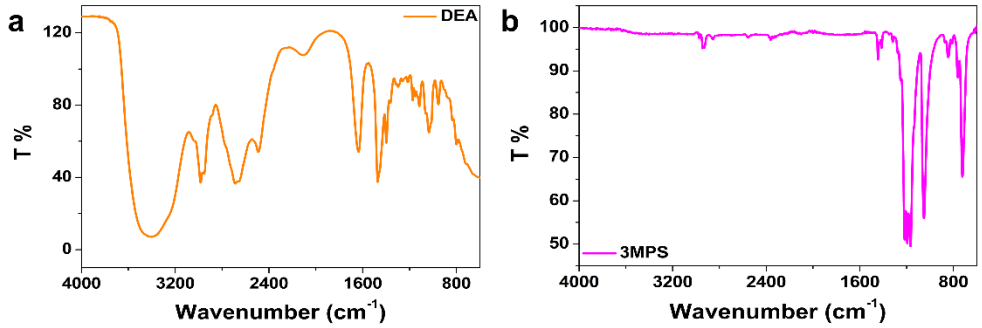

Figure A1. *FTIR spectra of a) DEA, b) 3MPS*

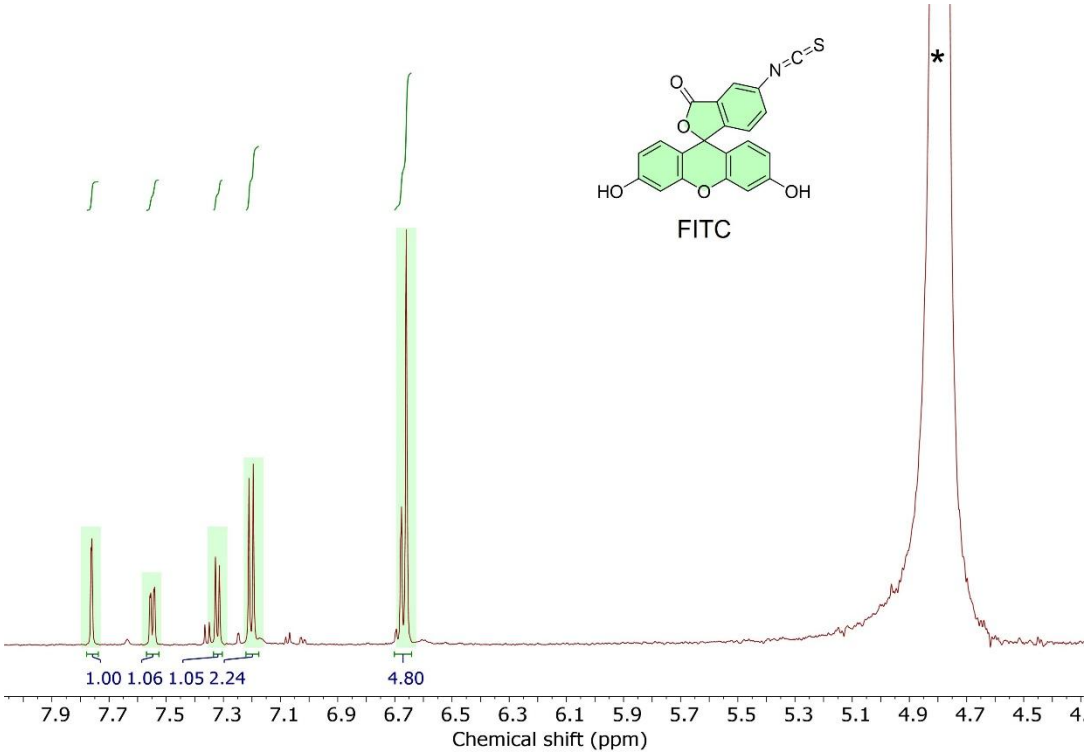

Figure A2. *^{1}H-NMR of FITC in D_2O + K_2CO_3.*

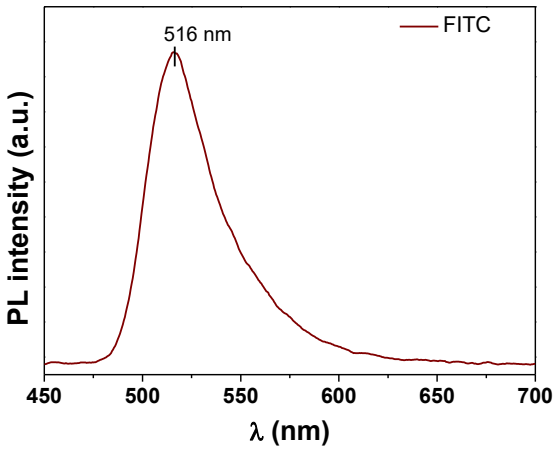

Figure A3. *FITC emission spectrum recorded with excitation wavelength: λ 440 nm. Spectrum recorded in H_2O phosphate buffer pH 8.*

A2. Instruments

UV–Visible. UV–Visible spectra were recorded using a Varian Cary 100 (wavelength range of 190–900 nm) UV–vis spectrophotometer at room temperature. Quartz cells with a 1.5 mL volume and 1 cm optical path length were used. For cell availability test, the multi-mode plate reader spectrophotometer Synergy HT Bioteck was used.

Fourier Transform infrared spectroscopy. FT-IR experiments were conducted with a Bruker Vertex 70. The samples were deposited on KRS-5 cells and analysed from 4000 to 400 cm^{-1}. Spectra in attenuated 263 total reflectance (ATR) mode were recorded in the 4000–600 cm^{-1} range. The resolution is 4 cm^{-1} with a minimum of 16 scans. FTIR spectra were recorded on a Bruker Vertex 70 instrument in the ATR mode in the 4000−600 cm^{-1} or in transmittance mode in the 4000−400 cm^{-1} range, 32 scans and 4 cm^{-1} resolution. The samples were deposited as solid powders on the sample holder for the ATR mode, as an organic suspension on a thallium Bromo iodide (KRS-5) plate for the FTIR mode, or as an aqueous film on a polyethylene plate for far-FTIR.

Dynamic light scattering (DLS) and ζ-potential. The hydrodynamic diameters ($<2R_H>$, nm) and ζ-potentials (ζ-pot, mV) of AuNPs were measured on a Malvern Zetasizer Nano ZS90 instrument at 25 °C using a 4 mW laser light with the wavelength of 632.8 nm and an automatic attenuator. Measurements were done in triplicate and reported as mean ± standard deviation (SD). DLS considers that particles in a medium diffuse with Brownian motion, where the diffusion can be correlated to the hydrodynamic radius (which takes into account the solvation shell of the particle) *via* the Stokes-Einstein equation:

$$R_H = K_B T / 6\pi\eta D$$

Where K_B is the Boltzmann constant, T is the temperature in K, D is the translational diffusion coefficient, the speed of the particles; η is the viscosity of the solvent; R_H is the hydrodynamic diameter of the particle.

Small-Angle X-ray scattering. SAXS measurements were performed at SAXSLab Sapienza with a Xenocs Xeuss 2.0 Q-Xoom system (Xenocs SA, Sassenage, France), equipped with a micro-focus Genix 3D X-ray Cu source (λ = 0.1542 nm), a two-dimensional Pilatus3 R 300 K detector placed at variable distance from the sample (Dectris Ltd., Baden, Switzerland). The beam size was selected using the two-pinhole collimation system equipped with "scatterless" slits to be 0.5 mm × 0.5 mm. Calibration of the scattering vector q range, where $q = (4\pi \sin\theta)/\lambda$, 2θ being the scattering angle, was performed using silver behenate. Measurements with two different sample-detector distances were performed so that the overall explored q region was $0.0042\ nm^{-1} < q < 1.75\ nm^{-1}$. Samples were loaded into glass capillaries with a nominal thickness of 1.5 mm and sealed with hot glue. They were subsequently placed in the instrument sample chamber at reduced pressure (~0.2 mbar) at 25 °C. The two-dimensional scattering patterns were subtracted for the "dark" counts, and then masked, azimuthally averaged, and normalised for transmitted beam intensity, exposure time and subtended solid angle per pixel, by using the FoxTrot software developed at SOLEIL synchrotron facility. The intensity vs. q profiles obtained from the subsequent frames were averaged after checking they were superimposable and were then subtracted for empty capillary and solvent contributions and put in absolute scale units (cm^{-1}) by dividing for the sample thickness estimated by scanning the capillary with the X-ray beam. The different angular ranges were merged using the SAXS utilities tool. The measurements were repeated on the same samples across an overall time of 24 h from the initial loading.

Grazing Incidence Small- and Wide-Angle X-Ray Scattering. GISAXS and GIWAXS measurements were performed at beamline P03 (MINAXS) at the synchrotron PETRA III at Deutsches Elektronen-Synchrotron DESY in Hamburg (Germany)[310]. Samples were prepared by drop casting on SiO/SiO_2 substrate from their aqueous dispersion. X-ray beam with the energy 11.83 keV (wavelength λ = 1.048 Å, Δλ/λ = 10−4) was focused on the detector by beryllium compound refractive lenses (CRL) with a beam size (V × H) 25 × 35 μm^2. Sample-Detector Distance (SDD) was 4190 ± 2 mm for GISAXS and 220.5 mm for GIWAXS. Pilatus 2 M (Dectris Ltd., Switzerland) with the pixel size 172 × 172 μm^2 and pixel array format (V × H) 1475 × 1679 pix^2 was used as a 2D detector for GISAXS mode.

GIWAXS 2D images was performed using a Lambda 9 M detector with a pixel size 55 × 55 μm^2. The reciprocal q-space and sample-to-detector distance were calculated using Ag-behenate, CeO and LaB_6 as calibrant. Azimuthally averaged radial distribution of intensity was performed after the analysis of X-ray data using the DPDAK software package[311].

Morphological and Structural studies. Morphology was assessed by an Auriga Zeiss field-emission scanning electron microscope (FESEM) instrument. The samples were drop casted on conducting silicon substrate. Further characterisation was performed by transmission electron microscopy JEOL 2100 LaB TEM operating at 200 kV equipped with an Energy Dispersive X-ray (EDX) detector. AuNPs internalised into IMR5 cells were prepared by a well-established analytical protocol to be observed by Zeiss EM10 TEM, operating at 60 kV.

High-resolution Transmission Electron Microscopy. HR-TEM images were acquired using FEI Talos F200S Field Emission Gun (FEG) microscope operating at 200 keV on samples deposited on Ni-support grid coated with a carbon amorphous film. Energy dispersive X-ray spectroscopy (EDX) compositional analysis maps were collected using a Super-X energy dispersive X-ray spectrometry system which includes two silicon drift detectors, coupled to the microscope in the Scanning Transmission Electron Microscopy (STEM) mode, using spatial drift correction and a dwell time of 0.2 s.

XPS μ-liquid jet measurements. The XPS μ-LJ measurements were performed at the French synchrotron radiation facility SOLEIL (Paris, France) at the PLÉIADES beamline which is dedicated to spectroscopic studies of dilute systems (atoms, molecules, ions, clusters). Details of the experimental setup have been previously reported.[312] The spectra were collected with a hemispherical electron analyser VG-Scienta R4000 with the axis of detection perpendicular to the propagation direction of the X-ray beam. The pass energy of the electron analyser and the monochromator slit were chosen to optimise the resolution and signal-to-noise ratio. XPS liquid-jet measurements were carried out at the C1s, N1s, Au4f and S2p edges using 400 eV and 1000 eV for C1s, 600 eV for N1s, 625 eV for Au4f and 400 eV photon energy for S2p. Curve-fitting analysis of the C1s, N1s, S2p, Au4f spectra was performed using Gaussian profiles as fitting functions, after subtraction of a polynomial background. The $S2p_{3/2}$-$S2p_{1/2}$ and $Au4f_{7/2}$- $A4f_{5/2}$ doublets were fitted using the same full width at half maximum (FWHM) for the two spin-orbit components of the same signal, a spin-orbit splitting of 1.2 eV for S2p and 3.8 eV for Au4f and the branching ratios $S2p_{3/2}/S2p_{1/2} = 2$ and $Au4f_{7/2}/Au4f_{5/2} = 1.3$. When several different species were identified in a spectrum, the same FWHM value was used for all individual photoemission bands.

Gas sensing measurement setup for BTX. AuNPs suspensions in CH_2Cl_2 (10 µL at concentration 1 mg/mL) were deposited by drop casting onto homemade transducers, based on interdigitated pairs of gold/chromium fingers implemented by lithography on passivated silicon substrates. The following geometry of metal electrodes was used: fingers width and gaps 20 µm, length 5640 µm, thickness 100 nm. AuNPs films were air dried, inserted into a measurement chamber and connected to a Keithley Model 595 Quasi-static CV Meter. Changes in the flowing current by applying a fixed voltage (0.5 V) were monitored at 20 °C by exposure to different analytes concentrations (benzene, toluene, range 0–5%; 0–1.7% respectively). Vapours of the selected analyte was mixed with synthetic air or N_2 using a MKS mass-flow controller and maintaining the total flux at 200 SCCM (standard cubic centimetres per minute). Both nitrogen and synthetic air were used as carrier gases without finding any differences in the electrical response of the sensitive layer of AuNPs. I/V and current response curves were carried out under dry N2 conditions (2000 SCCM) at 20 °C with a HP 3458A multimeter and a Keithley 230 programmable voltage source.

Setup for electrical measurements of blends. To analyse the electrical and chemical-sensory characteristics, the blends suspensions were deposited by drop casting onto homemade transducers. The transducers were based on interdigitated pairs of gold/chromium fingers implemented on passivated silicon substrate by conventional lithography with the following geometry: finger width and gaps 20 µm, length 5640 µm, thickness 200 nm. After drop casting of the blends onto the transducer (5 µL of samples suspensions in $CHCl_3$ at a 5 mg/mL concentration), films were air dried, inserted into a measurement chamber, and connected to a Keithley model 595 Quasi-static CV Meter.

Nuclear magnetic resonance. NMR spectra were recorded D_2O at 298 K on a Jeol JNM-ECZ 600R spectrometer operating at the proton frequency of 600 MHz and equipped with a multinuclear z-gradient inverse probe head. Monodimensional ^1H NMR spectra were acquired with a spectral width of 15 ppm (9013.7 Hz), 64 k data points and 128 scans. The recycle delay was set to 7.7 s to achieve complete resonance relaxation between successive scansions. Another instrument was also used, a 400.13 MHz Bruker Avance III spectrometer at 9.4 T. The samples were prepared in 600 µL of D_2O. The acquisition parameters for ^1H monodimensional experiments 264 recorded at 295 K were: spectral width of 15 ppm, 16 scans, 6.55 s repetition time to achieve full relaxation for all resonances.

X-Ray photoelectron spectroscopy. XPS analysis was performed with a homemade instrument, consisting of preparation and analysis UHV chambers separated by a gate valve. The analysis chamber is equipped with a six-degree-of freedom manipulator and a 150 mm

mean radius hemispherical electron analyzer with a five-lens output system combined with a 16-channel detector giving a total instrument resolution of 1.0 eV as measured at the Ag $3d_{5/2}$ core level. Samples were introduced in the preparation chamber and left outgassing overnight at a base pressure of about 10^{-8} Torr, before introduction in the analysis chamber. Typical vacuum pressure in the analysis chamber during measurements was in the 10^{-8}-10^{-9} Torr range. The used X-ray radiation is a non-monochromatized Mg K_α (1253.6 eV). Calibration of the energy scale was made referencing the spectra to the C1s core level signal of aliphatic C atoms, found at 285.00 eV, for all samples. Curve-fitting analysis of the C1s, O1s, S2p, Si2p, Ti2p and Ag3d spectra was performed using Gaussian profiles as fitting functions, after subtraction of a polynomial-type background. $S2p_{3/2,1/2}$ doublets were fitted by using the same Full Width at Half-Maximum (FWHM) for each pair of components of the same core level, a spin-orbit splitting of 1.2 eV and a branching ratios $S2p_{3/2}/S2p_{1/2}$ = 2/1. $Si2p_{3/2,1/2}$ doublet was fitted as a singlet because of its low spin-orbit splitting. $Ti2p_{3/2,1/2}$ doublets were fitted by using a spin-orbit splitting of 5.8 eV and a branching ratios $Ti2p_{3/2}/Ti2p_{1/2}$ = 2/1. The $Ag3d_{5/2,3/2}$ doublets were fitted by using the same FWHM for each pair of components of the same core level, a spin-orbit splitting of 6.0 eV and branching ratio $Ag3d_{5/2}/Ag3d_{3/2}$ = 3/2. When several different species were identified in a spectrum, the same FWHM value was set for all individual photoemission bands.

Synchrotron radiation-induced X-ray photoelectron spectroscopy. SR-XPS data were collected using a VG-Scienta R3000 hemispherical electron energy analyser in fixed angular mode (A21, the utilised pass energy was 50 eV), with the entrance and exit slits of the monochromator fixed at 30 μm and 20 μm, respectively. XPS measurements were carried out at the BACH (Beamline for Advanced DiCHroism) beamline at the ELETTRA facility in Trieste (Italy). The BACH beamline exploits the intense radiation emitted from an undulator front-end. XPS Photon energy of 360 eV was used for C1s, S2p, Au4f, spectral regions with a total binding energy resolution of 0.17 eV; for N1s and O1s spectral regions photon energy values of respectively 520 eV and 596 eV were selected, as to maximise signals intensities. The total binding energy resolution was about 0.22 eV. The energy scale was calibrated using as reference the C1s aliphatic signal at 285 eV and the $Au4f_{7/2}$ signal of AuNPs arising by metallic gold atoms, always found at 83.96 eV. Curve-fitting analysis of the C1s, S2p, N1s, O1s, Au4f spectra was performed using Gaussian curves as fitting functions. S2p3/2, S2p1/2 and Au4f7/2, Au4f5/2 doublets were fitted by using the same full width at half-maximum (FWHM) for each pair of components of the same core level, a spin–orbit splitting of 1.2 eV and 3.7 eV respectively and branching ratios $S2p_{3/2}/S2p_{1/2}$ of 2/1,

$Au4f_{7/2}$/$Au4f_{5/2}$ of 4/3. When several different species were individuated in a spectrum, the same FWHM value was used for all individual photoemission bands.

Circular Dichroism measurements were acquired with a Jasco J-715 spectropolarimeter (Jasco Inc.). The instrument was equipped with a high-intensity UV lamp emitting photons across a wide wavelength range, from the UV, below 180 nm, to above 800 nm in the visible. A monochromator equipped with variable aperture slits scanned the wavelength over the spectral window of interest at variable velocity (50 nm^{-1} in the present case). In the optical path, a photoelastic modulator, oscillating at 50 kHz, generated circularly polarized light, which was directed toward the sample compartment. The sample was contained by suprasil quartz cuvettes of 10 mm optical path. The transmitted light was then detected by a photomultiplier tube. The acquisition was performed by averaging multiple (2 to 8) subsequent accumulations. The CD was reported in units of ellipticity, defined as

$$[\theta] = \Delta A \left(\frac{ln10}{4}\right)\left(\frac{180°}{\pi}\right)$$

with $\Delta A = A_L - A_R$, $A_{L(R)}$ being the absorbance of left (right) circularly polarized light.

To obtain the anisotropy factor g, defined as

$$g = 2 \cdot \frac{A_L - A_R}{A_L + A_R}$$

the differential absorption ΔA, calculated from the ellipticity using the above equation, was normalized by the optical extinction, collected in the same spectral range and under the same experimental conditions.

Atomic Force Microscopy. AFM was performed on a Veeco AFM Multimode equipped with Nanoscope IIIa on spin-coated samples on glass substrates, from CH_2Cl_2 suspensions. The measurements were acquired in tapping mode using RTESP Bruker tips (nominal parameters r = 8 nm, f = 300 kHz, k = 40 N m^{-1}) with a 512 × 512 pixels resolution. Post-capture correction by polynomial background filters and analysis was performed by using the software Gwyddion 2.56.

Photoluminescence spectroscopy. Steady-state emission spectra were recorded on a PerkinElmer LS50 luminescence spectrometer using a quartz cuvette with a 1 mm optical path for the excitation. Monochromator slits resolution was set at 2.5 nm for both excitation and emission. Excitation wavelength was set according to the UV-Vis absorption maxima for each sample, using CH_2Cl_2 as solvent.

Appendix B

B1. Synthetic procedures of ligands

B1.1. Synthesis of FITC derivatives

B1.1.1. CysFITC

Synthesis of Cystamine dihydrochloride (Cys2) (1a)

In a round bottomed flask, cysteamine hydrochloride (Cys) (0.5000 g, 5.10 mmol) was dissolved in 2.5 mL of dry DMSO. Heat the reaction mixture to 90 °C, the reaction carried out under stirring overnight and turns from white to yellow. Then the reaction mixture was cool down to room temperature and the product separated by precipitation adding EtOH. Wash the precipitate several time with EtOH dry it. The reaction is quantitative.

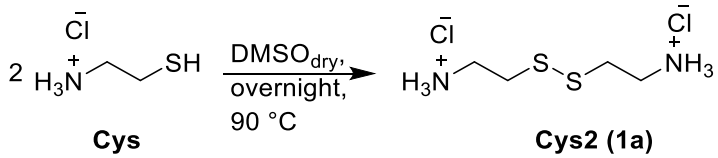

Cys
M.W. 113.61 g/mol

Cys2 (1a)
M.W. 225.22 g/mol

Synthesis of 1-(3',6'-dihydroxy-3-oxo-3H-spiro[isobenzofuran-1,9'-xanthen]-5-yl)-3-(2-(methylthio)ethyl)thiourea (CysFITC) (1)

In a round bottomed flask, cysteamine hydrochloride (Cys2) (20 mg, 0.09 mmol) and fluorescein 5(6)-isothiocyanate (FITC) (70 mg, 0.180 mmol) were dissolved in 0.350 mL of DMF and then Et_3N (0.02 mL) was added. The reaction carried out under stirring overnight. Due to the poor solubility of FITC in many solvents, chromatographic purification of the synthetic products was not feasible. Instead, the compounds were isolated by acidic precipitation using HCl 1M and washed twice with HCl 0.01 M and once with water and the dried. The product is an orange solid.

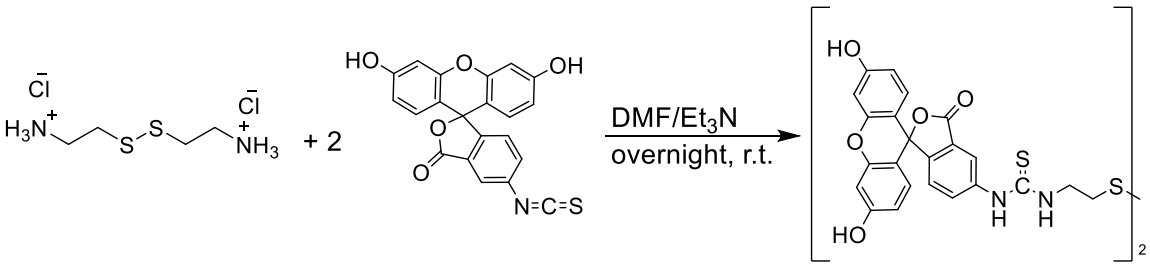

Cys2 (1a)
M.W. 225.22 g/mol

FITC
M.W. 389.38 g/mol

CysFITC (1)
M.W. 931.04 g/mol

Reaction yield: 50%

Physical properties and spectral data: **^{1}H-NMR** (600 MHz, D_2O + K_2CO_3, δ): 7.57 (s, 2H), 7.38 (d, 2H), 7.20 (d, 2H), 6.98 (d, 4H), 6.59 (m, 8H), 3.92 (s, 4H), 3.01 (t, 2H), 3.05 (q,

Et_3N), 1.21 (t, Et_3N);**^{13}C NMR** (600 MHz, D_2O + K_2CO_3, δ): 182.7 (s, C=S), 168.3 (s, K_2CO_3)[313], **UV–Vis** (H_2O): λ = 493 (max) nm; **PL** (H_2O): λ = 514 (max) nm.

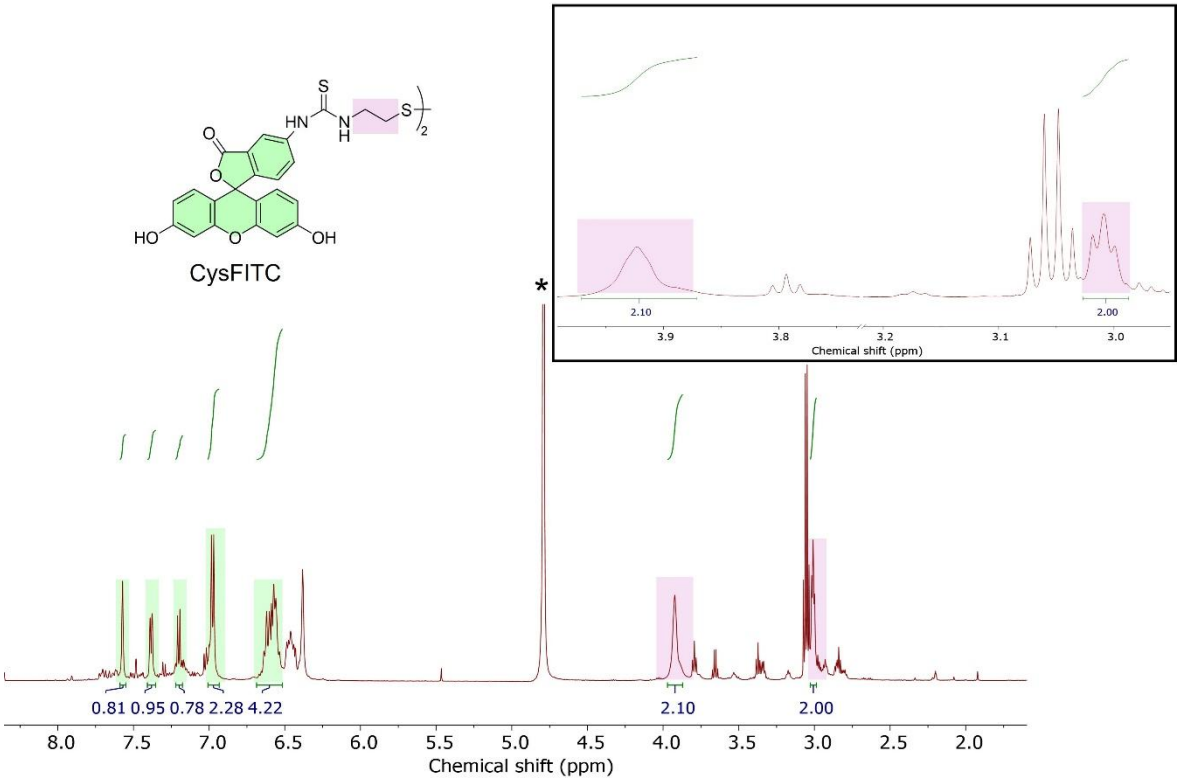

Figure B1. *^{1}H-NMR of CysFITC in D_2O + K_2CO_3.*

B1.1.2. AniFITC

Synthesis of 1-(3',6'-dihydroxy-3-oxo-3H-spiro[isobenzofuran-1,9'-xanthen]-5-yl)-3-(4-(methylthio)phenyl)thiourea (AniFITC) (2)

In a round bottomed flask, 4-Aminophenyl disulfide (Ani2) (22 mg, 0.09 mmol) and fluorescein 5(6)-isothiocyanate (FITC) (70 mg, 0.180 mmol) were dissolved in 0.350 mL of DMF and then Et_3N (0.02 mL) was added. The reaction carried out under stirring overnight. Due to the poor solubility of FITC in many solvents, chromatographic purification of the synthetic products was not feasible. Instead, the compounds were isolated by acidic precipitation using HCl 1M and washed twice with HCl 0.01 M and once with water and the dried. The product is an orange solid.

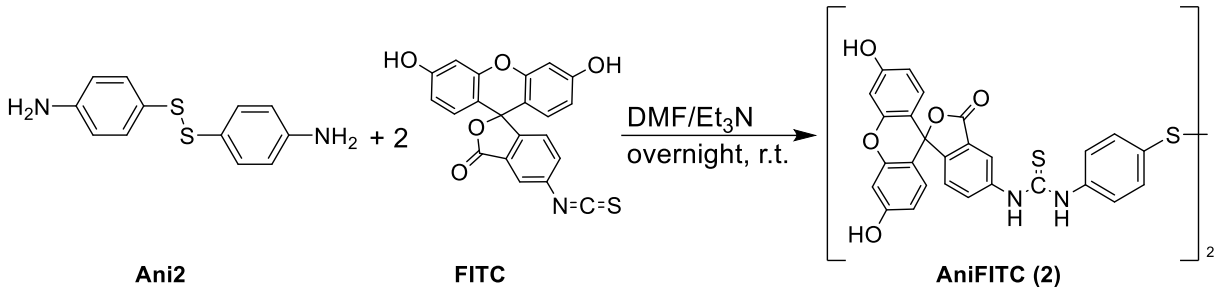

Physical properties and spectral data: **^{1}H-NMR** (600 MHz, D_2O + K_2CO_3, δ): 7.72 (s, 2H), 7.63 (s, 4H), 7.42 (d, 2H), 7.26 (d, 2H), 7.07 (m, 8H), 6.63 (m, 8H), 33.05 (q, Et_3N), 1.21 (t, Et_3N);**^{13}C NMR** (600 MHz, D_2O + K_2CO_3, δ): 182.7 (s, C=S), 168.3 (s, K_2CO_3)[313], **UV–Vis** (H_2O): λ = 492 (max) nm; **PL** (H_2O): λ = 514 (max) nm.

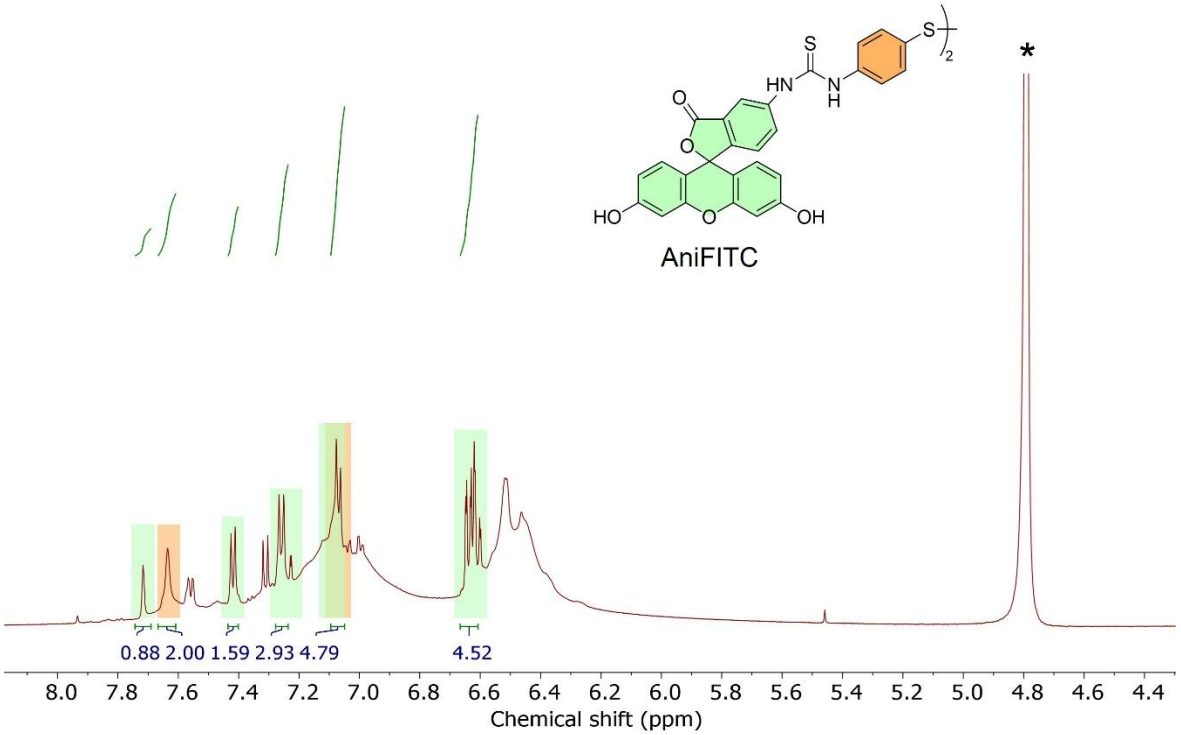

Figure B2. *^{1}H-NMR of AniFITC in D_2O + K_2CO_3.*

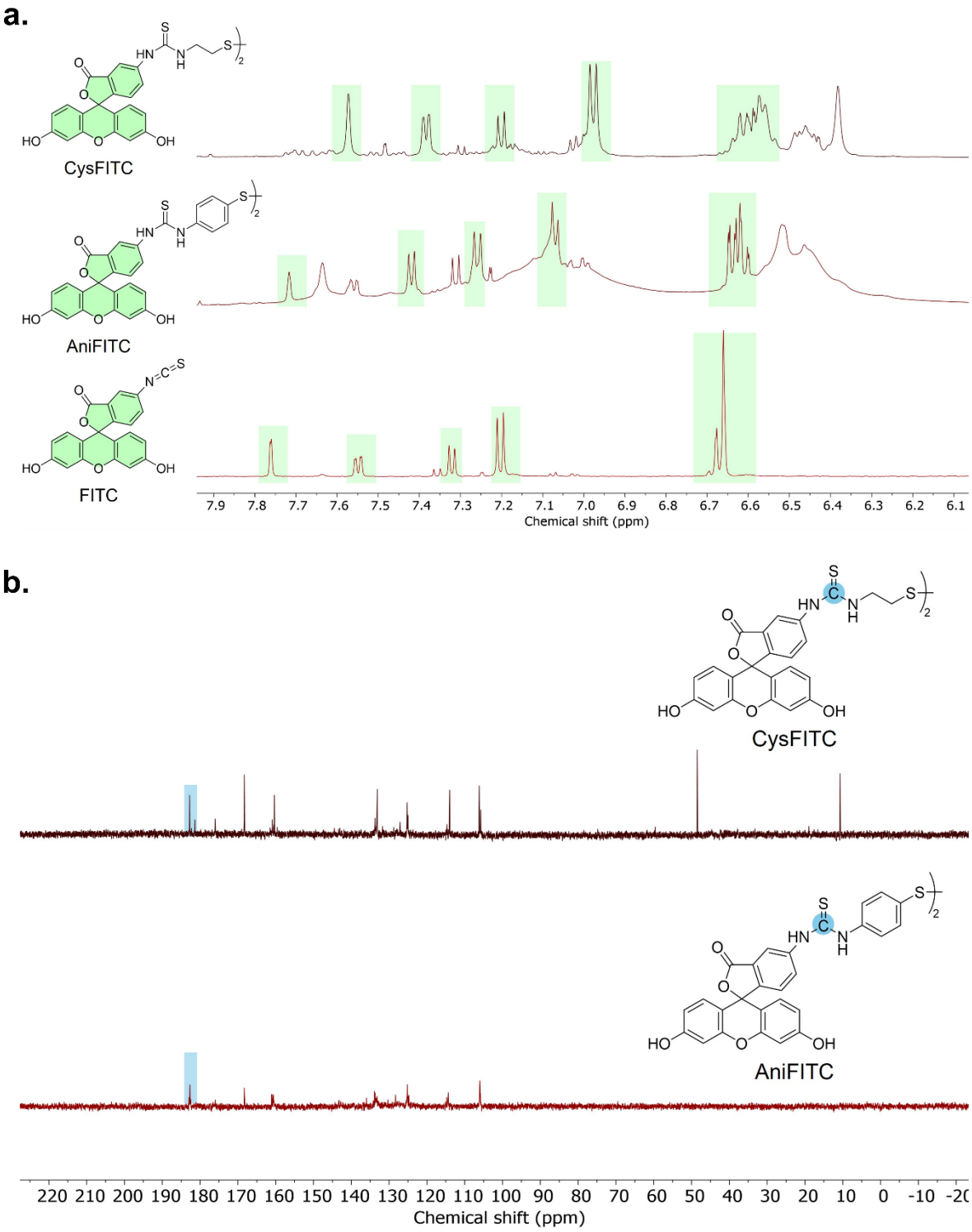

Figure B3. *a) ^{1}H-NMR spectra of CysFITC (top), AniFITC (center) and FITC (bottom); b) ^{13}C-NMR spetra of CysFITC (top) and AniFITC (bottom). All spectra are collected in D_2O + K_2CO_3.*

B1.2. Synthesis of fluorene derivatives

B1.2.1. Synthesis of 9,9-didodecyl-2,7-bis(acetylthio)fluorene (FL)

In a round bottomed flask, 9,9-didodecyl-2,7-dibromo-fluorene (FL-Br) (0.5000 g, 0.7500 mmol) was dissolved in 15 mL of dry DMI. After heating to 120 °C under Ar atmosphere sodium methanethiolate (0.5180 g, 7.500 mmol, 10 eq.) was added portionwise and the reaction mixture was stirred for approximately 24 hours. The reaction mixture turns from yellow to brown. TLC was used to monitor the reaction with a mobile phase petroleum ether/CH_2Cl_2 3:1 v/v. Then the reaction mixture was cool down to room temperature and 0.532 mL of acetyl chloride (7.50 mmol, 10 eq.) were added (under Ar flux), and the solution was stirred for 3 hours at room temperature. TLC was used to monitor the reaction (petroleum ether/CH_2Cl_2 3:1.5). At the end, the crude mixture was washed three times with ice/water, the organic layer was dried over Na_2SO_4, filtered and concentrated under reduced pressure. Purification by chromatography on silica gel (petroleum ether/CH_2Cl_2 with a gradient from 90/10 to 70/30) afforded 9,9-didodecyl-2,7-bis(acetylthio)fluorene (FL) (1) as a yellow oil.

Reaction yield: 0.155 g (32%).

Physical properties and spectral data: **^{1}H-NMR** (400 MHz, $CDCl_3$, δ): 7.74 (d, 2H, H-3), 7.40 (m, 4H, H-1, H-2), 2.43 (s, 6H, H-8), 1.96 (m, 4H, H-4), 1.33-1.1 (m, 36, H-6), 0.88 (t, 6H, CH_3), 0.68 (m, 4H, H-5); **FTIR** (film from CH_2Cl_2): ν = 3405 (w, (–OH)), 3061 (w, $(–CH)_{Ar}$), 2955 (s; $\nu_{as}(–CH_3)$), 2922 (s; $\nu_{as}(–CH_2)$), 2855 (s; $\nu_s(–CH_2)$), 1715 (s; ν(C=O)), 1602 (w; $\nu(CC)_{Ar}$), 1570 (w; $\nu(CC)_{Ar}$), 1485 (w; $\nu(CC)_{Ar}$), 1456 (s, $\delta_s(–CH_2)$), 1405 (m; $\delta(–CH_3)$, $\gamma(–CH_2)$), 1380 (m; $\delta(–CH_3)$, $\gamma(–CH_2)$), 1262 (m; ν_{as}(C–C–C), 1120 (s; in-plane δ(=CH)), 1005 (s; in-plane δ(=CH)), 886 (m; def. modes $(CC)_{Ar}$), 815(s; def. modes $(CC)_{Ar}$), 723 (m, out-of-plane $\delta(–CH)_{Ar}$), 615 (s, ν(=C–S)); **Far-IR** (PE) [1–4]: ν = 581 (s; in-plane ring deformation mode), 520 (s; out-of-plane δ(C=O), out-of-plane ring deformation), 435 (m; δ(C–S) of O=C–S, 327 (s; ring in-plane bending), 280 (w, ρ(–CH2)), 250 (w, ρ(–CH2)), 225 (w, ρ(–CH2)), **UV–vis** (CH_2Cl_2): λ = 293, 318 (max) nm

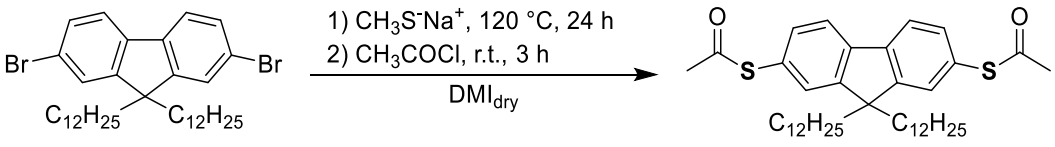

FL-Br
M.W. 660.65 g/mol

FL (1)
M.W. 651.07 g/mol

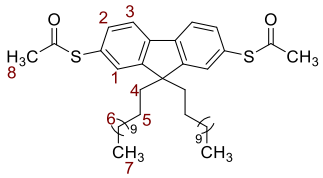

FL (1)

^{1}H-NMR ($CDCl_3$)

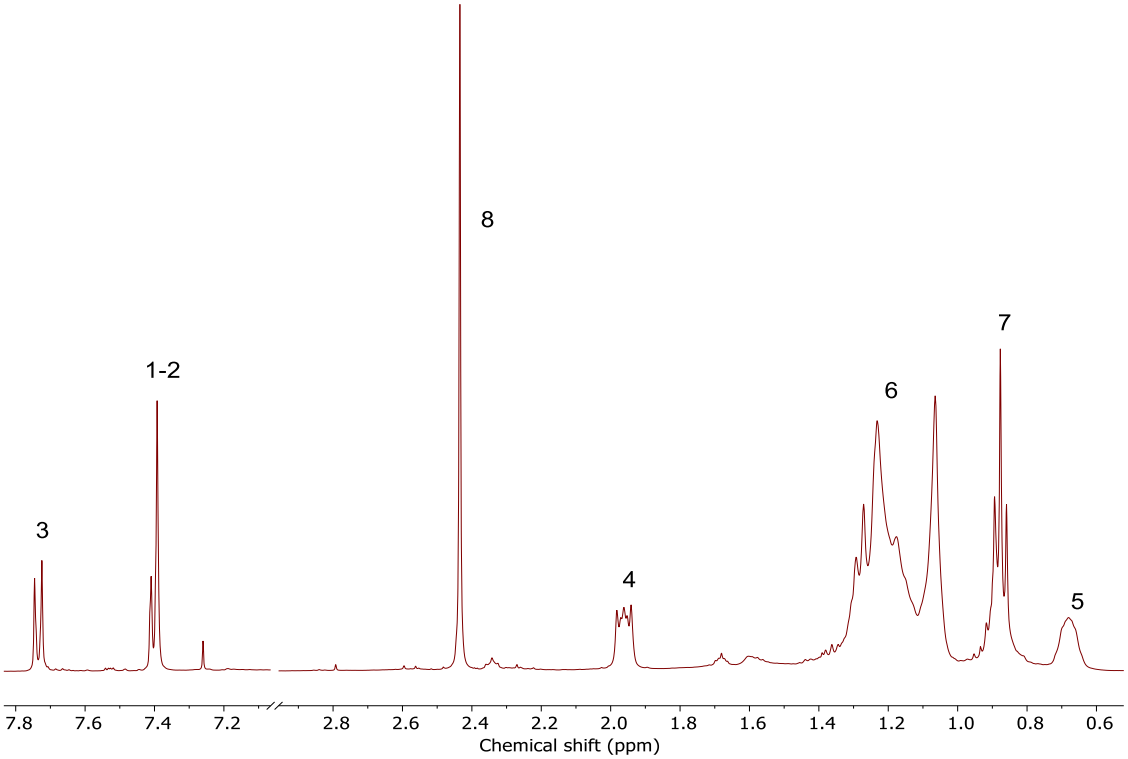

FTIR (film from CH_2Cl_2)

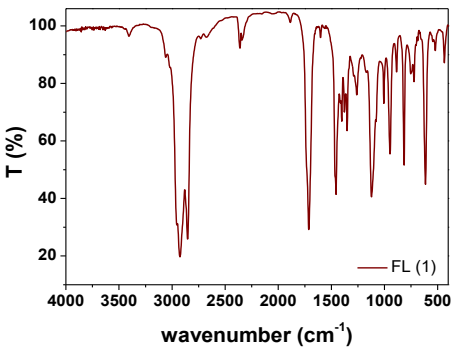

UV-Vis (CH_2Cl_2)

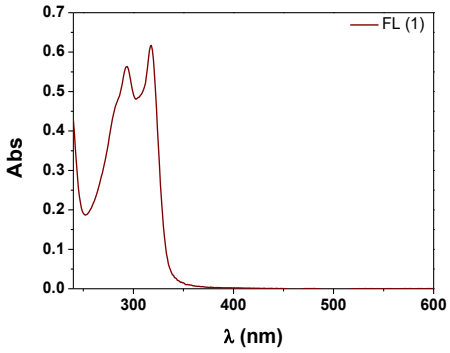

B1.2.2. 2,7-Bis[2-(trans-acetylthio-bis-(tributylphosphine)platinumII)ethynyl]-9,9-didodecyl-9H-fluorene (PtFL)

Synthesis of square planar cis- and trans-dichlorobis(tri-n-butylphosphine)platinum(II)

In a flask K_2PtCl_4 (1.00 g, 2.409 mmol) was dissolved in 60 ml of H_2O_{UP} and vacuum filtered with cellulose filter (pores ≤ 2 μm). The mixture was transferred to a round bottomed flask under Ar atmosphere and degassed for 10 minutes. Two equivalents (1.2 ml) of tributylphosphine were added by three aliquots (0.4 ml each) using a syringe, under Ar atmosphere and vigorous stirring; then the mixture was allowed to react overnight, in dark. The reaction mixture was vacuum filtered by Buchner funnel and cellulose filter (< 2μm) in a flask, the precipitate on the filter was collected in a flask using the minimum amount of EtOH and it was stored in freezer to promote crystallization of the cis isomer.

Reaction yield: 0.5834 g (36%).

Physical properties and spectral data: **^{1}H-NMR** (400 MHz, $CDCl_3$, δ): 1.99ppm (m, 3H, H-1), 1.55 ppm (m, 2H, H-2), 1.44 ppm (m, 2H, H-3), 0.92 ppm (m, 2H, H-4); **^{13}C NMR** ($CDCl_3$, 600 MHz): δ (ppm) = 13.86, 20.32, 24.38, 25.95, 26.70; **^{31}P NMR** ($CDCl_3$, 600 MHz): δ (ppm)= 5.07, 1.59; **FTIR** (film from CH_2Cl_2): $\bar{\nu}$ (cm^{-1}): 460, 726, 781, 795, 905 (ν (P-CH_3)), 964, 1009, 1053, 1089, 1206, 1278, 1304, 1341, 1377, 1400, 1420, 1456 (δ (-CH_2)), 2864 (ν_s (-CH_2)), 2928 (ν_{as} (-CH_2)), 2958 (ν_{as} (-CH_3)); **Far-IR** (film from CH_2Cl_2): $\bar{\nu}$ (cm^{-1}): 459, 406, 307, 281; **UV–vis** (CH_2Cl_2): λ(max) = 263, 321 nm;

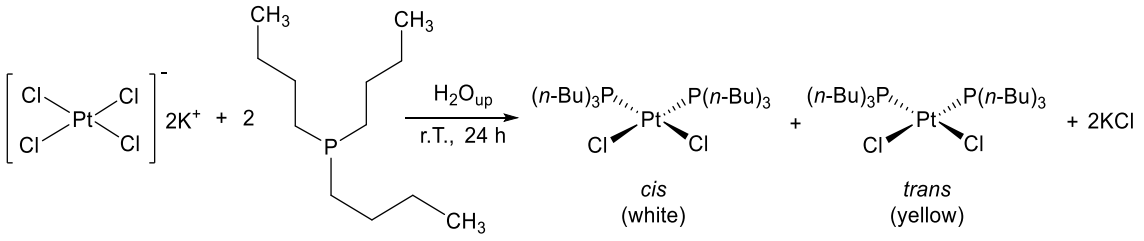

^{1}H-NMR ($CDCl_3$)

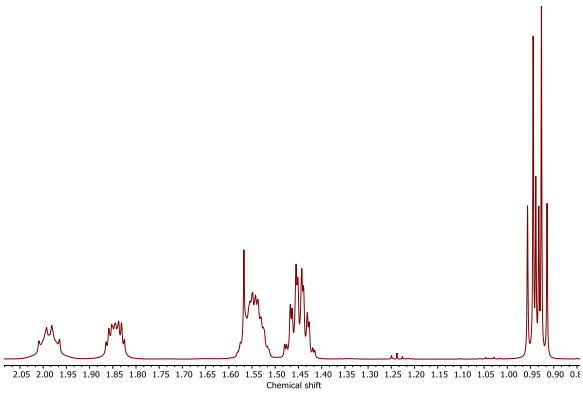

^{13}C-NMR ($CDCl_3$)

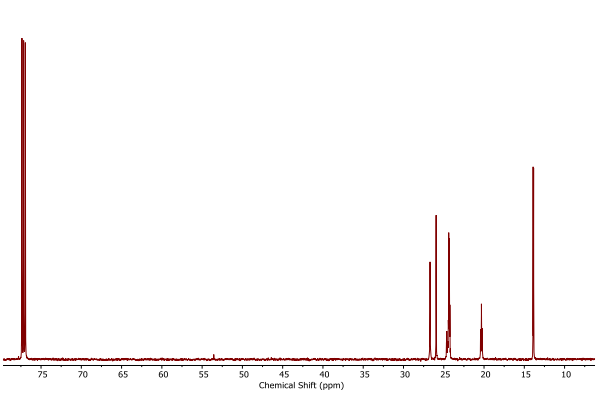

^{31}P-NMR ($CDCl_3$)

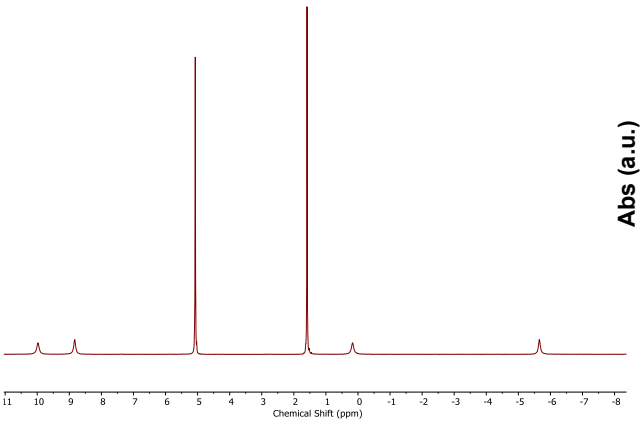

UV-Vis (CH_2Cl_2)

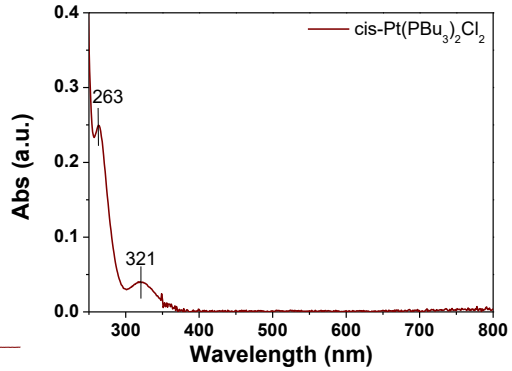

Far-IR (film from CH_2Cl_2)

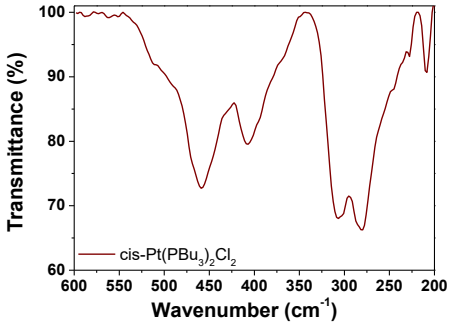

FTIR (film from CH_2Cl_2)

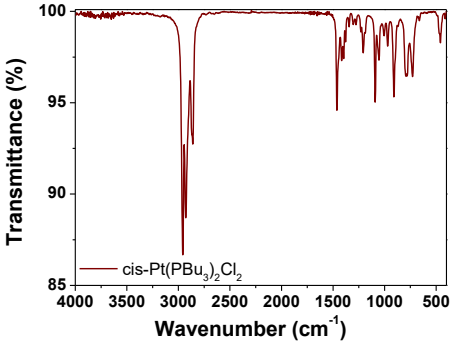

(9,9-didodecyl-9H-fluorene-2,7-diyl)bis(trimethyl silane) (2a)

In a dried round bottomed flask, 9,9-didodecyl-2,7-dibromo-fluorene (FL-Br, 0.600 g, 0.908 mmol) was dissolved in 6 mL of diisopropylamine (distilled over KOH under Ar atmosphere). The palladium complex (trans-[Pd(PPh_3)Cl_2], 0.064 g, 0.0908 mmol) and

copper(I) iodide (CuI, 0.023 g, 0.122 mmol)) were added. The reaction mixture was heated to 75 °C and under stirring the trimethylsilyl acetylene (TMSA, 0.4 mL, 3.6 mmol) was added dropwise. The reaction mixture was stirred at 75 °C overnight, then was added Et_2O, filtered on celite and washed with H_2O. The organic layer was dried over Na_2SO_4, filtered and concentrated under reduced pressure. The crude product was purified by column chromatography (silica gel, hexane) obtaining (9,9-didodecyl-9H-fluorene-2,7-diyl)bis(trimethyl silane) (2a) as yellow solid.

Reaction yield: 0.567 g (90%).

Physical properties and spectral data: **^{1}H-NMR** ($CDCl_3$, 600 MHz): δ (ppm) = 7.59 (d, 2H, H-3), 7.45 (dd, 2H, H-2), 7.41 (s, 2H, H-1), 1.92 (m, 4H, H-4),1.19 (m, 36H, H-6), 0.87 (t, 6H, H-7), 0.52 (m, 2H, H-5), 0.28 (s, 18H, H-8); **^{13}C-NMR** ($CDCl_3$, 600 MHz): δ (ppm) = 0.19 (CH_3, C-13), 14.2 (CH_3, C-10), 22.8, 23.8, 29.5, 29.8 (m), 30.2, 32.0, 40.5 (CH_2, C-8,C-9), 55.4 (C7), 94.4 (Ar-C≡C, C-11), 106.3 (C≡C-Si, C-12), 120, 122, 126.4, 131.4, 141.1, 151.1 (Ar, C-1-6); **FTIR** (film from CH_2Cl_2), $\bar{\nu}$ (cm^{-1}): 3064 (w; (-CH)$_{Ar}$), 2924 (s; ν_{as} (-CH_2)), 2852 (s; ν_s (-CH_2)), 2155 (s; ν (C≡C)), 1464 (s; δ (-CH_2)), 1419 (w; δ (-CH_3) γ (-CH_2)), 1377 (m; δ (-CH_3) γ (-CH_2)), 1248, 848, 760, 648, 555. **UV–vis** (CH_2Cl_2): λ = 308, 326, 341 (max) nm.

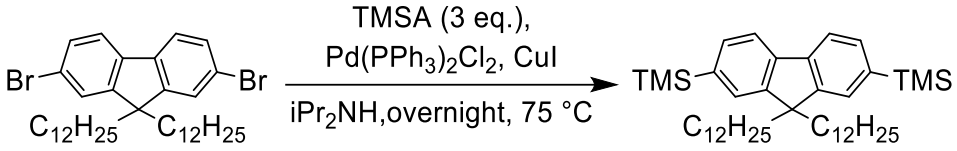

FL-Br
M.W. 660.65 g/mol

2a

^{1}H-NMR ($CDCl_3$)

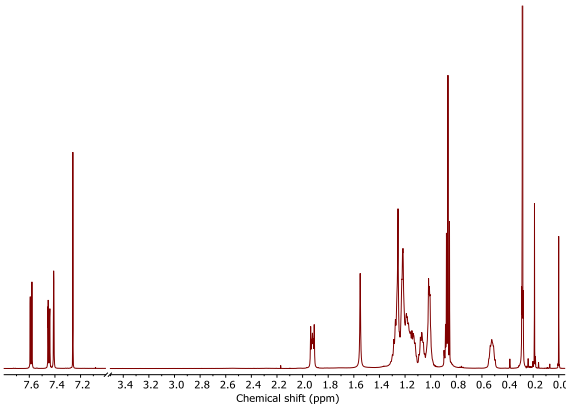

^{13}C-NMR ($CDCl_3$)

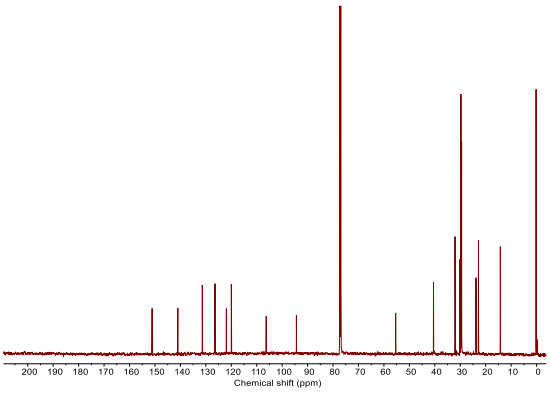

FTIR (film from CH_2Cl_2)

UV-Vis (CH_2Cl_2)

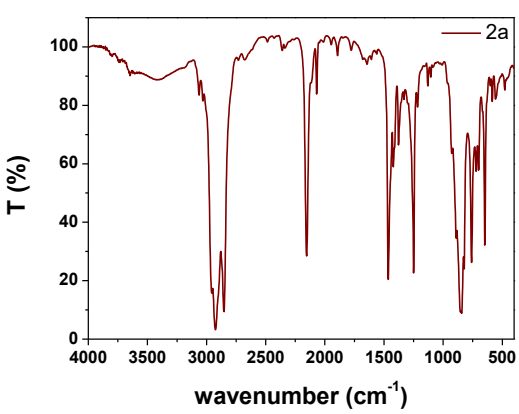

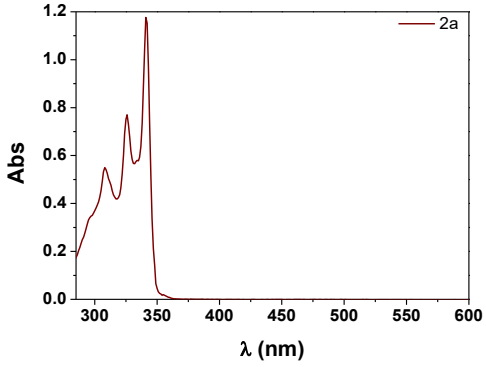

9,9-didodecyl-2,7-diethynyl-9H-fluorene (2b)

(9,9-didodecyl-9H-fluorene-2,7-diyl)bis(trimethyl silane) (2a) (0.567 g, 0.817 mmol) was dissolved in 18 mL of Et_2O in a round bottomed flask. K_2CO_3 (113 mg, 0.817 mmol) was dissolved in 18 mL of MeOH and was added into the reaction mixture. The reaction mixture stirred for 3 h at r.t. then the solvents were evaporated under vacuum and added DCM. The organic phase was washed 3 times with H_2O, was dried over Na_2SO_4, filtered and concentrated under reduced pressure. 9,9-didodecyl-2,7-diethynyl-9H-fluorene (2b) was obtained as yellow solid.

Reaction yield: 0.450 g (quantitative).

Physical properties and spectral data: **^{1}H-NMR** ($CDCl_3$, 600 MHz): δ (ppm) = 7.63 (d, 2H, H-3), 7.48 (dd, 2H, H-2), 7.46 (s, 2H, H-1), 3,14 (s, 2H, H-8), 1.92 (m, 4H, H-4),1.19 (m, 36H, H-6), 0.87 (t, 6H, H-7), 0.56 (m, 4H, H-5); **^{13}C-NMR** ($CDCl_3$, 600 MHz): δ (ppm) = 14.2 (CH_3, C-10), 22.8, 23.8, 29.5, 29.8 (m), 30.5, 32.0, 40.3 (CH_2, C-8, C-9), 55.9 (C-7), 77.4 (C≡C-H, C-12), 84.7 (Ar-C≡C, C-11), 120.1, 121, 126.7, 131.4, 141.2, 151.3 (Ar, C-1-6). **FTIR** (film from CH_2Cl_2), $\bar{\nu}$ (cm^{-1}): 3312 (s; (≡CH)), 3065 (w; $(-CH)_{Ar}$), 2926 (s; ν_{as} ($-CH_2$)), 2852 (s; ν_s ($-CH_2$)), 2106 (s; ν (C≡C)), 1609 (w; ν $(C-C)_{Ar}$), 1464 (s; δ ($-CH_2$)), 1416 (w; δ ($-CH_3$) γ ($-CH_2$)), 1377 (m; δ ($-CH_3$) γ ($-CH_2$)), 1263 (w; ν_{as} (C-C-C)), 891 (m; def. modes $(CC)_{Ar}$), 823 (s; def. modes $(CC)_{Ar}$), 646, 603. **UV–vis** (CH_2Cl_2): λ = 291, 303, 316, 330 (max) nm;

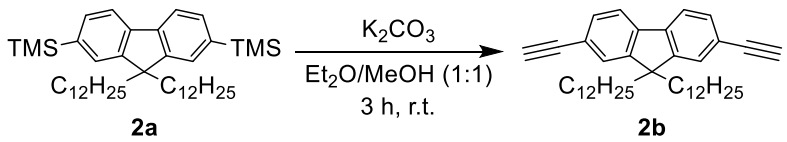

^{1}H-NMR ($CDCl_3$)

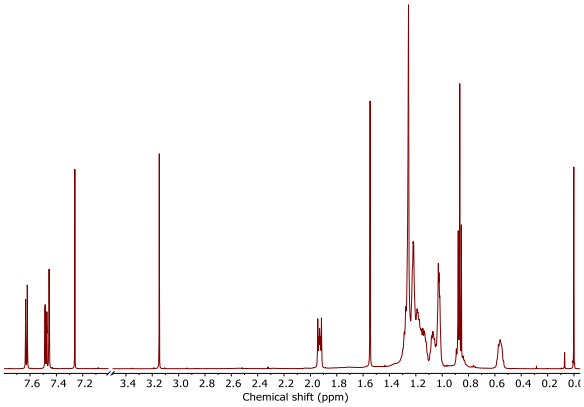

^{13}C-NMR ($CDCl_3$)

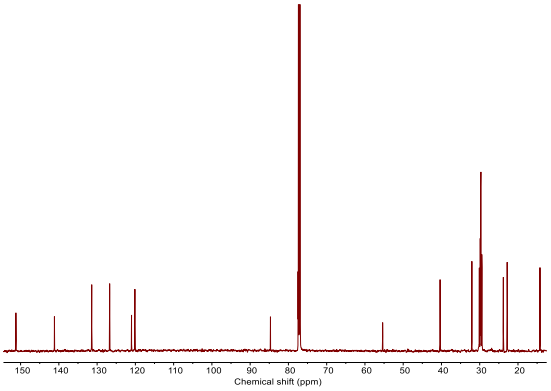

FTIR (film from CH_2Cl_2)

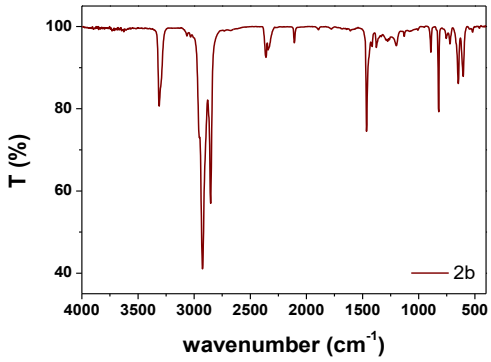

UV-Vis (CH_2Cl_2)

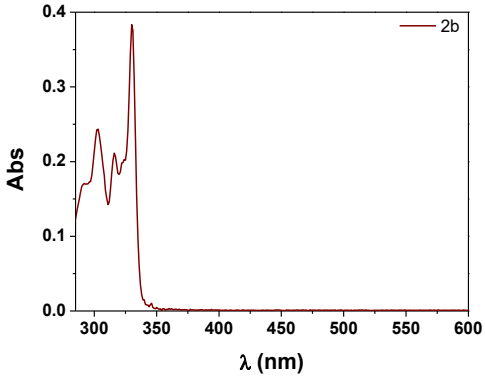

2,7-Bis[2-(trans-bis-(tributylphosphine)chloride-platinumII)ethynyl]-9,9-didodecyl-9H-fluorene (2c)

9,9-didodecyl-2,7-diethynyl-9H-fluorene (2b) (0.300 g, 0.544 mmol) and *cis*-[Pt(PBu_3)$_2$$Cl_2$] (730 g, 1.09 mmol) were stirred in a mixture of distilled diisopropylamine (60 mL) and anhydrous CH_2Cl_2 (60 mL) under an Argon atmosphere at 35 °C for 96 h. The solvent was removed under vacuum and the crude product was purified by column chromatography (silica gel, petroleum ether/dichloromethane with gradient from 4:1 to 2:1) affording as a yellow oil.

Reaction yield: 0.362 g, yield 36%.

Physical properties and spectral data: **^{1}H-NMR** ($CDCl_3$, 600 MHz): δ (ppm) = 7.45 (d, 2H, H-3), 7.18+7.16 (m, 4 H, H-1, H-2), 2.05 (m, 24H, H-8), 1.84 (m, 4H, H-4), 1.60 (m, , 24H, H-9), 1.46, (m, 24H, H-10), 1.29-1.00 (m, 36H, H-6), 0.93 (t, 42H, H-11), 0.86 (t, 6H, H-7), 0.61 (m, 4H, H-5). **^{13}C-NMR** ($CDCl_3$, 600 MHz): δ (ppm) = 13.94 (CH_3, C-17), 14.23 (CH_3, C-11), 22.2 (t, PCH_2CH_2, C-15, C-16), 22.8, 24.0 (CH_2), 24.5 (t, PCH_2CH_2, C-14), 26.3,

29.5, 29.8 (m), 30.5, 32.0, 35.2, 40.8 (CH_2), 53.5 (C-7), 96.5 (C≡C-Ar, C-12),106.9 (Pt-C≡C, C-13), 119, 125.1, 126.9, 129.8, 138.6,150.6 (Ar). **^{31}P-NMR** ($CDCl_3$, 600 MHz): δ (ppm) = 7.4 ($J_{P\text{-}Pt}$ = 2377.2 Hz). **FTIR** (film from CH_2Cl_2), $\bar{\nu}$ (cm^{-1}): 3055 (w; $(-CH)_{Ar}$), 2959 (s; ν_{as} $(-CH_3)$), 2928 (s; ν_{as} $(-CH_2)$), 2857 (s; ν_s $(-CH_2)$), 2113 (s; ν (C≡C)), 1605 (w; ν $(C\text{-}C)_{Ar}$), 1462 (s; δ $(-CH_2)$), 1415 (m; δ $(-CH_3)$ γ $(-CH_2)$), 1377 (m; δ $(-CH_3)$ γ $(-CH_2)$), 1262 (m; ν_{as} (C-C-C)), 1092 (s; δ (=CH), 1005 (s; in-plane δ(=CH)), 904 (m; def. modes $(CC)_{Ar}$), 817 (s; def. modes $(CC)_{Ar}$), 721 (m, out-of-plane δ$(–CH)_{Ar}$). **UV-Vis** (CH_2Cl_2), λ = 328, 358, 374 (max) nm;

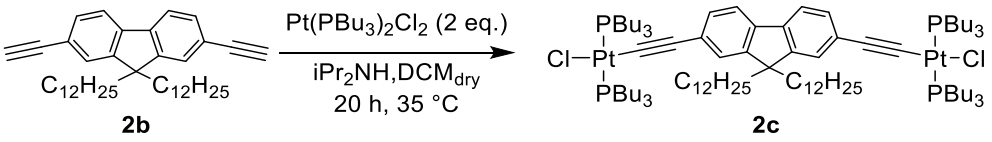

^{1}H-NMR ($CDCl_3$)

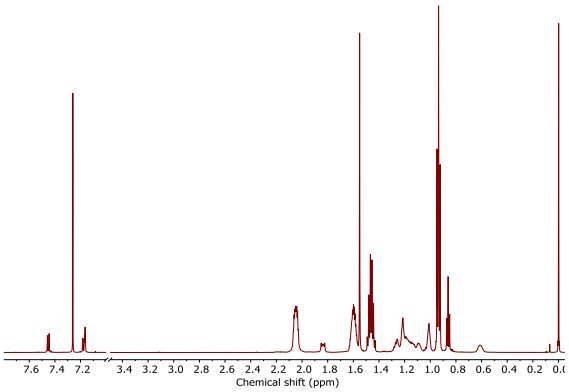

^{13}C-NMR ($CDCl_3$)

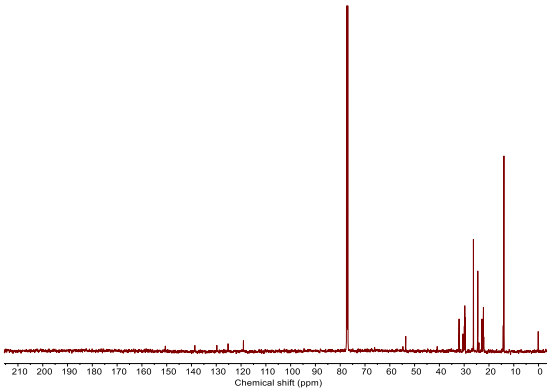

^{31}P-NMR ($CDCl_3$)

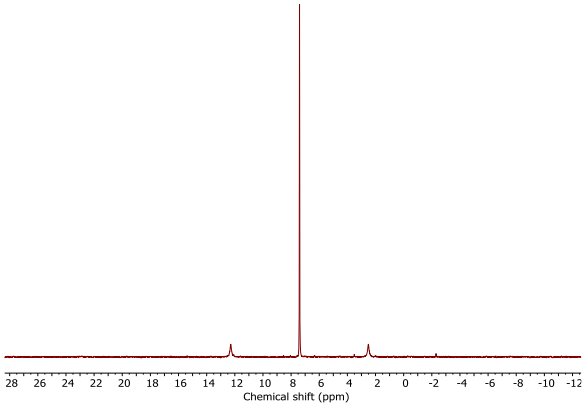

FTIR (film from CH_2Cl_2)

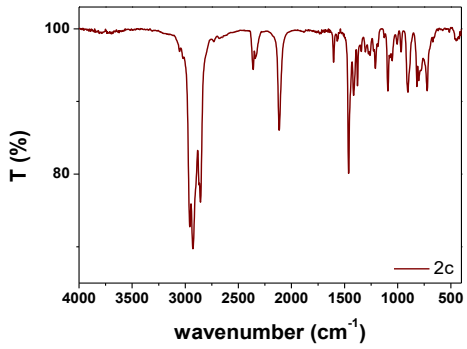

UV-Vis (CH_2Cl_2),

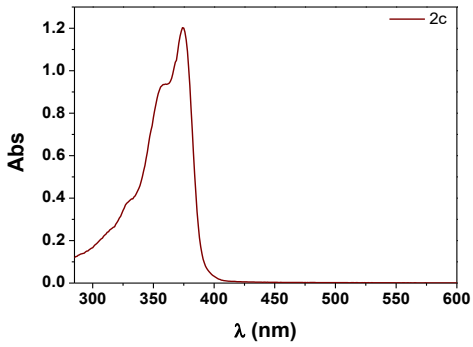

2,7-Bis[2-(trans-acetylthio-bis-(tributylphosphine)platinumII)ethynyl]-9,9-didodecyl-9H-fluorene (2) (PtFL)

2,7-Bis[2-(trans-bis-(tributylphosphine)chloride-platinumII)ethynyl]-9,9-didodecyl-9H-fluorene (2c) (0.300 g, 0.165 mmol) and potassium thioacetate (0.056 g, 0.50 mmol) were stirred in a mixture of degassed ethanol (15 mL) and dry CH_2Cl_2 (60 mL) under Argon atmosphere at 45 °C for 24 h. Upon filtration, the solution was washed with H_2O and the organic phase dried over Na_2SO_4 to give 2,7-Bis[2-(trans-acetylthio-bis-(tributylphosphine)platinumII)ethynyl]-9,9-didodecyl-9H-fluorene (2) as a yellow oil.

Reaction yield: 0.302 g, 96% yield.

Physical properties and spectral data: **^{1}H-NMR** ($CDCl_3$, 600 MHz): δ (ppm) = 7.46 (d, 2H, H-3), 7.19 (m, 4H, H-1, H-2), 2.35 (s, 6H, H-12), 2.06 (m, 24H, H-8), 1.84 (m, 4H, H-4), 1.60 (m, 24H + H_2O, H-9), 1.44 (m, 24H, H-10), 1.29-1.00 (m, 36H, H-6), 0.93 (t, 42H, H-11), 0.86 (t, 6H, H-7), 0.63 (m, 4H, H-5). **^{13}C-NMR** ($CDCl_3$, 600 MHz): δ (ppm) = 13.96 (CH_3, C-17), 14.23 (CH_3, C-11), 22.82 (CH_3, C-19), 22.85 (t, PCH_2CH_2, C-15, C-16), 24.0 (CH_2), 24.53 (t, PCH_2CH_2, C-14), 26.4, 29.47, 29.63, 29.79, 29.94, 30.49, 32.03, 35.26, 40.82 (CH_2), 54.7 (C-7), 96.5 (C≡C-Ar, C-12),106.9 (Pt-C≡C, C-13), 119, 125.1, 126.9, 129.5, 138.6,150.6 (Ar), 204.4 (CO, C-18). **^{31}P-NMR** ($CDCl_3$, 600 MHz): δ (ppm) = 4.53 (JP-Pt = 2392 Hz). **FTIR** (film from CH_2Cl_2), $\bar{\nu}$ (cm^{-1}): 3055 (w; $(-CH)_{Ar}$), 2954 (s; ν_{as} ($-CH_3$)), 2929 (s; ν_{as} ($-CH_2$)), 2857 (s; ν_s ($-CH_2$)), 2112 (s; ν (C≡C)), 1631 (s; ν (C=O)), 1603 (w; ν $(C-C)_{Ar}$), 1462 (s; δ ($-CH_2$)), 1415 (m; δ ($-CH_3$) γ ($-CH_2$)), 1377 (m; δ ($-CH_3$) γ ($-CH_2$)), 1262 (m; ν_{as} (C-C-C)), 1107 (s; δ (=CH), 1005 (s; in-plane δ(=CH)), 904 (m; def. modes $(CC)_{Ar}$), 819 (s; def. modes $(CC)_{Ar}$), 723 (m, out-of-plane δ$(–CH)_{Ar}$), 648 (s, ν(=C–S)). **UV-Vis** (CH_2Cl_2), λ = 328, 358, 374 (max) nm;

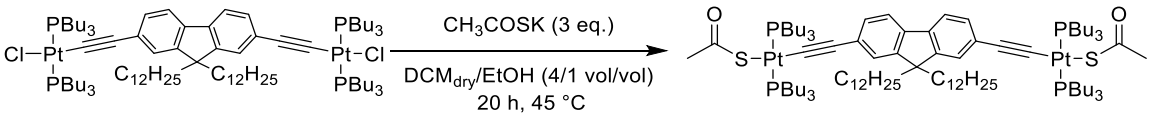

2c

PtFL (2)
M.W. 1898.52 g/mol

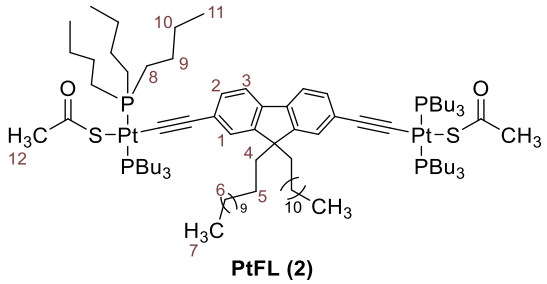

PtFL (2)

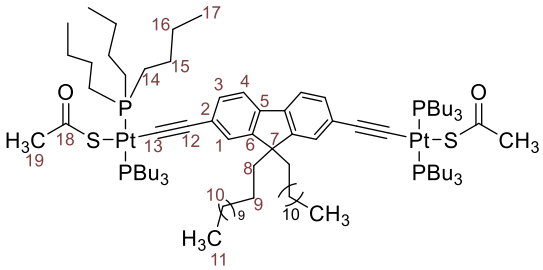

PtFL (2)

^{1}H-NMR ($CDCl_3$)

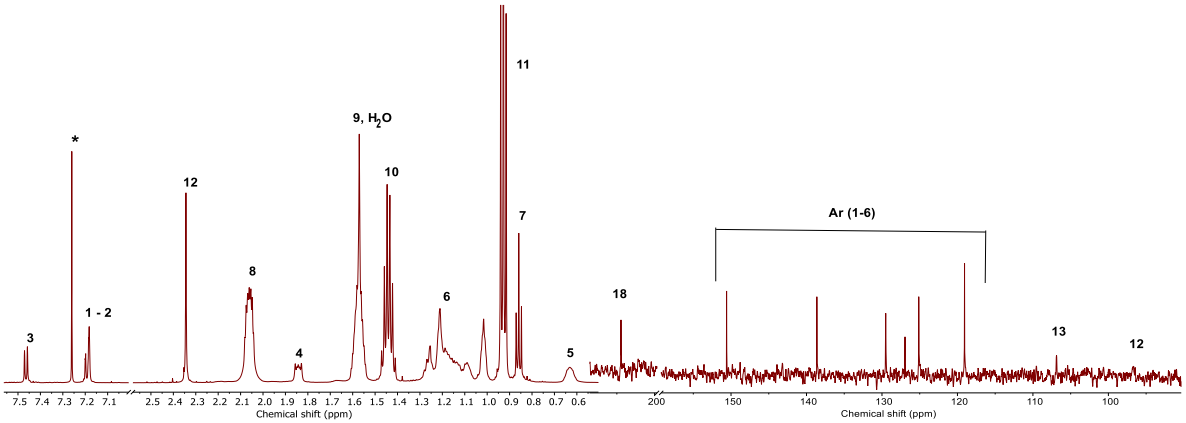

^{13}C-NMR ($CDCl_3$)

^{31}P-NMR ($CDCl_3$)

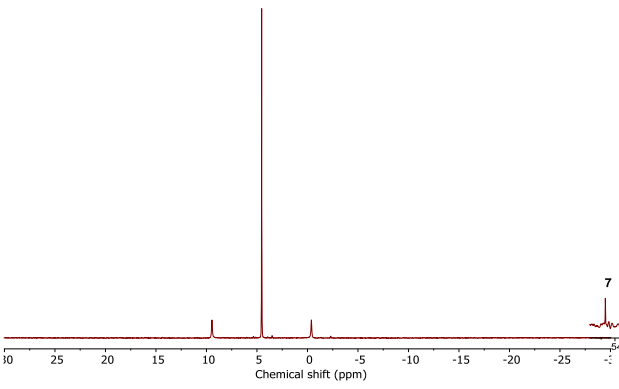

^{13}C-NMR ($CDCl_3$)

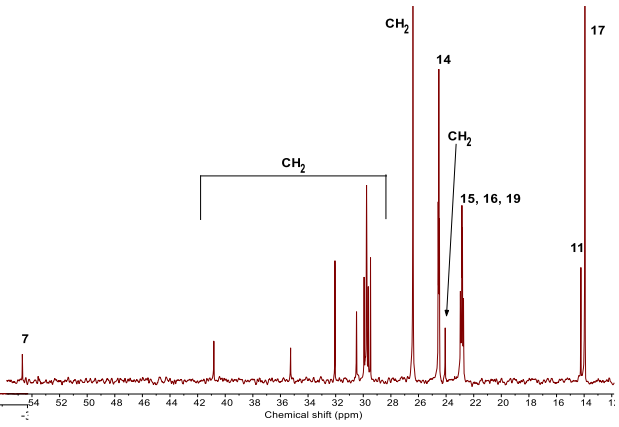

FTIR (film from CH_2Cl_2) UV-Vis (CH_2Cl_2)

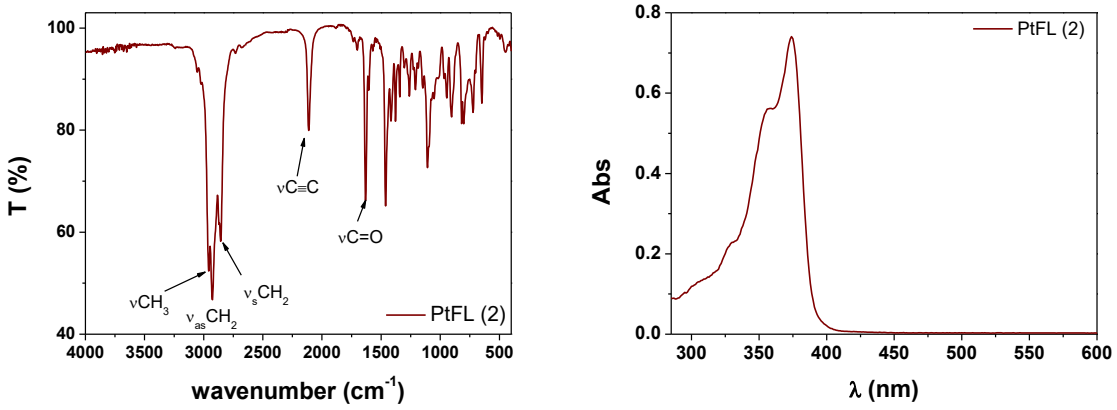

B1.3. Synthesis of DEBP derivatives

Bifunctional thiol *trans,trans*-[dithioacetyldibis(tributylphosphine)diplatinum(II)-4,4'-diethynylbiphenyl] (PtDEBP) was prepared according to a previously published procedure [287] and schematically reported below. The reaction is carried out in two steps: (i) the synthetic square-planar complex *cis*-$Pt(PBu_3)_2Cl_2$ undergoes to a dehydroalogenation reaction in the presence of 4,4'-diethynylbiphenyl (H-C≡C-C_6H_4-C_6H_4-C≡C-H, DEBP) to obtain the *trans,trans*-[$ClPt(PBu_3)_2$-C≡C-C_6H_4-C_6H_4-C≡C-$Pt(PBu_3)_2Cl$] complex; (ii) ligand exchange reaction of [$ClPt(PBu_3)_2$-C≡C-C_6H_4-C_6H_4-C≡C-$Pt(PBu_3)_2Cl$] complex in presence of potassium thioacetate led to the final Pt-$DEBP_n(SCOCH_3)_2$ ligand.

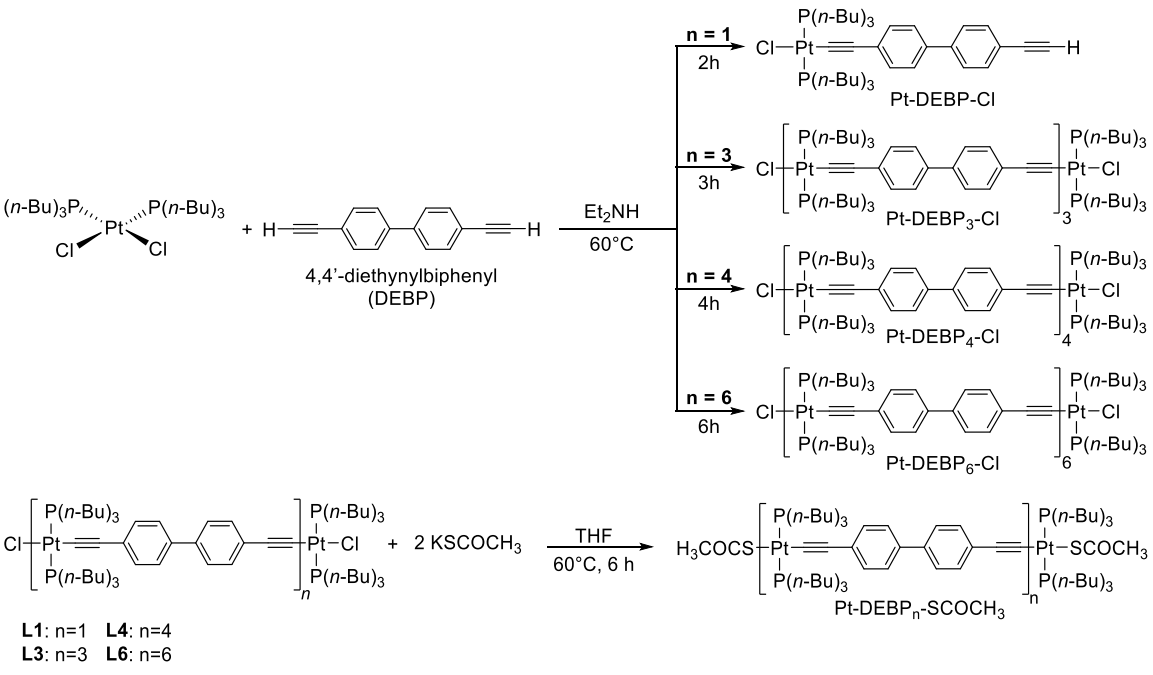

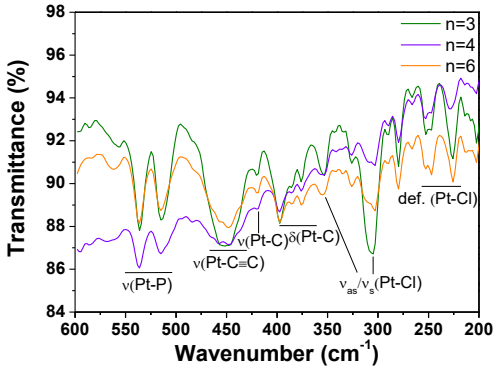

Figure B4. *Far-IR Spectra of Cl-Pt-DEBP$_n$ (n = 3, 4, 6).*

B1.4. Synthesis of PCP derivative

[2.2]Paracyclophan-4-yl)methanethiol PCP_2 (PCP) [305]

(±)-[2.2]paracyclophane-4-carboxaldehyde 1(+/-)

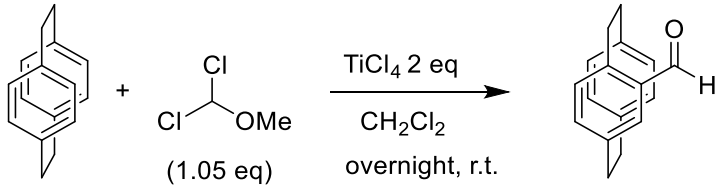

1 (+/-)

In a dried round bottomed flask, [2.2]paracyclophane (5g, 24 mmol, 1 eq) was dissolved in dry CH_2Cl_2 (220 mL) and cooled to 0 °C. The titanium (IV) chloride (5.26 mL, 48 mmol, 2 eq) and the dichloromethoxymethane (2.28 mL, 25.2 mmol, 1.05 eq) were added dropwise. The reaction mixture was stirred at room temperature overnight, poured into crushed ice (100 mL) and stirred for another 2 hours. The two layers were separated, and the aqueous layer was extracted with CH_2Cl_2 (2 x 50 mL). the combined organic layers were dried over $MgSO_4$, filtered and concentrated under reduced pressure. Purification by chromatography on silica gel (pentane/CH_2Cl_2, 1:1) afforded the desired formyl[2.2]PCP **1** as white solid.

Reaction yield: 79% yield.

Physical properties and spectral data: **^{1}H-NMR** ($CDCl_3$, 600 MHz): δ (ppm) = 9.95 (s, 1H, CHO), 7.01 (d, 1H), 6.73 (dd, 1H), 6.59 (d, 1H), 6.56 (dd, 1H), 6.50 (dd, 1H), 6.43 (dd, 1H), 6.37 (dd, 1H), 4.10 (ddd, 1H), 3.24-3.28 (m, 1H), 3.17-3.21 (m, 2H),3.01-3.11 (m, 3H), 2.92-2.98 (m, 1H). **^{13}C-NMR** ($CDCl_3$, 151 MHz): δ (ppm) = 192.09 (C=O), 143.39, 140.81, 139.66, 139.60, 138.23, 136.73, 136.50, 136.28, 133.42, 133.07, 132.53, 132.31, 35.42, 35.31, 35.15, 33.78.

^{1}H-NMR ($CDCl_3$)

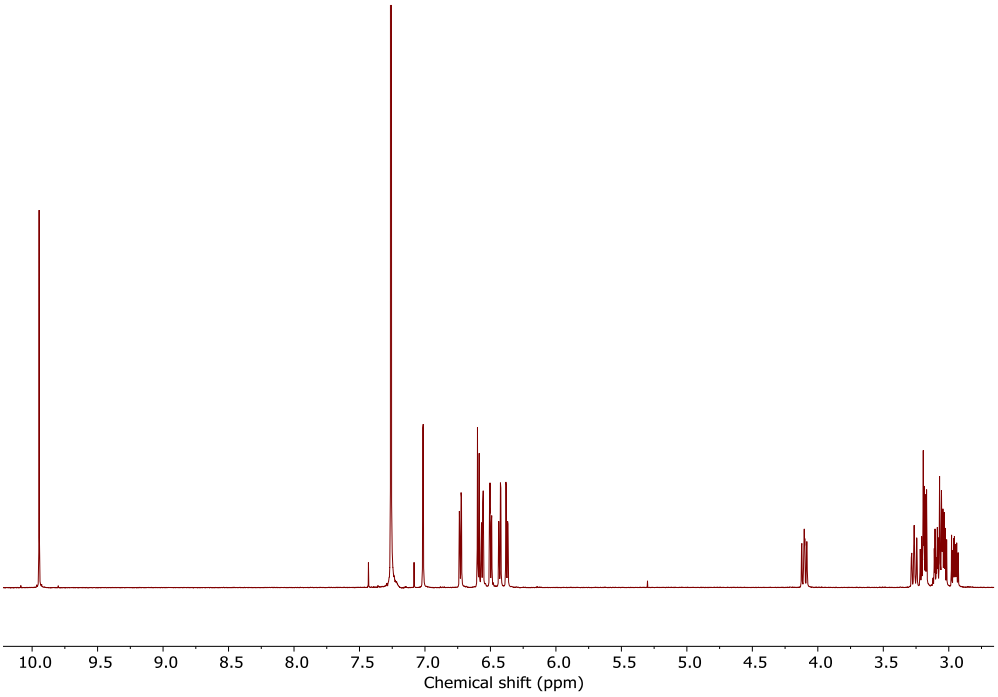

^{13}C-NMR ($CDCl_3$)

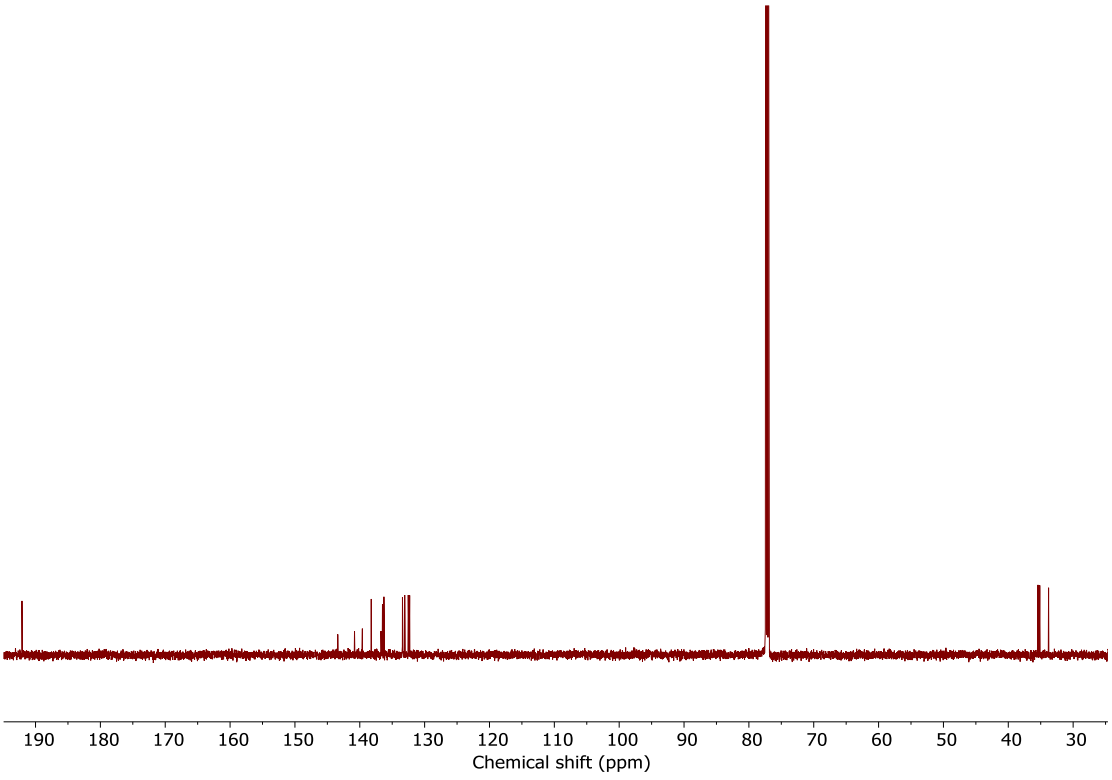

3-([2.2]Paracyclophan-4-yl)methylsulfanylpropionic Acid Methyl Ester 2 (+/-)

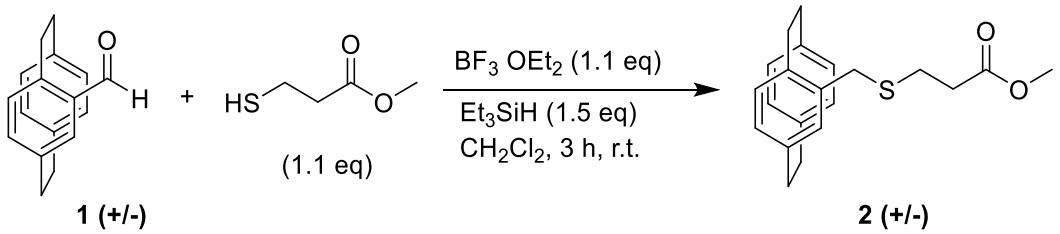

1 (+/-) **2 (+/-)**

In a two-necked round bottomed flask **1(+/-)** (100 mg, 0.423 mmol, 1 eq) was dissolved in dry CH_2Cl_2 (1.66 mL). 3-sulfanylpropionic acid methyl ester (51.3 µL, 0.47 mmol, 1.1 eq) was added into the reaction mixture then $BF_3 \cdot OEt_2$ (57.3 µL, 0.47 mmol, 1.1 eq) was added dropwise and finally triethylsilane (101.3 µL, 0.63 mmol, 1.5 eq) was added. The mixture was stirred for 5 hours. The reaction was monitored with TLC (eluent pentane:AcOEt 80:20). After 5 hours a saturated solution of $NaHCO_3$ was added into the reaction mixture with CH_2Cl_2. The two layers were separated, and the aqueous layer was extracted with CH_2Cl_2 (2 x 50 mL). The combined organic layers were dried over $MgSO_4$, filtered and concentrated under reduced pressure. Purification by chromatography on silica gel (pentane/AcOEt, 95:5 to 80:20) afforded the desired **2(+/-)** as white solid.

Reaction yield: 84% yield.

Physical properties and spectral data: **^{1}H-NMR** ($CDCl_3$, 600 MHz): δ (ppm) = 6.65 (dd, 1H), 6.55–6.43 (m, 4H), 6.41 (dd, 1H), 6.26 (s, 1H), 3.72 (d, 1H), 3.67 (s, 3H), 3.41 (d, 1H) 3.45–3.39 (m, 1H), 3.18–3.14 (m, 1H), 3.09–2.94 (m, 5H), 2.86 (ddd, 1H), 2.61–2.57 (m, 2H), 2.51–2.46 (m, 2H). **^{13}C-NMR** ($CDCl_3$, 151 MHz): δ (ppm) = 172.4, 140.0, 139.5, 139.3, 137.9, 137.2, 135.3, 135.1, 133.5, 133.3, 132.2, 131.7, 128.9, 51.8, 35.3, 35.2, 35.0, 34.5, 34.4, 33.4, 26.4.

^{1}H-NMR ($CDCl_3$)

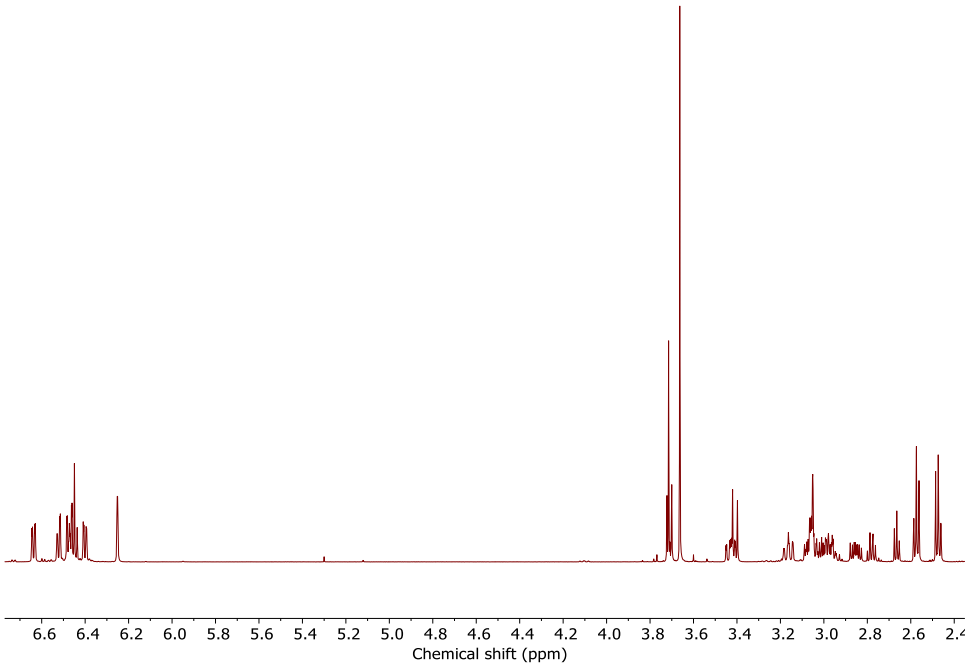

^{13}C-NMR ($CDCl_3$)

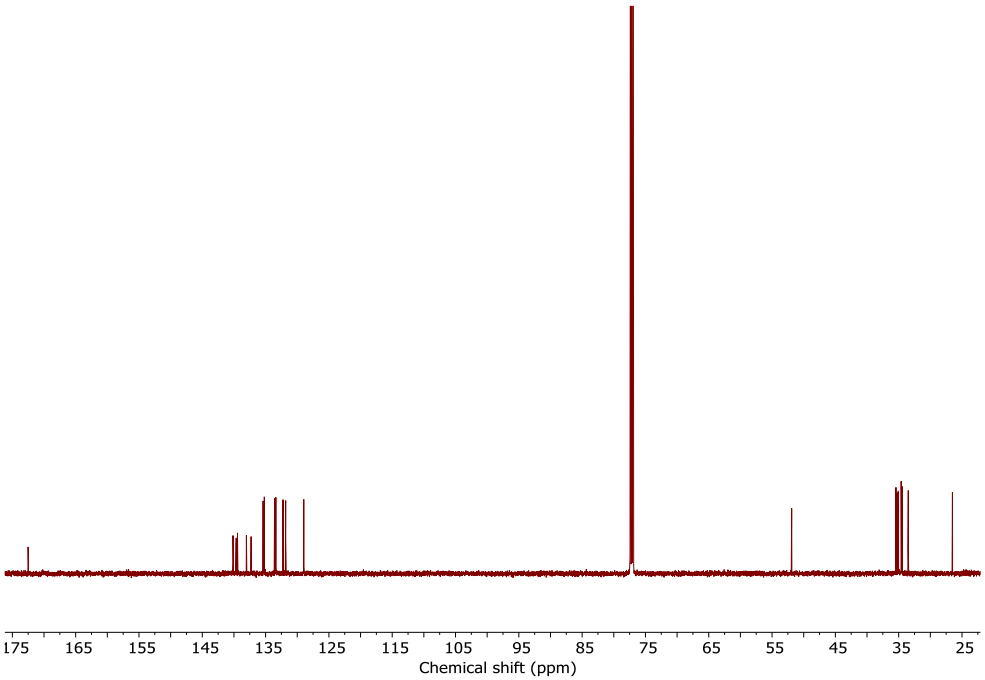

[2.2]Paracyclophan-4-yl)methanethiol PCP_2 (PCP)

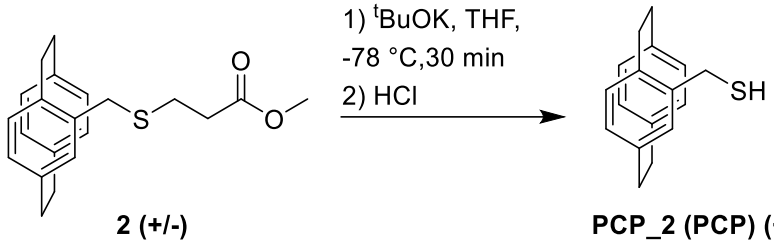

2 (+/-) **PCP_2 (PCP) (+/-)**

In a two-necked round-bottomed flask, **2 (+/-)** (100 mg, 0.33 mmol, 1 eq) was diluted in dry THF (1.4 mL). After cooling to −78 °C, *t*-BuOK (0.56 mL of a 1 M solution in THF, 2 eq) was added dropwise. The reaction mixture was stirred at −78 °C for 30 min and then directly poured onto an aqueous 1 M HCl solution (5.5 mL). The resulting mixture was extracted with CH_2Cl_2 (3 × 20 mL), and the collected organic layers were dried over $MgSO_4$ and concentrated under a vacuum. The resulting crude product was then purified by column chromatography on silica gel (pentane/CH_2Cl_2, 80:20) to afford the expected thiol.

Reaction yield: 80% yield.

Physical properties and spectral data: **^{1}H-NMR** ($CDCl_3$, 600 MHz): δ (ppm) = 6.63 (dd, 1H), 6.53–6.44 (m, 4H), 6.41 (dd, 1H), 6.30 (s, 1H), 3.73 (dd, 1H), 3.49–3.38 (m, 2H), 3.23–3.13 (m, 1H), 3.12–2.94 (m, 5H), 2.93–2.82 (ddd, 1H), 1.54 (t, 1H). **^{13}C-NMR** ($CDCl_3$, 151 MHz): δ (ppm) = 140.5, 140.3, 139.7, 139.4, 137.1, 135.5, 134.1, 133.6, 133.4, 132.3, 131.8, 128.9, 35.4, 35.1, 34.5, 33.3, 27.8. **FTIR** (ATR, deposited on glass), $\bar{\nu}$ (cm^{-1}): 2924 (ν_{as} (-CH_2)), 2853 (ν_s (-CH_2)), 2565 (ν (S-H)), 1616 (ν (C-C)$_{Ar}$), 1499 (s; δ (-CH_2)), 1412 (γ (-CH_2)), 1365 (γ (-CH_2)), 899 (def. modes (CC)$_{Ar}$), 796 (def. modes (CC)$_{Ar}$), 716 (out-of-plane δ(–CH)$_{Ar}$), 638 (s, ν(-C–S)). **UV-Vis** (CH_2Cl_2), λ = 288, 310 nm.

^{1}H-NMR ($CDCl_3$)

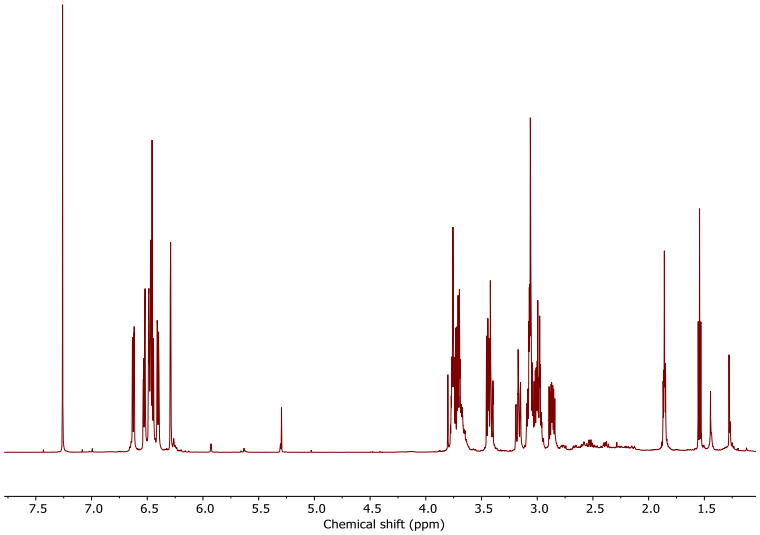

^{13}C-NMR ($CDCl_3$)

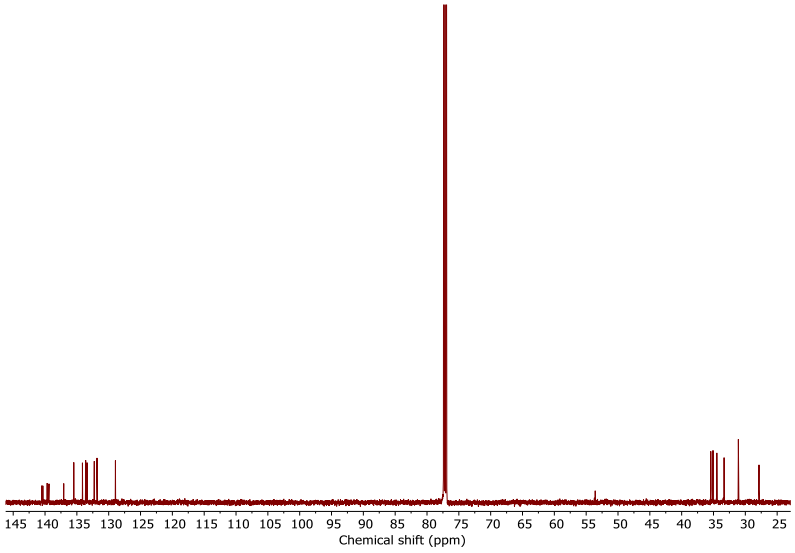

FTIR (film from CH_2Cl_2)

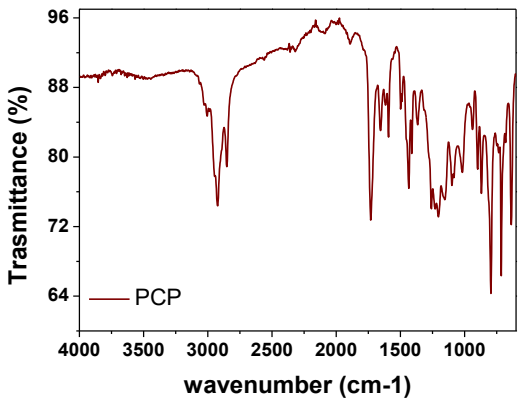

UV-Vis (CH_2Cl_2)

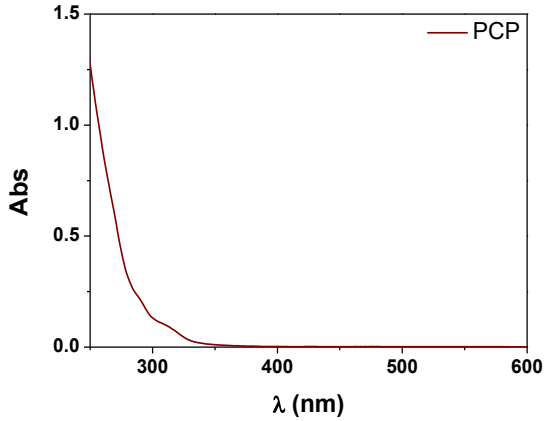

Resolution of racemic 2 (+/-)

The racemic sulfanyl ester **2 (+/-)** was dissolved in the minimum amount of a 60:40 n-heptane/ ethanol mixture. Aliquots of the resulting solution were repeatedly injected into the semipreparative HPLC apparatus equipped with an IA column (5 μm; size = 250 mm × 20 mm) eluting with 60:40 nheptane/ethanol at 1 mL min−1 (20 °C) and with UV monitoring at 229 nm. The collected fractions of each enantiomer, eluted at 5.96 and 17.91 min, were concentrated in vacuo. The deprotection to obtain of the enantiopure forms of PCP_2 was carried out as described before with the racemic material.

Appendix C

C1. Synthetic procedures of Hydrophilic Nanoparticles

C1.1. Synthesis of AuNPs stabilized by 3MPS and DEA

Synthesis of gold nanoparticles functionalised with 3MPS and DEA mixed thiols was carried out following a wet reduction procedure in water and it is reported for the molar ratio Au/3MPS/DEA = 1/4/10. In detail, in a 100 mL two-neck round bottom flask, 0.100 g ($2.54 \cdot 10^{-4}$ mol) of $HAuCl_4 \cdot 3H_2O$ were dissolved in 10 mL of H_2O_{up}. To the gold precursor solution, 0.1811 g ($1.02 \cdot 10^{-3}$ mol) of 3MPS and 0.4311 g ($2.54 \cdot 10^{-3}$ mol) of DEA were subsequently added in 10 mL of H_2O_{up} each. After 10 minutes of degassing with Argon, 0.0961 g ($2.54 \cdot 10^{-3}$ mol) of sodium borohydride in 10 mL of H_2O_{up} were added in the flask to reduce the gold. The reaction occurred for 2 hours under vigorous stirring at room temperature. After the 2 hours the AuNPs were purified to remove unreacted thiols and by-products from the solution and to isolate smaller nanoparticles: firstly, a centrifuge at 7000 rpm and with a controlled temperature of +5°C was performed on the crude mixture to eliminate larger nanoparticles; subsequently, the supernatant (10 mL) was transferred to a dialysis tube for purification with distilled water (500 mL) for 7 days under mild agitation at room temperature, removing the external water and adding fresh distilled water at a regular interval of time of 24 h.

Physical and spectral data of AuNPs-3MPS-DEA (1/4/10 molar ratio). **UV–Vis** (H_2O): λ_{max} = 520 nm; **DLS** (H_2O): $<2R_H>$ = (9 ± 2) nm; **yield**: 29 ± 8 % wt; **FTIR** (ATR, solid): ν = 3060 (w), 3020 (w), 1584 (m), 1472 (s), 807 cm^{-1} (s).

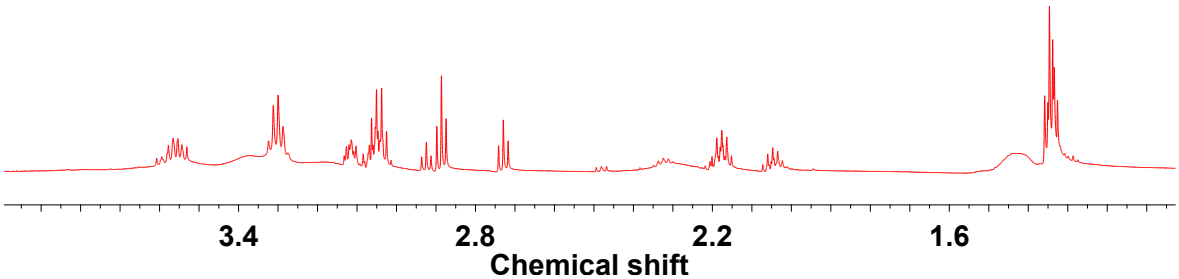

Figure C1. *^1H full spectrum of AuNPs-3MPS-DEA in D_2O.*

C1.2. Synthesis of AuNPs stabilized by 3MPS and FITC derivates

AuNPs-3MPS-CysFITC and AuNPs-3MPS-AniFITC were synthesized following one-pot wet chemical reduction method.

Tetrachloroauric acid (III) trihydrate ($HAuCl_4 \cdot 3H_2O$) was used as metal precursor, sodium 3-mercapto-1-propanesulfonate (3MPS) and fluoresceine isothiocyanate organic dye derivatized with cysteamine (CysFITC) or with 4-Aminothiophenol (AniFITC) were used as capping agents. AuNPs-3MPS-CysFITC and AuNPs-3MPS-AniFITC were prepared with $Au/S_{3MPS}/S_{Dye}$ 1/4/0.5 molar ratio. Briefly, in 100 mL two-neck round bottom flask 50 mg of $HAuCl_4 \cdot 3H_2O$ (0.12 mmol) were dissolved in 3 mL H_2O_{up}/MeCN (1/1 vol/vol). 85.5 mg of 3MPS (0.48 mmol) in 3 mL H_2O_{up}/MeCN (1/1 vol/vol) were added into the gold solution. The reaction mixture was degassed with argon for 10 minutes under stirring. The derivatized dye (0.03 mmol; CysFITC 29.5 mg, or AniFITC 32.4 mg) was solubilized in 3 mL of H_2O_{up}/MeCN (1/1 vol/vol) and before adding into the mixture of reactants was pre-reduced with 150 μL of $NaBH_4$ 0.33 M (dissolved in H_2O_{up}/MeCN 1/1 vol/vol) to reduce the disulphuric bonding. After 10 minutes the reduced FITC derivate was added to the mixture with gold and 3MPS. Finally, the 45.4 mg of $NaBH_4$ (1.2 mmol) in 3 mL H_2O_{up}/MeCN (1/1 vol/vol) were added to reduce Au^{III} to Au^0. Thus, the mixture was stirred for 2 h at room temperature. After the 2 hours, the crude mixture was transferred to centrifuge tube. One centrifuge at 7000 rpm and with a controlled temperature of +5°C was performed to eliminate larger nanoparticles. The supernatant was transferred to a dialysis tube for purification with distilled water for 7 days.

Physical and spectral data of AuNPs-3MPS-CysFITC. **UV–Vis** (H_2O, pH = 8 phosphate buffer): λ= 513 nm $\lambda_{SPR} \approx$ 545 nm; **PL** (H_2O, pH = 8 phosphate buffer): λ_{em} = 513 nm ; **DLS** (H_2O): $<2R_H>$ = (28 ± 14) nm; **ζ-pot** (H_2O): (-49 ± 9) mV.

Physical and spectral data of AuNPs-3MPS-AniFITC. **UV–Vis** (H_2O, pH = 8 phosphate buffer): λ= 512 nm $\lambda_{SPR} \approx$ 550 nm; **PL** (H_2O, pH = 8 phosphate buffer): λ_{em} = 512 nm; **DLS** (H_2O): $<2R_H>$ = (68 ± 20) nm, (295 ± 19) nm; **ζ-pot** (H_2O): (-30 ± 9) mV.

C2. Synthetic procedures of Hydrophobic Nanoparticles

C2.1. Synthesis of gold nanoparticles stabilized by Ani and DDT

Gold nanoparticles functionalised with *p*-aminothiophenol (Ani) and 1-dodecanethiol (DDT) were synthesized using a modified Brust's two-phase method introducing the two thiols in mixture. Tetrachloroauric(III) acid trihydrate ($HAuCl_4 \cdot 3H_2O$), 1-dodecanethiol ($CH_3(CH_2)_{11}SH$, DDT), and 4-Aminophenyl disulfide ($(H_2NC_6H_4S\text{-})_2$, Ani2) were used as precursors and hereafter the synthetic procedures for the $Au/S_{DDT}/S_{Ani}$ = 1/4/2 molar ratio is described. Briefly, 25 mg of $HAuCl_4 \cdot 3H_2O$ (0.06 mmol) were solved in 2 mL H_2O_{up} in air

in a reaction flask (gold precursor solution concentration 0.03 M). 32.8 mg of TOAB (0.06 mmol) in 3 mL of toluene were added under vigorously stirring and after the quantitative transfer of the gold into the organic phase, the capping thiols (48.6 mg of DDT, 0.24 mmol, and 14.9 mg of Ani, 0.06 mmol, in 2.5 mL of toluene each) were added in mixture. The biphasic solution was degassed for 10 minutes with Argon and then 22.7 mg of $NaBH_4$ (0.6 mmol) in 2.5 mL H_2O_{up} were added to reduce Au^{III} to Au° and Ani2 to Ani, with the contemporary surface capping reaction. The colour of the solution shifted from yellow, $HAuCl_4$ only, to orange with TOAB, to white after the ligands were added, and finally dark brown following reduction of the gold. The reaction occurs for 2 hours, at room temperature, in the dark (4-Aminophenyl disulfide is light sensitive). After the 2 hours the entire aqueous phase was removed, and the organic phase with the AuNPs was washed with H_2O_{up} 5 times to remove by-products. To purify the AuNPs, almost all the toluene was evaporated from organic phase and 10 mL of ethanol was added, the suspension was transferred to centrifuge tube. Five centrifuges at 13400 rpm per 10 min were performed to remove unreacted thiols and by-products. The purified nanoparticles were suspended in organic solvent *i.e.* CH_2Cl_2, $CHCl_3$ or toluene.

Physical and spectral data of AuNPs-DDT-Ani. **UV–Vis** (CH_2Cl_2): λ_{SPR} = 512 nm; **DLS** (CH_2Cl_2): $\langle 2R_H \rangle = (4 \pm 1)$ nm; **FT-IR** (ATR, deposited on glass): 3350 (w), 3170 (w), 3042 (w), 2954 (s), 2916 (s), 2848 (s), 1616 (w), 1591 (w), 1493 (w), 1456, 1375, 1294, 1182, 800, 667; **yield**: 34 ± 5 % wt/wt

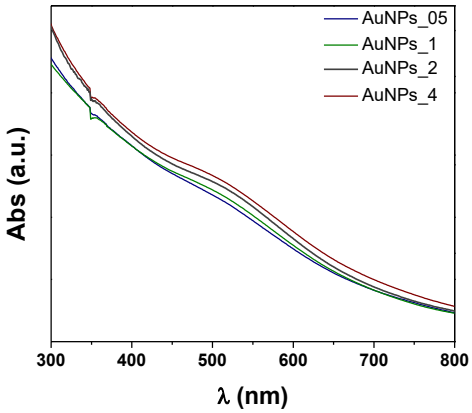

Figure C2. *UV-Vis spectra of AuNPs with different Au/S_{DDT}/S_{Ani} molar ratio: AuNPs_05 = 1/4/0.5, AuNPs_1 = 1/4/1, AuNPs_2 = 1/4/2, AuNPs_4 = 1/4/4.*

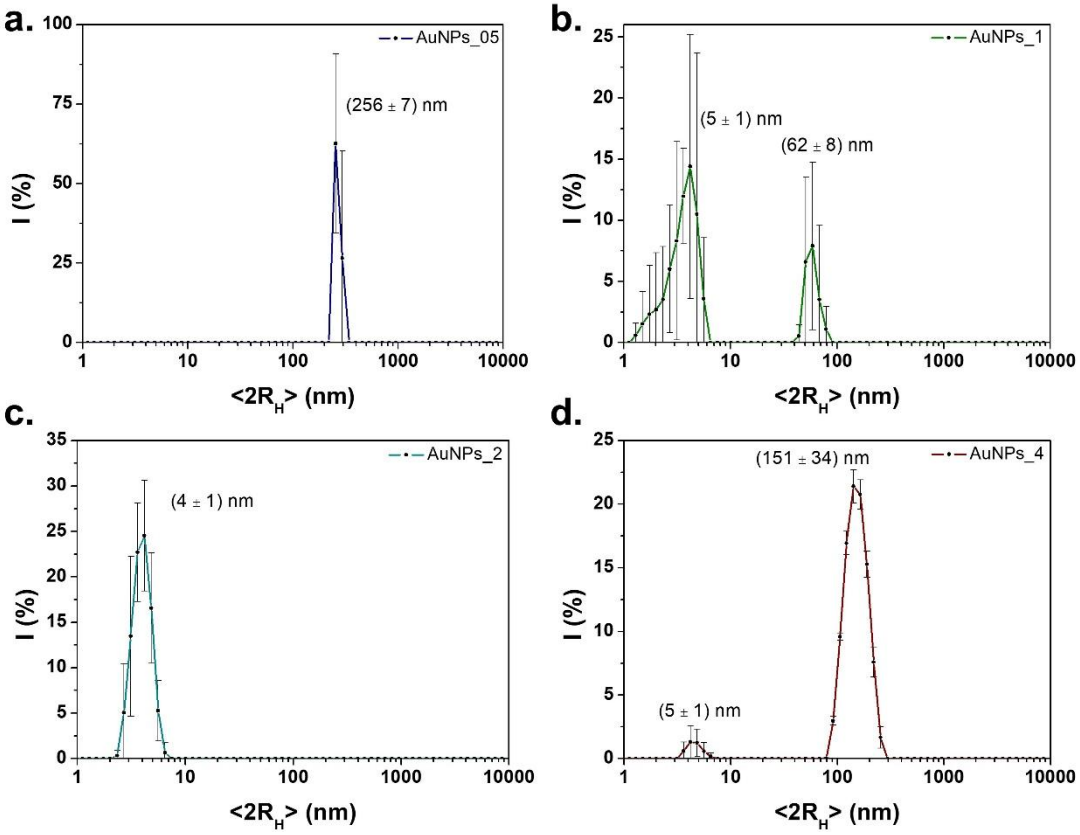

Figure C3. *DLS graphs of AuNPs with different Au/S_{DDT}/S_{Ani} molar ratio: a) AuNPs_05 = 1/4/0.5, <2R_H> = (256 ± 7) nm; b) AuNPs_1 = 1/4/1, <2R_H> = (5 ± 1) (62 ± 8) nm; c) AuNPs_2 = 1/4/2, <2R_H> = (4 ± 1) nm; d) AuNPs_4 = 1/4/4, <2R_H> = (5 ± 1) (151 ± 34) nm.*

ID Sample	Au/S_{DDT}/ S_{Ani} molar ratio	λ_{LSPR} (nm, DCM)	<2R_H> (nm, DCM)	Yield % wt/wt
AuNPs_05	1/4/0.5	515	(256 ± 7)	(29 ± 9)
AuNPs_1	1/4/1	515	(5 ± 1), (62 ± 8)	(39 ± 9)
AuNPs_2	**1/4/2**	**512**	**(4 ± 1)**	**(34 ± 5)**
AuNPs_4	1/4/4	512	(5 ± 1), (151 ± 34)	(18 ± 2)

Table C1. *AuNPs prepared with DDT and Ani functionalizing thiols and main characterizations.*

FT-IR		
Ani[314]	DDT	AuNPs
ν NH_2 3439	ν_{as} -CH_3 2954	ν NH_2 3350
ν NH_2 3358	ν_{as} -CH_2 2926	ν NH_2 3170
ν NH_2 3290	ν_s -CH_3 2872	ν C-H_{ar} 3042
ν C-H_{ar} 3026	ν_s -CH_2 2855	ν_{as} -CH_3 2954
ν S-H 2550	ν S-H 2575	ν_{as} -CH_2 2916
ν C-$H_{ar\ overtone}$ 1883	δ_s -CH_2 1466	ν_s -CH_2 2848
ν C-C_{ar} 1620	δ_{as} -CH_2 1377	ν C-C_{ar} 1616
ν C-C_{ar} 1595	ν C-S 654	ν C-C_{ar} 1591
ν C-C_{ar} 1494		ν C-C_{ar} 1493
ν C-N 1283		δ_{as} -CH_2 1456
ν S-C_{arom} 1090		δ_s -CH_2 1375
γ C-H_{Ar} 824		ν C-N 1260
		γ C-H_{Ar} 800
		ν C-S 667

Table C2. *FT-IR band assignments for Ani, DDT and AuNPs*

C2.2. Synthesis of Au-, Ag- and Pd-nanoparticles stabilized by PtDEBP

The gold, silver and palladium nanoparticles were prepared following a two-phase Schiffrin-Brust synthesis procedure. The molar ratio between the metal precursor and the PtDEBPligand was 4/1. The PdNPs synthesis is presented as a typical procedure: an aqueous solution of K_2PdCl_4 (67.9 mg, 0.206 mmol) ($AgNO_3$ for AgNPs and $HAuCl_4 \cdot 3H_2O$ for AuNPs) in deionized water (5 mL), was mixed with a solution of tetraoctylammonium bromide (TOAB) (134.8 mg, 0.251 mmol) in toluene (10 mL). The mixture was vigorously stirred until all the tetrachloropalladate was transferred into the organic phase and a solution of Pt-DEBP$(SCOCH_3)_2$ (80.2 mg, 0.052 mmol) in toluene (5 mL) was then added. The mixture was kept under Ar_2 flux for 15 minutes and an aqueous solution of $NaBH_4$ (77.8 mg, 2.06 mmol) in deionized water (5 mL) was added under vigorous stirring. The reaction mixture was stirred for 3 h at room temperature. Then, the organic phase was separated, washed with water (7 × 10 mL) and further purified by repetitive centrifugation steps (10 × 10 mL ethanol) at 13,400 rpm, 15 min. The solid precipitate was collected and dried *in vacuo*. Yield: PdNPs = 12% (calculated as PdNPs/K_2PdCl_4 weight ratio).

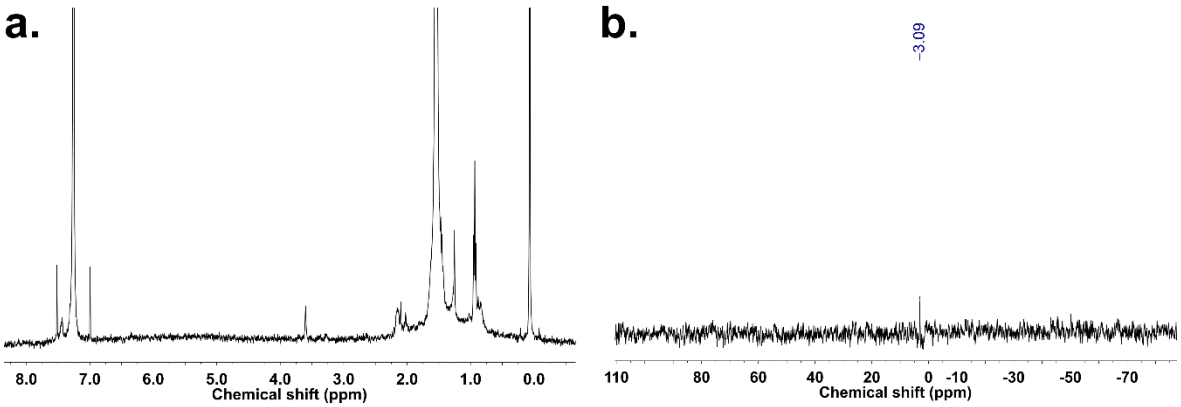

Figure C4. *a) ^{1}H-NMR spectrum of AuNPs-PtDEBP. b) ^{31}P-NMR of AuNPs-PtDEBP. (Denominations of the protons are shown in the structure inset in the NMR spectrum.)*

Sample	Signal	BE (eV)	FWHM (eV)	I ratio[a] (%)	Assignment
AuNPs	Au4f	83.87	1.01	68.48	Au(0)
		84.47	1.01	31.52	Au(δ^+)
	S2p	160.81	1.24	100	S-Au
	P2p	130.43	1.13	100	$P(Bu)_3$
AgNPs	Ag3d	367.99	1.07	69.50	Ag(0)
		368.59	1.07	30.50	Ag(δ^+)
	S2p	161.66	2.66	100	S-Ag
	P2p	131.65	1.36	100	$P(Bu)_3$
PdNPs	Pd3d	334.85	1.09	61.60	Pd(0)
		335.48	1.09	38.40	Pd(δ^+)
	S2p	161.23 162.97	1.66 1.66	76.98 23.02	S-Pd RS-H
	P2p	130.54	1.97	100	$P(Bu)_3$

Table C3*. XPS BE, FWHM, atomic ratio values and assignments collected on Au, Ag-, and PdNPs-Pt-DEBP. [a] I ratio = I_{peak}/I_{tot} signal for the selected element.*

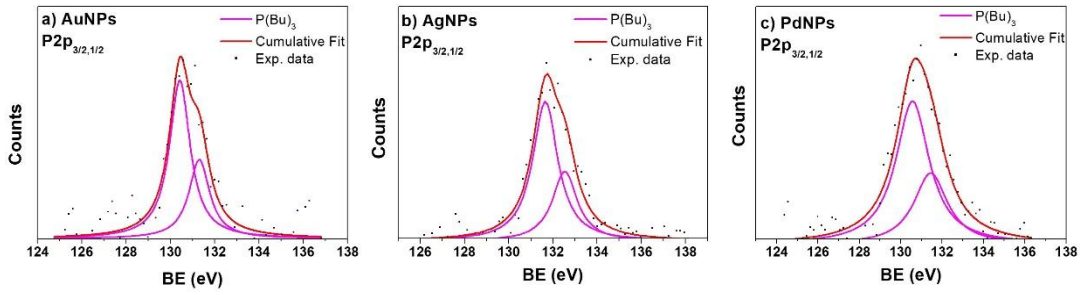

Figure C5. *P2p core level XPS spectra collected on a) AuNPs-Pt-DEBP, b) AgNPs-Pt-DEBP and c) PdNPs-Pt-DEBP.*

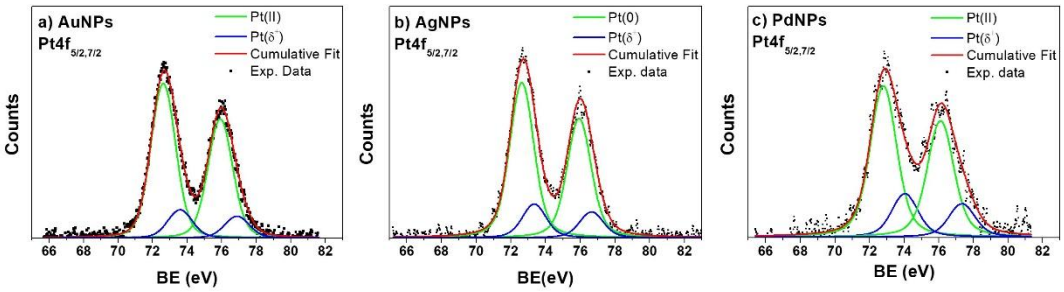

Figure C6. *Pt4f core level XPS spectra collected on a) AuNPs-Pt-DEBP, b) AgNPs-Pt-DEBP and c) PdNPs-Pt-DEBP.*

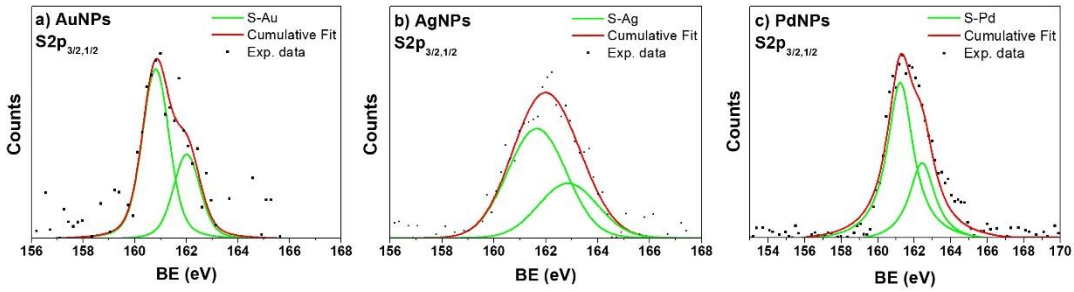

Figure C7. *S2p core level XPS spectra collected on a) AuNPs-Pt-DEBP, b) AgNPs-Pt-DEBP and c) PdNPs-Pt-DEBP.*

C2.3. Synthesis of AuNPs stabilized by FL, PtFL, DDT-FL, DDT-PtFL

In this work, four different AuNPs systems were synthesized: AuNPs functionalized with 9,9-didodecyl-2,7-bis(acetylthio)fluorene, AuNPs-FL, AuNPs functionalized 2,7-Bis[2-(trans-acetylthio-bis-(tributylphosphine)platinumII)ethynyl]-9,9-didodecyl-9H-fluorene, AuNPs-PtFL and two systems were functionalized with a bifunctional ligand in mixture with the monofunctional ligand 1-Dodecanethiol (DDT) *i.e.* AuNPs-FL-DDT, AuNPs-PtFL-DDT. AuNPs were obtained following a two-phase wet chemical reduction method using $HAuCl_4 \cdot 3H_2O$ as metallic precursor, tetraoctylammonium bromide (TOAB) as the phase transfer agent and sodium borohydride ($NaBH_4$) as the reducing agent. Thioesters or thioesters in mixture with DDT were used for a covalent stabilization of the colloids. Different molar ratio between metallic precursor and stabilizers were explored: Au/S molar ratio = 1/2 for AuNPs-FL and AuNPs-PtFL, and $Au/S_{FL}/S_{DDT}$ = 1/2/1 for AuNPs-DDT-FL $Au/S_{PtFL}/S_{DDT}$ = 1/1/1 for AuNPs-DDT-PtFL. Briefly in a round bottomed flask, a solution of $HAuCl_4 \cdot 3H_2O$ (50 mg, 0.127 mmol) in H_2O_{up} (5 mL) was mixed with a solution of TOAB (69 mg, 0.127 mmol) in toluene (10 mL). The mixture was vigorously stirred, then a thioester

solution (83 mg, 0.127 mmol, of FL or 241 mg, 0.127 mmol of PtFL, 0.127 mmol in 10 mL toluene) or a thioester solution (83 mg, 0.127 mmol, of FL or 121 mg, 0.064 mmol of PtFL in 5 mL of toluene) and DDT solution (26 mg, 0.127 mmol of DDT in 5 mL toluene) were added. The two-phase mixture was degassed for 10 minutes with Ar and then 48 mg of $NaBH_4$ (1.27 mmol) in 5 mL of H_2O_{up} were added under vigorous stirring to reduce Au^{III} to Au° and to hydrolyse the thioesters into thiols. The reaction mixture allowed to react for 3 h at room temperature. At the end, the organic phase was separated and washed with water. The organic phase was reduced under vacuum and 20 mL of ethanol were added. The mixture was centrifuged at 10000 rpm for 15 min (×10) to remove excess of reagents and byproducts. After removal of the supernatant, nanoparticles suspension was obtained with 10 mL of DCM.

AuNPs-FL

Physical properties and spectral data: **UV–vis** (CH_2Cl_2), λ = 330, 520 (max) nm; **<2R_H>** (DLS, CH_2Cl_2): (16 ± 8), (113 ± 29) nm; PDI (0.125 ± 0.009) **FTIR** (film from CH_2Cl_2) = $\bar{\nu}$ (cm^{-1}):: 3061 (w, $(–CH)_{Ar}$), 2955 (s; $\nu_{as}(–CH_3)$), 2922 (s; $\nu_{as}(– CH_2)$), 2851 (s; $\nu_s(–CH_2)$), 1712, 1695 (s; ν(C=O)), 1597 (w; $\nu(CC)_{Ar}$), 1450 (s, $\delta_s(–CH_2)$), 1404 (m; $\delta(–CH_3)$, $\gamma(–CH_2)$), 1377 (m; $\delta(–CH_3)$, $\gamma(–CH_2)$), 1259 (m; ν_{as}(C–C–C), 1005 (s; in-plane δ(=CH)), 885 (m; def. modes $(CC)_{Ar}$), 808 (s; def. modes $(CC)_{Ar}$), 721 (m, out-of-plane $\delta(–CH)_{Ar}$), 615 (s, ν(=C–S)). **yield**: (59 ± 2) % wt/wt.

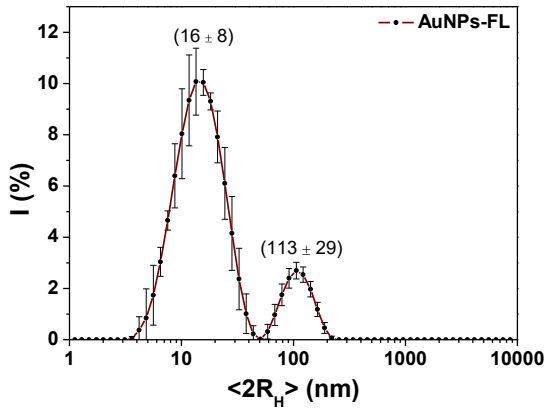

Figure C8. *DLS graph of AuNPs-FL in CH_2Cl_2.*

AuNPs-PtFL

Physical properties and spectral data: **UV–vis** (DMF), λ = 357, 540 (max) nm; **<2R$_H$>** (DLS, DMF): (69 ± 35) nm; PDI (0.353 ± 0.009), **FTIR** (film from CH_2Cl_2) = $\bar{\nu}$ (cm^{-1}): 2957 (s; ν_{as} (-CH_3)), 2926 (s; ν_{as} (-CH_2)), 2855 (s; ν_s (-CH_2)), 2098 (s; ν (C≡C)), 1603 (w; ν (C-C)$_{Ar}$), 1462 (s; δ (-CH_2)), 1414 (m; δ (-CH_3) γ (-CH_2)), 1377 (m; δ (-CH_3) γ (-CH_2)), 1261 (m; ν_{as} (C-C-C)), 1092 (s; δ (=CH), 904 (m; def. modes (CC)$_{Ar}$), 800 (s; def. modes (CC)$_{Ar}$), 721 (m, out-of-plane δ(–CH)$_{Ar}$).

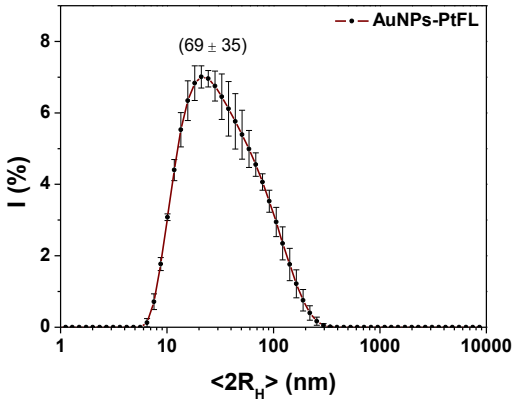

Figure C9. *DLS graph of AuNPs-PtFL in CH_2Cl_2.*

AuNPs-FL-DDT

Physical properties and spectral data: **UV–vis** (CH_2Cl_2), λ = 336, 515 (max) nm; **<2R$_H$>** (DLS, CH_2Cl_2): (2.0 ± 0.4), (10 ± 4), (38 ± 14) nm; PDI (0.443 ± 0.179); **FTIR** (film from CH_2Cl_2): ν = 3070 (w, (–CH)$_{Ar}$), 2959 (s; ν_{as}(–CH_3)), 2924 (s; ν_{as}(– CH_2)), 2853 (s; ν_s(–CH_2)), 1697 (s; ν(C=O)), 1454 (s, δ_s(–CH_2)), 1417 (m; δ(–CH_3), γ(–CH_2)), 1261 (m; ν_{as}(C–C–C), 1095 (s; in-plane δ(=CH)), 1016 (s; in-plane δ(=CH)), 800 (s; def. modes (CC)$_{Ar}$), 721 (m, out-of-plane δ(–CH)$_{Ar}$), 658 (s; ν (-$C_{aliphtic}$-S)). 626 (s, ν(=$C_{aromatic}$–S)); **TEM** (film from CH_2Cl_2): <2R> = (2.7 ± 0.6) nm; interparticle distance (1.3 ± 0.3) nm; **yield**: 79 % wt/wt

AuNPs-PtFL-DDT

Physical properties and spectral data: **UV–vis** (CH_2Cl_2), λ = 385, 530 (max) nm; **<2R$_H$>** (DLS, CH_2Cl_2): (4 ± 1), (33 ± 9) nm; PDI (0.844 ± 0.137); **FTIR** (film from CH_2Cl_2): $\bar{\nu}$ (cm^{-1}): 3051 (w; (-CH)$_{Ar}$), 2957 (s; ν_{as} (-CH_3)), 2924 (s; ν_{as} (-CH_2)), 2853 (s; ν_s (-CH_2)), 2099 (s; ν (C≡C)), 1462 (s; δ (-CH_2)), 1417 (m; δ (-CH_3) γ (-CH_2)), 1377 (m; δ (-CH_3) γ (-CH_2)), 1262 (m; ν_{as} (C-C-C)), 1093 (s; δ (=CH), 1005 (s; in-plane δ(=CH)), 906 (m; def. modes

$(CC)_{Ar}$), 802 (s; def. modes $(CC)_{Ar}$), 721 (m, out-of-plane δ(–CH)$_{Ar}$) 664 (ν (C-S)); **TEM** (film from CH_2Cl_2): <2R> = (3.6 ± 1.0) nm; interparticle distance (1.6 ± 0.5) nm.

C2.4. Synthesis of AuNPs stabilized by FL and 2AET

Hydrophobic gold nanoparticles were synthesized using a modified two-phase Brust-Shiffrin procedure. $HAuCl_4$ (0.0500 g, $1.27 \cdot 10^{-4}$ mol) was dissolved in 5 mL of H_2O_{up} and mixed with 0.0694 g of TOAB as phase-transfer agent solubilized in 5 mL of toluene ($HAuCl_4$:TOAB 1:1 mol/mol). The aqueous/toluene mixture was stirred for 5 min to allow the complete transfer of $[(CH_3(CH_2)_7)_4N]^+$ $[AuCl_4]^-$ complex in the organic phase. Then, the FL thioacetate ligand and the 2AET dye were dissolved in 5 mL of toluene (each) and added to the reaction mixture with different molar ratios between reagents $HAuCl_4$/2AET/FL: 1:0.5:0.5 (AuNPs-2AET-FL_1), 1:0.5:1 (AuNPs-2AET-FL_2), and 1:0.5:2 (AuNPs-2AET-FL_4). The reaction was degassed under Ar flux for 15 min, and 0.0480 g of $NaBH_4$ ($1.27 \cdot 10^{-3}$ mol, $HAuCl_4$:$NaBH_4$ 1:10 mol/mol) in 5 mL of H_2O_{up} were injected dropwise with a syringe to achieve gold precursor reduction in the presence of thiols as functionalizing agents. The synthesis mixture was vigorously stirred for 3 hours at room temperature, turning from orange to dark brown. In the end, the crude mixture was transferred into a separatory funnel and repeatedly washed with brine (5× ca. 10 mL). The organic phase was separated and removed by a rotary evaporator. The as-synthesized thiol-functionalized AuNPs were recovered with 20 mL of ethanol, split into centrifuge tubes, and purified by repeated centrifuges (4×, 10 000 rpm, 9503 g, 10 min, +8 °C). After purification steps, ethanol was removed under reduced pressure, and nanoparticles were redispersed in CH_2Cl_2 for further use.

Physical properties and spectral data of AuNPs-2AET-FL_1. **UV–Vis** (CH_2Cl_2): λ_{SPR} = 533 nm (fresh), 630 nm (aged, 1 year); **PL** (CH_2Cl_2): λ_{ex} = 333 nm, λ_{em} = 362, 395, 418 (max), 440 nm, λ_{ex} = 370 nm, λ_{em} = 398, 418 (max), 440 nm; **FT-IR** (KRS-5): ν = 3061 (w, (–CH) aromatic), 2955 (w; ν_{as}(–CH_2)), 2926 (s; ν_{as}(–CH_2)), 2852 (m; ν_s(–CH_2)), 1731 (m; ν(C=O)), 1671 (m; ν(CC) Ar), 1592 (m; ν(CC) Ar), 1490 (w; ν(CC) Ar), 1461 (s; δ_s(–CH_2)), 1406 (w; δ(–CH_3), γ(–CH_2)), 1377 (w; δ(–CH_3), γ(–CH_2)), 1262 (m; ν_{as}(C–C–C), 1095 (m; *in-plane* δ(=CH)), 1032 (s; *in-plane* δ(=CH)), 886 (w; def. modes (CC) Ar), 807 (s; def. modes (CC) Ar), 733 (m, *out-of-plane* δ(–CH) Ar), 663 (w, ν(C–S)); 616 (w, ν(=C–S)); **Far-IR** (PE, i-PrOH): ν = 590 (w; *in-plane* ring deformation mode), 521 (w; *out-of-plane* ring deformation), 485 (w; *in-plane* ring deformation mode), 415 (w; *out-of-plane* C–C

deformation), 377 (w, ρ(–CH_2)), 326 (w; ring *in-plane* bending), 309 (w, –S–C–C deformation), 280 (m; ρ(–CH_2)), 243 (m; ν(Au–S)); <$2R_H$> (**DLS**, CH_2Cl_2): (12 ± 2) nm; (60 ± 25) nm; (185 ± 65) nm; yield: 34%w/w. Yield was calculated as gold nanoparticles/gold precursor weight ratio.

Physical properties and spectral data of AuNPs-2AET-FL_2. **UV–Vis** (CH_2Cl_2): λ_{SPR} = 533 nm (fresh), 545 nm (aged, 1 year); **PL** (CH_2Cl_2): λ_{ex} = 333 nm, λ_{em} = 345, 362 (max), 377, 408 (tail) nm, λ_{ex} = 370 nm, λ_{em} =394, 415 (max), 440 nm; **FT-IR** (KRS-5): ν = 3061 (w, (–CH) aromatic), 2955 (w; ν_{as}(–CH_2)), 2926 (s; ν_{as}(–CH_2)), 2852 (m; ν_s(–CH_2)), 1710 (m; ν(C=O)), 1663 (m; ν(CC) Ar), 1594 (m; ν(CC) Ar), 1482 (w; ν(CC) Ar), 1465 (s; δ_s(–CH_2)), 1403 (w; δ(–CH_3), γ(–CH_2)), 1381 (w; δ(–CH_3), γ(–CH_2)), 1260 (m; ν_{as}(C–C–C), 1093 (m; *in-plane* δ(=CH)), 1020 (s; *in-plane* δ(=CH)), 880 (w; def. modes (CC) Ar), 805 (m; def. modes (CC) Ar), 735 (w, *out-of-plane* δ(–CH) Ar), 654 (w, ν(C–S)); 613 (w, ν(=C–S)); **Far-IR** (PE, i-PrOH): ν = 587 (w; *in-plane* ring deformation mode), 523 (w; *out-of-plane* ring deformation), 477 (w; *in-plane* ring deformation mode), 385 (w, ρ(–CH_2)), 326 (w; ring *in-plane* bending), 288 (w; ρ(–CH_2)), 242 (m; ν(Au–S)); <$2R_H$> (**DLS**, CH_2Cl_2): (30 ± 5) nm; (68 ± 15) nm; (260 ± 70) nm; yield: 34%wt. Yield was calculated as gold nanoparticles/gold precursor weight ratio.

Physical properties and spectral data of AuNPs-2AET-FL_4. **UV–Vis** (CH_2Cl_2): λ_{SPR} = 533 nm (fresh), 620 nm (aged, 1 year); **PL** (CH_2Cl_2): λ_{ex} = 333 nm, λ_{em} = 345, 362 (max), 377, 408 (tail) nm, λ_{ex} = 370 nm, λ_{em} = 394, 415 (max), 440 nm; **FT-IR** (KRS-5): ν = 3058 (w, (–CH) aromatic), 2955 (w; ν_{as}(–CH_2)), 2926 (s; ν_{as}(–CH_2)), 2852 (m; ν_s(–CH_2)), 1732 (m; ν(C=O)), 1669 (m; ν(CC) Ar), 1595 (m; ν(CC) Ar), 1490 (w; ν(CC) Ar), 1461 (s; δ_s(–CH_2)), 1404 (w; δ(–CH_3), γ(–CH_2)), 1377 (w; δ(–CH_3), γ(–CH_2)), 1260 (m; ν_{as}(C–C–C), 1099 (m; *in-plane* δ(=CH)), 1032 (s; *in-plane* δ(=CH)), 883 (w; def. modes (CC) Ar), 805 (s; def. modes (CC) Ar), 730 (m, *out-of-plane* δ(–CH) Ar), 661 (w, ν(C–S)); 605 (w, ν(=C–S)); **Far-IR** (PE, i-PrOH): ν = 573 (w; *in-plane* ring deformation mode), 539 (w; *out-of-plane* ring deformation), 482 (w; *in-plane* ring deformation mode), 326 (w; ring *in-plane* bending), 309 (w, –S–C–C deformation), 278 (w; ρ(–CH_2)), 241 (m; ν(Au–S)); <$2R_H$> (**DLS**, CH_2Cl_2): (3 ± 1) nm; (37 ± 5) nm; (205 ± 30) nm; yield: 20%w/w. Yield was calculated as gold nanoparticles/gold precursor weight ratio.

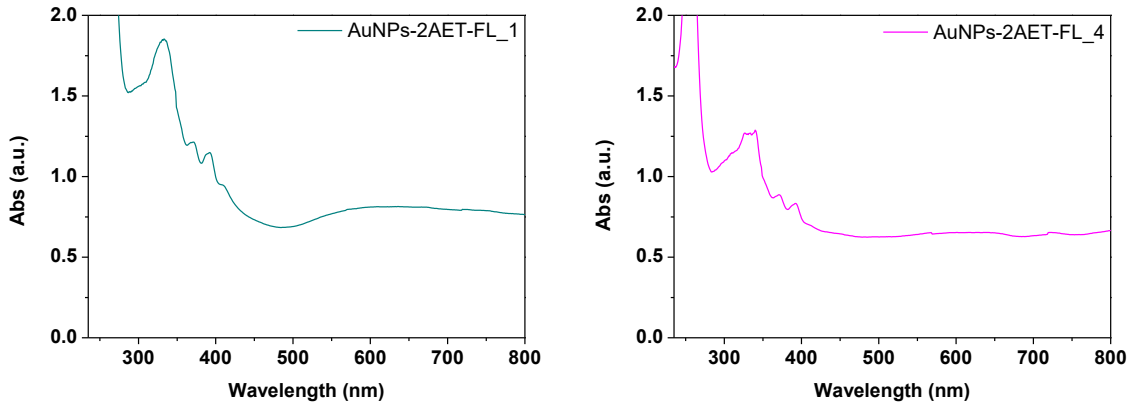

Figure C8. *UV-Visible spectra of AuNPs after one year aging of a) AuNPs-2AET-FL_1 and b) AuNPs-2AET-FL_4.*

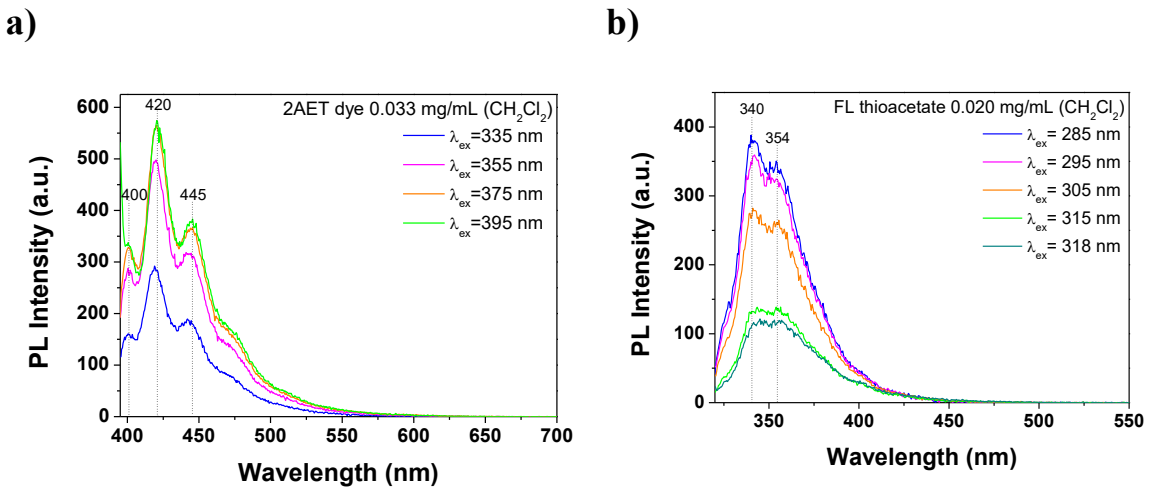

Figure C9. *a) Excitation-Emission Matrix photoluminescence spectra (λ_{ex} = 335-395 nm) of 2AET in CH_2Cl_2 at concentration 0.033 mg/mL; b) Excitation-Emission Matrix photoluminescence spectra (λ_{ex} = 295-318 nm) of FL in CH_2Cl_2 at concentration 0.020 mg/mL*

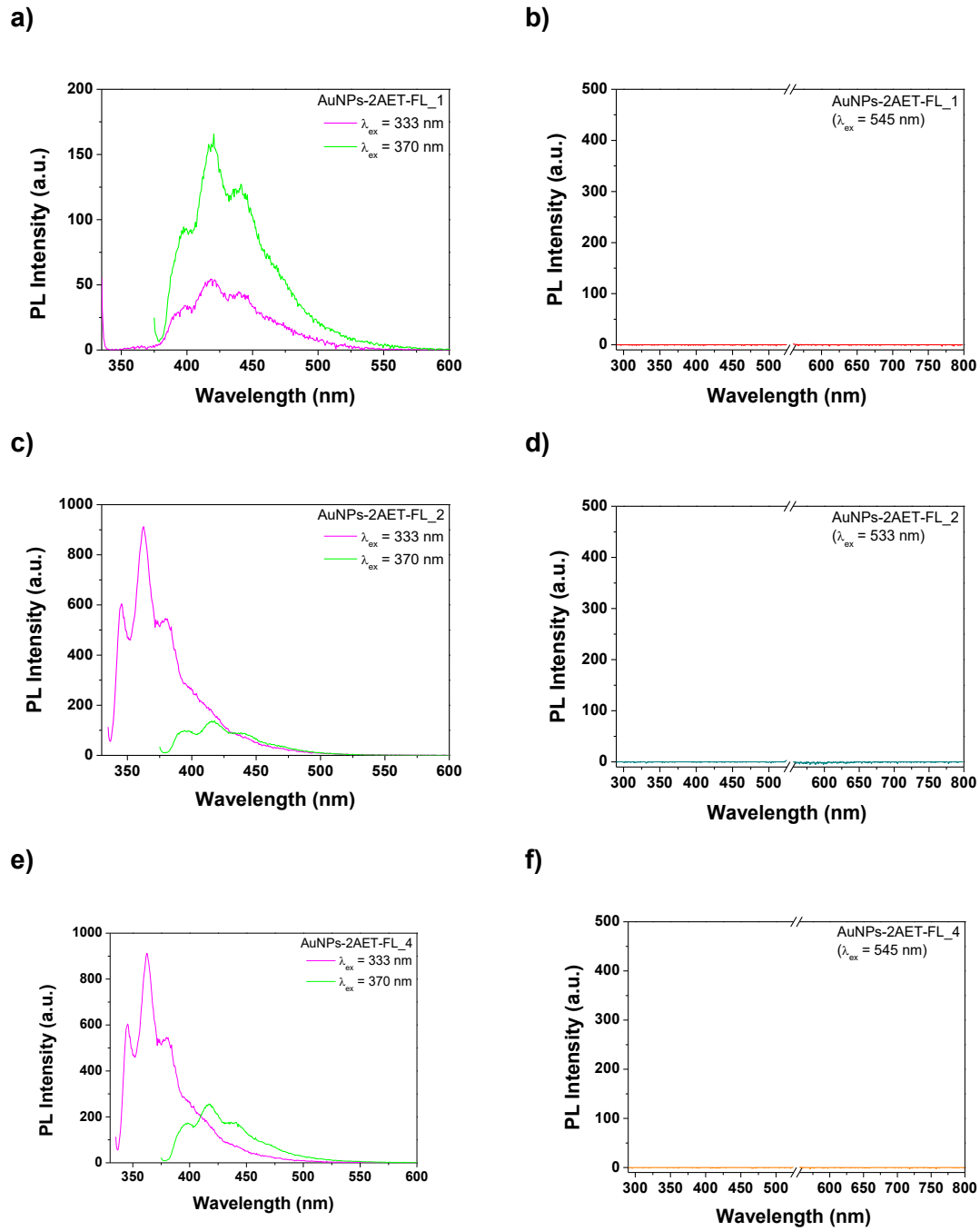

Figure C10. *Photoluminescence spectra in CH_2Cl_2 of a) AuNPs-2AET-FL_1 (λ_{ex}=333 nm, 370 nm). b) AuNPs-2AET-FL_1 (λ_{ex}=545 nm). c) AuNPs-2AET-FL_2 (λ_{ex}=333 nm, 370 nm). d) AuNPs-2AET-FL_2 (λ_{ex}=533 nm). e) AuNPs-2AET-FL_4 (λ_{ex}=333 nm, 370 nm). f) AuNPs-2AET-FL_4 (λ_{ex}=545 nm).*

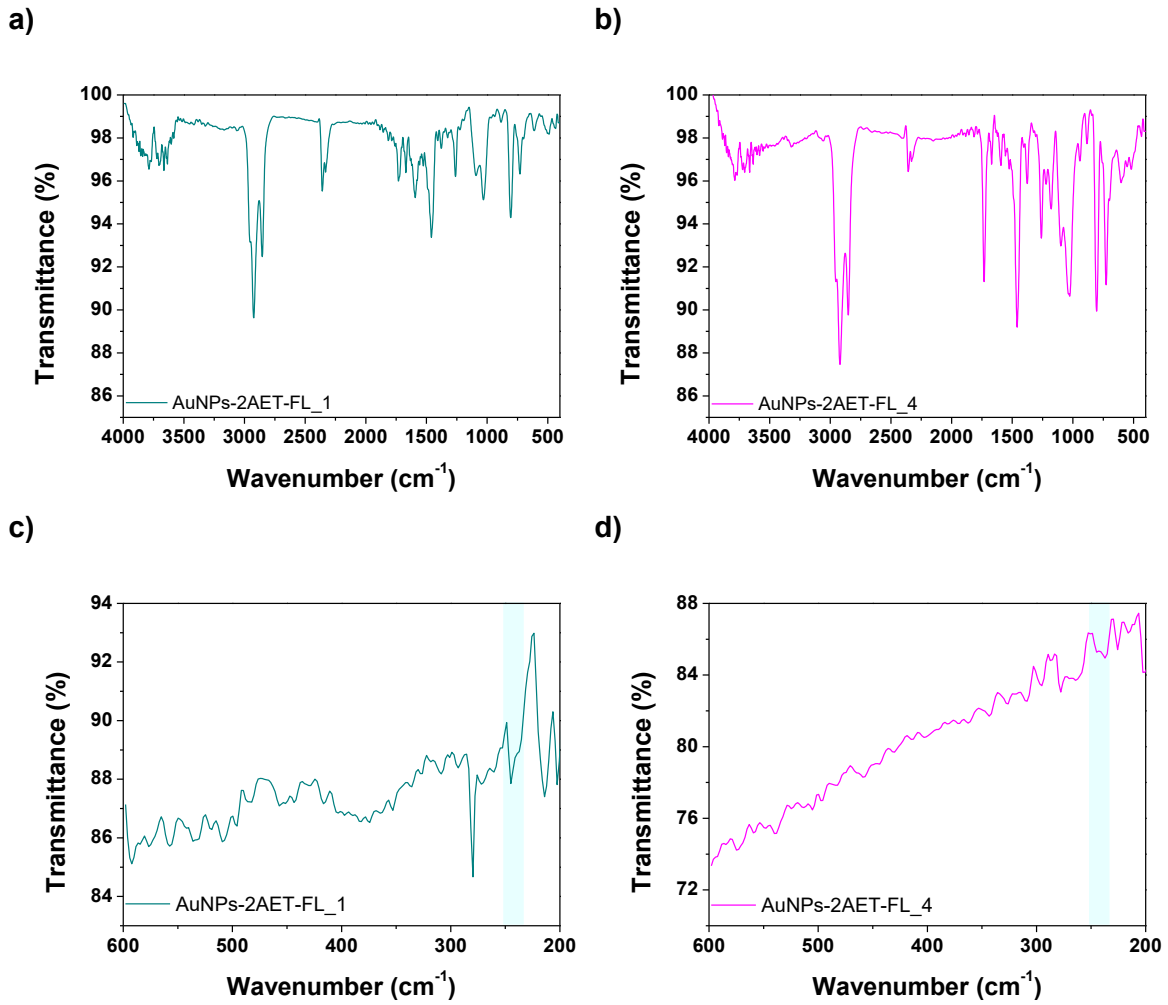

Figure C11. *a) FTIR in transmittance mode of AuNPs-2AET-FL_1 on KRS-5, film from CH_2Cl_2. b) FTIR in transmittance mode of AuNPs-2AET-FL_4 on KRS-5, film from CH_2Cl_2. c) Far-IR spectrum of AuNPs-2AET-FL_1 on polyethylene (PE) disk, film from i-PrOH. Au–S stretching vibration at ca. 242 cm^{-1} is evidenced. d) Far-IR spectrum of AuNPs-2AET-FL_4 on polyethylene (PE) disk, film from i-PrOH. Au–S stretching vibration at ca. 242 cm^{-1} is evidenced.*

Signal	Assignment	FWHM	BE (eV)	Internal Atomic Ratios (%)
C1s	C=C, C-S	1.50	284.7	95
	C-O		286.8	3
	COOH		288.9	2
S2p	Au-S	1.41	161.4	18
	-SH		163.0	21
	S_{ox}		168.1	9
	S_{ox}		169.4	14
	S_{ox}		171.6	38
Au4f	Au(0)	0.76	83.0	84
	Au(δ+)		83.7	16

Table C4. *SR-XPS data collected on AuNPs-2AET-FL_2: assignments, FWHM and Binding energies (BE) values.*

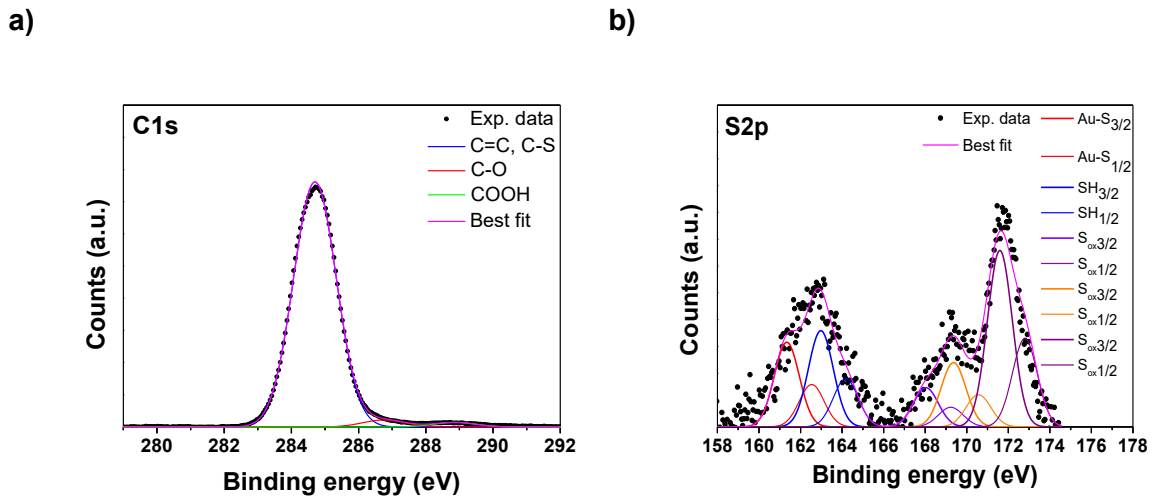

Figure C12. *SR-XPS spectra of AuNPs-2AET-FL_2 at: a) C1s core level and b) S2p core level.*

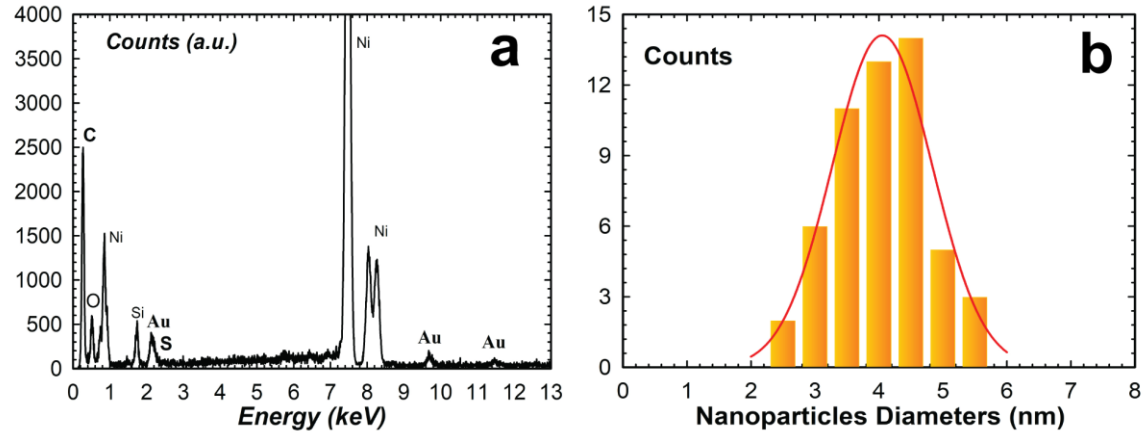

Figure C13. *Morpho-chemical characterizations of AuNPs-2AET-FL_2. a) EDX spectral image taken from Figure 3c. b) Plot showing the frequency distribution of the nanoparticle size histogram.*

C2.5. Synthesis of AuNPs stabilized by $PtDEBP_n$

AuNPs capped with the organometallic complex Pt-$DEBP_n$ (n=3, 4, 6) were synthesized. The AuNPs-$PtDEBP_3$ synthesis is reported as a typical procedure: an aqueous solution of $HAuCl_4$ (0.100 g, $2.54 \cdot 10^{-4}$ mol) in ultrapure water (10 mL) was mixed with a solution of tetraoctylammonium bromide (TOAB) ($2.54 \cdot 10^{-4}$ mol, Au/TOAB 1/1 molar ratio) in toluene (20 mL). The two-phase mixture was vigorously stirred until all the metal ion precursor was transferred into the organic layer. Subsequently, a solution of Pt-$DEBP_3$ ($6.387 \cdot 10^{-5}$ mol, Au/S 1/1 molar ratio) dissolved in 20 mL of toluene was added. The mixture was kept under Ar atmosphere for 15 minutes, then an aqueous solution of sodium borohydride ($2.54 \cdot 10^{-3}$ mol, Au/$NaBH_4$ 1/10 molar ratio) in ultrapure water (10 mL) was added under vigorous stirring. After further stirring for 3h at room temperature, the aqueous phase was discarded, and the organic phase separated and washed repeatedly with fresh water. The organic phase was reduced to 2 mL in a rotary evaporator, and 40 mL of ethanol were added. The mixture was kept overnight at -18 °C and then centrifuged at 10,000 rpm for 15 min to remove the solvent, while the precipitate was repeatedly washed with ethanol by centrifugation at 13,400 rpm (17,063 ×g) for 10 min. After purification, the colloidal precipitate was redispersed in dichloromethane, obtaining a ruby red suspension of Pt-DEBP-capped AuNPs.

C2.6. Synthesis of AuNPs stabilized by FL and 4BBT

AuNPs functionalised with FL and 4BBT (AuNPs-FL-4BBT) were obtained *via* the two phase Schiffrin–Brust method, as described below. Briefly, 0.1000 g (2.54×10^{-4} mol) of

$HAuCl_4 \cdot 3H_2O$ were dissolved in 5 mL of deionised water and put in a two-neck round-bottom flask under vigorous stirring at room temperature. The reagents were added in the following order: 0.1670 g (3.05×10^{-4} mol) of TOAB dissolved in 10 mL of toluene, 0.0827 g (1.27×10^{-4} mol) of FL in 10 mL of toluene, and 0.0240 g (1.27×10^{-4} mol) of 4BBT in 10 mL of toluene. Sodium borohydride (0.0965 g, 2.54×10^{-3} mol), dissolved in 5 mL of deionised water, was then added under an inert atmosphere to reduce Au^{3+} to Au^0. The colour of the solution shifted from yellow ($HAuCl_4$ only) to orange with TOAB, white after the ligands were added, and finally dark brown following reduction of the gold. The solution was stirred for 3 h before the purification processes. First, the product was purified *via* extractions in a separating funnel (5 times) to eliminate water soluble by-products, and the aqueous phase was discarded; the organic phase was then reduced *via* rotary evaporation. Subsequently, the product was dissolved in ethanol and centrifuged (*ca.* 15 times) to further eliminate unwanted products, and the purified nanoparticles were dissolved in DCM.

Physical properties and spectral data of AuNPs-4BBT-FL: **UV-Vis** (CH_2Cl_2): λ_{LSPR} = 523 nm; **FT-IR** (film from CH_2Cl_2): 3000-2800 cm^{-1}, sp^3 CH stretching; 615 cm^{-1}, C-S stretching; 813 cm^{-1}, aromatic CH out of plane bending; 480 cm^{-1}, C-Br stretching. DLS (CH_2Cl_2): $\langle 2R_H \rangle$ = (44 ± 24) nm.

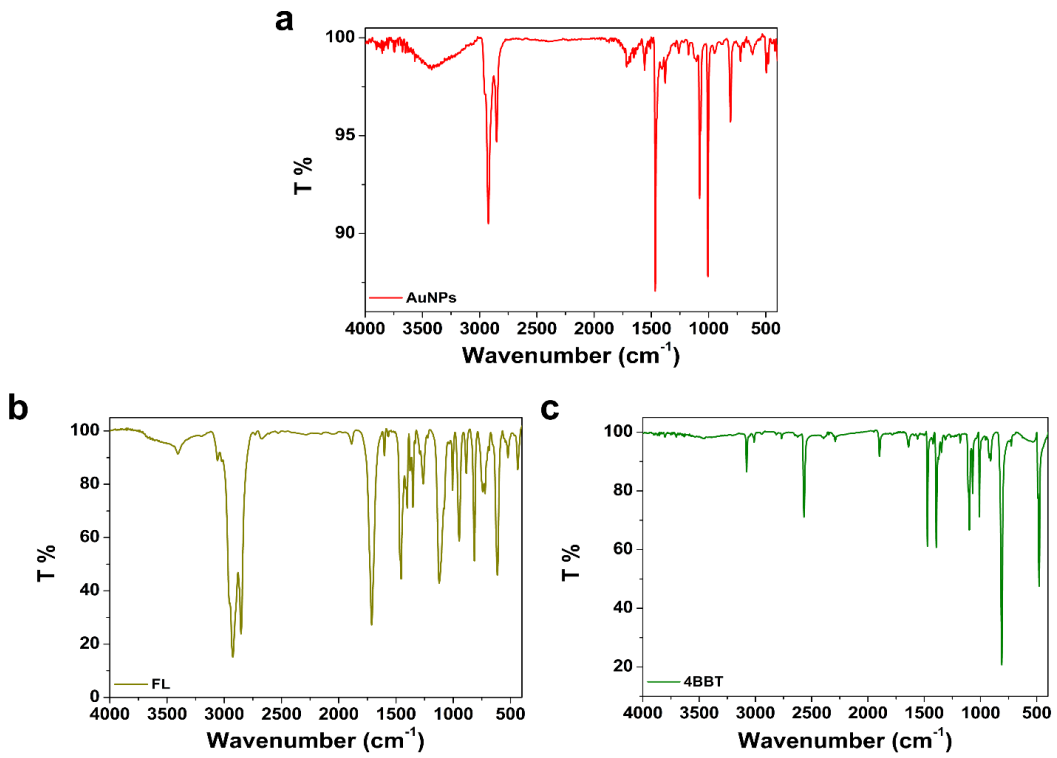

Figure C14. *Infrared spectra of a) AuNPs, b) FL and c) 4BBT. Deposited from CH_2Cl_2 film.*

C2.7. Synthesis of AuNPs stabilized by PCP_1 or PCP_2

Gold nanoparticles functionalised with thiol derivate of [2.2]paracyclophane were synthesized using a modified Brust's two-phase method. Briefly, 25 mg of $HAuCl_4 \cdot 3H_2O$ (0.06 mmol) were solved in 2 mL H_2O_{up} in air in a reaction flask (gold precursor solution concentration 0.03 M). 32.8 mg of TOAB (0.06 mmol) in 3 mL of toluene were added under vigorously stirring and after the quantitative transfer of the gold into the organic phase, the capping thiol (15.3 mg of PCP_1 or 16.1 mg of PCP_2) was added. The biphasic solution was degassed for 10 minutes with Argon and then 22.7 mg of $NaBH_4$ (0.6 mmol) in 2.5 mL H_2O_{up} were added to reduce Au^{III} to Au°. The reaction occurs for 2 hours, at room temperature. After the 2 hours the entire aqueous phase was removed, and the organic phase with the AuNPs was washed with H_2O_{up} 5 times to remove by-products. To purify the AuNPs, almost all the toluene was evaporated from organic phase and 10 mL of ethanol was added, the suspension was transferred to centrifuge tube. Six centrifuges at 13400 rpm per 10 min were performed to remove unreacted thiols and by-products. The purified nanoparticles were suspended in CH_2Cl_2.

AuNPs-PCP_1: the nanoparticles aggregate during the synthesis

AuNPs-PCP_2 rac

Physical and spectral data. **UV–Vis** (CH_2Cl_2): λ_{SPR} = 515 nm; **DLS** (CH_2Cl_2): $\langle 2R_H \rangle$ = (4 ± 1) (125 ± 2) nm; **FT-IR** (ATR, deposited on glass): 2963, 2922, 2850, 1730, 1593, 1450, 1411, 1259, 794; **yield**: 45 % wt/wt

AuNPs-PCP_2 Rp

Physical and spectral data. **UV–Vis** (CH_2Cl_2): λ_{SPR} = 515 nm; **DLS** (CH_2Cl_2): $\langle 2R_H \rangle$ = (4 ± 1) (376 ± 90) nm; **FT-IR** (ATR, deposited on glass): 3026, 2954, 2920, 2850, 1732, 1686, 1591, 1487, 1450, 1411,1259, 867, 795, 715, 632; **yield**: 49 % wt/wt

AuNPs-PCP_2 Sp

Physical and spectral data. **UV–Vis** (CH_2Cl_2): λ_{SPR} = 515 nm; **DLS** (CH_2Cl_2): $\langle 2R_H \rangle$ = (4 ± 1) (159 ± 11) nm; **FT-IR** (ATR, deposited on glass): 3026, 2964, 2922, 2850, 1732, 1686, 1591, 1454, 1411,1259, 796, 717, 632; **yield**: 31 % wt/wt

Appendix D

D1. Other procedures with Hydrophilic Nanoparticles

D1.1. μ-liquid jet XPS technique

The XPS μ-LJ measurements were performed at the French synchrotron radiation facility SOLEIL (Paris, France) at the PLÉIADES beamline. The liquid samples are injected into an evacuated experimental chamber through a 28 μm diameter glass capillary and collected by a heated copper-beryllium catcher, and electrons collected by a 300 μm stainless-steel skimmer. The liquid was injected into the glass capillary through a non-conductive PEEK line and pushed into the system using either an HPLC pump for all solutions without nanoparticles or a set of two Cetoni Nemesys Mid-pressure syringe pumps operating in continuous flow mode. The switch between the two systems is operated *via* a USB controlled high pressure valve (Rheodyne MXP790II). The spectra were collected with a hemispherical electron analyser VG-Scienta R4000 with LV polarization, with lens axis of the electron spectrometer parallel to the polarization vector of the light. Pass energy of the electron analyser, monochromator slit, resolution and energy beam data are reported in table S1. XPS liquid-jet measurements were carried out at the C 1s, N 1s, S 2p and Au 4f edges using 400, 600 and 625 eV photon energy. The spectra at 400 eV were energy referenced to the $1b_1$ peak of the liquid-phase water in the valence band spectrum, fixed at 11.16 eV[315]. For the spectra at 800 eV, calibration was made referring to the O1s component (BE = 538.1 eV)[316] of liquid-phase water. XPS μ-LJ data (BE, FWHM, atomic ratios) are reported in Table D2. It is important to emphasize that absolute BE values of XPS μ-LJ data differ from those obtained *via* solid-state XPS measurements due to the different calibration energy scale, *i.e.*, solid state spectra were calibrated using the C 1s signal of aliphatic C atoms having a BE = 285.0 eV, whereas in the case of XPS μ-LJ data calibration were done according to Winter *et al.*.[315, 316] Due to differences in absolute BE values, in the present study, we refer to spectral energy shifts (core-level energy shifts, ΔBE) of photoemission peaks. The spectra at 400 eV were energy referenced to the $1b_1$ peak of the liquid-phase water in the valence band spectrum, fixed at 11.16 eV[315]. For the spectra at 600 eV, calibration was made referring to the O1s component (BE = 538.1 eV)[316] of liquid-phase water.

Sample	Region	Pass energy (eV)	Spectral range (eV)	Photon energy (eV)	Monochromator slit	Photon resolution (meV)
DEA, pH 3.5, native	C1s	50	202-216	399.99	600	95.356
DEA, pH 3.5, native	S2p	50	320-340	400.01	600	95.366
DEA, pH 3.5, native	N1s	50	287-297	600.01	600	171.07
DEA, pH 5	C1s	50	202-216	400.00	600	95.363
DEA, pH 5	S2p	50	320-240	400.01	600	95.36
DEA, pH 5	N1s	50	287-297	599.96	600	171.05
DEA, pH 9	C1s	50	202-216	400.00	600	95.361
DEA, pH 9	S2p	50	320-340	400.00	600	95.361
DEA, pH 9	N1s	50	288-300	599.99	600	171.06
AuNPs, pH 5 native	Au 4f	100	526-540	625	600	182.61
AuNPs, pH 5native	S2p	100	221-237	400.01	600	95.365
AuNPs, pH 5 native	C1s	100	104-116	400	600	95.36
MIX pH 4.25, native	S2p	50	320-340	400	600	95.36

MIX pH 4.25, native	C1s	50	202-216	400.01	600	95.365
MIX pH 4.25, native	N1s	50	287-297	600.01	600	171.07
3MPS pH 2.9, native	S2p	100	220-237	399.98	600	40.421
3MPS pH 2.9, native	C1s	100	106-114	399.98	600	40.422
3MPS pH 10.25	C1s	100	105-113	400	600	40.424
3MPS pH 10.25	S2p	100	220-237	400	600	40.423
3MPS pH 5.44	S2p	100	221-236	400.00	600	40.424
3MPS pH 5.44	C1s	100	106-113	400.00	600	40.423

Table D1. XPS μ-LJ experimental parameter thiols and AuNPs.

Sample	Signal	BE (eV)	FWHM (eV)	Atomic ratio % (exp)	Assignment	Chemical shift
DEA native pH (3.5)	C1s 400eV	291.4 290.2	1.25 1.25	59% 41%	C-N C-C, C-S	1.2
	N1s 600eV	406.9	1.27		$N\text{-}R_3H^+$	
	S2p $_{3/2}$ 400eV	168.8	1.11		-SH	
DEA pH 5	C1s 400ev	291.4 290.3	1.24 1.24	59% 41%	C-N C-C, C-S	1.1

	S2p $_{3/2}$ 400eV	168.8	1.08		-SH	
	N1s 600eV	407.0	1.33		N-R_3H^+	
DEA pH 9	C1s 400eV	291.4 290.6 289.9	0.96 0.96 0.96	5% 64% 31%	C oxidized C-N C-C, C-S	0.8 0.7
	N1s 600eV	406.9 404.3	1.0 1.0	93% 7%	N-R_3H^+ N-R_3	2.6 2.6
	S2p $_{3/2}$ 400eV	168.7	0.8		-SH	
MIX DEA+3MPS native pH (4.25)	C1s 400eV	291.8 290.8	1.15 1.15	40% 60%	C-N C-C, C-S	1.0
	S2p $_{3/2}$ 400eV	172.8 168.6	0.97 0.97	26% 74%	-SO_3^- -SH	4.2
	N1s 600eV	406.7	1.14		N-R_3H^+	
AuNPs native pH (5)	C1s 400eV	291.4 290.0	1.38 1.38	44% 56%	C-N C-C, C-S	1.4
	S2p $_{3/2}$ 400eV	173.2	2.11	44%	-SO_3^-	4.4
	S2p $_{3/2}$ 400eV	168.8	2.11	56%	-SH	
	N1s	---	---	---	---	---
	Au4f 625 eV	89.5 90.1	0.7 0.7	83% 17%	Au^0 $Au^{\delta+}$	0.6

Table D2. XPS μ-LJ data collected on thiols and AuNPs.

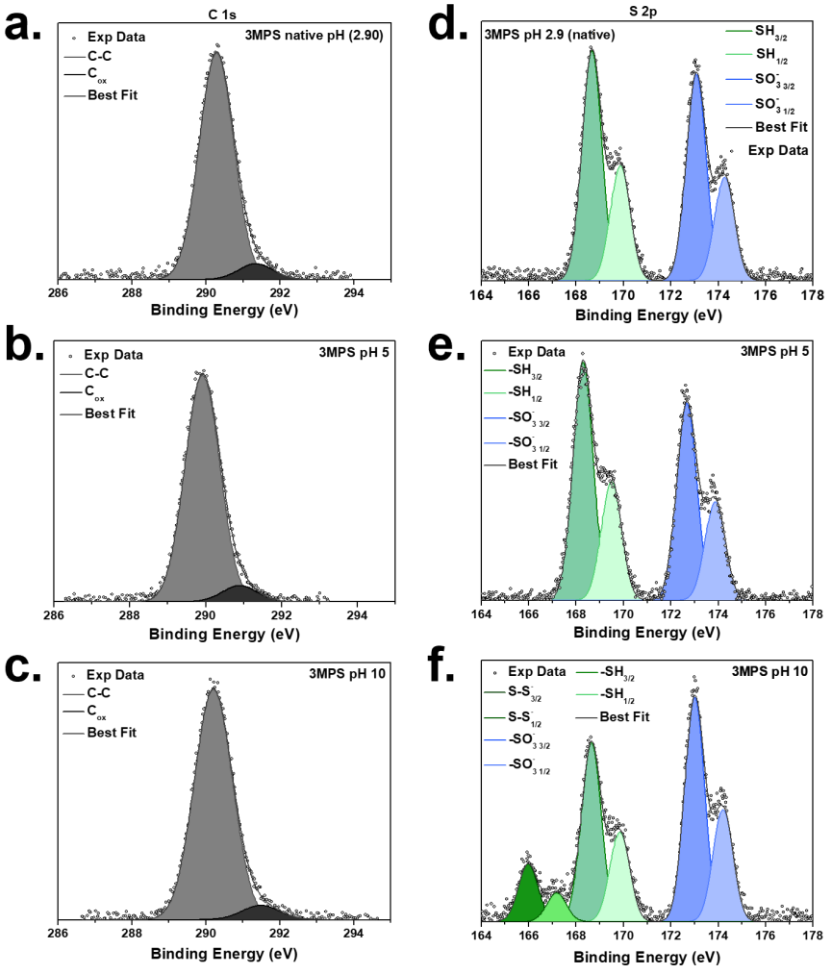

Figure D1. *M-LJ XPS spectra of 3MPS at C 1s core level at a) pH native (2.90), b) pH 5, c) pH 10 and at S 2p core level at at d) pH native (2.90), e) pH 5, f) pH 10.*

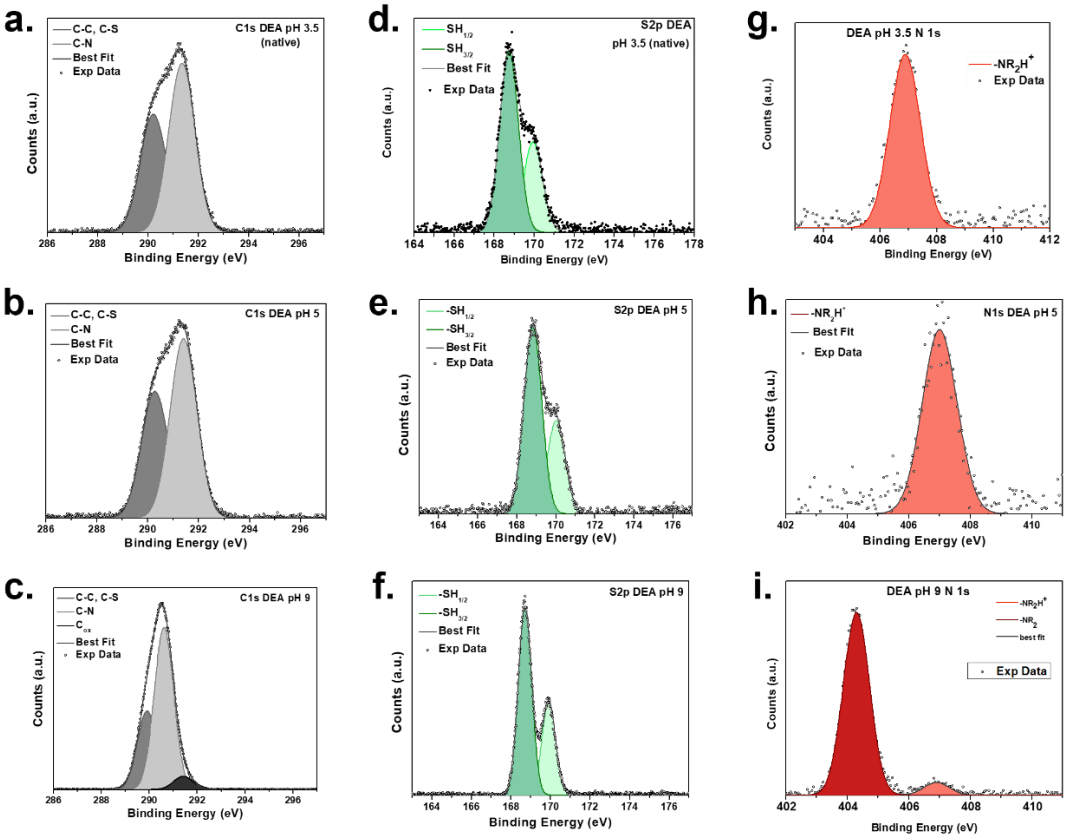

Figure D2. *M-LJ XPS spectra of DEA at C 1s core level at a) pH native (2.90), b) pH 5, c) pH 10 and at S 2p core level at at d) pH native (2.90), e) pH 5, f) pH 10, at N 1s core level at f) pH native (2.90), g) pH 5, h) pH 10 and at S 2p core level at at d) pH native (2.90), e) pH 5, f) pH 10*

D1.2. Conjugation of AuNPs-DOTA

In a round-bottomed flask, 6 mg of AuNPs functionalized with 3MPS and DEA were suspended in 6 mL of ultrapure water. A solution of 3 mg of the DOTA derivative (DOTA_1 or DOTA_2) in 1.5 mL of DMSO was then added to the reaction mixture, which was stirred for 24 hours. The resulting colloidal product was subsequently purified by dialysis against water, replacing the external medium every 24 hours for 5 days, in order to remove residual DMSO and unreacted DOTA derivative.

D1.3. Loading and release of methotrexate on AuNPs-3MPS-DEA

Cells and cell culture

Two Neuroblastoma (NB) cell lines, *i.e.,* SJNKP (a non-amplified NB cell line) and IMR5 (a n-Myc amplified NB cell line) were a kind gift from Dr. N. Crescenzio (Department of Paediatrics, University of Turin, Regina Margherita Children's Hospital, Turin, Italy) and Dr F. Timeus (Paediatric Haematology-Oncology, Regina Margherita Children's Hospital)[317]. SJNKP and IMR5 cell lines were maintained in monolayer cultures in RPMI-1640 medium supplemented with FBS 10% (v/v), 2 mM L-glutamine, 100 µg/mL streptomycin, and 100 IU/mL penicillin. A humidified atmosphere with 5% CO_2 in a water-jacketed incubator at 37˚C was used for cell incubation. For each passage, exponentially growing SJNKP and IMR5 cells were harvested with EDTA 10 mM and by further addition of trypsin solution 0.10%. Trypsin activity was quenched by the addition of complete RPMI-1640 medium; after centrifuge separation, cells were plated with DMEM-F12. Cells were centrifuged with a Thermo-Scientific centrifuge Megafuge ST Plus Series working at 1,000 rpm (233 g), 2 mins, at room temperature.

Experimental

To carry out *in vitro* test, MTX was loaded on AuNPs. Three concentrations of AuNPs were used: 0.5, 10, 50 µg/mL; with three different AuNPs/MTX weight ratio: 1/20, 1/1 and 5/1, respectively. As an example, only the loading of MTX on AuNPs 50 µg/mL is briefly reported. A stock solution (400 µg/mL) of MTX in 0.1 M HEPES buffer, was diluted with H_2O_{up} to 120 µg/mL and 500 µL of this solution are added – under stirring – to a round bottom flask containing 500 µL of an aqueous solution of AuNPs at a concentration of 600 µg/mL; the mixture was allowed to react, under stirring, in the dark at room temperature for 2 h. After 2 h, the solution is inserted in a dialysis membrane to remove the free MTX that is released from the membrane into the outside water (100 mL of distilled water for 30 min under stirring at room temperature). The AuNPs-MTX nanoconjugate (AuNPs concentration is 300 µg/mL) is then stored at −18 °C to avoid the release of the drug. For *in vitro* tests, AuNPs 50 µg/mL were necessary, so the AuNPs-MTX conjugate was diluted in 3 mL of DMEM-F12. To evaluate the loading of MTX on the nanoparticles, the outside solution of dialysis is collected, and the water is removed under vacuum. The recovered MTX is dissolved in 3 mL of HEPES buffer 0.1 M, and its quantity is evaluated via UV–Vis, comparing the maximum at λ = 303 nm (present in MTX spectrum, **Figure D3a**), using the calibration curve reported in **Figure D3b**.

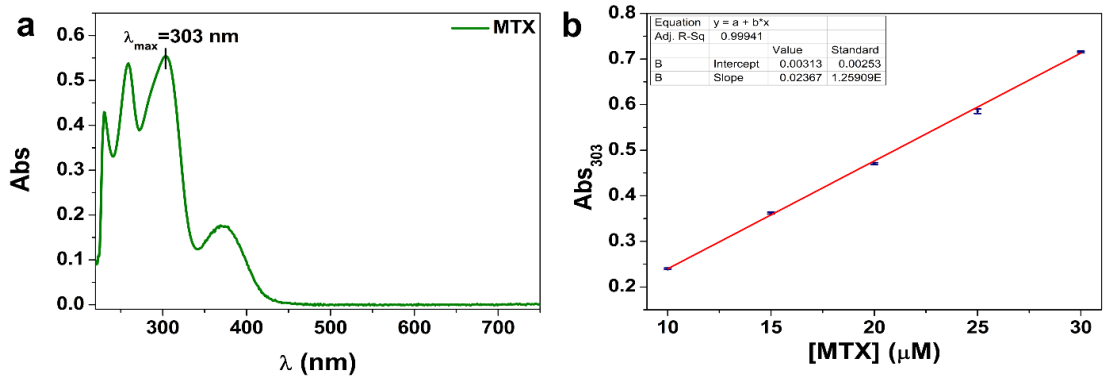

***Figure D3**. a) UV-Vis spectrum of MTX in water and b) calibration curve in HEPES 0.1 M at 303 nm. (R^2=0.9994; ε_0 = (20,540 ± 2630) M^{-1} cm^{-1}).*

The drug loading percentage was calculated using the following equation:

$$Loading\ \% = \frac{mol\ drug_{initial} - mol\ drug_{supernatant}}{mol\ drug_{initial}}\ x\ 100$$

The results are reported in **Table D3** for all weight ratio studied.

Release was studied following the ζ-potential signal. An AuNPs-MTX solution was left to stir mildly for 48 h at room temperature; after 2 and 4 h a 1 mL sample was collected and measured, after 48 h the stirring was stopped, and 1 mL of the solution was measured.

AuNPs* (μg/mL)	**AuNPs/MTX (wt/wt ratio)**	**η ± SD (%)**
3	1/20	61 ± 5
60	1/1	66 ± 2
300	5/1	74 ± 4

***Table D3.** Encapsulation efficiency of AuNPs-MTX at different AuNPs concentrations and AuNPs/MTX weight ratios. *The final nanoconjugate is diluted to the desired concentration prior to MTT assays.*

D1.4. XPS studies of MTX, AuNPs-3MPS-DEA pristine and loaded with MTX

XPS experiments were carried out with a homemade instrument, with preparation and analysis ultra-high vacuum (UHV) chambers separated by a gate valve. The analysis chamber contains a six-degree-of freedom manipulator and a 150 mm mean radius hemispherical electron analyser with a five-lens output system and a 16-channel detector giving a total instrument resolution of 1.0 eV as measured at the $Ag3d_{5/2}$ core level. Measurements were carried out on samples deposited onto TiO_2/Si(111) wafers by following

a drop-casting procedure; the use of titania substrates allows to avoid signals interference and minimize charging effects due to thick layers of organic molecules. 3MPS and DEA free thiols were drop cast deposited on Au/Si(111) substrates. Samples were inserted in the preparation chamber and left outgassing overnight at a base pressure of about 10^{-8} Torr, before insertion in the analysis chamber. Vacuum pressure in the analysis chamber during measurements was in the range of 10^{-9}–10^{-10} Torr. The X-ray radiation is a non-monochromatised Mg Kα (1253.6 eV). C1s signal of aliphatic C atoms having a binding energy of 285.0 eV was used as a reference. Atomic ratio values were calculated from peak intensities. Curve-fitting analysis of the C1s, N1s, O1s, S2p and Au4f spectra was performed using Gaussian profiles as fitting functions, after subtraction of a polynomial background. The $S2p_{3/2,1/2}$ doublets were fitted using the same Full Width at Half-Maximum (FWHM) for both components, a spin−orbit splitting of 1.2 and a branching ratio ($2p_{3/2}/2p_{1/2}$) of 1/2. For the $Au4f_{7/2,5/2}$ doublets, a splitting of 3.7 eV, a branch ratio $4f_{7/2}/4f_{5/2}$ of 4/3 and the same FWHM values for both spin−orbit components were applied. When several different species were identified in a spectrum, the same FWHM value was set for all individual photoemission bands.

Sample	**Signal**	**Assignment**	**FWHM (eV)**	**BE (eV)**
AuNPs-3MPS-DEA	C1s	C-C/S C-N/O COOH	1.96	285.0 286.7 288.5
	N1s	C-N $-N^+$	2.31	399.9 401.6
	O1s	TiO_2 S=O -OH	1.96	530.9 532.4 534.0
	$S2p_{3/2}$	RS-H $-SO_3^-$	1.90	163.4 168.6
	$Au4f_{7/2}$	Au^0 $Au^{\delta+}$	1.23	83.9 84.9

Table D4. *XPS data of AuNPs-3MPS-DEA deposited on TiO_2 substrate.*

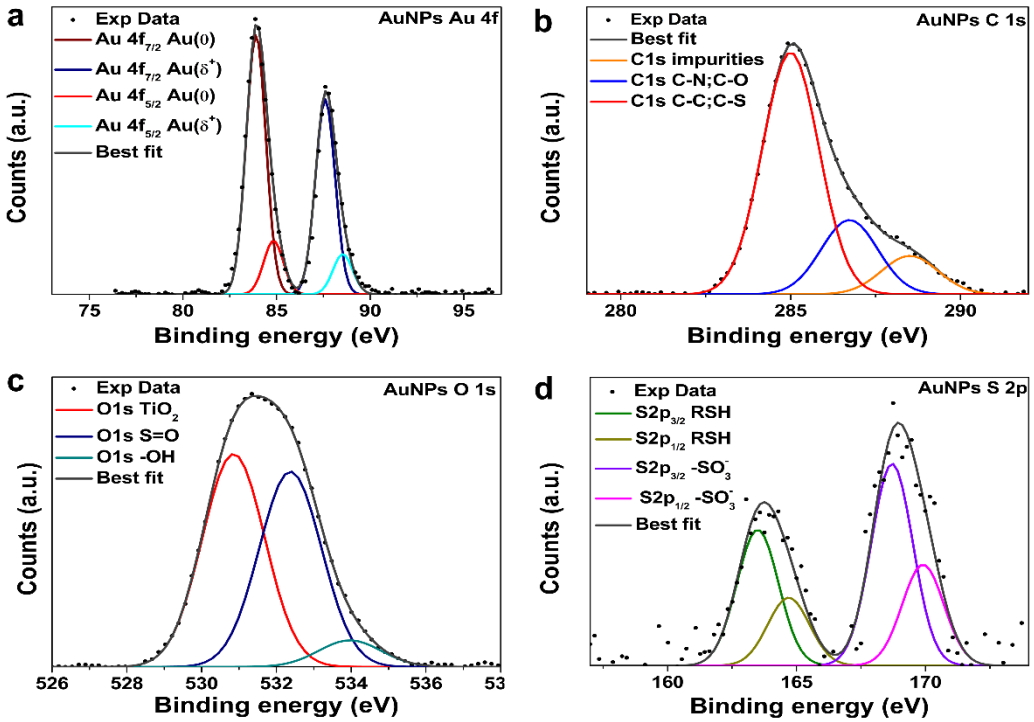

Figure D4. *XPS spectra of a, AuNPs at Au4f core level; b, AuNPs at C1s core level; c, AuNPs at O1s core level; d, AuNPs at S2p core level.*

Sample	Signal	Assignment	FWHM	BE (eV)
AuNPs-MTX	C1s	C-C/S	1.67	285.0
		C-N/O		286.4
		C=N/O		287.5
		COOH		288.8
	N1s	C-N; N-ring	2.40	400.3
	O1s	TiO_2	2.20	530.2
		C/S=O		532.0
		-OH		533.5
	$S2p_{3/2}$	Au-S	1.90	161.9
		RS-H		164.5
		$-SO_3^-$		168.7
	$Au4f_{7/2}$	Au^0	1.32	83.7
		$Au^{\delta+}$		84.7

Table D5. *XPS data of AuNPs-MTX deposited on TiO_2 substrate.*

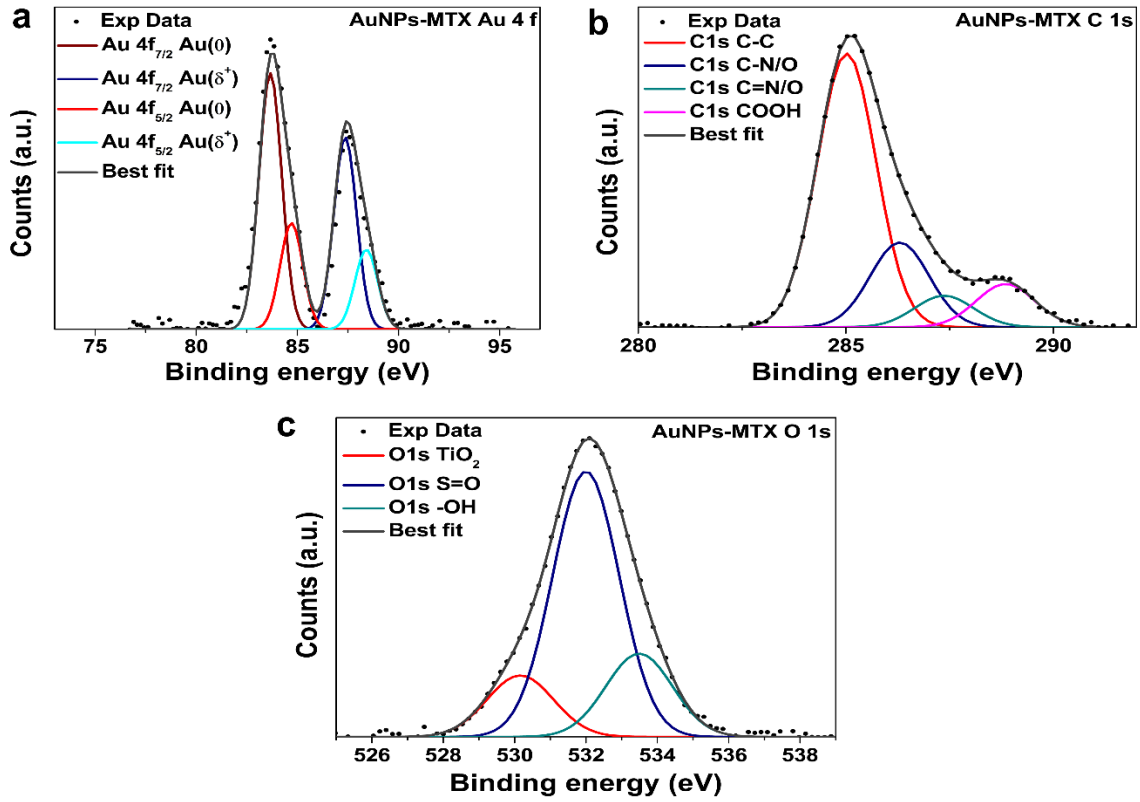

Figure D5. *XPS spectra of a) AuNPs-MTX at Au4f core level; b) AuNPs-MTX at C1s core level; c, AuNPs-MTX at O1s core level.*

Sample	**Signal**	**Assignment**	**FWHM (eV)**	**BE (eV)**
MTX	C1s	C-C C-N/O C=N/O COOH	1.65	285.0 286.5 287.7 288.8
	N1s	C-N; N-ring	2.33	400.9
	O1s	C=O -OH H_2O	2.24	531.4 533.3 534.9

Table D6. *XPS data of MTX deposited on TiO_2 substrate.*

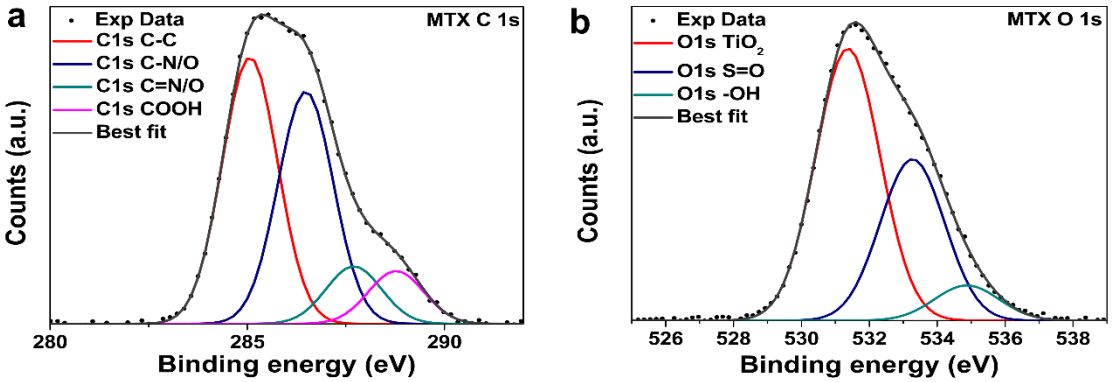

Figure D6. *XPS spectra of a, MTX at C1s core level; b, MTX at O1s core level.*

D1.5. X-ray Studies (SAXS, GISAXS, GIWAXS) on AuNPs-3MPS-DEA pristine and loaded with MTX

Small-Angle X-ray scattering. SAXS measurements were performed at SAXSLab Sapienza with a Xenocs Xeuss 2.0 Q-Xoom system (Xenocs SA, Sassenage, France), equipped with a micro-focus Genix 3D X-ray Cu source (λ = 0.1542 nm), a two-dimensional Pilatus3 R 300 K detector placed at variable distance from the sample (Dectris Ltd., Baden, Switzerland). The beam size was selected using the two-pinhole collimation system equipped with "scatterless" slits to be 0.5 mm x 0.5 mm. Calibration of the scattering vector q range, where $q = (4\pi \sin\theta)/\lambda$, 2θ being the scattering angle, was performed using silver behenate. Measurements with two different sample-detector distances were performed so that the overall explored q region was $0.0042\ nm^{-1} < q < 1.75\ nm^{-1}$. Samples were loaded into glass capillaries with a nominal thickness of 1.5 mm and sealed with hot glue. They were subsequently placed in the instrument sample chamber at reduced pressure (~0.2 mbar) at 25°C. The two-dimensional scattering patterns were subtracted for the "dark" counts, and then masked, azimuthally averaged, and normalised for transmitted beam intensity, exposure time and subtended solid angle per pixel, by using the FoxTrot software developed at SOLEIL synchrotron facility. The intensity *vs.* q profiles obtained from the subsequent frames were averaged after checking they were superimposable and were then subtracted for empty capillary and solvent contributions and put in absolute scale units (cm^{-1}) by dividing for the sample thickness estimated by scanning the capillary with the X-ray beam. The different angular ranges were merged using the SAXS utilities tool. The measurements were repeated on the same samples across an overall time of 24 hours from the initial loading.

Grazing Incidence Small- and Wide-Angle X-Ray Scattering. GISAXS and GIWAXS measurements were performed at beamline P03 (MINAXS) at the synchrotron PETRA III at Deutsches Elektronen-Synchrotron DESY in Hamburg (Germany)[310]. Samples were prepared by drop casting on SiO/SiO_2 substrate from their aqueous dispersion. X-ray beam with the energy 11.83 keV (wavelength $\lambda = 1.048$ Å, $\Delta\lambda/\lambda = 10^{-4}$) was focused on the detector by beryllium compound refractive lenses (CRL) with a beam size (V x H) 25×35 μm^2. Sample-Detector Distance (SDD) was 4190 ± 2 mm for GISAXS and 220.5 mm for GIWAXS. Pilatus 2M (Dectris Ltd., Switzerland) with the pixel size 172×172 μm^2 and pixel array format (V x H) 1475×1679 pix^2 was used as a 2D detector for GISAXS mode. GIWAXS 2D images was performed using a Lambda 9M detector with a pixel size 55×55 μm^2. The reciprocal q-space and sample-to-detector distance were calculated using Ag-behenate, CeO and LaB_6 as calibrant. Azimuthally averaged radial distribution of intensity was performed after the analysis of X-ray data using the DPDAK software package[311].

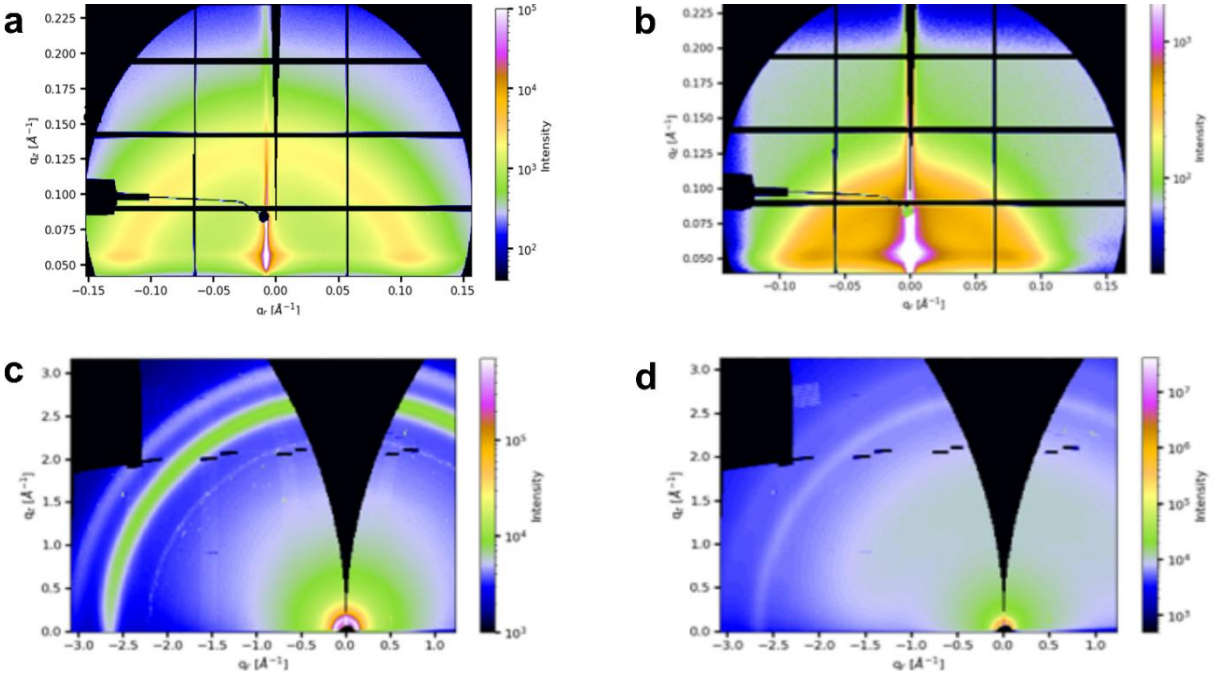

Figure D7. *GISAXS 2D profiles of AuNPs (a) and AuNPs-MTX (b); GIWAXS 2D profiles of AuNPs (c) and AuNPs-MTX (d).*

AuNPs		
Model	**Sphere**	
q range (nm^{-1})	0.3-10	
Reduced χ^2	68	
Parameters		
SLD_{sphere} (nm^{-2})	$124.8 \cdot 10^{-4}$	Fixed
$SLD_{solvent}$ (nm^{-2})	$9.4 \cdot 10^{-4}$	Fixed
Background (cm^{-1})	0.0003	Fixed
p	1	Fixed
$<R>_{sphere}$ (nm)	2.531 ± 0.017	Optimised
N	0.751 ± 0.016	Optimised
s	0.230 ± 0.023	Optimised
Model	**Sphere + Sphere with Mass Fractal Structure Factor** (model 4.4.4. Sasfit 0.94.11 manual page 146)	
q range (nm^{-1})	0.04-10	
Reduced χ^2	3.5	
Parameters		
SLD_{sphere} (nm^{-2})	$124.8 \cdot 10^{-4}$	Fixed
$SLD_{solvent}$ (nm^{-2})	$9.4 \cdot 10^{-4}$	Fixed
Background (cm^{-1})	0.0003	Fixed
$<R>_{sphere}$ (nm)	2.53	Fixed
s	0.23	Fixed
p	1	Fixed
Isolated spheres		
N	0.500	Optimised
Clustered spheres		
N	0.201	Optimised
r_0 (nm)	5.06	Fixed
x_i (nm)	106.85± 0.31	Optimised
D	1.278 ± 0.028	Optimised

Table D7*. Fit Parameters for SAXS measurements of AuNPs.*

AuNPs-MTX		
Model	**Sphere**	
q range (nm^{-1})	0.3-10	
Reduced χ^2	57	
Parameters		
SLD_{sphere} (nm^{-2})	$124.8 \cdot 10^{-4}$	Fixed
$SLD_{solvent}$ (nm^{-2})	$9.4 \cdot 10^{-4}$	Fixed
Background (cm^{-1})	0.0003	Fixed
p	1	Fixed
$<R>_{sphere}$ (nm)	2.486 ± 0.025	Optimised
N	0.453 ± 0.015	Optimised
s	0.208 ± 0.040	Optimised
Model	**Sphere + Sphere with Mass Fractal Structure Factor** (model 4.4.4. Sasfit 0.94.11 manual page 146)	
q range (nm^{-1})	0.04-10	
Reduced χ^2	1.35	
Parameters		
SLD_{sphere} (nm^{-2})	$124.8 \cdot 10^{-4}$	Fixed
$SLD_{solvent}$ (nm^{-2})	$9.4 \cdot 10^{-4}$	Fixed
$<R>_{sphere}$ (nm)	2.49	Fixed
s	0.21	Fixed
p	1	Fixed
Isolated spheres		
N	0.215	Optimised
Clustered spheres		
N	0.182	Optimised
r_0 (nm)	5.06	Fixed
x_i (nm)	65.06± 0.14	Optimised
D	1.308 ± 0.023	Optimised

Table D8. Fit Parameters for SAXS measurements of AuNPs-MTX.

D1.6. Cell viability and permeation studies on neuroblastoma cells (AuNPs-MTX)

Pristine and MTX-loaded AuNPs were tested on NB cell lines and results compared with free MTX drug. SJNKP and IMR5 cells at a concentration of 5,000 cells per well, were seeded in 96-multiwell plates and treated for 48 h with three different concentrations of gold nanoparticles, named as AuNPs (pristine) 0.5 µg/mL, AuNPs 10 µg/mL and AuNPs 50 µg/mL and AuNPs-MTX with a 0.015, 0.031, 0.124 µM on AuNPs 0.5 µg/mL, 10 µg/mL, 50 µg/mL, respectively. Cells were treated with unloaded nanoparticles and free drug separately, as a control. After 48 h, growing medium was discarded and replaced with MTT solution to assess the cell viability. MTT reading wavelength was set at 577 and 660 nm, then processed according to Kanamori *et al.*[318]. Cell viability was analysed by GraphPad Prism and reported as % of viable cells, where control cells are 100 %.

To assess the permeation of nanoparticles inside the cells, for the highest concentration (50 µg/mL) the growing medium was separated and analysed via UV–vis. The absorbance of AuNPs and AuNPs-MTX inside the separated growing medium was compared to the 50 µg/mL stock solution of AuNPs. Permeation % (P%) was calculated as follows:

$$P\% = 100 - \frac{Abs_0}{Abs_1} \cdot 100$$

Where Abs_0 is the absorbance value at 520 nm of the AuNPs stock, and Abs_i is the value of the AuNPs or AuNPs-MTX solutions after the treatment at 24 or 48 h.

MTT assays were carried out least three times for statistical analysis and results were expressed as mean values ± SD. The Student's t-test was used to analyse the statistical significance and differences between the test and control groups were considered to be significant at $*p < 0.05$ and very significant at $**p < 0.01$. One-way Anova, Dunnett's and Sidak's multiple comparisons test were performed for statistical analysis.

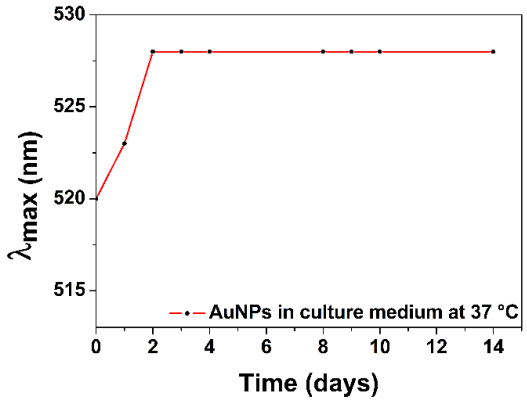

Figure D8. *Stability studies of AuNPs 50 μg/mL at 37°C in DMEM-F12 (0-14 days).*

D1.7. Loading and release of trastuzumab on AuNPs-3MPS-DEA

Two different weight ratios were tested to obtain the nanoconjugate: AuNPs-TZ 2:1 and AuNPs-TZ 1:1. The loading and release details are reported only for 1:1 ratio.

50 µl of an aqueous 1 mg/ml stock solution of AuNPs was added to 50 µl of a 1 mg/ml stock solution of TZ in H_2O_{up}. The solution was diluted with 0.1 M HEPES buffer to obtain 1 ml total. The obtained mixture was gently stirred for 3 hours and centrifuged at 13400 rpm and 5 °C for 20 minutes to precipitate the AuNPs-TZ nanoconjugate. The AuNPs-free supernatant, containing the unbound antibody was mixed with a Bradford assay solution following the manufacturer's instructions to quantify the unbound TZ and, thus, the loading percentage. All loading experiments were carried out in triplicates. The equation used to calculate loading is:

$$\text{Drug Loading (\%)} = L\% = \frac{wt_{TZ_{AuNPs}}}{wt_{TZ_{initial}}} \cdot 100$$

The release study was carried out at 37 °C after the loading and centrifugation of several samples (one per set time point: 1 h, 2 h, 4 h, 24 h, 28 h) of the AuNPs-TZ, the conjugates were kept at 37 °C resuspended in a known volume of 0.1 M HEPES. At the desired time point, the corresponding sample was centrifuged at 13400 rpm for 20 minutes at 5 °C and the Bradford assay was performed at set times on the supernatant. The release was calculated as a percentage of the weight of the loading (calculated for each time point sample).

D1.8. Cells culture, cell viability and apoptosis assays (AuNPs-TZ)

The wtBRCA1 gene-carrying ovarian serous adenocarcinoma cell line SKOV3 was used (purchased from ATCC® (HTB77™)). The cells were cultured in RPMI-1640 with L-

glutamine (Sigma-Aldrich), supplemented with 10% FBS (Corning), and 1% Penicillin Streptomycin (100x) (Sigma-Aldrich). They were incubated at 37°C and 5% CO_2.

SKOV3 cells were transfected with pCMVmiR-200c (OriGene) carrying the miR-200c precursor and the corresponding empty vector, pCMV (OriGene).

SKOV3, vector, and miR-200c transfected cells were treated with AuNPs, AuNPs-TZ, and TZ. The cell viability was assessed using Cell Proliferation Kit I (Merck), according to the manufacturer's instructions. SKOV3 cells were seeded in a 96-multiwell plate in triplicates at a concentration of 1.5 x 10^4 cells in 200 µl per well. The following day, they were treated for 24, 48, and 72 hours with three different concentrations of AuNPs loaded with trastuzumab (0.1 µg/ml, 0.5 µg/ml, 1 µg/ml for AuNPs, corresponding to 0.041 µg/ml, 0.205 µg/ml and 0.410 µg/ml of loaded antibody, respectively). Cells were treated with unloaded nanoparticles and free antibodies separately as a control. After 24, 48, and 72 hours, 20 µl of MTT solution was added to each well and incubated at 37° C for 3 hours. Subsequently, 100 µl solubilization buffer was added to each well and incubated at 37° C overnight. The following day, the absorbance was measured at 560 in a GloMax® Discover Microplate Reader (Promega). The results were plotted as a mean ± SD of three replicates measured at A560 per condition, and the treatments were repeated at least three times.

SKOV3 cells, empty vector, and miR-200c transfected were seeded in a 6-well plate at a concentration of 1.5 x 10^5 cells in 2 ml per well and duplicates. Following the 48-hour incubation, with AuNPs, AuNPs-TZ, and TZ, the cells were harvested and centrifuged at 1200 rpm for 5 minutes at room temperature. Subsequently, the pellet was suspended in cold PBS and centrifuged once more. The cells were then suspended in the BD Pharmingen™ PE Annexin V Apoptosis Detection Kit I Binding Buffer at 1 x 10^6 cells/ml. To 100 µl of the cell suspension, 5 µL of PE Annexin V and 5 µL of 7-AAD were added and incubated at room temperature for 15 minutes in the dark. After adding 400 µL of the binding buffer to each test tube, the samples were analysed by a BD Accuri™ C6 Plus Flow Cytometer to assess the number of cells undergoing apoptosis (Annexin V positive) and the amount of non-viable cells (7-AAD labelled). The experiment was repeated at least three times.

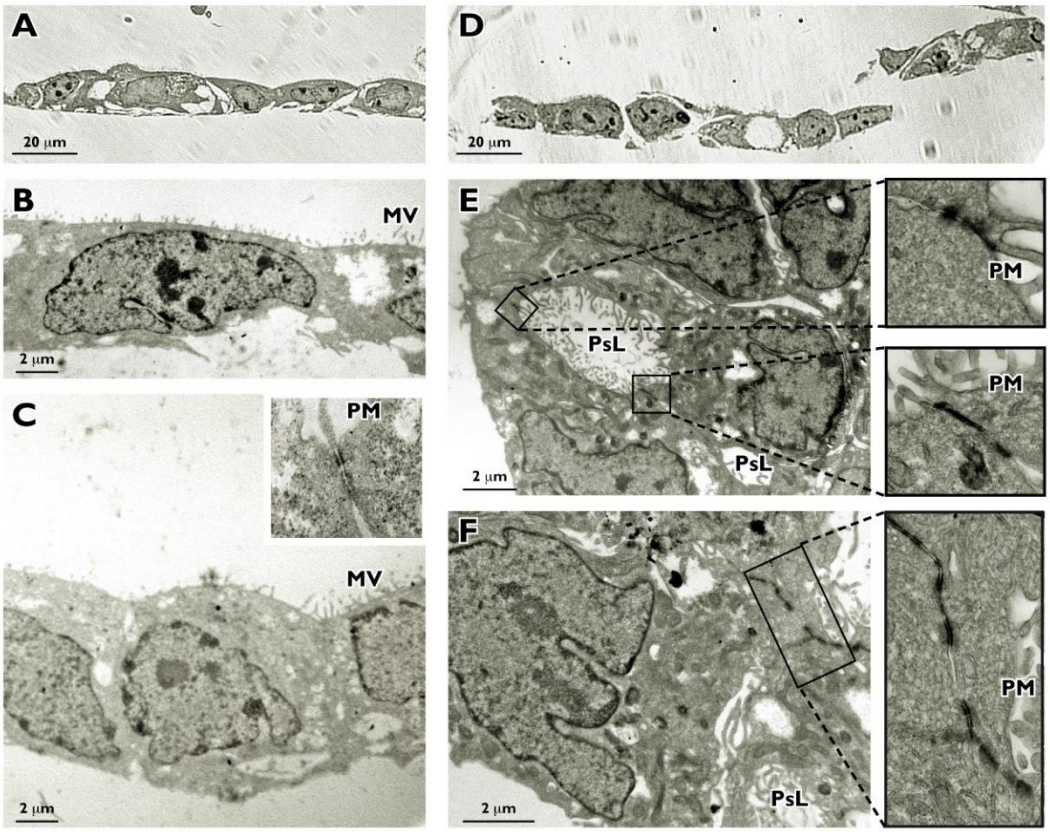

Figure D9. *A-C: SKOV3 parental cells show large nuclei compared to their cytoplasm, only a few small surface microvilli, and very simple cell-to-cell connections. D-F: In contrast, SKOV3 miR-200c cells look more differentiated: they form pseudolumina with many well-organized microvilli and have longer, more developed junctions between neighboring cells. [Legend: MV: microvilli; PM: plasma membrane; PsL: pseudolumen; A and D: semi-thin sections; staining: toluidine blue; B, C, E, and F: TEM micrographs; staining: uranyl acetate/lead citrate].*

D2. Other procedures with Hydrophilic Nanoparticles

D2.1. Kinetics of SSA, CSA and cTSA

In all kinetics experiments, Ani concentration was used instead AuNPs concentration, and it was calculated considering that all amount of Ani used during the AuNPs synthesis was capped on gold surface. In every experiment the molar ratio between Ani/Linker/H^+ = 1/0.5/1 (H^+ = TFA or TBA).

The experiments conducting in CH_2Cl_2 were characterized with UV-Vis, DLS, HR-TEM, FESEM, FT-IR, XPS, GIWAXS and GISAXS. For SAXS characterization the experiments were conducted in Toluene and for NMR ones were conducted in $CDCl_3$. In every experiment, dry solvents were used. For Covalent Self-Assembly and Dynamic Self-

Assembly studies, AuNPs and Linker were let equilibrate for 3 days at room temperature, and then the acid (TFA for CoSA, and TBA for DySA) was added. The mixtures were monitored for 24 h after acid addition. All the amounts of Ani (AuNPs), Linker and Acid (TFA or TBA) are reported in **TableD9**.

[Ani] mM ([AuNPs] mg/mL)*	[Linker] mM (when used)	[TFA] or [TBA] mM	Solvent
5 mM (~ 0.3 mg/mL)	2.5 mM	5 mM	CH_2Cl_2 (3 mL)
154 mM (10 mg/mL)	77 mM	154 mM	$CDCl_3$ (1 mL)
15.4 mM (1 mg/mL)	7.7 mM	15.4 mM	Toluene (1 mL)

Table D9. *Experimental amount of Ani (AuNPs), Linker and Acid (TFA or TBA), *[Ani] was calculated to obtain a suspension of AuNPs compatible with the characterization technique.*

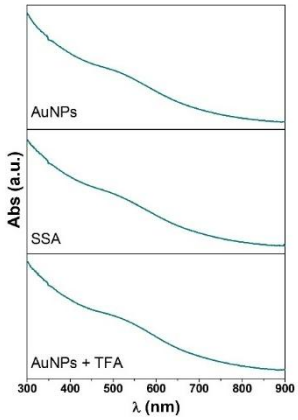

Figure D10. *UV-Vis spectra of AuNPs (top), SSA (middle) and AuNPs + TFA (bottom) in DCM.*

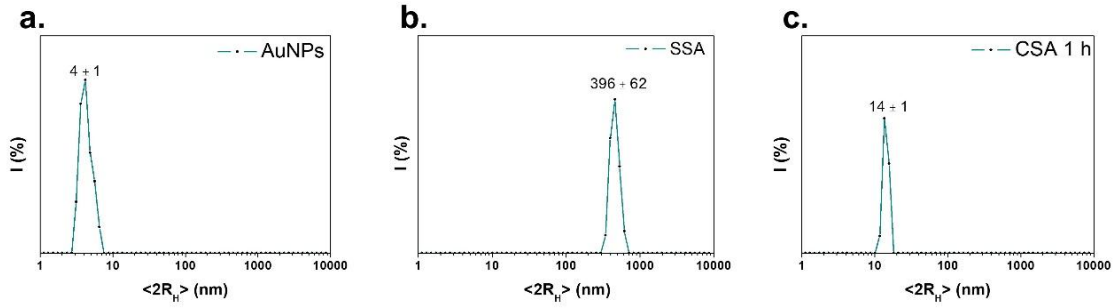

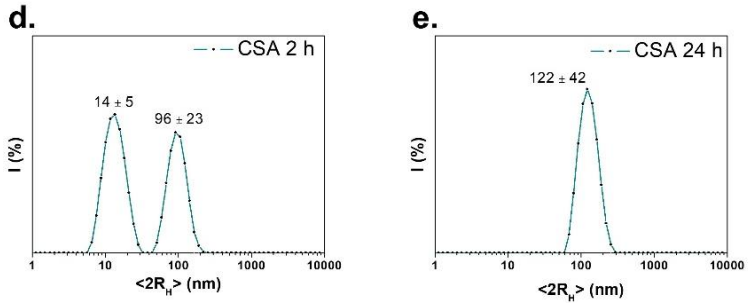

Figure D11. *DLS graph of a) AuNPs; b) SSA; c) CSA after 1 h of TFA interaction; d) CSA after 2 h of TFA interaction; e) CSA after 24 h of TFA interaction. All measurement in DCM.*

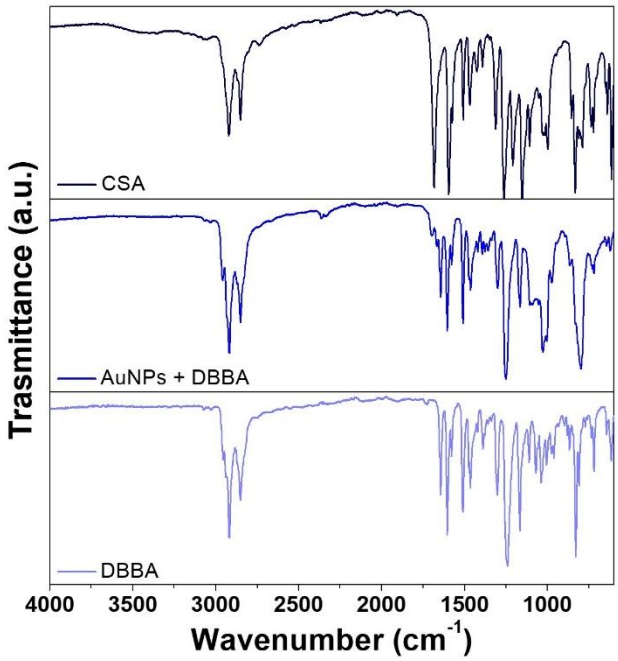

Figure D12. *FTIR spectra (ATR, deposited on glass): DBBA precursor linker spectrum (bottom), AuNPs + DBBA mixture (middle) and CSA of AuNPs (top).*

DBBA Linker[319]	AuNPs-CSA
ν (=C-H_{imine}) 3071	ν NH_2 3360 (N-butylamine) [320]
ν (=C-H_{ar}) 3029	ν (=C-H_{imine}) 3076
ν_{as} -CH_3 2954	ν (=C-H_{ar}) 3053
ν_{as} -CH_2 2918	ν_{as} -CH_2 2920
ν_s -CH_3 2872	ν_s -CH_3 2868
ν_s -CH_2 2850	ν_s -CH_2 2850
ν C=N 1605	ν C=O 1684
ν C-C_{ar} 1577	ν C=N 1595

ν C-C_{ar} 1510	ν C-C_{ar} 1576
δ_s -CH_2 1466	ν C-C_{ar} 1509
δ_{as} -CH_2 1389	δ_s -CH_2 1467
ν_{as} C-O-C 1242	δ_{as} -CH_2 1390
β(CH Ar) 1167	ν C_{ar}-N 1313
β(CH Ar) 1110	β(CH Ar) 1152
ν C-N 1071	β(CH Ar) 1136
ν_s C-O-C 1040	ν_{as} C-O-C 1251
	ν Ar-COH 1209
	ν C-N 1107 (N-butylamine)
	ν_s C-O-C 1030

Table D10. *FT-IR band assignments for DBBA linker and AuNPs-CSA.*

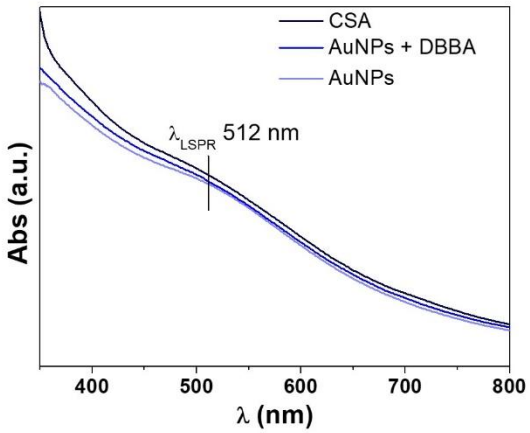

Figure D13. *UV-Vis spectra of AuNPs, AuNPs + DBBA mixture and CSA after 24 h of TFA interaction. All measurement in DCM.*

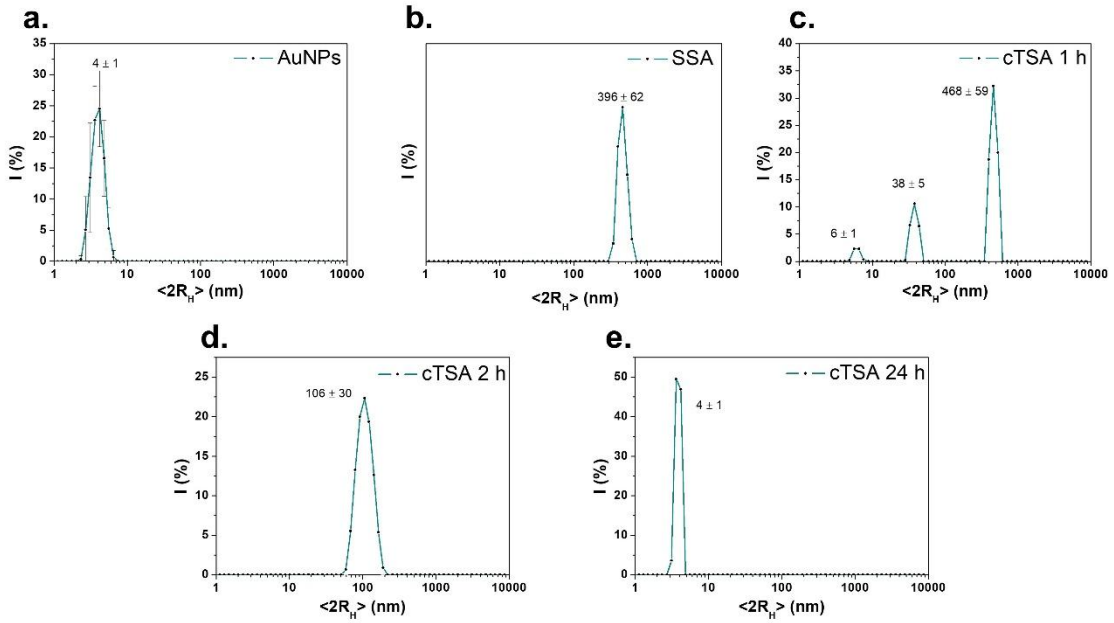

Figure D14. *DLS graph of a) AuNPs; b) SSA; c) cTSA after 1 h of TBA interaction; d) cTSA after 2 h of TBA interaction; e) cTSA after 24 h of TBA interaction. All measurement in DCM.*

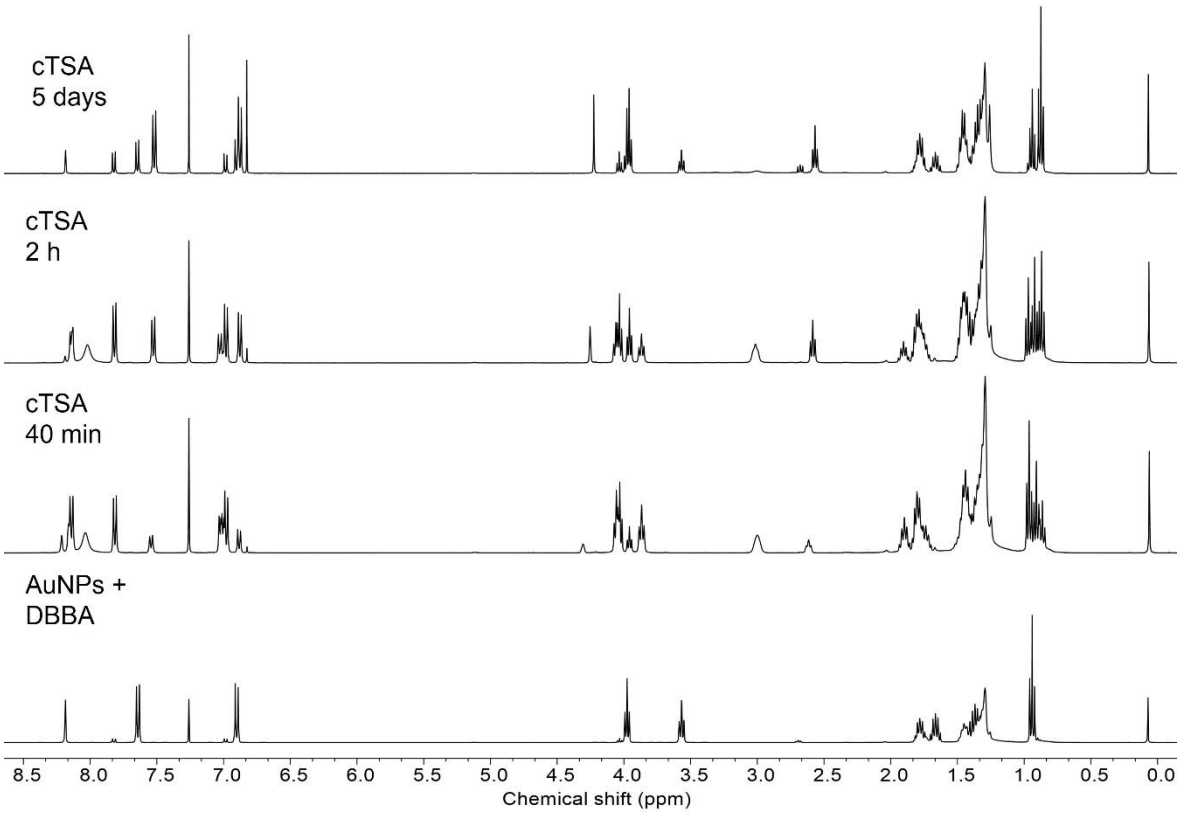

Figure D15. *^{1}H-NMR spectra (from bottom to top) of AuNPs + DBBA, cTSA after 40 min of TBA interaction, cTSA after 2 h of TBA interaction, cTSA after 5 days of TBA interaction. All measurement in $CDCl_3$.*

D2.2. Preparation of SAMs and multilayers of rod-like Pt(II) dithiol on polycrystalline gold surface.

In order to prepare the self-assembled monolayer (SAM), the terminal thiol compound *trans,trans*-[(HS)-Pt(PBu_3)$_2$-C≡C-C_6H_4-C_6H_4-C≡C-Pt(PBu_3)$_2$(SH)] was obtained *in situ* by a deacetylation procedure carried out on the thioacetate precursor and allowed to self-assemble on polycrystalline gold surfaces (Au/Si(111) wafers surfaces). In a typical procedure, the Pt-DEBP($SCOCH_3$)$_2$ ligand (30 mg, 0.019 mmol) was dissolved in 20 mL of THF and 260 µL of NH_4OH (30%) was added. The PtDEBP solution was stirred at 30°C for 2 h and filtered on celite. Gold-coated silica wafers were prepared by growing Au film 4000 Å thick onto Si(111) substrates and cut into slices (ca. 1 cm^2), washed with several organic solvents (acetone, ethanol, chloroform), and blown dry with nitrogen. Freshly prepared gold substrates were dipped into the Pt-DEBP(SH)$_2$ solution for 4 h to achieve the anchoring of thiol on Au surface. The obtained multilayer was rinsed (ethanol, THF and acetone) to achieve the formation of a film in the monolayer thickness regime (SAM). The same procedure, without the final washing step, was applied to obtain Multilayer (MUL) sample.

D2.3. Sensing Measurements

AuNPs suspensions in CH_2Cl_2 (10 µLat concentration 1 mg mL^{-1}) were deposited by drop casting onto homemade transducers, based on interdigitated pairs of gold/chromium fingers implemented by lithography on passivated silicon substrates. The following geometry of metal electrodes was used: fingers width and gaps 20 µm, length 5640 µm, thickness 100 nm. AuNPs films were airdried, inserted into a measurement chamber and connected to a Keithley Model 595 Quasi-static CV Meter. Changes in the flowing current by applying a fixed voltage (1 V) were monitored at 20 °C by exposure to different analytes concentrations (benzene, toluene). Vapours of the selected analyte was mixed with synthetic air or N_2 using a MKS mass-flow controller and maintaining the total flux at 200 SCCM (standard cubic centimetres per minute). Both nitrogen and synthetic air were used as carrier gases without finding any differences in the electrical response of the sensitive layer of AuNPs. I/V and current response curves were carried out under R.H. 60% at 20 °C with a HP 3458A multimeter and a Keithley 230 programmable voltage source.

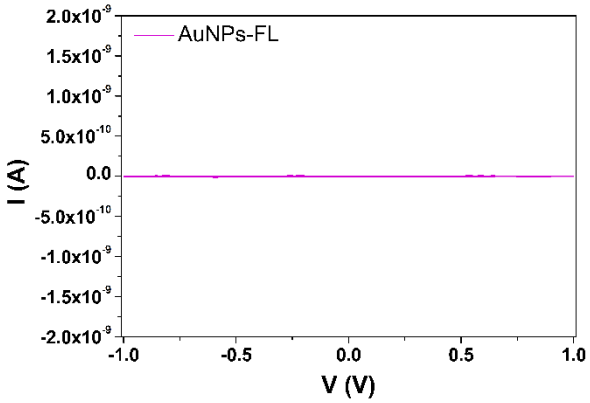

Figure D16. *I/V curve of AuNPs-FL.*

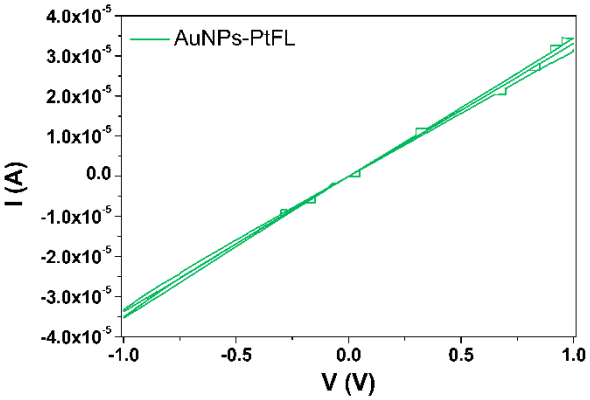

Figure D17. *I/V curve of AuNPs-PtFL.*

D2.4. AuNPs/PPA nanocomposite blend synthesis

Gold nanoparticles/poly(phenylacetylene) (AuNPs/PPA) nanocomposite material was synthesized following a single-step blending approach at room temperature. A 2 mg/mL of PPA solution and a 2 mg/mL of AuNPs suspension in $CHCl_3$ were used as stock solutions for the preparation of 2 mL of nanocomposites with different AuNPs/PPA weight ratios (%wt.): 10/90, 30/70, 50/50, 70/30, 90/10. The mixture was gently stirred for 3 hours at room temperature under Ar atmosphere. Then, the final blend was stored for further use at +4 °C under inert atmosphere.

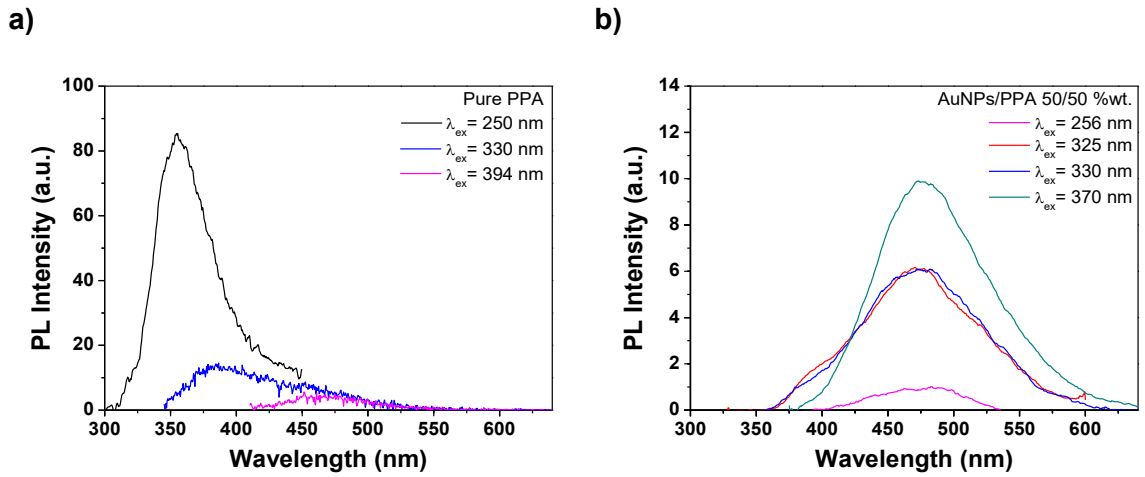

Figure D18. *Photoluminescence spectra in CH_2Cl_2 of a) pure PPA and b) B50 sample at different excitation wavelengths.*

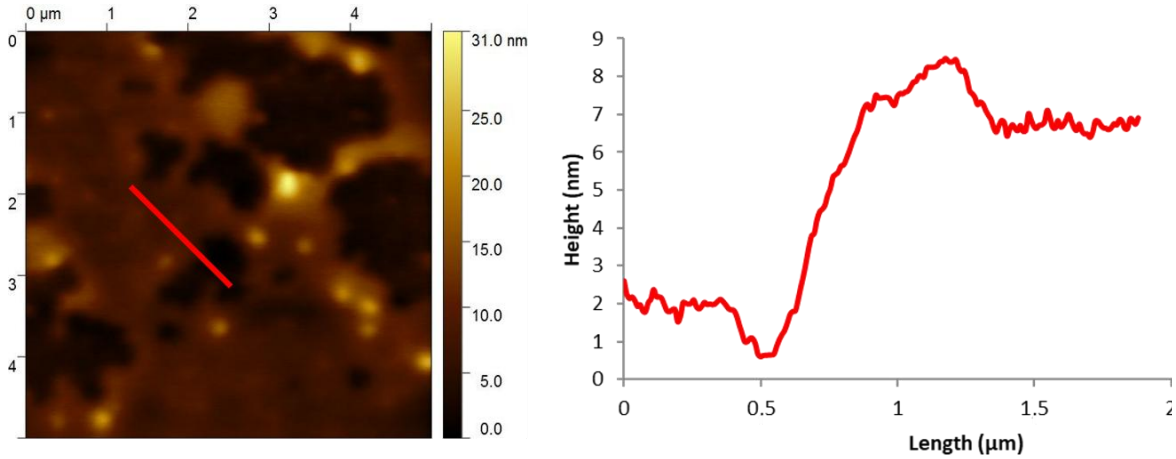

Figure D19. *Representative thickness profile of AuNPs-2AET-FL_2/PPA 50:50 %wt. (B50 sample) spin-coated film on Si/SiO_2 substrate taken from AFM image.*

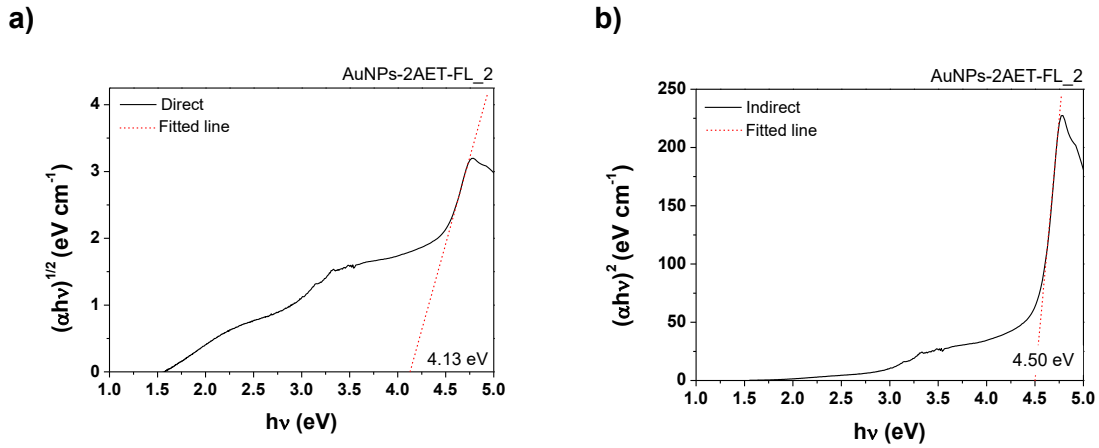

c)

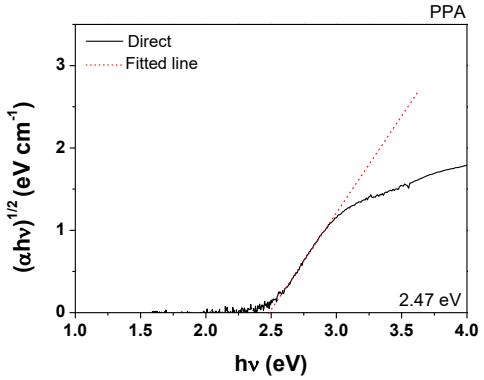
PPA
Direct
Fitted line
2.47 eV
(αhν)^1/2 (eV cm^-1)
hν (eV)

d)

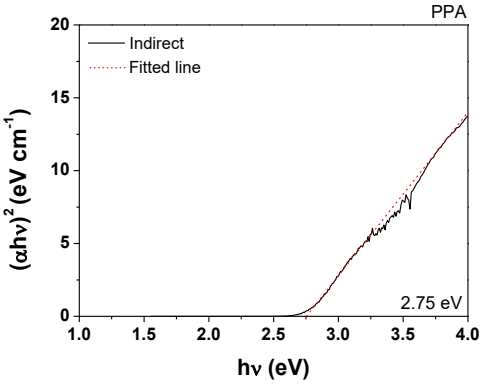
PPA
Indirect
Fitted line
2.75 eV
(αhν)^2 (eV cm^-1)
hν (eV)

e)

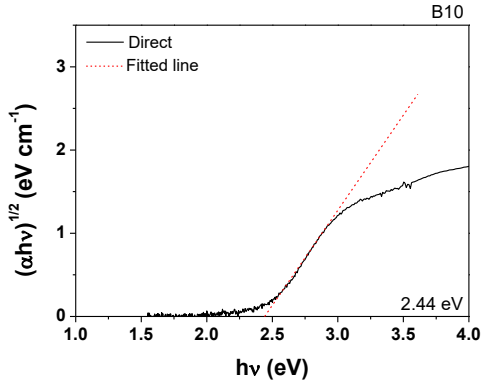
B10
Direct
Fitted line
2.44 eV
(αhν)^1/2 (eV cm^-1)
hν (eV)

f)

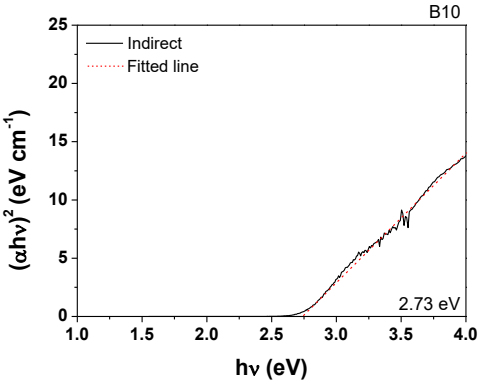
B10
Indirect
Fitted line
2.73 eV
(αhν)^2 (eV cm^-1)
hν (eV)

g)

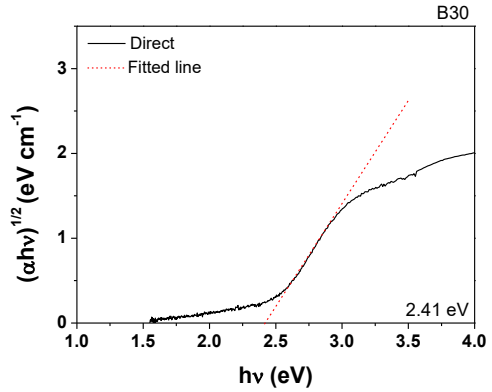
B30
Direct
Fitted line
2.41 eV
(αhν)^1/2 (eV cm^-1)
hν (eV)

h)

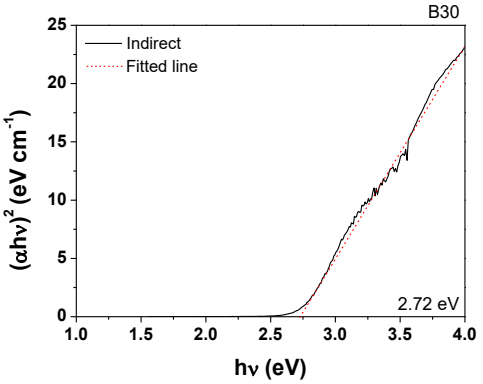
B30
Indirect
Fitted line
2.72 eV
(αhν)^2 (eV cm^-1)
hν (eV)

i)

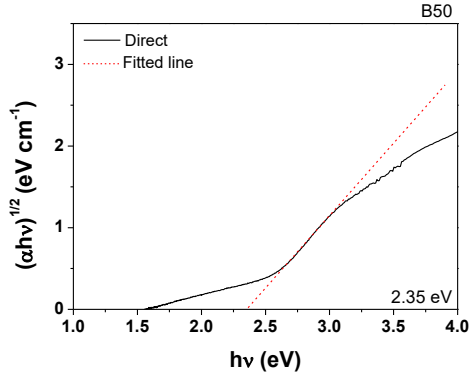
B50
Direct
Fitted line
2.35 eV
(αhν)^1/2 (eV cm^-1)
hν (eV)

l)

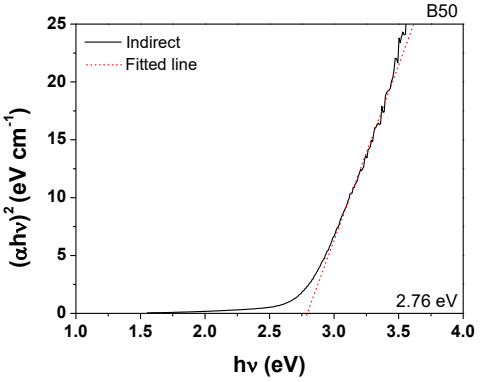
B50
Indirect
Fitted line
2.76 eV
(αhν)^2 (eV cm^-1)
hν (eV)

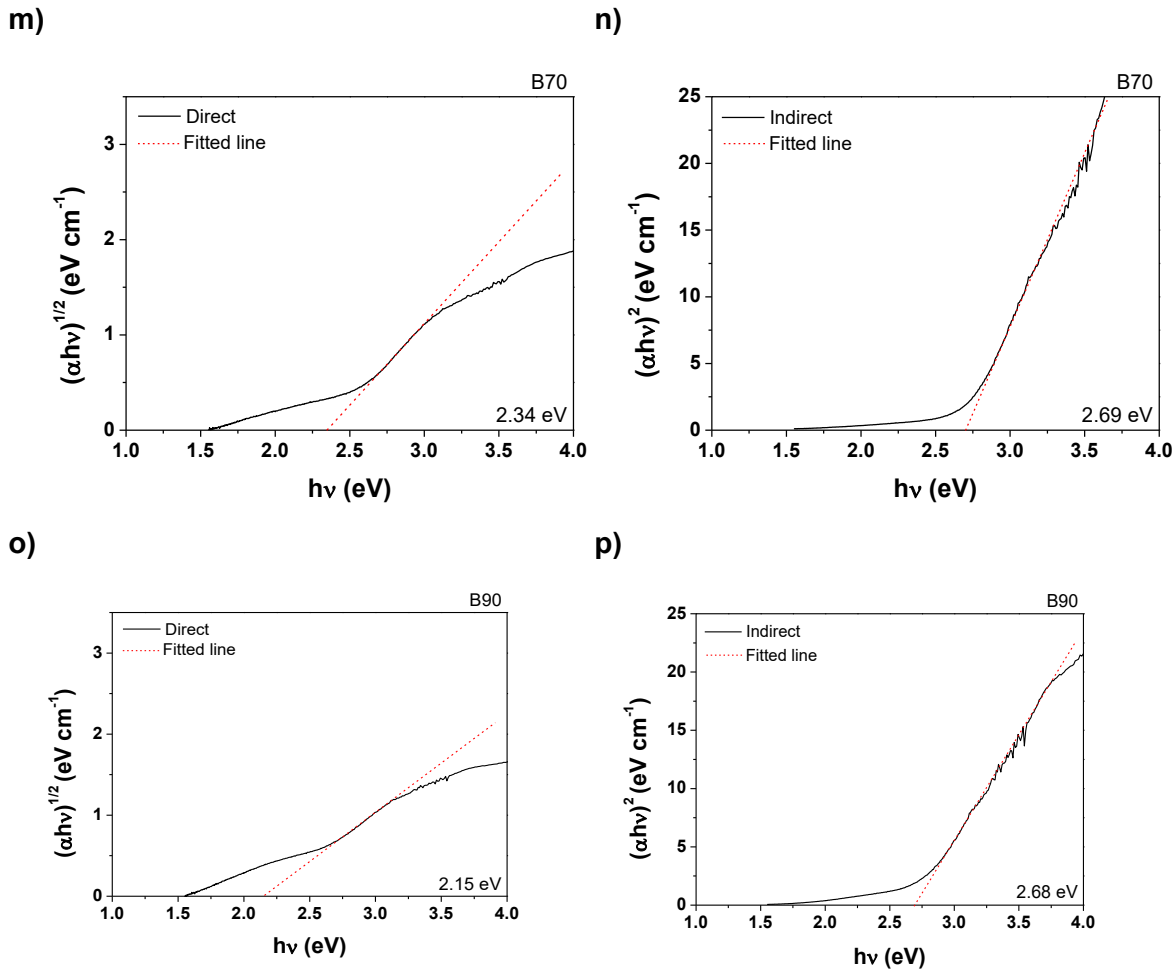

Figure D20. *Tauc's plot for band gap energies calculation: (a,b) direct and indirect plot for AuNPs-2AET-FL_2, (c,d) direct and indirect plot for pure PPA, (e,f) direct and indirect plot for B10 nanocomposite, (g,h) direct and indirect plot for B30 nanocomposite, (i,l) direct and indirect plot for B50 nanocomposite, (m,n) direct and indirect plot for B70 nanocomposite, (o,p) direct and indirect plot for B90 nanocomposite samples.*

Sample	σ (S/m) ·10^{-8}
AuNPs-2AET-FL_2	9.4 ± 0.9
PPA	9.3 ± 0.9
B10	9.6 ± 0.9
B30	8.6 ± 0.9
B50	12 ± 1
B70	18 ± 2
B90	23 ± 2

Table D11. *Electrical conductivity values calculated for pristine AuNPs-2AET-FL_2, pure PPA and related nanocomposite blends.*

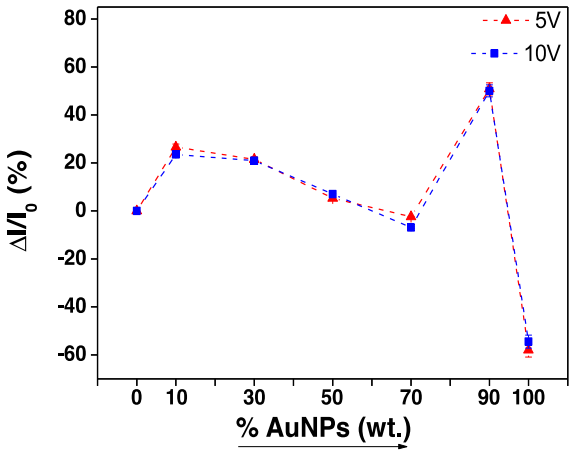

Figure D21. *Dependence of relative current (%) on the AuNPs concentration in PPA blends. (0% stands for PPA only, taken as a reference).*

D2.5. AuNPs/P3HT nanocomposite blend synthesis

Nanocomposite AuNPs-PtDEBP$_n$ (n= 3, 4, 6)/P3HT polymer blends were synthesized through one-step blending approach at room temperature. 0.0040 g of P3HT were dissolved in $CHCl_3$ at a concentration of 2 mg/mL. Similarly, a 2 mg/mL $CHCl_3$ suspension of AuNPs was prepared redispersing 0.0040 g of AuNPs-PtDEBP$_n$ in 2 mL of organic solvent. Then, P3HT and AuNPs suspensions were mixed in a total volume of 1 mL exploring different AuNPs/P3HT weight ratios: 10/90, 30/70, 50/50, 70/30, 90/10 %wt. The mixture was gently stirred for 3 h at room temperature and in the dark. Each nanocomposite suspension was dried using a rotary evaporator and stored at +4°C for further use.

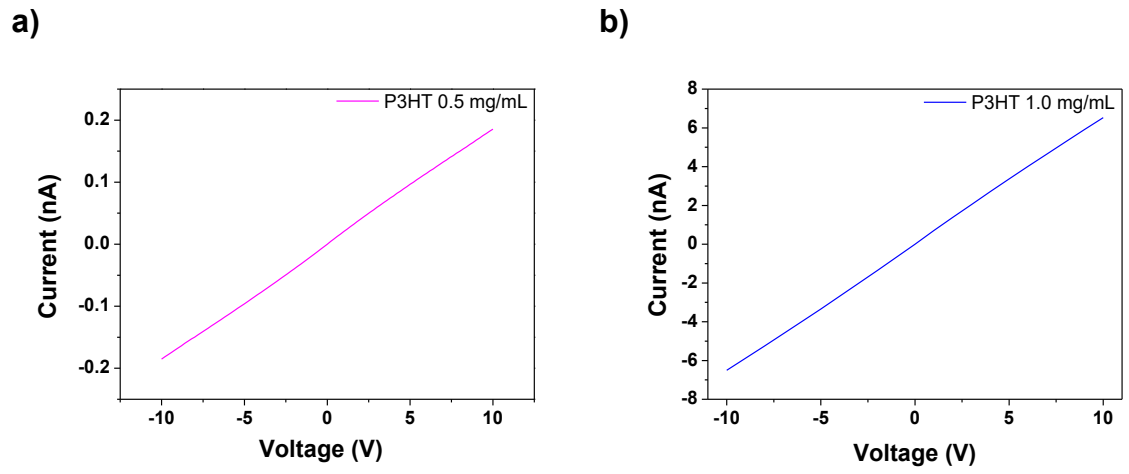

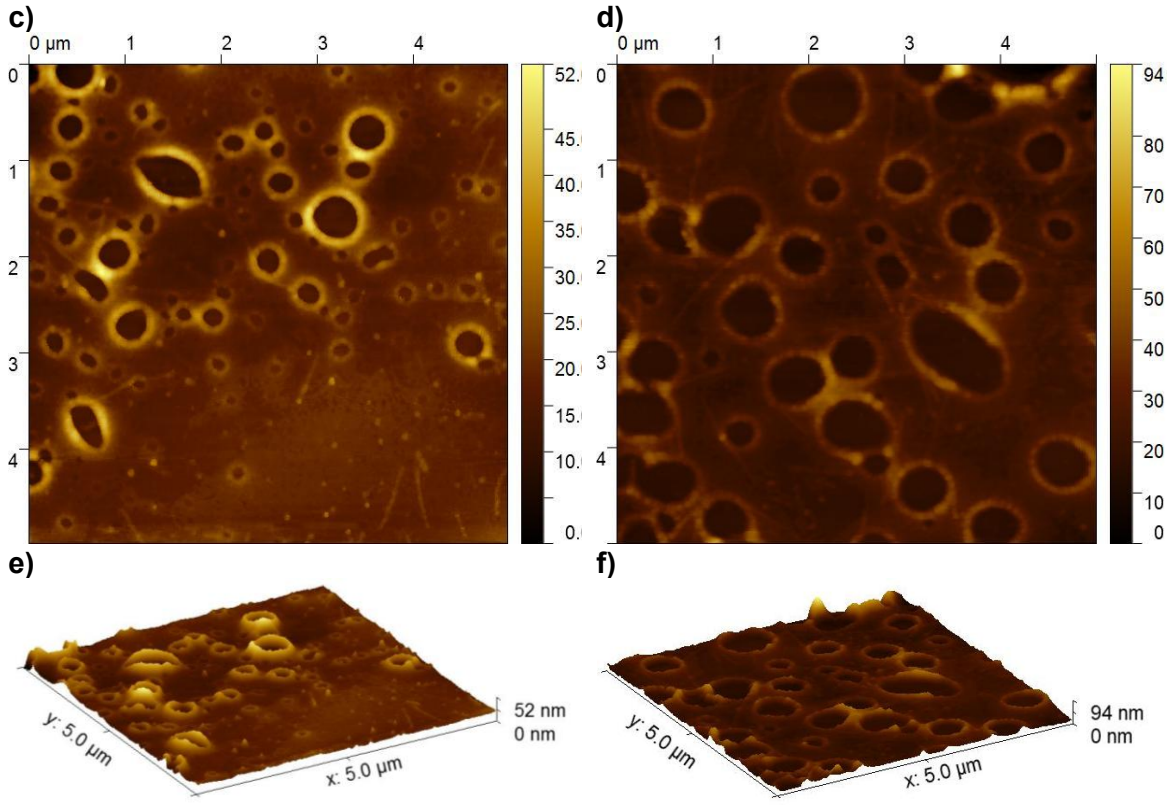

Figure D22. *Electrical measurements of regioregular pristine P3HT at two different concentrations: a) 0.5 mg/mL, and b) 1.0 mg/mL spin-coated onto interdigitated electrodes from $CHCl_3$. c) AFM topography of P3HT spin coated onto Si/SiO_2 substrate at 0.5 mg/mL and 600 rpm. d) AFM topography of P3HT spin coated onto Si/SiO_2 substrate at 1 mg/mL and 600 rpm. e) 3D profile of c). f) 3D profile of d).*

D2.6. AuNPs/P3HT/PLA nanocomposite blend synthesis

Spin coating of polymer/AuNPs blends

The thin films of P3HT-PLA-AuNPs were prepared *via* spin coating. As an example, the preparation of a thin film of P3HT-PLA-AuNPs 45/45/10 is described. 0.0090 g of P3HT, 0.0090 g of PLA and 0.0020 g of AuNPs-FL-4BBT were mixed in 4 mL of $CHCl_3$ (for the 5 mg/mL sample, for more concentrated samples, *i.e.* 10 mg/mL, 2 mL of $CHCl_3$ were used) and stirred (after 1 minute of ultrasound bath) for 30 minutes to obtain a uniform dispersion. The blend was then spin-coated with a SCI spin-coater from KLM GmbH (Germany), at 1000 rpm on either a SiO_2 wafer or homemade transducers to allow for the formation of the thin film.

Table D12 shows a summary of the examined blends, obtained by varying the P3HT, PLA, and AuNPs content. The effect of the molecular weight of PLA was also studied (with number average molecular weight M_n equal to 85-95 kDa (PLA_1) and 15-25 kDa (PLA_2).

Sample ID	P3HT content (wt %)	PLA content (wt %)	AuNPs content (wt %)	M_n PLA (kDa)
BB_1 50	50	50	0	85-95
BB_2 50	50	50	0	15-25
BB_2 10	10	90	0	15-25
BB_2 40	40	60	0	15-25
HB 5	47.5	47.5	5	15-25
HB 10	45	45	10	15-25
HB 10b	10	80	10	15-25
HB 25	37.5	37.5	25	15-25
HB 33	33.3	33.3	33.3	15-25
HB 50	25	25	50	15-25

Table D12. *Summary of the studied binary blends (BB) and hybrid blends (HB).*

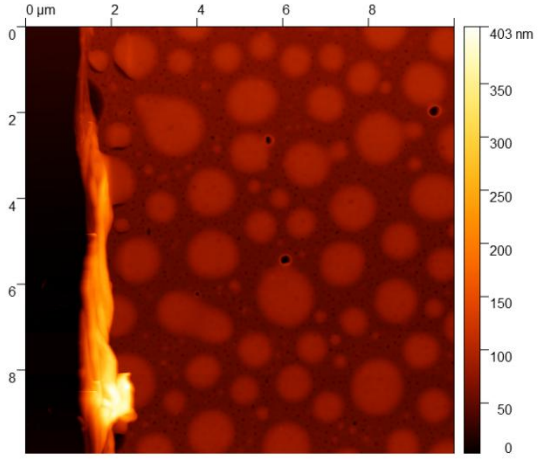

Figure D23. *Binary blends, BB_1 50. as-spun PLA/P3HT blend.*

List of Publications

1. Salamone, T. A.; Rutigliano, L.; Pennacchi, B.; Cerra, S.; Matassa, R.; Nottola, S.; Sciubba, F.; Battocchio, C.; Marsotto, M.; Del Giudice, A.; Chumakov, A.; Davydok, A.; Grigorian, S.; Canettieri, G.; Agostinelli, E.; Fratoddi, I. Thiol Functionalised Gold Nanoparticles Loaded with Methotrexate for Cancer Treatment: From Synthesis to in Vitro Studies on Neuroblastoma Cell Lines. *Journal of Colloid and Interface Science* **2023**, *649*, 264–278. https://doi.org/10.1016/j.jcis.2023.06.078.

This paper deals with the synthesis and thorough characterisation of a novel multi-functionalised AuNPs system. Two hydrophilic thiols stabilised and provided the surface functionality necessary for the use of the gold nanoparticles as drug delivery agents, in this respect, a lipophilic drug, MTX, was successfully loaded on the AuNPs, enhancing its bioavailability and obtaining a system that was successfully tested in vitro against two neuroblastoma cell lines. (vd. Paragraphs 2.1. and 2.2.1)

2. Cerra, S.; Carlini, L.; Salamone, T. A.; Hajareh Haghighi, F.; Mercurio, M.; Pennacchi, B.; Sappino, C.; Battocchio, C.; Nottola, S.; Matassa, R.; Fratoddi, I. Noble Metal Nanoparticles Networks Stabilized by Rod-Like Organometallic Bifunctional Thiols. *ChemistrySelect* **2023**, *8* (13), e202300874. https://doi.org/10.1002/slct.202300874.

This paper shows the synthesis and physico-chemical characterisation of metal (Au, Pd, Ag) nanoparticles networks functionalised by organometallic bifunctional, rigid, π-conjugated ligands, as well as the synthesis of the ligands. XPS data showed, interestingly, an interaction between the aromatic moieties of the backbone and the metal centre of the ligand (Pt), stabilising the organic network. (vd. Paragraph 3.2.1.)

3. Cerra, S.; Cirri, D.; Gabbiani, C.; Pratesi, A.; Grigorian, S.; Matassa, R.; Lozano, J. G.; Beltrán, A. M.; Capocefalo, A.; Fasolato, C.; Scaramuzzo, F. A.; Marsotto, M.; Battocchio, C.; Salamone, T. A.; Pennacchi, B.; Mercurio, M.; Fratoddi, I. Hydrophobic Gold Nanoparticles Coupled with Fluorescent Dyes: A Smart Tool for Optoelectronic Applications. *Inorganica Chimica Acta* **2025**, *579*, 122553. https://doi.org/10.1016/j.ica.2025.122553.

This paper highlights the possibilities of bifunctional π-conjugated ligands to functionalise AuNPs, coupled with a monofunctional fluorescent ligand to add further functionality. The optical properties are underscored by the fluorescence response of the system. The electronic properties, as thin films of blends with a semiconducting polymer (PPA), showed an increase in conductivity (2.5 times) of the blended system compared to pristine PPA. (vd. Paragraph 3.2.3.a.)

4. Salamone, T. A.; Marotta, S.; Mrmić, S.; Raffa, S.; Cerra, S.; Pennacchi, B.; Mercurio, M.; Visco, V.; Alimandi, M.; Ricciardi, M. R.; Taurino, M.; Fratoddi, I.; Trivedi, P.; Anastasiadou, E. MiR-200c Synergizes with Trastuzumab-Loaded Gold Nanoparticles to Overcome Resistance in Ovarian Cancer Cells. *Cancer Nano* **2025**, *16* (1), 29. https://doi.org/10.1186/s12645-025-00330-5.

This paper shows the use of a very stable multi-functionalised gold nanoparticles system (published in paper no. 1) as a platform for the delivery of an antibody, trastuzumab, and its synergy with the use of microRNAs for the in vitro treatment of ovarian cancer. The outstanding results in terms of cell toxicity and cell penetration open new pathways for the synergistic use of AuNPs and bioactive agents, including microRNAs. (vd. Paragraph 2.2.2.)

References

[1] El-Khawaga, A. M.; Zidan, A.; El-Mageed, A. I. A. A. Preparation Methods of Different Nanomaterials for Various Potential Applications: A Review. *Journal of Molecular Structure* **2023**, *1281*, 135148. https://doi.org/10.1016/j.molstruc.2023.135148.

[2] Mekuye, B.; Abera, B. Nanomaterials: An Overview of Synthesis, Classification, Characterization, and Applications. *Nano Select* **2023**, *4* (8), 486–501. https://doi.org/10.1002/nano.202300038.

[3] Baig, N.; Kammakakam, I.; Falath, W. Nanomaterials: A Review of Synthesis Methods, Properties, Recent Progress, and Challenges. *Mater. Adv.* **2021**, *2* (6), 1821–1871. https://doi.org/10.1039/D0MA00807A.

[4] Jamkhande, P. G.; Ghule, N. W.; Bamer, A. H.; Kalaskar, M. G. Metal Nanoparticles Synthesis: An Overview on Methods of Preparation, Advantages and Disadvantages, and Applications. *Journal of Drug Delivery Science and Technology* **2019**, *53*, 101174; 10.1016/j.jddst.2019.101174.

[5] Saleh, T. A. Nanomaterials: Classification, Properties, and Environmental Toxicities. *Environmental Technology & Innovation* **2020**, *20*, 101067. https://doi.org/10.1016/j.eti.2020.101067.

[6] Joudeh, N.; Linke, D. Nanoparticle Classification, Physicochemical Properties, Characterization, and Applications: A Comprehensive Review for Biologists. *J Nanobiotechnol* **2022**, *20* (1), 262. https://doi.org/10.1186/s12951-022-01477-8.

[7] Wu, Q.; Miao, W.; Zhang, Y.; Gao, H.; Hui, D. Mechanical Properties of Nanomaterials: A Review. *Nanotechnology Reviews* **2020**, *9* (1), 259–273. https://doi.org/10.1515/ntrev-2020-0021.

[8] El-Kady, M. M.; Ansari, I.; Arora, C.; Rai, N.; Soni, S.; Verma, D. K.; Singh, P.; Mahmoud, A. E. D. Nanomaterials: A Comprehensive Review of Applications, Toxicity, Impact, and Fate to Environment. *Journal of Molecular Liquids* **2023**, *370*, 121046. https://doi.org/10.1016/j.molliq.2022.121046.

[9] Paras; Yadav, K.; Kumar, P.; Teja, D. R.; Chakraborty, S.; Chakraborty, M.; Mohapatra, S. S.; Sahoo, A.; Chou, M. M. C.; Liang, C.-T.; Hang, D.-R. A Review on Low-Dimensional Nanomaterials: Nanofabrication, Characterization and Applications. *Nanomaterials* **2022**, *13* (1), 160. https://doi.org/10.3390/nano13010160.

[10] Aubert, T.; Golovatenko, A. A.; Samoli, M.; Lermusiaux, L.; Zinn, T.; Abécassis, B.; Rodina, A. V.; Hens, Z. General Expression for the Size-Dependent Optical Properties of Quantum Dots. *Nano Lett.* **2022**, *22* (4), 1778–1785. https://doi.org/10.1021/acs.nanolett.2c00056.

[11] Pabari, C. Size Dependent Properties of Metallic Nanoparticles. *Materials Today: Proceedings* **2022**, *55*, 98–101. https://doi.org/10.1016/j.matpr.2021.12.375.

[12] Barhoum, A.; García-Betancourt, M. L.; Jeevanandam, J.; Hussien, E. A.; Mekkawy, S. A.; Mostafa, M.; Omran, M. M.; S. Abdalla, M.; Bechelany, M. Review on Natural, Incidental,

Bioinspired, and Engineered Nanomaterials: History, Definitions, Classifications, Synthesis, Properties, Market, Toxicities, Risks, and Regulations. *Nanomaterials* **2022**, *12* (2), 177. https://doi.org/10.3390/nano12020177.

[13] Khan, Y.; Sadia, H.; Ali Shah, S. Z.; Khan, M. N.; Shah, A. A.; Ullah, N.; Ullah, M. F.; Bibi, H.; Bafakeeh, O. T.; Khedher, N. B.; Eldin, S. M.; Fadhl, B. M.; Khan, M. I. Classification, Synthetic, and Characterization Approaches to Nanoparticles, and Their Applications in Various Fields of Nanotechnology: A Review. *Catalysts* **2022**, *12* (11), 1386. https://doi.org/10.3390/catal12111386.

[14] Kolahalam, L. A.; Kasi Viswanath, I. V.; Diwakar, B. S.; Govindh, B.; Reddy, V.; Murthy, Y. L. N. Review on Nanomaterials: Synthesis and Applications. *Materials Today: Proceedings* **2019**, *18*, 2182–2190. https://doi.org/10.1016/j.matpr.2019.07.371.

[15] Sajid, M. Nanomaterials: Types, Properties, Recent Advances, and Toxicity Concerns. *Current Opinion in Environmental Science & Health* **2022**, *25*, 100319. https://doi.org/10.1016/j.coesh.2021.100319.

[16] K Karunakar, K.; Cheriyan, B. V.; R, K.; M, G.; B, A. Therapeutic Advancements in Nanomedicine: The Multifaceted Roles of Silver Nanoparticles. *Biotechnology Notes* **2024**, *5*, 64–79. https://doi.org/10.1016/j.biotno.2024.05.002.

[17] Lopes, T. S.; Alves, G. G.; Pereira, M. R.; Granjeiro, J. M.; Leite, P. E. C. Advances and Potential Application of Gold Nanoparticles in Nanomedicine. *J of Cellular Biochemistry* **2019**, *120* (10), 16370–16378. https://doi.org/10.1002/jcb.29044.

[18] Zhao, Q.; Yu, H.; Hu, D.; Li, L.-L.; Jin, J.; Ai, M.-J.; Wei, J.; Song, K. Recent Advances in Electrochemical Sensors Based on Palladium Nanoparticles. *Chinese Journal of Analytical Chemistry* **2022**, *50* (11), 100144. https://doi.org/10.1016/j.cjac.2022.100144.

[19] Marin, M.; Nikolic, M. V.; Vidic, J. Rapid Point-of-need Detection of Bacteria and Their Toxins in Food Using Gold Nanoparticles. *Comp Rev Food Sci Food Safe* **2021**, *20* (6), 5880–5900. https://doi.org/10.1111/1541-4337.12839.

[20] Kaushik, T.; Ghosh, S.; Dolkar, T.; Biswas, R.; Dutta, A. Noble Metal Plasmon–Molecular Catalyst Hybrids for Renewable Energy Relevant Small Molecule Activation. *ACS Nanosci. Au* **2024**, *4* (5), 273–289. https://doi.org/10.1021/acsnanoscienceau.4c00009.

[21] Heiligtag, F. J.; Niederberger, M. The Fascinating World of Nanoparticle Research. *Materials Today* **2013**, *16* (7–8), 262–271. https://doi.org/10.1016/j.mattod.2013.07.004.

[22] Freestone I., Meeks N., Sax M., Higgitt C., The Lycurgus Cup — A Roman nanotechnology, *Gold Bull*, **2007**, 40, 270-277. https://doi.org/10.1007/BF03215599.

[23] Cai, Y.; Choi, Y. C.; Kagan, C. R. Chemical and Physical Properties of Photonic Noble-Metal Nanomaterials. *Advanced Materials* **2023**, *35* (34), 2108104. https://doi.org/10.1002/adma.202108104.

[24] Mori, T.; Hegmann, T. Determining the Composition of Gold Nanoparticles: A Compilation of Shapes, Sizes, and Calculations Using Geometric Considerations. *J Nanopart Res* **2016**, *18* (10), 295. https://doi.org/10.1007/s11051-016-3587-7.

[25] Stewart, S.; Wei, Q.; Sun, Y. Surface Chemistry of Quantum-Sized Metal Nanoparticles under Light Illumination. *Chem. Sci.* **2021**, *12* (4), 1227–1239. https://doi.org/10.1039/D0SC04651E.

[26] Sarfraz, N.; Ibrahim Khan, I. Plasmonic Gold Nanoparticles (AuNPs): Properties, Synthesis and their Advanced Energy, Environmental and Biomedical Applications. *Chem Asian J*, **2021**, 16, 720 – 742. https://doi.org/10.1002/asia.202001202720.

[27] Khurana, K.; Jaggi, N. Localized Surface Plasmonic Properties of Au and Ag Nanoparticles for Sensors: A Review. *Plasmonics* **2021**, *16* (4), 981–999. https://doi.org/10.1007/s11468-021-01381-1.

[28] Hou, W.; Cronin, S. B. A Review of Surface Plasmon Resonance-Enhanced Photocatalysis. *Adv Funct Materials* **2013**, *23* (13), 1612–1619. https://doi.org/10.1002/adfm.201202148.

[29] Kuiri, P. K. Control of Ultraviolet Surface Plasmon Absorption of Al Nanoparticles by Changing Particle Size, Shape, Interaction, and Medium Dielectric Constant. *Plasmonics* **2020**, *15* (4), 933–940. https://doi.org/10.1007/s11468-019-01113-6.

[30] Amendola, V.; Meneghetti, M. Laser Ablation Synthesis in Solution and Size Manipulation of Noble Metal Nanoparticles. *Phys. Chem. Chem. Phys.* **2009**, *11* (20), 3805. https://doi.org/10.1039/b900654k.

[31] Sardar, R.; Funston, A. M.; Mulvaney, P.; Murray, R. W. Gold Nanoparticles: Past, Present, and Future. *Langmuir* **2009**, *25* (24), 13840–13851. https://doi.org/10.1021/la9019475.

[32] Alkilany, A. M.; Lohse, S. E.; Murphy, C. J. The Gold Standard: Gold Nanoparticle Libraries To Understand the Nano–Bio Interface. *Acc. Chem. Res.* **2013**, *46* (3), 650–661. https://doi.org/10.1021/ar300015b.

[33] Amin, M. U.; Fang, J. Self-Assembled Gold Nano-Bipyramids for Solution-Based Surface-Enhanced Raman Spectroscopy Detection. *ACS Appl. Nano Mater.* **2022**, *5* (8), 10421–10430. https://doi.org/10.1021/acsanm.2c01779.

[34] Mosquera, J.; Wang, D.; Bals, S.; Liz-Marzán, L. M. Surfactant Layers on Gold Nanorods. *Acc. Chem. Res.* **2023**, *56* (10), 1204–1212. https://doi.org/10.1021/acs.accounts.3c00101.

[35] Wu, Y.; Yang, Q.; Chen, J.; Bi, L.; Zhang, Z.; Zhou, N.; Ostovan, A.; Arabi, M.; Chen, L.; Choo, J. Surface-Enhanced Raman Scattering-Based Lateral Flow Assay Strips Using Highly Symmetric Gold Nanostars. *ACS Appl. Nano Mater.* **2024**, *7* (23), 27134–27141. https://doi.org/10.1021/acsanm.4c05151.

[36] Alba-Molina, D.; Giner-Casares, J. J.; Cano, M. Bioconjugated Plasmonic Nanoparticles for Enhanced Skin Penetration. In *Surface-modified Nanobiomaterials for Electrochemical and Biomedicine Applications*; Puente-Santiago, A. R., Rodríguez-Padrón, D., Eds.; Topics in Current

Chemistry Collections; Springer International Publishing: Cham, **2020**; pp 219–235. https://doi.org/10.1007/978-3-030-55502-3_7.

[37] Jain, P. K.; Huang, W.; El-Sayed, M. A. On the Universal Scaling Behavior of the Distance Decay of Plasmon Coupling in Metal Nanoparticle Pairs: A Plasmon Ruler Equation. *Nano Lett.* **2007**, *7* (7), 2080–2088. https://doi.org/10.1021/nl071008a.

[38] Link, S.; El-Sayed, M. A. Size and Temperature Dependence of the Plasmon Absorption of Colloidal Gold Nanoparticles. *J. Phys. Chem. B* **1999**, *103* (21), 4212–4217. https://doi.org/10.1021/jp984796o.

[39] Yockell-Lelièvre, H.; Lussier, F.; Masson, J.-F. Influence of the Particle Shape and Density of Self-Assembled Gold Nanoparticle Sensors on LSPR and SERS. *J. Phys. Chem. C* **2015**, *119* (51), 28577–28585. https://doi.org/10.1021/acs.jpcc.5b09570.

[40] Jain, P. K.; El-Sayed, M. A. Plasmonic Coupling in Noble Metal Nanostructures. *Chemical Physics Letters* **2010**, *487* (4–6), 153–164. https://doi.org/10.1016/j.cplett.2010.01.062.

[41] Ghosh, S. K.; Nath, S.; Kundu, S.; Esumi, K.; Pal, T. Solvent and Ligand Effects on the Localized Surface Plasmon Resonance (LSPR) of Gold Colloids. *J. Phys. Chem. B* **2004**, *108* (37), 13963–13971. https://doi.org/10.1021/jp047021q.

[42] Zhang, H.; Chen, H.-J.; Du, X.; Wen, D. Photothermal Conversion Characteristics of Gold Nanoparticle Dispersions. *Solar Energy* **2014**, *100*, 141–147. https://doi.org/10.1016/j.solener.2013.12.004.

[43] Kader, Md. A.; Suhaity Azmi, N.; Kafi, A. K. M. Recent Advances in Gold Nanoparticles Modified Electrodes in Electrochemical Nonenzymatic Sensing of Chemical and Biological Compounds. *Inorganic Chemistry Communications* **2023**, *153*, 110767. https://doi.org/10.1016/j.inoche.2023.110767.

[44] Coetzee, D.; Venkataraman, M.; Militky, J.; Petru, M. Influence of Nanoparticles on Thermal and Electrical Conductivity of Composites. *Polymers* **2020**, *12* (4), 742. https://doi.org/10.3390/polym12040742.

[45] Ijaz, I.; Gilani, E.; Nazir, A.; Bukhari, A. Detail Review on Chemical, Physical and Green Synthesis, Classification, Characterizations and Applications of Nanoparticles. *Green Chemistry Letters and Reviews* **2020**, *13* (3), 223–245. https://doi.org/10.1080/17518253.2020.1802517.

[46] Vinukonda, A.; Bolledla, N.; Jadi, R. K.; Chinthala, R.; Devadasu, V. R. Synthesis of Nanoparticles Using Advanced Techniques. *Next Nanotechnology* **2025**, *8*, 100169. https://doi.org/10.1016/j.nxnano.2025.100169.

[47] Gain, A. K.; Cui, Y.; Zhang, L.; Li, Z. Mechanical Properties of Additively Manufactured Ultrafine Grain Stainless Steel-Titanium Boride (SS–TiB2) Nanocomposites. *Materials Science and Engineering: A* **2024**, *911*, 146961. https://doi.org/10.1016/j.msea.2024.146961.

[48] Yadwade, R.; Gharpure, S.; Lestari, G. A. D.; Sur, U. K.; Sarma, L. S.; Singh, S. C. E.; Sarmah, J. K.; Mohanta, D.; Ankamwar, B. Seed-Mediated Synthesis and Biosynthesis of Iron Oxide Nanoparticles. *3 Biotech* **2025**, *15* (8), 258. https://doi.org/10.1007/s13205-025-04431-1.

[49] Guo, Q.; Huang, D.; Kou, X.; Cao, W.; Li, L.; Ge, L.; Li, J. Synthesis of Disperse Amorphous SiO2 Nanoparticles via Sol–Gel Process. *Ceramics International* **2017**, *43* (1), 192–196. https://doi.org/10.1016/j.ceramint.2016.09.133.

[50] Chandekar, K. V.; Yadav, S. P.; Chinke, S.; Shkir, Mohd. Impact of Co-Doped NiFe2O4 (CoxNi1−xFe2O4) Nanostructures Prepared by Co-Precipitation Route on the Structural, Morphological, Surface, and Magnetic Properties. *Journal of Alloys and Compounds* **2023**, *966*, 171556. https://doi.org/10.1016/j.jallcom.2023.171556.

[51] Tirkey, A.; Babu, P. J. Synthesis and Characterization of Citrate-Capped Gold Nanoparticles and Their Application in Selective Detection of Creatinine (A Kidney Biomarker). *Sensors International* **2024**, *5*, 100252. https://doi.org/10.1016/j.sintl.2023.100252.

[52] Pradeepa; Vasappa, R. K.; Mohan, D. S.; Krishnaswamy, M. B.; Srinivasalu, A. K. H.; Kamath Halladi, V.; Gamana, G.; Muddappa, V. S. Ascorbic Acid - Sodium Borohydride Coupled Supersensitive Gold Nanoparticles for Water Quality Assurance. *Nanotechnol. Environ. Eng.* **2025**, *10* (1), 12. https://doi.org/10.1007/s41204-025-00406-y.

[53] Newman, J. D. S.; Blanchard, G. J. Formation and Encapsulation of Gold Nanoparticles Using a Polymeric Amine Reducing Agent. *J Nanopart Res* **2007**, *9* (5), 861–868. https://doi.org/10.1007/s11051-006-9145-y.

[54] Daruich De Souza, C.; Ribeiro Nogueira, B.; Rostelato, M. E. C. M. Review of the Methodologies Used in the Synthesis Gold Nanoparticles by Chemical Reduction. *Journal of Alloys and Compounds* **2019**, *798*, 714–740. https://doi.org/10.1016/j.jallcom.2019.05.153.

[55] Lu, J.; Dreisinger, D. B.; Cooper, W. C. Cobalt Precipitation by Reduction with Sodium Borohydride. *Hydrometallurgy* **1997**, *45* (3), 305–322. https://doi.org/10.1016/S0304-386X(96)00086-2.

[56] Chen, Y.-C.; Chen, J.-Y.; Wu, W.-W. In Situ Observation of Au Nanostructure Evolution in Liquid Cell TEM. *J. Phys. Chem. C* **2017**, *121* (46), 26069–26075. https://doi.org/10.1021/acs.jpcc.7b07956.

[57] Karimadom, B. R.; Kornweitz, H. Mechanism of Producing Metallic Nanoparticles, with an Emphasis on Silver and Gold Nanoparticles, Using Bottom-Up Methods. *Molecules* **2021**, *26* (10), 2968. https://doi.org/10.3390/molecules26102968.

[58] Gorkanti, S.; Dasari, A.; Padma, S. M. Design, Synthesis, Characterization, Catalytic, Fluorometric Sensing, Antimicrobial and Antioxidant Activities of Schiff Base Ligand Capped AgNPs. *J Fluoresc* **2022**, *32* (6), 2363–2378. https://doi.org/10.1007/s10895-022-03026-w.

[59] Jose, P. A.; Sankarganesh, M.; Raja, J. D.; Senthilkumar, G. S. Synthesis of Methoxy Substituted Pyrimidine Derivative Imine Stabilized Copper Nanoparticles in Organic Phase and Its Biological

Evaluation. *Journal of Molecular Liquids* **2020**, *305*, 112821. https://doi.org/10.1016/j.molliq.2020.112821.

[60] Gavia, D. J.; Shon, Y.-S. Controlling Surface Ligand Density and Core Size of Alkanethiolate-Capped Pd Nanoparticles and Their Effects on Catalysis. *Langmuir* **2012**, *28* (40), 14502–14508. https://doi.org/10.1021/la302653u.

[61] Brust, M.; Walker, M.; Bethell, D.; Schiffrin, D. J.; Whyman, R. Synthesis of Thiol-Derivatised Gold Nanoparticles in a Two-Phase Liquid–Liquid System. *J. Chem. Soc., Chem. Commun.* **1994**, *0* (7), 801–802. https://doi.org/10.1039/C39940000801.

[62] Perala, S. R. K.; Kumar, S. On the Mechanism of Phase Transfer Catalysis in Brust–Schiffrin Synthesis of Metal Nanoparticles. *Langmuir* **2013**, *29* (48), 14756–14762. https://doi.org/10.1021/la403652k.

[63] Corbierre, M. K.; Lennox, R. B. Preparation of Thiol-Capped Gold Nanoparticles by Chemical Reduction of Soluble Au(I)−Thiolates. *Chem. Mater.* **2005**, *17* (23), 5691–5696. https://doi.org/10.1021/cm051115a.

[64] Patil, T.; Gambhir, R.; Vibhute, A.; Tiwari, A. P. Gold Nanoparticles: Synthesis Methods, Functionalization and Biological Applications. *J Clust Sci* **2023**, *34* (2), 705–725. https://doi.org/10.1007/s10876-022-02287-6.

[65] Yazdani, S.; Daneshkhah, A.; Diwate, A.; Patel, H.; Smith, J.; Reul, O.; Cheng, R.; Izadian, A.; Hajrasouliha, A. R. Model for Gold Nanoparticle Synthesis: Effect of pH and Reaction Time. *ACS Omega* **2021**, *6* (26), 16847–16853. https://doi.org/10.1021/acsomega.1c01418.

[66] Frenkel, A. I.; Nemzer, S.; Pister, I.; Soussan, L.; Harris, T.; Sun, Y.; Rafailovich, M. H. Size-Controlled Synthesis and Characterization of Thiol-Stabilized Gold Nanoparticles. *The Journal of Chemical Physics* **2005**, *123* (18), 184701. https://doi.org/10.1063/1.2126666.

[67] Fratoddi, I. Hydrophobic and Hydrophilic Au and Ag Nanoparticles. Breakthroughs and Perspectives. *Nanomaterials* **2017**, *8* (1), 11. https://doi.org/10.3390/nano8010011.

[68] Lee, J. W.; Choi, S.-R.; Heo, J. H. Simultaneous Stabilization and Functionalization of Gold Nanoparticles via Biomolecule Conjugation: Progress and Perspectives. *ACS Appl. Mater. Interfaces* **2021**, *13* (36), 42311–42328. https://doi.org/10.1021/acsami.1c10436.

[69] Carone, A.; Emilsson, S.; Mariani, P.; Désert, A.; Parola, S. Gold Nanoparticle Shape Dependence of Colloidal Stability Domains. *Nanoscale Adv.* **2023**, *5* (7), 2017–2026. https://doi.org/10.1039/D2NA00809B.

[70] Segets, D.; Marczak, R.; Schäfer, S.; Paula, C.; Gnichwitz, J.-F.; Hirsch, A.; Peukert, W. Experimental and Theoretical Studies of the Colloidal Stability of Nanoparticles−A General Interpretation Based on Stability Maps. *ACS Nano* **2011**, *5* (6), 4658–4669. https://doi.org/10.1021/nn200465b.

[71] Dinkel, R.; Braunschweig, B.; Peukert, W. Fast and Slow Ligand Exchange at the Surface of Colloidal Gold Nanoparticles. *J. Phys. Chem. C* **2016**, *120* (3), 1673–1682. https://doi.org/10.1021/acs.jpcc.5b11055.

[72] Al-Johani, H.; Abou-Hamad, E.; Jedidi, A.; Widdifield, C. M.; Viger-Gravel, J.; Sangaru, S. S.; Gajan, D.; Anjum, D. H.; Ould-Chikh, S.; Hedhili, M. N.; Gurinov, A.; Kelly, M. J.; El Eter, M.; Cavallo, L.; Emsley, L.; Basset, J.-M. The Structure and Binding Mode of Citrate in the Stabilization of Gold Nanoparticles. *Nature Chem* **2017**, *9* (9), 890–895. https://doi.org/10.1038/nchem.2752.

[73] Heuer-Jungemann, A.; Feliu, N.; Bakaimi, I.; Hamaly, M.; Alkilany, A.; Chakraborty, I.; Masood, A.; Casula, M. F.; Kostopoulou, A.; Oh, E.; Susumu, K.; Stewart, M. H.; Medintz, I. L.; Stratakis, E.; Parak, W. J.; Kanaras, A. G. The Role of Ligands in the Chemical Synthesis and Applications of Inorganic Nanoparticles. *Chem. Rev.* **2019**, *119* (8), 4819–4880. https://doi.org/10.1021/acs.chemrev.8b00733.

[74] Njoki, P. N.; Luo, J.; Kamundi, M. M.; Lim, S.; Zhong, C.-J. Aggregative Growth in the Size-Controlled Growth of Monodispersed Gold Nanoparticles. *Langmuir* **2010**, *26* (16), 13622–13629. https://doi.org/10.1021/la1019058.

[75] Silva, L. I. M.; Pérez-Gramatges, A.; Larrude, D. G.; Almeida, J. M. S.; Aucélio, R. Q.; Da Silva, A. R. Gold Nanoparticles Produced Using NaBH4 in Absence and in the Presence of One-Tail or Two-Tail Cationic Surfactants: Characteristics and Optical Responses Induced by Aminoglycosides. *Colloids and Surfaces A: Physicochemical and Engineering Aspects* **2021**, *614*, 126174. https://doi.org/10.1016/j.colsurfa.2021.126174.

[76] Zürbes, K. R.; Mani, E.; Bandyopadhyay, S. Synthesis of Anisotropic Gold Nanoparticles in Binary Surfactant Mixtures: A Review on Mechanisms of Particle Formation. *RSC Adv.* **2025**, *15* (6), 4377–4407. https://doi.org/10.1039/D4RA06358A.

[77] Ulman, A. Formation and Structure of Self-Assembled Monolayers. *Chem. Rev.* **1996**, *96* (4), 1533–1554. https://doi.org/10.1021/cr9502357.

[78] Zhang, B.; Chen, J.; Cao, Y.; Chai, O. J. H.; Xie, J. Ligand Design in Ligand-Protected Gold Nanoclusters. *Small* **2021**, *17* (27), 2004381. https://doi.org/10.1002/smll.202004381.

[79] Tang, C.; Ku, K. H.; Lennon Luo, S.-X.; Concellón, A.; Wu, Y.-C. M.; Lu, R.-Q.; Swager, T. M. Chelating Phosphine Ligand Stabilized AuNPs in Methane Detection. *ACS Nano* **2020**, *14* (9), 11605–11612. https://doi.org/10.1021/acsnano.0c04154.

[80] Porcheron, A.; Sadek, O.; Sowid, S. B.; Bridonneau, N.; Hippolyte, L.; Mercier, D.; Marcus, P.; Mutalliev, L.; Chauvier, C.; Chanéac, C.; Fensterbank, L.; Ribot, F. Direct Synthesis of Mesoionic Carbene (MIC)-Stabilized Gold Nanoparticles from 1,2,3-Triazolium Salts. *Chem. Mater.* **2023**, *35* (17), 6865–6876. https://doi.org/10.1021/acs.chemmater.3c01162.

[81] Crudden, C. M.; Horton, J. H.; Ebralidze, I. I.; Zenkina, O. V.; McLean, A. B.; Drevniok, B.; She, Z.; Kraatz, H.-B.; Mosey, N. J.; Seki, T.; Keske, E. C.; Leake, J. D.; Rousina-Webb, A.; Wu, G. Ultra Stable Self-Assembled Monolayers of N-Heterocyclic Carbenes on Gold. *Nature Chem* **2014**, *6* (5), 409–414. https://doi.org/10.1038/nchem.1891.

[82] Smith, C. A.; Narouz, M. R.; Lummis, P. A.; Singh, I.; Nazemi, A.; Li, C.-H.; Crudden, C. M. *N* -Heterocyclic Carbenes in Materials Chemistry. *Chem. Rev.* **2019**, *119* (8), 4986–5056. https://doi.org/10.1021/acs.chemrev.8b00514.

[83] Chatterjee, S.; Lou, X.-Y.; Liang, F.; Yang, Y.-W. Surface-Functionalized Gold and Silver Nanoparticles for Colorimetric and Fluorescent Sensing of Metal Ions and Biomolecules. *Coordination Chemistry Reviews* **2022**, *459*, 214461. https://doi.org/10.1016/j.ccr.2022.214461.

[84] Hernández-Esparza, M. J.; Fratoddi, I.; Cerra, S.; Juarez-Moreno, K.; Huirache-Acuña, R. Hybrid AuNPs-3MPS-MTX Nanosystem and Its Evaluation for Treating Cervical Cancer and Melanoma. *Nanoscale Adv.* **2023**, *5* (24), 7077–7085. https://doi.org/10.1039/D3NA00605K.

[85] Ngernpimai, S.; Puangmali, T.; Kopwitthaya, A.; Tippayawat, P.; Chompoosor, A.; Teerasong, S. Enhanced Stability of Gold Nanoparticles with Thioalkylated Carboxyl-Terminated Ligands for Applications in Biosensing. *ACS Appl. Nano Mater.* **2024**, *7* (11), 13124–13133. https://doi.org/10.1021/acsanm.4c01631.

[86] Fratoddi, I.; Battocchio, C.; Iucci, G.; Catone, D.; Cartoni, A.; Paladini, A.; O'Keeffe, P.; Nappini, S.; Cerra, S.; Venditti, I. Silver Nanoparticles Functionalized by Fluorescein Isothiocyanate or Rhodamine B Isothiocyanate: Fluorescent and Plasmonic Materials. *Applied Sciences* **2021**, *11* (6), 2472. https://doi.org/10.3390/app11062472.

[87] Khosroshahi, M. E.; Morison, V. W.; Chabok, R.; Patel, Y.; Mohmedi, T. Observation and Biomedical Application of Plasmon-Enhanced Fluorescence Induced Multiple Stimulated Stokes Raman Scattering in FITC-Conjugated Gold Nanoparticles Solution. *Laser Phys.* **2022**, *32* (10), 105601. https://doi.org/10.1088/1555-6611/ac9373.

[88] Liao, J.; Blok, S.; Van Der Molen, S. J.; Diefenbach, S.; Holleitner, A. W.; Schönenberger, C.; Vladyka, A.; Calame, M. Ordered Nanoparticle Arrays Interconnected by Molecular Linkers: Electronic and Optoelectronic Properties. *Chem. Soc. Rev.* **2015**, *44* (4), 999–1014. https://doi.org/10.1039/C4CS00225C.

[89] Wang, H.; Liu, Y.; Yu, J.; Luo, Y.; Wang, L.; Yang, T.; Raktani, B.; Lee, H. Selectively Regulating the Chiral Morphology of Amino Acid-Assisted Chiral Gold Nanoparticles with Circularly Polarized Light. *ACS Appl. Mater. Interfaces* **2022**, *14* (2), 3559–3567. https://doi.org/10.1021/acsami.1c22191.

[90] Huang, R.; Wang, D.; Liu, S.; Guo, L.; Wang, F.; Lin, Z.; Qiu, B.; Chen, G. Preparative Separation of Enantiomers Based on Functional Nucleic Acids Modified Gold Nanoparticles. *Chirality* **2013**, *25* (11), 751–756. https://doi.org/10.1002/chir.22208.

[91] Chen, X.; Würbser, M. A.; Boekhoven, J. Chemically Fueled Supramolecular Materials. *Acc. Mater. Res.* **2023**, *4* (5), 416–426. https://doi.org/10.1021/accountsmr.2c00244.

[92] Zhao, Y.; Cui, C.; Fan, G.; Shi, H. Stimuli-triggered Self-Assembly of Gold Nanoparticles: Recent Advances in Fabrication and Biomedical Applications. *Chemistry An Asian Journal* **2024**, *19* (7), e202400015. https://doi.org/10.1002/asia.202400015.

[93] Grzelczak, M.; Liz-Marzán, L. M.; Klajn, R. Stimuli-Responsive Self-Assembly of Nanoparticles. *Chem. Soc. Rev.* **2019**, *48* (5), 1342–1361. https://doi.org/10.1039/C8CS00787J.

[94] Lee, M. S.; Yee, D. W.; Ye, M.; Macfarlane, R. J. Nanoparticle Assembly as a Materials Development Tool. *J. Am. Chem. Soc.* **2022**, *144* (8), 3330–3346. https://doi.org/10.1021/jacs.1c12335.

[95] Zhao, H.; Sen, S.; Udayabhaskararao, T.; Sawczyk, M.; Kučanda, K.; Manna, D.; Kundu, P. K.; Lee, J.-W.; Král, P.; Klajn, R. Reversible Trapping and Reaction Acceleration within Dynamically Self-Assembling Nanoflasks. *Nature Nanotech* **2016**, *11* (1), 82–88. https://doi.org/10.1038/nnano.2015.256.

[96] Wang, L.; Wang, Y.; Dong, S.; Deng, Y.; Hao, J. Nanocapsules of Magnetic Au Self-Assembly for DNA Migration and Secondary Self-Assembly. *ACS Appl. Mater. Interfaces* **2018**, *10* (6), 5348–5357. https://doi.org/10.1021/acsami.7b18689.

[97] Cho, E. C.; Choi, S.-W.; Camargo, P. H. C.; Xia, Y. Thiol-Induced Assembly of Au Nanoparticles into Chainlike Structures and Their Fixing by Encapsulation in Silica Shells or Gelatin Microspheres. *Langmuir* **2010**, *26* (12), 10005–10012. https://doi.org/10.1021/la100127w.

[98] Jin, Y.; Yu, C.; Denman, R. J.; Zhang, W. Recent Advances in Dynamic Covalent Chemistry. *Chem. Soc. Rev.* **2013**, *42* (16), 6634. https://doi.org/10.1039/c3cs60044k.

[99] Kim, G.-H.; Kim, M.; Hyun, J. K.; Park, S.-J. Directional Self-Assembly of Nanoparticles Coated with Thermoresponsive Block Copolymers and Charged Small Molecules. *ACS Macro Lett.* **2023**, *12* (7), 986–992. https://doi.org/10.1021/acsmacrolett.3c00221.

[100] Roy, S.; Gravener, L.; Philp, D.; Kay, E. R. A Dissipative Reaction Network Drives Transient Solid–Liquid and Liquid–Liquid Phase Cycling of Nanoparticles. *Angew Chem Int Ed* **2023**, *62* (22), e202217613. https://doi.org/10.1002/anie.202217613.

[101] Edward, A. K.; Ettlinger, R.; Janczuk, Z. Z.; Hua, G.; Morris, R. E.; Kay, E. R. Chemospecific Heterostructure and Heteromaterial Assembly of Metal–Organic Framework Nanoparticles. *J. Am. Chem. Soc.* **2025**, *147* (6), 5114–5124. https://doi.org/10.1021/jacs.4c15261.

[102] Grötsch, R. K.; Wanzke, C.; Speckbacher, M.; Angı, A.; Rieger, B.; Boekhoven, J. Pathway Dependence in the Fuel-Driven Dissipative Self-Assembly of Nanoparticles. *J. Am. Chem. Soc.* **2019**, *141* (25), 9872–9878. https://doi.org/10.1021/jacs.9b02004.

[103] Van Ravensteijn, B. G. P.; Hendriksen, W. E.; Eelkema, R.; Van Esch, J. H.; Kegel, W. K. Fuel-Mediated Transient Clustering of Colloidal Building Blocks. *J. Am. Chem. Soc.* **2017**, *139* (29), 9763–9766. https://doi.org/10.1021/jacs.7b03263.

[104] Sawczyk, M.; Klajn, R. Out-of-Equilibrium Aggregates and Coatings during Seeded Growth of Metallic Nanoparticles. *J. Am. Chem. Soc.* **2017**, *139* (49), 17973–17978. https://doi.org/10.1021/jacs.7b09111.

[105] Grötsch, R. K.; Angı, A.; Mideksa, Y. G.; Wanzke, C.; Tena-Solsona, M.; Feige, M. J.; Rieger, B.; Boekhoven, J. Dissipative Self-Assembly of Photoluminescent Silicon Nanocrystals. *Angew Chem Int Ed* **2018**, *57* (44), 14608–14612. https://doi.org/10.1002/anie.201807937.

[106] Chandrakala, V.; Aruna, V.; Angajala, G. Review on Metal Nanoparticles as Nanocarriers: Current Challenges and Perspectives in Drug Delivery Systems. *emergent mater.* **2022**, *5* (6), 1593–1615. https://doi.org/10.1007/s42247-021-00335-x.

[107] Amina, S. J.; Guo, B. A Review on the Synthesis and Functionalization of Gold Nanoparticles as a Drug Delivery Vehicle. *IJN* **2020**, *Volume 15*, 9823–9857. https://doi.org/10.2147/IJN.S279094.

[108] Bansal, S. A.; Kumar, V.; Karimi, J.; Singh, A. P.; Kumar, S. Role of Gold Nanoparticles in Advanced Biomedical Applications. *Nanoscale Adv.* **2020**, *2* (9), 3764–3787. https://doi.org/10.1039/D0NA00472C.

[109] Priya, M. R. K.; Ashokkumar, M.; Precilla, L. K.; Hanna, L. E.; Iyer, P. R. Nanomedicine Perspective in HIV Therapy: Biosynthesized Gold Nanoparticles Exhibiting Enhanced Anti-HIV Property. *Beni-Suef Univ J Basic Appl Sci* **2021**, *10* (1), 23. https://doi.org/10.1186/s43088-021-00105-y.

[110] Bahrami, A.; Delshadi, R.; Jafari, S. M. Active Delivery of Antimicrobial Nanoparticles into Microbial Cells through Surface Functionalization Strategies. *Trends in Food Science & Technology* **2020**, *99*, 217–228. https://doi.org/10.1016/j.tifs.2020.03.008.

[111] Fratoddi, I.; Cerra, S.; Salamone, T. A.; Fioravanti, R.; Sciubba, F.; Zampetti, E.; Macagnano, A.; Generosi, A.; Paci, B.; Scaramuzzo, F. A.; Matassa, R.; Familiari, G.; Battocchio, C.; Marsotto, M.; Papa, P.; Bearzotti, A. Functionalized Gold Nanoparticles as an Active Layer for Mercury Vapor Detection at Room Temperature. *ACS Appl. Nano Mater.* **2021**, *4* (3), 2930–2940. https://doi.org/10.1021/acsanm.1c00074.

[112] Li, Z.; Lu, J.; Ruan, X.; Wu, Y.; Zhao, J.; Jiao, X.; Sun, J.; Sun, K. Exposure to Volatile Organic Compounds Induces Cardiovascular Toxicity That May Involve DNA Methylation. *Toxicology* **2024**, *501*, 153705. https://doi.org/10.1016/j.tox.2023.153705.

[113] Wu, Y.; Yang, J.; Wu, G.; Gao, W.; Silva Lora, E. E.; Isa, Y. M.; Subramanian, K. A.; Kozlov, A.; Zhang, S.; Huang, Y. Benzene, Toluene, and Xylene (BTX) Production from Catalytic Fast Pyrolysis of Biomass: A Review. *ACS Sustainable Chem. Eng.* **2023**, *11* (32), 11700–11718. https://doi.org/10.1021/acssuschemeng.3c01202.

[114] Zhao, Y.; Liu, Y.; Han, B.; Wang, M.; Wang, Q.; Zhang, Y. Fiber Optic Volatile Organic Compound Gas Sensors: A Review. *Coordination Chemistry Reviews* **2023**, *493*, 215297. https://doi.org/10.1016/j.ccr.2023.215297.

[115] Moon, Y. K.; Kim, K. B.; Jeong, S.-Y.; Lee, J.-H. Designing Oxide Chemiresistors for Detecting Volatile Aromatic Compounds: Recent Progresses and Future Perspectives. *Chem. Commun.* **2022**, *58* (36), 5439–5454. https://doi.org/10.1039/D2CC01563C.

[116] Neri, G. First Fifty Years of Chemoresistive Gas Sensors. *Chemosensors* **2015**, *3* (1), 1–20. https://doi.org/10.3390/chemosensors3010001.

[117] Singh, S.; S, S.; Varma, P.; Sreelekha, G.; Adak, C.; Shukla, R. P.; Kamble, V. B. Metal Oxide-Based Gas Sensor Array for VOCs Determination in Complex Mixtures Using Machine Learning. *Microchim Acta* **2024**, *191* (4), 196. https://doi.org/10.1007/s00604-024-06258-8.

[118] Jian, Y.; Hu, W.; Zhao, Z.; Cheng, P.; Haick, H.; Yao, M.; Wu, W. Gas Sensors Based on Chemi-Resistive Hybrid Functional Nanomaterials. *Nano-Micro Lett.* **2020**, *12* (1), 71. https://doi.org/10.1007/s40820-020-0407-5.

[119] Park, S. Y.; Kim, Y.; Kim, T.; Eom, T. H.; Kim, S. Y.; Jang, H. W. Chemoresistive Materials for Electronic Nose: Progress, Perspectives, and Challenges. *InfoMat* **2019**, *1* (3), 289–316. https://doi.org/10.1002/inf2.12029.

[120] Khatib, M.; Haick, H. Sensors for Volatile Organic Compounds. *ACS Nano* **2022**, *16* (5), 7080–7115. https://doi.org/10.1021/acsnano.1c10827.

[121] Rath, R. J.; Farajikhah, S.; Oveissi, F.; Dehghani, F.; Naficy, S. Chemiresistive Sensor Arrays for Gas/Volatile Organic Compounds Monitoring: A Review. *Adv Eng Mater* **2023**, *25* (3), 2200830. https://doi.org/10.1002/adem.202200830.

[122] George, G.; G. R., R.; Thomas, N. R.; Ede, S. R.; B., S.; Nair, A. K.; T., S. Gold Nanoparticles-Based Gas Sensors: A Comprehensive Review of Design, Mechanisms, and Applications. *Critical Reviews in Analytical Chemistry* **2025**, 1–39. https://doi.org/10.1080/10408347.2025.2512174.

[123] Cerra, S.; Salamone, T. A.; Bearzotti, A.; Hajareh Haghighi, F.; Mercurio, M.; Marsotto, M.; Battocchio, C.; Fioravanti, R.; Diociaiuti, M.; Fratoddi, I. Thiol-Functionalized Palladium Nanoparticles Networks: Synthesis, Characterization, and Room Temperature (Toxic) Vapor Detection. *Part & Part Syst Charact* **2023**, *40* (4), 2200189. https://doi.org/10.1002/ppsc.202200189.

[124] Lee, D.; Kim, S. H.; Han, S. K.; Mun, J.; Rho, J.; Cho, K.; Rhee, H.; Jeong, M. S.; Oh, D. X. Effect of Hot-Electron Injection on the Excited-State Dynamics of a Hybrid Plasmonic System Containing Poly(3-Hexylthiophene)-Coated Gold Nanoparticles. *J. Phys. Chem. C* **2019**, *123* (43), 26564–26570. https://doi.org/10.1021/acs.jpcc.9b08639.

[125] Zhang, R.-C.; Sun, D.; Zhang, R.; Lin, W.-F.; Macias-Montero, M.; Patel, J.; Askari, S.; McDonald, C.; Mariotti, D.; Maguire, P. Gold Nanoparticle-Polymer Nanocomposites Synthesized by Room Temperature Atmospheric Pressure Plasma and Their Potential for Fuel Cell Electrocatalytic Application. *Sci Rep* **2017**, *7* (1), 46682. https://doi.org/10.1038/srep46682.

[126] Shumbula, N. P.; Ndala, Z. B.; Nkabinde, S. S.; Kolokoto, T.; Shumbula, P. M.; Mdluli, P. S.; Hlatshwayo, T.; Mlambo, M.; Moloto, N. Experimental and Theoretical Studies of 1-Alkanethiols SAMs of Various Chain-Lengths on Gold Nanoparticles and Their Effect on SERS, Stability and Surface Properties. *Journal of Molecular Structure* **2020**, *1221*, 128801. https://doi.org/10.1016/j.molstruc.2020.128801.

[127] Yu, L.; Song, Z.; Peng, J.; Yang, M.; Zhi, H.; He, H. Progress of Gold Nanomaterials for Colorimetric Sensing Based on Different Strategies. *TrAC Trends in Analytical Chemistry* **2020**, *127*, 115880. https://doi.org/10.1016/j.trac.2020.115880.

[128] Atta, M. R.; Alsulami, Q. A.; Asnag, G. M.; Rajeh, A. Enhanced Optical, Morphological, Dielectric, and Conductivity Properties of Gold Nanoparticles Doped with PVA/CMC Blend as an Application in Organoelectronic Devices. *J Mater Sci: Mater Electron* **2021**, *32* (8), 10443–10457. https://doi.org/10.1007/s10854-021-05701-3.

[129] Venditti, I.; Fontana, L.; Fratoddi, I.; Battocchio, C.; Cametti, C.; Sennato, S.; Mura, F.; Sciubba, F.; Delfini, M.; Russo, M. V. Direct Interaction of Hydrophilic Gold Nanoparticles with Dexamethasone Drug: Loading and Release Study. *Journal of Colloid and Interface Science* **2014**, *418*, 52–60. https://doi.org/10.1016/j.jcis.2013.11.063.

[130] Kluenker, M.; Mondeshki, M.; Nawaz Tahir, M.; Tremel, W. Monitoring Thiol–Ligand Exchange on Au Nanoparticle Surfaces. *Langmuir* **2018**, *34* (4), 1700–1710. https://doi.org/10.1021/acs.langmuir.7b04015.

[131] Cerra, S.; Matassa, R.; Beltrán, A. M.; Familiari, G.; Battocchio, C.; Pis, I.; Sciubba, F.; Scaramuzzo, F. A.; Del Giudice, A.; Fratoddi, I. Insights about the Interaction of Methotrexate Loaded Hydrophilic Gold Nanoparticles: Spectroscopic, Morphological and Structural Characterizations. *Materials Science and Engineering: C* **2020**, *117*, 111337. https://doi.org/10.1016/j.msec.2020.111337.

[132] Ali, H.; Seidel, R.; Pohl, M. N.; Winter, B. Molecular Species Forming at the α-Fe_2 O_3 Nanoparticle–Aqueous Solution Interface. *Chem. Sci.* **2018**, *9* (19), 4511–4523. https://doi.org/10.1039/C7SC05156E.

[133] Söderström, J.; Ottosson, N.; Pokapanich, W.; Öhrwall, G.; Björneholm, O. Functionalized Nanoparticles in Aqueous Surroundings Probed by X-Ray Photoelectron Spectroscopy. *Journal of Electron Spectroscopy and Related Phenomena* **2011**, *184* (7), 375–378. https://doi.org/10.1016/j.elspec.2011.02.006.

[134] Ali, H.; Seidel, R.; Bergmann, A.; Winter, B. Electronic Structure of Aqueous-Phase Anatase Titanium Dioxide Nanoparticles Probed by Liquid Jet Photoelectron Spectroscopy. *J. Mater. Chem. A* **2019**, *7* (12), 6665–6675. https://doi.org/10.1039/C8TA09414D.

[135] Olivieri, G.; Kladnik, G.; Cvetko, D.; Brown, M. A. Determination of the Valence Band Edge of Fe Oxide Nanoparticles Dispersed in Aqueous Solution through Resonant Photoelectron Spectroscopy from a Liquid Microjet. *Nanoscale Adv.* **2021**, *3* (15), 4513–4518. https://doi.org/10.1039/D1NA00275A.

[136] Carlini, L.; Fasolato, C.; Postorino, P.; Fratoddi, I.; Venditti, I.; Testa, G.; Battocchio, C. Comparison between Silver and Gold Nanoparticles Stabilized with Negatively Charged Hydrophilic Thiols: SR-XPS and SERS as Probes for Structural Differences and Similarities. *Colloids and Surfaces A: Physicochemical and Engineering Aspects* **2017**, *532*, 183–188. https://doi.org/10.1016/j.colsurfa.2017.05.045.

[137] Song, Y.; Zemlyanov, D.; Chen, X.; Nie, H.; Su, Z.; Fang, K.; Yang, X.; Smith, D.; Byrn, S.; Lubach, J. W. Acid–Base Interactions of Polystyrene Sulfonic Acid in Amorphous Solid Dispersions Using a Combined UV/FTIR/XPS/ssNMR Study. *Mol. Pharmaceutics* **2016**, *13* (2), 483–492. https://doi.org/10.1021/acs.molpharmaceut.5b00708.

[138] Elzey, S.; Tsai, D.-H.; Rabb, S. A.; Yu, L. L.; Winchester, M. R.; Hackley, V. A. Quantification of Ligand Packing Density on Gold Nanoparticles Using ICP-OES. *Anal Bioanal Chem* **2012**, *403* (1), 145–149. https://doi.org/10.1007/s00216-012-5830-0.

[139] Kehrer, M.; Duchoslav, J.; Hinterreiter, A.; Cobet, M.; Mehic, A.; Stehrer, T.; Stifter, D. XPS Investigation on the Reactivity of Surface Imine Groups with TFAA. *Plasma Processes & Polymers* **2019**, *16* (4), 1800160. https://doi.org/10.1002/ppap.201800160.

[140] Darrah Thomas, T.; Weightman, P. Valence Electronic Structure of AuZn and AuMg Alloys Derived from a New Way of Analyzing Auger-Parameter Shifts. *Phys. Rev. B* **1986**, *33* (8), 5406–5413. https://doi.org/10.1103/PhysRevB.33.5406.

[141] Baranyai, Z.; Tircsó, G.; Rösch, F. The Use of the Macrocyclic Chelator DOTA in Radiochemical Separations. *Eur J Inorg Chem* **2020**, *2020* (1), 36–56. https://doi.org/10.1002/ejic.201900706.

[142] Perton, F.; Palluel, M.; Kiefer, C.; Freis, B.; Mertz, D.; Begin-Colin, S. One Pot Synthesis of Dithiolane Dendron Functionalized Gold Nanoparticles. *Eur J Inorg Chem* **2021**, *2021* (41), 4286–4297. https://doi.org/10.1002/ejic.202100650.

[143] Beik, J.; Khateri, M.; Khosravi, Z.; Kamrava, S. K.; Kooranifar, S.; Ghaznavi, H.; Shakeri-Zadeh, A. Gold Nanoparticles in Combinatorial Cancer Therapy Strategies. *Coordination Chemistry Reviews* **2019**, *387*, 299–324. https://doi.org/10.1016/j.ccr.2019.02.025.

[144] Dreaden, E. C.; Alkilany, A. M.; Huang, X.; Murphy, C. J.; El-Sayed, M. A. The Golden Age: Gold Nanoparticles for Biomedicine. *Chem. Soc. Rev.* **2012**, *41* (7), 2740–2779. https://doi.org/10.1039/C1CS15237H.

[145] Alam, A.-M.; Shon, Y.-S. Water-Soluble Noble Metal Nanoparticle Catalysts Capped with Small Organic Molecules for Organic Transformations in Water. *ACS Appl. Nano Mater.* **2021**, *4* (4), 3294–3318. https://doi.org/10.1021/acsanm.1c00335.

[146] Sztandera, K.; Gorzkiewicz, M.; Klajnert-Maculewicz, B. Gold Nanoparticles in Cancer Treatment. *Mol. Pharmaceutics* **2019**, *16* (1), 1–23. https://doi.org/10.1021/acs.molpharmaceut.8b00810.

[147] Jiang, Y.; Zhao, W.; Zhou, H.; Zhang, Q.; Zhang, S. ATP-Triggered Intracellular In Situ Aggregation of a Gold-Nanoparticle-Equipped Triple-Helix Molecular Switch for Fluorescence Imaging and Photothermal Tumor Therapy. *Langmuir* **2022**, *38* (12), 3755–3764. https://doi.org/10.1021/acs.langmuir.1c03331.

[148] Luan, S.; Xie, R.; Yang, Y.; Xiao, X.; Zhou, J.; Li, X.; Fang, P.; Zeng, X.; Yu, X.; Chen, M.; Gao, H.; Yuan, Y. Acid-Responsive Aggregated Gold Nanoparticles for Radiosensitization and Synergistic

Chemoradiotherapy in the Treatment of Esophageal Cancer. *Small* **2022**, *18* (19), 2200115. https://doi.org/10.1002/smll.202200115.

[149] Bertrand, N.; Wu, J.; Xu, X.; Kamaly, N.; Farokhzad, O. C. Cancer Nanotechnology: The Impact of Passive and Active Targeting in the Era of Modern Cancer Biology. *Advanced Drug Delivery Reviews* **2014**, *66*, 2–25. https://doi.org/10.1016/j.addr.2013.11.009.

[150] Cryer, A. M.; Chan, C.; Eftychidou, A.; Maksoudian, C.; Mahesh, M.; Tetley, T. D.; Spivey, A. C.; Thorley, A. J. Tyrosine Kinase Inhibitor Gold Nanoconjugates for the Treatment of Non-Small Cell Lung Cancer. *ACS Appl. Mater. Interfaces* **2019**, *11* (18), 16336–16346. https://doi.org/10.1021/acsami.9b02986.

[151] Fratoddi, I.; Benassi, L.; Botti, E.; Vaschieri, C.; Venditti, I.; Bessar, H.; Samir, M. A.; Azzoni, P.; Magnoni, C.; Costanzo, A.; Casagrande, V.; Federici, M.; Bianchi, L.; Pellacani, G. Effects of Topical Methotrexate Loaded Gold Nanoparticle in Cutaneous Inflammatory Mouse Model. *Nanomedicine: Nanotechnology, Biology and Medicine* **2019**, *17*, 276–286. https://doi.org/10.1016/j.nano.2019.01.006.

[152] Taran, Z.; Yektaniroumand Digehsaraei, S.; Salouti, M.; Amini, B.; Mahmazi, S.; Kalantari, M. Methotrexate Loaded in Alginate Beads for Controlled Drug Release against Breast Cancer. *Gene* **2023**, *851*, 146941. https://doi.org/10.1016/j.gene.2022.146941.

[153] Venditti, I.; Cartoni, A.; Cerra, S.; Fioravanti, R.; Salamone, T. A.; Sciubba, F.; Tabocchini, M. A.; Dini, V.; Battocchio, C.; Iucci, G.; Carlini, L.; Faccini, R.; Collamati, F.; Mancini Terracciano, C.; Solfaroli Camillocci, E.; Morganti, S.; Giordano, A.; Scotognella, T.; Maccora, D.; Rotili, D.; Marchese, C.; Anastasiadou, E.; Trivedi, P.; Fratoddi, I. Hydrophilic Gold Nanoparticles as Anti-PD-L1 Antibody Carriers: Synthesis and Interface Properties. *Part & Part Syst Charact* **2022**, *39* (4), 2100282. https://doi.org/10.1002/ppsc.202100282.

[154] İlgar, M.; Karakuş, S.; Kilislioğlu, A. Design, Characterization and Evaluation of the Drug-Loaded Chitosan/Cerium Oxide Nanoparticles with pH-Controlled Drug Release. *Polym. Bull.* **2022**, *79* (8), 6693–6708. https://doi.org/10.1007/s00289-021-03839-y.

[155] Venditti, I.; Iucci, G.; Fratoddi, I.; Cipolletti, M.; Montalesi, E.; Marino, M.; Secchi, V.; Battocchio, C. Direct Conjugation of Resveratrol on Hydrophilic Gold Nanoparticles: Structural and Cytotoxic Studies for Biomedical Applications. *Nanomaterials* **2020**, *10* (10), 1898. https://doi.org/10.3390/nano10101898.

[156] Venditti, I.; Testa, G.; Sciubba, F.; Carlini, L.; Porcaro, F.; Meneghini, C.; Mobilio, S.; Battocchio, C.; Fratoddi, I. Hydrophilic Metal Nanoparticles Functionalized by 2-Diethylaminoethanethiol: A Close Look at the Metal–Ligand Interaction and Interface Chemical Structure. *J. Phys. Chem. C* **2017**, *121* (14), 8002–8013. https://doi.org/10.1021/acs.jpcc.7b01424.

[157] Silverstein R., Webster F., Kiemle, D., Infrared Spectrometry. In: R. Silverstein, F. Webster and D. Kiemle, ed., Spectrometric identification of organic compounds, 2005, 7th ed. Hoboken, USA: Wiley, pp.72-126

[158] Masoodi, H. R.; Bagheri, S. Interplay between Π···π Stacking and Cation···π Interaction: A Theoretical NMR Study. *J IRAN CHEM SOC* **2015**, *12* (10), 1883–1892. https://doi.org/10.1007/s13738-015-0663-3.

[159] Wei, D.; Ma, F.; Wang, R.; Dou, S.; Cui, P.; Huang, H.; Ji, J.; Jia, E.; Jia, X.; Sajid, S.; Elseman, A. M.; Chu, L.; Li, Y.; Jiang, B.; Qiao, J.; Yuan, Y.; Li, M. Ion-Migration Inhibition by the Cation–π Interaction in Perovskite Materials for Efficient and Stable Perovskite Solar Cells. *Advanced Materials* **2018**, *30* (31), 1707583. https://doi.org/10.1002/adma.201707583.

[160] Cooper, I.; Fridkin, M.; Shechter, Y. Conjugation of Methotrexate-Amino Derivatives to Macromolecules through Carboxylate Moieties Is Superior Over Conventional Linkage to Amino Residues: Chemical, Cell-Free and In Vitro Characterizations. *PLoS ONE* **2016**, *11* (7), e0158352. https://doi.org/10.1371/journal.pone.0158352.

[161] Najdian, A.; Shakourian-Fard, M.; Fattahi, A. Cooperativity Effects of Intramolecular OH…O Interactions on p K_a Values of Polyolalkyl Sulfonic Acids in the Gas Phase and Solution: A Density Functional Theory Study: COOPERATIVITY EFFECTS OF INTRAMOLECULAR OH…O INTERACTIONS ON p K_a VALUES. *J. Phys. Org. Chem.* **2014**, *27* (7), 604–612. https://doi.org/10.1002/poc.3307.

[162] Rayer, A. V.; Sumon, K. Z.; Jaffari, L.; Henni, A. Dissociation Constants (p K_a) of Tertiary and Cyclic Amines: Structural and Temperature Dependences. *J. Chem. Eng. Data* **2014**, *59* (11), 3805–3813. https://doi.org/10.1021/je500680q.

[163] Chakraborty, C.; Sharma, A. R.; Sharma, G.; Sarkar, B. K.; Lee, S.-S. The Novel Strategies for Next-Generation Cancer Treatment: miRNA Combined with Chemotherapeutic Agents for the Treatment of Cancer. *Oncotarget* **2018**, *9* (11), 10164–10174. https://doi.org/10.18632/oncotarget.24309.

[164] Mongroo, P. S.; Rustgi, A. K. The Role of the miR-200 Family in Epithelial-Mesenchymal Transition. *Cancer Biology & Therapy* **2010**, *10* (3), 219–222. https://doi.org/10.4161/cbt.10.3.12548.

[165] Prinz, F.; Jonas, K.; Balihodzic, A.; Klec, C.; Reicher, A.; Barth, D. A.; Riedl, J.; Gerger, A.; Kiesslich, T.; Mayr, C.; Rinner, B.; Kargl, J.; Pichler, M. MicroRNA Mimics Can Distort Physiological microRNA Effects on Immune Checkpoints by Triggering an Antiviral Interferon Response. *RNA Biology* **2022**, *19* (1), 1305–1315. https://doi.org/10.1080/15476286.2022.2152978.

[166] Luistro, L. L.; Rosinski, J. A.; Bian, H.; Bishayee, S.; Rameshwar, P.; Ponzio, N. M.; Ritland, S. R. Development and Characterization of a Preclinical Ovarian Carcinoma Model to Investigate the Mechanism of Acquired Resistance to Trastuzumab. *International Journal of Oncology* **2012**, *41* (2), 639–651. https://doi.org/10.3892/ijo.2012.1463.

[167] Emami, F.; Banstola, A.; Vatanara, A.; Lee, S.; Kim, J. O.; Jeong, J.-H.; Yook, S. Doxorubicin and Anti-PD-L1 Antibody Conjugated Gold Nanoparticles for Colorectal Cancer Photochemotherapy. *Mol. Pharmaceutics* **2019**, *16* (3), 1184–1199. https://doi.org/10.1021/acs.molpharmaceut.8b01157.

[168] Nkune, N. W.; Abrahamse, H. The Phototoxic Effect of a Gold-Antibody-Based Nanocarrier of Phthalocyanine on Melanoma Monolayers and Tumour Spheroids. *RSC Adv.* **2024**, *14* (27), 19490–19504. https://doi.org/10.1039/D4RA03858D.

[169] Muradova, A. G.; Al-Hilali, H. A.; Andreeva, P. A.; Sharapaev, A. I.; Khakimov, K. T.; Bai, X.; Finko, A. V. Fluorescent Composite Nano- and Microparticles Based on Xanthene Dyes and Iron Oxides. *Chem Eng & Technol* **2024**, *47* (7), 952–960. https://doi.org/10.1002/ceat.202300465.

[170] Le Guern, F.; Mussard, V.; Gaucher, A.; Rottman, M.; Prim, D. Fluorescein Derivatives as Fluorescent Probes for pH Monitoring along Recent Biological Applications. *IJMS* **2020**, *21* (23), 9217. https://doi.org/10.3390/ijms21239217.

[171] Xu, W.; Riikonen, J.; Nissinen, T.; Suvanto, M.; Rilla, K.; Li, B.; Wang, Q.; Deng, F.; Lehto, V.-P. Amine Surface Modifications and Fluorescent Labeling of Thermally Stabilized Mesoporous Silicon Nanoparticles. *J. Phys. Chem. C* **2012**, *116* (42), 22307–22314. https://doi.org/10.1021/jp303199s.

[172] Xu, W.; Riikonen, J.; Nissinen, T.; Suvanto, M.; Rilla, K.; Li, B.; Wang, Q.; Deng, F.; Lehto, V.-P. Amine Surface Modifications and Fluorescent Labeling of Thermally Stabilized Mesoporous Silicon Nanoparticles. *J. Phys. Chem. C* **2012**, *116* (42), 22307–22314. https://doi.org/10.1021/jp303199s.

[173] Chayah, M.; Camacho, M. E.; Carrión, M. D.; Gallo, M. A. ^{1}H and ^{13}C NMR Spectral Assignment of *N* , *N* ′-disubstituted Thiourea and Urea Derivatives Active against Nitric Oxide Synthase. *Magnetic Reson in Chemistry* **2016**, *54* (10), 793–799. https://doi.org/10.1002/mrc.4455.

[174] Biagini, C.; Di Stefano, S. Abiotic Chemical Fuels for the Operation of Molecular Machines. *Angewandte Chemie* **2020**, *132* (22), 8420–8430. https://doi.org/10.1002/ange.201912659.

[175] Del Giudice, D.; Di Stefano, S. Dissipative Systems Driven by the Decarboxylation of Activated Carboxylic Acids. *Acc. Chem. Res.* **2023**, *56* (7), 889–899. https://doi.org/10.1021/acs.accounts.3c00047.

[176] Berrocal, J. A.; Biagini, C.; Mandolini, L.; Di Stefano, S. Coupling of the Decarboxylation of 2-Cyano-2-phenylpropanoic Acid to Large-Amplitude Motions: A Convenient Fuel for an Acid–Base-Operated Molecular Switch. *Angew Chem Int Ed* **2016**, *55* (24), 6997–7001. https://doi.org/10.1002/anie.201602594.

[177] Del Giudice, D.; Valentini, M.; Melchiorre, G.; Spatola, E.; Di Stefano, S. Dissipative Dynamic Covalent Chemistry (DDCvC) Based on the Transimination Reaction. *Chemistry A European J* **2022**, *28* (26), e202200685. https://doi.org/10.1002/chem.202200685.

[178] Valentini, M.; Ercolani, G.; Di Stefano, S. Kinetic Trapping of an Out-of-Equilibrium Dynamic Library of Imines by Changing Solvent. *Chemistry A European J* **2024**, *30* (37), e202401104. https://doi.org/10.1002/chem.202401104.

[179] Melchiorre, G.; Visieri, L.; Valentini, M.; Cacciapaglia, R.; Casnati, A.; Baldini, L.; Berrocal, J. A.; Di Stefano, S. Imine-Based Transient Supramolecular Polymers. *J. Am. Chem. Soc.* **2025**, *147* (13), 11327–11335. https://doi.org/10.1021/jacs.5c00274.

[180] Cerra, S.; Carlini, L.; Salamone, T. A.; Hajareh Haghighi, F.; Mercurio, M.; Pennacchi, B.; Sappino, C.; Battocchio, C.; Nottola, S.; Matassa, R.; Fratoddi, I. Noble Metal Nanoparticles Networks Stabilized by Rod-Like Organometallic Bifunctional Thiols. *ChemistrySelect* **2023**, *8* (13), e202300874. https://doi.org/10.1002/slct.202300874.

[181] Salamone, T. A.; Rutigliano, L.; Pennacchi, B.; Cerra, S.; Matassa, R.; Nottola, S.; Sciubba, F.; Battocchio, C.; Marsotto, M.; Del Giudice, A.; Chumakov, A.; Davydok, A.; Grigorian, S.; Canettieri, G.; Agostinelli, E.; Fratoddi, I. Thiol Functionalised Gold Nanoparticles Loaded with Methotrexate for Cancer Treatment: From Synthesis to in Vitro Studies on Neuroblastoma Cell Lines. *Journal of Colloid and Interface Science* **2023**, *649*, 264–278. https://doi.org/10.1016/j.jcis.2023.06.078.

[182] Trofimov, B. A.; Sinegovskaya, L. M.; Gusarova, N. K. Vibrations of the S–S Bond in Elemental Sulfur and Organic Polysulfides: A Structural Guide. *Journal of Sulfur Chemistry* **2009**, *30* (5), 518–554. https://doi.org/10.1080/17415990902998579.

[183] Sharma, L.; Kimura, T. FT-IR Investigation into the Miscible Interactions in New Materials for Optical Devices. *Polymers for Advanced Techs* **2003**, *14* (6), 392–399. https://doi.org/10.1002/pat.347.

[184] Zhang, Z.; Xu, P.; Yang, X.; Liang, W.; Sun, M. Surface Plasmon-Driven Photocatalysis in Ambient, Aqueous and High-Vacuum Monitored by SERS and TERS. *Journal of Photochemistry and Photobiology C: Photochemistry Reviews* **2016**, *27*, 100–112. https://doi.org/10.1016/j.jphotochemrev.2016.04.001.

[185] Ciaccia, M.; Di Stefano, S. Mechanisms of Imine Exchange Reactions in Organic Solvents. *Org. Biomol. Chem.* **2015**, *13* (3), 646–654. https://doi.org/10.1039/C4OB02110J.

[186] Matassa, R.; Familiari, G.; Battaglione, E.; Sibilia, C.; Leahu, G.; Belardini, A.; Venditti, I.; Fontana, L.; Fratoddi, I. Electron Microscopy Reveals a Soluble Hybrid Network of Individual Nanocrystals Self-Anchored by Bifunctional Thiol Fluorescent Bridges. *Nanoscale* **2016**, *8* (42), 18161–18169. https://doi.org/10.1039/C6NR06260A.

[187] Matassa, R.; Orlanducci, S.; Reina, G.; Cassani, M. C.; Passeri, D.; Terranova, M. L.; Rossi, M. Structural and Morphological Peculiarities of Hybrid Au/Nanodiamond Engineered Nanostructures. *Sci Rep* **2016**, *6* (1), 31163. https://doi.org/10.1038/srep31163.

[188] Sharma, R.; Holland, G. P.; Solomon, V. C.; Zimmermann, H.; Schiffenhaus, S.; Amin, S. A.; Buttry, D. A.; Yarger, J. L. NMR Characterization of Ligand Binding and Exchange Dynamics in Triphenylphosphine-Capped Gold Nanoparticles. *J. Phys. Chem. C* **2009**, *113* (37), 16387–16393. https://doi.org/10.1021/jp905141h.

[189] Lukasiewicz, A. Reactions of Trihalogenoacetic Acids—III. *Tetrahedron* **1965**, *21* (3), 193–202. https://doi.org/10.1016/S0040-4020(01)98259-6.

[190] Kawawaki, T.; Takahashi, Y.; Tatsuma, T. Enhancement of Dye-Sensitized Photocurrents by Gold Nanoparticles: Effects of Plasmon Coupling. *J. Phys. Chem. C* **2013**, *117* (11), 5901–5907. https://doi.org/10.1021/jp3120836.

[191] Carone, A.; Emilsson, S.; Mariani, P.; Désert, A.; Parola, S. Gold Nanoparticle Shape Dependence of Colloidal Stability Domains. *Nanoscale Adv.* **2023**, *5* (7), 2017–2026. https://doi.org/10.1039/D2NA00809B.

[192] Battocchio, C.; Fratoddi, I.; Fontana, L.; Bodo, E.; Porcaro, F.; Meneghini, C.; Pis, I.; Nappini, S.; Mobilio, S.; Russo, M. V.; Polzonetti, G. Silver Nanoparticles Linked by a Pt-Containing Organometallic Dithiol Bridge: Study of Local Structure and Interface by XAFS and SR-XPS. *Phys. Chem. Chem. Phys.* **2014**, *16* (23), 11719–11728. https://doi.org/10.1039/C4CP01264J.

[193] Battocchio, C.; D'Acapito, F.; Fratoddi, I.; La Groia, A.; Polzonetti, G.; Roviello, G.; Russo, M. V. Platinum (II) Dialkynyl Bridged Binuclear Complex and Related Multinuclear Oligomer: Comparison of EXAFS and X-Ray Crystal Structure Studies. *Chemical Physics* **2006**, *328* (1–3), 269–274. https://doi.org/10.1016/j.chemphys.2006.07.011.

[194] Kamatham, N.; Ibraikulov, O. A.; Durand, P.; Wang, J.; Boyron, O.; Heinrich, B.; Heiser, T.; Lévêque, P.; Leclerc, N.; Méry, S. On the Impact of Linear Siloxanated Side Chains on the Molecular Self-Assembling and Charge Transport Properties of Conjugated Polymers. *Adv Funct Materials* **2021**, *31* (6), 2007734. https://doi.org/10.1002/adfm.202007734.

[195] Roy, S.; Lopez, A. A.; Yarnell, J. E.; Castellano, F. N. Metal–Metal-to-Ligand Charge Transfer in Pt(II) Dimers Bridged by Pyridyl and Quinoline Thiols. *Inorg. Chem.* **2022**, *61* (1), 121–130. https://doi.org/10.1021/acs.inorgchem.1c02469.

[196] Mauro, M.; Aliprandi, A.; Septiadi, D.; Kehr, N. S.; De Cola, L. When Self-Assembly Meets Biology: Luminescent Platinum Complexes for Imaging Applications. *Chem. Soc. Rev.* **2014**, *43* (12), 4144–4166. https://doi.org/10.1039/C3CS60453E.

[197] Zhu, Y.; Luo, K.; Zhao, L.; Ni, H.; Li, Q. Binuclear Platinum(II) Complexes Based on 2-Mercaptobenzothiazole 2-Mercaptobenzimidazole and 2-Hydroxpyridine as Brigding Ligands: Red and near-Infrared Luminescence Originated from MMLCT Transition. *Dyes and Pigments* **2017**, *145*, 144–151. https://doi.org/10.1016/j.dyepig.2017.05.052.

[198] Suleymanova, A. F.; Yakovleva, Y. A.; Eltsov, O. S.; Lantushenko, A. O.; Evstigneev, M. P.; Donnio, B.; Heinrich, B.; Kozhevnikov, V. N. Comparative Analysis of Self-Aggregation of Liquid Crystalline Pt(II) Complexes in Solution and in Neat Films. *Journal of Organometallic Chemistry* **2021**, *938*, 121750. https://doi.org/10.1016/j.jorganchem.2021.121750.

[199] Gwo, S.; Chen, H.-Y.; Lin, M.-H.; Sun, L.; Li, X. Nanomanipulation and Controlled Self-Assembly of Metal Nanoparticles and Nanocrystals for Plasmonics. *Chem. Soc. Rev.* **2016**, *45* (20), 5672–5716. https://doi.org/10.1039/C6CS00450D.

[200] Battocchio, C.; Fratoddi, I.; Russo, M. V.; Carravetta, V.; Monti, S.; Iucci, G.; Borgatti, F.; Polzonetti, G. Binuclear Transition Metal Complexes on Gold: Molecular Orientation by Angular

Dependent NEXAFS Spectroscopy. *Surface Science* **2007**, *601* (18), 3943–3947. https://doi.org/10.1016/j.susc.2007.04.154.

[201] Li, D.; Zhou, H.; Ren, Z.; Lee, C. Advances in MEMS, Optical MEMS, and Nanophotonics Technologies for Volatile Organic Compound Detection and Applications. *Small Science* **2025**, *5* (4), 2400250. https://doi.org/10.1002/smsc.202400250.

[202] Liu, J.; Wang, T.; Zhong, L.; Serageldin, M. A.; Pan, W.-P. Review of Organic Pollutants in Coal Combustion Processes and Control Technologies. *Progress in Energy and Combustion Science* **2025**, *109*, 101231. https://doi.org/10.1016/j.pecs.2025.101231.

[203] Han, B.; Rupam, T. H.; Chakraborty, A.; Saha, B. B. A Comprehensive Review on VOCs Sensing Using Different Functional Materials: Mechanisms, Modifications, Challenges and Opportunities. *Renewable and Sustainable Energy Reviews* **2024**, *196*, 114365. https://doi.org/10.1016/j.rser.2024.114365.

[204] Rosario, W.; Singh, P. K.; Tiwari, A.; Jain, U.; Avasthi, D. K.; Chauhan, N. Nanomaterial-Based VOC Sensing Applications and a Deep Dive into Their Developmental Trends. *J. Mater. Chem. A* **2024**, *12* (17), 9979–10011. https://doi.org/10.1039/D3TA07171E.

[205] Liu, H.; Meng, G.; Deng, Z.; Nagashima, K.; Wang, S.; Dai, T.; Li, L.; Yanagida, T.; Fang, X. Discriminating BTX Molecules by the Nonselective Metal Oxide Sensor-Based Smart Sensing System. *ACS Sens.* **2021**, *6* (11), 4167–4175. https://doi.org/10.1021/acssensors.1c01704.

[206] Carlos Braga Alves, I.; Ribamar Nascimento Dos Santos, J.; Pereira Marques, E.; Carvalho Martiniano De Azevedo, L.; Azevedo Beluomini, M.; Ramos Stradiotto, N.; Lopes Brandes Marques, A. Simultaneous Determination of Benzene, Toluene and Xylene (BTX) by Au Nanoparticles (AuNP) Anchored in Reduced Graphene Oxide Electrode. *Electroanalysis* **2024**, *36* (2), e202300260. https://doi.org/10.1002/elan.202300260.

[207] Chen, Y.; Xu, J.; Pan, Y.; Cao, Q.; Yuan, K. Trace Detection of Benzene, Toluene and Xylene (BTX) by Chemiresistive Metal Oxide-Based Gas Sensors: Recent Advances in Heterojunction Materials Design. *Chinese Chemical Letters* **2024**, 110606. https://doi.org/10.1016/j.cclet.2024.110606.

[208] Krishna, K. G.; Parne, S. R.; Nagaraju, P. ZnO/CdO Island-like Porous Nanocomposite as an Ultra-Sensitive Sensor for BTX Detection at Room Temperature. *Surfaces and Interfaces* **2024**, *44*, 103631. https://doi.org/10.1016/j.surfin.2023.103631.

[209] Gounder Thangamani, J.; Khadheer Pasha, S. K. Hydrothermal Synthesis of Copper (II) Oxide-Nanoparticles with Highly Enhanced BTEX Gas Sensing Performance Using Chemiresistive Sensor. *Chemosphere* **2021**, *277*, 130237. https://doi.org/10.1016/j.chemosphere.2021.130237.

[210] Acharyya, S.; Nag, S.; Kimbahune, S.; Ghose, A.; Pal, A.; Guha, P. K. Selective Discrimination of VOCs Applying Gas Sensing Kinetic Analysis over a Metal Oxide-Based Chemiresistive Gas Sensor. *ACS Sens.* **2021**, *6* (6), 2218–2224. https://doi.org/10.1021/acssensors.1c00115.

[211] Marikutsa, A.; Novikova, A.; Rumyantseva, M.; Khmelevsky, N.; Gaskov, A. Comparison of Au-Functionalized Semiconductor Metal Oxides in Sensitivity to VOC. *Sensors and Actuators B: Chemical* **2021**, *326*, 128980. https://doi.org/10.1016/j.snb.2020.128980.

[212] Xu, F.; Li, W.; Sun, S.; Zhong, A.; Cheng, X.; Shi, J.; Li, Z.; Li, J.; Zhang, W.; Wang, X.; Ma, Y.; Ho, A. H.-P. Expanding Selectivity Functionality of a ZnO Nanotetrapod-Based Volatile Organic Compound Sensor Using Au Nanoparticle Decoration. *ACS Appl. Nano Mater.* **2023**, *6* (10), 8335–8345. https://doi.org/10.1021/acsanm.3c00576.

[213] Mirzaei, A.; Kim, J.-H.; Kim, H. W.; Kim, S. S. Resistive-Based Gas Sensors for Detection of Benzene, Toluene and Xylene (BTX) Gases: A Review. *J. Mater. Chem. C* **2018**, *6* (16), 4342–4370. https://doi.org/10.1039/C8TC00245B.

[214] Schlicke, H.; Bittinger, S. C.; Noei, H.; Vossmeyer, T. Gold Nanoparticle-Based Chemiresistors: Recognition of Volatile Organic Compounds Using Tunable Response Kinetics. *ACS Appl. Nano Mater.* **2021**, *4* (10), 10399–10408. https://doi.org/10.1021/acsanm.1c01892.

[215] Fratoddi, I.; Matassa, R.; Fontana, L.; Venditti, I.; Familiari, G.; Battocchio, C.; Magnano, E.; Nappini, S.; Leahu, G.; Belardini, A.; Li Voti, R.; Sibilia, C. Electronic Properties of a Functionalized Noble Metal Nanoparticles Covalent Network. *J. Phys. Chem. C* **2017**, *121* (33), 18110–18119. https://doi.org/10.1021/acs.jpcc.7b07176.

[216] Cerra, S.; Fontana, L.; Rossi, E.; Bassetti, M.; Battocchio, C.; Venditti, I.; Carlini, L.; Matassa, R.; Familiari, G.; Fratoddi, I. Binuclear Organometallic Pt(II) Complexes as Stabilizing Ligands for Gold and Silver Metal Nanoparticles. *Inorganica Chimica Acta* **2021**, *516*, 120170. https://doi.org/10.1016/j.ica.2020.120170.

[217] Amendola, V.; Pilot, R.; Frasconi, M.; Maragò, O. M.; Iatì, M. A. Surface Plasmon Resonance in Gold Nanoparticles: A Review. *J. Phys.: Condens. Matter* **2017**, *29* (20), 203002. https://doi.org/10.1088/1361-648X/aa60f3.

[218] Abbas, M. A.; Kamat, P. V.; Bang, J. H. Thiolated Gold Nanoclusters for Light Energy Conversion. *ACS Energy Lett.* **2018**, *3* (4), 840–854. https://doi.org/10.1021/acsenergylett.8b00070.

[219] Muniz-Miranda, M.; Muniz-Miranda, F.; Pedone, A. Spectroscopic and Computational Studies on Ligand-Capped Metal Nanoparticles and Clusters. In *Metal Nanoparticles and Clusters*; Deepak, F. L., Ed.; Springer International Publishing: Cham, 2018; pp 55–87. https://doi.org/10.1007/978-3-319-68053-8_3.

[220] Vijayakumar, C.; Balan, B.; Saeki, A.; Tsuda, T.; Kuwabata, S.; Seki, S. Gold Nanoparticle Assisted Self-Assembly and Enhancement of Charge Carrier Mobilities of a Conjugated Polymer. *J. Phys. Chem. C* **2012**, *116* (33), 17343–17350. https://doi.org/10.1021/jp3039253.

[221] Ba, M.; Erouel, M.; Mansouri, S.; Chouiref, L.; Jdir, M.; El Mir, L. Channel Length Effect of P3HT:ZnO Hybrid Blend Layer on Electrical Characteristics of Thin-Film Transistors. *Sens. Actuator A: Phys.* **2023**, *359*, 114470. https://doi.org/10.1016/j.sna.2023.114470.

[222] Riaz, S.; Ansari, M. A.; Raja, D. A.; Tahir, H.; Malik, M. I. Poly(3-Hexylthiophene) Incorporated with Metallic Nanoparticles: Optoelectronic Properties in Context of Organic Solar Cell. *Opt Quant Electron* **2023**, *55*, 700. https://doi.org/10.1007/s11082-023-04981-9.

[223] King, M.; Gottlieb, D.; Boucher, D. Impact of Regioregularity on the Solubility Parameters of Poly(3-hexylthiophene). *J. Polym. Sci.* **2022**, *60*, 2769–2783. https://doi.org/10.1002/pol.20220235.

[224] Thakur, A. K.; Mukherjee, A. K.; Preethichandra, D. M. G.; Takashima, W.; Kaneto, K. Charge Injection Mechanism across the Au-Poly(3-Hexylthiophene-2,5-Diyl) Interface. *J. Appl. Phys.* **2007**, *101*, 104508. https://doi.org/10.1063/1.2734955.

[225] C. Cametti, P. Codastefano, R. D'Amato, A. Furlani, M.V. Russo, Static and dynamic light scattering measurements of polyphenylacetylene (PPA) in different organic solvents (tetrahydrofuran, toluene and chloroform), *Synth. Met.* **2000**, *114*, 173–179. https://doi.org/10.1016/S0379-6779(00)00245-9.

[226] Muhammed Shameem, M.; Sasikanth, S. M.; Annamalai, R.; Ganapathi Raman, R. A Brief Review on Polymer Nanocomposites and Its Applications. *Materials Today: Proceedings* **2021**, *45*, 2536–2539. https://doi.org/10.1016/j.matpr.2020.11.254.

[227] Tan, B.; Pan, H.; Li, H.; Minus, M. L.; Budhlall, B. M.; Sobkowicz, M. J. Improving Charge Carrier Mobility of Polymer Blend Field Effect Transistors with Majority Insulating Polymer Phase. *J. Phys. Chem. C* **2018**, *122*, 2918–2930. https://doi.org/10.1021/acs.jpcc.7b09775.

[228] Hintz, H.; Egelhaaf, H.-J.; Lüer, L.; Hauch, J.; Peisert, H.; Chassé, T. Photodegradation of P3HT−A Systematic Study of Environmental Factors. *Chem. Mater.* **2011**, *23*, 145–154. https://doi.org/10.1021/cm102373k.

[229] Saifuddin, M.; Biswas, A.; Roy, S.; Mandal, S.; Hazra, S. Nanoparticle Mediated Improved Crystallinity and Connectivity of Semiconducting Polymer Thin Films. *ACS Appl. Polym. Mater.* **2023**, *5*, 3359–3369. https://doi.org/10.1021/acsapm.3c00049.

[230] Vohra, V.; Notoya, O.; Huang, T.; Yamaguchi, M.; Murata, H. Nanostructured Poly(3-Hexylthiophene-2,5-Diyl) Films with Tunable Dimensions through Self-Assembly with Polystyrene. *Polymer* **2014**, *55* (9), 2213–2219. https://doi.org/10.1016/j.polymer.2014.03.030.

[231] Perry, S. C.; Arumugam, S.; Beeby, S.; Nandhakumar, I. Template-Free Nanostructured Poly-3-Hexylthiophene (P3HT) Films via Single Pulse-Nucleated Electrodeposition. *Journal of Electroanalytical Chemistry* **2023**, *933*, 117278. https://doi.org/10.1016/j.jelechem.2023.117278.

[232] Hu, J.; Clark, K. W.; Hayakawa, R.; Li, A.-P.; Wakayama, Y. Enhanced Electrical Conductivity in Poly(3-Hexylthiophene)/Fluorinated Tetracyanoquinodimethane Nanowires Grown with a Porous Alumina Template. *Langmuir* **2013**, *29* (24), 7266–7270. https://doi.org/10.1021/la304499k.

[233] Ok, S.; Vayer, M.; Sinturel, C. A Decade of Innovation and Progress in Understanding the Morphology and Structure of Heterogeneous Polymers in Rigid Confinement. *Soft Matter* **2021**, *17* (32), 7430–7458. https://doi.org/10.1039/D1SM00522G.

[234] Takahashi, A.; Rho, Y.; Higashihara, T.; Ahn, B.; Ree, M.; Ueda, M. Preparation of Nanoporous Poly(3-Hexylthiophene) Films Based on a Template System of Block Copolymers via Ionic Interaction. *Macromolecules* **2010**, *43* (11), 4843–4852. https://doi.org/10.1021/ma100957q.

[235] Apelt, S.; Höhne, S.; Mehner, E.; Böhm, C.; Malanin, M.; Eichhorn, K.; Jehnichen, D.; Uhlmann, P.; Bergmann, U. Poly(Vinylidene Fluoride-co-trifluoroethylene) Thin Films after Dip- and Spin-Coating. *Macro Materials & Eng* **2022**, *307* (10), 2200296. https://doi.org/10.1002/mame.202200296.

[236] Vital, A.; Vayer, M.; Tillocher, T.; Dussart, R.; Boufnichel, M.; Sinturel, C. Morphology Control in Thin Films of PS:PLA Homopolymer Blends by Dip-Coating Deposition. *Applied Surface Science* **2017**, *393*, 127–133. https://doi.org/10.1016/j.apsusc.2016.09.151.

[237] Navarro-Baena, I.; Sessini, V.; Dominici, F.; Torre, L.; Kenny, J. M.; Peponi, L. Design of Biodegradable Blends Based on PLA and PCL: From Morphological, Thermal and Mechanical Studies to Shape Memory Behavior. *Polymer Degradation and Stability* **2016**, *132*, 97–108. https://doi.org/10.1016/j.polymdegradstab.2016.03.037.

[238] Rinehart, S. J.; Yuan, G.; Dadmun, M. D. The Interplay of Thermodynamics and Kinetics: Imparting Hierarchical Control over Film Formation of Self-Stratified Blends. *Soft Matter* **2020**, *16* (5), 1287–1297. https://doi.org/10.1039/C9SM01147A.

[239] Xue, L.; Zhang, J.; Han, Y. Phase Separation Induced Ordered Patterns in Thin Polymer Blend Films. *Progress in Polymer Science* **2012**, *37* (4), 564–594. https://doi.org/10.1016/j.progpolymsci.2011.09.001.

[240] Sinturel, C.; Vayer, M.; Morris, M.; Hillmyer, M. A. Solvent Vapor Annealing of Block Polymer Thin Films. *Macromolecules* **2013**, *46* (14), 5399–5415. https://doi.org/10.1021/ma400735a.

[241] Rinehart, S. J.; Yuan, G.; Dadmun, M. D. Elucidating the Kinetic and Thermodynamic Driving Forces in Polymer Blend Film Self-Stratification. *Macromolecules* **2018**, *51* (19), 7836–7844. https://doi.org/10.1021/acs.macromol.8b01397.

[242] Grigorian, S.; Fontana, L.; Cerra, S.; Pietsch, U.; Scaramuzzo, F. A.; Fratoddi, I. Superior Transport Behavior of Gold Nanoparticles/P3HT Blends by Tuning Optical and Structural Properties. *Synthetic Metals* **2022**, *283*, 116973. https://doi.org/10.1016/j.synthmet.2021.116973.

[243] M. Núñez-Martínez, S. Arias, J. Bergueiro, E. Quiñoá, R. Riguera, F. Freire, The Role of Polymer–AuNP Interaction in the Stimuli-Response Properties of PPA–AuNP Nanocomposites, *Macromol. Rapid Commun.* **2022**, *43*, 2100616. https://doi.org/10.1002/marc.202100616.

[244] D.E. Mustafa, T. Yang, Z. Xuan, S. Chen, H. Tu, A. Zhang, Surface Plasmon Coupling Effect of Gold Nanoparticles with Different Shape and Size on Conventional Surface Plasmon Resonance Signal, *Plasmonics* **2010**, *5*, 221–231. https://doi.org/10.1007/s11468-010-9141-z.

[245] S.K. Ghosh, T. Pal, Interparticle Coupling Effect on the Surface Plasmon Resonance of Gold Nanoparticles: From Theory to Applications, *Chem. Rev.* **2007**, *107*, 4797–4862. https://doi.org/10.1021/cr0680282.

[246] A. Bearzotti, P. Papa, A. Macagnano, E. Zampetti, I. Venditti, R. Fioravanti, L. Fontana, R. Matassa, G. Familiari, I. Fratoddi, Environmental Hg vapours adsorption and detection by using functionalized gold nanoparticles network, *J. Environ. Chem. Eng.* **2018**, *6*, 4706–4713. https://doi.org/10.1016/j.jece.2018.07.013.

[247] J.A. Balderas-López, M.R. Jaime-Fonseca, P. Abrica-González, A. Mandelis, On the Importance of Using Reliability Criteria in Photothermal Experiments for Accurate Thermophysical Property Measurements, Int. J. Thermophys. **2024**, *45*, 56. https://doi.org/10.1007/s10765-024-03348-w.

[248] R.R. Naujok, R.V. Duevel, R.M. Corn. Fluorescence and Fourier Transform Surface-Enhanced Raman Scattering Measurements of Methylene Blue Adsorbed onto a Sulfur-Modified Gold Electrode, *Langmuir* **1993**, *9*, 1771–1774. https://doi.org/0743-7463/93/2409-1771$04.00/0.

[249] M. Marchioni, C. Battocchio, Y. Joly, C. Gateau, S. Nappini, I. Pis, P. Delangle, I. Michaud-Soret, A. Deniaud, G. Veronesi, Thiolate-Capped Silver Nanoparticles: Discerning Direct Grafting from Sulfidation at the Metal–Ligand Interface by Interrogating the Sulfur Atom, *J. Phys. Chem. C* 2020, 124, 13467–13478. https://doi.org/10.1021/acs.jpcc.0c03388.

[250] F. Ishii, S. Matsunami, M. Shibata, T. Kakuchi, UV-vis Absorption Study of cis- and trans Poly(phenylacetylene)s Based on CNDO/S Calculation, *Polym. J.* **1999**, *31*, 84–88. https://doi.org/10.1295/polymj.31.84.

[251] C.W. Lee, K.S. Wong, W.Y. Lam, B.Z. Tang, Light-emitting properties of stereoregular cis-rich poly(phenylacetylene)s, *Chem. Phys. Lett.* **1999**, *307*, 67–74. https://doi.org/10.1016/S0009-2614(99)00463-7.

[252] M.K. Corbierre, N.S. Cameron, M. Sutton, K. Laaziri, R.B. Lennox, Gold Nanoparticle/Polymer Nanocomposites: Dispersion of Nanoparticles as a Function of Capping Agent Molecular Weight and Grafting Density, *Langmuir* **2005**, *21*, 6063–6072. https://doi.org/10.1021/la047193e.

[253] A.A. Al-Shamari, A.M. Abdelghany, H. Alnattar, A.H. Oraby, Structural and optical properties of PEO/CMC polymer blend modified with gold nanoparticles synthesized by laser ablation in water, *J. Mater. Res. Technol.* **2021**, *12*, 1597–1605. https://doi.org/10.1016/j.jmrt.2021.03.050.

[254] O. Trhlíková, J. Zedník, J. Vohlídal, J. Sedláček, Molecular weight and configurational stability of poly(phenylacetylene) prepared with Rh catalyst, *Polym. Degrad. Stab*. **2011**, 96, 1310–1320. https://doi.org/10.1016/j.polymdegradstab.2011.04.003.

[255] O. Trhlíková, J. Zedník, J. Vohlídal, J. Sedláček, SEC/DAD and ^{1}H NMR Study of Molecular Weight and Configurational Stability of Poly(2,4-difluorophenylacetylene) and Polyphenylacetylene Prepared with Rh Catalyst, *Macromol. Chem. Phys.* **2011**, 212, 1987–1998. https://doi.org/10.1002/macp.201100228.

[256] O. Dammer, B. Vlčková, M. Procházka, D. Bondarev, J. Vohlídal, J. Pfleger, Effect of preparation procedure on the structure, morphology, and optical properties of nanocomposites of poly[2-methoxy-5-(2-ethylhexyloxy)-1,4-phenylenevinylene] with gold nanoparticles, *Mater. Chem. Phys.* **2009**, *115*, 352–360. https://doi.org/10.1016/j.matchemphys.2008.12.021.

[257] B. Sun, T. Tao, L. Liu, R. Ding, Y. Mao, Electron Transfer Facilitated by π–π Stacking during the Nitrobenzene Recognition Process of an MOF Sensor, *J. Phys. Chem. C* **2021**, *125*, 12433–12440. https://doi.org/10.1021/acs.jpcc.1c02942.

[258] S. Bhattacharyya, T. Sen, A. Patra, Host−Guest Energy Transfer: Semiconducting Polymer Nanoparticles and Au Nanoparticles, *J. Phys. Chem. C* **2010**, *114*, 11787–11795. https://doi.org/10.1021/jp1030398.

[259] J.-H. Liu, J.-J. Yan, E.-Q. Chen, J.W.Y. Lam, Y.-P. Dong, D.-H. Liang, B.Z. Tang, Chain helicity of a poly(phenylacetylene) with chiral centers between backbone and mesogenic groups on side chains, *Polymer* **2008**, *49*, 3366–3370. https://doi.org/10.1016/j.polymer.2008.06.007.

[260] Davis, E. A.; Mott, N. F. Conduction in Non-Crystalline Systems V. Conductivity, Optical Absorption and Photoconductivity in Amorphous Semiconductors. *Philosophical Magazine* **1970**, *22* (179), 0903–0922. https://doi.org/10.1080/14786437008221061.

[261] Sangiorgi, N.; Aversa, L.; Tatti, R.; Verucchi, R.; Sanson, A. Spectrophotometric Method for Optical Band Gap and Electronic Transitions Determination of Semiconductor Materials. *Optical Materials* **2017**, *64*, 18–25. https://doi.org/10.1016/j.optmat.2016.11.014.

[262] Darwesh, A. H. A.; B.Aziz, S.; Hussen, S. A. Insights into Optical Band Gap Identification in Polymer Composite Films Based on PVA with Enhanced Optical Properties: Structural and Optical Characteristics. *Optical Materials* **2022**, *133*, 113007. https://doi.org/10.1016/j.optmat.2022.113007.

[263] Kang, E. T.; Bhatt, A. P.; Villaroel, E.; Anderson, W. A.; Ehrlich, P. Electrical Properties of Thin Films of Polyphenylacetylene Doped with Iodine or Arsenic Pentafluoride. *Molecular Crystals and Liquid Crystals* **1982**, *83* (1), 307–308. https://doi.org/10.1080/00268948208072180.

[264] Gal, Y.-S.; Lee, W.-C.; Jin, S.-H.; Park, Y.-I.; Park, J.-W.; Lim, K. T.; Kim, S. Y. Electro-Optical and Electrochemical Properties of Poly(Phenylacetylene). *Molecular Crystals and Liquid Crystals* **2009**, *513* (1), 293–300. https://doi.org/10.1080/15421400903217231.

[265] Canto-Reyes, D.; Soberanis-Ortiz, R. A.; Riech, I.; Mendez-Gamboa, J. A.; Acosta, M. Photocurrent Enhancement Estimation of P3HT:PCBM:Au Films as a Function of Gold Nanoparticles Concentration. *Gold Bull* **2020**, *53* (3–4), 141–145. https://doi.org/10.1007/s13404-020-00284-z.

[266] Kaçuş, H.; Baltakesmez, A.; Çaldıran, Z.; Aydoğan, Ş.; Yılmaz, M.; Sevim, M. Optical and Electrical Characterization of Organic Solar Cells Obtained Using Gold and Silver Metal Nanoparticles. *Materials Today: Proceedings* **2021**, *46*, 6986–6990. https://doi.org/10.1016/j.matpr.2021.03.276.

[267] Aruna, P.; Joseph, C. M. Optical and Photosensing Properties of Gold Nanoparticles Doped Poly (3-Hexylthiophene-2, 5-Diyl) Thin Films. *Materials Letters* **2021**, *295*, 129726. https://doi.org/10.1016/j.matlet.2021.129726.

[268] Farea, M. O.; Abdelghany, A. M.; Oraby, A. H. Optical and Dielectric Characteristics of Polyethylene Oxide/Sodium Alginate-Modified Gold Nanocomposites. *RSC Adv.* **2020**, *10* (62), 37621–37630. https://doi.org/10.1039/D0RA07601E.

[269] Mejias, S. H.; López-Martínez, E.; Fernandez, M.; Couleaud, P.; Martin-Lasanta, A.; Romera, D.; Sanchez-Iglesias, A.; Casado, S.; Osorio, M. R.; Abad, J. M.; González, M. T.; Cortajarena, A. L. Engineering Conductive Protein Films through Nanoscale Self-Assembly and Gold Nanoparticles Doping. *Nanoscale* **2021**, *13* (14), 6772–6779. https://doi.org/10.1039/D1NR00238D.

[270] Clausi, M.; Santonicola, M. G.; Laurenzi, S. Fabrication of Carbon-Based Nanocomposite Films by Spin-Coating Process: An Experimental and Modeling Study of the Film Thickness. *Composites Part A: Applied Science and Manufacturing* **2016**, *88*, 86–97. https://doi.org/10.1016/j.compositesa.2016.05.026.

[271] Yang, Y.; Deng, H.; Fu, Q. Recent Progress on PEDOT:PSS Based Polymer Blends and Composites for Flexible Electronics and Thermoelectric Devices. *Mater. Chem. Front.* **2020**, *4* (11), 3130–3152. https://doi.org/10.1039/D0QM00308E.

[272] Backes, I. K.; González-García, L.; Holtsch, A.; Müller, F.; Jacobs, K.; Kraus, T. Molecular Origin of Electrical Conductivity in Gold–Polythiophene Hybrid Particle Films. *J. Phys. Chem. Lett.* **2020**, *11* (24), 10538–10547. https://doi.org/10.1021/acs.jpclett.0c02831.

[273] Zhang, T.; Li, Z.; Li, K.; Yang, X. Flexible Pressure Sensors with Wide Linearity Range and High Sensitivity Based on Selective Laser Sintering 3D Printing. *Adv Materials Technologies* **2019**, *4* (12), 1900679. https://doi.org/10.1002/admt.201900679.

[274] Abdelghany, A. M.; Elashmawi, I. S.; Al-Shamari, A. A.; Alnattar, H. Dielectric Behavior and AC Conductivity of PEO/CMC Polymer Blend Incorporated with Gold Nanoparticles Produced by Laser Ablation. *J Mater Sci: Mater Electron* **2023**, *34* (5), 388. https://doi.org/10.1007/s10854-022-09797-z.

[275] Benito, J.; Berenguer, J. R.; Forniés, J.; Gil, B.; Gómez, J.; Lalinde, E. Synthesis, Characterization and Luminescence Properties of Homoleptic Platinum(ii) Acetylide Complexes. *Dalton Trans.* **2003**, 22, 4331–4339. https://doi.org/10.1039/B308291A.

[276] Zhao, T.; Liu, R.; Shi, H.; Shu, M.; Hu, J.; Li, H.; Zhu, H. Synthesis, Tunable Photophysics and Nonlinear Absorption of Terpyridyl Pt(II) Complexes Bearing Different Acetylide Ligands. *Dyes Pigm.* **2016**, *126*, 165–172. https://doi.org/10.1016/j.dyepig.2015.11.021.

[277] Avram, M.; Mateescu, G. D.; *Infrared Spectroscopy: Applications in Organic Chemistry*, Repr. ed.; Krieger: Huntington, N. Y, **1978**.

[278] Petroski, J.; Chou, M.; Creutz, C. The Coordination Chemistry of Gold Surfaces: Formation and Far-Infrared Spectra of Alkanethiolate-Capped Gold Nanoparticles. *J. Organomet. Chem.* **2009**, *694*, 1138–1143. https://doi.org/10.1016/j.jorganchem.2008.11.057.

[279] Shurvell, H.F. Spectra–Structure Correlations in the Mid- and Far-infrared in *Handbook of Vibrational Spectroscopy*; Chalmers, J. M., Ed.; Wiley: Chichester Weinheim, **2002**, pp. 1783–1816.

[280] Pradilla-Sorzano, J.; Fackler, J. P. Far Infrared Spectra of Olefin-Pt(II) Complexes. Normal Coordinate Analysis of Zeise's Salt. *J. Mol. Spectrosc.* **1967**, *22*, 80–98. https://doi.org/10.1016/0022-2852(67)90150-6.

[281] Taylor, M. J.; Odell, A.L; Raethel, H.A. Assignment of the stretching frequencies in some chlorine-bridged platinum(II) complexes, $Pt_2Cl_4L_2$,with phosphorus and arsenic ligands. *Spectrochim. Acta* **1968**, *24A*, 1855-1861. https://doi.org/10.1016/0584-8539(68)80242-9.

[282] Adams, D.M.; Cornell, J.B. Metal-Sulphur Vibrations. Part I. Far-infrared Spectra of Some Complexes of Thiourea and Ethylenethiourea (Imidazolidine-2-thione). *J. Chem. Soc. A* **1967**, 884-889. https://doi.org/10.1039/J19670000884.

[283] Allen, A. D.; Theophanides, T. Platinum(II) Complexes: Infrared Spectra in the 300–800 cm^{-1} Region. *Can. J. Chem.* **1964**, *42* (7), 1551–1554. https://doi.org/10.1139/v64-238.

[284]. Tang, J.; Gao, K.; Ou, Q.; Fu, X.; Man, S.-Q.; Guo, J.; Liu, Y. Calculation Extinction Cross Sections and Molar Attenuation Coefficient of Small Gold Nanoparticles and Experimental Observation of Their UV–Vis Spectral Properties. Spectrochim. Acta A 2018, 191, 513-520. Doi: https://doi.org/10.1016/j.saa.2017.10.047.

[285] Cirri, A.; Hernández, H. M.; Johnson, C. J. High Precision Electronic Spectroscopy of Ligand-Protected Gold Nanoclusters: Effects of Composition, Environment, and Ligand Chemistry. *J. Phys. Chem. A* **2020**, *124*, 1467–1479. https://doi.org/10.1021/acs.jpca.9b09164.

[286] Zhang, Y. J. Comparing the Interparticle Coupling Effect on Sensitivities of Silver and Gold Nanoparticles. *J. Quant. Spectrosc. Radiat. Transf.* **2012**, *113*, 578–581. https://doi.org/10.1016/j.jqsrt.2012.02.018.

[287] Fratoddi, I.; Venditti, I.; Battocchio, C.; Polzonetti, G.; Bondino, F.; Malvestuto, M.; Piscopiello, E.; Tapfer, L.; Russo, M. V. Gold Nanoparticle Dyads Stabilized with Binuclear Pt(II) Dithiol Bridges. *J. Phys. Chem. C* **2011**, *115* (31), 15198–15204. https://doi.org/10.1021/jp202717t.

[288] Oliveira, J. P.; Prado, A. R.; Keijok, W. J.; Ribeiro, M. R. N.; Pontes, M. J.; Nogueira, B. V.; Guimarães, M. C. C. A Helpful Method for Controlled Synthesis of Monodisperse Gold Nanoparticles through Response Surface Modeling. *Arab. J. Chem.* **2020**, *13*, 216–226. https://doi.org/10.1016/j.arabjc.2017.04.003.

[289] Wu, W.-T.; Chen, C.-H.; Chiang, C.-Y.; Chau, L.-K. Effect of Surface Coverage of Gold Nanoparticles on the Refractive Index Sensitivity in Fiber-Optic Nanoplasmonic Sensing. *Sensors* **2018**, *18*, 1759. https://doi.org/10.3390/s18061759.

[290] Li Voti, R.; Leahu, G.; Sibilia, C.; Matassa, R.; Familiari, G.; Cerra, S.; Salamone, T. A.; Fratoddi, I. Photoacoustics for Listening to Metal Nanoparticle Super-Aggregates. *Nanoscale Adv.* **2021**, *3*, 4692–4701. https://doi.org/10.1039/D1NA00333J.

[291] Fitzgerald, S. A.; Xiao, X.; Zhao, J.; Horton, P. N.; Coles, S. J.; Knighton, R. C.; Ward, B. D.; Pope, S. J. A. Organometallic Platinum(II) Photosensitisers That Demonstrate Ligand-Modulated Triplet-Triplet Annihilation Energy Upconversion Efficiencies. *Chem. A Eur. J.* **2023**, *29* (9), e202203241. https://doi.org/10.1002/chem.202203241.

[292] Thorp-Greenwood, F. L.; Balasingham, R. G.; Coogan, M. P. Organometallic Complexes of Transition Metals in Luminescent Cell Imaging Applications. *J. Organomet. Chem.* **2012**, *714*, 12–21. https://doi.org/10.1016/j.jorganchem.2012.01.020.

[293] Cerra, S.; Cirri, D.; Gabbiani, C.; Pratesi, A.; Grigorian, S.; Matassa, R.; Lozano, J. G.; Beltrán, A. M.; Capocefalo, A.; Fasolato, C.; Scaramuzzo, F. A.; Marsotto, M.; Battocchio, C.; Salamone, T. A.; Pennacchi, B.; Mercurio, M.; Fratoddi, I. Hydrophobic Gold Nanoparticles Coupled with Fluorescent Dyes: A Smart Tool for Optoelectronic Applications. *Inorg. Chim. Acta* **2025**, *579*, 122553. https://doi.org/10.1016/j.ica.2025.122553.

[294] Rausch, A. F.; Murphy, L.; Williams, J. A. G.; Yersin, H. Improving the Performance of Pt(II) Complexes for Blue Light Emission by Enhancing the Molecular Rigidity. *Inorg. Chem.* **2012**, *51* (1), 312–319. https://doi.org/10.1021/ic201664v.

[295] Chen, X. C.; Green, P. F. Control of Morphology and Its Effects on the Optical Properties of Polymer Nanocomposites. *Langmuir* **2010**, *26* (5), 3659–3665. https://doi.org/10.1021/la903108u.

[296] Paruzel, B.; Pavlova, E.; Pfleger, J.; Šlouf, M.; Halašová, K.; Mikmeková, Š. Poly(3-Hexylthiophene)/Gold Nanoparticle Nanocomposites: Relationship between Morphology and Electrical Conductivity. *Chem. Pap.* **2017**, *71* (2), 401–408. https://doi.org/10.1007/s11696-016-0101-8.

[297] Ishikawa, K. Structure and Electrical Properties of Au2S. *Solid State Ionics* **1995**, *79*, 60–66. https://doi.org/10.1016/0167-2738(95)00030-A.

[298] Cho, C.-J.; Chen, S.-Y.; Kuo, C.-C.; Veeramuthu, L.; Au-Duong, A.-N.; Chiu, Y.-C.; Chang, S.-H. Morphology and Optoelectronic Characteristics of Organic Field-Effect Transistors Based on Blends of Polylactic Acid and Poly(3-Hexylthiophene). *Polym J* **2018**, *50* (10), 975–987. https://doi.org/10.1038/s41428-018-0087-x.

[299] Heriot, S. Y.; Jones, R. A. L. An Interfacial Instability in a Transient Wetting Layer Leads to Lateral Phase Separation in Thin Spin-Cast Polymer-Blend Films. *Nature Mater* **2005**, *4* (10), 782–786. https://doi.org/10.1038/nmat1476.

[300] Su, S.; Kopitzky, R.; Berrenrath, C. Experimental Determination of Molecular Weight-Dependent Miscibility of PBAT/PLA Blends. *Polymers* **2021**, *13* (21), 3686. https://doi.org/10.3390/polym13213686.

[301] Coleman, M. M.; Serman, C. J.; Bhagwagar, D. E.; Painter, P. C. A Practical Guide to Polymer Miscibility. *Polymer* **1990**, *31* (7), 1187–1203. https://doi.org/10.1016/0032-3861(90)90208-G.

[302] Xue, L.; Yu, X.; Han, Y. Different Structures and Crystallinities of Poly(3-Hexylthiophene) Films Prepared from Aged Solutions. *Colloids and Surfaces A: Physicochemical and Engineering Aspects* **2011**, *380* (1–3), 334–340. https://doi.org/10.1016/j.colsurfa.2011.03.003.

[303] Noriega, R.; Rivnay, J.; Vandewal, K.; Koch, F. P. V.; Stingelin, N.; Smith, P.; Toney, M. F.; Salleo, A. A General Relationship between Disorder, Aggregation and Charge Transport in Conjugated Polymers. *Nature Mater* **2013**, *12* (11), 1038–1044. https://doi.org/10.1038/nmat3722.

[304] P3HT Revisited – From Molecular Scale to Solar Cell Device*s*; Ludwigs, S., Ed.; Advances in Polymer Science; Springer Berlin Heidelberg: Berlin, Heidelberg, **2014**; Vol. 265. https://doi.org/10.1007/978-3-662-45145-8.

[305] Deschamps, D.; Lohier, J.-F.; Richards, C. J.; Gaumont, A.-C.; Perrio, S. Functionalization of [2.2]Paracyclophanes via a Reductive Sulfanylation Reaction. *J. Org. Chem.* **2021**, *86* (1), 507–514. https://doi.org/10.1021/acs.joc.0c02235.

[306] Hassan, Z. Molecular Insights into [2.2]Paracyclophane-Based Functional Materials: Chemical Aspects Behind Functions. *Adv Funct Materials* **2024**, *34* (47), 2311828. https://doi.org/10.1002/adfm.202311828.

[307] Vincent, A.; Deschamps, D.; Martzel, T.; Lohier, J.-F.; Richards, C. J.; Gaumont, A.-C.; Perrio, S. Enantiomerically Pure [2.2]Paracyclophane-4-Thiol: A Planar Chiral Sulfur-Based Building Block Readily Available by Resolution with an Amino Acid Chiral Auxiliary. *J. Org. Chem.* **2016**, *81* (9), 3961–3966. https://doi.org/10.1021/acs.joc.6b00560.

[308] Lohier, J.-F.; Foucoin, F.; Jaffrès, P.-A.; Garcia, J. I.; Sopková−de Oliveira Santos, J.; Perrio, S.; Metzner, P. An Efficient and Straightforward Access to Sulfur Substituted [2.2]Paracyclophanes: Application to Stereoselective Sulfenate Salt Alkylation. *Org. Lett.* **2008**, *10* (6), 1271–1274. https://doi.org/10.1021/ol800161m.

[309]. Russo, M. V.; Lo Sterzo, C.; Franceschini, P.; Biagini, G.; Furlani, A. Synthesis of Highly Ethynylated Mono and Dinuclear Pt(II) Tethers Bearing the 4,4′-Bis(Ethynyl)Biphenyl (Debp) Unit as Central Core. *Journal of Organometallic Chemistry* **2001**, *619*, 49–61. https://doi.org/10.1016/S0022-328X(00)00533-7.

[310] Buffet, A.; Rothkirch, A.; Döhrmann, R.; Körstgens, V.; Abul Kashem, M. M.; Perlich, J.; Herzog, G.; Schwartzkopf, M.; Gehrke, R.; Müller-Buschbaum, P.; Roth, S. V. P03, the Microfocus and Nanofocus X-Ray Scattering (MiNaXS) Beamline of the PETRA III Storage Ring: The Microfocus Endstation. *J Synchrotron Rad* **2012**, *19* (4), 647–653. https://doi.org/10.1107/S0909049512016895.

[311] Benecke, G.; Wagermaier, W.; Li, C.; Schwartzkopf, M.; Flucke, G.; Hoerth, R.; Zizak, I.; Burghammer, M.; Metwalli, E.; Müller-Buschbaum, P.; Trebbin, M.; Förster, S.; Paris, O.; Roth, S. V.; Fratzl, P. A Customizable Software for Fast Reduction and Analysis of Large X-Ray Scattering Data Sets: Applications of the New *DPDAK* Package to Small-Angle X-Ray Scattering and Grazing-Incidence Small-Angle X-Ray Scattering. *J Appl Crystallogr* **2014**, *47* (5), 1797–1803. https://doi.org/10.1107/S1600576714019773.

[312] Lindblad, A.; Söderström, J.; Nicolas, C.; Robert, E.; Miron, C. A Multi Purpose Source Chamber at the PLEIADES Beamline at SOLEIL for Spectroscopic Studies of Isolated Species: Cold Molecules, Clusters, and Nanoparticles. *Review of Scientific Instruments* **2013**, *84* (11), 113105. https://doi.org/10.1063/1.4829718.

[313] Stueber, D.; Patterson, D.; Mayne, C. L.; Orendt, A. M.; Grant, D. M.; Parry, R. W. Carbonates, Thiocarbonates, and the Corresponding Monoalkyl Derivatives. 1. Their Preparation and Isotropic ^{13}C NMR Chemical Shifts. *Inorg. Chem.* **2001**, *40* (8), 1902–1911. https://doi.org/10.1021/ic0012266.

[314] Rosario-Castro, B. I.; Fachini, E. R.; Hernández, J.; Pérez-Davis, M. E.; Cabrera, C. R. Electrochemical and Surface Characterization of 4-Aminothiophenol Adsorption at Polycrystalline Platinum Electrodes. *Langmuir* **2006**, *22* (14), 6102–6108. https://doi.org/10.1021/la0522193.

[315] Winter, B.; Weber, R.; Widdra, W.; Dittmar, M.; Faubel, M.; Hertel, I. V. Full Valence Band Photoemission from Liquid Water Using EUV Synchrotron Radiation. *J. Phys. Chem. A* **2004**, *108* (14), 2625–2632. https://doi.org/10.1021/jp030263q.

[316] Winter, B.; Aziz, E. F.; Hergenhahn, U.; Faubel, M.; Hertel, I. V. Hydrogen Bonds in Liquid Water Studied by Photoelectron Spectroscopy. *The Journal of Chemical Physics* **2007**, *126* (12), 124504. https://doi.org/10.1063/1.2710792.

[317] Hayes, J.; Peruzzi, P. P.; Lawler, S. MicroRNAs in Cancer: Biomarkers, Functions and Therapy. *Trends in Molecular Medicine* **2014**, *20* (8), 460–469. https://doi.org/10.1016/j.molmed.2014.06.005.

[318] Kanamori, Y.; Dalla Via, L.; Macone, A.; Canettieri, G.; Greco, A.; Toninello, A.; Agostinelli, E. Aged Garlic Extract and Its Constituent, S-allyl-L-cysteine, Induce the Apoptosis of Neuroblastoma Cancer Cells Due to Mitochondrial Membrane Depolarization. *Exp Ther Med* **2019**. https://doi.org/10.3892/etm.2019.8383.

[319] Youming, Z.; Xinrong, D.; Liangcheng, W.; Taibao, W. Synthesis and Characterization of Inclusion Complexes of Aliphatic-Aromatic Poly(Schiff Base)s with β-Cyclodextrin (Highlight). *J Incl Phenom Macrocycl Chem* **2008**, *60* (3–4), 313–319. https://doi.org/10.1007/s10847-007-9379-z.

[320] Yang, L.; May, P. W.; Yin, L.; Smith, J. A.; Rosser, K. N. Ultra Fine Carbon Nitride Nanocrystals Synthesized by Laser Ablation in Liquid Solution. *J Nanopart Res* **2007**, *9* (6), 1181–1185. https://doi.org/10.1007/s11051-006-9192-4.